University of Alberta

Rapid Densification of the Oil Sands Mature Fine Tailings (MFT) by Microbial Activity

by

Chengmai Guo

A thesis submitted to the Faculty of Graduate Studies and Research
in partial fulfillment of the requirements for the degree of

Doctor of Philosophy

In

Geotechnical Engineering

Civil and Environmental Engineering

Fall 2009

Edmonton, Alberta

Examining Committee

Dr. Rick Chalaturnyk, Supervisor, Civil and Environmental Engineering

Dr. Don Scott, Civil and Environmental Engineering

Dr. David. Sego, Civil and Environmental Engineering

Dr. Selma E. Guigard, Civil and Environmental Engineering

Dr. Julia Foght, Biological Sciences

Dr. Loretta Li, External Examiner, University of British Columbia

ABSTRACT

The Mildred Lake Settling Basin (MLSB) is the largest disposal site for mature fine tailings (MFT) at the Syncrude Canada Ltd oil sands plant. Since 1996, MFT densification in the MLSB has significantly accelerated due to microbial activity. Methane-producing microorganisms, known as methanogens, have become very active. A field and laboratory research program has been performed to study the mechanisms leading to the rapid densification.

This research program consisted of historical monitoring data analyses, field investigations, small-scale column tests, and gas MFT densification tests. The field investigations have shown that the rapid densification of the MFT has occurred in the southern part of the pond ranging from 8 m to 15 m below the water surface. A connection existed between the rapid densification zone and the zone with intense microbial activity at the pond. The small-scale column tests demonstrated that, with increases of biogas generation, water drainage from the MFT was enhanced. Gas MFT densification tests showed that, stress histories and total pressure affected MFT densification property during microbial activity. Under high total pressure (6-7 m below pond surface) gas bubbles had difficulty to release. For MFT without pre-consolidation or under a preloading, during rapid gas generation, water was rapidly drained out. For over-consolidated MFT, water flowed back into MFT quickly during intense biogas generation. The concept of operative stress, the difference between the total stress and pore water pressure for the soil with large gas bubbles, was introduced to analyze the densification behavior of gassy MFT. Under high

total pressure and under a preloading (1 kPa), excess pore pressure increased and operative stress decreased during rapid gas generation while water drainage from the MFT was accelerated. Total pressure and stress history also affected the structure and permeability of the MFT during microbial activity. Under low total pressure (1 m below pond surface) and without pre-consolidation, the MFT permeability increased after intense microbial activity.

ACKNOWLEDGEMENTS

I wish to express my deepest gratitude to Dr. R.J.Chalaturnyk for his guidance and encouragement during my Ph.D. program. His courage, enthusiasm, and insight are invaluable. I would also like to appreciate the guidance provided by my co-supervisor, Dr. J.D. Scott, who has patiently helped me professionally and personally. The technical support from Mr. Gerry Cyre is especially appreciated. The field and laboratory experiments have very much benefited from his wisdom and hardwork. Special thanks to Dr. Fedorak for his guidance in the microbiological aspect. Many thanks to Dr. Irene Meglis for her generous support in data analyses and report editing.

Financial support provided by Syncrude Canada Ltd., Canadian Natural Resources Ltd., and Suncor Energy Inc. for this research is gratefully acknowledged. Special thanks to Dr. Mike MacKinnon, Mr. Jonathan Matthews, and Mr. Geoff Halferdahl at Syncrude Canada Ltd. The guidance, encouragement, and friendship are greatly appreciated.

Many people have given me assistance during my laboratory experiments: Steve Gamble, Christine Hereygers, Gilbert Wong and Ken Leung (Geotechnical Engineering group), and Debbi Coy (Biological Sciences group). In particular, the patience and kindness of Steve Gamble are unforgettable. Thanks to my fellow colleagues, Silawat Jeeravipoolvarn, Yetimgeta Mihiretu, and Santiago Paz for their generous help and friendship.

I will always remember the support and influence of my mother and late father. During those tough years in life, they still encouraged me to seek knowledge and to get a good education. Finally, I feel very much indebted to my daughter, Changchang. I would like to tell you “Dad loves you forever.”

TABLE OF CONTENTS

LIST OF TABLES

LIST OF FIGURES

LIST OF SYMBOLS

MLSB	Mildred Lake Settling Basin (tailings pond)
WIP	West In Pit (tailings pond)
MFT	Mature Fine Tailings
CT	Composite tailings (Syncrude), consolidated tailings (Suncor)
LVDT	Linear variable differential transducer
LP	Linear potentiometer
STP	Standard temperature (25^{o}C) and pressure (atmospheric pressure)
MPN	Maximum probable number (of bacteria)
GC	Gas chromatography
SRB	Sulphate-reducing bacteria
σ	Total stress
σ_{op}	Operative stress
u	Pore water pressure
h_o	Initial sample height at time 0
h_{y0}	Hydrostatic head above the MFT interface at time 0.
γ_0	Unit weight of the sample at time 0
A	Cross sectional area of test cell
A_1	Cross sectional area of released gas cylinder
A_2	Cross sectional area of water collection standpipe
A_3	Cross sectional area of plastic tube
T_1	Differential pressure transducer at the bottom (E1)
T_2	Differential pressure transducer at 1.45 cm elevation (E2) above the bottom of the sample
T_3	Differential pressure transducer at 3.95 cm elevation (E3) above the bottom of the sample
T_4	Differential pressure transducer to measure hydrostatic changes in test cell.
T_5	Differential pressure transducer to measure water volume in the standpipe
V_0	Total sample volume at time 0
m_0	Total sample mass at time 0
m_{w0}	Water mass in the sample at time 0

V_{w0}	Water volume in the sample at time 0
m_s	Solids mass in the sample
V_s	Solids volume in the sample
V_h	Total water volume in the cell space above the interface, in plastic tube, and in standpipe at time 0.
Δh	Interface movements of the MFT at time t
V_t	Total MFT volume at time t
L_t	Water front movement in plastic tube at time t (relative to time 0)
h_{pt}	Water level change in water collection standpipe at time t
h_{rt}	Released gas thickness in gas collection cylinder at time t
V_{rt}	Released gas volume at time t
V_{wt}	Water volume in the MFT at time t
h_{yt}	Hydrostatic head above the MFT interface at time t
V_{dt}	Drained water volume from the MFT at time t
V_{tgt}	Trapped gas volume in the MFT at time t
V_{tgst}	Trapped gas volume at standard condition (STP, 25^o C and 1 atm.) at time t
V_{rst}	Released gas volume converted to STP condition
V_{gst}	Total gas volume (trapped gas + released gas) at STP at time t
ρ_t	Bulk density of the sample at time t
γ_t	Unit weight of the sample at time t
SC_t	Total solids content of the sample at time t
GC_t	Trapped gas content in the sample at time t
e_{wt}	Water void ratio at time t
e_{gt}	Gas void ratio at time t
e_t	Total void ratio at time t
S_r	Degree of saturation of the sample at time t
σ_0	Total stress at bottom at time 0
σ_L	Surcharge applied on the sample
u_{s0}	Hydrostatic pore pressure at the bottom at time 0
u_{w0}	Pore pressure at the bottom at time 0
u_{e0}	Excess water pressure at the bottom at time 0

σ_{op0}	Operative stress at time 0
σ_t	Total stress at the bottom at time t
u_{wt}	Pore pressure at the bottom at time t
u_{st}	Hydrostatic pore pressure at the bottom at time t
u_{et}	Excess pore pressure at the bottom at time t
σ_{opt}	Operative stress at the bottom at time t

CHAPTER 1

1 INTRODUCTION

1.1 Statement of the Problem

The Mildred Lake Settling Basin (MLSB) is the largest disposal site for tailings at the Syncrude Canada Ltd. oil sands plant containing over 200 $\times 10^6$ m^3 mature fine tailings (MFT) that has been accumulating since Syncrude started production in 1978. The tailings pond has a water area of about 11 km^2 and a maximum depth of MFT of approximately 50 m. Until the Southwest Sand Storage (SWSS) Facility was commissioned in 1991, all extraction tails were discharged into the MLSB. By 1999, only a small fraction of whole Syncrude tailings were input to the MLSB. As well, starting in 1995, some MFT has been transferred (> 130 Mm^3) to the West In pit (WIP). Because of the low permeability of the fines fraction, and the considerable depth and chemical properties of the MFT, its densification is slow. It was estimated that the complete consolidation of the MFT could take 120-150 years (Eckert et al., 1996). Figure 1.1 shows the relative locations of Syncrude's tailings ponds. Stations 1, 2 and 3 indicate the three locations used for long-term monitoring and field investigating at the MLSB. Sta. 1 is located at the southern part of the pond and close to the MFT pumping barge. Sta. 3 is located at northern part of the MLSB, and Sta. 2 is approximately midway between Sta. 1 and Sta. 3. In the early 1990's, methane evolution was noted at the southern part of the tailings pond, and was increasingly spreading northward (Holowenko et al., 2000). In the mid to late 1990's (since 1996) methane producing microorganisms, known as methanogens, had become active in southern part of the pond. Bubbles of the released methane emanating from the MFT became very noticeable during this period, as illustrated in Figure 1.2. After 1996, the measurements of fine/(fines + water) in the southern part of the MLSB were much greater than predicted by an empirical equation proposed by MacKinnon et al. (1993):

$$F=17.4+8.86 \ln (Y) \qquad [1\text{-}1]$$

where F = % fines {f/(f+water); f = fines <44 μm}

Y = years since deposition

Since 1996, the MFT densification in the southern part of MLSB has increased in comparison to initial expected densification rates. From 1996 to 1999, % fines at 2-5 m depth zone below mudline surface at Sta. 1 increased about 14% (Figure 1.3) which was much greater than the prediction (less than 3%) by the equation above.

The potential positive effect of the rapid densification of the MFT is considerable. It may greatly accelerate the reclamation of the fine tailings. The rapid densification can significantly reduce MFT volume and increase the released water volume. This will benefit both the tailings storage and oil sands extraction (the released water from tailing pond is recycled to the plant for bitumen extraction). On the other hand, some negative effects also exist. This rapid densification has caused pumping challenges in the transfer of fine tailings from the MLSB for the creation of composite tailings; and the released gas comprised mainly of methane, is a greenhouse gas.

Some questions related to the rapid densification phenomenon need to be answered before it can be utilized to improve the tailings management:

- What is the distribution and characteristics of the densified MFT in the tailings pond?
- What is the mechanism leading to the rapid densification phenomenon?
- What is required to initiate reclamation?
- And can we utilize the mechanism to improve the reclamation and management of the oil sands tailings?

The technical issues associated with these questions must be addressed before moving forward with effective, realistic tailings management strategies that take advantage of biogenic gas activity. In addition, this research may help to understand the behaviors of some other organic soils such as estuarine and marine sediments with microbial activity and biogas generation.

1.2 Oil Sands and Oil Sands Tailings

1.2.1 Oil Sands Industry in Alberta

The oil sands deposits in northern Alberta represent a huge petroleum resource. It is estimated that over 1.7 trillion barrels of bitumen are contained in the oil sands deposits in Alberta, of which about 300 billion barrels, an amount similar to the proven reserves of Saudi Arabia in size, are recoverable by existing technologies (ACR, 1995). Currently, the oil sands supply about 26 percent of Canada petroleum production (AOSD, 1998). In Alberta, the oil sands deposits mainly exist in three areas (Athabasca, Cold Lake, and Peace River.) as shown in Figure 1.4. The Athabasca deposits contain about 869 billion barrels of bitumen (FTFC, 1995), which is the largest of the three deposits. The oil sands reserves at or near the surface can be recovered by surface mining techniques, while the deeper reserves can be recovered by in situ methods of extraction such as Steam-assisted Gravity Drainage (SAGD).

Since Suncor Energy Ltd. started to extract bitumen from oil sands in Athabasca deposit in 1967, a number of other companies have joined the development of the oil sands resource in northern Alberta. They include: Syncrude Canada Ltd., Albian Sands Energy Inc., Canadian Natural Resource Ltd., as well as many other companies at their initial plan and design stage**.** Among them Syncrude Canada Ltd. is the largest company in oil sands surface mining with about 350,000 barrels (2007) of crude oil produced per day from Athabasca oils sands deposits.

1.2.2 Oil Sands

Crude bitumen is a type of heavy oil defined as a viscous mixture of hydrocarbons. Under its natural state it will not flow to a well (EUB, 2004). Crude bitumen is found in oil sands deposits in northern Alberta.

The Athabasca oil sands deposits belong to lower Cretaceous McMurray formation. The thickness of the formation varies from 30 m to 90 m. About

10% of the deposits have an overburden less than 45 m, which makes surface mining economically feasible. The oil sands deposits were formed in variable depositional environments. In the Syncrude and Suncor surface mining areas, the oil sands were formed in fluvial, estuarine, and marine environments (FTFC, 1995).

The oil sands sediments consist of quartz sand, silt, clay, water and bitumen. The sand particles are covered by a thin layer of water which is then enveloped by bitumen (Pollock, 1988). The oil sands structure is illustrated in Figure 1-5. The sand is locked sand with small amounts of fines filling with particle contacts (Touhidi, 1998; Jeeravipoolvarn, 2004). More commonly, the bitumen-bearing sediments are interbedded with clay-rich fine-grained sediments, like clay shale. During surface mining, the interbedded clay shale is usually mixed with oil sand ore, and sent to extraction plant (FTFC, 1995). The average bitumen content in oil sands is greater than 10 weight percent (FTFC, 1995), and water content varies from 3-6% and average about 5%. The commercial oil sands consist of about 70% sands and 14% fines (<45um), and clay accounts for approximately 32% of fines (Nagula, 1995). The clay minerals in Athabasca oil sands deposits are mainly kaolinite and illite, with minor and trace amounts of smectite, chlorite, vermiculite (TFTC, 1995).

1.2.3 Oil Sands Operations

For the oil sands deposits which are close to the surface, surface mining and the Clark hot water extraction method are used to recover bitumen. For the deep deposits, in situ methods such as steam injection through vertical and horizontal wells are used to extract bitumen. The recovery rate of bitumen by the surface mining method is more than 90%, and that by in situ method varies from 25 to 75% (Petroleum Communication Foundation, 2000). About two tonnes of oil sands must be mined to make one 159-litre barrel of crude oil (Petroleum Communication Foundation, 2000).

In surface mining operation, mining shovels dig into the oil sands and load it into huge trucks. In early 2000, 380 tonne trucks started to operate in Syncrude. The huge trucks move the oil sands to the crushers and hot water is added to oil sands, and then the mixture is transported to the extraction plant by pipeline. The truck and shovel mining method has proven more effective than the previous dragline method.

At the extraction plant, bitumen is extracted by the hot water method which was initially invented by Dr. Karl Clark who used hot water, steam, and caustic to separate bitumen from the oil sands (TFTC, 1995). Figure 1.6 shows a schematic flow diagram of bitumen extraction process in the plant. The extraction process mainly consists of three stages: conditioning, primary separation, and secondary separation.

In the conditioning stage, oil sands are mixed with hot water, steam, and caustic soda (NaOH), and the mixture is hydrotransported to extraction plant. The introduction of steam raises the temperature of the slurry to about 80°C, and the addition of caustic soda increases the pH to the range of 9.0 to 11.0 (Luo, 2004). During this stage, the silts and clay particles become well dispersed, which makes bitumen separation easy.

After conditioning stage, the slurry is discharged onto vibrating screens to remove some undigested large slumps and rocks. Additional hot water is added to further dilute the slurry, and then the slurry is pumped to the primary separation vessel where bitumen floats to the surface as primary froth, and sand particles settle to the bottom as primary tailings. The middlings (the middle part of the slurry in the primary vessels) combined with the primary tailings are introduced into large deep cone vessels where the bitumen is recovered as secondary froth. After bitumen recovery, the slurry is discharged as tailings.

Both the primary and secondary froths contain significant amounts of water and fines. They must be removed prior to the upgrading process where

bitumen is converted into light synthetic crude oil. This process generates froth treatment tailings as shown in Figure 1.6. After bitumen extraction, the tailings are pumped into the settling basins where the released water is recycled into the extraction plant.

1.2.4 Oil Sands Tailings

After bitumen extraction from the oil sands, a warm aqueous suspension (about 25 to 35^{o}C) consisting of sand, silt, water and residual bitumen is produced, which is referred to as oil sands tailings. Some large lumps and boulders from the extraction plant are sent back to a mined-out pit, and all the other tailings are pumped into large settling basins (Figure 1-7) where the coarse particles settle out to form dykes and beaches, and the fine mineral particles and water flow into the tailings pond as a thin slurry stream with a solids content of approximately 8%.

The fines particles in thin slurry stream remain suspended during the early period ranging from several hours to 3 months. Then, after 2-3 years, dewatering occurs rapidly to reach a solids content of about 30% which marks the formation of mature fine tailings (MFT). After that, dewatering rate for MFT is extremely slow due to its dispersive structure, extremely low permeability and large depth. It's estimated that hundreds of years are required for MFT to develop the properties associated with soft soils (Sheeran, 1993).

Figure 1.7 shows the characteristic three zones in the tailings pond. The upper zone with a thickness 3-4 m is the released water from the MFT. The released water is recycled to the extraction plant for bitumen recovery. Below the released water is a transitional zone which is an immature fine tailings slurry with a thickness about 1-2 m. Below the transitional zone is the MFT zone which is about 15-20 m thick, and consists of water, fines (silts and clay), sands, residual bitumen and other organic compound like naphthenic acid. In the MFT zone, fines particles are by far the major component of the solids, and the sands are wind blown sands from the beach and dyke of the tailings

pond. With depth increasing, the solids content and bulk density increase mainly due to the increase of sands particles. Below the MFT zone is very sandy material or the sand beach. The maximum depth of the MLSB is about 50 m.

As a gross average, the bitumen content in fine tailings is about two percent of the total mass (Mackinnon and Sethi, 1993). The presence of bitumen is an important factor leading to its thixotropic behavior and extremely low permeability (Suthaker, 1995). The clay minerals in oil sands tailings are similar to those in McMurray Formation oil sands deposits with kaolinite and illite minerals dominating and other minerals such as smectite and vermiculite existing as minor ingredients.

Due to continuous accumulation and very slow dewatering rate, a large inventory (more than 500 Mm^3) of fine tailings has been accumulated in the tailings ponds at Syncrude and Suncor. The continuous increase of oil sands tailings pose a major environmental concern in the development of oil sands industry. Due to their toxic nature, oil sands tailings are not allowed to be discharged into the environment. To densify the MFT and accelerate the reclamation of the disturbance areas has been a major challenge facing surface mining oil sands industry.

In early 1990's, methane gas was detected at the southern part of the MLSB. Over the past decade, the release of methane gas has become very active in this area and the activity is spreading northward. Coincident with increasing microbial activity, the densification of the MFT has been significantly accelerating (Guo et al., 2002). This rapid densification may help reduce total MFT inventory and accelerate tailings pond reclamation. The focus of this research program is to study the MFT densification property and mechanism during microbial activity.

1.2.5 Major Options for MFT Treatment

Over the past two decades, tremendous work has been carried out to find effective methods to densify the MFT and to reduce its inventory. Two major methods in current oil sands tailings practice are discussed in the following.

1.2.5.1 Composite Tailings (CT)

Composite Tailings (CT) is a mixture of MFT, tailings sand, and gypsum. It's usually called Composite Tailings in Syncrude, also called Consolidated Tailings in Suncor

With the addition of divalent cations like Ca^{2+}, the thickness of double diffuse layer will decrease and the attractive forces between the clay particles increase (Mitchell, 1991). This will lead to the formation of flocculated structure which is strong enough to support the surcharge from the sands. In CT technology, the sands particles and the fines settle simultaneously to form uniform non-segregating deposit (TFTC, 1995). By introducing sand particles into the fine tailings, an internal stress is applied to the structure, which causes a significant increase in its densification rate. This process can significantly increase the permeability of the tailings (TFTC, 1995).

During the development of CT process, various chemicals have been used, including sulphuric acid, gypsum and organic polymers. It has been proved that gypsum is a robust, effective and readily available chemical to make CT (Luo, 2004).

In 1996, Suncor began to use CT technology to treat the fine tailings in the tailings ponds on a commercial scale. In 1997/1998, Syncrude successfully demonstrated a full-scale prototype operation of CT test. Under the present plans, a large part of the extraction tailings will be treated by CT technology at Syncrude (MacKinnnon et al., 2000).

With the addition of chemical coagulants such as gypsum, the dewatering rate of the MFT can be increased significantly. However, the addition of chemical additives in CT process can significantly change the released water quality. It can increase the salinity, corrosion potential, SO_4^{2-} concentration of the

released water, and affect bitumen recovery at the plant (Mackinnon et al., 2000)

1.2.5.2 Freeze-Thaw Dewatering of the Fine Tailings

Freeze-thaw is an effective method to accelerate water release from the MFT and to increase its strength. Laboratory experiments have demonstrated that suctions are created between ice and unfrozen liquid water. These suctions cause water to flow to the growing ice lenses which form a three dimensional reticulate ice network surrounding blocks of over-consolidated MFT (Dawson et al., 1999; Proskin, 1998). During freeze-thaw process, the MFT structure was observed to change from disaggregated cardhouse structure to a compact, aggregated structure. Also, freeze-thaw process can significantly increase its hydraulic conductivity as high as 100 folds (Proskin, 1998). Laboratory tests suggested that freeze-thaw increased the solids content from 35% to approximately 44-48%, and additional mechanisms of consolidation and surface drying further increased the solids to 70% (TFTC, 1995).

When ice lenses are formed, they force the clay particles together and disrupt the floc structure. During freeze-thaw processes, water is released from the MFT suspension rapidly. During freezing, the ice crystals mechanically force clay flocs or aggregates together. This results in ion concentration increase. The increasing ionic strength also provide additional chemical driving for dewatering (Mikula, et al., 1996)

Laboratory tests suggested that dewatering can be significantly improved by chemical treatment of the MFT before freeze-thaw process. The field tests at Suncor from 1991-1993 showed that freeze-thaw dewatering of acid/lime fine tailings can treat up to 3 times the volume of fine tailings (without chemical treatment) for per unit surface area. After the combined treatment processes, the solids content increased significantly from 35% to about 70%. A mineral free, easily detoxified run off water was produced (TFTC, 1995).

Although freeze-thaw can enhance water drainage from the MFT, the feasible large-scale implementation is not easy. Major restriction is large surface area required to treat the huge amount of MFT. For this reason, there has been no large scale operation during the past two decades. With more mine sites and tailings ponds near closure, more land will become available. Freeze-thaw combined with evaporation is becoming a promising technology for MFT treatment (Wells, et al., 2007).

1.3 Research Scope

The scope of this research is restricted specifically to in situ field investigations conducted within Syncrude Mildred Lake Settling Basin (MLSB) and state-of-the-art experimental tests for studying the mechanisms of rapid densification of MFT due to biological gas generation. This research will not pursue the development of numerical models for simulating gassy MFT behaviour.

Chemical changes within the aqueous will not be the focus of this research program. Aqueous chemistry, however, is an important aspect of tailings behaviour and existing chemistry data will be utilized to analyze the depositional environments and to interpret the behaviour of gassy MFT. More detailed chemical research during microbial activity is expected in future program.

Microbiological aspects of this research have been conducted in close association with Dr. Phil Fedorak at the Department of Biological Science. The scientific basis for the microbiological processes occurring within this research program has been conducted in complementary research programs under the supervision of Dr. Fedorak and will be used in the interpretation of the densification mechanism.

The research program mainly consists of the following parts:

- Systematic field investigations, including sampling, cone penetration tests (CPT), earth pressure measurements, pore water pressure measurements, steel plate penetration tests (SPP), in-situ temperature measurements, field vane shear tests and field mapping of the released gas bubbles on the water surface of the pond;
- Small-scale column tests to model the microbial activity and to provide preliminary data on its influence on MFT densification;
- Gas MFT densification tests to study the mechanism of the rapid densification of the MFT;
- Permeability tests to study the influence of microbial activity on hydraulic conductivity of the MFT;
- Visual observations and SEM tests to study the influence of microbial activity on MFT structure; and
- Discussion, conclusions and suggestions for future research and MFT reclamation.

1.4 Organization of the Thesis

Chapter 2 introduces the recent development on the researches of the soils containing occluded gas bubbles. Some test techniques and concepts are demonstrated, also some microbiological aspects related to biogas generation are introduced.

In Chapter 3, some historical monitoring data in the MLSB including MFT densification, temperature, gas content, pH, concentrations of some important ions are analyzed. This chapter will reveal the physical and chemical environmental changes affecting microbial activity and MFT densification in the MLSB.

Systematic field investigations were conducted in the MLSB in 2000, 2001 and 2002. Chapter 4 describes the techniques used in the field investigations. The test results including piston sampling and freezing sampling, cone penetration testing (CPT), steel plate penetration (SPP) testing, field vane

shear testing, earth pressure measurements, piezometer, field mapping of gas bubble distribution and in situ temperature measurements are presented.

Small-scale column tests were used to model the microbial activity and to preliminarily study its influences on MFT densification. The test methods and results are presented in Chapter 5.

Gas MFT densification tests were used to comprehensively study the mechanisms leading to the rapid densification of the MFT during microbial activity. The tests modeled the microbial activities of the MFT with different stress histories and different depths. Various parameters including densification properties, operative stress, permeability and pore water chemistry were measured during microbial activity, and the macro- and micro-structural changes were observed. Chapters 6, 7, 8 and 9 describe the test methods and present the results of the gas MFT densification tests.

In Chapter 10, the results from historic monitoring, field investigating and laboratory testing are discussed. The mechanisms leading to rapid densification of the MFT are analyzed and summarized. Suggestions for oil sands tailings reclamation and future research are proposed.

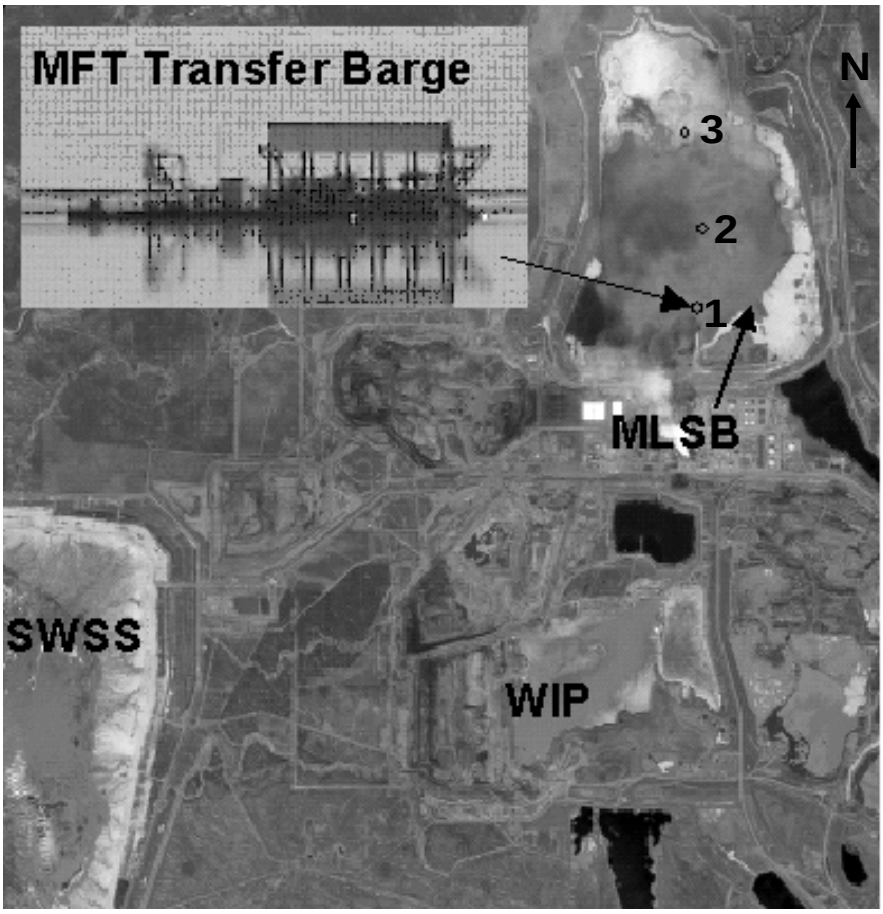

Figure 1-1 Syncrude's Storage and Settling Basins

Figure 1-2 Gas Bubbles on the Water Surface of Southern Part of the MLSB

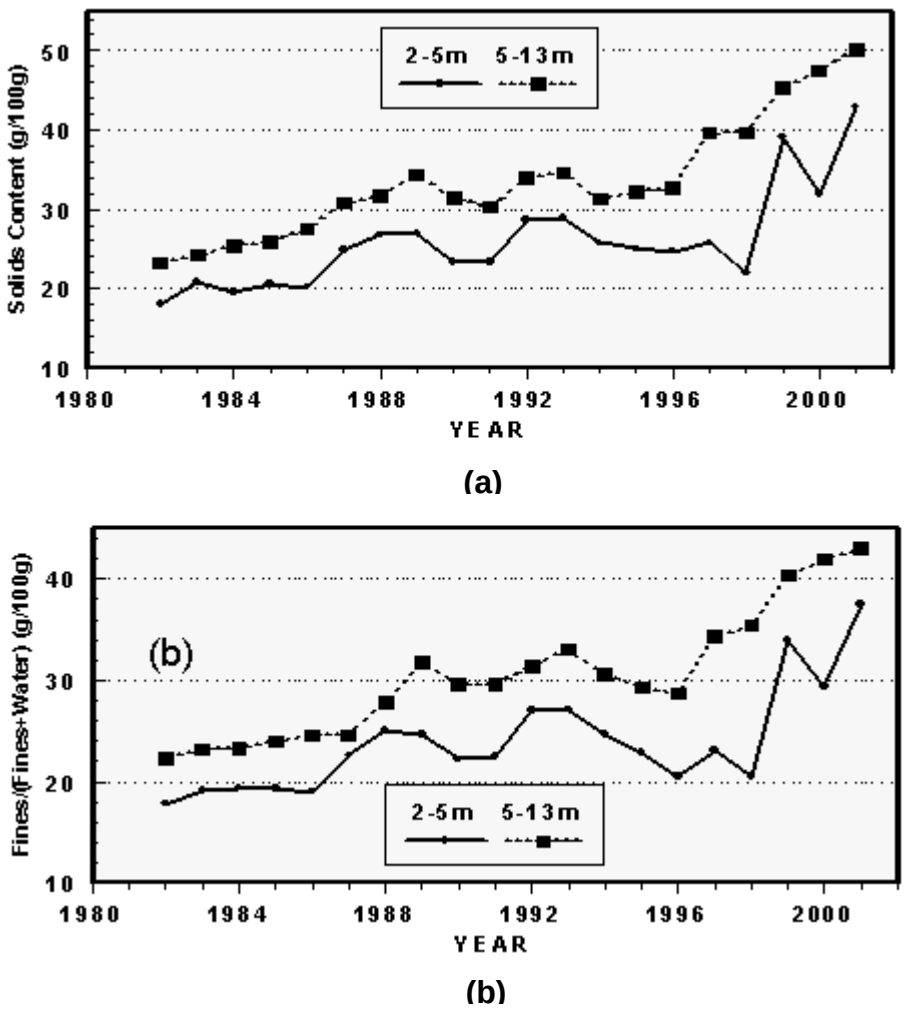

Figure 1-3 Changes in (a) Solids and (b) Fines Contents Averaged by Depth Zones in the Fines Tailings at Sta. 1
(Provided by MacKinnon, 2003)

Figure 1-4 Oil Sands Distribution in Alberta

(Modified from AEUB, 2004)

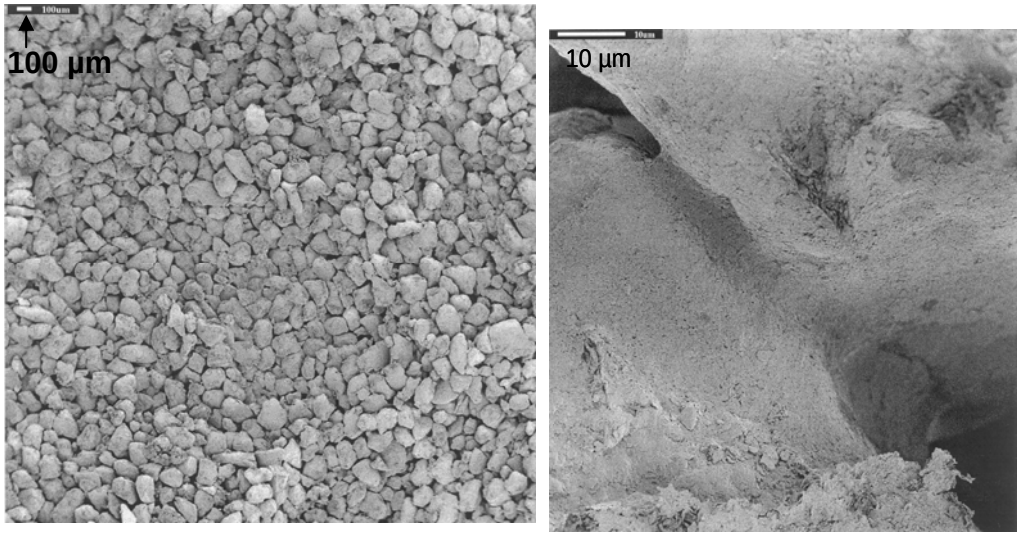

a) **b)**

Figure 1-5 Scanning Electron Microscope of Bitumen-Free McMurray Formation Oil Sand a) Overview of Sand Structure b) Fines in Sand Structure

(Modified from Touhidi, 1998)

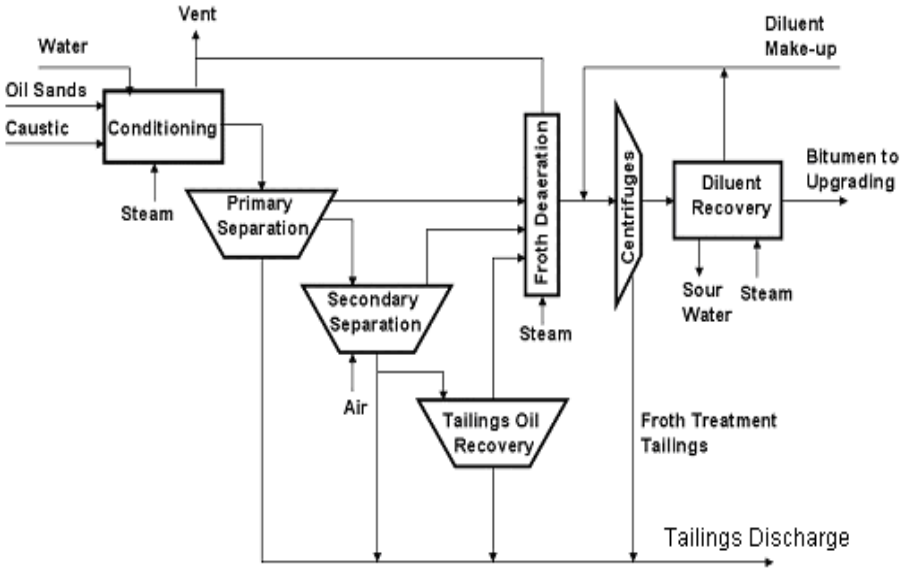

Figure 1-6 Generalized Scheme of Clark Hot Water Extraction Process

(Adapted from Jeeravipoolvarn, 2004)

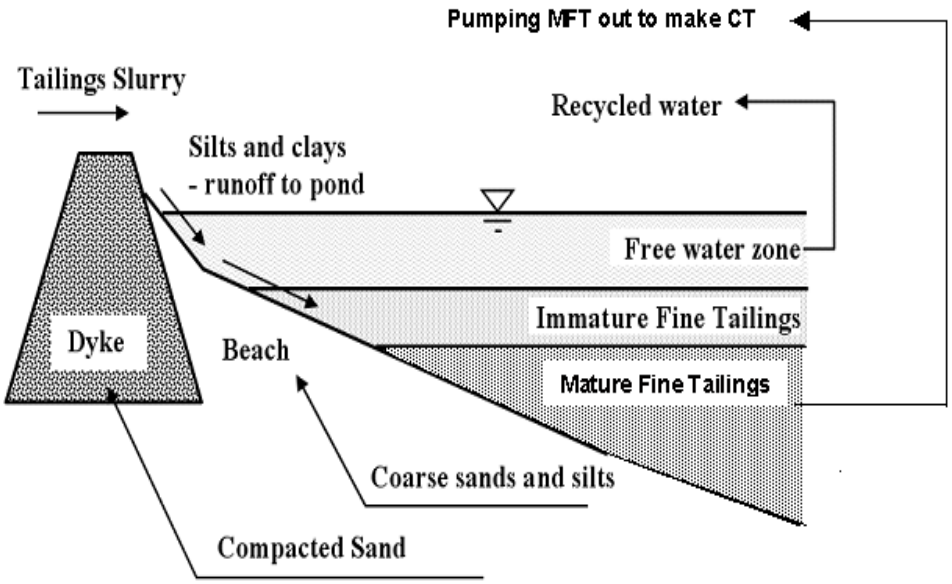

Figure 1-7 A Sketch of the Oil Sands Tailings Storage and Settling Basin (Adapted from Jeeravipoolvarn, 2004)

CHAPTER 2

2 LITERATURE REVIEW

The presence of gas bubbles have been reported in many locations: the marine sediments of the Gulf of Mexico (Esrig & Kirby, 1977), the mouth of some rivers such as Mississippi delta (Whelan et al., 1977), and estuarine clayey silt dredged from Rotterdam harbour (Sills et al., 2001). The presence of gas bubbles can significantly affect the consolidation and strength properties of the soils (Sills et al., 2001).

The existence of biogenic gas bubbles in the oil sands tailings was probed by geophysical survey. According to a report (AGRA, 1997), it became difficult to locate the pond bottom of the MLSB by geophysical method in the early 1990's, and by 1994 it was almost impossible to determine the pond bottom due to the presence of large amount of gas bubbles in the MFT. This phenomenon started as in Suncor's tailings pond in 1980's with gas bubbles observed on pond surface (Sheeran, 2003, personal communications).

About the source of the gas bubbles, Holowenko et al. (2000) indicated about 60-80% of the flux gas across the surface of the MLSB was methane, and the volume of carbon dioxide was approximate 10% of the volume of methane (Holowenko et al., 2000).The methanogenesis in the Mildred Lake Settling Basin (MLSB) appears to have started after the sulfate concentration dropped (Holowenko et al., 2000). This is due to the competition between methanogens and sulphate-reducing bacteria (SRB). SRB obtain more energy for a given substrate than do methanogens. If abundant sulphate exists in the habitat, SRB out-compete methanogens for the substrate (Fedorak et al., 2002). Methanogens are usually considered the last players in the decomposition of the organic matter in anaerobic ecosystems. They use the endproducts (acetate and H_2) of other strictly anaerobic bacteria as food to produce methane and CO_2 as waste (Fedorak et al., 2000).

The soil containing gas phase is defined as unsaturated soil. Unsaturated soil can be divided into three classifications (Wheeler, 1988): (1) continuous gas and discontinuous water (dry soil); (2) continuous gas and water; (3) continuous water and discontinuous gas. Sparks (1963) suggested that the critical degree of saturation for type (3) is about 85%. The theory of two independent stress variables (σ-u_a) and (u_a-u_w) fits very well for the type (2) (Matyas & Rcdhakrishna, 1968; Fredlund, 1985), but it is not suitable for type (3) (Wheeler, 1988).

For soil type (3), the soil is formed by a two phase system: the large gas cavity surrounded by a continuum of saturated soil (Wheeler, 1988; Sill et al., 1991). It can be further divided into two sub-types. For the first sub-type, very small occluded gas bubbles fitted within the normal pore voids, and the radius of curvature of the gas-water interface is equal to the radius of the gas bubble. For this type of soil, the theory of effective stress is still suitable. The presence of gas bubbles can only affect the compressibility of the soil. For the second sub-type: the size of gas bubbles is much larger than the size of soil particles. The radius of curvature of the water-gas interface is not equal to the radius of the gas bubbles. For this type of soil, the effect of the large gas bubbles is more complex than that of small gas bubbles. The oil sands mature tailings (MFT) containing large gas bubbles belongs to the second sub-type. Figures 2.1 and 2.2 illustrate soil type (2) and type (3), respectively.

For soil type (3), a new concept "operative stress" which is defined as the difference between the total stress and pore water pressure was introduced by Sills et al. (1991). For saturated soil, effective stress "σ' is the exclusive cause of ----all the measurable effects of a change in stress, such as compression, distortion, and a change in shearing resistance" (Terzaghi, 1923). For gassy soil, the strength and strain properties are not uniquely determined by operative stress, but for any initial gas content, the water void ratio is solely determined by operative stress (Sills et al., 1991).

The current researches on gassy soils mainly include the following aspects: the undrained shear strength, consolidation, the acoustic response, and gas bubble

migration. The influences of gas bubbles on engineering properties of soils have been studied at Oxford University, Queen's University of Belfast, and Shefield University (Sills et al., 1991).

Thomas (1987) carried out a one-dimensional consolidation program by using an oedometer. The gassy sample was prepared by using zeolite, an inert chemical which has strong affinity for water. When the methane-saturated zeolite is mixed with soil, methane is rapidly replaced by water. It takes a few hours for the methane to be released from the zeolite. The test results were modeled using the concept of operative stress (Sills et al., 1991). The compressibilities of the gas and the surrounding saturated matrix are considered independently. The compressibility of gas is assumed related to the change of total mean stress, and the consolidation of the saturated soil matrix is controlled by operative stress. The gas pressure is dependent on the change of total stress.

Sills et al. (2001**)** carried out a series of settling column tests with estuarine clayey silt dredged from Rotterdam Harbour. The influence of biogenic gas production on self-weight consolidation and strength of the soil was studied. Three different temperatures, 10^{o} C, 20^{o}C and 30^{o}C, were used to control the rate of gas generation. While changing the generation rate, the temperature can also change the viscosity of the pore water, so, it is not appropriate to compare the time-dependent behaviour under different temperatures (Sills et al., 2001). The experiments showed that the excess pore water pressure decreased quickly during gas production period. At the bottom of the column, the excess pore water pressure became negative when gas was produced. This phenomenon was explained as "an effective stress increase is necessary to resist the expansion (caused by gas production), this requires a reduction in pore pressure." (Sills et al., 2001). Observation of the soil structure change showed that gas morphology depends on production rate and ambient temperature. At low rate, gas bubbles tend to be spherical, at high rate, they are irregular, ellipsoidal, elongated, even branched shapes.

Wichman et al. (2000) developed a self-weight consolidation computer program to simulate the consolidation of the gassy sludge from Rotterdam harbour. Some assumptions were made for modeling: gas voids are fixed in the soil skeleton, gas void ratio is constant across the bed height, in-situ gas pressure is equal to the total vertical stress plus atmospheric pressure, the initial increase in gas content occurred instantaneously and gas void ratio at atmospheric pressure remained constant. The computer simulation and laboratory tests demonstrated that the effect of the gas is to retard the self-weight consolidation.

For the rapid densification phenomenon occurring in the MLSB, it was assumed that the gas helps, and does not hinders the water release from the MFT in a report (AGRA, 1997). But this was just an assumption, there was no experimental and theoretical evidence to confirm this. Since there were more than 3 m water cap above the MFT surface in the MLSB, freeze-thawing should not be a factor for the rapid MFT densification.

Based on the pore water pressure response of the gaseous marine soils with S_r greater than 90% to wave overpressure, Esrig et al. (1977) concluded that the gaseous-laden submarine soils have higher effective stress and greater stability than their fully saturated counterpart, and the prediction of slope stability of the gaseous soils based on the effective stress theory and the assumption of fully saturated soils will be conservative.

Wheeler (1988) conducted triaxial tests on gassy samples of Combwich mud prepared using the Zeolite method. He indicated that the undrained shear strength of the gassy soils can be either higher or lower than that of the saturated matrix, depending on both the operative stress and the cell pressure. Theoretical lower and higher bounds of the undrained strength were derived. The gas pressure was always greater than the pore water pressure.

Wheeler (1990) suggested two independent sets of limits for gas pressure: the surface tension effect limits the difference between gas pressure and pore water pressure, the gas pressure is always greater than the pore water pressure;

cavity expansion and contraction limit the difference between gas pressure and total stress. When gas pressure lies inside the limits of surface tension and cavity expansion and contract, the gas pressure is less affected by the change of total stress. For very soft soil, the difference between gas pressure and total stress is very small.

Wheeler (1988) suggested a conceptual model of the soils containing large gas bubbles. He pointed out that the stress concentration caused by gas cavity can cause a varying field of pore water pressure, and the equalization of the local pore water pressures will lead to localized consolidation. Gas bubble flooding can occur at two different conditions: when the difference between gas pressure and water pressure (u_a-u_w) reaches a lower limit (-T/R_c, T is surface tension between gas bubble and water, and R_c is minimum radius of the meniscus), a sudden flooding of water into the bubble cavity will occur; when the pressure difference (u_a-u_w) reaches a upper limit (T/ R_c), there will be a sudden encroach of gas into the surrounding soil. The second case rarely occurs.

Wheeler (1990) summarized four possible mechanisms for the migration of the large bubbles in unsaturated fine grained sediments: (1) dissolved gas moves with water due to hydraulic gradient; (2) dissolved gas moves relative to water due to concentration gradient; (3) undissolved small gas bubbles move through void spaces under buoyancy; (4) large gas bubbles moves upward under buoyancy. Based on theoretical analysis and experimental tests of the reconstituted kaolin containing methane bubbles zeolite method, he indicated that bubbles with realistic size should move upward only in extremely weak sediment, the application of cyclic loading can reduce the critical size for the gas bubble moving upward, but even under cyclic load bubbles with realistic size can move upward only in very weak soil such as, undrained strength is less than 0.1 kPa.

About acoustic response of the soils containing large gas bubbles, Gardner (1988) indicated that the signal attenuation can significantly occur due to the

presence of the gas bubble cavities. The bulk modulus k of the gassy soil is much lower than that of the saturated soil.

In summary, extensive research have been done on the behaviour of the soils containing large gas bubbles, but most of the current research focus on observations, empirical analysis and conceptual model. Although numerical modeling has been conducted by some researchers, simplified assumptions (some of them are far different from the real conditions) have to be used. Also, in most of the previous experimental researches, the gas bubbles were produced using the zeolite method in which the gas bubbles were released to the soil rapidly. This is different from the actual biogas activity at the MLSB. This research program uses nutrients to stimulate microbial activity. The MFT densification property during microbial activity is studied.

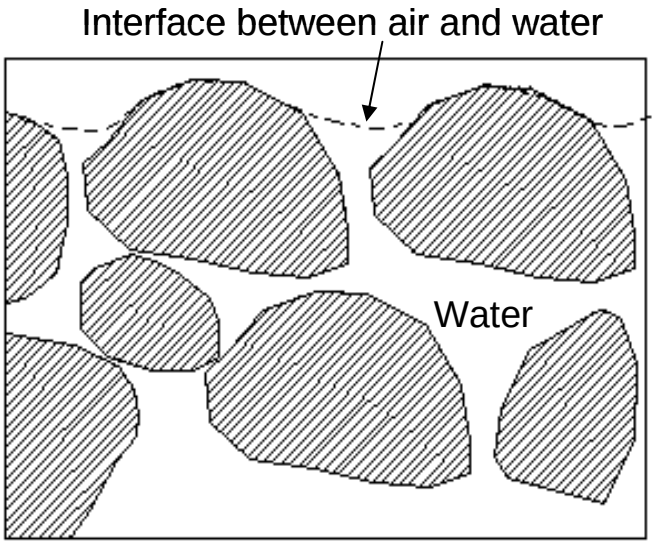

Figure 2-1 Demonstration of Unsaturated Soil Type 2

(modified from Fredlund, et. al. 1993)

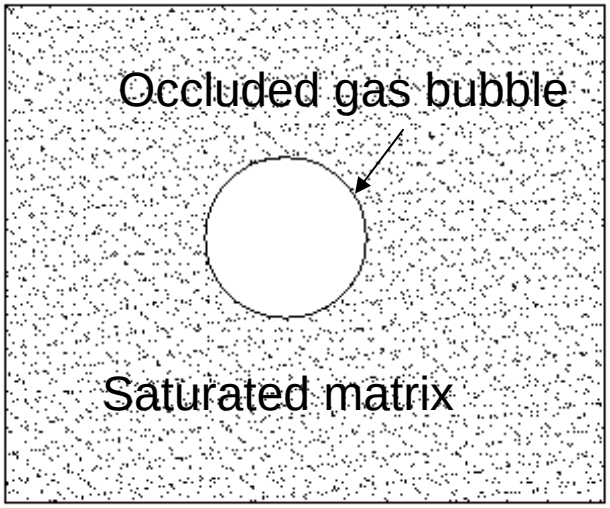

Figure 2-2 Demonstration of Unsaturated Soil Type 3

(modified from Wheeler, 1988)

CHAPTER 3

3 SYNTHESIS OF SOME HISTORICAL MONITORING DATA IN THE MLSB

3.1 Introduction

Over the past years (since 1996) remarkable changes have occurred in the Mildred Lake Settling Basin (MLSB) operated by Syncrude Canada Ltd. Microbial activity known as methanogenesis has become active at the southern part of the tailings pond, where the densification of the MFT has been accelerated.

In order to understand the mechanism causing the accelerated densification phenomenon, it is necessary to know the densification properties of the MFT and the depositional environments at the tailings pond. Since early 1980's, Syncrude Canada Ltd. has been monitoring the MFT properties at the three stations shown in Figure 1.1. Valuable data (both physical and chemical data) has been accumulated over the past two decades. In this chapter the historical monitoring data is used to evaluate the densification properties of the MFT and the depositional environmental changes within the tailings pond.

The three stations used for long-term monitoring are not fixed points in the tailings pond. Due to the complexities of the field conditions (pumping operation, weather and other factors), the location of each station is variable within a certain range (up to 1000 m). Sta. 1 is at the southern part of the pond and close to the pump barge. As the pump barge moves, the location of Sta. 1 varies. Sta. 3 is at the northern part of the tailings pond, and Sta. 2 is in the middle. At each station, samples at different depths were obtained 2-3 times (in April, July, and September, respectively) every year. These samples were shipped to Syncrude Research Center where physical and chemical parameters (like solids content, fines content, bitumen content, p, EC, were measured using standard industrial procedures (Syncrude Canada Ltd., 1995).

Through these measurements, valuable information can be obtained for understanding the physical and chemical conditions at the tailings pond. Based on the historical monitoring data, some parameters including solids content, fines/(fines + water), temperature, gas content and pore water chemistry are synthesized in this chapter.

By following Syncrude's analysis protocol, the parameters at two depth zones, 2-5 m and 5-13 m (below water-MFT interface), are analyzed in this research. The average of a parameter within each depth zone is used to study the variation trend of this parameter.

3.2 MFT Densification Properties

In the oil sands industry, two parameters are usually used to determine the density of the MFT: total solids content and the ratio of fines/(fines + water). Solids content was defined as the percentage of the solid particle mass to total MFT mass. The fines are defined as the particles smaller than 44 μm. The fines content of a sample can be obtained from the plot of particle size distribution. Since segregation of coarse particles (>44μm) can lead to the change of solids content, the ratio of fines/(fines + water) reflects the densification property of the MFT better than total solids content does. In this research, the densification properties at Sta. 1 and Sta. 3 of the MLSB are analyzed and compared.

Figure 3.1 shows the elevaion profiles of solids and fines/(fines + water) at Sta. 1 in different years. Significant increases in both solids and fines/(fines + water) occurred within the elevation range from 330 m to 340 m after 1996. For example, the ratio of fine/(fines + water) at 336 m elevation increased about 30% during the period from 1996 to 2002. This was much faster than the predicted increase (less than 7%) by Equation 1.1.

Figure 3.2 and Figure 3.3 show the changes of solids contents and fines/(fines + water), respectively, at 336 m elevation (about 7-8 m below water-MFT

interface) at Sta. 1 and Sta. 3. The densification parameters at these two stations were close in 1995. Since then, the densification rates at the both stations have been accelerated. But the densification at Sta. 1 was more significant than that at Sta. 3. In 2002 the ratio of fine/(fines + water) at Sta. 1 was much larger than that at Sta. 3.

Figure 3.4 shows the elevation profiles of fines/(fines + water) at Sta.1 and Sta.3 in 2002. The densification of the MFT at Sta. 1 was more than that at Sta. 3. In the elevation profile of fines/(fines+ water) at Sta. 1 a peak value was reached at 5-6 m depth below water-MFT interface.

3.3 MFT Temperature Change and Reason Analyses

3.3.1 MFT Temperature Change

Over the past two decades, Syncrude Canada Ltd. has performed MFT sampling 2-3 times per year from different depths of the three stations at the MLSB. When a sample was brought out of water surface and retrieved on the testing boat, the temperature of the sample was immediately measured using a thermometer. The results can be used to analyze the temperature variation trend at the tailings pond.

Figure 3.5 shows the changes of temperature averaged by two depth zones, 2-5 m and 5-12 m below water-MFT interface at Sta. 1. Before 1994, the temperatures at the two depth zones ranged from 10^{o}C to 16^{o}C, and the variations were relatively small. This is likely a reason for weak microbial activity at the tailings pond in the early 1990's. From 1994 to 1997, the temperatures rapidly increased. In 1997 the temperature at Sta. 1 approached 23.5^{o}C. Although the measured temperatures after 1997 showed fluctuations and decreases, they were still higher than the temperatures before 1994. From 1998 to 2002, the measured temperatures showed fluctuations ranging from 17^{o}C to 22.5^{o}C.

Temperature is an important factor affecting microbial activity and biogas generation in the MFT. It is often assumed that there is no (or very weak) microbial activity below 4°C. The optimum temperatures for methanogenesis range from 33°C to 35°C (Cooper & Harrington, 1988). The microbial activity of methane bacteria becomes negligible below approximately 15°C (Marison, 1988). However, microbial activity has also been detected at lower temperature below 2°C (Tiner, R.W. 1999).The remarkable temperature increase at the southern part of the pond could be a factor to accelerate microbial activity after mid 1990's.

3.3.2 Reasons of the Rapid Temperature Changes

Two potential factors might contribute to the temperature increases in the MFT: released heat from microbial activity, and artificial activities such as oil sands tailings discharging into the pond. The tailings stream discharged into the pond has a temperature ranging from 25-35 °C. (MacKinnon, 2003, Personal Communications).

Methanogen bacteria use the metabolic end products (mainly acetate, CO_2, and H_2) of other strictly anaerobic bacteria as nutrients to produce methane and CO_2 (Zinder, 1993; Fedorak et al., 2000). The energy produced during the methanogenesis for the production of methane can be expressed in the following equations (Fedorak et al., 2000):

$$4H_2+HCO_3^- + H^+ \rightarrow CH_4 +3H_2O \quad \text{Methanogenesis} \qquad (3.1)$$

$\Delta G^{0'}$=-135 kJ/reaction

$$CH_3COO^- + H_2O \rightarrow CH_4 + HCO_3^- \quad \text{Methanogenesis} \qquad (3.2)$$

$\Delta G^{0'}$=-31 kJ/reaction

In Equation (3.1), methanogen bacteria use H_2 and CO_2 as nutrient to produce methane, for each reaction 135 kJ heat is produced; in Equation (3.2), methanogen bacteria use acetate as nutrient to produce methane and CO_2, for each reaction 31 kJ heat is produced. The reaction in Equation (3.1) produces more heat than that in Equation (3.2). The above equations are two possible reactions for methanogenesis. Which reaction is the dominant microbial activity at the tailings pond is not unclear (Fedorak, 2003, Personal communications.)

The methane yields in the MFT at the MLSB ranges from 0.13 to 0.24 mL methane/mL MFT at atmospheric pressure and room temperature (Fedorak et al., 2000). In order to estimate the maximum potential temperature increase, it's assumed that 0.24 mL methane/mL MFT is produced.

For 1.0 L MFT (about 1200 g), the maximum methane production under 1.0 atmospheric pressure and room temperature is about 240 mL which is equivalent to 0.01071 mol. In order to calculate the maximum possible temperature increase, Equation (3.1) is assumed as the main reaction for methanogenesis. After microbial activity the maximum heat produced in 1.0 L MFT is about 1.4445 kJ (345.2 Cal).The specific heat of water is 1 cal/g/^{o}C. The MFT is a slurry with very high water content. By assuming the specific heat of the MFT is about 1.2 cal/g/^{o}C. and the total mass of 1.0 L MFT is about 1200 g, the maximum temperature increase after microbial activity is about 0.24^{o}C. This is very small relative to the actual temperature increases (more than 8^{o}C) occurring in the tailings pond after 1994.

Since the influence of microbial activity itself on MFT temperature is very small, the rapid temperature increases in the tailings pond must be caused by some external factors such as warm tailings (about 25 to 35^{o}C.) discharging into the pond (MacKinnon, 2003, Personal Communications). Before 1994 the tailings discharge was distributed around the tailings pond. After 1994 the tailings discharge was focused at the southern part of the pond. The released heat from the warm tailings stream was likely an important reason for the rapid temperature increase at the southern part of the pond. The obvious

temperature fluctuations after 1998 might be caused by temperature fluctuations of the discharged tailings and discharging location changes (MacKinnon, 2003, Personal Communications).

3.4 Total Gas Contents within the MFT

Syncrude Canada Ltd. started to measure the gas volumes in the MFT in 1996. The MFT samples were obtained using a piston sampler or large diameter bucket sampler. When the MFT sample was retrieved on the testing boat, an air-tight piston syringe with needle was used to collect part of the MFT sample which was then sealed and delivered to the laboratory. Gas analysis was performed after vacuum stripping the sample. The total gas volume and the volumes of different components were measured by Gas Chromatography (GC) analysis. Although some of the gas bubbles released to the atmosphere during sampling, most of the gas bubbles would remain in the syringe if sampling operations were conducted rapidly. This is an approximate method to determine the gas contents in the MFT, and is used only for the purpose of comparison between successive sampling. More accurate methods of in situ gas sampling are necessary to determine the gas volume in the future.

Although the trapped gas volume within the MFT is not the total gas production since part of the produced gas might have released from the MFT and CO_2 may have dissolved as HCO_3^-, the gas volume within the MFT can still be used to approximately estimate the intensity of microbial activity and the relative gas production, especially in the early periods of microbial activity when most of the generated gas was trapped in the MFT.

Figure 3.6 shows the elevation profiles of total gas contents in different years at Sta. 1. The gas content is defined as the ratio of total gas volume at standard pressure and temperature (STP, 25^{o}C and 1 atmospheric pressure) to total sample volume (at STP) in percentage. The in situ gas content is defined as the ratio of in situ gas volume (at in situ pressure and temperature) to in situ MFT volume. From 1996 to 1999, the measured gas contents at a depth from 5 m to

10 m below water-MFT interface rapidly increased. This demonstrates the rapid gas generation and intense microbial activity at the southern part of the pond. The gas contents in 2000 and 2002 were obviously lower than those in 1999. This was likely caused by the intense gas release from the MFT. At the upper parts of the profiles gas contents rapidly increased with depth. At about 5-6 m depth below water-MFT interface the gas contents reached maximum values in most of the profiles. This suggests that microbial activity at about 5-6 m depths (below water-MFT interface) was the most intense in the profiles. The depth zone with the most intense microbial activity was also the zone with the most significant measured densification.

Figure 3.7 shows the elevation profiles of gas content in different years at Sta. 3. Similar to Sta. 1, gas contents increased from 1996 to 1999. But the increases at Sta. 3 were less significant relative to Sta. 1.

Figure 3.8 shows the changes of maximum gas contents (at the spike points of the profiles) in different years. From 1996 to 1999, the gas contents at both Sta. 1 and Sta. 3 increased with time, but the increases at Sta. 1 were more rapid than those at Sta. 3. After 1999, the gas contents at Sta.1 significantly decreased. This was likely due to the intense gas release from the MFT.

3.5 Changes of Some Chemical Parameters

3.5.1 Introduction

Chemical changes in the tailings pond might have important influence on the microbial activity and the densification of the MFT. Four groups of anaerobic microorganisms (denitrifiers, Fe(III)-reducer, SRB and methanogens) were found in the oil sands tailings. Sulphate-reducing Bacteria (SRB) and methanogens were more important groups existing in MFT and CT samples (Fedorak et al., 2000). Methanogens utilize the end products (mainly acetate and H_2) of other strictly anaerobic bacteria as nutrients to produce methane (Zinder, 1993; Fedorak, 2000). Sulfate-reducing Bacteria (SRB) are an

important group of microorganisms in anaerobic ecosystems that contain high sulphate. SRB use a wide range of organic compounds as their energy sources compared to methanogens and they produce sulphide as their waste product (Fedorak, 2000). In the sediments with abundant sulphate, SRB can obtain more energy for a given substrate than do methanogens, they out-compete methanogens for the substrate. Fedorak et al. (2002) has demonstrated that high sulphate concentration inhibited methanogen activity, and that methane was produced after the sulphate concentration dropped to approximately 20 mg/L. This indicates the strong dependence of microbial activity on water chemistry of the MFT.

The knowledge of the chemical changes at the tailings pond can provide important information for the initiation and development of microbial activity. Over the past two decades, Syncrude Canada Ltd. has been monitoring the physical and chemical changes at the three stations in the MLSB as shown in Figure 1.1. Samples from different depths of the three sites were used to measure various chemical parameters including pH, electric conductivity (EC), and the concentrations of different ions. These tests were performed at Syncrude Edmonton Research Centre using established company protocols and methods (Syncrude Canada Ltd., 1995; Fedorak et al., 2000). In this section, the changes of some parameters including pH and concentrations of some major cations and anions are analyzed.

3.5.2 pH and Electrical Conductivity (EC)

Figure 3.9 shows the pH changes averaged at two depth zones (2-5 m and 5-13 m below MFT interface) at Sta. 1. At shallow depth zone, the pH was about 8.4 before 1999, and remained relatively stable. After 1999, the pH decreased. In 2003 the average pH at this zone was about 8.0. In the 5~13 m depth zone, the pH decreased from 8.6 to 7.8 from 1992 to 2003. The pH decreases might have been related to microbial activity and dissolved CO_2 in the solution (MacKinnon, 2003, Personal Communications).

Figure 3.10 shows the depth profiles of electrical conductivity at Sta.1 of the MLSB. The electrical conductivity at a depth increased with time, and the increases after 1995 accelerated. This indicates that the pore water salinity increased in the tailings pond. With time the tailing pond became more brackish.

The pH change could have significant influence on the depositional environment of the MFT. Bjerrum (1967) has shown that the pH value of pore water is a basic factor governing the chemical stability of minerals in clay. The pH decrease of the pore water would increase the disintegration of the clay minerals. In addition, the increase of H^+ ion can decrease the repulsive forces between clay particles. A low pH promotes a positive edge to negative surface interaction, often leading to flocculated structure (Mitchell, 1993).

3.5.3 Concentrations of Ions Na^+, K^+, Ca^{2+}, Mg^{2+}

The negatively charged clay particle surface and the dispersed layer of cations form diffuse double layer. The Gouy-Chapman theory provides a basis for understanding the influence of clay-water electrolyte on the soil structure. An increase of electrolyte concentration or valence can decrease the thickness of diffuse double layer, thus leading to the decrease of inter-plate repulsion (Mitchell, 1993). A net repulsive force between clay particles will lead to stable dispersed structure, on the contrary, the net attractive force between clay particles will lead to flocculated structure.

Figure 3.11 shows the changes of Na^+ concentrations averaged in 2-5 m depth zones at Sta. 1 and Sta. 3. Na^+ concentrations increased with time at the both sites. Before 1991, the concentrations at the two sites were similar. At Sta. 1, Na^+ concentration rapidly increased during two periods: from 1991 to 1993 and from 1997 to 1999. Figure 3.12 show the Na^+ concentration averaged in 5-13 m depth zone. From 1993 to 2001, Na^+ concentration rapidly increased from 526 mg/L to 1106 mg/L at Sta.1. The changes of Na^+ concentration at Sta. 1 were more obvious than those at Sta. 3.

Figure 3.13 shows the changes of Ca^{2+} concentrations averaged in 2-5 m depth zone at Sta. 1 and Sta. 3. Before 1997, the Ca^{2+} concentrations were relatively stable. From 1997 to 2002 the Ca^{2+} concentration at 2-5 m zone at Sta.1 increased from 6 mg/L to 25 mg/L, and at Sta. 3 it increased from 4.5 mg/L to 11 mg/L. In 5-13 m depth zone, the Ca^{2+} concentrations at both Sta. 1 and Sta. 3 obviously increased after 1995 (Figure 3.14). The increases at Sta. 1 were more obvious than those at Sta.3.

Figure 3.15 shows the changes of Mg^{2+} concentration at 2-5 m depth zone at Sta. 1 and Sta. 3. At Sta.1, Mg^{2+} concentration rapidly increased from 6.5 mg/L to 31.5 mg/L from 1998 to 2002. At Sta. 3 the changes of Mg^{2+}concentration were less obvious. Figure 3.16 shows the Mg^{2+} concentration changes at 5-13 m depth zone**.** Similar changes as at 2-5 m depth zone can be seen.

Figure 3.17 shows the changes of K^{+} concentrations at 2-5 m depth zone at Sta. 1 and Sta. 3. Figure 3.18 shows the changes of K^{+} concentrations at 5-13 m. Relative to Na^{+}, Ca^{2+}, and Mg^{2+}, K^{+} concentrations were relatively stable. After 1993 K^{+} concentration at Sta. 1 slightly increased.

Several reasons may contribute to the rapid changes of cation concentrations. Firstly, the changes in oil sands ore properties might be an important reason. Over this period, the mineral ore resources have become more brackish (MacKinnon, 2003. Personal Communications). Secondly, the extraction process and water management could cause the water chemical changes of the MFT. Since the released water is recycled to the extraction plant for bitumen recovery, with time, the pore water chemistry will become more brackish (TFTC, 1995); part of the CT release water (Syncrude started to produce CT in 1998) discharged into the MLSB could also increase some cation concentrations especially Ca^{2+}. Thirdly, the rapid increase in temperature and decrease in pH might be another reason for the rapid changes of the water chemistry. Temperature increase and pH decrease could accelerate mineral disintegration causing more ions dissolved in the solution.

3.5.4 Concentrations of Ions HCO_3^-, SO_4^{2-}, Cl^-, and Naphtha

Bicarbonate (HCO_3^-) is the most abundant anion in the MFT. It affects the MFT behaviour through the control of pH (FTFC, 1995). Figure 3.19 shows the changes of HCO_3^- concentration at 2-5 m depth zone at Sta.1 and Sta. 3. Before 1991, the HCO_3^- concentrations at the two sites were close, and remained stable. From 1991 to 2003, the concentration at Sta. 1 rapidly increased from 720 mg/L to 1600 mg/L, and at Sta. 3 it increased from 720 mg/L to 1100 mg/L. The changes of bicarbonate concentration at 5-13 m depth zone are shown in Figure 3.20. The increases at Sta. 1 were more obvious than those at Sta. 3.

Sulphate concentration has important influence on microbial activity in the MFT. Fedorak et al. (2000) has shown that the increase of sulphate concentration inhibits the methanogenesis, and SRB out-compete the methanogens for energy sources at high sulphate concentration.

Figure 3.21 and Figure 3.22 show the changes of sulphate concentrations averaged in 2-5 m depth zone at Sta. 1 and Sta. 3, respectively. The fitted curves by third order polynomial equations are also shown in the figures. In 1985 the sulphate concentration at Sta. 1 was about 40 mg/L. It decreased with time, and was about 20 mg/L in 1995. Figure 3.23 and Figure 3.24 show the changes of sulphate concentrations averaged in 5-13 m depth zone at Sta. 1 and Sta. 3, respectively. The concentrations at the two stations decreased with time, and they became lower than 20 mg/L after 1995.

Figure 3.25 shows Cl^- concentration changes at 2-5 m depth zone. From 1993 to 1999 the concentration at Sta. 1 increased from 170 mg/L to 600 mg/L, and at Sta. 3 it increased from 135 mg/L to 250 mg/L. the changes of Cl^- concentration at 5 –13 m zone are shown in Figure 3.26, similar changes to those at 2-5 m zone can be seen.

Naphtha is used as a chemical additive to improve bitumen extraction. After bitumen extraction, part of the added Naphtha flows into the tailings pond

along with oil sands tailings. Siddique et al. (2007) suggested that, microbial communities in the MFT can rapidly utilize certain fractions of uncovered naphtha in oil sands tailings and support methanogenesis in the tailings pond. Figure 3.27 shows the elevation profiles of Naphtha contents in different years at Sta. 1. From 1996 to 2002, the naphtha concentrations obviously decreased with time. Large portion of Nathan could be biodegraded into methane (Siddique, et al., 2006).

3.5.5 Discussion

The rapid changes of pore water chemistry of the MFT at the MLSB since early 1990's might be attributed to the following reasons:

- The major source of inorganic ions comes from oil sands connate water (Mikula et al., 1996). Changes in oil sands ore properties could lead to the water chemistry changes of oil sands tailings, especially Cl^- and Na^+ concentrations **.**
- Bitumen extraction process in the plant and water management affected the pore water chemistry in the MFT. The released water from the MFT is recycled to the plant for bitumen extraction. With repeated use of the released water, the tailings pond becomes more brackish (Mikula et al., 1996). Chemicals like NaOH are added during hot water extraction process. This can lead to the increase of the Na^+ concentration. Adsorption of CO_2 during aeration in the conditioning stage in the extraction can lead to increase of bicarbonate concentration.
- Microbial activity could change the water chemistry in the MFT. The anaerobic tailing pond is rich with microorganisms. Sulphate Reducing Bacteria (SRB) and methanogens are two important microorganisms at the tailings pond. At high sulphate environment, SRB out-compete methanogens for energy resource. With SRB activity proceeding, SO_4^{2-} concentration decreased with time. When SO_4^{2-} concentration was reduced to about 20 mg/L of MFT, methanogenesis was initiated within large regions of the tailing pond (Fedorak et al., 2002).

- The differences in MFT water chemistry between Sta. 1 (southern station) and Sta. 3 (northern station) might be related to tailings discharge into the pond. Since 1995 the tailings discharge has occurred primarily in the southern part of the tailings pond. Consequently, the water chemistry at Sta. 1 was likely more affected by changes in oil sands ore properties and extraction process than that at Sta.3.

The pore water chemistry in the tailings ponds was affected by various factors including the ore composition, bitumen extraction, water management, and microbial activity. Water chemistry changes controlled the microbial activity. Analyses of the long-term monitoring data suggest that the chemical changes at the tailings pond since early 1990's have created a favorable environment for methanogen bacteria activity and had beneficial effects on MFT densification.

3.6 Summary

From the synthesis of long-term historical data, the following conclusions can be obtained:

- Rates of MFT densification at both Sta. 1 and Sta. 3 accelerated after 1996 with Sta.1 exhibiting a larger increase than Sta. 3.
- The temperature of the MFT at southern part of the tailings pond increased rapidly after 1994. The rapid temperature increase was mainly caused by oil sands tailings discharge. The rapid temperature increase at the southern part of the pond was a factor for the rapid increase of microbial activity.
- With increasing microbial activity, the measured gas contents increased rapidly from 1996 to 1999. The gas generation rates at the southern part of the tailings pond were more rapid than those at the northern part of the pond.
- The similarity between the depth profiles of gas content and the corresponding profiles of fines/(fines + water) demonstrates that the rapid

densification of the MFT at the southern part of the pond was closely related to biogas generation.

- The pH at the southern part of the pond has obviously decreased since 1998.
- The concentrations of Na^+, Ca^{2+}, Mg^{2+}, HCO_3^-, Cl^- at the southern part of the tailing pond have increased since mid 1990's. Various factors including oil sands ore changes, bitumen extraction process, microbial activity, and temperature changes might be the reasons for the increases.
- The sulphate concentration in the MFT decreased to about 20 mg/L after 1995. This might be a reason for methanogenesis initiation and acceleration.
- The physical and chemical changes at the southern part of the pond including decrease of sulphate concentration and increase of temperature have created favourable environments for methanogenesis and MFT densification.

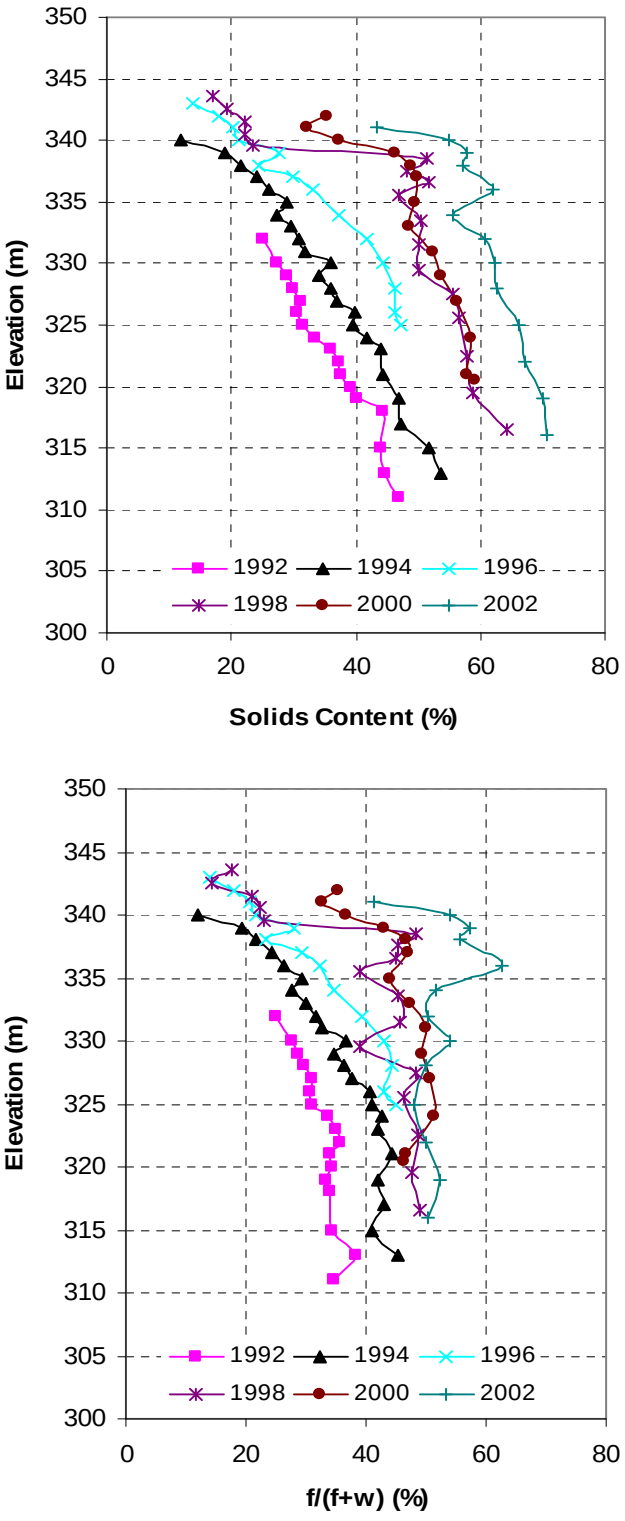

Figure 3-1 Changes in (a) Solids and (b) Fines/(Fines + Water) (Fines<44um) Contents by Elevation for Various Years at Sta. 1

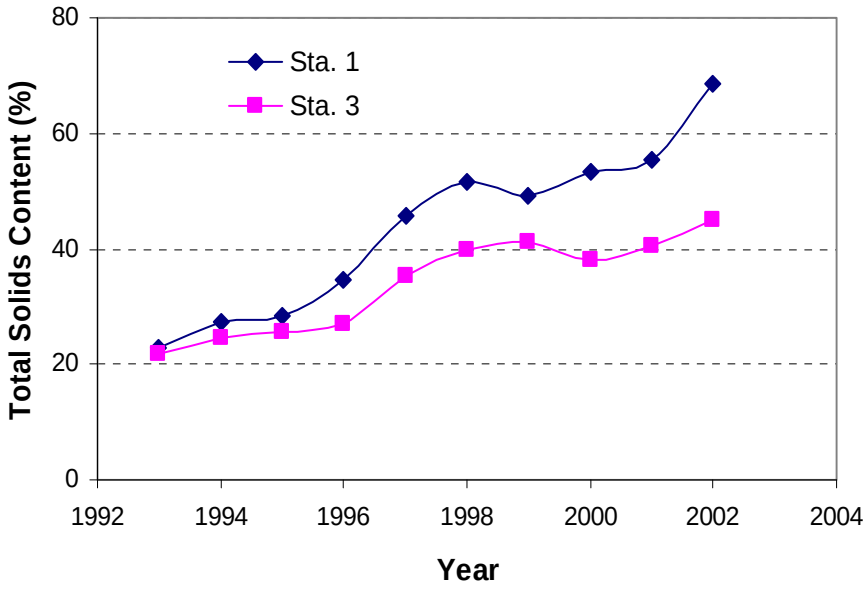

Figure 3-2 Total Solids Content Changes at 336 m Elevation of Sta. 1 and Sta. 3

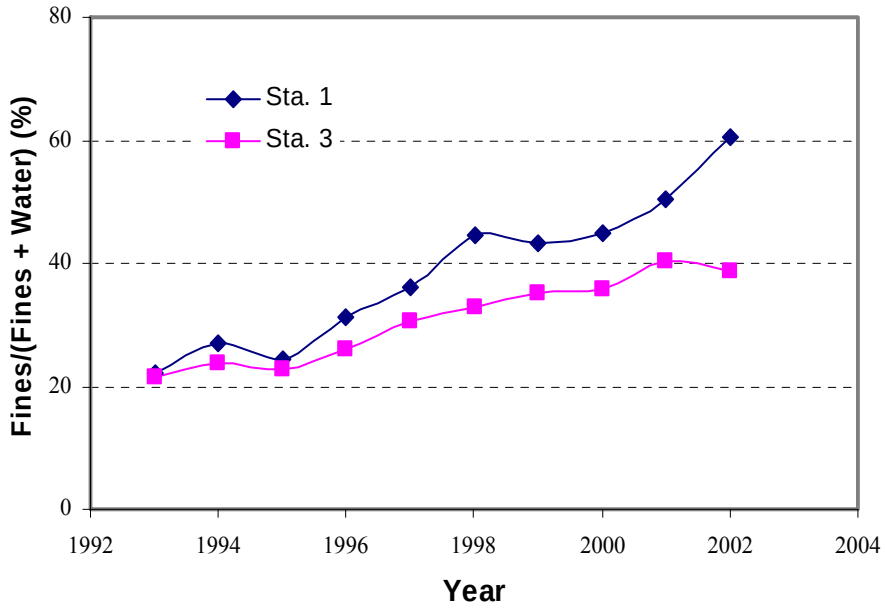

Figure 3-3 Changes of fines/(fines + water) with years at 336 m Elevation of Sta. 1 and Sta. 3

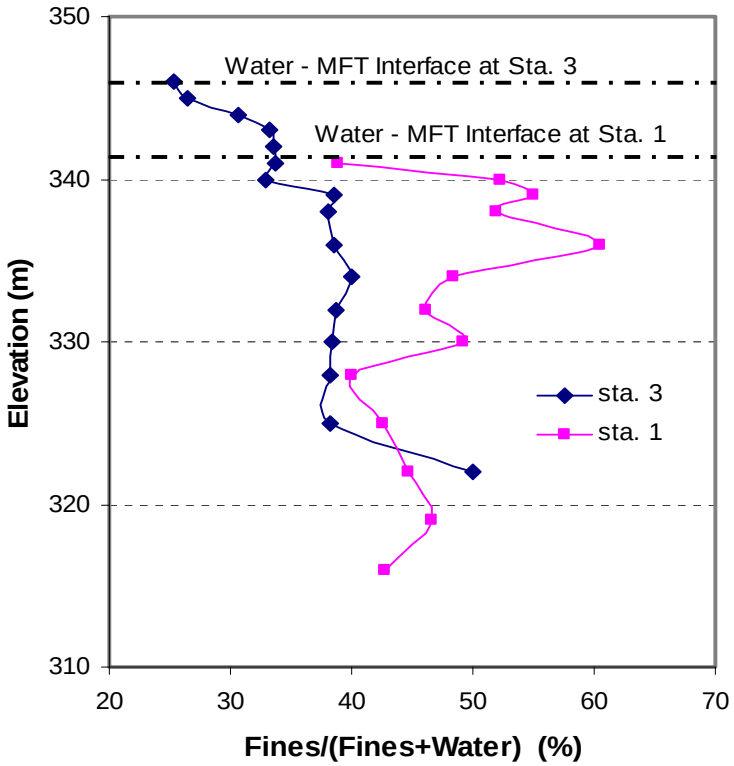

Figure 3-4 Depth Profiles of fines/(fines + water) at Site 1 and Site 3 in 2002

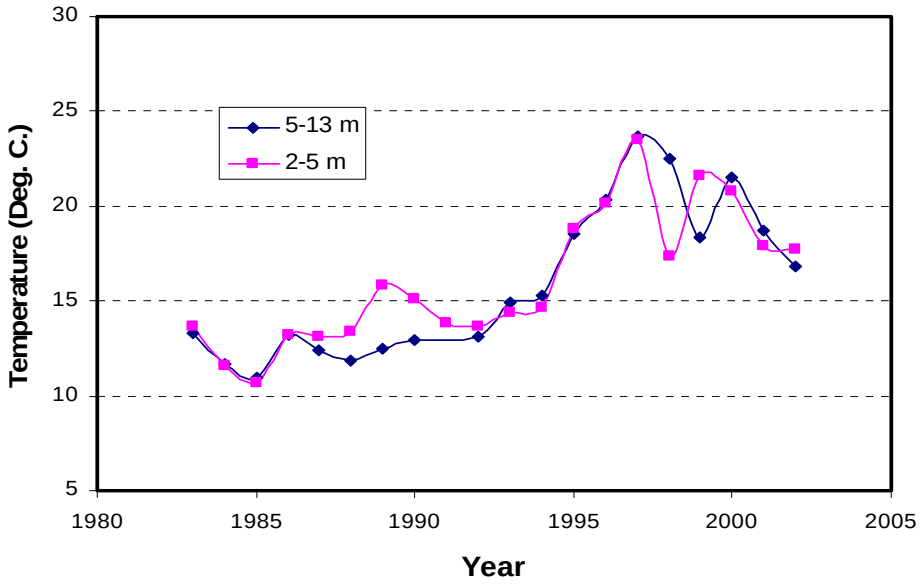

Figure 3-5 Changes in Temperature Averaged by Depth Zones in the Fines Tailing at Sta. 1

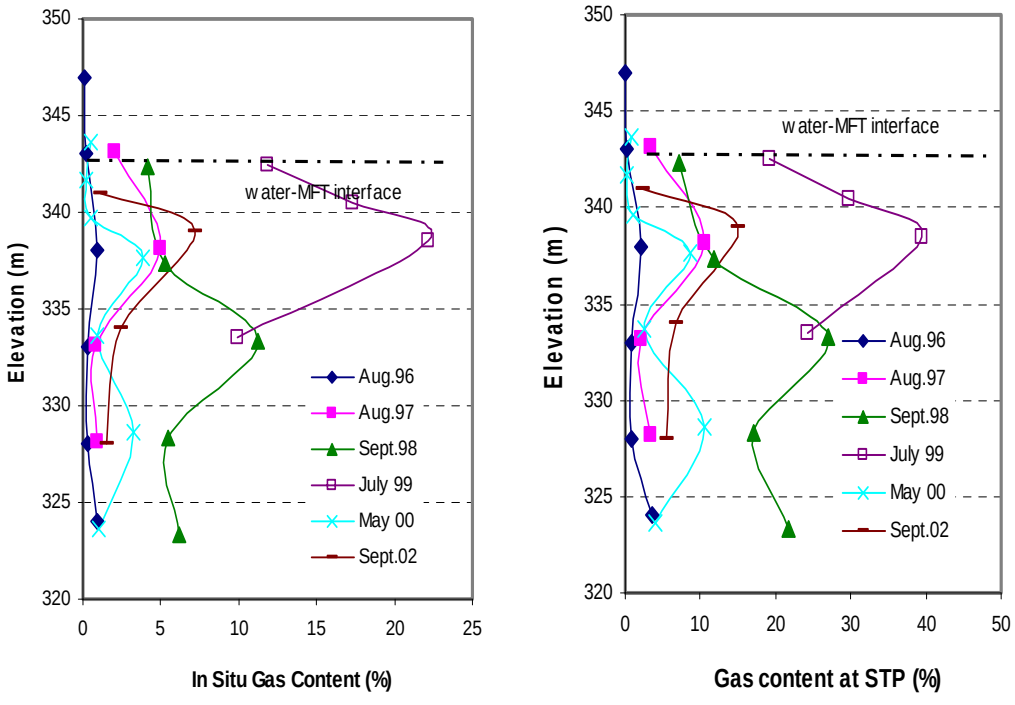

(a) (b)

Figure 3-6 Elevation Profiles of Gas Content in the MFT at Sta.1 (a) In Situ Gas Content (b) Gas Content at STP

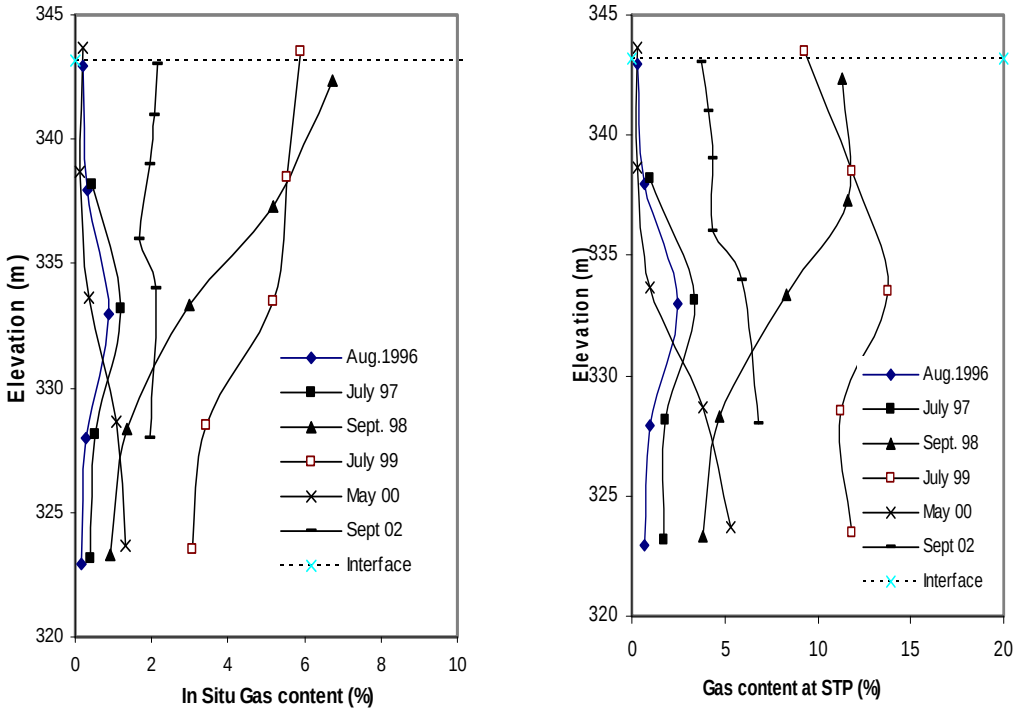

(a) (b)

Figure 3-7 Elevation Profiles of Gas Content in the MFT at Sta.3 (a) In Situ Gas Content (b) Gas Content at STP

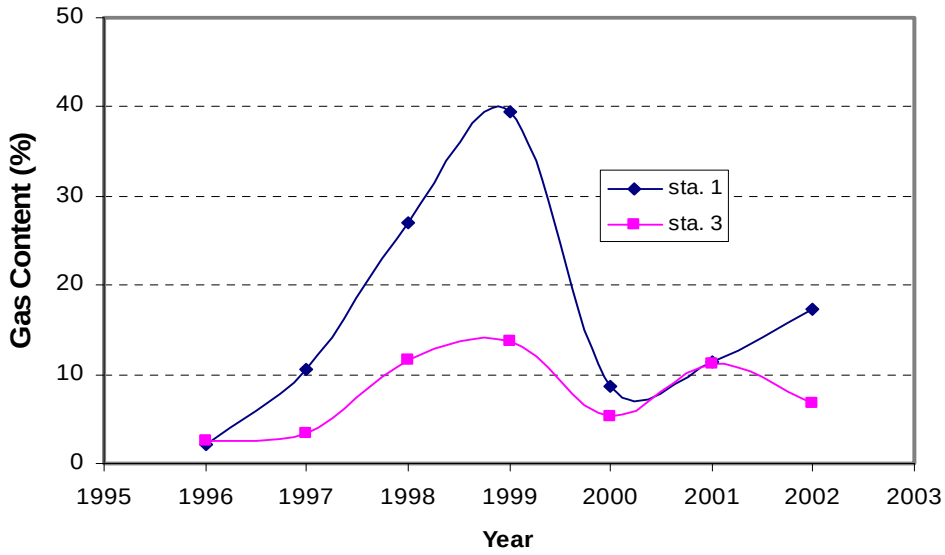

Figure 3-8 Changes of the Maximum Gas Contents at Sta. 1 and Sta. 3

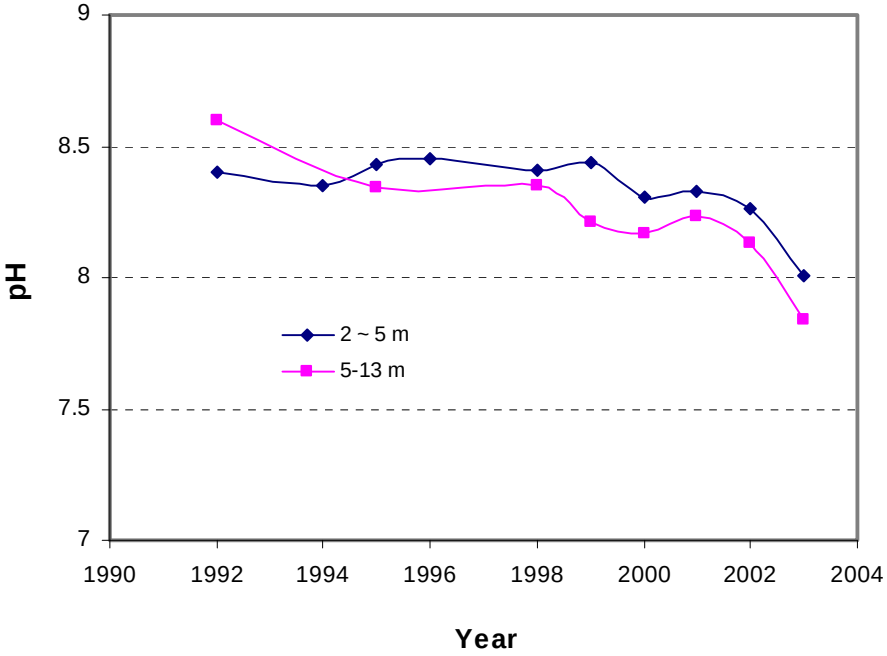

Figure 3-9 Changes in pH Values Averaged by Depth Zones at Sta. 1

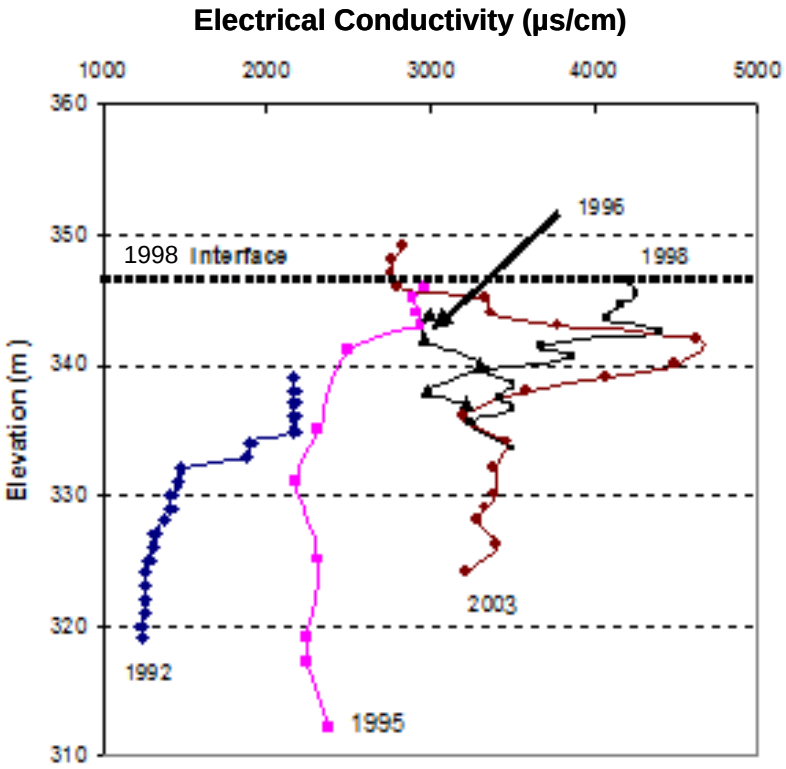

Figure 3-10 Depth Profiles of Electrical Conductivity at Sta. 1 of MLSB

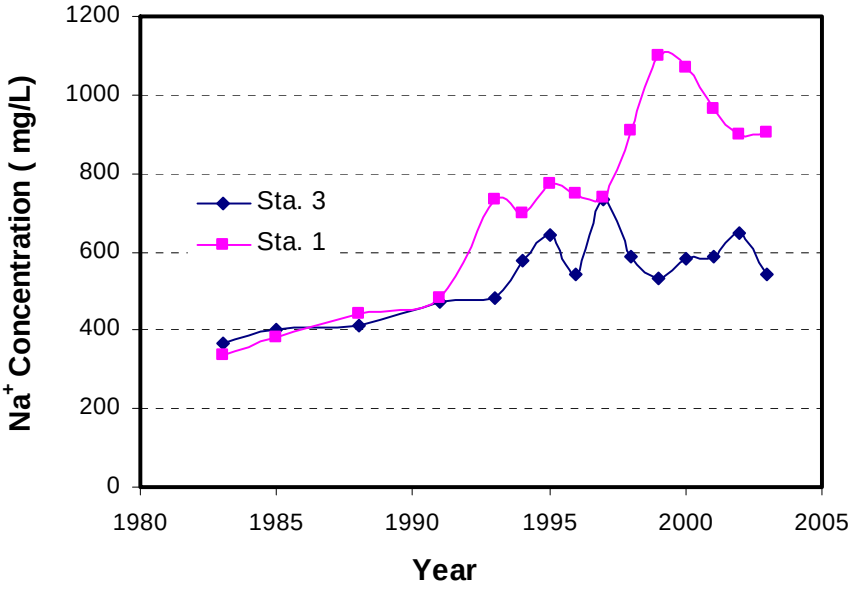

Figure 3-11 Changes of Na^+ Concentration Averaged within 2-5 m Depth Zone

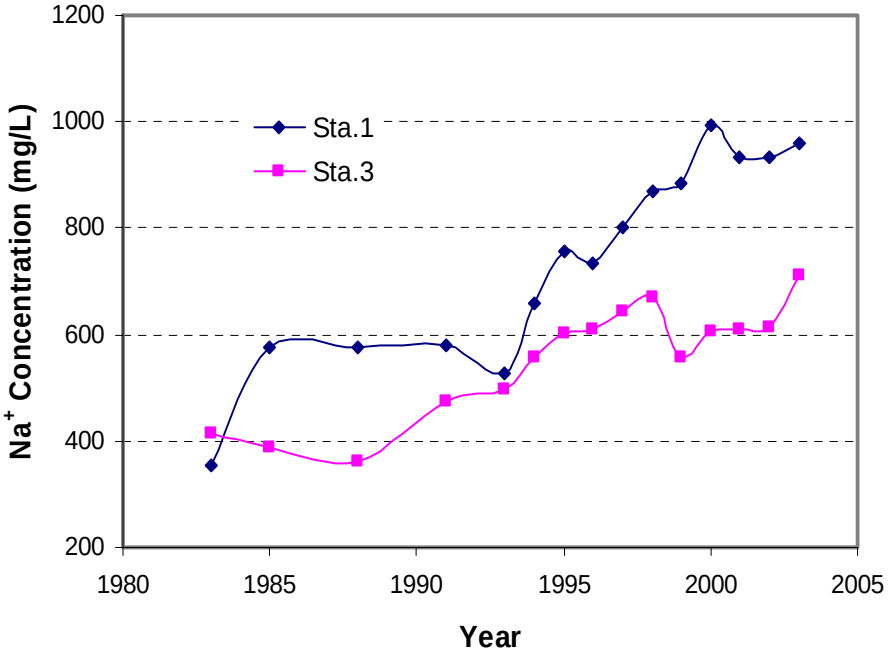

Figure 3-12 Changes of Na^+ Concentration Averaged within 5-13 m Depth Zone

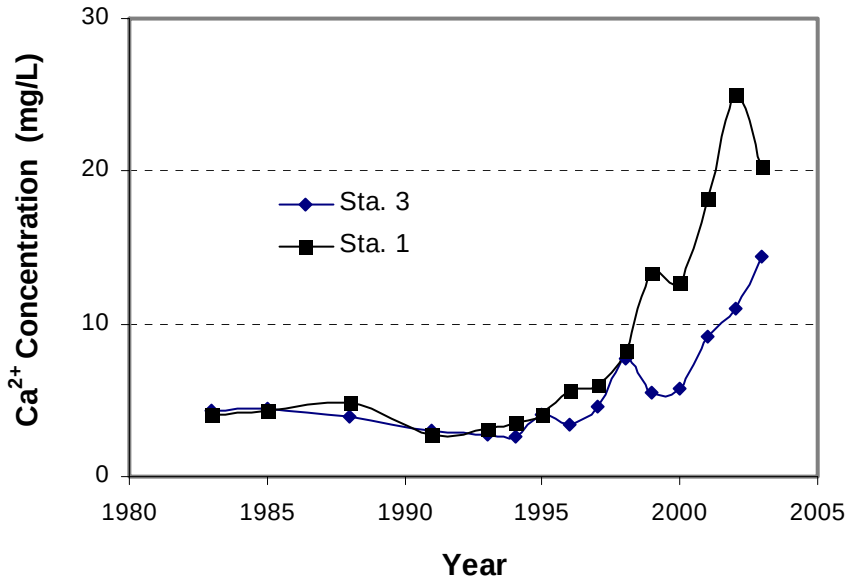

Figure 3-13 Changes of Ca^{2+} Concentration Averaged within 2-5 m Depth Zone

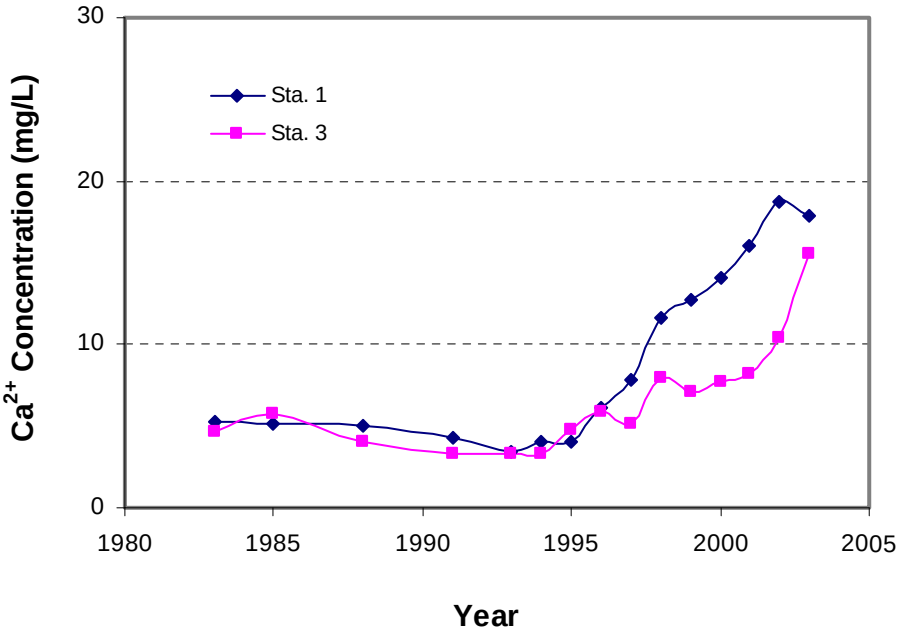

Figure 3-14 Changes of Ca^{2+} Concentration Averaged within 5-13 m Depth Zone

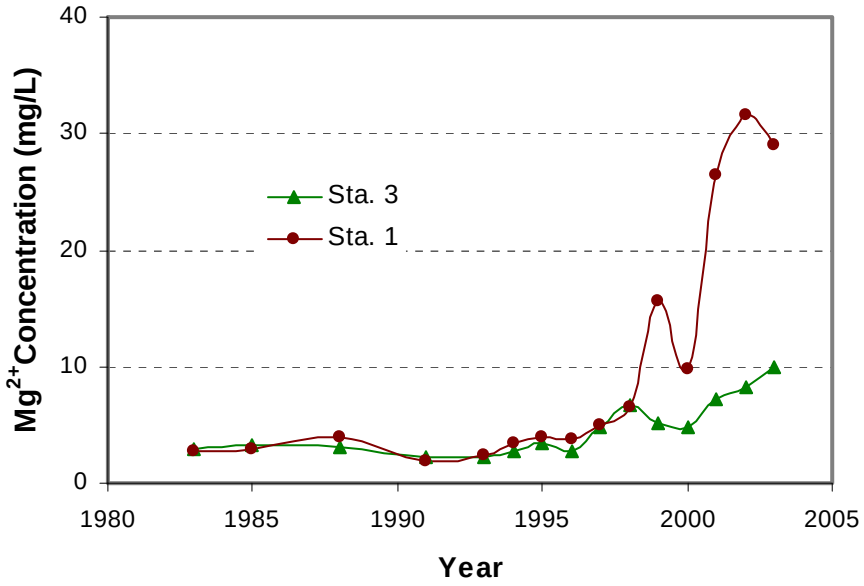

Figure 3-15 Changes of Mg^{2+} Concentration Averaged within 2-5 m Depth Zone

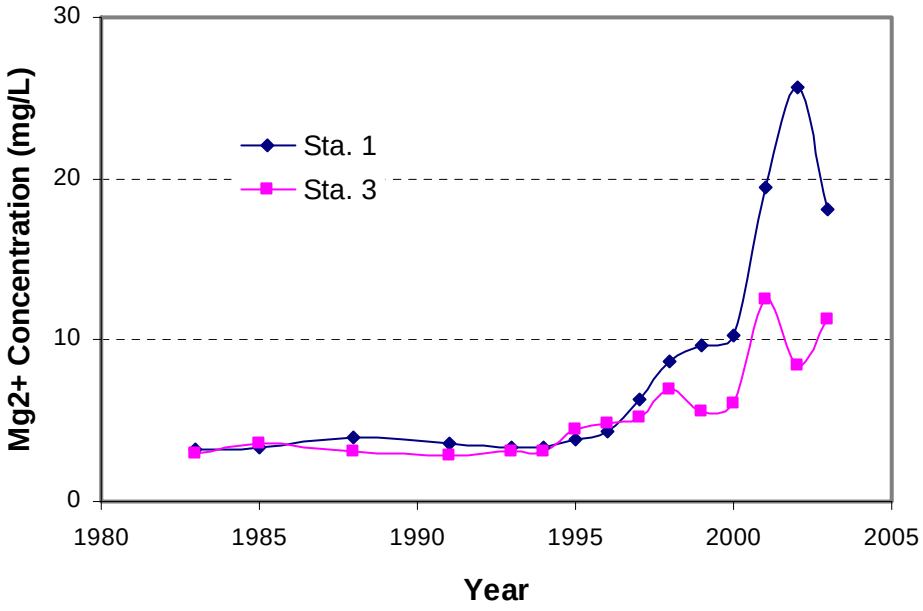

Figure 3-16 Changes of Mg^{2+} Concentration Averaged within 5-13 m Depth Zone

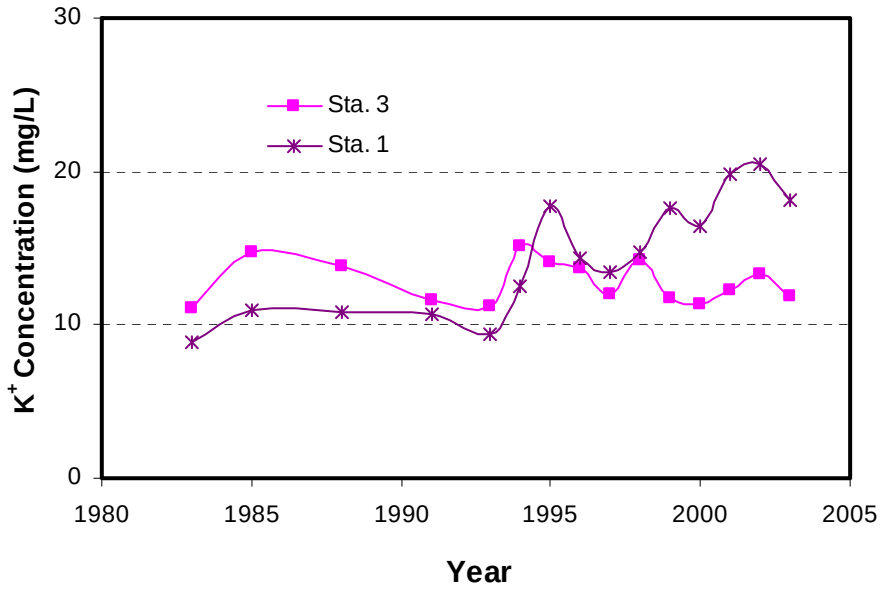

Figure 3-17 Changes of K^+ Concentration Averaged within 2-5 m Depth Zone

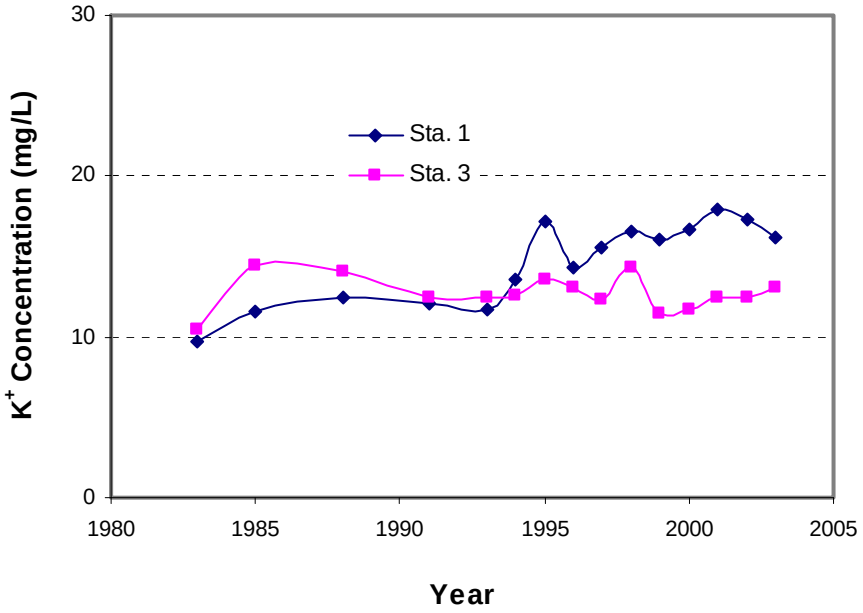

Figure 3-18 Changes of K^+ Concentration Averaged within 5-13 m Depth Zone

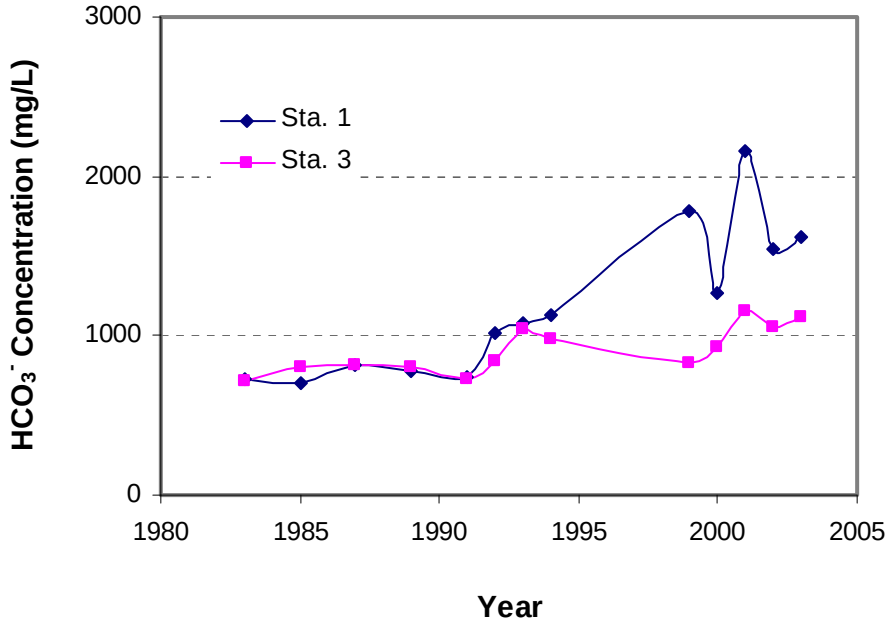

Figure 3-19 HCO_3^- Concentration Averaged within Depth Zone 2-5 m below the Interface

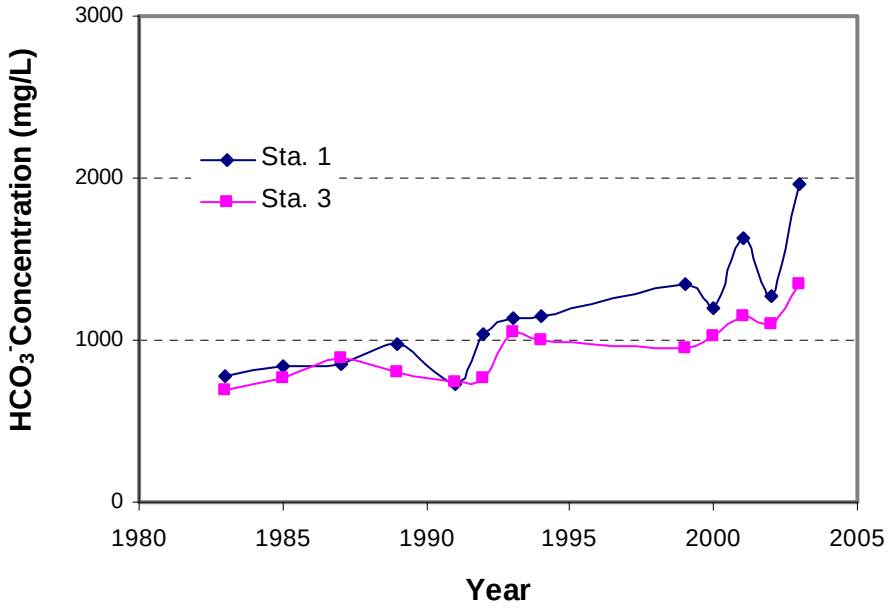

Figure 3-20 HCO_3^- Concentration Averaged within Depth Zone 5-13 m below the Interface

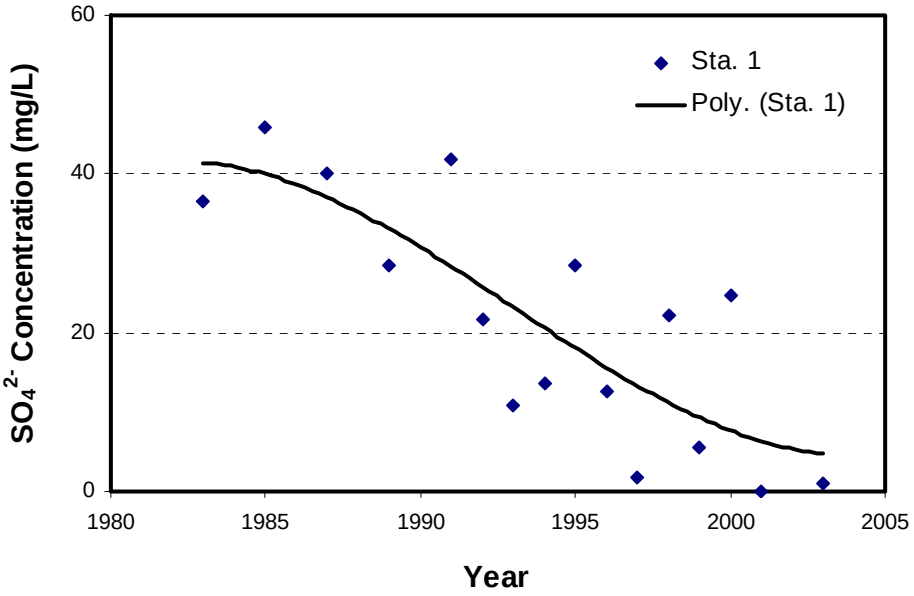

Figure 3-21 SO_4^{2-} Concentration Averaged within 2-5 m Depth Zone below the Interface at Sta.1
(Poly. is the fitted curve by polynomial equation to show the trend)

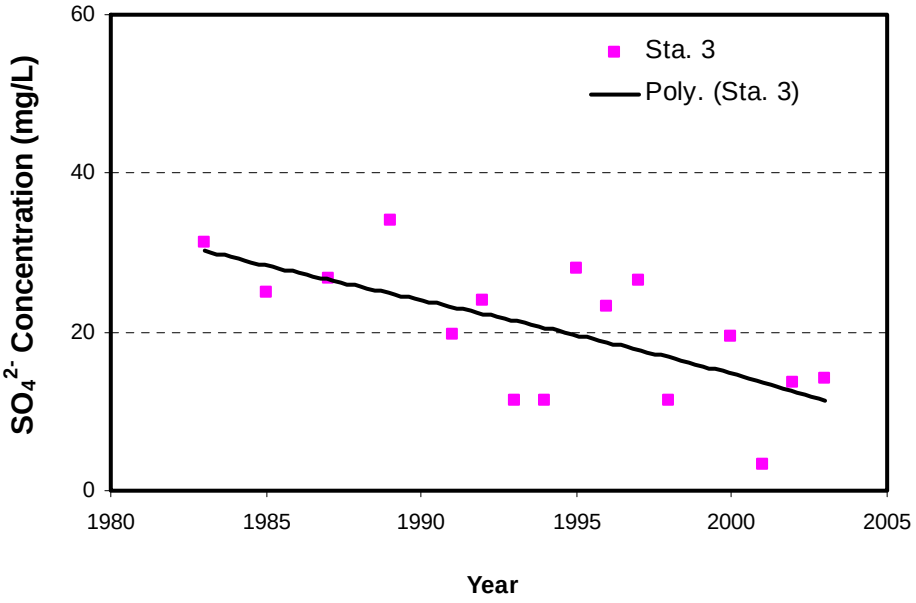

Figure 3-22 SO_4^{2-} Concentration Averaged within 2-5 m Depth Zone below the Interface at Sta.3

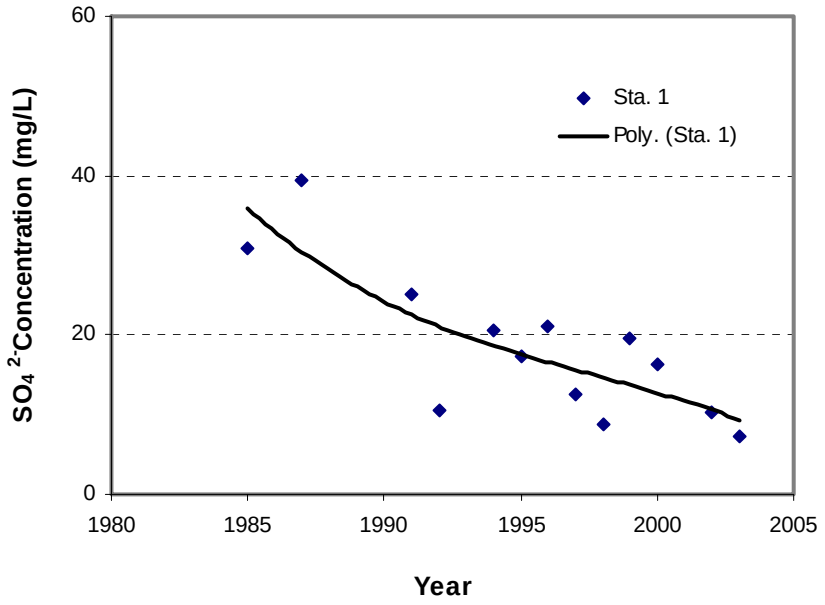

Figure 3-23 SO_4^{2-} Concentration Averaged within 5-13 m Depth Zone below the Interface at Sta. 1

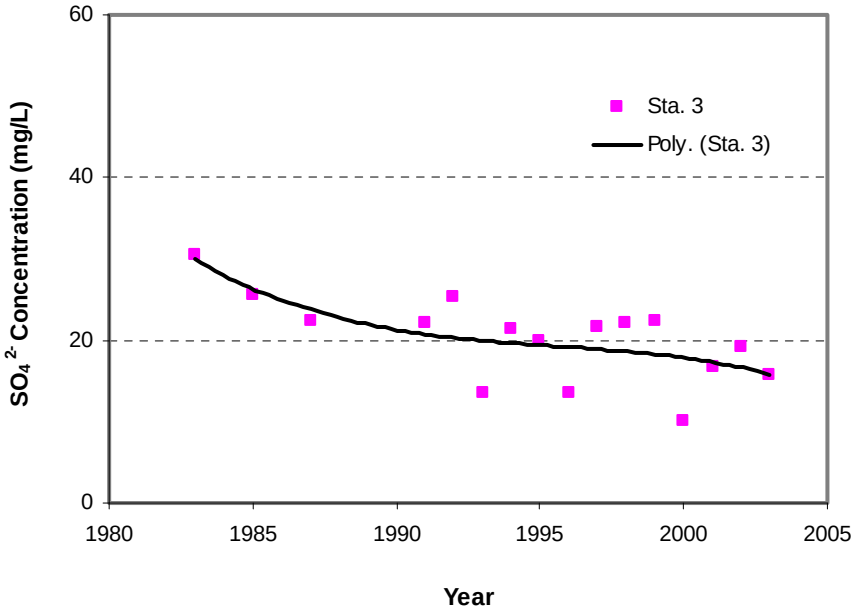

Figure 3-24 SO_4^{2-} Concentration Averaged within 5-13 m Depth Zone below the Interface at Sta. 3

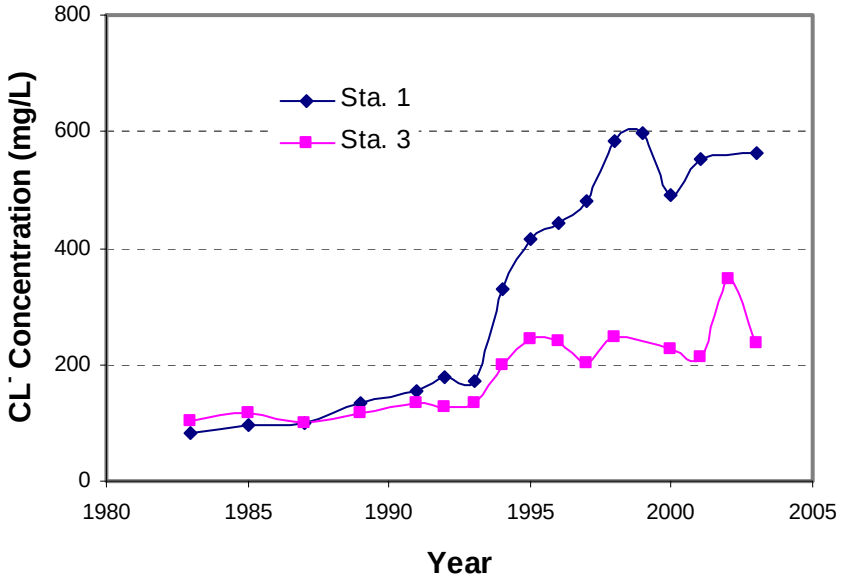

Figure 3-25 Cl^- Concentration Averaged within Depth Zone 2-5 m below the Interface

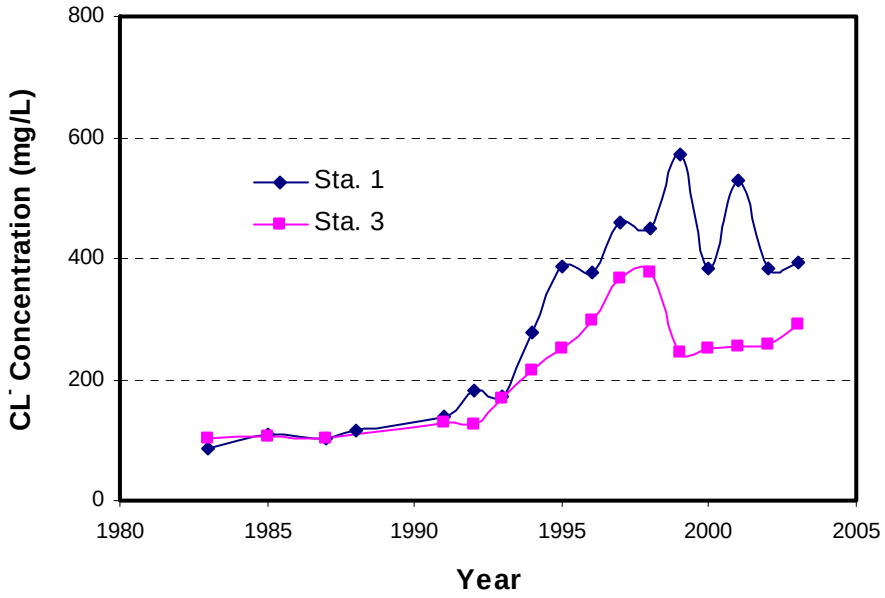

Figure 3-26 Cl^- Concentration Averaged within Depth Zone 5-13 m below the Interface

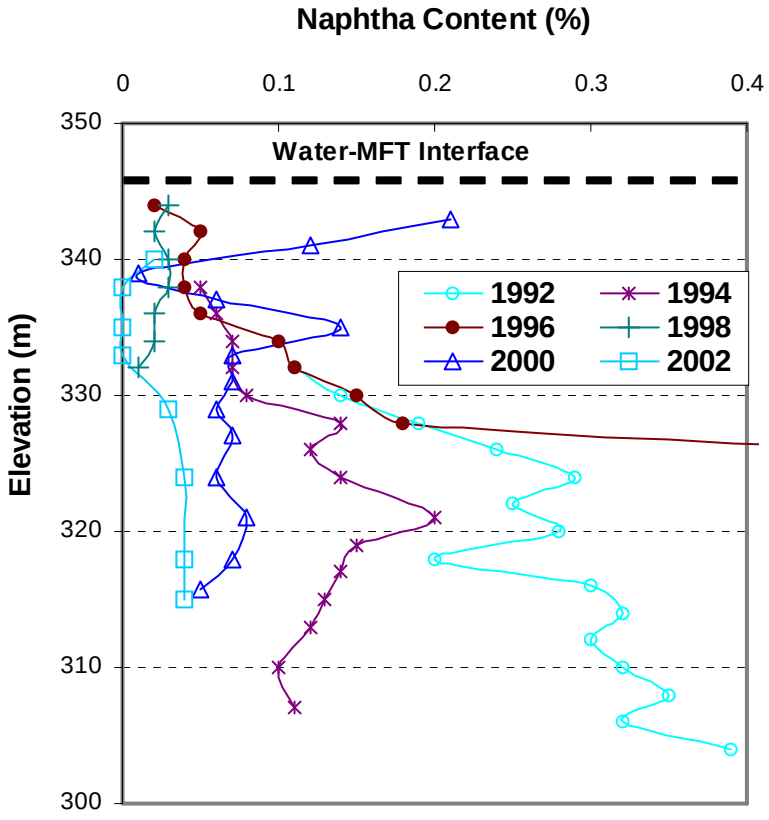

Figure 3-27 Depth Profiles of Naphtha Contents (Weight %) at Sta. 1

CHAPTER 4

4 FIELD INVESTIGATIONS OF THE RAPID DENSIFICATION OF THE MFT IN THE MLSB

4.1 Objectives

To study and understand the mechanism for the rapid densification of MFT in the MLSB, it is necessary to assess the distribution and properties of the dense zones in the pond. Through the field investigation, samples were obtained to test the geotechnical and geochemical properties of the MFT. The field investigations were conducted to determine the shear strength, pore water pressure, in situ stress, in situ temperature, and other properties of the MFT at the tailings pond.

4.2 Overview of the Field Investigations

The geotechnical field investigations were carried out in 2000, 2001, and 2002 as summarized in Table 4.1. During the field investigations various types of field tests were used:

- Piston sampling
- Freeze sampling
- Field vane shear tests
- Steel plate penetration tests (SPP)
- Piezometer and earth pressure measurements
- Cone penetration tests (CPT)
- In situ temperature measurements
- Gas bubble distribution mapping

4.3 Sampling

4.3.1 Piston Sampling

4.3.1.1 Introduction

Piston sampling is a simple sampling method to obtain disturbed samples. The piston samples have been used in determining the chemical and physical properties of MFT, including pH, conductivity, major ions, trace metals, organic components, solids content, bitumen content, particle size distribution, mineralogy and methylene blue absorption. Sub-samples were also taken for measurement of the biogenic gas content. In the field, the piston samples were used to visually identify the densification properties of the MFT using field observations of the MFT physical properties as demonstrated Table 4.2.

Figure 4.1 and Figure 4.2 show a photo and schematic of the U of A piston sampler, respectively. The sampler had an internal diameter of 5 cm and was 55 cm long with a sampling capacity of about 1000 mL. The piston sampler penetrated into the MFT under its own weight. The sampler was stopped at the target depth, and the piston was held in place by rods or air pressure. The piston was then allowed to move, and the MFT sample entered the sampler under the action of in situ stress.

When the samples were retrieved on the testing boat, glass jars (approximately 1000 mL) were used to hold the MFT samples. The jar was filled near the top of the mouth. The temperature of each sample was measured. The samples were sealed, and their individual information was documented. The samples were delivered to the Syncrude Edmonton Research Centre and the University of Alberta separately for physical, chemical and geotechnical tests.

4.3.1.2 Field Observation and Classification

The densification properties of the MFT were identified by field observation methods. In field sampling, the samples were approximately identified and classified based on the properties given in Table 4.2. When classifying the MFT samples in the field, the properties, including the solids content, relative components (sands and fines), and physical states, were taken into account.

Figure 4.3 shows the MFT sample from 6 m depth below the water surface at the barge location in the MLSB. The solids content was within the range of 30-40%, and the MFT was easy to move and deform. Figure 4.4 shows the photo of a relatively dense sample. It had a solids content within the range of 40-50%, was quite viscous but deformed easily.

Figures 4.5 to 4.8 show the rapidly dense MFT samples in the MLSB. The samples were mainly composed of fines particles and had solids contents close to or more than 60%.

According to Suthaker (1995), the MFT sample at the MLSB had Liquid limit 59% and Plastic limit 23%. The physical condition of the dense MFT was close to a plastic state. The trapped gas voids were clearly visible. Figure 4.7 shows the gas voids on the surface of the piston sample. Figure 4.8 shows the gas voids inside the piston sample. The maximum diameter of the gas voids is about 5 mm and most of them have a round or elliptical shape.

Based on the descriptive classifications defined in Table 4.2, the MFT properties at different locations were visually identified and described. Appendix A provides an example of MFT classification for a field investigation conducted in May 2001. At the time of field investigation, there was very thin tailings slurry within about 1-2 m below the water-MFT interface at the MLSB. With increasing depth, the densification of the MFT also increased. There existed a very dense MFT layer from about 8 to 12 m at Sta. 1. The dense MFT layer was identified from 14 to 15 m at Sta. 2. No dense MFT layer was found at Sta. 3.

4.3.2 Freeze Sampling

Undisturbed samples could not be obtained by piston sampling because of immediate gas release, swelling of the sample and disturbances when sampling. Fourie et al. (2001) reported the successful recovery of undisturbed samples of oil sands tailings by freezing the tailings in situ. In this program,

freeze sampling method was used to obtain samples for MFT structural analyses.

During freeze sampling, a one meter long steel pipe was connected in series with PVC tubing. The steel pipe was inserted to the required sampling depth, and was then fixed to a static object such as the barge or boat. Dry ice (CO_2) with -80^{o}C was poured into the PVC tubing from the surface. The dry ice contacted the steel pipe, reducing its temperature and causing the adjacent MFT to freeze. The dry ice was replenished periodically; after a few hours, a frozen sample formed around the pipe. The pipe was then carefully pulled up, and the frozen sample retrieved. After repeating this process, all the frozen samples were brought to the surface where they were divided into individual blocks and stored in coolers containing dry ice. The frozen samples were shipped to the University of Alberta. They were used to perform the analyses of macro- and micro- structures, density, and gas contents.

A frozen sample obtained from a depth of 9.2 m at Sta.1 of the MLSB in August 2001 is shown in Figure 4.9 and Figure 4.10. When the frozen MFT was removed from the sampling pipe, numerous gas voids were visible. The gas voids had different sizes and shapes. Their maximum diameter was about 1 cm.

From the samples, it can also be seen that the distribution of bitumen in the MFT was not uniform. Figure 4.11 shows the vertical gas voids with a maximum diameter of about 2 mm. Figure 4.12 shows some vertical fractures in the frozen sample. It is possible that when the microbial activity caused the expansion of the MFT, the corresponding local and tensile stress concentrations fractured the MFT structure. Figure 4.13 shows the frozen sample from a depth of 10 m and near the pumping barge (Sta.1) in August 2002. Most of the macro gas voids ranged from 1-2 mm in diameter, but a few large gas voids had diameters close to 4-5 mm.

Figures 4.14 and 4.15 show the Scanning Electrical Microscopy (SEM) photos of the dense MFT samples (horizontal plane in the field), retrieved from a depth of 10 m near the pumping barge (Sta. 1) in August 2002. The MFT

consists of clay particle assemblages, large gas voids and inter-particle voids. Within the particle assemblages, the closely packed clay platelets with face-face contacts can be observed as shown in Figure 4.16 (horizontal plane in the field). Small voids with the size of the clay particles exist within the clay particle assemblages. Relatively large pores and voids exist between the clay particle assemblages.

Some large gas voids and gas bubbles can also be seen in these images. The gas bubble in Figure 4.14 has a diameter of about 0.3 mm. The non-circular shape of the bubbles seen in the image may indicate that the original gas bubble was partially flooded (failed) due to non-equilibrium between the gas pressure and surrounding pressures. Wheeler (1988) suggested a conceptual model for gas bubble flooding.

$$-2T/R_C \leq u_g - u_w \leq 2T/R_c$$

where, T is the surface tension between gas-water interface, R_C is the minimum radius of meniscus which bridge the gaps between the particles, u_g is gas pressure, and u_w is pore water pressure. If the pressure difference $(u_g - u_w)$ reaches the lower limit, collapse of gas bubble roof will occur, leading to a sudden flood of water into the bubble. If pressure difference $(u_g - u_w)$ reaches the upper limit, there will be a sudden encroachment of gas into the surrounding soil skeleton. But there's little chance of this occurring (Wheeler, 1988).

In Figure 4.14, some small bitumen blocks can be seen around the gas bubble. It is likely that the gas bubbles existed in the relatively high hydrocarbon environment which provided the nutrient resource for the bacterial activity. Figure 4.15 shows a dish-shaped gas void. The interesting phenomenon is that some fissures and cracks appear at the bottom of the gas voids. This demonstrates that the formation and growth of the gas bubble can cause tensile stress within the surrounding area. The tensile stress can then cause fissures and fractures around the gas bubbles. Near the large gas bubbles, an

approximately circular void can be seen. It might be formed by gas bubble release or migration from lower levels.

In addition to its application for viewing the in situ structure of the MFT, the frozen sample can also be used to determine the in situ density and gas content of the MFT. For example, a frozen sample retrieved from a depth of 9.2 m below the water surface at Sta. 1 of the MLSB was used to determine the in situ density of the gassy MFT. The sample had a solids content of 58.1% and bitumen content of 3.99%. The mass of the frozen MFT block was 329.5 g. The volume of the frozen block, determined by measuring the submerged mass of the sample, was 234.2 mL. The wet volume (before freezing) of the MFT block was 222.2 mL. As such, the in situ density of the MFT at this depth was 1.48 g/cm^3. From the measured density and other parameters, including the bitumen and solids content, the gas content in the MFT was calculated to be 3.41% of the total MFT volume. It appears that only a small part of the generated gas remained in the MFT near the pump barge.

4.4 Field Vane Shear Tests

4.4.1 Introduction

MFT has a high moisture content, is thixotropic, highly compressible soil structure, making it difficult to obtain undisturbed samples. The samples used for laboratory tests are usually different from in situ tailings both in structure and mechanical properties. Due to the existence of gas bubbles in the MFT, it is difficult to get undisturbed samples from the tailings pond.

The vane shear test is the most widely used method of in situ determination of the un-drained shear strength of very soft clays. Originally used in Sweden in 1919, it has been employed extensively since the late 1940s. The standard vane consists of four blades set at right angles with a height-to-width (or diameter) ratio, H/D, of 2:1. The blade thickness is typically 1.5 mm. The usual equilibration period following vane insertion is 5 min.

Assuming that the shear strength distributes uniformly on the cylindrical surface (H=2D), the total torque can be expressed as:

$$M = C_u * (\pi D) * H * D/2 + \int_0^{D/2} 2C_u * 2\pi r^2 dr = \frac{7}{6}\pi D^3 C_u$$

$$C_u = \frac{6M}{7\pi D^3}$$

where, C_u is the un-drained shear strength, and M is the maximum recorded torque (Chandler, 1987).

The field vane tests were performed from a boat at the MLSB. Table 4.3 gives a summary of the field vane tests in 2001 and 2002. Two different vane sizes, 60 mm × 120 mm and 80 mm × 160 mm, were used. Each vane was connected to a steel rod which was enclosed by a steel sleeve that isolated the rod from the MFT. During testing, each vane was inserted to the required depth under self-weight. After about five minutes of inserting the vane at a target depth, rotational torque was applied to the vane to shear the MFT. At the top of the vane, a transducer was used to measure the torque, while on the boat, a data dolphin recorded the readings. The test at each depth point lasted from two to four min. The schematic of the field vane test apparatus is shown in Figure 4.17.

4.4.2 Calibration

Before the field test, the equipment was calibrated. A fixed incremental load was applied to the torque cell. The torque can be calculated by the force times the length of the moment arm. The relationships between the output (mv) and the torque (N.m) in field vane shear tests in 2001 and 2002 are shown in Appendix D. The calibration equation used in 2001 was:

M=1.701* R

The calibration equation used in 2002 was:

M= -2.131* R

where, M is the torque (N.m) and R is the Readings (mv)

4.4.3 Results of Field Vane Shear Tests

Figure 4.18 shows the plot of the vane shear stress vs. rotation angle, measured at 12 m depth below the water surface and near the barge of the MLSB in May 2001. Normally, the peak strength was reached at an angular rotation of about 30^o to 60^o. The peak vane strength was 3.5 kPa, and the post-peak strength was about 1.5 kPa. Figure 4.19 shows the results in August 2001 at a depth of 12.8 m and near the barge. The peak strength was 3.0 kPa, and the post-peak strength was about 1.5 kPa. The results at the pumping barge in May and August are comparable.

Figure 4.20 and Figure 4.21 show the vane shear strength vs. depth at the barge in the MLSB in May and August 2001, respectively. In May, the strength was 0.2 - 0.3 kPa from 5 to 7 m depth, 2 - 2.5 kPa from 9 to 11 m depth, and 3.5 kPa at a depth of 12m . In August, from 7.5 to 8.5 m depth, the strength was about 0.3 - 0.4 kPa. From 9.5 to 13.5 m depth, the shear strength ranged from 1.8 to 3.0 kPa. Below 14.5 m depth, the vane shear strength decreased greatly.

Figure 4.22 shows a plot of the vane shear strength vs. depth at the 3 stations in the MLSB in August 2002. At Sta. 3, the peak vane shear strength was close to zero, and there was no obvious increase in strength with depth. This indicates that the densification phenomenon of the MFT at Sta. 3 was not measured. At Sta. 1, the vane shear strength rapidly increased with depth from 8 to 12.5 m, and the maximum strength (at 12.5 m) was greater than 2 kPa. The shape of the depth profile of vane shear strength at Sta. 1 in 2002 is very similar to that of the depth profile of fines/(fines + water), as shown in Figure 3.4. This indicates that there existed dense MFT from 8 m to 15 m depth at this location. The vane shear strength was higher at the site in the south end of the pond and decreased toward the north end.

4.5 Steel Plate Penetration Tests

4.5.1 Introduction

In the MLSB the densification properties of the MFT are not uniform, due to different depositional environments such as temperature, different chemical and microbiological activities, and external disturbances, such as tailings discharge and pumping. To understand the mechanism for the rapid densification phenomenon observed in some locations in the MLSB, the distribution of the MFT properties, both laterally and vertically, must be determined. The steel plate penetration (SPP) test is a simple, practical, and effective method to investigate the range of the dense MFT over a wide region, as well as to estimate its shear strength. Guo et al. (2002 and 2004) describe the test method and application on geotechnical investigation in oil sands tailings.

Figure 4.23 shows a sketch of the steel plate penetration test and Figure 4.24 gives a photo of the test on the boat. The steel plate is connected to a wire rope which goes over a pulley/depth encoder. The upward drawing force of the wire rope is negligible. On average, the penetration rate is about 30 cm/sec. When a relatively stiff layer is encountered, the penetration rate is adjusted if necessary.

When the MFT layer is sufficiently dense, the steel plate will stop penetration and settle at very slow rates. If the plate is penetrating at a rate of less than 5 cm/minute the test is considered complete and the depth is recorded. The plate size and weight are also confirmed at that time. The next heavier plate is then tested using the same procedure. If there is no "stiff" layer to stop the penetration, the steel plate will drop down to the pond bottom. Plates with different weights are used. In this way, the "dense" layers can be found, and the un-drained shear strengths can be approximated.

The steel plate penetration tests were carried out in 2000, 2001, and 2002. In 2000, steel plates with two different sizes were used to penetrate the MFT, but the irregular shapes and large thicknesses of the plates restricted their applications. The steel plates were re-designed with thin steel plate in a circular shape to reduce the side friction acting on them. Four steel plates

(made by the University of Alberta) with different shapes and weights, as summarized in Table 4.4**,** were used to penetrate the MFT at 55 locations throughout the pond in 2001. After the successful application of the steel plate penetration tests in 2001, five similar steel plates with base stresses of 0.5 kPa, 1.0 kPa , 3.0 kPa, 5.0 kPa, and 10 kPa, were made at Sycrude's Tailings Department as useful investigation tools for oil sands tailings. In this section, the results of the steel plate penetration tests in 2001 and 2002 are presented. The calculation method of the un-drained shear strength using the steel plate penetration test is shown in Appendix B.

4.5.2 Test Results of Steel Plate Penetration Tests

The results of the steel plate penetration tests can be used to determine the extent of the dense MFT zone, both laterally and vertically. The un-drained shear strengths can be approximated.

Figure 4.25 shows the penetration depths of Plate 1 from August 2001. At the time, the net base stress was 2.2 kPa. The tests were performed at 55 sites throughout the pond. In Zone A, the penetration depths were less than 8 m; in Zone B the penetration depths were greater than 8 m.

Figure 4.26 shows the penetration depths of Plate 2 with a net base stress of 3.8 kPa. In Zone A, the penetration depths at most of the sites were less than 10 m. In Zone B, the penetration depths at most of the sites were greater than 10 m.

Figure 4.27 shows the penetration depths of Plate 3 where the net base resistance was 5.4 kPa. In Zone A, the penetration depths at most of the sites ranged from 5 m to 15 m. In Zone B, the steel plate penetrated to the bottom of the pond at most sites. The un-drained shear strengths at the locations where the steel plates were stopped were greater than 1.0 kPa. This bearing capacity analysis calculates a lower bound of the un-drained shear strength of the MFT, since it is possible that a heavier steel plate might also stop at the layer.

Figure 4.28 shows the penetration depths of Plate 4 when the net base stress is 10.3 kPa. In Zone A, the penetration depths at most sites ranged from 8 m to 17 m. In Zone B, the steel plate penetrated to the bottom of the pond at most sites. The undrained shear strengths at the locations where the steel plates were stopped were greater than 2.0 kPa.

These figures show that there was a distinct difference in the densification of the MFT in different parts of the pond. The dense MFT was found mainly in the southwestern part of the pond ranging from 8 m to 15 m depths. The ranges of the dense MFT in the pond, as determined by the four plates, were very similar.

In the field investigation of August 2002, the steel plate penetration (SPP) tests were performed at three sites. Five different plates made by Syncrude's Tailings Department were used for each site. The base stress of the plates were 0.5 kPa, 1.0 kPa , 3.0 kPa, 5.0 kPa, and 10 kPa . The depth below the water surface at which each plate stopped is shown in Table 4.5.

Figure 4.29 shows a diagram of the penetration depths of the five steel plates with different base stresses. At Sta. 1 and Sta. 2 the steel plate with 10 kPa base stress stopped at a depth of 10-11 m. However, at Sta. 3, the 10 kPa steel plate went down to the bottom.

The results of these steel plate penetration tests show that rapid densification has progressed the most in the southern region of the pond, with an approximate area extent of about 3 km^2. The depths of the dense zone ranged from 8 to 15m.

4.6 Piezometer and Earth Pressure Measurements

4.6.1 Introduction

Natural stress states and changes during microbial activity and artificial activities, such as those brought about by the pumping operation, may be

closely connected to the gas migration, water drainage, densification and strength of the MFT. Due to microbial activities and the pumping operation, the stress states of the MFT are very complex. To understand the mechanisms leading to the phenomenon of rapid densification, it is necessary to take into account these stress states.

In situ earth pressures (both lateral and vertical) and pore water pressures were measured to determine the stress states in the MFT in 2001 and 2002. In 2001, lateral earth pressures were measured at four locations near the pumping barge, as summarized in Table 4.6. Lateral and vertical earth pressures, as well as pore water pressures were measured at Stations 1-3 in 2002, as shown in Table 4.7.

An IRAD GAGE, a vibrating wire oil-filled earth pressure cell, was used in 2001. The aspect ratio (the ratio of cell thickness to active diameter) of which was 0.03, and the stiffness was roughly 20,000. An earth pressure cell with a small aspect ratio has the least disturbance on the stress field in the MFT. There are two types of readings with this cell: normal mode readings, and linear mode readings. For these tests, the linear mode reading was selected. When temperature measurements are required, thermistors, mounted inside the pressure housing, can be read with the IRAD GAGE thermistor read-out unit. However, temperature changes were not significant during these tests, therefore no thermistor readings were made. During testing, the earth pressure cell penetrated into the MFT under its self-weight. In the very dense MFT layer, the earth pressure cell was pushed into the required depths.

In 2002, vibrating wire-line (VW) piezometers and vibrating wire total pressure cells from the Slope Indicator Company, were used to measure the pore water pressures and horizontal and vertical pressures at different depths in the MFT. The VW piezometer converts water pressure to a frequency signal via a diaphragm and tensioned steel wire. The piezometer is designed so that a change in pressure on the diaphragm causes a change of tension in the wire. When excited by a magnetic coil, the wire vibrates at its natural frequency. The vibration of the wire in the proximity of the magnetic coil

generates a frequency signal that is transmitted to the readout device. The readout device processes the signal and displays a reading. The VW piezometer is equipped with two sensing elements: a pressure transducer and a temperature transducer. The pressure transducer is attached to the fluid–filled total pressure cell. Soil pressure on the walls of the cell is converted to fluid pressure and measured by the piezometer.

Before testing, the piezometer was saturated with de-aerated water. During testing, the piezometer was attached to the total pressure cell, as shown in Figure 4.30, at which time the relative position between the total pressure cell and the piezometer was measured. Wire lines connected the piezometers and the total pressure cells to the readout, which was placed on the boat or the barge. The total pressure cell penetrated into the MFT under self-weight. At the very dense MFT zone, the earth pressure cell was pushed into the required depths. The total pressure cell and the piezometer remained in the MFT until a stable reading was achieved.

At the pump barge, the vertical stress was measured by placing the total pressure cell horizontally. This was done using a specific penetration method. The total pressure cell was connected to a series of steel pipes, and was then allowed to slip into the MFT at a certain angle relative to the horizontal. This took place until the pipes became vertical (i.e. the pressure cell became horizontal). The depths of the cell and the piezometer were then measured. The piezometer was bound to the total pressure cell before penetration. This made the total pressure cell and piezometer stay at the same depth during testing. Figure 4.31 shows a photo of the total pressure cell before slipping into the MFT.

4.6.2 Calibration

Before testing in 2001, the IRAD GAGE earth pressure cell was placed into water to perform the calibration. Because the lateral stress in water is equal to the hydrostatic pressure, the calibration relationship between the readings and the lateral pressure can be determined. The location for the calibration test

was the pumping barge in the MLSB. The interface of the MFT was more than 6 m below the surface of the water. The calibration curve is shown Appendix D.

$$P = 0.4414\ F - 2631.2$$

Where P is the lateral earth pressure (kPa), F is the output readings (mv).

The VW earth pressure cells and piezometers, used in 2002, were calibrated by the manufacturer, Slope Indicator Company. The pore pressure or the total pressure can be calculated using the following equation:

$$P = A \times F^2 + B \times F + C$$

where, P is the pore pressure (or total pressure) in kPa, and F is frequency readings (mv), and A, B, and C are conversion factors with reference to standard atmosphere. The calibration coefficients of the piezometers and total earth pressure cells used in 2002 are shown in Appendix D. The calibrations were conducted at temperatures ranging from 21.9 to 23^{o}C and standard atmospheric pressure. When the in situ temperatures were different from the calibration temperatures, the measured pressures were calibrated. The temperature calibration coefficients are also shown in Appendix D.

4.6.3 Lateral Earth Pressure Measurements in 2001

Lateral earth pressures at different depths were measured at four locations in 2001, as summarized in Table 4.6. Locations 1-3 were close to the pumping barge and location 4 was about 650 m north of the barge.

Before the testing was complete, the pressure cell was emplaced at a depth of 14.6 m (below the water surface) to check the response rate of the pressure cell to the equilibrium of the pressure in the MFT. Readings were made twice, two hours apart. The measurements indicate that the two readings are very close. Thus, the lateral stress cell equilibrates to the stress state quickly

enough that it is possible to do continuous measurements along a depth profile within a short period.

Figure 4.32 shows the results of the lateral pressure measurements at Location 1 (near the pump barge). Readings were taken as the pressure cell was emplaced at different depths. Measurements were repeated as the cell was removed. There was no MFT transfer via pump barge during testing. The data measured during emplacement and removal shows notable agreement. Above 6 m depth, the lateral stresses in the MFT were almost equal to the hydrostatic pressure. These measurements show that the interface of the MFT was about 6 m below the water surface.

Since any effective stress in the MFT would be very small (if in existence), and the earth pressure coefficient at rest is close to 1.0 **(**Guo et al., 2002), the total lateral pressure measurements can be used to approximate the unit weights of the MFT at different depths. Figure 4.33 shows the estimated unit weights of the MFT at Sta. 1:

- Above 6 m depth the unit weights are close to 9.8 kN/m^3
- From 6 m to 10 m the unit weights of the MFT increase rapidly from 9.8 to 16.3 kN/m^3.
- From 10 m to 14 m depth, the unit weights fluctuate around 15.5 kN/m^3.
- From 14 m to 15 m depth, the unit weights of the MFT rapidly increase again.
- Below 15 m depth, the estimated unit weights are greater than 17.0 kN/m^3.

The rapid increase in density of the MFT from 6 m to 10 m indicated the densification phenomenon. The densified layer ranged from approximately 9 m to 14 m depth. The rapid increases below 14 m depth might be related to the increases in content of coarse (sand) materials and decreases in gas content within the MFT.

Figure 4.34 shows the influence of the pumping operation on the total lateral pressure of the MFT near the pumping barge. The pressure cell was placed at a depth of 10.3 m, approximately the same depth as the intake depth of the pump. Before pumping, a reasonably stable lateral earth pressure of 115.2 kPa was recorded. After pumping was initiated, the lateral earth pressure decreased. During the initial period, some fluctuations, caused by adjustments of the pump intake elevation, were evident. When the intake elevation was close to the elevation of the earth pressure cell, the measured lateral earth pressure decreased. After about 30 minutes of pumping, the lateral earth pressure reached a stable value of 102.6 kPa, a decrease of 12.6 kPa. Clearly, the lateral earth pressure cell was sufficiently sensitive to record small fluctuations in earth pressure in the soft MFT. The pumping operation can be said to have significantly changed the stress state of the MFT near the barge.

Figure 4.35 and Figure 4.36 show the lateral earth pressure measurements and the estimated unit weights at Location 3, which was close to Location 1. Similar results as those found at Location 1 can be observed.

Figure 4.37 compares the results of lateral earth pressure measurements at Location 3 (near the barge) and Location 4 (about 650 m north of the barge). Above 7 m and below 11 m depth the results at the two locations are consistent. But from 7 m to 11 m depth, the lateral earth pressures at Location 3 were less than those at Location 4. The maximum difference for the same depth between the two sites was about 9 kPa. This might be caused by the pumping operation, since pumping was occurring during testing and Location 3 was closer to the pumping barge. The decrease of lateral earth pressures near the barge during the pumping operation can be explained by: (1) a large pumping cone possibly forming near the intake point, so that closer to the intake point, the MFT interface becomes deeper; (2) the MFT structure being disturbed and becoming loose during the pumping operation. This might have reduced the confining pressure in the MFT.

4.6.4 Piezometer and Total Earth Pressure Measurements in 2002

4.6.4.1 Introduction

Although the total lateral earth pressures were measured in 2001, the stress states, especially that of the effective stress, were still not clear. Most of the tests in 2001 were focused near the pumping barge. The stress conditions at other parts of the tailings pond were unknown. In order to better understand the stress conditions in the tailings pond, more tests, including the measurements of vertical and lateral earth pressure, and pore water pressure, were performed in 2002.

4.6.4.2 Total Lateral Earth Pressure and Pore Water Pressure Measurements

To measure the total lateral pressure of the MFT, a total pressure cell was pushed down to the required depth with the diaphragm surface oriented vertically. The piezometer was bound together with the total pressure cell, approximately 30-40 cm above the centre of the total pressure cell.

Figure 4.38 shows the results of the total lateral pressure tests at 9.9 m, and the pore water pressure tests at 9.47 m depth below the water surface at Sta.1. The total lateral pressure at 9.9 m was 105.5 kPa, and the pore water pressure at 9.47 m was 103.2 kPa (at 9.9 m the pore water pressure was approximately 107.6 kPa). Given the precision of the total pressure cell and the piezometer, the difference between the total lateral pressure and the pore water pressure was small.

The results of the total lateral pressure and the pore water pressure tests at the three stations are summarized in Table 4.8. Figure 4.39 shows a comparison of the lateral earth pressure and pore water pressure at different depths of the three stations. From these results, it can be seen that the total lateral pressure was close to the pore water pressure at each depth for all three of the sites. The detailed test results at different depths of the three locations are shown in Appendix C.

Since the effective stress in MFT is small (if, in fact, there is any effective stress), the pore water pressure at each depth is close to the total vertical pressure. The unit weights of the gassy MFT can be approximately determined from these readings. The unit weights calculated from the lateral pressure and pore water pressure measurements are presented in Table 4.9. For each depth, the unit weight of MFT, determined by lateral earth pressure, is close to that determined by pore water pressure. At Sta.2, the unit weights from 10 to 11 m obviously increased, indicating the existence of a dense MFT zone at this site.

4.6.4.3 Total Vertical Pressure and Pore Water Pressure

In order to determine the effective stress in the MFT, the total vertical pressure and pore water pressure were measured at selected depths. A special penetration method, as described above, was used to ensure the diaphragm surface was horizontal and the MFT was minimally disturbed during tool emplacement. In this test the total pressure cell and the piezometer were at the same depth.

Figures 4.40 and 4.41 show the test results of the total vertical pressure and pore water pressure measurements at a depth of 8.19 m, and near the pumping barge (Sta.1). Figures 4.42 and 4.43 show the results at a depth of 8.75 m, and near the pump barge. These tests were performed in August and September 2002. The results are summarized in Table 4.10. The data indicate a small difference between the total vertical pressure and the pore water pressure.

If effective stress existed in the dense MFT, it was likely small. The precision of the measurements was about ± 0.5%, and any disturbance from tool emplacement might also have affected the results. From the total vertical pressure measurements at the two different depths at Site 1 the average unit weight of the MFT can be calculated. The average unit weight from 8.19 m to 8.75 m was approximately 11.96 kN/m^3. The total pressure cell had difficulty

penetrating further into these depths. The operative stress and effective stresses at deeper levels of the dense MFT need to be further investigated.

4.7 Cone Penetration Test (CPT)

4.7.1 Introduction

In a Cone Penetration Test (CPT), a cone mounted on the end of a series of rods is pushed into sediment at a constant rate. Continuous or intermittent measurements of the resistance of the sediment to the penetration of the cone are made. The resistance acting on the cone (q_c), and the sleeve friction (fs) can both be measured. With a piezocone penetrometer (CPTU), pore pressure can be measured as well.

The first cone penetrometer tests were carried out in Holland in 1932, by P. Barentsen . In 1965, an electrical cone was developed by Fugro, in cooperation with the Dutch state Research Institute. Since then, CPT/CPTU tests have been important methods of geotechnical investigation. They can provide continuous or near continuous data, and quick, cost efficient measurements. The standard rate of CPT penetration is 2 cm/sec. The CPT parameters are usually used to determine the stratigraphy, undrained shear strength (C_u), bearing capacity of shallow or deep foundations, or deformation modulus of sediment. The CPTU test can be used to determine the pore pressure, hydraulic gradient, permeability, and coefficient of consolidation. CPT/CPTU tests on land are common. Some applications of geotechnical investigation with CPT or CPTU were reported on tailings dams or on the beach of tailings ponds (Campanella, , 1984; Vidic, 1995),but few CPT tests have been performed on fine tailings in situ.

Because the MFT is a high water content slurry, the skin friction is small. Measuring skin friction requires high accuracy and sensitivity in the equipment. Therefore, in this test only the tip resistance was measured. The cone resistance was converted into electrical signals which were transmitted through a cable inside the hollow penetrometer rods. The CPT tests were done

from a special test boat. The cone was emplaced under self-weight of the steel rods and sleeves at a controlled rate using a cable and reel. During penetration, the cone resistance was measured, and the corresponding penetration time and depth were recorded.

Due to the inner geometry of a cone penetrometer, the ambient pore water pressure acts on the shoulder area behind the cone and on the ends of the friction sleeve. The effect is usually referred as "the unequal area effect" (Lunne et al., 1997**)**. For cone resistance, the unequal area is represented by the cone area ratio *a*, which is approximately equal to the ratio of the cross-sectional area of the load cell, divided by the projected area of the cone. The corrected total cone resistance (q_t) is given by:

$q_t = q_c + u\,(1-a)$

where, u is the pore pressure acting behind the cone, and *a* is the cone area ratio.

4.7.2 Calibration

The calibration between cone resistance (q_c) and the measured output (mv) was done by applying a series of loads to the cone and recording the readings. The calibration results of the 1.5" cone used in 2000 and 2001 are shown in Appendix D.

In order to determine the cone area ratio, *a*, the penetrometer is put into water in a calibration vessel. Water pressure (u) is applied, and the corresponding cone resistance (q_c) is measured. By plotting the relationship between applied water pressure and measured resistance, the area ratio can be determined **(**Lunne et al., 1997). The calibration result of the area ratio, *a,* of the 1.5" cone is shown in Appendix D. In 2000, both 1.5" and 2" cones were used. However, because the calibration (area ratio) for a 2" cone is not available, the data of the 2" CPT cannot be used.

4.7.3 Test Results

Cone penetration tests were conducted in both the MLSB and WIP. Some typical results of the tests are presented in this section. From the cone penetration tests the CPT profiles (cone resistance (q_t)-depth (h)) can be plotted. Approximations of the un-drained shear strength are obtained from the total cone resistance, given by the following equation (Lunne et al., 1997):

$$s_u = \frac{(q_t - \sigma_{v0})}{N_{kt}}$$

Where, s_u is the undrained shear strength estimated from CPT profiles

σ_{v0} is the total in situ vertical stress

q_t is the corrected total cone resistance

N_{kt} is the empirical cone coefficient with an average of 15 assumed

When the undrained shear strength is estimated using the above equation, the in situ vertical stress is determined by assuming the MFT is saturated. Due to the existence of gas bubbles, the actual in situ bulk densities might be different from the assumed values.

Figure 4.44 shows a CPT profile at the southern end of the MLSB. The MFT interface was about 3.5 m below the water surface in this case. From 3.5 m to 14 m, the cone resistance increased approximately linearly with depth. But from 14 m to 17 m, the cone resistance greatly increased, showing a relatively dense MFT layer.

From the results of the cone penetration test, shown in Figure 4.44, the undrained shear strength can be calculated. Near the site of the CPT test, steel plate penetration (SPP) tests were also conducted. The un-drained shear strength can also be estimated using the SPP results, using the method shown in Appendix B. The results are shown in Figure 4.45. There is notable agreement between the undrained shear strengths from the CPT and from the steel plate penetration tests in the dense MFT for the higher shear strength material.

Figure 4.45 shows a dense MFT layer ranging from 12 m to 17 m at this site. The maximum undrained shear strength estimated from the CPT was greater than 2.0 kPa. Figure 4.46 and Figure 4.47 shows typical CPT test results in the northern part of the MLSB. The cone resistance is shown to have increased linearly with depth. Above 17 m depth, the un-drained shear strengths of the MFT were close to 0. This shows that there was no dense MFT layer in the northern part of the MLSB.

4.8 Mapping of Gas Bubble Distribution in the MLSB

Since the mid 1990s, the microbial activity in some parts of the MLSB has significantly increased. This microbial activity generates gas. When gas accumulation within the MFT reaches a critical state, part of the generated gas will be released from the MFT. The distribution of the gas bubbles on the water surface, and the ongoing gas bubble release, directly reflect the microbial activity within the MFT.

Field observations were used to map the gas bubble distribution in 2002. The presence and relative number of the gas bubbles, and the ongoing gas bubble release rate were characterized. The coordinates of the boundary locations were determined using a GPS. Two zones were outlined, as shown in Figure 4.48. Zone B is the region with intense gas activity in which a lot of gas bubbles were visible on the surface, and significant ongoing gas bubble release occurred. The average distance between neighboring gas bubbling points was about 1-2 m. Zone A had only slight gas activity with fewer gas bubbles visible on the water surface and very infrequent gas bubble release. The average distance between neighboring gas bubbling points was more than 10 m. The photos of the water surfaces at Zone A and Zone B are shown in Figure 4.49 and Figure 4.50. The results of gas bubble distribution mapping indicate that the microbial activity at the southern part of the pond was more intense than that at the northern part.

4.9 In Situ Temperature Measurements

The temperature of MFT has an important influence on microbial activity and therefore may impact the gas production and densification rate. Previous temperature measurements in MFT at the MLSB were made primarily in recovered MFT samples. The temperatures measured by this method were affected by those of the atmosphere. The in situ temperatures of MFT can be measured quickly and accurately using an electrical thermister. In situ temperatures were measured at different depths at the three stations of the MLSB in September 2002. Before field testing, the thermister was calibrated in a temperature-controlled chamber. The temperatures and corresponding output readings were recorded. The calibration results are shown in Appendix D.

Figure 4.51 shows that there were significant differences in the temperatures of the MFT above 15 m depth among the three sites, with temperature increasing from the north to the south. From 10 m to 15 m, the temperatures at Site 1 were around 20^{o}C, while at Site 3 the temperatures were less than 14^{o}C.

The in situ temperature measurements matched the results of historical monitoring data, as demonstrated in Chapter 3. The factors causing the obvious temperature differences among the three stations have been discussed in Chapter 3. The temperature differences were likely an important aspect leading to different levels of microbial activity in the tailings pond.

4.10 Discussion and Conclusions

The field investigations performed from 2000 to 2002 have greatly improved our understanding of the rapid densification phenomenon occurring at the MLSB. In this section, the results from the field investigations are discussed and some conclusions are drawn.

The comprehensive field investigations, including sampling, field vane shear tests, steel plate penetration tests (SPP), piezometer and total earth pressure measurements, and cone penetration tests (CPT), have clearly verified the

presence of MFT which has rapidly become more dense at the southern part of the MLSB.

There existed obvious vane shear strengths from 8 m to 15 m at Sta. 1 and Sta. 2 of the MLSB. The maximum vane shear strength at Sta. 1 was more than 2 kPa. At Sta.3 of the MLSB, the vane shear strength of the MFT was negligible at the testing times. The results of the field vane shear tests demonstrate that the "high strength" MFT was mainly at the southern part of the MLSB, ranging from 8 m to 15 m below the water surface.

The "high strength" MFT had a moisture content of about 65%, which is close to the liquid limit of MFT (about 60%, according to Suthaker (1995)). Field observations of the MFT samples have shown that the dense MFT was close to a plastic state. According to Head (1989), at the liquid limit (I_L=1), the shear strength of a soil is abut 2 kPa. This value matches the results of the field vane tests in the dense MFT.

The steel plate penetration test (SPP) is an effective tool to identify the presence and range of the rapidly dense MFT. The undrained shear strengths of the dense MFT can be approximated from these measurements. The successful application of the SPP in the MLSB shows the useful potential of this testing method in future investigations. SPP tests showed that the MFT densification zone was primarily at the southern part of the MLSB. The depths of densification ranged from 8 m to 15 m.

The total lateral stress measurements in the MFT can be indirectly used to calculate the unit weights (or density) of the gassy MFT at different depths. The rapid increase of the unit weights from 8 m to 15 m was caused by the rapid densification of the MFT. The higher unit weights of the MFT below 15 m depth might be caused by the higher coarse particle content and relatively low gas content.

In situ earth pressure and pore water pressure measurements show that the vertical pressure, lateral pressure and the corresponding pore water pressure

were very close at a certain depth of the MLSB. If there existed effective (or operative) stress, it should be a very small value (at 8-9 m at the pumping barge it was about 0.5-1.0 kPa). Further field tests are required to measure the effective (operative) stress at the lower part of the dense MFT layer.

The pumping operation can significantly change the stress state within the MFT near the pumping barge. If this acts to accelerate the gas bubble release, it could contribute to an increase in the density of the MFT, thus benefiting its densification.

Cone penetration tests (CPT) can be used to calculate the undrained shear strength of the MFT empirically. The results of the CPT show that there was obvious shear strength in the dense MFT at the southern part of the MLSB, and that the undrained shear strengths of the MFT at the northern part were negligible at testing times.

Gas bubble mapping demonstrates a strong correlation between the intense microbial activity zone and the zone of rapid densification (as indicated by the Steel Plate Penetration tests). It supports the hypothesis that microbial activity and corresponding gas bubble generation, migration, and release, can contribute to the acceleration of densification of MFT.

The temperatures of the MFT increased significantly from the north to the south of the pond. The temperature difference might be one factor contributing to the non-uniform distributions of the microbial activity, and the correspondingly different densification rates throughout the pond.

Many large gas voids and bubbles existed within recovered samples of the dense MFT. The maximum void diameter observed was close to 5 mm. The gas bubbles tended to be surrounded by some bitumen blocks. The hydrocarbon was beneficial to the microbial activity and gas generation. Some evidence related to gas bubble cracking (or fissuring) and partial flooding was observed from the SEM images, and some macro-fractures were observed from the frozen sample. The fractures and the large gas voids might have

formed the drainage paths for the dewatering process necessary for the densification of MFT.

Table 4-1 Summary of the Field Investigations in the MLSB

Test Method	2000	2001	2002
Piston Sampling		6	3
Freeze Sampling			1
Vane Test		2	3
CPT	24	4	3
Piezo. Earth Press		2	4
SPP	24	55	3
Temperature			3
Gas Bubble Mapping			82

Table 4-2 Field Classifications Used for Characterization of the MFT

No.	Classification	Solids Content (%)	Properties
1	Light MFT	<30%	Thin slurry
2	Medium MFT	30~40%	Easily moves and deforms
3	Dense MFT	40~50%	Slowly or very slowly flows and deforms
4	Very dense MFT	50~65%	Holds a shape for a long time
5	Dense and sandy MFT	> 50%	Sandy when touching with hands. Difficult to keep shape. (Typically found below 15 m)

Table 4-3 Summary of the Field Vane Shear Tests in 2001 and 2002

Test Date	Location	Easting (m)	Northing (m)	Vane Size (mm)
May 25, 2001	MLSB Sta. 1	461927	6324940	60 × 120
August 18, 2001	MLSB Sta. 1	461934	6324932	60 × 120
August 20 2002	MLSB Sta. 1	461930	6324942	60 × 120
AUGUST 21 2002	MLSB Sta. 3	460042	6326983	60 × 120
August 22 2002	MLSB Sta. 2	460051	6326992	80 × 160

Table 4-4 Dimensions and Weights of the Penetration Plates Used in August 2001

Plate No.	Diameter (cm)	Area (cm^2)	Height (cm)	Volume (cm^3)	Weight (kg)	Resisting stress (kPa)
1	30	706.5	3	2295	18.1	2.2
2	20	314	5.2	1633	14.2	3.8
3	20	314	7.5	2355	20.0	5.4
4	20	314	15	4710	38.9	10.3

Table 4-5 Steel Plate Penetration Tests at the MLSB in 2002

Site No.	Northing (m)	Easting (m)	Penetration Depth (m)	Net Base stress (kPa)
1	461930	6324942	6.1	0.5
			7.2	1.0
			8.0	3.0
			9.1	5.0
			9.8	10.0
2	460051	6326992	3.7	0.5
			5.2	1.0
			6.1	3.0
			10.4	5.0
			11.0	10.0
3	0460042	6326983	3.4	0.5
			3.4	1.0
			19.2	3.0
			21.9	5.0
			25.6	10.0

Table 4-6 Lateral Stress Tests in the MFT in the MLSB in August 2001

Location No.	Date/time	Easting	Northing	Testing Depth	Pumping Operation
1	Aug.17, 15:00	461965	6324933	2 -18m	No pumping
2	Aug.18, 13:05	461934	6324932	10.3m	Start pumping
3	Aug. 19, 9:45	Close to the location of Test 1		4 -18 m	Pumping
4	Aug. 19, 11:00	461708	6325535	3 -17m	Pumping
Notes: Locations 1-3 were near the pumping barge, and Location 4 was about 650 m from the barge.					

Table 4-7 Summary of the Tests of the Piezometer and Total Pressure Cell in 2002

Site No.	Depth of Cell (m)	Serial No.	Depth of Piezometer	Serial No.	Total Stress Type
1	7	74515	6.55	74521	Horizontal
	8.65	74516	8.26	74520	
	9.9	74517	9.47	74518	
2	7.0	74515	6.55	74521	Horizontal
	9.6	74516	9.21	74520	
	11.1	74517	10.67	74518	
3	7.0	74515	6.55	74521	Horizontal
	10.0	74517	9.57	74518	
1	8.75	74515	8.75	74521	Vertical
	8.19	74517	8.19	74519	Vertical

Table 4-8 Summary of Total Lateral Pressure and Pore Water Pressure Tests in 2002

Site No.	Depth of Pressure Cell (m)	Total Lateral Pressure (kPa)	Depth of Piezometer (m)	Pore Water Pressure (kPa)
1	7	72.5	6.55	67.1
1	8.65	91.1	8.26	88.8
1	9.9	105.5	9.47	103.2
2	7	74.5	6.55	71.0
2	9.6	103.2	9.21	101.7
2	11.1	125.4	10.67	123.1
3	7	72.3	6.55	68.8

Table 4-9 Unit Weights of the MFT Determined by Lateral Earth Pressure and Pore Water Pressure Measurements

Sta. No	Depth Range (m)	Unit Weight from Piezometer (kN/m^3)	Unit Weight from Lateral Pressure (kN/m^3)	Average Unit Weight (kN/m^3)
1	7-8.65	12.7	11.3	11.95
1	8.65-9.9	11.9	11.52	12.12
2	7-9.6	11.8	11.1	11.41
2	9.6-11.1	14.65	14.8	14.32

Table 4-10 Summary of the Total Vertical Pressure and Pore Water Pressure Measurements in 2002

Test No.	Testing Date	Depth (m)	Total Vertical Pressure (kPa)	Pore Pressure (kPa)	Difference at Test End (kPa)
1	Sept.21, 2002	8.19	83.6	82.3	1.3
2	Aug.24, 2002	8.75	90.3	89.8	0.5

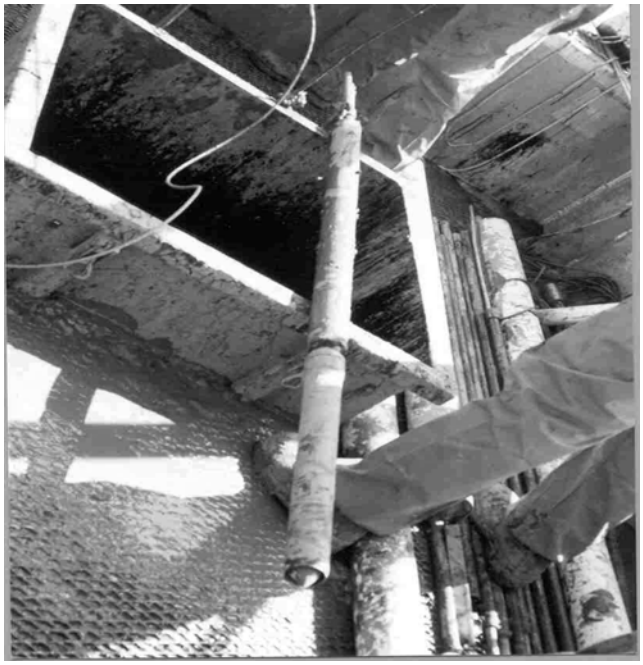

Figure 4-1 U of A Piston Sampler

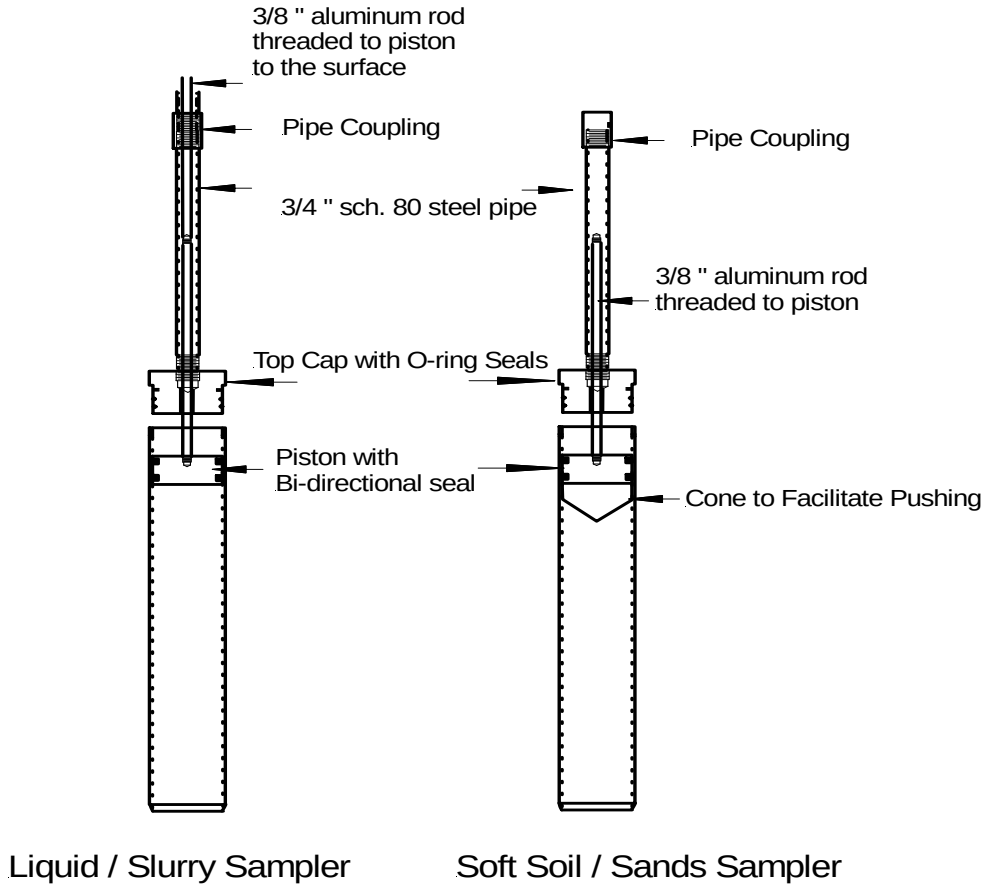

Figure 4-2 A Schematic of piston sampler

Figure 4-3 Piston Sample Recovered from 6 m Depth at the Barge in the MLSB

Figure 4-4 Dense MFT Recovered from 8 m Depth in the MLSB

Figure 4-5 Very Dense MFT Recovered from 10m Depth at the Barge in the MLSB

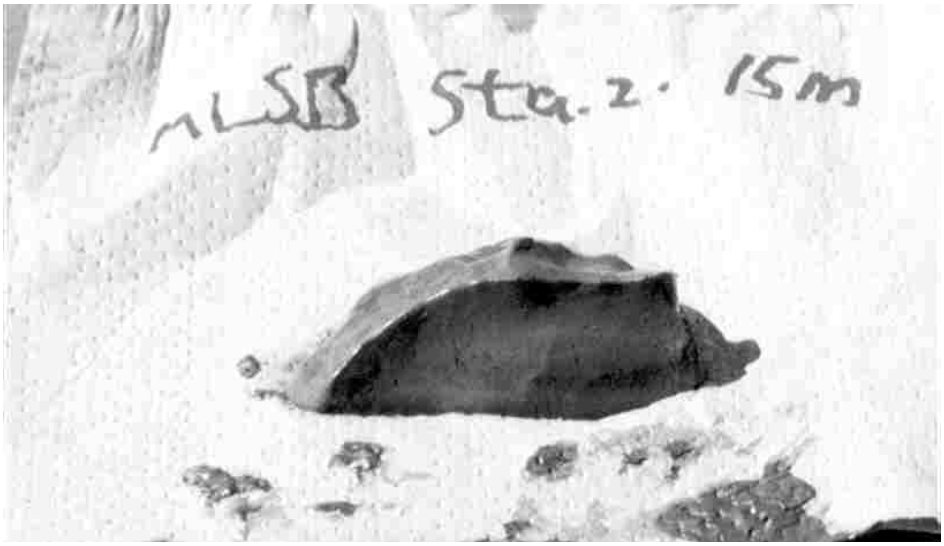

Figure 4-6 Very Dense MFT Recovered from 15m Depth in the MLSB

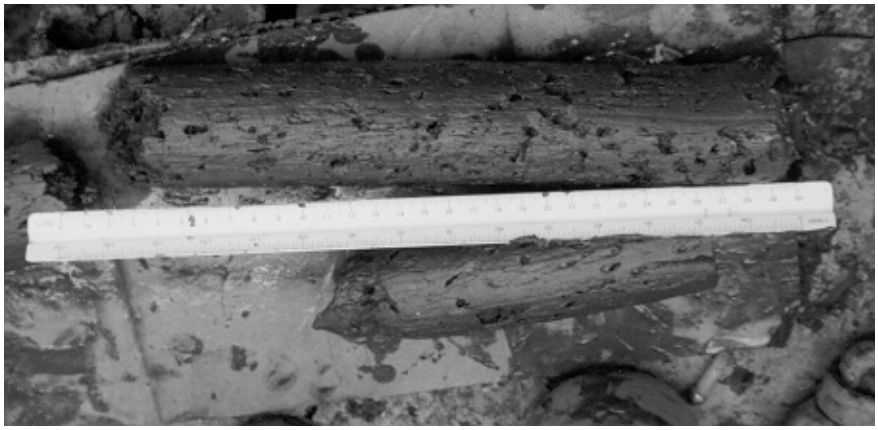

Figure 4-7 Piston Sample Retrieved from a Depth of 12 m near the Pumping Barge

Figure 4-8 Piston Sample Retrieved from a Depth of 12 m near the Pumping Barge

Figure 4-9 A Photo of the Frozen Sample at 9.2 m below the Water Surface at Sta. 1 in August 2001

Figure 4-10 Interior of a Frozen Sample at 9.2 m below the Water Surface at Sta. 1 in August 2001

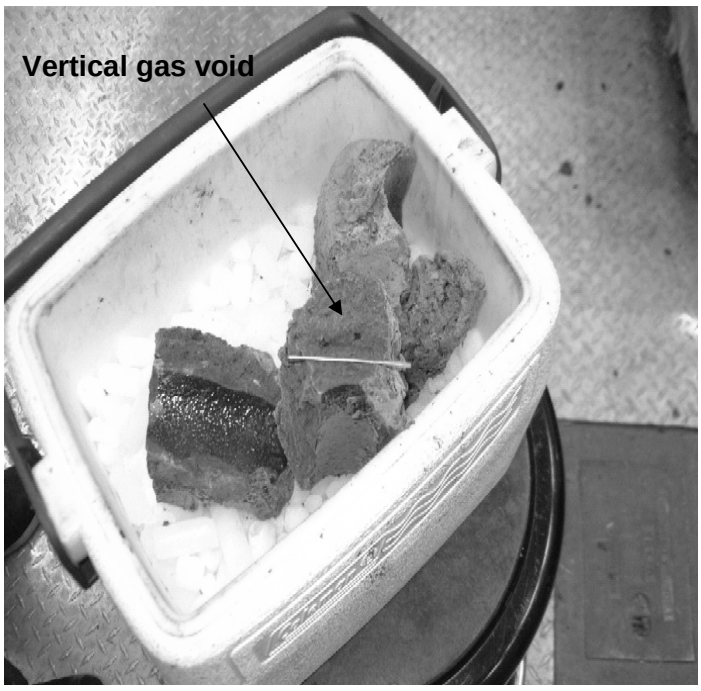

Figure 4-11 The Vertical Gas Voids in the Frozen Sample at 9.2 m below Water Surface at Sta. 1 in August 2001

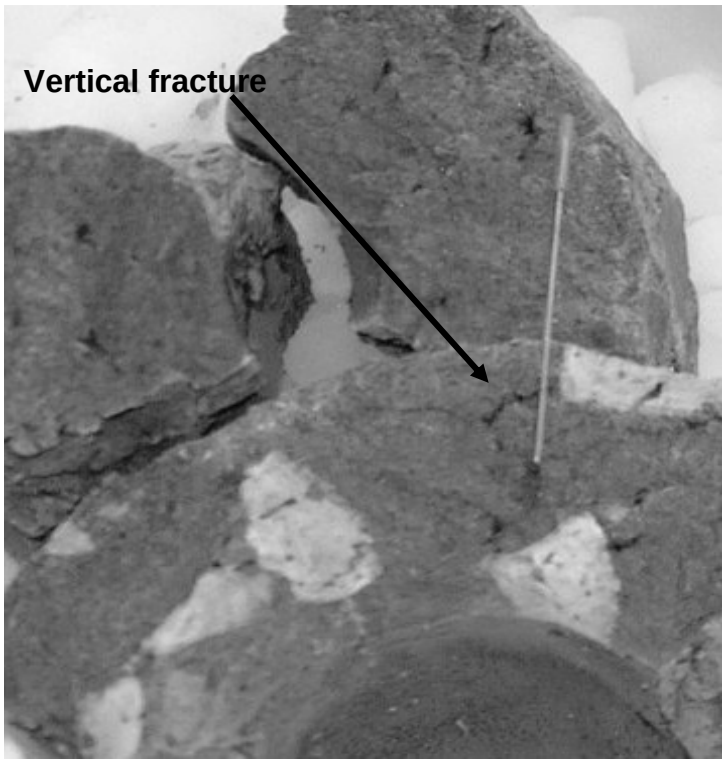

Figure 4-12 The Vertical Fractures in the Frozen Sample at 9.2 m below the Water Surface at Sta. 1 in August 2001

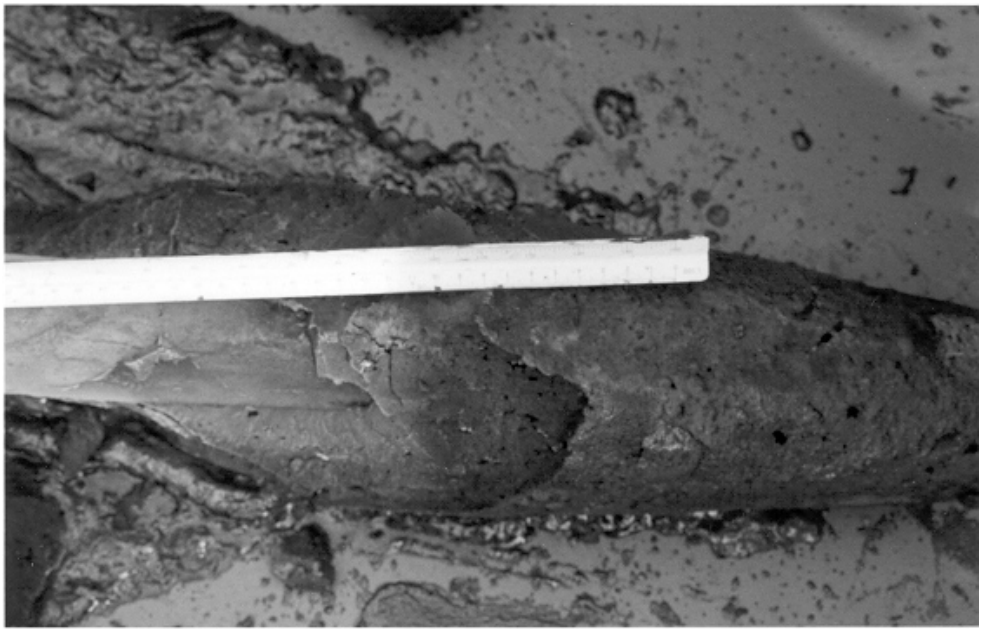

Figure 4-13 Frozen Sample Retrieved from 10m Depth near the Pumping Barge in August 2002

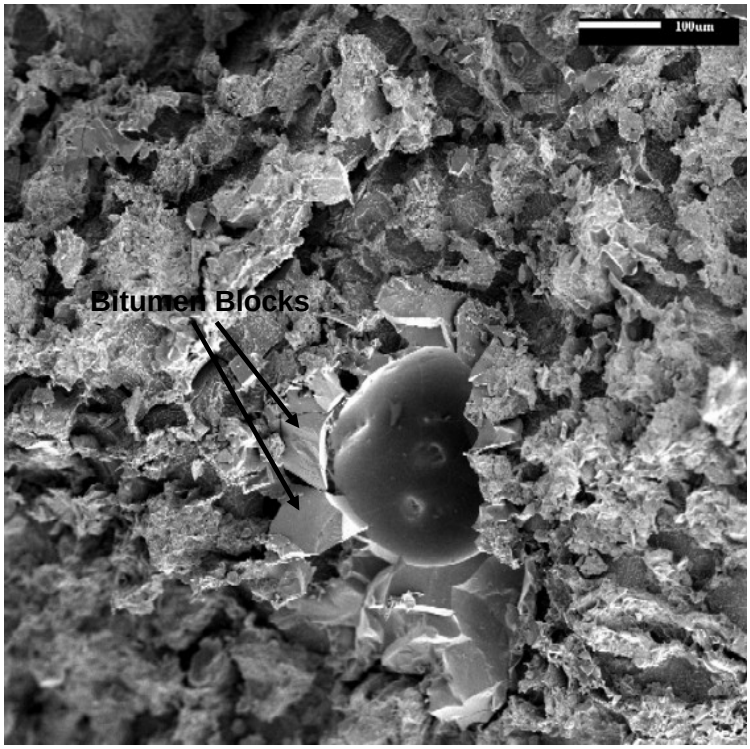

Figure 4-14 A SEM Image of the Frozen Sample at 10 m Depth below the Water Surface at Sta.1

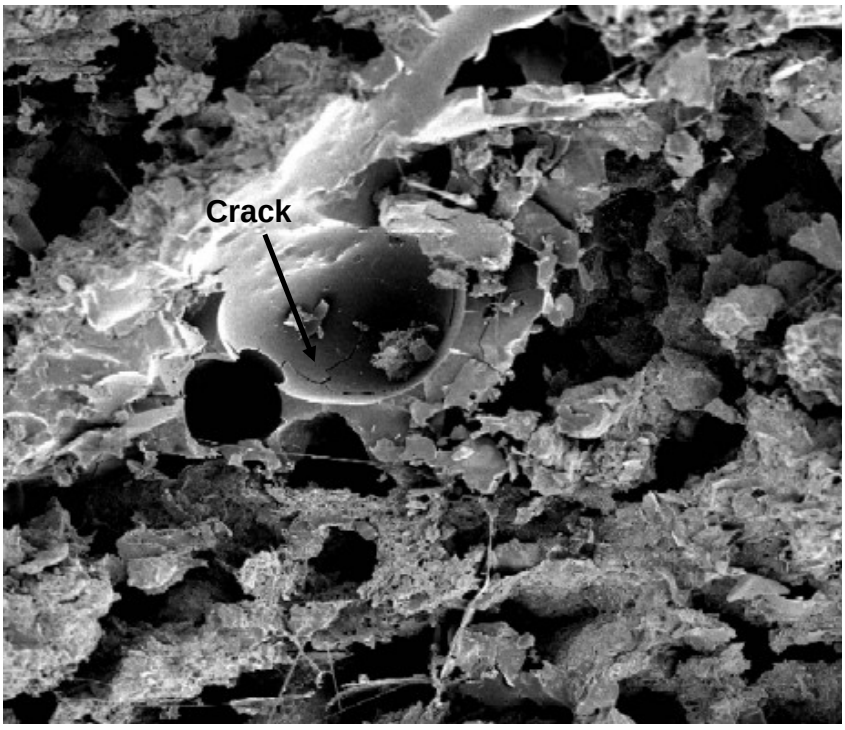

Figure 4-15 Large Gas Bubbles in the Frozen Sample at 10 m Depth below Water Surface at Sta.1
(the large gas bubble's size is about 150 μm)

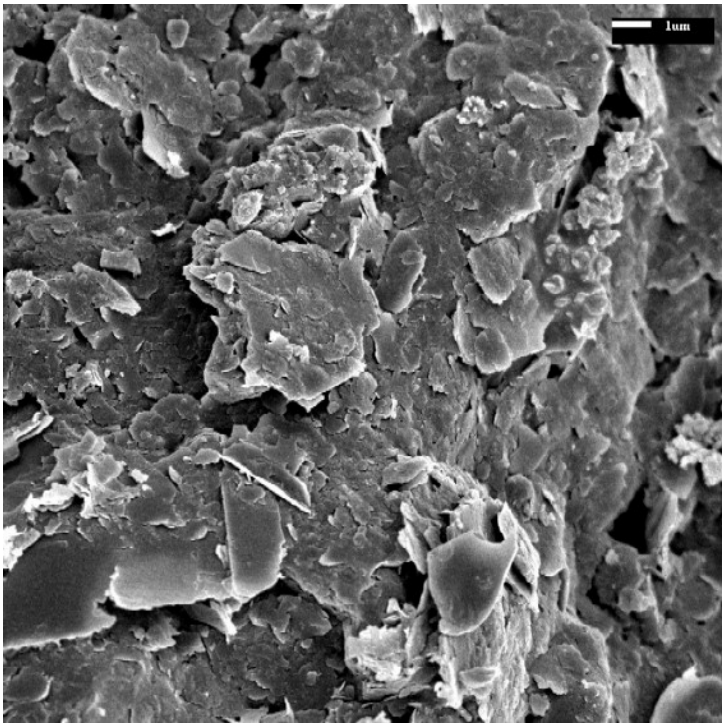

Figure 4-16 The Clay Platelets in the Frozen Sample at 10 m Depth below the Water Surface at Sta.1

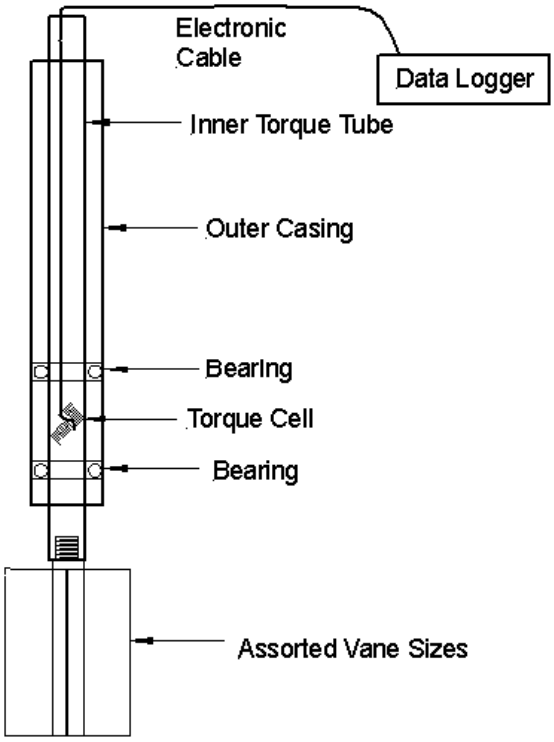

Figure 4-17 The Schematic of the Field Vane Test Apparatus

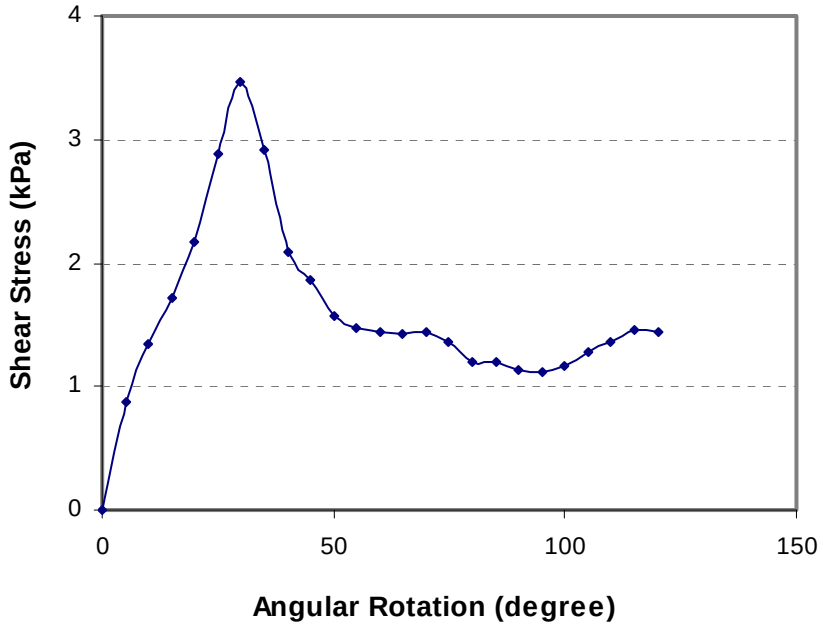

Figure 4-18 Vane Shear Test at 12.0 m Depth below the Water Surface at the Barge of the MLSB in May 2001

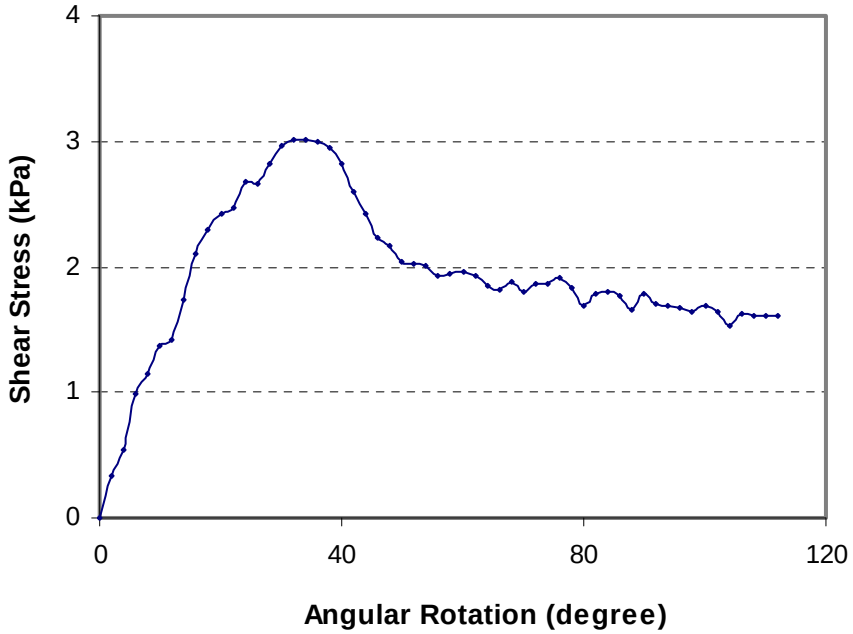

Figure 4-19 Vane Shear Test at 12.8 m Depth below the Water Surface at the Barge of the MLSB in August 2001

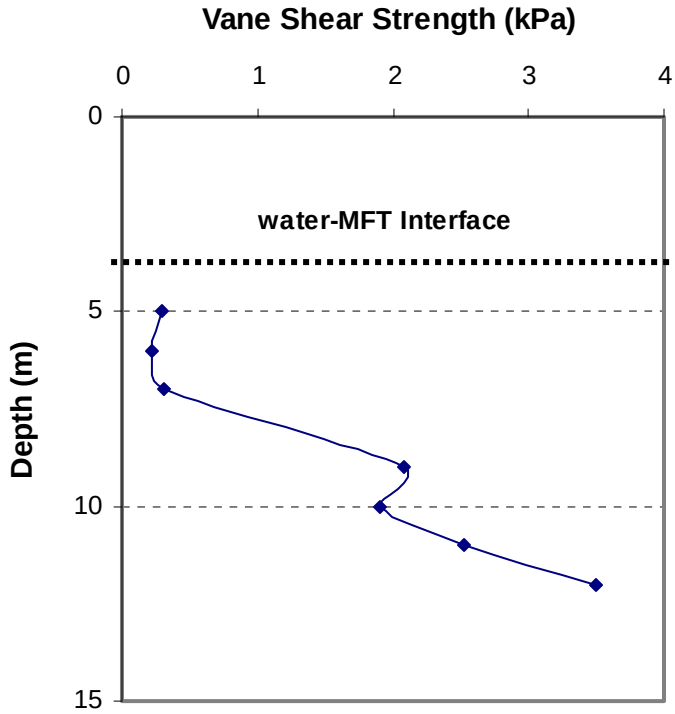

Figure 4-20 Vane Shear Strength vs. Depth below Water Surface at the Barge of the MLSB in May 2001

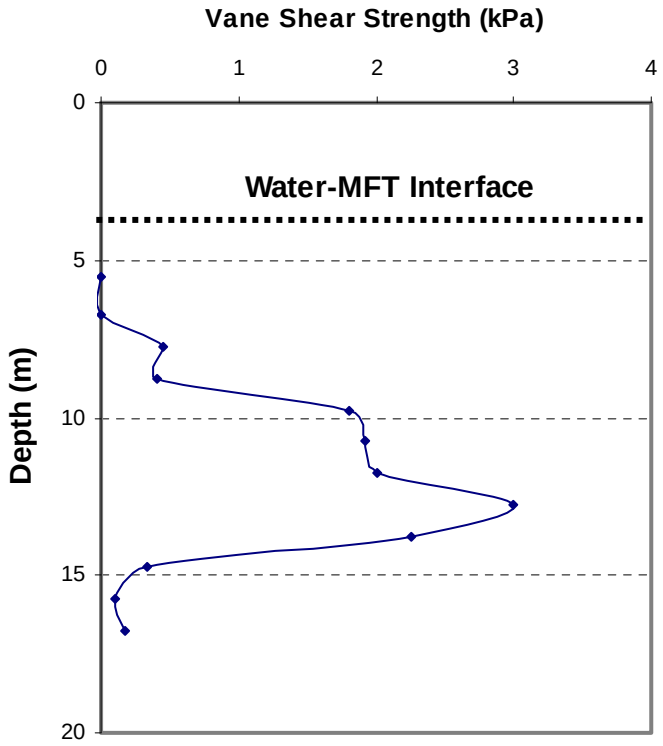

Figure 4-21 Vane Shear Strength vs. Depth below Water Surface at the Barge of the MLSB in August 2001

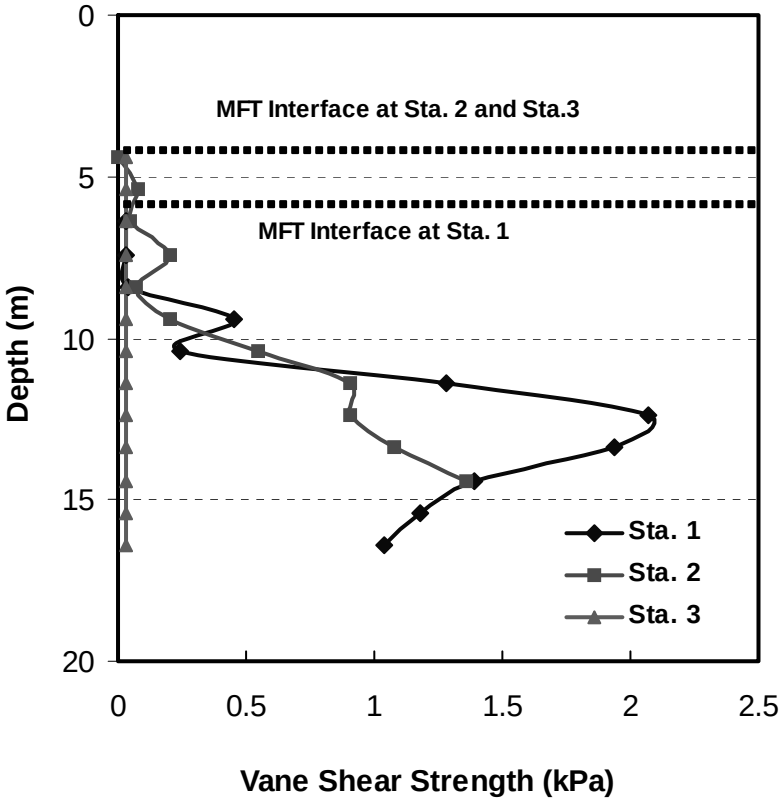

Figure 4-22 Depth Profiles of Vane Shear Strength at the three Stations in August 2002

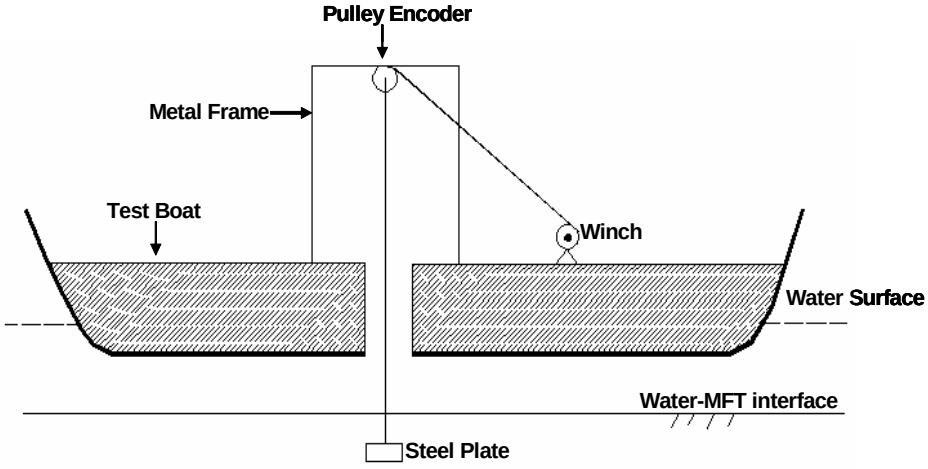

Figure 4-23 A Sketch of the Steel Plate Penetration Test

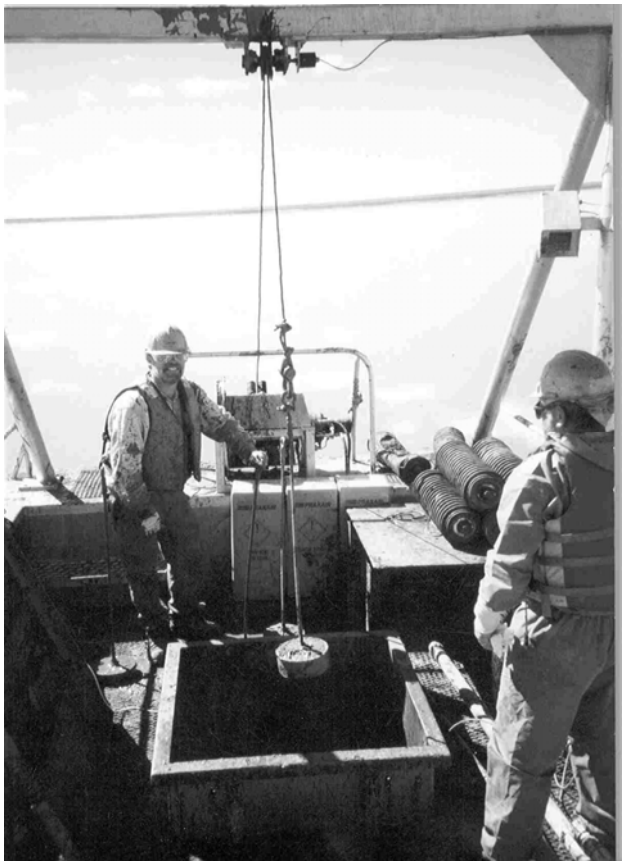

Figure 4-24 Steel Plate Penetration Test at the MLSB

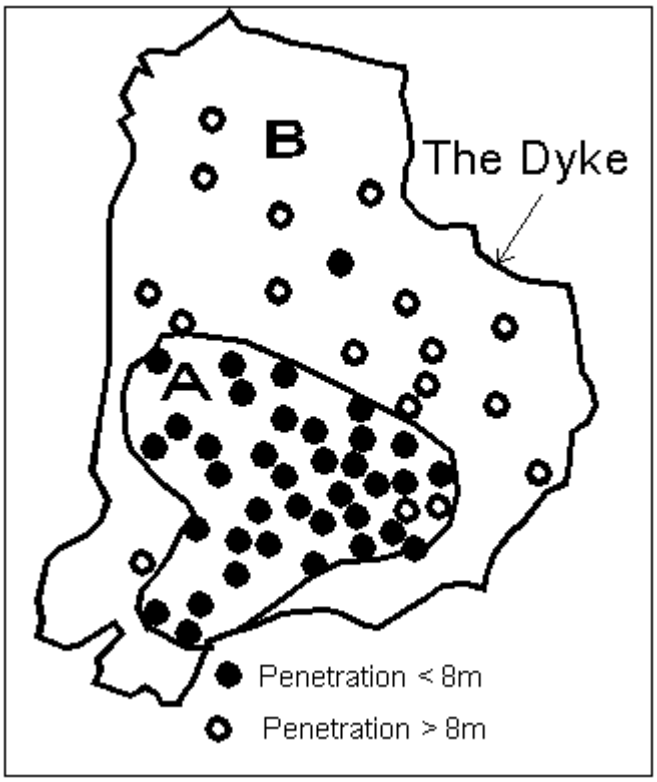

Figure 4-25 Penetration Depths of Plate 1 in August 2001

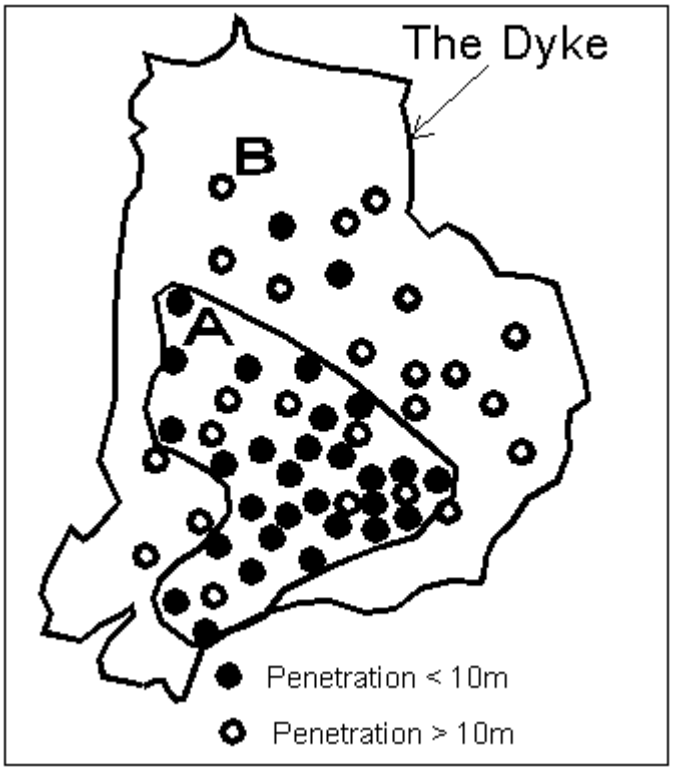

Figure 4-26 Penetration Depths of Plate 2 in August 2001

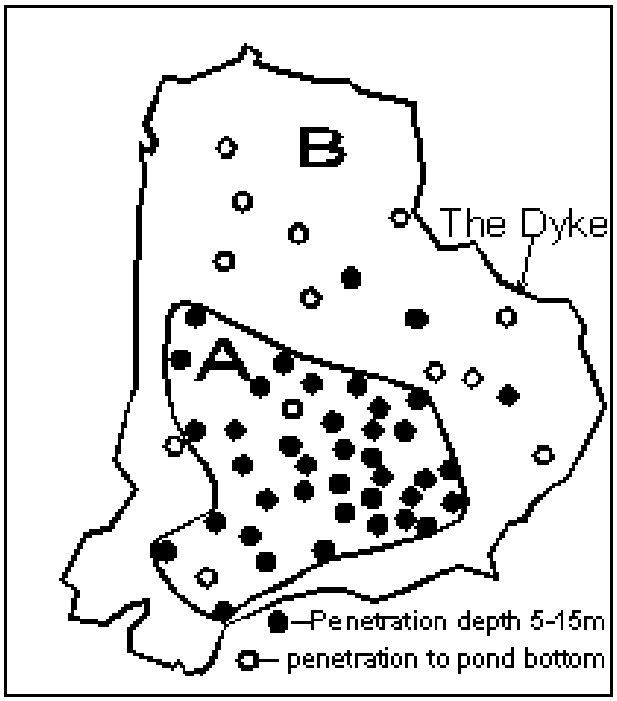

Figure 4-27 Penetration Depths of Plate 3 in August 2001

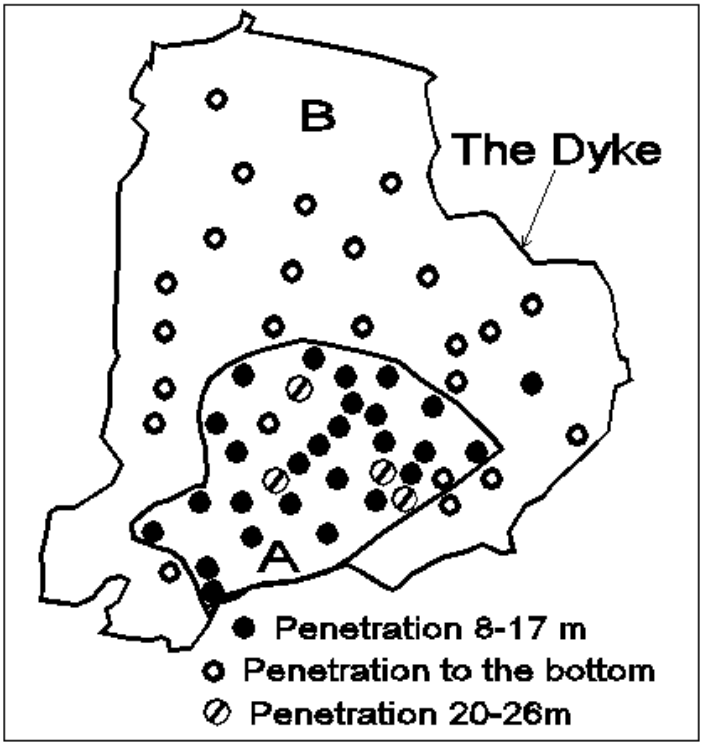

Figure 4-28 Penetration Depths of Plate 4 in August 2001

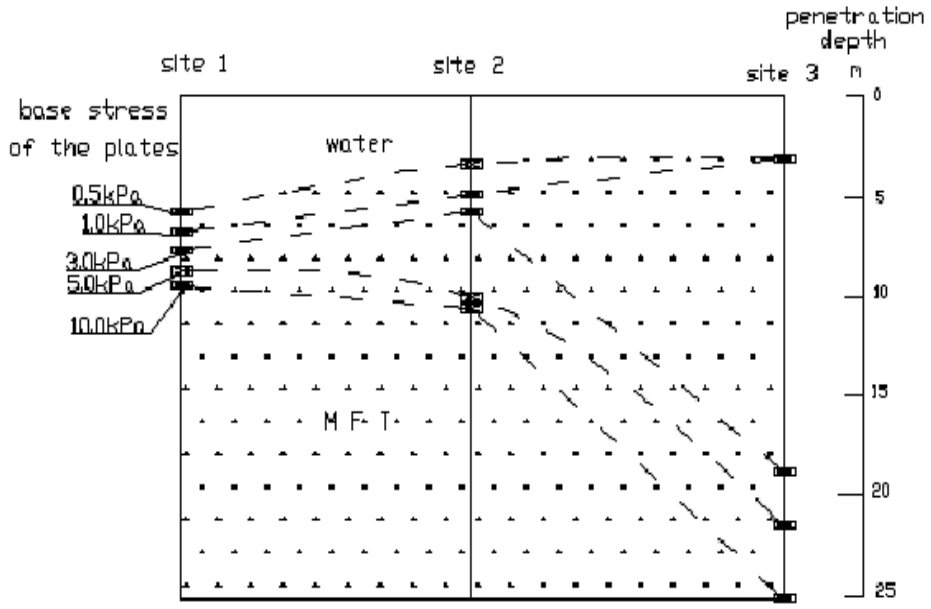

Figure 4-29 Penetration Depths of the Steel Plate Penetration Tests at Three Sites in 2002

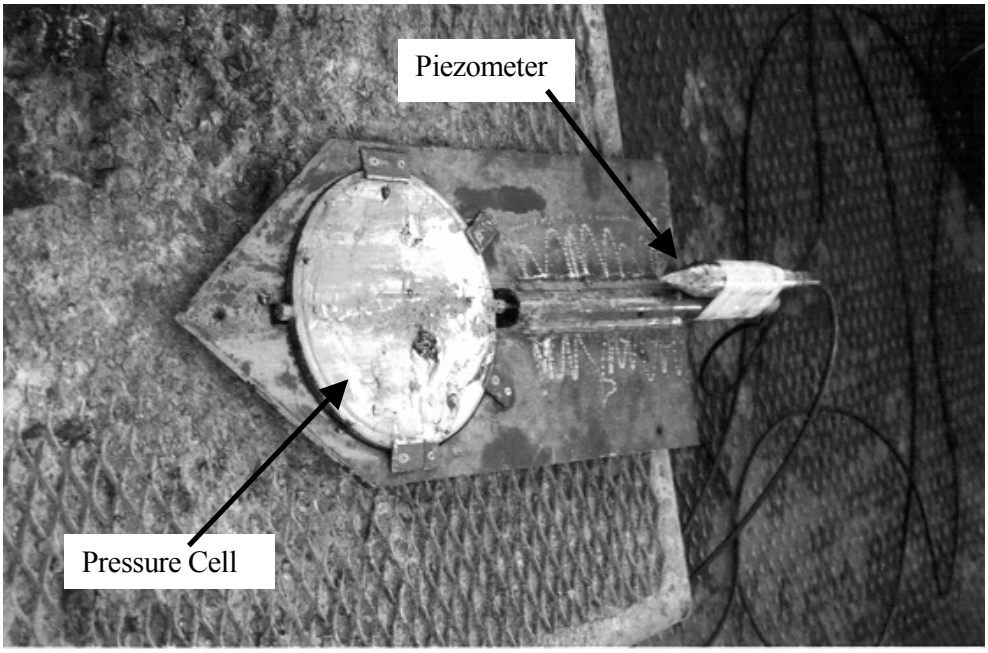

Figure 4-30 A Photo of the Total Pressure Cell and Piezometer

Figure 4-31 A Photo of the Total Pressure Cell before Total Vertical Pressure Test

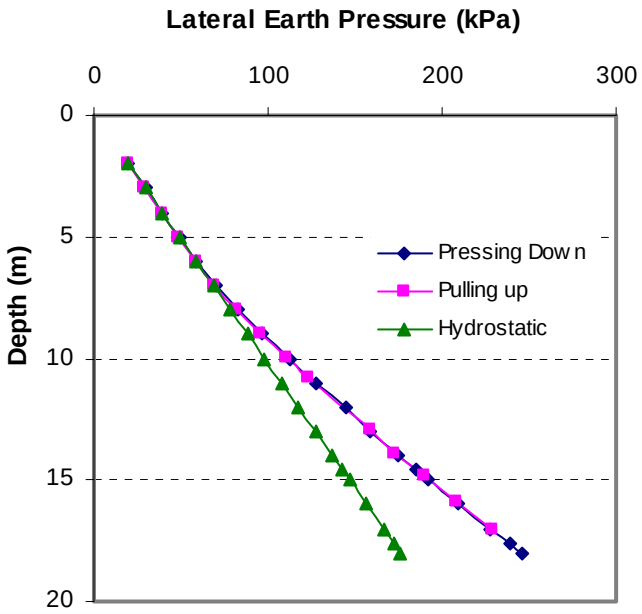

Figure 4-32 Depth Profiles of Lateral Earth Pressures and Hydrostatic Pressures at Location 1 in 2001

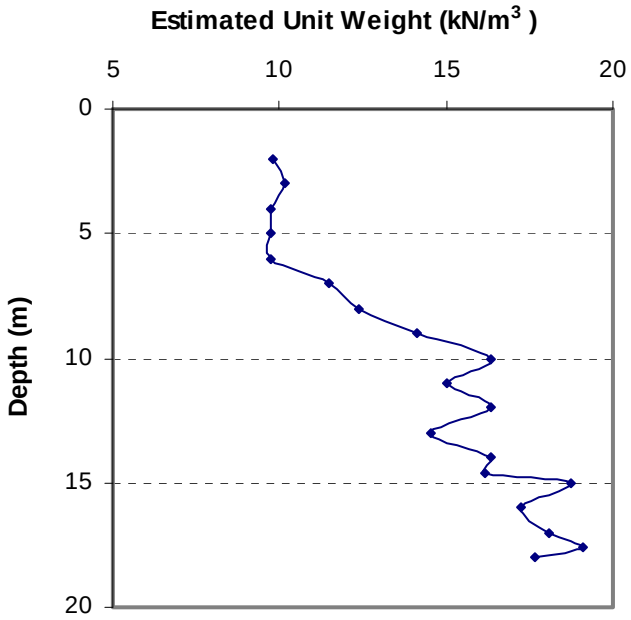

Figure 4-33 Estimation of the Unit Weights of the MFT at Location 1 (near the barge) in 2001.

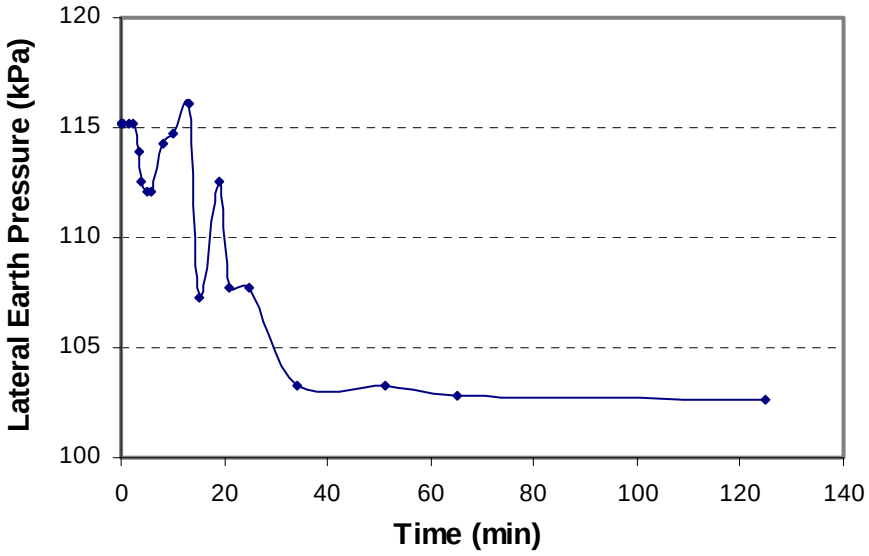

Figure 4-34 Influence of Pumping Operation on Lateral Earth Pressure of the MFT at Location 2 (near the barge)

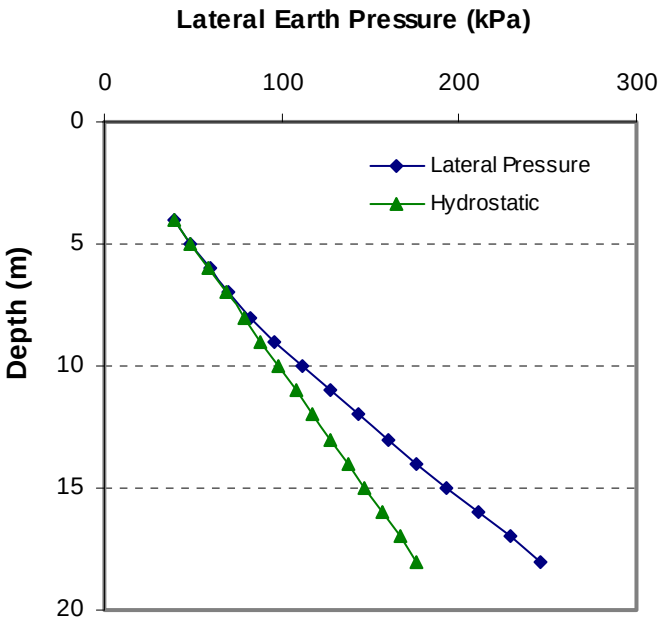

Figure 4-35 Depth Profiles of Lateral Earth Pressures and Hydrostatic Pressures at Location 3 (near the barge) in 2001

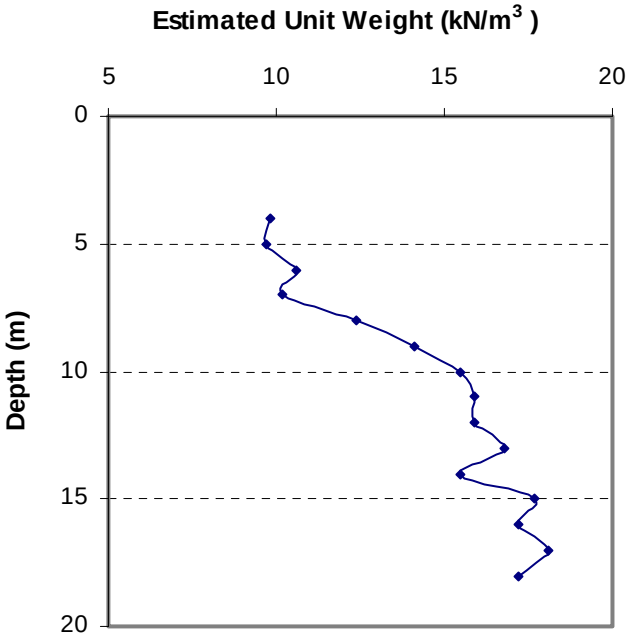

Figure 4-36 Estimation of the Unit Weights of the MFT at Location 3 (near the barge) in 2001

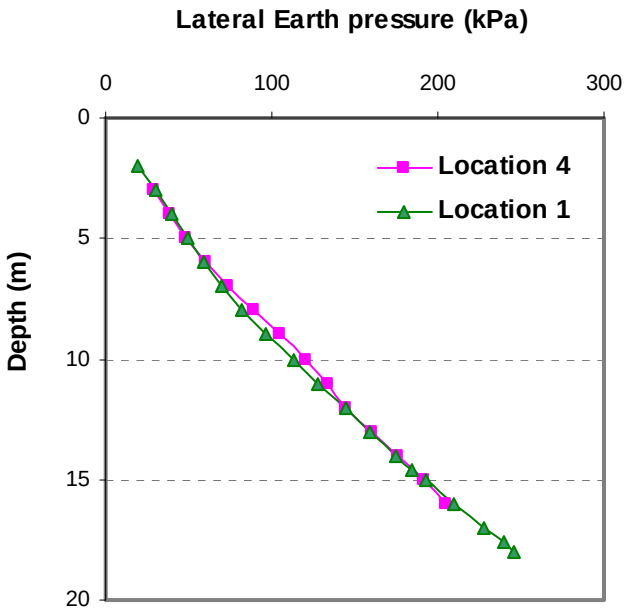

Figure 4-37 Comparison of the Lateral Earth Pressure Measurements between Location 1 and Location 4

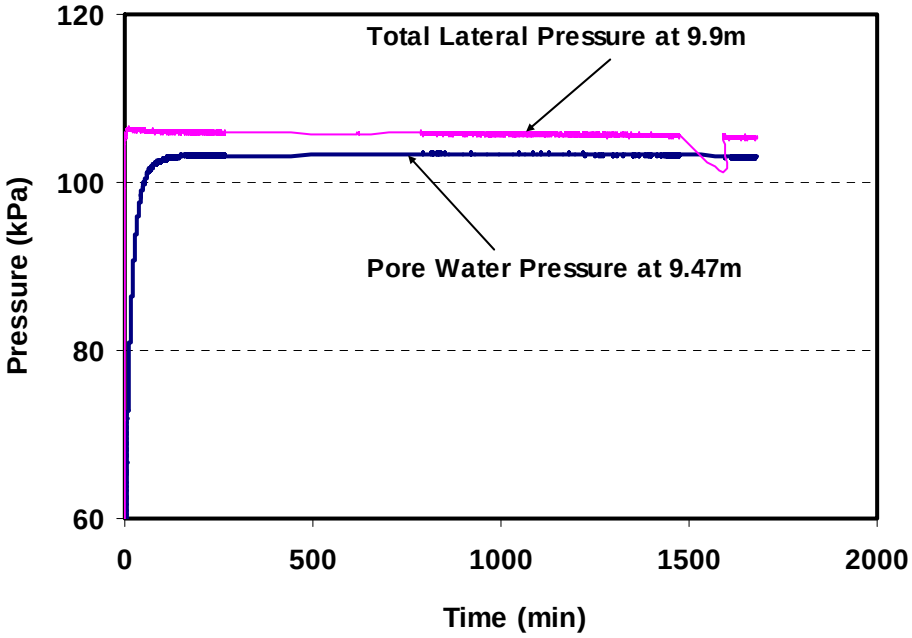

Figure 4-38 Total Lateral Pressure at 9.9 m and Pore Water Pressure at 9.47 m below the Water Surface at Sta. 1

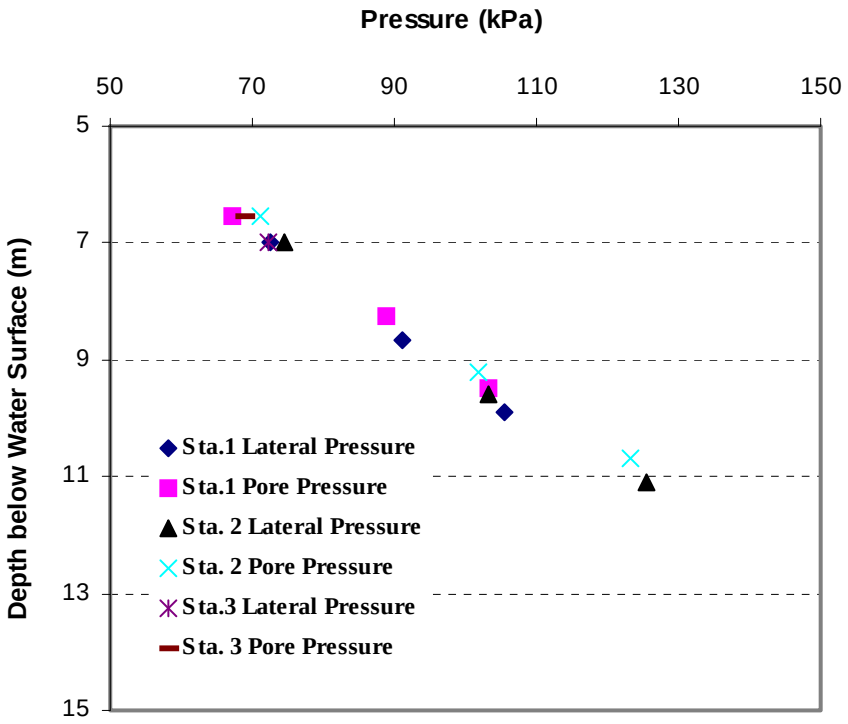

Figure 4-39 Comparison of Lateral Pressure and Pore Pressure with Depth at the Three Sites

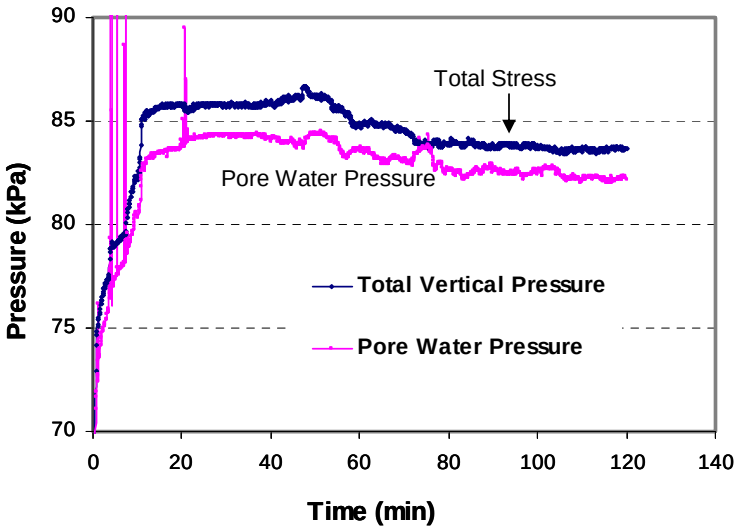

Figure 4-40 The Total Vertical Pressure and Pore Water Pressure with Time at a Depth of 8.19 m below the Water Surface at Sta. 1 in September 2002

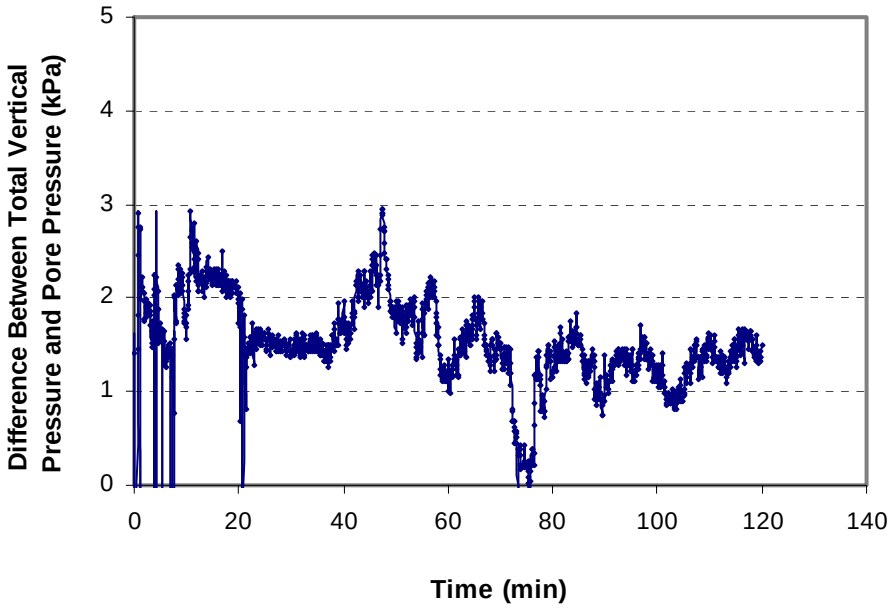

Figure 4-41 The Difference between Total Vertical Pressure and Pore Water Pressure at 8.19 m Depth at Sta.1

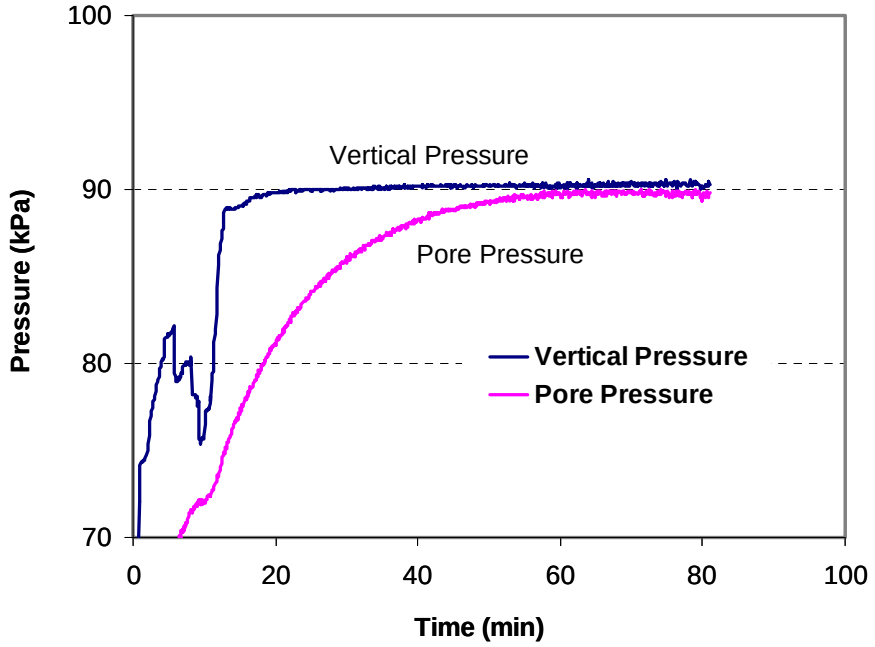

Figure 4-42 The Total Vertical Pressure and Pore Water Pressure with Time at a Depth of 8.75 m below Water Surface at Sta. 1 in September 2002

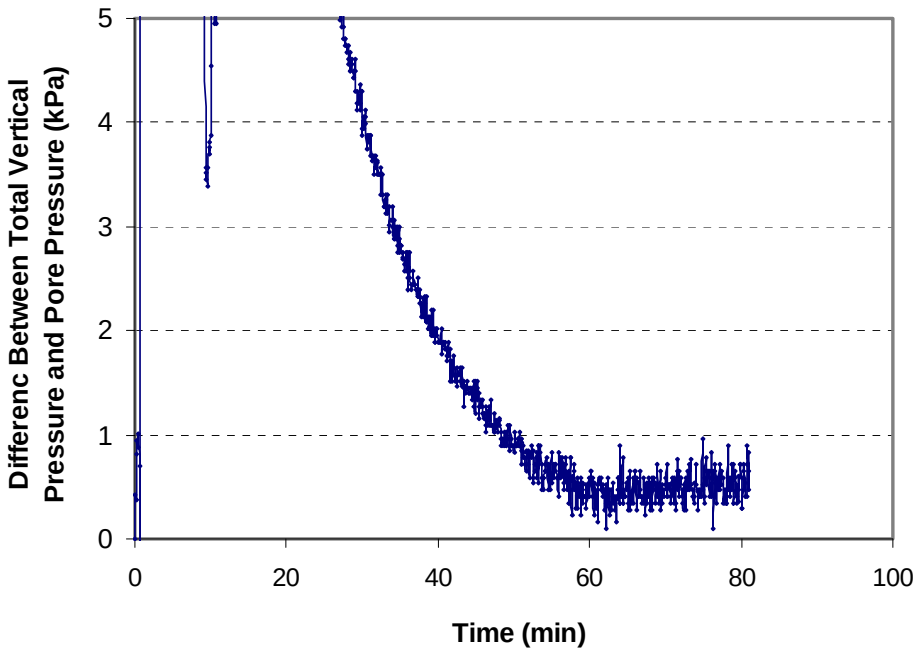

Figure 4-43 The Difference between Total Vertical Pressure and Pore Water Pressure at 8.75 m Depth at Sta.1

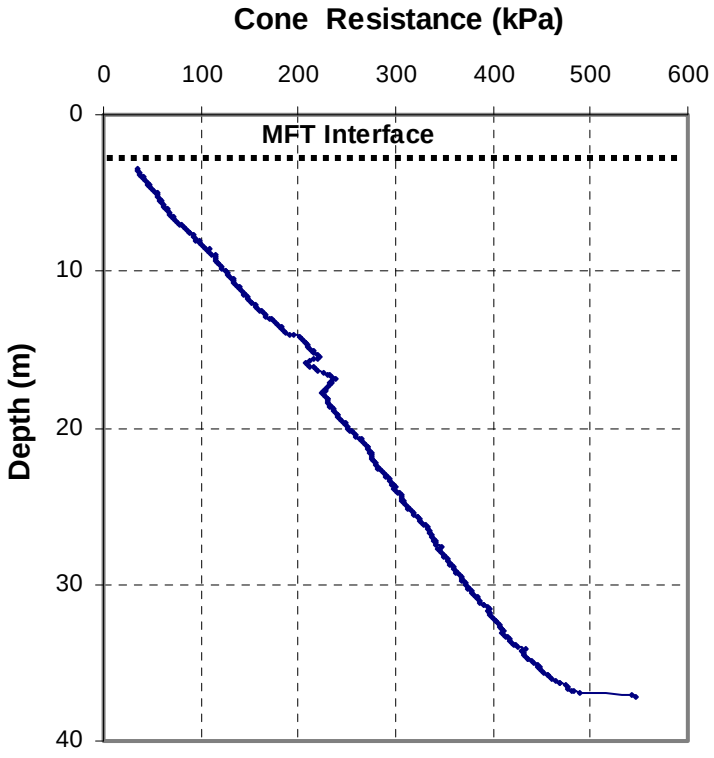

Figure 4-44 A CPT Profile at the Southern Part of the Pond

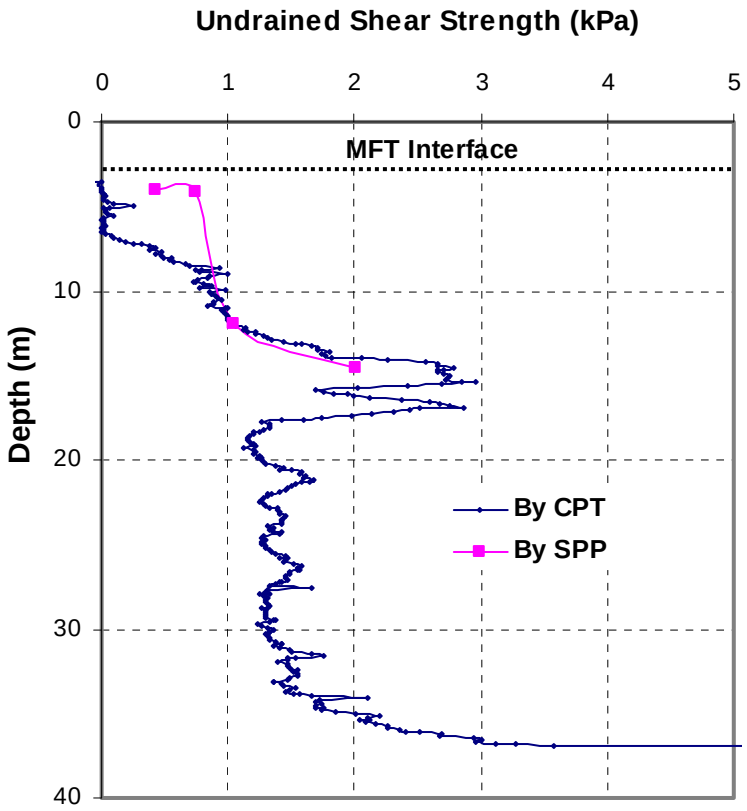

Figure 4-45 Measured Undrained Shear Strengths at Different Depths at the Southern Part of the Pond by CPT and SPP

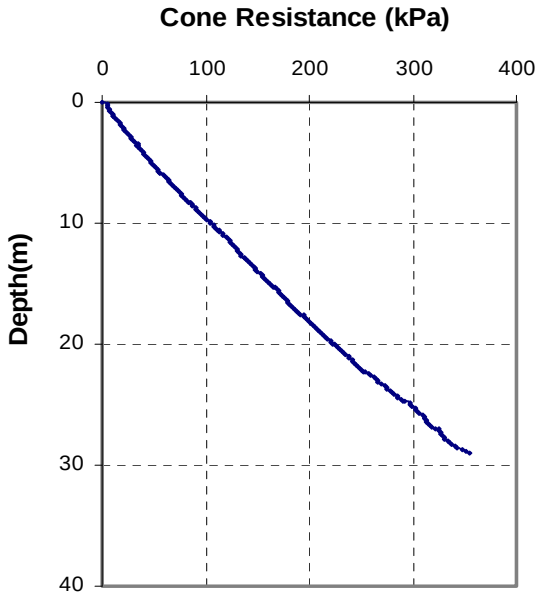

Figure 4-46 CPT Profile at the Northern Part of the Pond

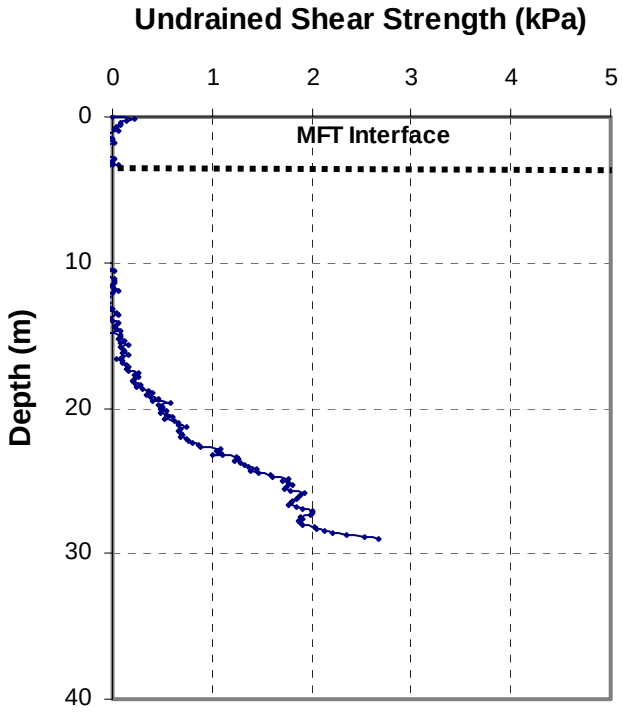

Figure 4-47 Measured Undrained Shear Strengths (by CPT) at Different Depths at the Northern Part of the Pond

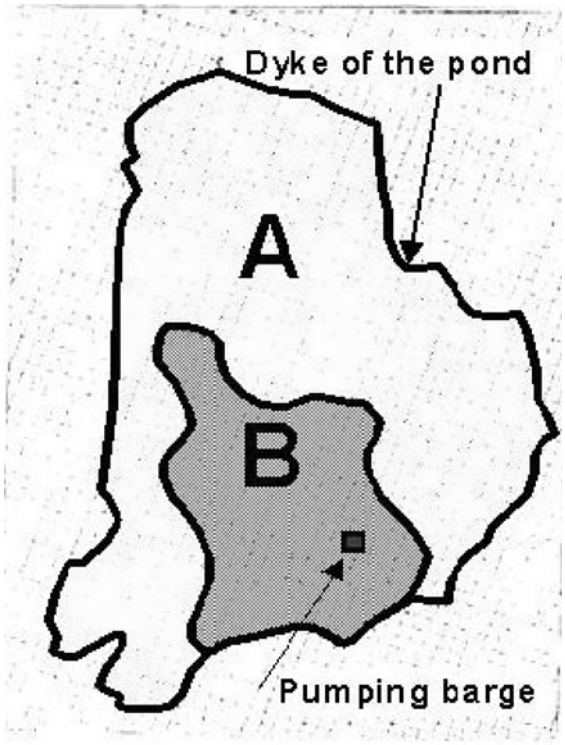

Figure 4-48 Mapping of Gas Bubble Distribution at the MLSB in 2002

Figure 4-49 A Photo of the Water Surface at Zone A

Figure 4-50 A Photo of the Water Surface at Zone B

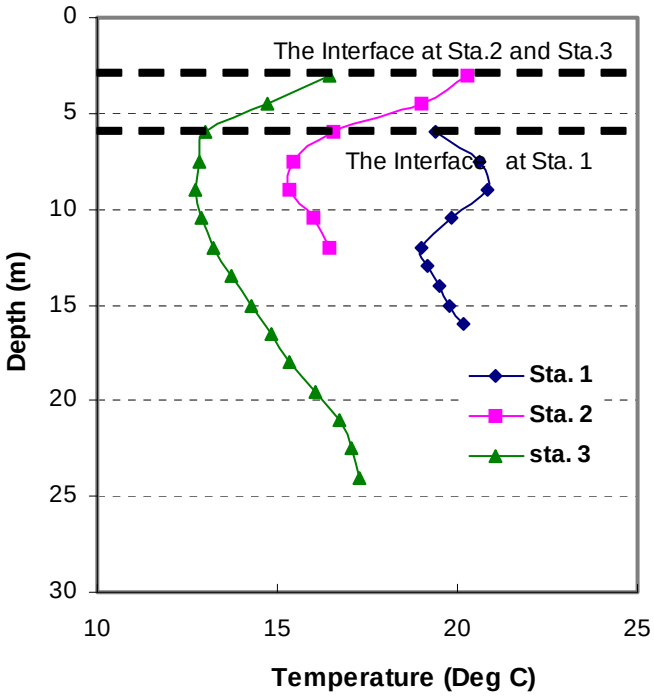

Figure 4-51 Depth Profiles of the In Situ Temperatures at the Three Stations in 2002

CHAPTER 5

5 SMALL-SCALE COLUMN TESTS

5.1 Introduction

Since the mid 1990s, microbial activity in some regions of the mature fine tailings (MFT) of the MLSB has been observed. A large number of gas bubbles have been observed on the water surface in some areas of the pond **(**Figure 1.2**)** and in recovered MFT samples (Figure 4.8 and Figure 4.10**)**. The phenomenon of rapid densification of the MFT at the southern part of the MLSB has been proven by field investigations (Guo et al., 2002).

Accumulation and release of biogenic gas is hypothesized to have a major influence on the densification rate of MFT. The objective of the small-scale column tests performed during field investigations was to study the effects of microbial activity on MFT densification under controlled laboratory conditions. More detailed physical and chemical properties of the MFT during microbial activity were studied by gas MFT densification tests as presented in Chapters 6 to 9.

A series of tests were conducted at Oxford University to study the consolidation of naturally gassy soft soil (Sills et al., 2001), and the behaviour of offshore soils containing gas bubbles (Sills et al., 1991). Both settling column tests and odometer tests were conducted in these studies. In the odometer tests, methane gas is introduced to make reconstituted samples by the zeolite method (Sills et al., 1991). The disadvantages of this approach are that it cannot model the natural process of microbiological gas production, and that the rate of gas production is much higher than the natural gas production occurring in the MLSB. Another approach to control the gas production rate is to regulate the temperature of the soil (Sills et al., 2001). However, changing the soil temperature will also change the viscosity of the pore fluid, and the permeability of the soil.

Sills et al. (2001) studied the consolidation of naturally gassy soft soil of estuarine origin, from the Slufter disposal site in the Netherlands, using

settling column tests. In these tests, biogas generation rates were either accelerated or reduced through controlling temperatures in the range of 10-30^{o}C. Structural changes were observed and the pore water pressure and density were measured. It was observed that when gas was produced, there was only a small increase in the bed height. This indicates that most of the gas volume was accommodated by expelling water from the bed. The pore water pressure measurements also show that the excess pore water pressures decreased rapidly during the gas production period.

Wichman (1999 and 2000) used the computer program FSCongas to model the consolidation of the mud in the Slufter disposal site, which is used to store polluted mud from Rotterdam harbour. In his modeling, it was assumed that large gas bubbles were fixed inside the soil skeleton and that the gas content was constant. It followed from the simulation that gas significantly retards the consolidation.

Fedorak et al. (2000) studied the microbial activity in sulphate-enriched tailings in the MLSB by laboratory mesocosms. They found that methanogenesis in the MLSB appears to have started after the sulphate concentration dropped. Special nutrients, including sodium acetate, were added to stimulate the activity of methane-producing microorganism, known as methanogens.

Microbial activity can be stimulated by controlling the temperature of MFT or by adding a nutrient such as sodium acetate. The method of nutrient addition is easier to implement than that of temperature control. At a temperature of 25^{o}C it may take half a year for gas accumulation within the MFT to reach a critical state for gas release. But by adding a suitable amount of sodium acetate, the time for gas release can be greatly shortened. Furthermore, a temperature change can alter the viscosity of the pore water. This makes it difficult to compare water drainage rates during different microbial activities.

Five small-scale column tests were conducted with different amounts of sodium acetate added, and different temperatures controlled in this research. Structural changes of the MFT were observed during microbial activity, and

densification properties were studied. Also, the effect of sodium acetate on MFT densification was analyzed.

5.2 Test Description

Five columns were set up, each with different amounts of sodium acetate added. A schematic of the test setup is shown in Figure 5.1. The test device consisted of a glass column with an inner diameter of 60 mm, in which the test materials were held, and graduated cylinder (an overflow water collection cylinder for gas volume measurement) of a small inner diameter. The height of the glass column was 50 cm. A glass tube connected the glass column to the water collection cylinder. A rubber stopper completely sealed the top of the glass column. Silicon sealant was used to prevent water or gas leakage.

Columns 1, 3 and 5 were kept in a room with a constant temperature of 25^{o}C. Columns 2 and 4 were kept in a room with a constant temperature of 4^{o}C. The test procedure was as follows:

- Measure the initial geotechnical parameters and weigh the samples.
- Mix sodium acetate into the MFT samples uniformly.
- Flush the column with nitrogen gas to create an anaerobic environment.
- Pour the MFT sample into the column, and pour recycle water from the MLSB above the MFT until the 2 L column is full.
- Seal the column with a rubber stopper, and place silicon sealant around the rubber stopper to prevent leakage. Put glass tubing through the rubber stopper so that the lower end of the tubing is submerged in water. The glass tubing connects the column to the water collection cylinder.
- Put the ruler vertically on the outside wall of the cylinder, and record the initial elevations of the MFT-water interface, and the water surface in the column.
- Incubate the column at constant temperature.

- Observe the structural changes, and measure the MFT-water interface movements, released gas volumes, and water volumes in the water collector during microbial activity.
- Sample the MFT material in the column for solids content measurements at the end of testing.

With different amounts of sodium acetate stimulating the activity of methanogens, biogas was produced at different rates. Before gas releasing (about 200 hours) from Column 5, the generated gas was trapped within the MFT, so the water-MFT interface expanded upward. Because the column was full of water, when the MFT expanded, some of the water at the headspace of the column was discharged into the water collector. Since the water drainage from the MFT interface did not affect the water volume in the water collector, the change in the water collector indicated that gas had been generated. The change in volume was attributed both to trapped gas and released gas.

When the generated gas accumulated to a critical state, some of it escaped from the MFT. The released gas volumes at the headspace, as well as the interface movements, were measured by eyes against a ruler. The discharged water volume in the water collector was measured in a graduated water cylinder.

Since the glass tubing was open to the atmosphere, the gas pressure at the headspace was close to atmospheric pressure. Due to the small size of the column, the difference between the gas pressure at the headspace and the gas pressure within the MFT was very small. It is reasonable to assume that the gas pressure in the column was approximately equal to atmospheric pressure.

5.3 Test Conditions and Initial Parameters

MFT samples were originally retrieved from a depth of about 2.5 m below the water-MFT interface at Sta. 2 of the MLSB. The samples were totally remoulded prior to standpipe testing. Fused crystals of sodium acetate (CH_3COONa) were uniformly mixed with the MFT samples before they were poured into the small columns. After the samples were completely remoulded

and mixed, some parameters were measured, as shown in Table 5.1. These parameters likely differ from those of the undisturbed MFT in the field, especially its density and void ratio.

The microbial activity was controlled by adding different amounts of acetate and incubating the MFT under different temperatures as demonstrated in Table 5.2. In Column 1 there was no acetate added, resulting in relatively slow gas production. In Column 3, 0.52 g sodium acetate was added for each litre MFT, which produced moderate microbial activity. In Column 5, 1.52 g acetate per litre MFT was added, which produced intense microbial activity. These three columns were incubated at 25^{o}C. For Columns 2 and 4, two different amounts of acetate were added and the incubation occurred at 4^{o}C. The purpose of these two tests was to determine the influence of acetate itself on MFT densification. A low temperature was used in order to ensure that microbial activity would not occur (or occur very slowly).

5.4 Determinations of Some Parameters during Microbial Activity

Before testing started, different parameters, including the solids content, density, and void ratio, were measured. As such, the initial total MFT volume, water volume and solids volume in each column were known. During microbial activity, the MFT-water interface movements, the released gas thickness, and the water volume in the water collector were all measured with time. From these measurements, the volumetric changes in the MFT were determined. It was assumed during testing the solids volume was constant. The water volume in the MFT was calculated by considering the total water mass balance in the whole test system, including the column, glass tubing and water collector. Knowing the total MFT volume, the water volume and the solids volume at one time, the trapped gas volume in the MFT was easily calculated.

The water void ratio is defined as the ratio of the water volume in the MFT to the solids volume, while the gas void ratio is defined as the ratio of the trapped

gas volume in the MFT to the total solids volume. The total void ratio is a combination of the water void ratio and gas void ratio. Since the columns were of small sizes and open to the atmosphere, it is reasonable to assume that the gas pressure was equal to the atmospheric pressure.

5.5 Test Results

The MFT-water interface movement, the released gas volumes, and the water volumes in the water collector were measured at different times during microbial activity. These measurements can be used to determine some parameters including the gas content, total void ratio, water void ratio, and gas void ratio, as demonstrated above.

Figure 5.2 shows the volume of produced gas as a percentage of the initial MFT volume. Some details about the gas generation are summarized in Table 5.3. The more acetate was added to the MFT, the more gas was generated, provided the temperature was sufficient to support microbial activity. The gas generation rate of the MFT with added acetate was much faster than of that without. In both Columns 2 and 4, large amounts of sodium acetate were added, but there was no visible gas generation at the low temperature (4^{o}C). This indicates that temperature is an important factor for microbial activity.

During microbial activity, changes in the level of the water-MFT interface were measured by observing the movements of the interface relative to the ruler fixed to the outside wall of the column. The thicknesses of the gas released at the headspace were also measured. Figure 5.3 shows the interface movements in Columns 1, 3 and 5. Figure 5.4 shows the changes in gas content during microbial activity. Figure 5.5 shows the released gas volume with time during testing.

Column 5 had the most intense microbial activity among the three columns. Three stages can be identified:

- The period from the start of incubation to 181 hours was a stage of rapid gas generation within the MFT. There was no visible gas released. The water-MFT interface moved upward, and the gas content within the MFT increased.
- Form 181 to 340 hours, the rate of gas release was greater than the rate of gas production. The interface of the MFT settled down, and the gas content decreased with time.
- After 340 hours, the microbial activity diminished. Both the MFT interface level and gas content remained relatively stable.

For Column 3, rapid gas generation lasted about seven days. Then, with the depletion of sodium acetate, microbial activity diminished. The gas accumulation in Column 3 did not reach a critical state for release. In Column 1, gas was generated slowly and there was no visible gas release.

Gas release began in Column 5 when the gas content reached 14.6%. In Column 3 the maximum gas content reached was only 12.5%, which was less than the peak gas content for Column 5. In Column 1 the maximum gas content after 17 days of incubation was only 2.4%. These results suggest that there may be a threshold gas content at which gas starts to escape for MFT with a certain structural strength.

Figure 5.6 shows the estimated water drainage volumes with time in Columns 1, 3 and 5. At the end of testing, the water drainage volume in Column 5 was much larger than that in Column 1. With the increase of microbial activity in the MFT, water drainage volumes increased. At the end of testing, the water drainage volumes from Columns 5, 3, and 1 were 48.8 mL, 30.9 mL and 7.1 mL, respectively.

Figure 5.7 shows variations of the total void ratio (a ratio of total void volume to solids volume) in the MFT with time. Columns 1, 3 and 5 all had the initial void ratio 4.43. After 182 hours the total void ratios in Columns 5 and 3 increased to 5.3 and 4.95, respectively. Then, due to gas release the total void

ratio in Column 5 decreased rapidly. At 340 hours, the total void ratio in Column 5 was 4.49, close to the initial value. After that time it remained stable. In Column 3, after 182 hours, the total void ratio remained almost stable. In Column 1, the total void ratio kept increasing slowly. At the end of testing, Column 5 had the lowest total void ratio among the three columns.

Figure 5.8 shows the variations in the water void ratio (a ratio of water volume to solids volume) during the test. The three columns had the same initial water void ratio 4.38. Due to water drainage from the interface of the MFT, the water void ratios decreased in all the columns. However, the water void ratio in Column 5 decreased more rapidly than in the others. At the end of testing the water void ratio in Columns 5, 3 and 1 were 4.0, 4.14 and 4.34, respectively.

Figure 5.9 shows the variations in the gas void ratio (a ratio of gas volume to solids volume) in the three columns. Although Column 5 had the highest gas production, its final gas void ratio was less than that in Column 3 due to large amounts of gas release. When the microbial activity diminished, the gas void ratios in both Columns 5 and 3 continued to increase, but at a slow rate, which was similar to that in Column 1.

In order to analyze the effects of microbial activity on MFT dewatering, and to prove the estimations illustrated in Figure 5.6, the MFT materials in the columns were sampled with a spoon sampler at the end of testing using the following procedures:

- Remove the rubber stopper on the top of the standpipe;
- Clear the water above the interface of the MFT using a small syringe pump;
- Sample the MFT in the column layer by layer;
- Measure the wet weights of the MFT samples, then dry them in the oven.

Figure 5.10 shows the solids contents at different elevations of the 5 columns by the spoon sampling done at the end of testing. The solids contents near the MFT-water interfaces in each column were lower than the initial solids

contents. This might have been caused by the following factors: a small amount of water possibly remaining above the water-MFT interface after cleaning; a small amount of water possibly entering the MFT through the cracks close to the interfaces.

The initial solids content of the MFT was 36%. After microbial activity, the solids contents in the columns varied considerably. For Columns 2 and 4, the final solids contents were very close to the initial value of 36%, though there was a slight increase. Although the amount of sodium acetate added to Column 4 was much larger than that added to Column 2, the final solids contents in the two columns were similar. This demonstrates that the sodium acetate alone has very little influence on the densification of the MFT, as it cannot act to stimulate gas generation.

For Columns 1, 3 and 5, with increasing amounts of sodium acetate, microbial activity was accelerated and the final solids contents also increased. Although no sodium acetate was added to Column 1, the final solids content was still higher than those in Column 2 and 4 which had acetate added. This demonstrates that the microbial activity within the MFT can be accelerated by temperature increase, and that water drainage from the MFT can also be improved, even if gas generation occurs at a relatively slow rate.

The sampling results can also help to answer the important question of whether water drainage from the MFT can be improved even if there is no gas released. Although all the generated gas in Column 3 remained within the MFT, its water drainage was still accelerated compared with that of Columns 1, 2 and 4.

Table 5.4 gives a summary of some parameters of the MFT in the five columns at the end of testing. These parameters are calculated from measurements that include MFT-water interface movements, released gas volumes, and water volumes in the water collector. The parameters given are the averages for each column. Since the size of each column is small, the MFT in each can be regarded as a single sample. Although there existed

variations in these parameters at different levels of the columns, the average values are helpful in characterizing the overall effect of microbial activity on MFT densification. With the increase in microbial activity, the final average solids contents in the five columns increased. The densities of the MFT in Columns 1, 3 and 5 decreased relative to the initial densities. The density of Column 5 was higher than that in Column 3. This is because a large amount of gas was released from the MFT in Column 5, while all the generated gas in Column 3 was trapped.

5.6 Summary and Conclusions

The small-scale column test is a simple and effective test method to preliminarily model the microbial activity under controlled laboratory conditions. From the five column tests of this study, some results can be summarized as follows:

- Sodium acetate can be used to effectively stimulate microbial activity at room temperature (25^{o}C). With the increase of added sodium acetate, the total amount of gas generated and gas production rate increased. There was no visible microbial activity and gas generation for the MFT incubated at a temperature of 4^{o}C, even though large amounts of sodium acetate were added. This indicates that temperature is an important factor for microbial activity.
- Among the five columns, Column 5 had the most intense microbial activity. Three stages can be discerned:
    - Gas bubbles increased rapidly without gas release from the MFT.
    - Gas generation reached a critical state; part of the generated gas was released from the MFT. During this stage, the gas release rate was higher than the gas generation rate. For Columns 1 and 3, gas accumulations within the MFT did not reach the critical state, so there was no visible gas release.
    - After microbial activity diminished, gas content within the MFT increased at slow rates.

- The detailed structure observations during biogas activity are demonstrated in Appendix E. The following process related to gas bubble activity is summarized:
    - ♦ Gas bubbles formed and increased.
    - ♦ Bubbles migrated and accumulated to form large gas voids or cracks. Gas bubbles tended to move upward and to migrate from small gas bubbles to large gas bubbles. This was attributed to the buoyancy acting on the gas bubbles and their different gas pressures. The small gas bubbles had higher gas pressures than the large gas bubbles. This led to a higher concentration of dissolved gas near the small gas bubbles, and thus, a steady diffusion of gas from small gas bubbles to large gas bubbles (Olson, 1986). The cracks and fractures in the MFT helped the gas bubbles to migrate.
    - ♦ Gas bubble accumulation led to an unstable MFT structure, so gas bubble flooding occurred and part of the gas was released. Some large gas bubbles and cracks disappeared and became smaller.
    - ♦ Gas bubbles continued to form, grow, accumulate and migrate.
    - ♦ A new critical state was reached, and more gas was released.

  This process continued until microbial activity diminished.
- At 25^{o}C room temperature, with the increases of microbial activity, water drainage volumes increased at the end of testing. This indicates that biogas generation helps (not retards) water drainage from the MFT.
- There were no obvious increases in solids content for the two columns incubated at 4^{o}C even though large amounts of acetate were added. This demonstrates that the drainage rate of the MFT without microbial activity and gas generation is slow, and that sodium acetate itself has very little influence on the densification of the MFT, except for its role in stimulating microbial activity.
- Rapid gas generation can improve water drainage from the MFT even if there is no visible gas release. This suggests that gas bubble formation and growth is an important factor leading to rapid water drainage from the MFT.

- Although the gas generation rate in the column without acetate added was slow, relative to those with acetate, the drainage was still improved relative to the MFT without visible gas production (incubated at $4^{o}C$).
- Although the microbial activity can be approximately modelled by small-scale column testing, the in-depth mechanisms leading the rapid densification phenomenon are still unclear. More sophisticated experiments are required to provide the answer.

Table 5-1 Initial Parameters of the Remoulded MFT Samples

Density g/cm^3	Solids Content (%)	Bitumen Content (%)	Void Ratio (e)	Particle Size Distribution		
				<2μm	<22μm	<44μm
1.262	36	4.82	4.43	51	89.9	93.1

Table 5-2 Summary of Some Initial Information of the Five Columns

Column No	Initial Sample Height	Acetate Addition	Incubation Temperature
	cm	g/L MFT	^oC
1	25.9	0	25
2	24.6	0.52	4
3	23.35	0.52	25
4	24.8	1.52	4
5	24.4	1.52	25

Table 5-3 Some Details about the Gas Production in the Five Columns

Column No.	Ratio of Total Gas Production Volume to Initial MFT Volume in %	Notes
1	2.3	Continue to slowly generate gas after 17 days.
2	0	No visible gas generation
3	14.2	Significant gas activity lasted 8 days
4	0	No visible gas generation
5	46	Dramatic gas activity lasted 15 days

Table 5-4 Final Parameters of the MFT Samples after Testing

Column No	Solids Content	Density (r)	Void Ratio (e)	Fluid Void Ratio (e_f)	Gas Void Ratio (e_g)	Degree of Saturation (Sr)	Water Content (w)	Gas Content
	(%)	g/cm3				(%)	(%)	(%)
1	36.3	1.24	4.51	4.34	0.17	95.7	175.5	2.41
2	36.1	1.27	4.41	4.38	0.03	99.3	177.0	0.54
3	38.0	1.09	4.96	4.14	0.82	81.4	163.3	12.47
4	36.1	1.27	4.40	4.38	0.03	99.5	177.2	0.38
5	39.7	1.15	4.46	4.00	0.46	85.1	151.9	7.56

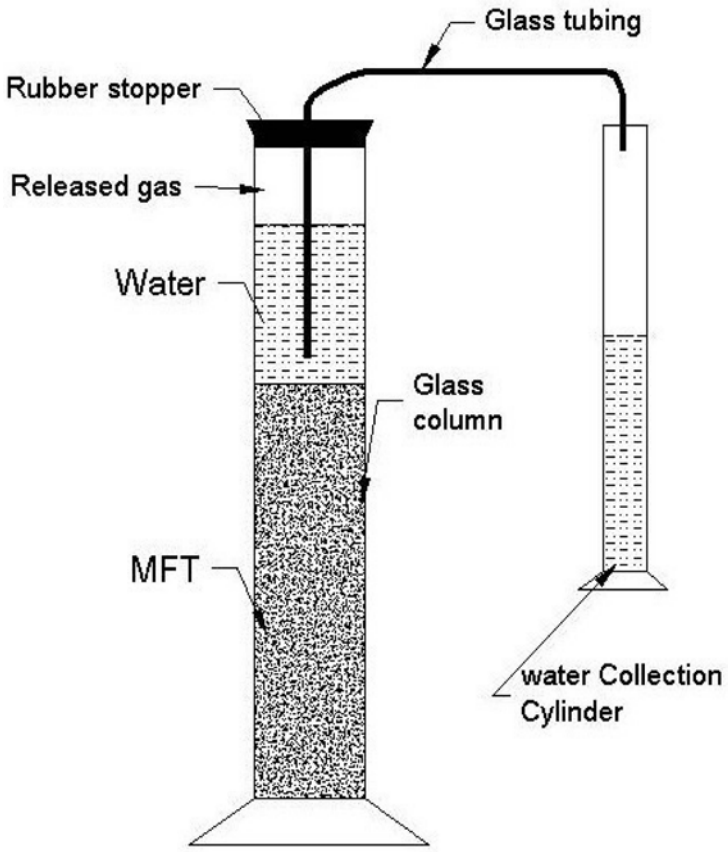

Figure 5-1 A Schematic of the Small-Scale Column Test

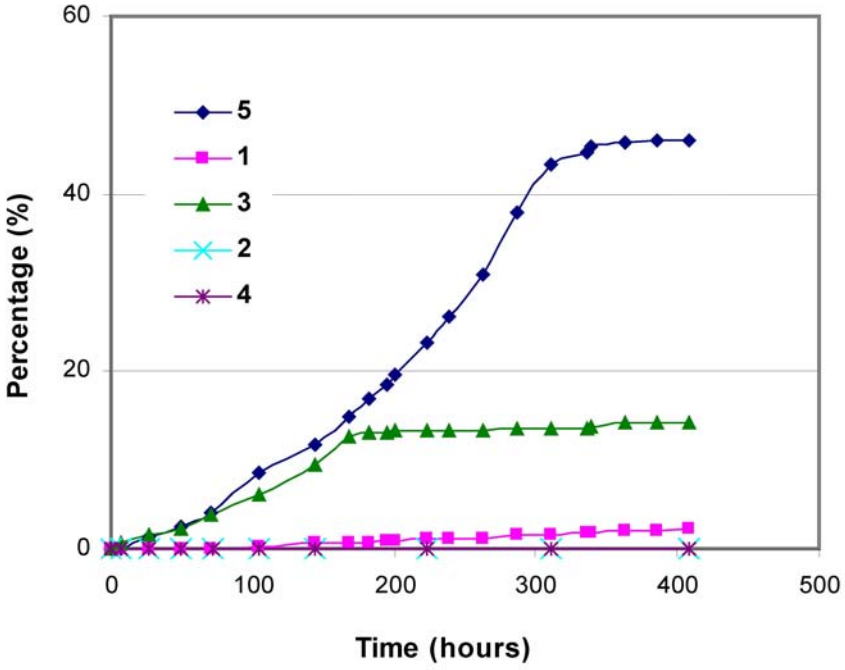

Figure 5-2 Ratio of Total Gas Production Volume to Initial MFT Volume in % for Different Columns

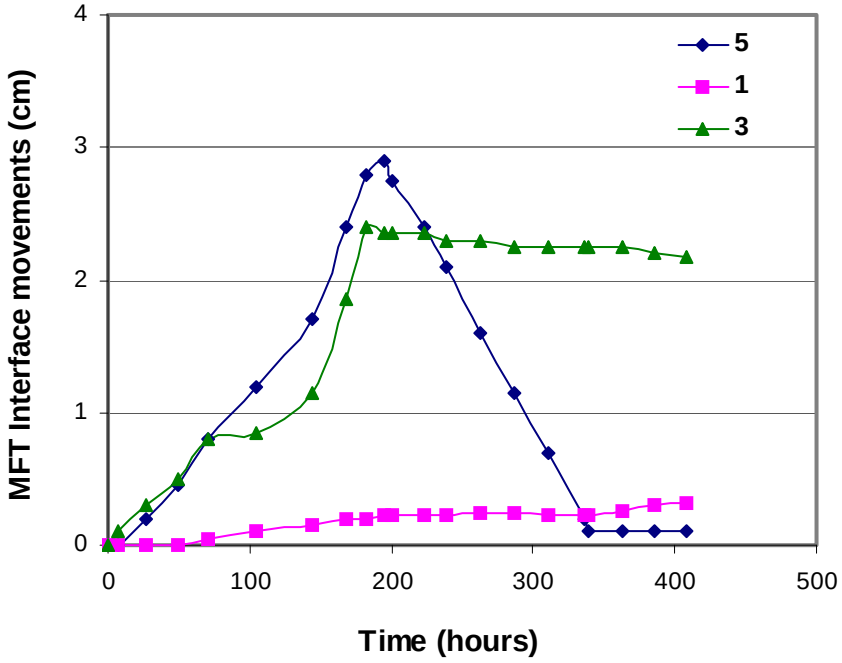

Figure 5-3 MFT Interface Movements vs. Time in Columns 1, 3 and 5

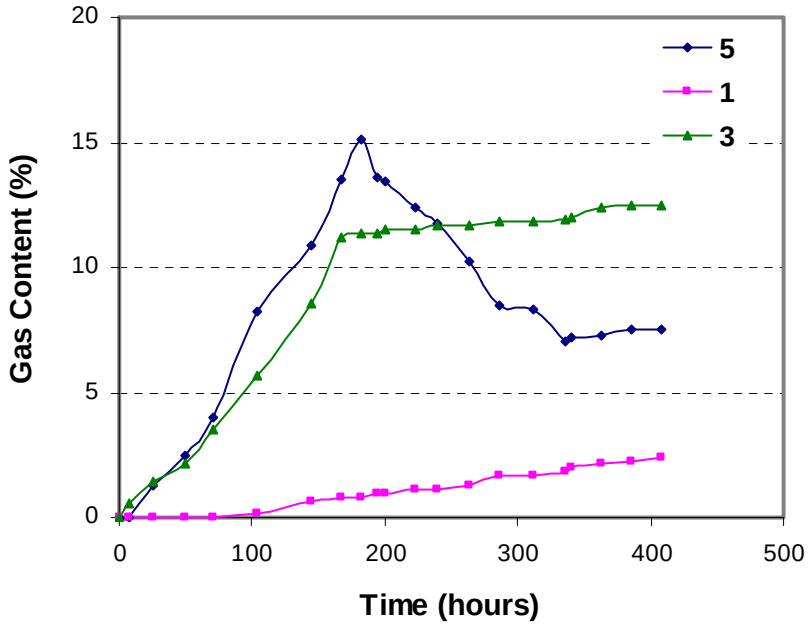

Figure 5-4 Gas Content within the MFT vs. Time in Columns 1, 3, and 5

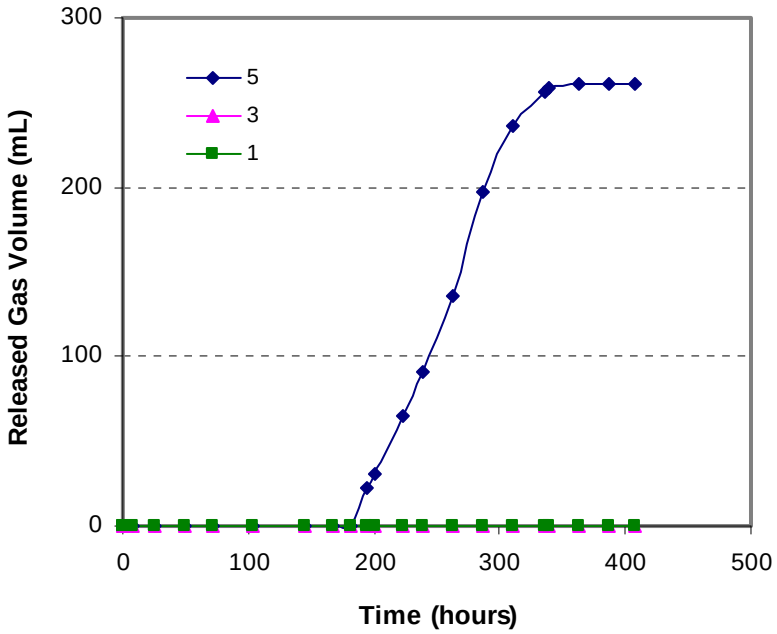

Figure 5-5 Released Gas Volume vs. Time in Columns 1, 3, and 5

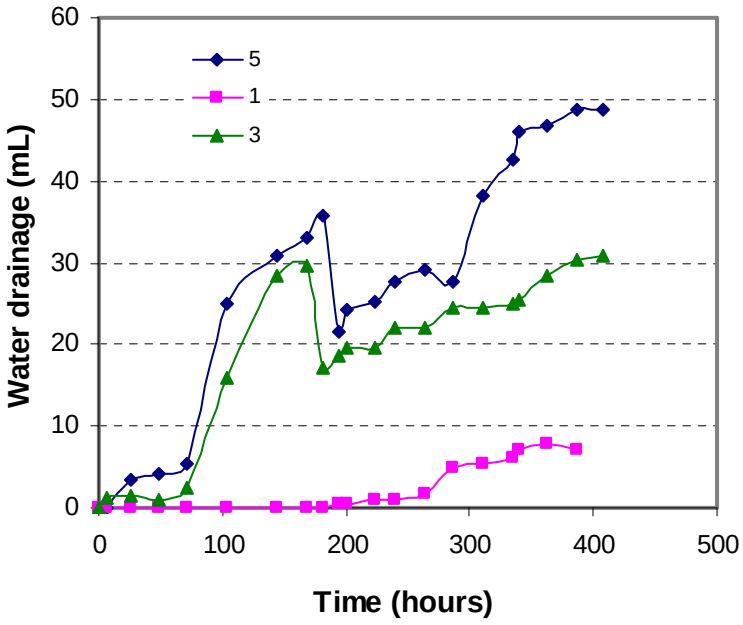

Figure 5-6 Estimated Water Drainage from the MFT in Columns 1, 3 and 5

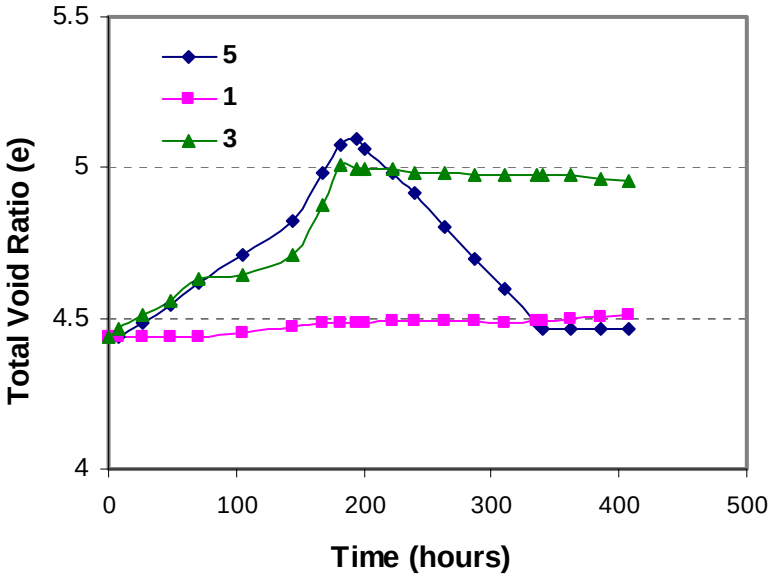

Figure 5-7 Variations of Total Void Ratios with Time in Columns 1, 3 and 5

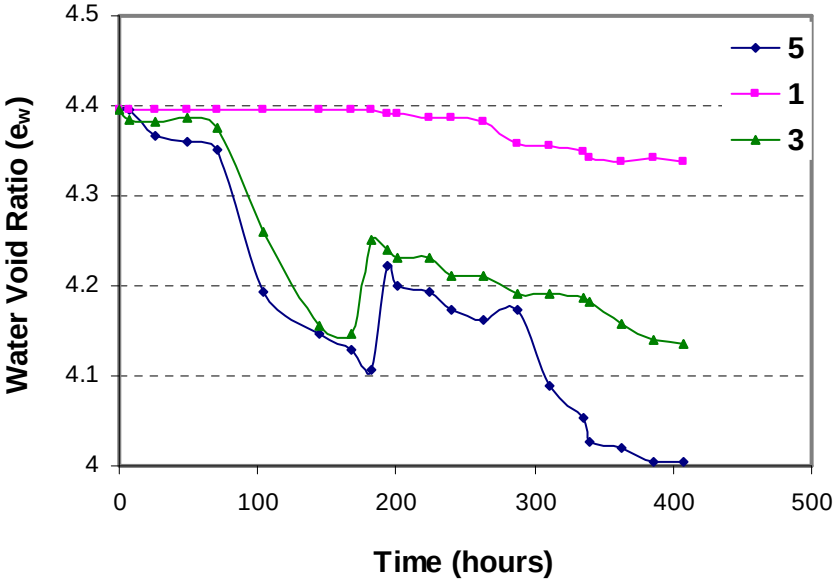

Figure 5-8 Variations of Water Void Ratios with Time in Columns 1, 3 and 5

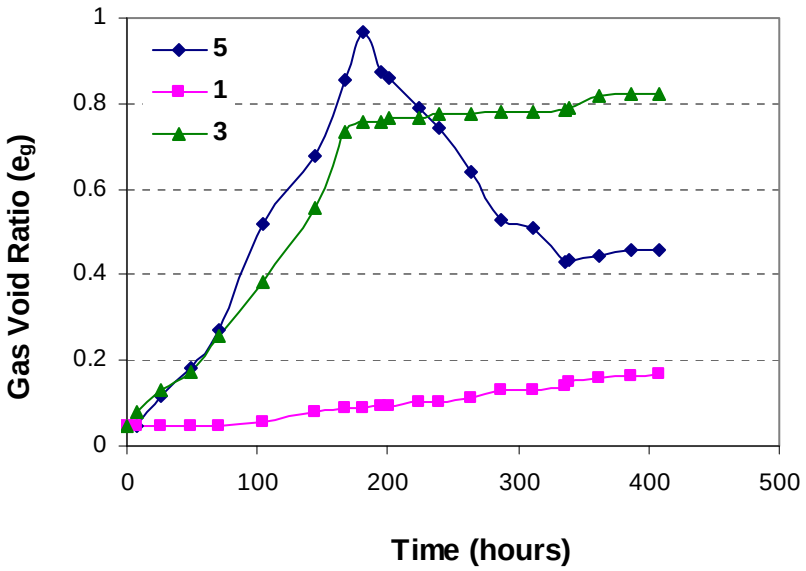

Figure 5-9 Variations of Gas Void Ratios with Time in Columns 1, 3 and 5

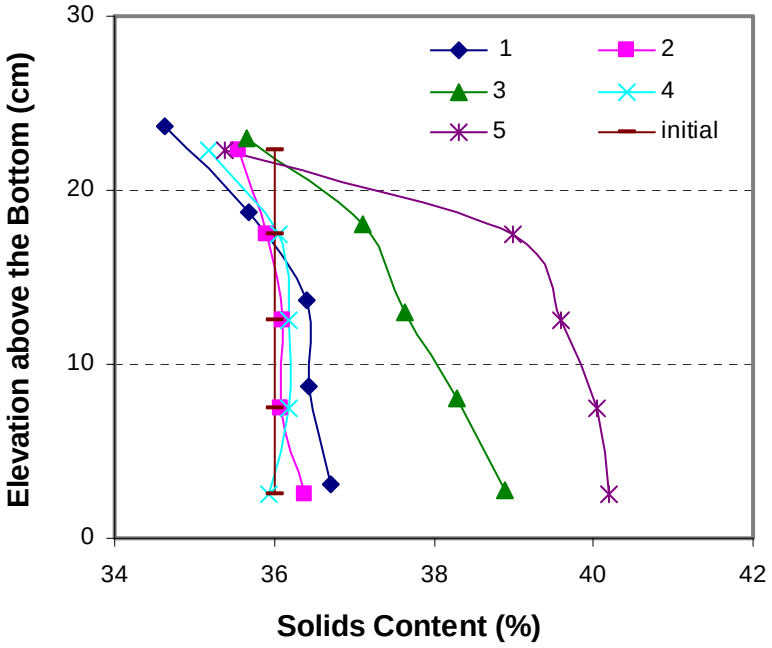

Figure 5-10 Profiles of Final Solids Contents (by Sampling) in Different Columns

CHAPTER 6

6 INTRODUCTION OF GAS MFT DENSIFICATION TESTS

6.1 Test Objective

Although the effects of microbial activity on MFT densification have been initially studied by small-scale column tests, the in-depth mechanisms leading to the rapid densification phenomenon remain unsolved. The following questions require clarification in order to move forward with effective, realistic tailings management strategies when biogenic activity may influence tailings behavior:

- How do the excess pore water pressure and operative stress change during microbial activity?
- How do different MFT structure strengths and stress histories affect MFT densification during biogas generation?
- How do the pore water chemical and microbiological properties change during microbial activity, and what are their effects on MFT densification? and
- How can the mechanisms be used to improve the reclamation and management of the oil sands tailings?

To answer these questions, a comprehensive experimental program of gas MFT densification tests has been developed.

A series of gas MFT densification tests have been carried out to model the microbial activities of the MFT under different conditions, including different stress histories and different depths in the tailings pond. The microbial activity of the MFT was stimulated by adding different amounts of sodium acetate and controlling the room temperature. In order to study the effects of different stress histories and structure strengths on gas evolution and MFT densification, the MFT samples were consolidated under different stresses (self-weight and 1.0 kPa) before microbial activity was initiated. Different back pressures (0 and 60 kPa) were applied to the test systems to model the microbial activity of the MFT at different depths at the tailings pond. During

microbial activity, various parameters, including volumetric changes, pore water pressures, and pore water chemical and microbiological properties were measured. This chapter describes the experimental program, test apparatus, and test method. The detailed test results are shown in Chapters 7 to 9.

6.2 Experimental Infrastructure

6.2.1 Introduction

A new test apparatus has been developed to study the densification properties of MFT with microbial activity under different conditions. As shown in Figure 6.1, the test apparatus consists of an acrylic cell of 15 cm inner diameter, an acrylic gas cylinder with an inner diameter of 1.92 cm or 3.809 cm, depending on expected gas volume, and a water collection standpipe with an inner diameter 1.11 cm. A plastic tube with 0.42 cm inner diameter connects the test cell to the standpipe in which the drained water is collected and measured during biogas generation. A submergible LVDT (Linear Variable Differential Transformer) was used to accurately measure the water-MFT interface movement. Three differential pressure transducers (T1, T2, T3) were used to measure the pore water pressures at different elevations (E1, E2, E3) in the sample. Transducer T4 was used to measure the hydrostatic changes in the test cell. Released gas thicknesses in the headspace were measured visually using a ruler taped on the outside wall of the gas cylinder. Water front movement in the plastic tube was also measured by visual observations. Figure 6.2 shows a photo of the gas MFT densification test in a temperature-controlled room.

At the time of testing, the space above the water-MFT interface was filled with pond water before microbial activity was initiated (by raising the room temperature from 4^{o}C to about 24^{o}C). Due to biogas generation, water in the test cell was partly pushed out into the water collection standpipe through the plastic tube. Water volumes in the water collection standpipe were measured using the pressure measurement from transducer T5.

In order to model biological activities at different depths of the pond, different air pressures, 0 and 60 kPa, were applied to the test system by a stable air pressure supply. An air cylinder, shown in Figure 6.1, was used to apply back pressure to the whole test system, including the test cell, released gas cylinder, water collection standpipe and the external ports of all differential pressure transducers. The air cylinder was connected to a plastic tube through which stable air pressure was input to the cylinder. From the cylinder, air pressure was applied to the whole test system using a series of small plastic tubes as shown in Figure 6-1. The pressure in the air pressure cylinder was controlled using a low-pressure regulator. When the air cylinder was open to the atmosphere, the gas MFT densification tests were carried out without air pressure being applied.

The samples were incubated at about 24^{o}C during microbial activity. When gas accumulation in the MFT reached a critical value, part of the generated gas was released to the headspace of the gas cylinder.

Before and after microbial activity, the room temperature was lowered to 4^{o}C to inhibit microbial activity. At this room temperature, hydraulic conductivity tests were conducted to measure the coefficients of permeability. Constant head differences were applied by fixing the inflowing tube (connected with a valve at the bottom of the cell) above the outflow tube to cause upward flow, as illustrated in Figure 6.1.

Two types of tests, gas MFT densification tests and chemical sampling tests, were conducted. Samples were obtained from chemical cells to study the chemical and microbiological properties of the MFT during microbial activity. The devices of chemical tests were similar to those of gas MFT densification tests as shown in Figure 6.1, except that pore water pressure changes and interface movements were not monitored in the chemical sampling tests.

6.2.2 Pore Pressure and Interface Movement Measurements

OMEGA PX26 series differential pressure transducers were used to measure the pore pressure changes at three different elevations: 0 cm, 1.45 cm, and 3.95 cm above the base of the cell. The transducers were also used to measure the hydrostatic pressure changes in the test cell (by T4), and pore pressure changes at the bottom of the water collection standpipe (by T5). The OMEGA differential pressure sensors used consisted of four active piezoresistive bridge devices. The changes of applied differential pressures are proportional to those of output voltages. There are two ports in each differential pressure sensor. If different pressures are applied to both sides of the transducer, the pressure sensor measures the pressure difference between the two ports. If one port is vented to the atmosphere, the measured pore pressure at another port is relative to the atmospheric pressure.

Two different models, PX26-001 GV and PX26-005GV, of OMEGA's differential pressure sensors were used in the tests. Model PX26-001 GV had a range of 1 psi (6.9 kPa), while model PX26-005GV had a range of 5 psi (34.5 kPa). The proof pressures for the two models were 20 psi (138 kPa). The accuracy of each model was 1% FS**.** The compensated temperatures ranged from 0^{o} C to 50^{o} C. Model PX26-005GV transducers were mainly used for T1, T2 and T3, while model PX26-001 GV transducers were mostly used for T4 and T5.

The transducers were calibrated at 24^{o}C room temperature before MFT samples were poured into the cell. They were saturated with de-aired pond water, and mounted at different elevations of the test cell and at the bottom of the water collection standpipe. The outside ports of the transducers were vented to the atmosphere. When calibrating, the test cell was filled with de-aired pond water and opened to the atmosphere. All the pressure transducers were connected to a data logger. By measuring output voltages of each sensor at different hydrostatic levels, the relationships between pore water pressure and output voltage were determined. When calibrating the transducers, the hydrostatic level changes were measured by visual observation using a ruler taped to the outside of the gas collection cylinder, and the voltage outputs

were recorded by the data logger. The calibration results are provided in Appendix F.

During consolidation tests (at 4^{o}C) and microbial activity (at 24^{o}C), a Schaevitz HCA500 Submersible Linear Variable Differential Transformer (LVDT) was used to measure the interface movements. An LVDT is an electromechanical device that produces an electrical output proportional to the displacement of a separate movable core. It has a range of ±12.7 mm, and a very high resolution. The LVDT can respond to even the most minute motion of the core to produce an output. When calibrating the LVDT, the displacements were measured using a precision micrometer, and the output voltages were measured by a voltmeter. During the consolidation tests of samples 10-12, a Novotechnik TR 25 Linear Potentiometer (LP) was used to measure the MFT interface movements. The LP has a range of 25 mm and a resolution of better than 0.01 mm. The calibration results of the sensors (LVDT and LP) are provided in Appendix F.

Figure F.1 (in Appendix F) shows a sketch of the displacement measurement system. The movable rod of the LVDT was connected to a hollow copper rod which was screwed into a small rectangular plastic plate. Another hollow copper rod connected the rectangular plate to a circular plastic plate which was seated on the MFT surface. Holes with 0.3-0.6 mm diameter were drilled in the circular plate to allow gas bubbles to escape during microbial activity. A filter paper was placed beneath the porous plate to keep soil particles in place.

6.2.3 Data Acquisition System

Figure F.2 (in Appendix F) shows a layout of the automatic data collecting and recording system. The monitoring signals from pressure transducers and LVDTs were controlled and processed by an excitation controller and signal conditioner. Conditioned signals were transferred to and stored in the Agilent 34970, a Data Acquisition/Switch Unit. The data was then transferred to a computer.

Agilent 34970 is a Data Acquisition/Switch Unit that combines precision measurement capacity with flexible signal connection for the test systems. It has convenient data logging features and flexible data acquisition/switching features. It can directly measure thermocouples, RTDS, thermistors, dv voltage, ac voltage, resistance, dc current, ac current, and frequency, and includes up to 60 channels per instrument. The reading rates are up to 600 readings per second on a single channel, and scan rates are up to 250 channels per second. By using Benchlink Data Logger Software, one can easily set up a test, display test results and download test data to a computer. A word of caution, however, data will be automatically deleted from the recording system after downloading, and if mistakes are made during downloading, the recorded data might be lost.

The aforementioned data collecting and recording system was used for most of the consolidation and gas densification tests. But, in consolidation Tests 10-12 (those conducted in the moisture room), the measurements of LP and pore pressure transducers were recorded by a data dolphin, which was connected to a computer. The data dolphin is a simple and portable data acquisition device. Most sensors (LVDT, LP and pore pressure transducers) can be directly connected to the data dolphin without any signal conditioning. After downloading data to the computer, the data can still be stored in the dolphin. However, usage of the data dolphin is restricted by its limited number of channels and high equipment cost.

6.3 Test Procedure and Schedule

Table 6.1 shows the sequences of the gas MFT densification tests and chemical sampling tests. A total of 27 tests were conducted: 18 densification tests and 9 chemical sampling tests. Different amounts of sodium acetate, 0, 0.6 and 1.75 g, per liter of MFT, were added to the samples before testing. Samples 1-6 and **7©~9©** (chemical sampling tests) were self-weight consolidated at 4^{o}C room temperature before microbial activity was initiated.

Samples 10-12, Samples 19-24 and Samples 25©~27© (chemical sampling tests) were consolidated under 1.0 kPa loading before microbial activity. For Tests 13-15 and Tests 16©~18©, microbial activities were stimulated shortly after the MFT was poured into the cells (without pre-consolidation). After the 1.0 kPa consolidation was finished, the loadings (by lead shots) on Samples 10-12 were released, and the microbial activities started. These three tests were used to model the stress condition of over-consolidated MFT.

During microbial activity, 60 kPa air pressure was applied to Samples 4-6, 22-24, and 25©-27© to model microbial activities at certain depths of the pond. For all other samples, microbial activities were under atmospheric pressure plus about 1.0 m water head. The overall procedure of the gas MFT densification tests can be summarized as follows:

- Sample preparation and initial parameter measurements.
- Consolidation under self-weight (Samples 1-6) or 1.0 kPa loading (Samples 10-12 and Samples 19-24) at 4^{o}C temperature. During consolidation, 1.0 kPa loading was applied at two steps.
- After 1.0 kPa consolidation, the loadings on Samples 10-12 were released.
- Permeability test at 4^{o}C.
- Microbial activity and biogas generation at 24^{o}C.
- Permeability test again at 4^{o}C.

Tests 1-6 and 7©~9© comprised the first sequence (biogas generation from Oct. 30 to Dec. 24 in 2003), Tests 10-15 and 16©~18© comprised the second sequence (biogas generation from Dec.24, 2003 to Feb. 12, 2004) and Tests 19-24 and 25©~27© were the final sequence (biogas generation from June 15 to Oct. 8 in 2004).

Table 6.2 shows the schedule of gas MFT densification tests and chemical sampling tests. The complete test program lasted approximately 14 months. Most of the tests (including consolidation and gas MFT densification tests) were carried out in a temperature-controlled cooler, but due to space and temperature factors, the consolidation tests (from 0.5 to 1.0 kPa) of Samples

10-12 were conducted in the moisture room (with 4^{o} C room temperature), which was used to store samples for the Geotechnical Group.

6.4 Characterization Equations for Gassy MFT Behavior

6.4.1 Introduction

During the gas MFT densification test (Figure 6.1), different methods of measurement were used for different variables. The interface movements were measured by a submergible LVDT, the released gas volumes by visual observations, the water level changes in the standpipe by pressure transducer T5, the pore pressure changes at the three different elevations, bottom (E1), 1.45 cm (E2) and 3.95 cm (E3) above the bottom of the sample, by pressure transducers T1, T2 and T3, respectively, the hydrostatic pressure changes in the test cell by pressure transducer T4, and the water front movements in the plastic tube by visual observations. From these measurements, some parameters (i.e. volumetric changes, pore pressures and operative stresses) were determined.

Figure 6.3 shows the conditions of the gas MFT densification tests at time 0 (initial time) and time t (some time during microbial activity). Some symbols and parameters in gas MFT densification test are explained in Table 6.3. This section demonstrates the calculation methods of some parameters of the MFT during microbial activity.

6.4.2 Volumetric Changes (Gas and Water)

The calculations of the volumetric parameters are based on water mass balance in the whole test system, including the MFT sample, cell space above the MFT interface, plastic tube, and water collection standpipe. This section presents the calculation methods of some volumetric parameters at time t during microbial activity. The meanings of the symbols are explained in Table 6.3.

1. Interface movements, Δh, are calculated by LVDT readings.
2. Total MFT Volume V_t

$$V_t = V_0 + \Delta h\ A \qquad [6\text{-}1]$$

3. Released gas volume at time t

$$V_{rt} = h_{rt}\ A_1 \qquad [6\text{-}2]$$

4. Water volume (V_{wt}) in the MFT at time t

Initial water volume in the whole system = $V_{w0} + V_h$

Water volume in the system at time t = $V_{wt} + V_h - V_{rt} + L_t\ A_3 + h_{pt}\ A_2 - \Delta h\ A$

Initial water volume in the system = water volume in the system at time t

$V_{w0} + V_h = V_{wt} + V_h - V_{rt} + L_t\ A_3 + h_{pt}\ A_2 - \Delta h\ A$

$$V_{wt} = V_{w0} + h_r A_1 - L_t\ A_3 - h_{pt}\ A_2 + \Delta h\ A \qquad [6\text{-}3]$$

5. Drained water volume (V_{dt}) from the MFT at time t

$$V_{dt} = V_{w0} - V_{wt} = h_{pt}\ A_2 + L_t\ A_3 - h_r A_1 - \Delta h\ A \qquad [6\text{-}4]$$

6. Trapped gas volume (V_{tgt}) in the MFT at time t

Total MFT volume at time t = $V_{w0} + V_s + \Delta h\ A$

Total MFT volume at time t = $V_{wt} + V_{tgt} + V_s$

$V_{w0} + V_s + \Delta h\ A = V_{wt} + V_{tgt} + V_s$

$V_{tgt} = V_{w0} - V_{wt} + \Delta h\ A$

$$V_{tgt} = V_{dt} + \Delta h\ A \qquad [6\text{-}5]$$

7. Trapped gas volume (V_{tgst}) at STP (25^o C and 1 atm.)

By combined gas law:

$$\frac{P_1 V_{tgt}}{273 + 24} = \frac{P_2 V_{tgst}}{273 + 25}$$

$P_1 = \sigma_t$

σ_t is the total stress (at time t) in the middle of the sample plus 1 atmosphere.

P_2 = 1 atmosphere

$$V_{tgst} = \frac{\sigma_t V_{tgt}}{103.12} \quad [6\text{-}6]$$

8. Released gas volume (V_{rst}) at STP (25°C and 1 atm.)

Similar to the trapped gas volume at STP

$$V_{rst} = \frac{\sigma_{rgt} V_{rt}}{103.12} \quad [6\text{-}7]$$

Where, σ_{rgt} is the pressure of the released gas at STP, V_{rt} is the released gas volume in the cell

9. Total gas volume at STP

$$V_{gst} = V_{tgst} + V_{rst} \quad [6\text{-}8]$$

10. Density (ρ_t) and unit weight (γ_t) of the sample at time t

$$\rho_t = \frac{m_0 - V_{dt}}{V_0 + \Delta h A} \quad \text{(g/ml)} \quad [6\text{-}9]$$

$\gamma_t = \rho_t * 9.8$ (kN/m^3)

11. Total solids content (SC_t) at time t

$$SC_t = \frac{m_s}{m_0 - V_{dt}\rho_w} * 100\% \quad [6\text{-}10]$$

12. Gas content (GC_t) in the sample

$$GC_t = \frac{V_{tgt}}{V_t} * 100\% \qquad [6\text{-}11]$$

13. Water void ratio

$$e_{wt} = \frac{V_{w0} - V_{dt}}{V_s} \qquad [6\text{-}12]$$

14. Gas void ratio

$$e_{gt} = \frac{V_{tgt}}{V_s} \qquad [6\text{-}13]$$

15. Total void ratio

$$e_t = e_{wt} + e_{gt} \qquad [6\text{-}14]$$

16. Degree of saturation

$$S_r = \frac{e_w}{e} * 100\% \qquad [6\text{-}15]$$

6.4.3 Excess Pore Water Pressure and Operative Stress

The concept of "operative stress" was proposed by Sills et al. (1991). It is based on the oedometer tests of Thomas (1988) in which gas bubbles were produced by the zeolite technique. The methane-saturated zeolite was introduced into reconstituted samples. Gas bubbles were released to the soil over a period of a few hours. During consolidation, incremental loadings were applied. There was very little gas released from the sample, and no biogenic gas was generated. As such, the gas content was almost constant. The operative stress was defined as:

$$\sigma_{op} = \sigma - u \quad [6\text{-}16]$$

where, σ_{op} is operative stress, σ is total stress, and u is pore water pressure.

It is considered that the "operative stress" concept is applicable for soils with occluded gas bubbles, and that for any initial gas content, water void ratio (e_w) is controlled by operative stress (Sills et al., 1991).

The operative stress approach is utilized to interpret the rapid densification of the MFT during biogas generation. The results of the gas MFT densification tests will be discussed using this approach. However, it should be noted that the test conditions in this research were different from those in Thomas's tests. For example, the gas void ratio significantly changed in testing conducted in this research.

This section demonstrates the calculation methods of excess pore water pressure and operative stress, at time t, for the gas MFT densification test, as illustrated in Figure 6.3. The changes in excess pore water pressure and operative stress at the bottom of the cell (E1) are considered below. For the other elevations (E2 and E3), the calculation methods are similar.

1. Initial total stress (σ_0) at the bottom

$$\sigma_0 = \gamma_0 h_0 + \gamma_w h_1 + \sigma_L \quad [6\text{-}17]$$

2. Initial hydrostatic pressure at the bottom

$$u_{s0} = (h_0 + h_1)\gamma_w \quad [6\text{-}18]$$

3. Initial pore water pressure (u_{w0})

For normally consolidated MFT, $u_{w0} = u_{s0}$ [6-19]

For MFT without pre-consolidation,

$$u_{w0} = u_{s0} + (\gamma_0 - \gamma_w) h_0 \quad [6\text{-}20]$$

4. Initial excess pore water pressure

For normally-consolidated MFT, $u_{e0}=0$ [6-21]

For MFT without pre-consolidation

$u_{e0}=(\gamma_0-\gamma_w)\,h_0$ [6-22]

5. Initial operative stress (σ_{op0})

$\sigma_{op0}=\sigma_0-u_{w0}$ [6-23]

6. Total stress (σ_t) at time t

$\sigma_t=\gamma_t(h_0+\Delta h)+\gamma_w h_{yt}+\sigma_L$ [6-24]

7. Pore water pressure at time t

u_{wt} = u_{w0} + pore water pressure change measured by T1

$u_{wt}=u_{w0}+K_{(T1)}$ (Volt (t)-Volt(0)) [6-25]

where, $K_{(T1)}$ is the calibration coefficient of transducer T1

Volt (t) and Volt (0) are the output readings of T1 at time t and time 0, respectively.

8. Hydrostatic pore water pressure (u_{st}) at time t

$u_{st}=u_{s0}+K_{(T4)}$ (Volt (t)-Volt(0)) [6-26]

where, $K_{(T4)}$ is the calibration coefficient of transducer T4

Volt (t) and Volt (0) are the output readings of T4 at time t and time 0, respectively.

9. Excess pore water pressure (u_{et}) at time t

$u_{et}=u_{wt}-u_{st}$ [6-27]

10. Operative stress (σ_{opt}) at time t

$$\sigma_{opt} = \sigma_t - u_{wt} \qquad [6\text{-}28]$$

From the above equations, the changes of total stress and pore water pressure can be calculated. The results are shown in Appendix H. The total stress and pore water pressure are used to calculate excess pore water pressure and operative stress, which will be analyzed for each test.

Table 6-1 Test Sequences of Gas MFT Densification Tests

Sodium Acetate	Self-Weight consolidation			Consolidation under 1 kPa Loading				Without Pre-consolidation	
	Sequence 1			Sequence 2	Sequence 3			Sequence 2	
g/L MFT	Air Pressure (kPa)								
	0	60	0	0	0	60	60	0	0
0	1	4	7 ©	10	19	22	25©	13	16©
0.6	2	5	8©	11	20	23	26©	14	17©
1.75	3	6	9©	12	21	24	27©	15	18©

Notes: 1- 27: Test identification number, 7©~9©, 16©~18©, 25©~27© are chemical sampling tests.
Sequence 1: biogas generation from Oct 30 to Dec. 24, 2003; Sequence 2: biogas generation from Dec 24, 2003 to Feb. 12, 2004; Sequence 3: biogas generation from June 15 to Oct. 8, 2004.

Table 6-2 Schedule of Gas MFT Densification Tests

Periods	Test No.	Activities
Aug. 7~ Oct 30, 2003	1-6, 7©~9©	Self-weight Consolidation at 4°C.
	10~12	0.5 kPa Consolidation at 4°C.
Oct 30 ~ Dec. 24, 2003	1~3, 7©~9© (Sequence 1)	Gas generation under atmospheric pressure at 24°C,
	4~6 (Sequence 1)	Gas generation under 60 kPa back pressure at 24°C,
	10~12	1.0 kPa Consolidation in moisture room at 4°C.
Dec. 24 ~ Feb.12, 2004	10-12 (Sequence 2)	Gas generation under atmospheric pressure at 24°C
	13~15, 16©~18© (Sequence 2)	Gas generation without pre-consolidation under atmosphere pressure at 24°C,
Feb 12~ June. 15, 2004	19~21, 22~24, 25©~27©	Consolidate to 1.0 kPa at 4°C.
June 15 ~ Oct. 8, 2004	19~21 (Sequence 3)	Gas generation under atmospheric pressure at 24°C,
	22~24, 25©~27© (Sequence 3)	Gas generation under 60 kPa back pressure at 24°C,

Table 6-3 Explanations of Some Symbols and Parameters

Symbol	Explanation
h_o	Initial sample height at time 0
h_{y0}	Hydrostatic head above the MFT interface at time 0.
γ_0	Unit weight of the sample at time 0
A	Cross sectional area of test cell
A_1	Cross sectional area of released gas cylinder
A_2	Cross sectional area of water collection standpipe
A_3	Cross sectional area of plastic tube
T_1	Differential pressure transducer at the bottom (E1)
T_2	Differential pressure transducer at 1.45 cm elevation (E2) above the bottom of the sample
T_3	Differential pressure transducer at 3.95 cm elevation (E3) above the bottom of the sample
T_4	Differential pressure transducer to measure hydrostatic changes in test cell.
T_5	Differential pressure transducer to measure water volume in the standpipe
V_0	Total sample volume at time 0
m_0	Total sample mass at time 0
m_{w0}	Water mass in the sample at time 0
V_{w0}	Water volume in the sample at time 0
m_s	Solids mass in the sample
V_s	Solids volume in the sample
V_h	Total water volume in the cell space above the interface, in plastic tube and in standpipe at time 0.
Δh	Interface movements of the MFT at time t
V_t	Total MFT volume at time t
L_t	Water front movements in plastic tube at time t (relative to time 0)
h_{pt}	Water level change in water collection standpipe at time t
h_{rt}	Released gas thickness in gas collection cylinder at time t
V_{rt}	Released gas volume at time t
V_{wt}	Water volume in the MFT at time t

Table 6.3 Explanations of Some Symbols and Parameters (Continuing)

h_{yt}	Hydrostatic head above the MFT interface at time t
V_{dt}	Drained water volume from the MFT at time t
V_{tgt}	Trapped gas volume in the MFT at time t
V_{tgst}	Trapped gas volume at standard condition (STP, 25^o C and 1 atm.) at time t
V_{rst}	Released gas volume converted to STP condition
V_{gst}	Total free gas volume (trapped gas + released gas) at STP at time t
ρ_t	Bulk density of the sample at time t
γ_t	Unit weight of the sample at time t
SC_t	Total solids content of the sample at time t
GC_t	Trapped gas content in the sample at time t
e_{wt}	Water void ratio at time t
e_{gt}	Gas void ratio at time t
e_t	Total void ratio at time t
S_r	Degree of saturation of the sample at time t
σ_0	Total stress at bottom at time 0
σ_L	Surcharge applied on the sample
u_{s0}	Hydrostatic pore pressure at the bottom at time 0
u_{w0}	Pore pressure at the bottom at time 0
u_{e0}	Excess water pressure at the bottom at time 0
σ_{op0}	Operative stress at time 0
σ_t	Total stress at the bottom at time t
u_{wt}	Pore pressure at the bottom at time t
u_{st}	Hydrostatic pore pressure at the bottom at time t
u_{et}	Excess pore pressure at the bottom at time t
σ_{opt}	Operative stress at the bottom at time t

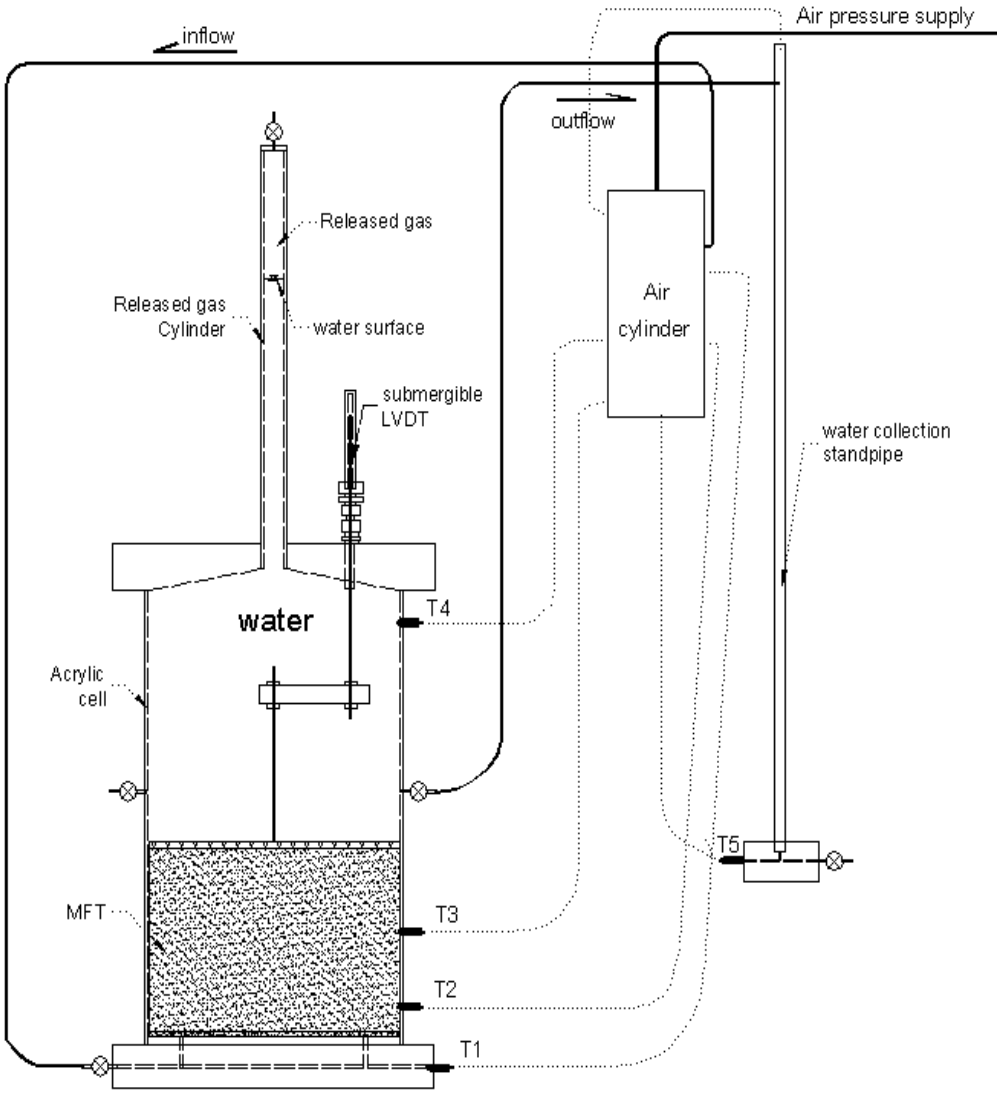

Figure 6-1 A Schematic of the Gas MFT Densification Test

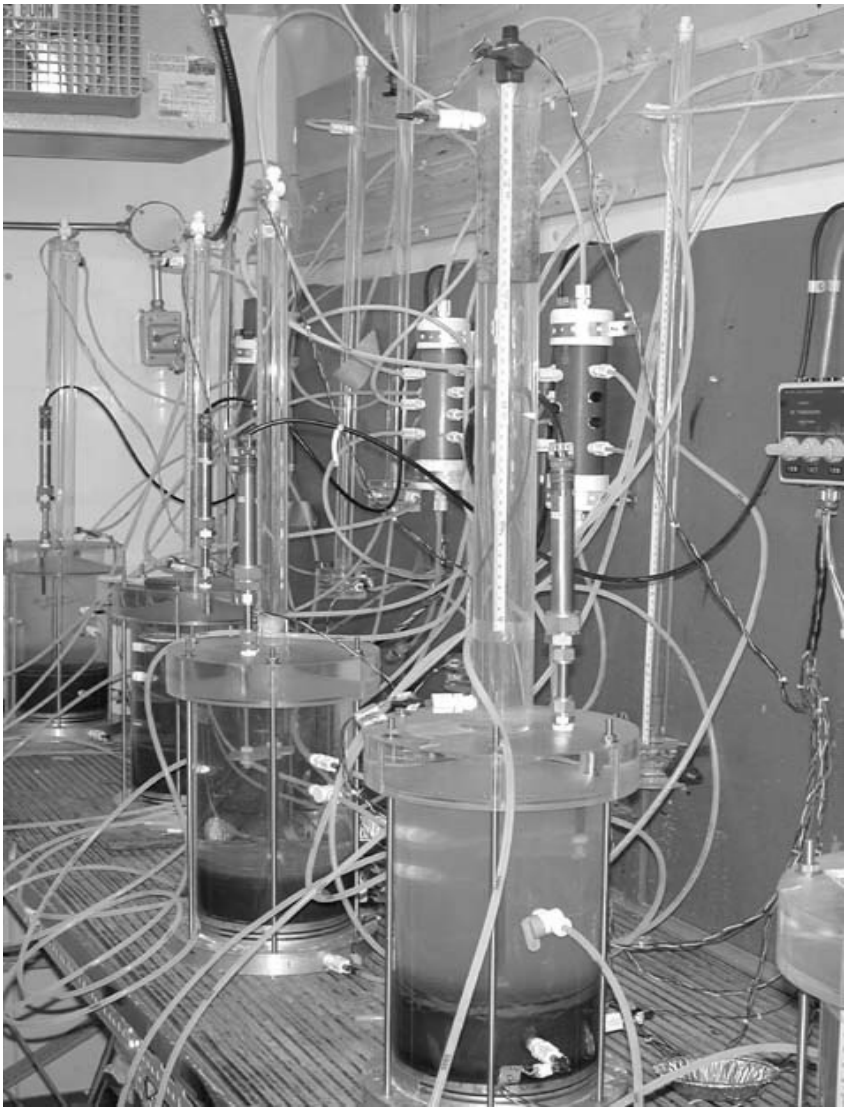

Figure 6-2 A Photo of Gas MFT Densification and Permeability Tests

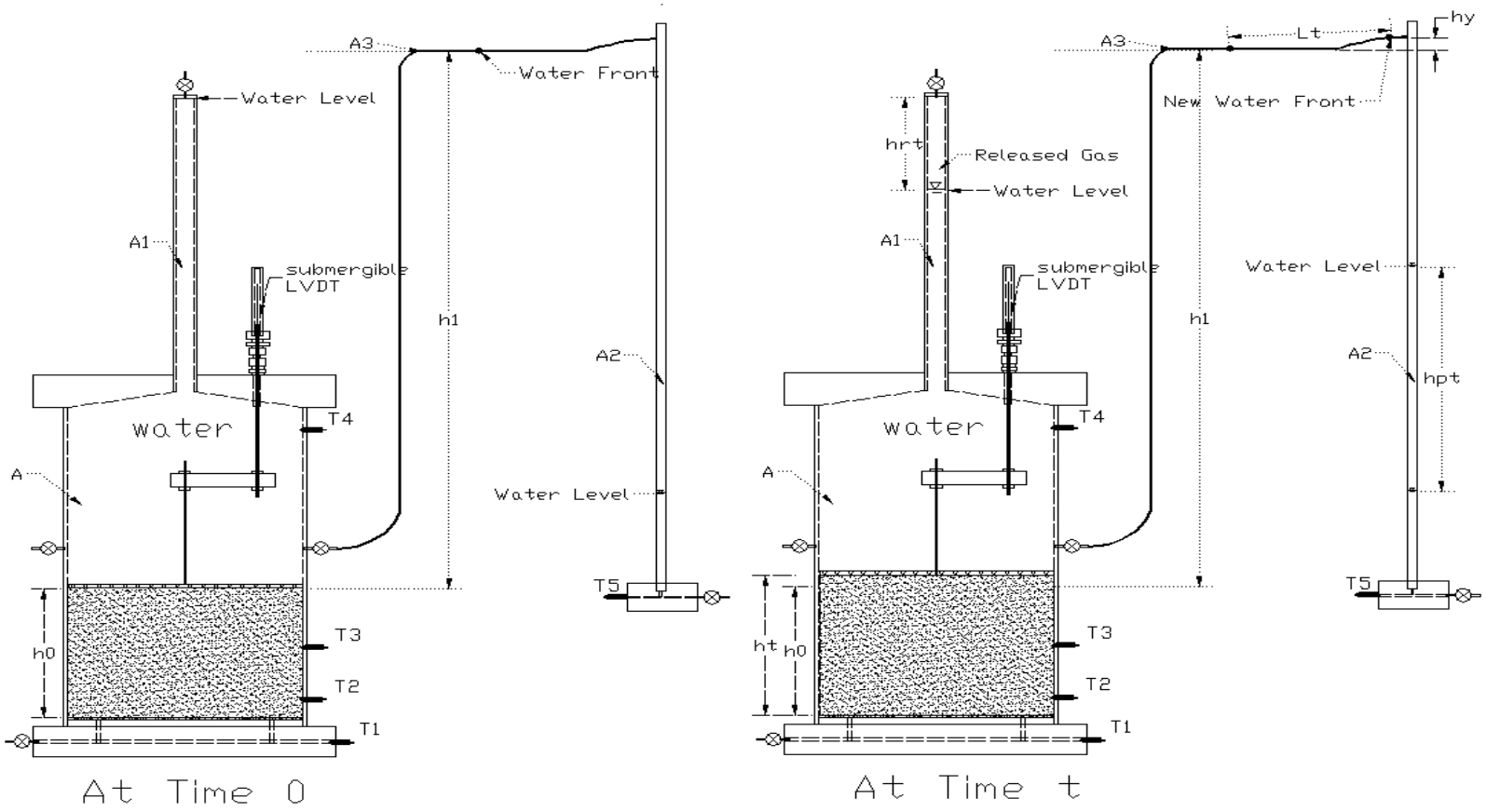

Figure 6-3 Conditions of Gas MFT Densification Tests at Time 0 and Time t

CHAPTER 7

7 INFLUENCE OF BIOLOGICAL GAS GENERATION FOLLOWING SELF WEIGTH CONSOLIDATION

7.1 Introduction

The influence of sodium acetate concentration under conditions of both atmospheric pressure and a fluid pressure of 60 kPa were examined in Tests 1 to 6, including the associated chemical sampling Tests 7©, 8©, and 9©.

Tests 1-6 were used to study the densification properties of the normally consolidated MFT (under self-weight) during microbial activity. Different amounts of sodium acetate, 0 g, 0.6 g, and 1.75 g per litre MFT, were added to control microbial activity. From August. 7 to October 30 in 2003, self-weight consolidation was carried out at 4^{o}C to create a certain structural strength. The room temperature was then raised to 24^{o}C to initiate microbial activity. For Tests 1-3, no air pressure was applied to the test system. As a result, microbial activity occurred under about 1.0 m hydrostatic head plus atmospheric pressure. The test conditions of Cells 7©-9© were as close as possible to the test conditions of Cells 1-3. Tests 7©-9© were used to provide chemical samples during microbial activity. After self-weight consolidation, 60 kPa air pressure was applied to Samples 4-6 to model the microbial activity of the MFT at about 6-7 m depth below the water surface of the tailings pond.

7.2 Test Materials and Sample Preparation

The initial sample was obtained from a depth of about 2.5 m below the water-MFT interface at Sta. 2 of the MLSB in July 2003. The solids content of the field MFT was 40.6%, and the bulk density of the completely remoulded MFT was 1.294 g/mL.

Figure 7.1 shows the grain size distribution of the initial MFT material from the tailings pond. It had a clay content of 53.63% and fines content (<44 μm) of 93.2%. The water content (percentage of water mass to solids mass in MFT sample) was 146.3%, and the ratio of fines/(fines + water) was 0.39. This was a relatively dense material for starting gas MFT densification testing since the ratio of fines/(fines + water) was about 0.3 (from historical monitoring data as shown in Fig. 1.3) when microbial activity began in the MLSB. To make the initial sample coincide with field conditions before microbial activity began, recycled water from the pond was added to the field MFT and the two were completely mixed. The mixed sample had a solids content of 34.6%, and ratio of fines/(fines + water) of 0.33. Initial parameters of the mixed sample are provided in Table 7.1. Before being poured into the test cell, the reconstituted sample was placed on a vibration table to accelerate the release of trapped air (or gas) bubbles from the MFT. Table 7.2 summarizes some information regarding Samples 1-6 before self-weight consolidation tests were started.

7.3 Self -Weight Consolidation

Figure 7.2 shows a sketch of the self-weight consolidation test. The inner diameter of the acrylic cell was 15 cm. A Schaevitz LVDT was used to measure the interface movements during consolidation. Pore water pressures in Sample 4 were monitored during the self-weight consolidation.

Water was drained out from the bottom and the top of the sample during the consolidation. A glass burette connected the cell bottom through a rubber tube kept the outflow at the same level as the water surface in the cell. Since the water level in the cell kept dropping during the consolidation test, the glass burette was frequently adjusted to keep it at the same level as the water surface in the cell.

Table 7.3 shows some parameters of Samples 1-3 after self-weight consolidation. After self-weight consolidation, the densification conditions of the three samples

were similar (the solids contents were about 38%). The detailed results of the consolidation tests (before microbial activity) are provided in Appendix G.

7.4 Constant Head Permeability Tests before Microbial Activity

In order to study the influence of microbial activity and biogas generation on MFT permeability, constant head permeability tests were carried out at 4^{o}C temperature before and after microbial activity. After self-weight consolidation was finished, the valve at the bottom of the cell was closed to stop the outflow. The apparatus for the gassy MFT densification and permeability tests, as shown previously in Figure 6.1, was installed. The cell space above the MFT interface was filled with pond water. A plastic tube connected to the bottom of the cell was used as an inflow burette, and another plastic tube connected to a valve above the MFT interface was used as an outflow burette. Both the plastic tubes were transparent so that the water front movement could be identified by visual observations. The two plastic burettes were horizontally fixed on the wall of the cold room with the inflow burette slightly above the outflow burette. An upward gradient of about 0.2 (Suthaker, 1995) was applied during permeability tests.

Permeability Tests 1-3 were performed with both the inflow and outflow burettes open to the atmosphere. The hydrostatic head was about 1 m above the MFT interface. Permeability and gassy MFT densification Tests 4-6 were performed with 60 kPa air pressure applied to the test system.

Recycled water from the tailings pond was used as permeant. During permeability tests, water front movements in both the inflow and outflow burettes were observed visually. The plastic tubes had an inner diameter of 4.24 mm. Assuming the accuracy of visual observations of the water front movements was about 0.1 mm, the measurement accuracy of the seepage water volume was about 1.4×10^{-3} mL.

Figure 7.3 shows the flow velocity vs. time in Tests 1-3, and Figure 7.4 shows the flow velocity vs. time in Tests 4-6. For each test, the inflow velocity was slightly higher than the outflow velocity at a steady state. It is likely that small part of the inflow water was used to fill some voids in the MFT. When both the inflow and outflow velocities became stable, the steady state seepage was reached. The average velocity of the inflow and outflow at the steady state was used to calculate the coefficient of permeability from Darcy's Law. The results of permeability Tests 1-6 (before microbial activity) are shown in Table 7.4. The coefficient of permeability of Sample 3 was slightly higher than those of Samples 1 and 2. This may be related to the large addition of sodium acetate in Sample 3. Despite this, the differences of the measured coefficients of permeability among the six samples were small.

7.5 Tests 1 to 3

After about 3 month consolidation under self-weight, the excess pore pressures in the MFT were close to zero. Samples 1 to 3 can be considered as normally consolidated soils. After the completion of self-weight consolidation and permeability tests as demonstrated above, the room temperature was raised to about 24^{o}C to activate microbiological activity. During microbial activity of the three tests, no air pressure was applied to the air cylinder (Figure 6.1). The MFT samples were under atmospheric pressure plus about 1 m water head. The objective of the tests was to study the behaviour of the self-weight consolidated MFT at shallow depths during microbial activity.

7.5.1 Test Results

After constant head permeability tests were finished, the room temperature was increased. It took about 24 hours for the room temperature to increase from 4^{o}C to 24^{o}C. Due to the defrosting operation of the temperature-controlling device,

the room temperature fluctuated about 2-3^{o}C for every 5 hours. Figure 7.5 shows the room temperature changes during these test series.

With temperature increasing, microbial activity was initiated, and gas was produced in the MFT. Figure 7.6 shows the changes of the total gas volume at standard temperature and pressure (STP, 25^{o}C and 1 atm.) with time in Samples 1 to 3. The total gas volumes, including the trapped gas volume and released gas volume are determined by Equation 6-8. It is assumed that gas bubbles (trapped gas and released gas) started to form only after the dissolved gas in the pore water had reached the solubility limit, and that most of the dissolved gas existed in the pore water of the MFT. According to Holowenko et al. (2000), the major component of the biogenic gas was methane. The solubility of methane gas in 25^{o}C water is 1.32×10^{-3} mol /bar/L water (Langmuir, 1996). For very soft soil, the gas pressure is approximately equal to the total stress (Wheeler et al., 1990). If the water volume and total stress in the MFT are known, the dissolved gas mass can be approximately determined using Henry's Law. Table 7.5 shows the equivalent gas volumes (at STP) of the dissolved gas in Samples 1 to 3. Once the dissolved gas volume reaches the solubility limit of the solution, it should be stable if the total stress and temperature are as well. Using Equations 6-6 and 6-7, the trapped and released gas volumes at standard temperature and pressure (25^{o}C and 1 atm.) can be calculated. The purpose of converting the total gas volumes to standard condition (STP) was the convenience of comparing the gas generation volumes under different conditions.

With an increase in sodium acetate concentration, the total gas volumes increased. Sample 3 which had the highest sodium acetate concentration, with a total gas volume of about 360 mL (at STP) was generated rapidly (the average gas generation rate was about 1 mL per hour) during the first 360 hours in this test, after which time the gas generation rate decreased. In Test 2, gas was generated at a rapid rate (the average rate was about 0.36 mL per hour) during the first 200 hours, and continued at a slower rate from that point. In Test 1, there was no

obvious increase in the total gas volume during the first 150 hours. It is likely that most of the generated gas in this period was dissolved in the solution. After 150 hours, the gas volume started to slowly increase at an approximately constant rate (about 0.04 mL per hour).

Figure 7.7 shows the changes of the released gas volume (at STP) with time. After about 200 hours, gas started to be released from Sample 3 at a rapid rate. The released gas volume was about 220 mL at the end of the test. Small amounts of gas started to be released from Sample 2 after about 400 hours. There was no visible gas release from Sample 1.

Figure 7.8 shows the changes in gas content (a ratio of trapped gas volume to total MFT volume in percentage) with time. In Sample 3, the gas content rapidly increased during the first 230 hours. After it reached the threshold value of 10.5%, it slightly decreased. This indicates that after 230 hours, gas release rates were higher than gas generation rates. At the end of testing, the gas contents in Samples 1, 2, and 3 were 2%, 7.5% and 10%, respectively. Figure 7.9 shows the changes of the gas void ratio with time. The final gas void ratios in Samples 1, 2, and 3 were 0.078, 0.353 and 0.484, respectively.

Figure 7.10 shows the MFT interface movements over time. In Test 3, the MFT interface moved upward during the first 230 hours, due to an increase in the trapped gas volume. The interface then settled because large amount of gas bubbles escaped from the MFT. After about 360 hours, the interface was stable. The final MFT interface was 3.1 mm above the initial level. In Test 2, the MFT interface moved up during the first 150 hours then became stable. Due to very slow gas generation, the MFT interface of sample 1 slowly settled during the test.

Figure 7.11 shows the drained water volumes from Samples 1, 2, and 3 at different times. At the end of testing, the drained water volumes from Samples 1, 2, and 3 were 47 mL, 57 mL and 72 mL, respectively. The water void ratios of

Samples 1, 2, and 3 were 3.41, 3.36 and 3.3, respectively. With the increase of microbial activity and biogas generation in each sample, the water drainage rates of the MFT increased.

Figure 7.12 shows the changes of bulk density with time. The changes of the bulk density of the MFT were related to the increase rates of the trapped gas volume in the samples. The bulk density of Sample 1 was relatively stable at the early period, but decreased slightly with time. During the first 230 hours, the bulk density of Sample 3 rapidly decreased from 1.263 g/mL to 1.14 g/mL, due to the rapid increase of the trapped gas volume. After 230 hours, the bulk density was relatively stable as the trapped gas volume stabilized. The bulk density of Sample 2 rapidly decreased with time, during the first 150 hours, and then decreased slowly. At the end of testing, the bulk densities of Samples 1, 2, and 3 were 1.25 g/mL, 1.18 g/mL and 1.15 g/mL, respectively.

Figures 7.13 to 7.15 show the volumetric changes (trapped gas, released gas and total gas volumes at STP, and water drainage volumes) in Tests 1-3, respectively. In Test 1, the water drainage volume rapidly increased during the first 40 hours, and then increased slowly at an almost constant rate. In Test 2, total gas volume rapidly increased during the first 200 hours, as did the water drainage volume. In Test 3, a clear connection between the gas generation rate and water drainage rate were observed.

Figures 7.16 to 7.18 show the changes of trapped gas volumes and total MFT volumes, with time, in Samples 1 to 3, respectively. In Sample 1, the trapped gas volume increased very slowly and the total MFT volume decreased with time. The very slow gas generation of this sample had little effect on the MFT behaviour. In Sample 2, both the trapped gas volume and total MFT volume rapidly increased with time during the first 150 hours, but the increase rate of total MFT volume lagged behind that of the trapped gas volume. As a result, water was rapidly pushed out of the MFT during this period. When the trapped gas

volume slowly increased, the total MFT volume stabilized. Water was drained out slowly. In Sample 3, both the trapped gas volume and global MFT volume rapidly increased during the first 230 hours, but the global expansion of the MFT matrix lagged behind the increase of the trapped gas volume. As such, part of the space required by the trapped gas bubbles was obtained by pushing water out of the MFT. From 230 hours to 360 hours, part of the generated gas escaped from the MFT. Both the trapped gas volume and global MFT volume decreased with time, but the total MFT volume decreased more rapidly than the trapped gas volume did. Thus, more water was rapidly drained out of the sample. After 360 hours, the total MFT volume was almost stable, and the trapped gas volume increased slowly. Water was drained out slowly during this period.

The changes of total stress and pore water pressure during microbial activity are shown in Appendix H. Figure 7.19 shows the changes of excess pore water pressure and operative stress at the bottom (Elevation 1, E1) of Sample 1. After self-weight consolidation, the excess pore water pressure in the MFT was approximately zero, and operative stress at the bottom (E1) of the sample was 0.177 kPa. During the first 25 hours, with temperature increasing, the excess pore water pressure at the bottom rapidly increased to 0.053 kPa, and operative stress decreased from 0.177 kPa to 0.124 kPa. After another 25 hours, the excess pore water pressure decreased to 0.026 kPa, because the excess pore water pressure was partly dissipated, and the temperature became stable. After about 50 hours, excess pore water pressure and operative stress were almost stable.

Figure 7.20 and Figure 7.21 show the changes of excess pore water pressure and operative stress at 1.45 cm elevation (Elevation 2, E2) above the bottom of Sample 1. After self-weight consolidation, the excess pore water pressure was zero, and the operative stress was 0.14 kPa. During the first 25 hours, excess pore water pressure increased to 0.114 kPa, and operative stress decreased from 0.14 kPa to 0.038 kPa, due to a temperature increase and gas generation. Within another 25 hours, with the MFT temperature stabilizing and excess pore water

pressure partly dissipating, the excess pore water pressure slightly decreased, and operative stress slightly increased. After 50 hours, the excess pore water pressure and operative stress were almost stable.

Figure 7.22 shows the changes of excess pore pressure and operative stress at 3.95 cm elevation (Elevation 3, E3) above the bottom of Sample 1. Similar changes to those at E1 and E2 are shown.

Figures 7.23 and 7.24 show the changes of excess pore pressure and operative stress, respectively, at the bottom (E1) of Sample 2 during microbial activity. Due to rapid gas generation and water being pushed out of the test cell, the total stress obviously decreased within the first 140 hours. The total stress then remained relatively stable. Any fluctuations mainly came from those of the hydrostatic level, caused by water front movements in the plastic tube (variable in elevation). During the first 35 hours, the excess pore water pressure showed some fluctuations, and then increased to about 0.1 kPa, due to a temperature increase and gas generation. During the same period, the operative stress decreased from 0.171 kPa to 0.074 kPa. From 35 hours to 140 hours, the excess pore water pressure decreased from 0.1 kPa to 0.063 kPa, while the operative stress increased, at a slow rate, from 0.074 kPa to 0.082 kPa. From 140 hours to 200 hours, the excess pore water pressure decreased from 0.063 kPa to 0.019 kPa, and the operative stress increased from 0.082 kPa to 0.119 kPa. During this period (140 to 200 hours), the increases of operative stress were more obvious than those that occurred from 35 to 140 hours. After 200 hours, the changes of operative stress and excess pore water pressure were slow.

Figure 7.25 shows the changes of excess pore water pressure and operative stress at 1.45 cm elevation (E2) above the bottom of Sample 2. From 35 to 140 hours, the total stress visibly decreased due to a rapid increase of trapped gas in the MFT. After 140 hours, the total stress stayed relatively stable. During the first 35 hours, excess pore water pressure increased to 0.04 kPa due to a rapid temperature

increase and gas generation. Correspondingly, the operative stress decreased from 0.134 kPa to 0.098 kPa. From 35 to 140 hours, the excess pore water pressure decreased to close to zero, while the operative stress increased very slowly. From 140 to 200 hours, the total stress became stable. Obvious decreases in the excess pore water pressure and increases in the operative stress were observed. The reason for the very slow increase in operative stress from 35 to 140 hours might be related to the total stress decrease and rapid structure dilation during this period.

Figure 7.26 shows the changes of the excess pore water pressure and operative stress at 3.95 cm elevation (E3) above the bottom of Sample 2. Similar changes to those that occurred at E1 and E2 are shown.

Figure 7.27 shows the changes of the excess pore water pressure and operative stress at the bottom (E1) of Sample 3. From 30 hours to 120 hours, the trapped gas volume slowly increased, and the total stress was relatively stable. From 120 hours to 230 hours, the total stress noticeably decreased due to a rapid increase of the trapped gas volume. After 230 hours, the total stress was relatively stable, except for fluctuations caused by hydrostatic changes in the plastic tubing. During the first 30 hours, the excess pore water pressure increased from 0 to 0.2 kPa due to a rapid temperature increase and gas bubble formation. The operative stress decreased from 0.17 to –0.016 kPa. From 30 to 230 hours, the excess pore water pressure rapidly decreased due to the excess pore water pressure dissipation and total stress decrease. The changes of operative stress were more complex and variable, since the total stress was not constant during microbial activity. From 30 hours to 120 hours, the operative stress increased more rapidly than from 120 to 230 hours. This is likely because the total stress decreased more clearly from 120 to 230 hours. After 360 hours, both the operative stress and excess pore water pressure were relatively stable.

Figure 7.28 shows the changes of the excess pore water pressure and operative stress at 1.45 cm elevation (E2) above the bottom of Sample 3. During the first 30 hours, due to a rapid temperature increase and biogas generation, the excess pore water pressure increased from 0 to 0.2 kPa, while the operative stress decreased from 0.135 kPa to –0.064 kPa. From 30 to 230 hours, the excess pore water pressure rapidly decreased from 0.2 kPa to 0.084 kPa, while the operative stress increased slowly. From 230 to 360 hours, there were obvious increases in the operative stress as the total stress became stable. After 360 hours, with microbial activity diminishing, the excess pore water pressure and operative stress became stable.

Figure 7.29 shows the changes of the excess pore water pressure and operative stress at 3.95 cm elevation (E3) above the bottom of Sample 3. Since E3 was at a higher level of the sample, the total stress at this location was less affected by biogas generation, and thus remained relatively stable. The decreases of the excess pore water pressure were close to the increases of the operative stress during microbial activity. After about 360 hours, with microbial activity diminishing, the operative stress became stable.

Table 7.6 shows some parameters of the MFT at the end of microbial activity. Sample 3 had the lowest water void ratio and the highest gas void ratio among the three samples.

7.5.2 Permeability Tests

After microbial activity diminished, the room temperature was lowered to 4^{o}C to further inhibit microbial activity, and constant head permeability tests were carried out.

Figure 7.30 shows the changes of flow velocities (inflow and outflow) at different times. The upward gradients were close to 0.2. In Tests 2 and 3, the outflow velocities were slightly higher than the inflow velocities. This indicates that there

might be very weak microbial activity and biogas generation, even at 4^{o} C temperature. The results of permeability Tests 1, 2, and 3 are summarized in Table 7.7. With the increase of microbial activity in Samples 1, 2, and 3, the coefficients of permeability increased. After microbial activity, the coefficient of permeability of Sample 3 was about five times greater than that before microbial activity.

7.5.3 Discussion of Tests 1 to 3

7.5.3.1 Volume Changes

After self-weight consolidation was finished, excess pore water pressures in Samples 1 to 3 were close to zero. They were thus regarded as normally consolidated soils. The densification states (void ratio, solids contents, etc.) of the three samples were very close.

Due to different sodium acetate additions, gas generation rates in the three samples were obviously different. Microbial activity in Sample 3 was much more intense than in Samples 1 and 2. For each sample, gas generation rates were variable with time during microbial activity. In Sample 3, gas was generated rapidly during the first 360 hours, but slowed after this point. In Sample 2, rapid gas generation occurred during the first 200 hours, and then slowed. In Sample 1, gas was generated slowly during the test.

There was a strong relationship between biogas generation and water drainage during microbial activity. With the increase of microbial activity and biogas generation in Samples 1 to 3, water drainage volumes increased. For each sample, water drainage rates were related to gas generation rates. In Sample 3, gas was generated rapidly during the first 360 hours, the same period in which rapid water drainage was observed. After 360 hours, with gas generation rates slowing down, water drainage rates obviously decreased. In Sample 2, both rapid

gas generation and rapid water drainage occurred during the first 200 hours after which time both slowed down.

The water drainage volume from the MFT was decided by the relative changes of the global MFT volume and trapped gas volume. During the periods of rapid increases of the trapped gas volume (the first 230 hours in sample 3 and 150 hours in Sample 2), the global MFT volume increases lagged behind those of the trapped gas volume. At the same time, water was rapidly pushed out of the samples. The physical process can be explained as follows:

The MFT sample was a multi-phase system consisting of solids, water and gas. During rapid gas generation, the trapped gas volume increased rapidly. However, due to structural resistance, the global matrix expansion lagged behind the trapped gas volume increase. Water was pushed out of the matrix by an increase in gas bubbles.

In Sample 3, the process of microbial activity can be divided into two periods, both of which saw rapid gas generation. During the first period (about 230 hours), most of the generated gas was trapped in the sample. The physical process in this period has been analyzed above. During the second period (from 230 to 360 hours), gas was intensely released from the MFT, and gas release rates were greater than gas generation rates. Both the trapped gas volume and total MFT volume decreased with time, but the total MFT volume decreased more rapidly than the trapped gas volume. Rapid water drainage occurred in the two periods. In the second period, the MFT structure visibly collapsed. In Sample 2, only a small amount of gas was released from the MFT. Rapid water drainage occurred mainly during the first period.

In Samples 2 and 3, when microbial activity and biogas generation diminished, both the trapped gas volumes and total MFT volumes became stable, and the

water drainage rates obviously decreased. Water drainage rates in Samples 2 and 3 were significantly affected by gas generation rates.

Gas generation in Sample 1 was very slow; the degree of saturation at the end of testing was greater than 98%. The behaviour of Sample 1 was similar to that of a saturated soil. While the trapped gas volume increased very slowly, the total MFT volume slowly decreased with time. The water drainage volumes were approximately equal to the total MFT volume decreases.

7.5.3.2 Excess Pore Water Pressure and Operative Stress

Due to temperature changes (temperature increase from 4 ^{o}C to 24 ^{o}C in the early period, and temperature fluctuation as shown in Figure 7.5 due to frosting operation of the temperature control system) and gas generation and release, the changes of the excess pore water pressure and operative stress were complex during microbial activity. In addition, during rapid biogas generation, water in the MFT was partly pushed out of the test cell by gas bubble growth, leading to a decrease in the total stress. All of these factors made the changes in the excess pore water pressure and operative stress very complex.

Mitchell (1993) describes the effects of rapid temperature changes on saturated soils as changes in their volume and excess pore water pressure. Temperature changes have two effects: firstly, they can generate positive excess pore water pressure; secondly, they can weaken the strength of individual particle contacts causing a partial structural collapse, and thus a void ratio decrease. The reason for the excess pore water pressure change is due to the different thermal expansion coefficients of pore water and mineral solids. When temperature is rapidly increased, positive excess pore water pressure will be generated. This is because the thermal expansion coefficient of pore water is greater than that of mineral solids. The major factors affecting excess pore water pressure during temperature change include thermal expansion of pore water, structural

compressibility of soil and initial effective stress. No literature has been found about excess pore water pressure changes when temperature change and gas generation occur at the same time. The concurrent changes of temperature and trapped gas volume in the MFT would make the changes of excess pore water pressure more complex. The effects of rapid temperature change on gassy MFT behaviour are not the focus of this research, but some phenomena will be evaluated.

In Samples 1 to 3, excess pore water pressures increased and the operative stress decreased with rapid temperature increases. The increases of excess pore water pressure in Sample 3 were more obvious than those in Samples 1 and 2. This was likely due to the rapid gas generation in Sample 3. The growth and expansion of small gas bubbles in the pore water might have increased the expansion of the water-gas mixture, and further increased the excess pore water pressure during the early period of gas generation.

In Sample 1, the temperature-induced excess pore water pressure slightly decreased within a short period (about 30 hours) after the temperature became stable. No obvious changes in the excess pore water pressure or operative stress were observed during the slow biogas generation.

The changes in the excess pore water pressure and operative stress in Samples 2 and 3 were more significant than those in Sample 1. In Sample 2, the temperature-induced excess pore water pressure obviously decreased from 35 to 140 hours, while the increases of operative stress were relatively slow. This is because the total stress was not constant. It decreased during rapid gas generation due to part of the water in the MFT being pushed out of the test cell. It can be suggested that if the total stress were constant, there would be obvious operative stress increases. This has been proven by changes during the subsequent period. From 140 to 200 hours, the total stress became relatively stable and the total MFT volume stopped expansion. Obvious decreases of excess pore water pressure and

increases of operative stress were observed. From 35 to 140 hours, the increases of operative stress at E3 were more obvious than those at E1 and E2. This is because the total stress at E3 (at an upper elevation of the sample) was less affected by gas generation than those at E1 and E2.

The changes of excess pore water pressure and operative stress in Sample 3 were similar to those in Sample 2, but more significant. In Sample 3, the excess pore water pressure rapidly decreased from 30 to 230 hours (before gas release), but the increases of operative stress were slow. This can be attributed, in part, to the total stress decreases during rapid gas accumulation in the MFT. When the total stress became relatively stable, there were obvious operative stress increases. After about 360 hours, with microbial activity diminishing, the excess pore water pressure and operative stress became stable, and water drainage from the MFT slowed.

Table 7.8 shows the overall changes of excess pore water pressure and operative stress after temperature became stable (from 30 hours to 750 hours). With the increases of microbial activity and biogas generation in Samples 1 to 3, the overall changes of excess pore water pressure and operative stress became more obvious.

The obvious fluctuations in the plots of excess pore water pressure vs. time and the plots of operative stress vs. time, were likely caused by two factors: (1) intense disturbances caused by gas release from the MFT; (2) hydrostatic fluctuations in the plastic tube. Due to the unsaturated behaviour of the gassy MFT, the pore water pressure reactions of the MFT were not equal to the hydrostatic changes (they were equal, however, for saturated soils). Hydrostatic fluctuations in the plastic tubes caused the fluctuations of excess pore pressure and operative stress. Although these fluctuations existed, the trends of excess pore water pressure and operative stress were still identified.

7.5.3.3 Structure Change and Permeability

The detailed structural changes of Samples 1 to 3 during microbial activity are shown in Appendix I. Microbial activity in sample 1 was much weaker than those in Samples 2 and 3. Most of the gas bubbles in Sample 1 were in a spherical shape, and there were no visible open structures (fissures, cracks) observed. In Sample 2, some large gas bubbles and cracks were observed during microbial activity, but most of the cracks were short and discontinuous. The structural changes in Sample 3 were more significant than those in Samples 1 and 2. Some large gas bubbles in ellipsoidal shapes and some interconnected cracks were observed. Since constant head permeability tests were conducted at 4^{o}C before and after microbial activity, the viscosities of the MFT were expected to be close. As such, the test results reflect the changes of intrinsic permeability. Figure 7.30 shows flow velocity vs. time in permeability Tests 1 to 3. Before microbial activity, the coefficients of permeability of the three samples were close. After microbial activity, the coefficients of permeability of Samples 2 and 3 had obviously increased, but the coefficient of permeability of Sample 1 had only slightly increased.

Previous research (Wichman et al., 2000) shows that the coefficient of permeability is controlled by the water void ratio, and furthermore, that with an increase in the water void ratio comes an increase in the coefficient of permeability of a gas soil. These results were obtained under the assumption that gas bubbles were fixed in the soil and unable to escape. These assumptions are not suitable to our experiments. Water void ratios in Tests 2 and 3 decreased after microbial activity while the coefficients of permeability significantly increased. During intense microbial activity, the coefficients of permeability of Samples 2 and 3 were mainly controlled by significant structural changes (cracks, fractures and gas release holes), not only by the water void ratio.

7.6 Tests 4 to 6

After self-weight consolidation and permeability tests were finished, the room temperature was raised to 24^{o}C to activate microbial activity. Air pressure (60 kPa) was applied to Samples 4 to 6 to model the microbial activity of MFT at 6-7 m depth below the water surface of the tailings pond.

7.6.1 Test Results

Henry's law was used to determine the dissolved gas mass in the MFT. Table 7.9 shows the equivalent volumes (at STP) of the dissolved gas in pore solutions of Samples 4 to 6. The dissolved gas masses in the solutions are converted to the equivalent gas volumes at standard temperature and pressure (STP) in the table. For very soft MFT material, it is reasonable to assume that gas pressure is approximately equal to the total vertical stress plus atmospheric pressure (Wheeler et al., 1990; Wichman et al., 2000). Since Samples 4 to 6 had higher gas pressures than Samples 1-3, more gas was dissolved in the pore solutions.

Figure 7.31 shows the changes of total gas generation volumes (trapped gas plus released gas at STP) in Samples 4 to 6 over time. In Sample 4, the gas volume increased approximately linearly with time, but at a very slow rate. In Sample 5, gas was generated rapidly during the first 140 hours, and then increased at much slower rates; in Sample 6, gas was generated rapidly during the first 360 hours, after which time gas generation rates visibly decreased. At the end of testing, the total gas generation volumes of Samples 4 to 6 were 11 mL, 74 mL and 300 mL, respectively.

Figure 7.32 shows the changes of gas content with time. The changes of gas content in each sample were similar to those of the total gas volume, since all the generated gas in Samples 4 to 6 was trapped in the MFT. At the end of testing, the gas contents in Samples 4 to 6 were 0.56%, 3.5% and 12.9%, respectively. It appears that under higher gas pressure (or total stress), gas bubbles had difficulty

escaping from the MFT. Figure 7.33 shows the changes of the gas void ratio with time in Samples 4 to 6. At the end of testing, the gas void ratios in Samples 4 to 6 were 0.025, 0.16 and 0.64, respectively.

Figure 7.34 shows the MFT interface movements during microbial activity. The interface of Sample 4 settled over time at a slow rate. In Sample 5, the interface moved up about 0.7 mm during the first 140 hours, due to rapid increases in the trapped gas volume. After 140 hours, with gas generation slowing down, the interface slowly settled with time. In Sample 6, the interface moved up about 6.3 mm during first 360 hours, and then with the gas generation rate decreasing, slightly settled with time. At the end of testing, the MFT interfaces of Samples 4 and 5 were about 2 mm and 0.2 mm below the initial levels, respectively, and the interface of Sample 6 was 5.9 mm above the initial level.

Figure 7.35 shows the changes of the water void ratio with time. In Sample 4, the water void ratio decreased with time and at a slow rate. In Sample 5, the water void ratio rapidly decreased during the first 140 hours, as did rapid gas generation. After this time, the water void ratio slowly decreased as gas generation slowed down. In Sample 6, the water void ratio rapidly decreased during the first 360 hours, along with rapid gas generation. This period was followed by a decrease that took place at slower rates. At the end of testing, the water void ratios of Samples 4 to 6 were 3.43, 3.4, and 3.31, respectively. For each sample, water drainage rates were related to gas generation rates.

Figures 7.36 to 7.38 show volumetric changes (total and trapped gas volumes at STP, and water drainage volumes) in Samples 4 to 6, respectively. Clear connections between gas generation rates and water drainage rates can be observed. During rapid biogas generation, there was a subsequent rapid increase in water drainage, and vice versa**.** In Samples 5 and 6, water drainage from the MFT was obviously controlled by microbial activity and biogas generation. The slow gas generation in Sample 4 had little effect on MFT densification, and water was drained out at slow rates.

Figures 7.39 to 7.41 show the changes of the total MFT volume and trapped gas volume with time in Samples 4 to 6, respectively. In Sample 4, while the trapped gas volume increased very slowly, the total MFT volume slowly decreased over time. In Sample 5, both the trapped gas volume and total MFT volume rapidly increased during the first 140 hours, but the increases of the total MFT volume lagged behind those of the gas generated in the MFT. Water was rapidly pushed out by gas bubble formation. After 140 hours, the trapped gas volume had slowly increased, and the total MFT volume had slightly decreased. As a consequence, water drained out slowly. In sample 6, during the first 360 hours, both the trapped gas volume and the total MFT volume rapidly increased with time, but the total MFT volume increases lagged behind the increases of the gas generation volume. There was rapid water drainage during this period. After 360 hours, the trapped gas volume slowly increased, but the total MFT volume was almost stable, so water drained out slowly.

Figures 7.42 and 7.43 show the changes of excess pore water pressure and operative stress at the bottom (E1) of Sample 4 at different times. During the first 24 hours, due to a rapid temperature increase, excess pore water pressure increased from 0 to 0.096 kPa. Correspondingly, the operative stress decreased from 0.167 to 0.067 kPa. After the temperature stabilized, there were only slight changes in the excess pore water pressure and operative stress within a short period (from 24 to 50 hours). Following this period, both the excess pore water pressure and operative stress remained relatively stable.

Figure 7.44 shows the changes of excess pore water pressure and operative stress at 1.45 cm elevation (E2) above the bottom of Sample 4. Figure 7.45 shows the changes of excess pore water pressure and operative stress at 3.95 cm elevation (E3) above the bottom of Sample 4. The changes of operative stress and excess pore water pressure at E2 and E3 were similar to those at E1.

Figure 7.46 shows the changes of excess pore water pressure and operative stress at the bottom (E1) of Sample 5. The changes of total stress and pore water pressure can be found in Appendix H. During the first 35 hours, due to a rapid temperature increase, excess pore water pressure increased from 0 to 0.152 kPa, and operative stress decreased from 0.181 to 0.027 kPa. From 35 to 140 hours, due to rapid gas generation, the bulk density of the MFT obviously decreased, as did the total stress. During this period, the excess pore water pressure slightly increased from 0.15 to 0.16 kPa, and the operative stress decreased from 0.027 to near 0. It appears that extra excess pore water pressure was generated during rapid gas generation. There was rapid water drainage from the MFT during this period. From 140 hours to 500 hours, with gas generation slowing down, the MFT interface slowly settled. During this period, the excess pore water pressure decreased from 0.16 to 0.081 kPa, and the operative stress increased from 0.005 to 0.08 kPa. After about 500 hours, with gas generation further diminishing, both the excess pore water pressure and operative stress stabilized.

Figure 7.47 shows the changes of the excess pore water pressure and operative stress at 1.45 cm elevation (E2) above the bottom of Sample 5. Figure 7.48 shows the changes of operative stress and excess pore water pressure at 3.95 cm above the bottom (E3) of Sample 5. The changes at E2 and E3 were similar to those observed at E1.

Due to sudden leakage shortly after applying 60 kPa air pressure to Sample 6, the water from the cell space flooded out of the cell and soaked the pore water pressure transducers in Cell 6. Also, the sudden pressure loss caused serious damage to the pressure transducers in Cell 6. Although the leakage was repaired later, the pressure transducers malfunctioned during the gas densification test. Unfortunately, no useful pore water pressure data was obtained in Test 6.

Table 7.10 shows some parameters of Samples 4 to 6 at the end of gas MFT densification tests. Sample 6 had the highest gas void ratio and lowest water void ratio among the 3 samples.

7.6.2 Permeability Tests

After microbial activity diminished, the room temperature was lowered to 4^{o}C to further inhibit microbial activity. Once the gas-liquid system became stable, constant head permeability tests were conducted.

Figure 7.49 shows the changes of flow velocities at different times in permeability Tests 5 and 6; the results of the permeability tests are summarized in Table 7.11. Due to slow leakage occurring in Cell 4 after the room temperature was lowered to 4^{o}C, constant head permeability was not performed in this cell. After microbial activity had stopped, the coefficients of permeability of Sample 5 and Sample 6 were close to one another, and to those before microbial activity. Unlike Samples 2 to 3, the coefficients of permeability of Samples 5 to 6 had no significant increases after microbial activity.

7.6.3 Discussion of Tests 4 to 6

7.6.3.1 Volume Changes

The microbial activities in Samples 4 to 6 were under higher total stress (or gas pressure) than those in Samples 1 to 3. Due to the variations in sodium acetate amendments, the intensities of microbial activity in Samples 4-6 were significantly different. In Sample 4, gas was generated at a very slow rate; in Sample 5, rapid gas generation lasted about 140 hours. In Sample 6, however, gas was generated very rapidly during the first 360 hours, and then obviously slowed down. The durations of rapid gas generation in Samples 5 and 6 were close to those in Samples 2 and 3, respectively.

Table 7.12 gives a comparison of gas generation and water drainage volumes between Samples 1 to 3 and Samples 4 to 6. The total equivalent gas volumes (trapped gas + dissolved gas + released gas at STP) of Samples 4 to 6 were close to those of Samples 1 to 3, respectively. This indicates that the changes in total stress did not significantly change the generated gas mass in the MFT when other conditions (sodium acetate, temperature, etc.) were constant. In contrast, different gas pressures clearly affected gas release from the MFT. The gas bubbles under lower pressure were released more easily from the MFT.

With the increases of microbial activity and biogas generation in Samples 4 to 6, water drainage volumes increased. For each sample, water drainage rates were related to gas generation rates. In Sample 6, gas was rapidly generated during the first 360 hours, which corresponded with rapid water drainage during this period. After 360 hours, with gas generation slowing down, water drainage rates obviously decreased. In Sample 5, rapid gas generation and rapid water drainage occurred during the first 140 hours, but then, as microbial activity diminished, water drainage rates decreased.

Water drainage from the MFT was decided by the relative changes of the trapped gas volume and total MFT volume during microbial activity. In Samples 5 and 6, during rapid gas generation (the first 140 hours for Sample 5 and 360 hours for Sample 6), both total MFT volumes and trapped gas volumes increased with time. On the contrary, the global MFT volume expansions lagged behind trapped gas volume increases, and as a result, water was rapidly pushed out of the MFT. With gas generation rates slowing down, trapped gas volumes slowly increased, and total MFT volumes slightly decreased (or remained stable) with time. Water was drained out of the MFT at slower rates.

7.6.3.2 Excess Pore Water Pressure and Operative Stress

The changes of excess pore water pressure and operative stress in Sample 4 were similar to those in Sample 1. Obvious changes occurred only during the early

period (about 50 hours). These changes were mainly caused by temperature variations. After temperature stabilized, there were no obvious changes in excess pore water pressure or operative stress. Weak microbial activity and slow gas generation occurred during this test.

The changes of excess pore water pressure and operative stress in Sample 5 were different from those in Sample 4. From 35 to 140 hours, gas was generated rapidly. While total stress decreased, excess pore water pressure slightly increased and operative stress slightly decreased. From 140 to 360 hours, both gas generation rates and the total MFT volume decreased with time. Excess pore water pressure rapidly decreased, and operative stress increased with time. Water drainage in this period however, was slower than that during the prior period (35 to 140 hours). After 360 hours, both excess pore water pressure and operative stress became stable.

During rapid gas generation (35 to 140 hours), there was rapid water drainage and a simultaneous decrease in operative stress with time. This phenomenon obviously contradicts the operative stress approach (Sills et al., 1991), and can be explained as follows:

- During rapid gas generation in Sample 5, the growth of gas bubbles was restricted by structural resistance. Some small gas bubbles pushed the pore water causing excess pore water pressure to increase.
- While excess pore water pressure was partly dissipated, at the same time, extra excess pore water pressure was likely generated. The increase of extra excess pore water pressure counteracted the excess pore water pressure dissipation.
- However, excess pore water pressure obviously decreased during rapid gas generation in Sample 2. The difference between Sample 2 and Sample 5 was likely due to their varying gas pressures during microbial activity.

- The coefficient of permeability of Sample 2 significantly increased due to remarkable structural changes, making excess pore water pressure easier to dissipate. In contrast, Sample 5 showed no obvious change in permeability during microbial activity.
- In addition, the sizes of gas bubbles in Sample 5 were much smaller than those in Sample 2, due to higher gas pressure. The growths of some very small gas bubbles pushed the pore water, thereby causing excess pore water pressure to increase. After 140 hours, with gas generation slowing down, no (or less) extra excess pore water pressure was produced, and as such, the dissipation of excess pore water pressure became obvious.

During rapid gas generation in the MFT, total stresses decreased as water was pushed out from the test cells. However, during the tests at the Oxford University, total stresses were kept stable. This might be another factor for the different behaviours in excess pore water pressure and operative stress between current tests and those at the Oxford University.

7.6.3.3 Structure Change and Permeability

The detailed structural changes of Samples 4 to 6 during microbial activity are shown in Appendix I. Due to the applied back pressure and weak microbial activity; there was no obvious structural change in Sample 4. In Sample 5, gas bubbles were small and occluded, and no obvious cracks were observed. Although large cracks were produced in Sample 6, most of them extended horizontally and were tightly filled with large ellipsoidal gas bubbles.

At the end of microbial activity the coefficients of permeability of Samples 5 and 6 were very close. They were also close to the coefficients of permeability before microbial activity. After intense microbial activity and rapid gas generation, the coefficients of permeability of Samples 5 and 6 had no obvious changes. Since cracks and fractures in Sample 4 to 6 were mostly at closed condition under the

application of back pressure, they could not act as convenient drainage paths. The coefficients of permeability of Samples 4 to 6 were mainly controlled by the pore voids.

7.7 Chemical Tests 7©, 8©, and 9©

Tests 1 to 6 were used to study the geotechnical properties of MFT during microbial activity. Since some geotechnical parameters, including pore water pressure and operative stress, are very sensitive to disturbance it is not appropriate to directly obtain chemical samples from Samples 1 to 6 during microbial activity. Tests 7© to 9© were used to sacrificially obtain chemical samples for Samples 1 to 3 during microbial activity. Tests 7© to 9© followed the same procedures as Tests 1 to 3. They can be considered the duplication of Tests 1 to 3. Different amounts of sodium acetate, 0, 0.6 g, and 1.75 g per litre MFT, were added to Samples 7© to 9©, respectively. The initial heights were about 7.5 cm (close to the initial heights of Samples 1 to 3). After self-weight consolidation finished at 4^{o}C, the room temperature was raised to 24^{o}C in order to start microbial activity.

A plastic piston syringe connected with a hollow copper tube with a small diameter was used as the sampler. When sampling, the small copper tube was inserted into the sample through a valve mounted at 1.45 cm elevation above the bottom of the sample. By pulling back the piston of the syringe, the MFT slurry was sucked into the sampler.

Due to the small sample size (less than 7 cm thick after self-weight consolidation), a significant amount of pond water entered the sampler from above the MFT interface when sampling. This led to considerable contaminations of the chemical samples. The measurements could not really reflect the chemical changes of the MFT during microbial activity. The prior consideration of using 7.5 cm as the initial height for Samples 7© to 9© was to match the height of Samples 1 to 3.

The pond water problem indicated that a relatively large sample size was required for chemical sampling.

7.8 Summary

Eighteen gas MFT densification tests and nine chemical sampling tests were carried out within 14 months. The MFT densification properties were studied under different conditions, such as different stress histories (normally consolidated Samples 1 to 6 and 19 to 24; under-consolidated Samples 13 to 15 and over-consolidated Samples 10 to 12), different pressures (0 and 60 kPa air pressures) and different microbial activities (0, 0.6 and 1.75 g sodium acetate added per liter MFT). During the densification tests, various parameters were measured and structural changes were observed. These sophisticated and comprehensive tests have greatly improved our understanding of MFT behaviors during microbial activity. The results of Tests 1 to 6 are summarized as follows:

1. With the increase of sodium acetate added to Samples 1 to 6, gas generation volumes increased. Sodium acetate amendments were seen to significantly accelerate microbial activity.
2. Gas generation volumes (at STP) and rates in Samples 4 to 6 were close to those in Samples 1 to 3, respectively. The pressure changes (by applying air pressure) did not obviously affect microbial activity.
3. Under high pressure (in Samples 4 to 6), gas bubbles were released from the MFT with more difficulty than observed in the low pressure tests.
4. With the increases of microbial activity and gas generation in Samples 1 to 6, water drainage volumes increased.
5. For each sample, water drainages rates were related to gas generation rates. During rapid gas generation, there existed rapid water drainage.
6. During microbial activity, water drainage from the MFT was decided by relative changes between the trapped gas volume and total MFT volume. Since microbial activities were very weak in Samples 1 and 4, the MFT

behavior was similar to that of a saturated soil. Water drainage volume increases in the two samples were approximately equal to MFT volume decreases. During rapid gas generation in Samples 2, 3, 5 and 6, MFT volume expansions lagged behind trapped gas volume increases. As a result, water was rapidly pushed out.

7. There was rapid water drainage during intense microbial activity and rapid gas generation regardless of whether gas bubbles were mostly trapped or intensely released.
8. Due to very slow gas generation in Samples 1 and 4, there were no obvious changes in excess pore water pressure or operative stress after the temperature became stable.
9. In Samples 2 and 3, excess pore water pressure obviously decreased during rapid gas generation, while operative stress increased very slowly. This was mainly caused by total stress decreases during rapid gas generation. When total stress stabilized, operative stress obviously increased. When microbial activity diminished in Samples 2 and 3, both excess pore pressure and operative stress became stable and water drainage was very slow.
10. In Sample 5, excess pore water pressure slightly increased and operative stress slightly decreased during rapid gas generation. It is likely that extra excess pore pressure was generated during rapid gas generation.
11. With the increases of microbial activity and gas generation in Samples 1 to 3, the macro-structural changes became more significant, and the coefficients of permeability obviously increased. The coefficients of permeability in Samples 2 and 3 were mainly controlled by structural changes (cracks, fractures and gas releasing holes), not only by water void ratios.
12. In Samples 4 to 6, the cracks and fractures were mostly in a closed condition and tightly filled with gas bubbles. There were no obvious changes in the coefficients of permeability of Samples 4 to 6 after microbial activity.

Table 7-1 Some Parameters of Samples 1-6 before Self-weight Consolidation

Solids Content (%)	Fines/(fines + water) (%)	Void Ratio (e)	Density (g/ml)	Water Content (%)	Bitumen Content (%)
34.6	0.33	4.165	1.233	189.02	4.285

Note: bitumen content = bitumen mass/total solids mass * 100%

Table 7-2 Summary of Some Initial Information of Samples 1-6

Test No	Total Mass (g)	Solids Mass (g)	Water Mass (g)	Total Volume (ml)	Solids Volume (ml)	Height (cm)	Sodium Acetate (g/L MFT)
1	1672.1	578.5	1093.6	1356.2	262.6	7.46	0
2	1670.5	578	1092.5	1354.9	262.4	7.48	0.6
3	1679.9	581.2	1098.7	1362.5	263.8	7.57	1.75
4	1665.7	576.3	1089.4	1350.9	261.5	7.44	0
5	1743.8	603.4	1140.4	1414.3	273.9	7.87	0.6
6	1775.9	614.4	1161.5	1440.3	278.8	7.94	1.75

Table 7-3 Some Parameters of Samples 1-3 after Self-weight Consolidation

Test No	Sample Height (cm)	Density (g/ml)	Void Ratio (e)	Solids Content (%)
1	6.63	1.262	3.59	38.03
2	6.63	1.263	3.58	38.11
3	6.7	1.263	3.57	38.15

Table 7-4 Results of Permeability Tests 1-6 before Microbial Activity

Test No	1	2	3	4	5	6
Gradient	0.204	0.211	0.209	0.204	0.201	0.214
Average Flow Velocity (10^{-9} m/s)	0.653	0.54	0.834	0.719	0.631	0.724
Coefficient of Permeability (10^{-9} m/s)	3.2	2.56	3.99	3.52	3.14	3.38

Table 7-5 Dissolved Gas Volumes in Samples 1 to 3

Test No	1	2	3
Dissolved Methane gas (10^{-3} mol)	1.399	1.327	1.378
Equivalent Vol. at STP (ml)	34.2	33.5	33.7

Table 7-6 Some Parameters of Samples 1 to 3 after Microbial Activity

Test NO	Solids Content (%)	Density (g/ml)	Water Void Ratio	Gas Void Ratio	Total Void Ratio	Degree of Saturation (%)
1	39.25	1.251	3.41	0.08	3.49	97.6
2	39.48	1.18	3.38	0.35	3.73	90.5
3	40.04	1.15	3.3	0.48	3.78	87.2

Table 7-7 Results of Permeability Tests 1 to 3 after Microbial Activity

Test No.	1	2	3
Gradient	0.216	0.219	0.20
Average Flow Velocity (10^{-9} m/s)	0.96	2.89	3.73
Coefficient of Permeability (10^{-9} m/s)	4.4	13.2	18.7

Table 7-8 Overall Changes of Excess Pore Pressure and Operative Stress in Samples 1-3 during Microbial Activity (after Temperature Stabilized)

Test No	Elevation	Excess Pore Water Pressure Change (kPa)	Operative Stress Change (kPa)
1	E1	-0.044	0.027
	E2	-0.039	0.023
	E3	-0.037	0.022
2	E1	-0.115	0.062
	E2	-0.1	0.055
	E3	-0.067	0.041
3	E1	-0.157	0.094
	E2	-0.157	0.104
	E3	-0.12	0.079

Table 7-9 Dissolved Gas Volumes in Samples 4-6

Test No	4	5	6
Dissolved Methane Gas (10^{-3} mol)	2.14	2.20	2.25
Equivalent Vol. at STP (ml)	52.3	53.9	55.0

Table 7-10 Some Parameters of Samples 4-6 after Microbial Activity

Test NO	Solids Content (%)	Density (g/ml)	Water Void Ratio	Gas Void Ratio	Total Void Ratio	Degree of Saturation (%)
4	39.1	1.264	3.43	0.025	3.46	99.1
5	39.3	1.229	3.39	0.16	3.55	95.5
6	40.0	1.114	3.31	0.64	3.95	83.8

Table 7-11 Results of Permeability Tests 5-6 after Microbial Activity

Test No.	5	6
Gradient	0.216	0.195
Average Flow Velocity (10^{-9} m/s)	0.946	0.906
Coefficient of permeability (10^{-9} m/s)	4.38	4.65

Table 7-12 A Comparison of Volumetric Changes in Samples 1-6 during Microbial Activity

Test No	Trapped Gas Volume at STP (ml)	Released Gas Volume at STP (ml)	Equivalent Volume at STP of Dissolved Gas (ml)	Total Gas Volume (trapped + released + dissolved) at STP (ml)	Water Drainage Volume (ml)
1	22.7	0	34.2	56.9	47.3
2	100.1	8.9	33.5	142.5	56.6
3	139.1	221.9	33.7	394.7	71.6
4	11.1	0	52.3	63.4	42.5
5	74	0	53.9	127.9	47.2
6	300.7	0	55	355.7	71.8

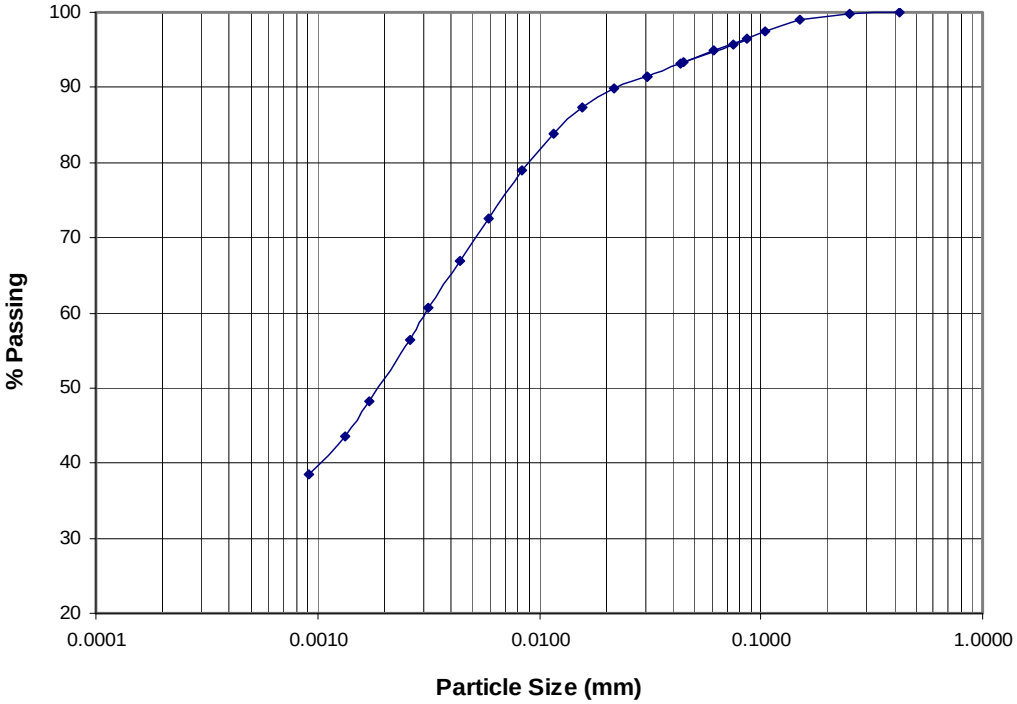

Figure 7-1 Grain Size Analysis of the Initial MFT Sample

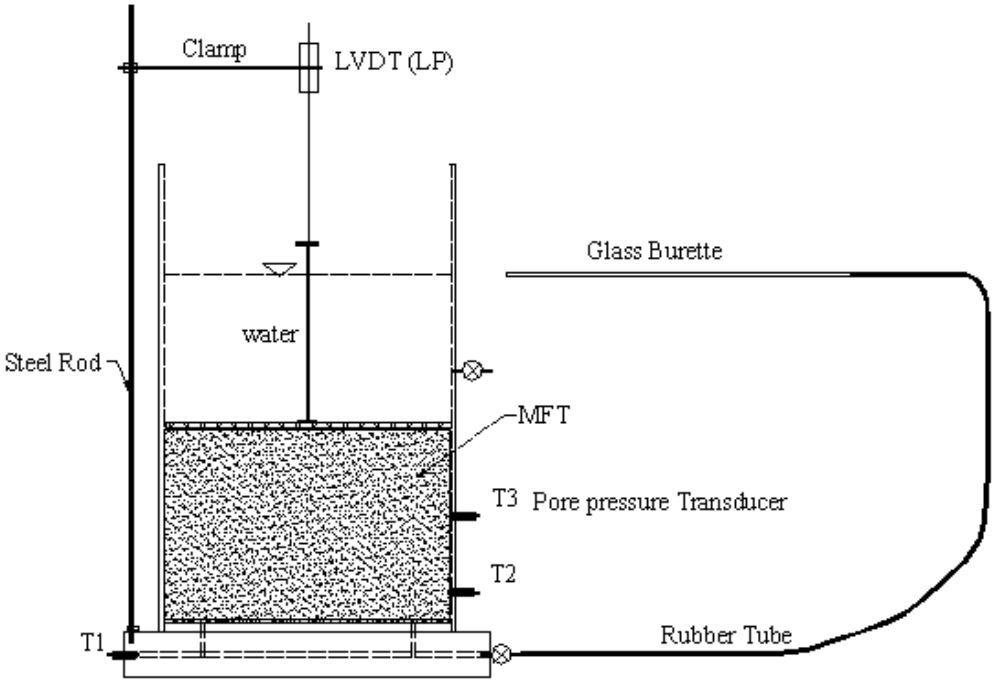

Figure 7-2 A Sketch of Self-Weight Consolidation Test

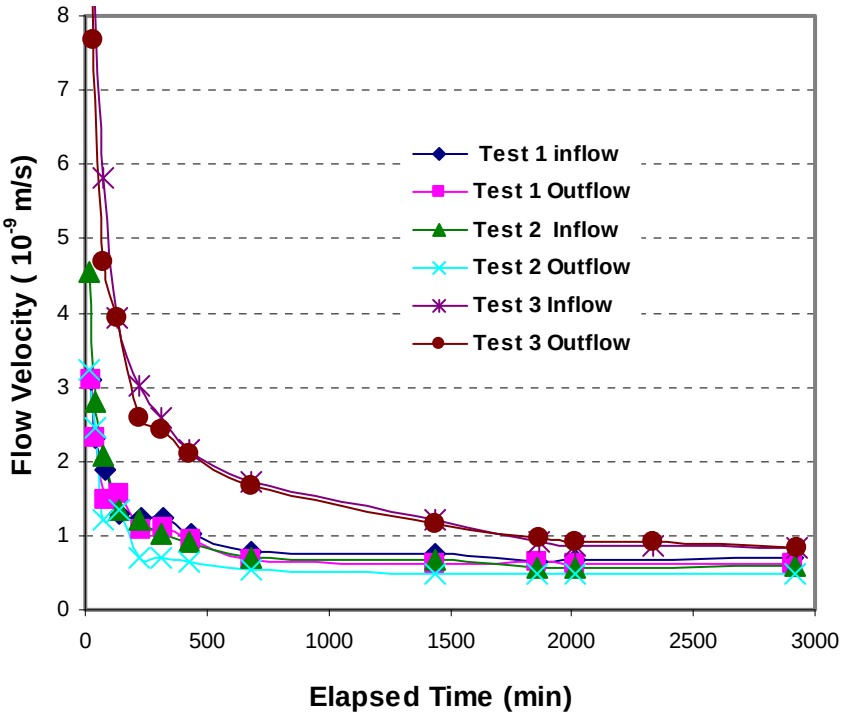

Figure 7-3 Flow Velocity vs. Time for Permeability Tests 1-3 before Microbial Activity

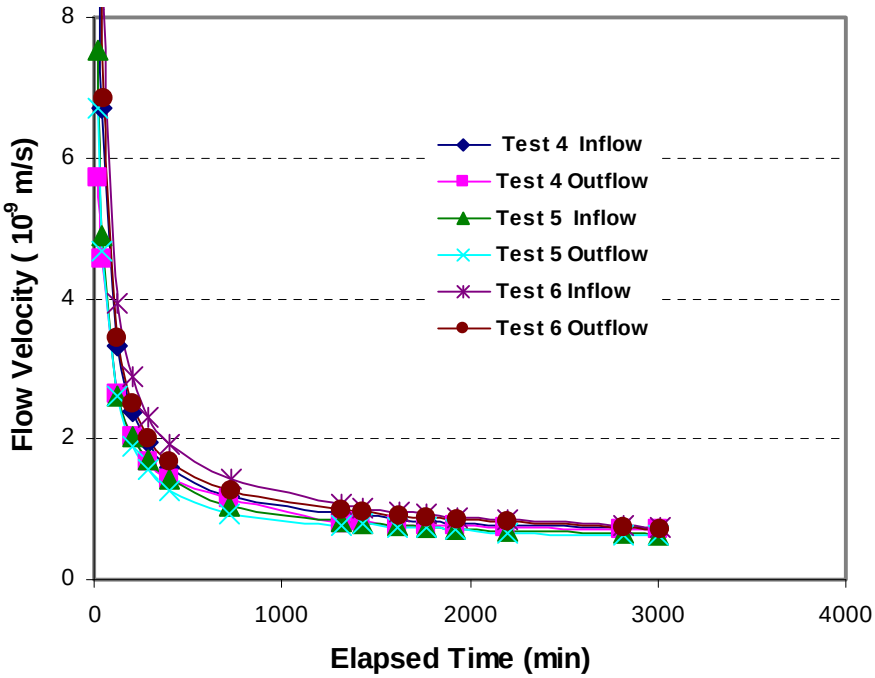

Figure 7-4 Flow Velocity vs. Time for Permeability Tests 4-6 before Microbial Activity

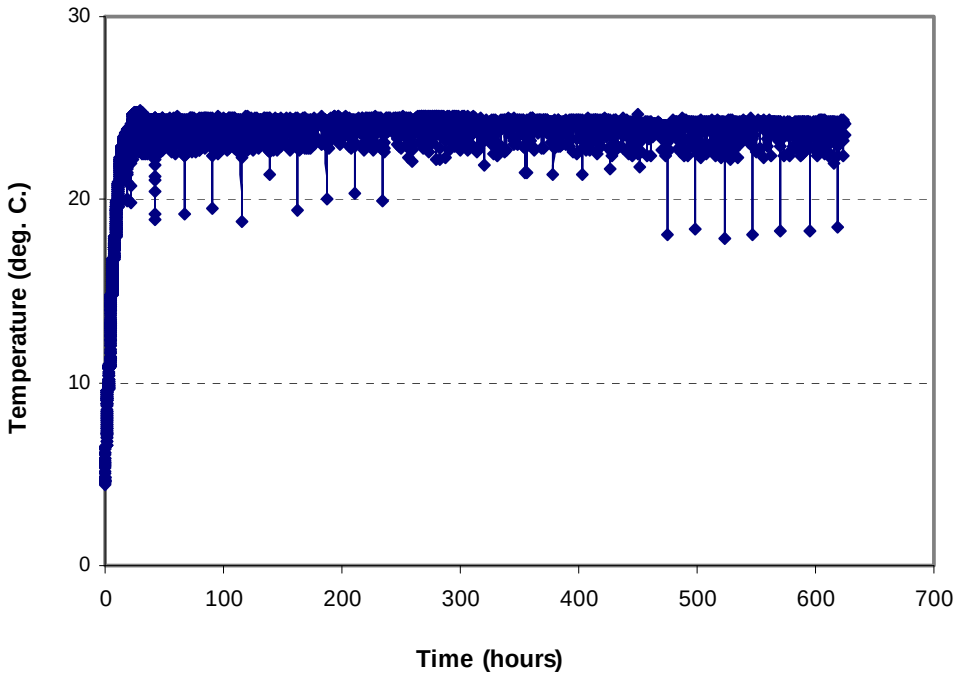

Figure 7-5 Temperature Changes during Microbial Activity of Samples 1-6

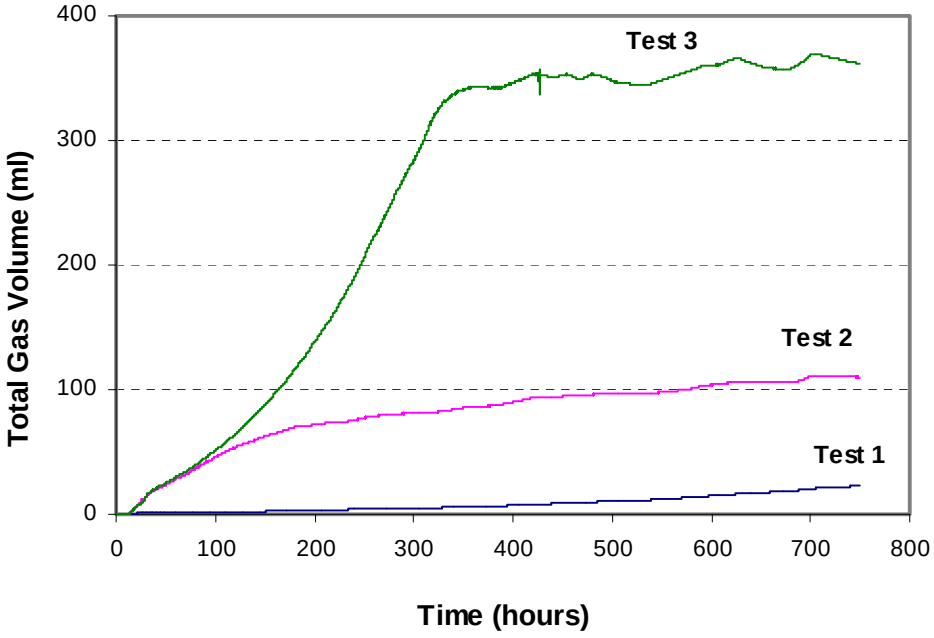

Figure 7-6 Total Gas Volume (trapped + released at STP) vs. Time in Samples 1-3

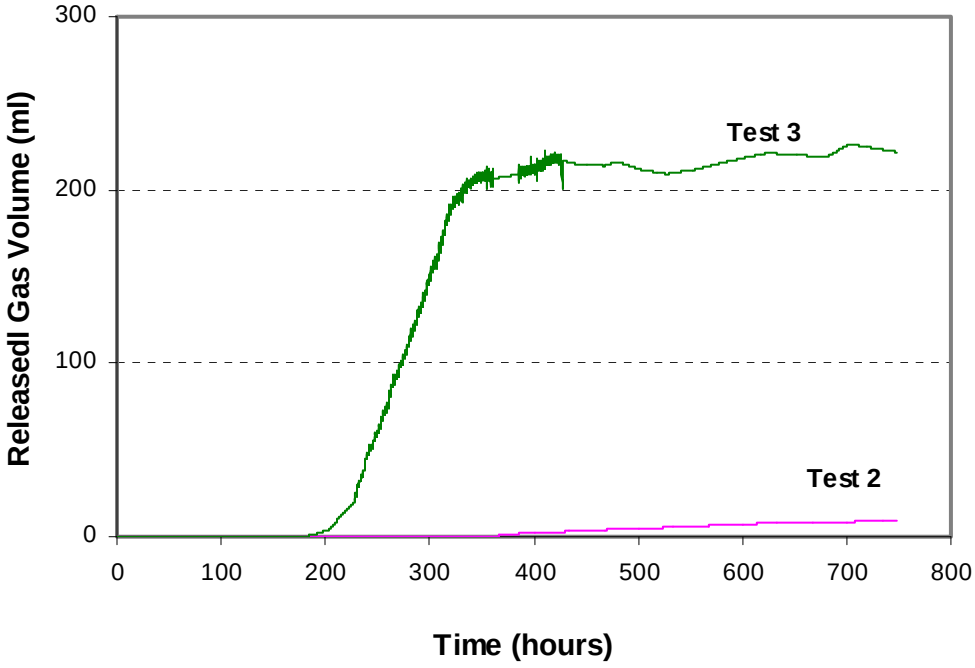

Figure 7-7 Released Gas Volume (at STP) vs. Time in Samples 2-3

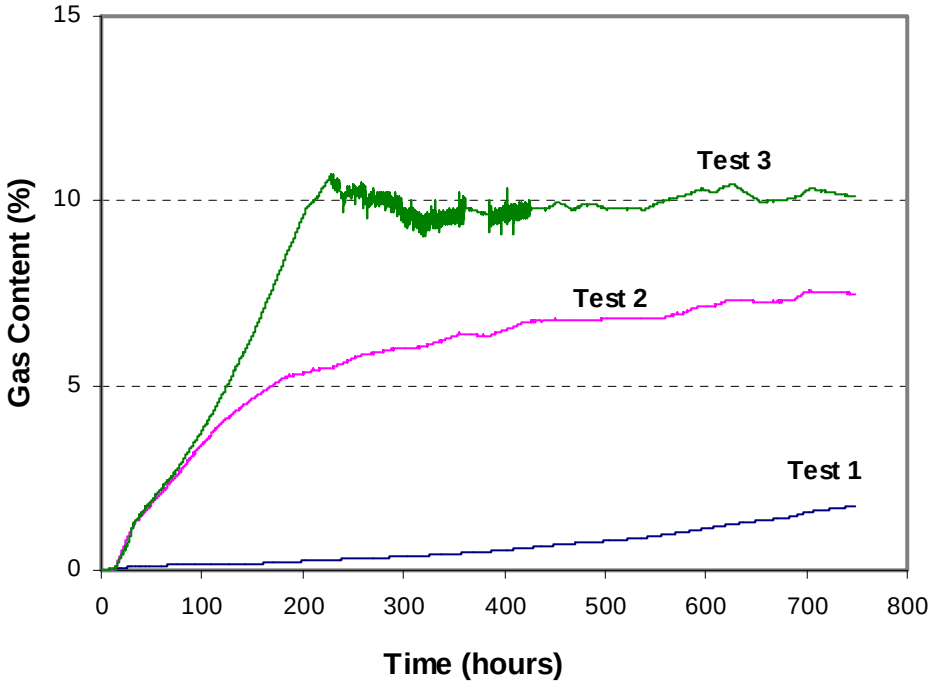

Figure 7-8 Gas Content vs. Time in Samples 1-3

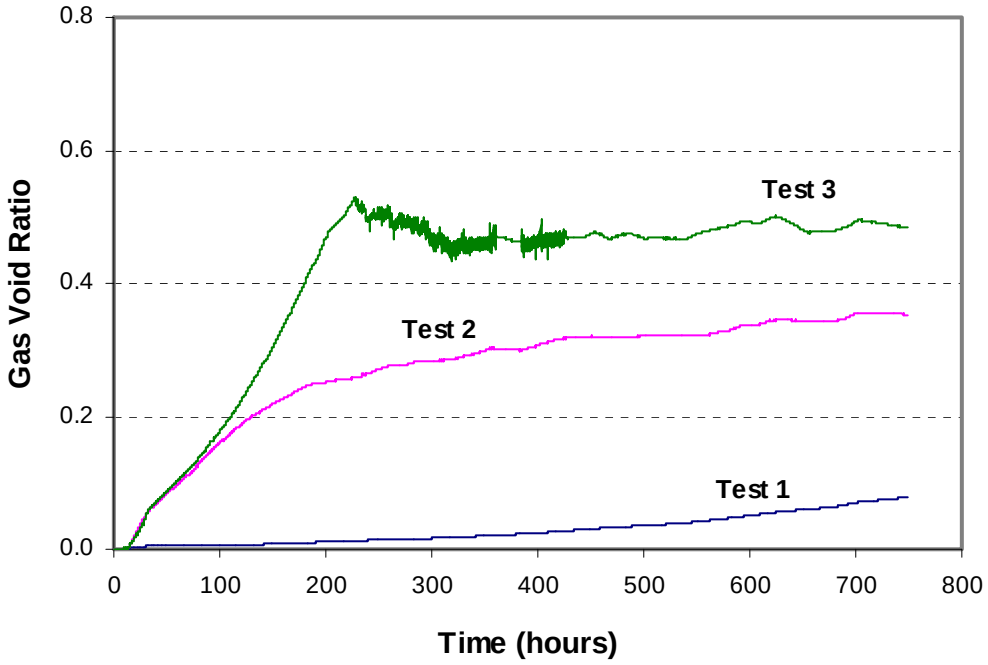

Figure 7-9 Gas Void Ratio vs. Time in Samples 1-3

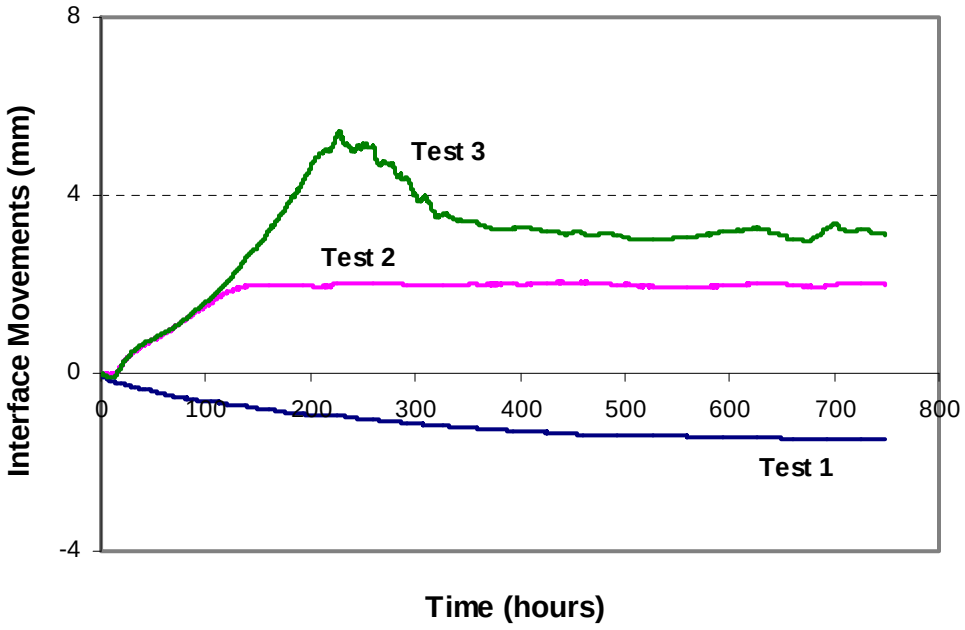

Figure 7-10 Interface Movements vs. Time in Samples 1-3

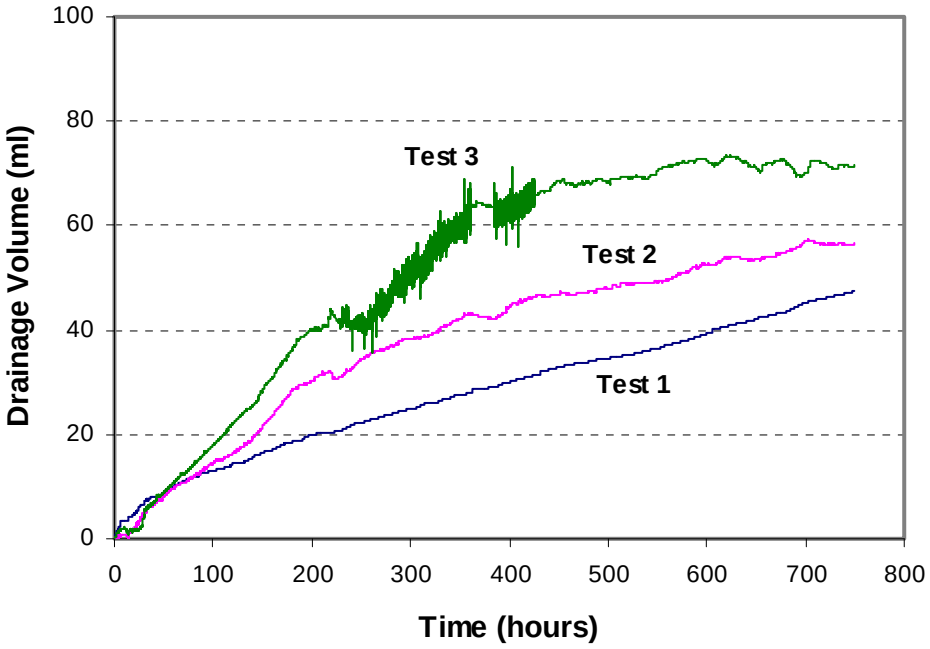

Figure 7-11 Water Drainage Volume vs. Time in Samples 1-3

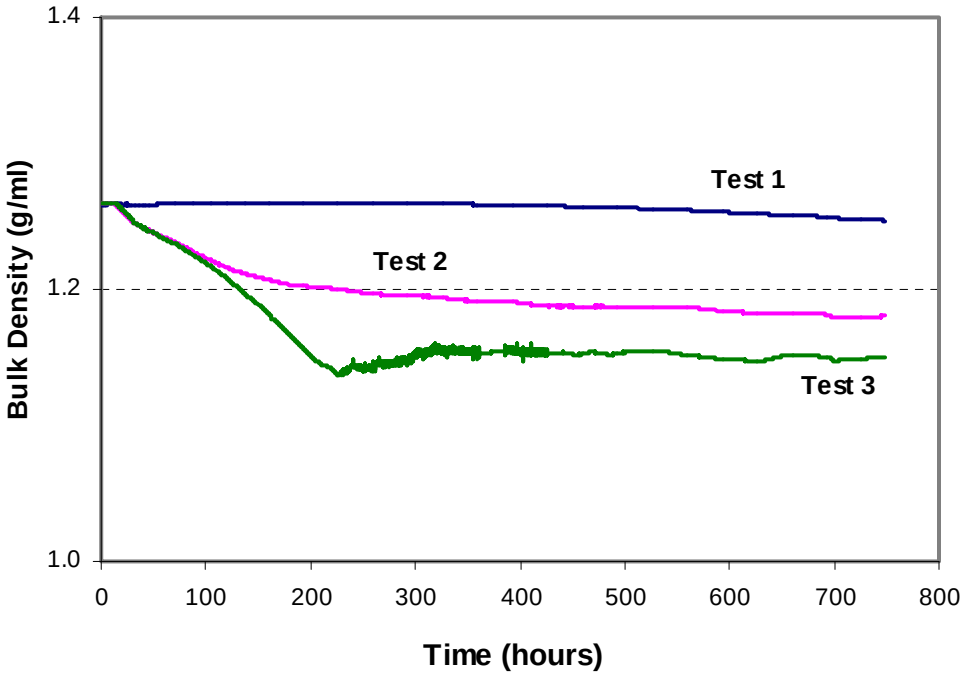

Figure 7-12 Bulk Density vs. Time in Samples 1-3

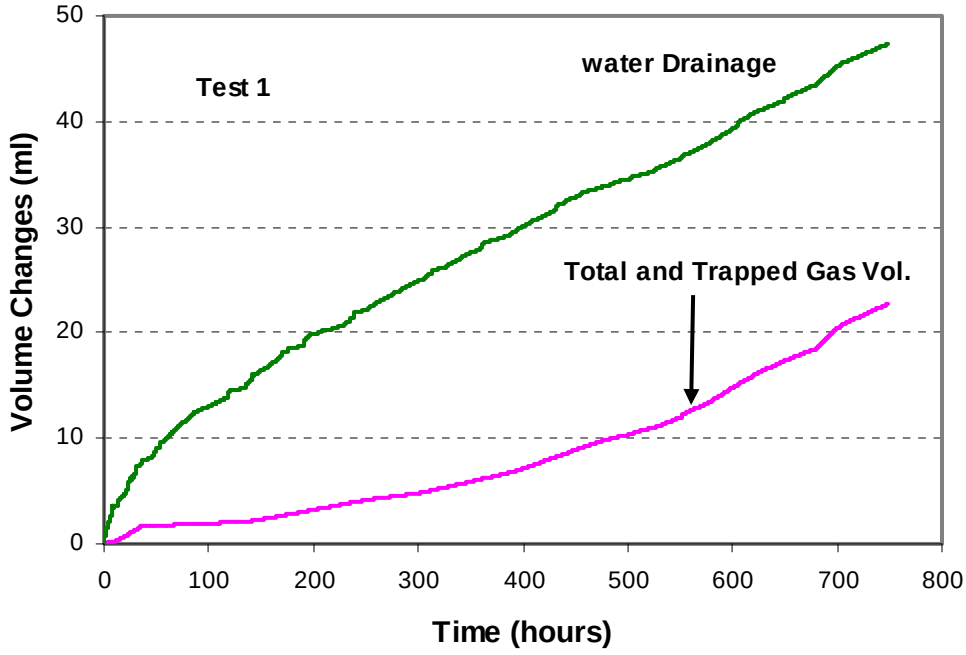

Figure 7-13 Volumetric Changes in Sample 1 during Microbial Activity

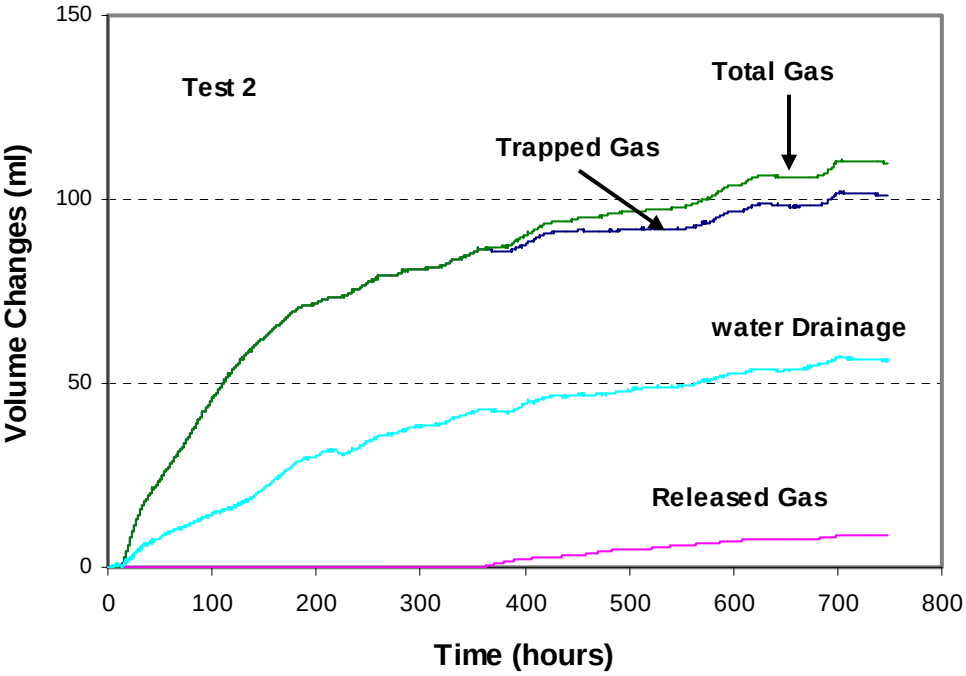

Figure 7-14 Volumetric Changes in Sample 2 during Microbial Activity

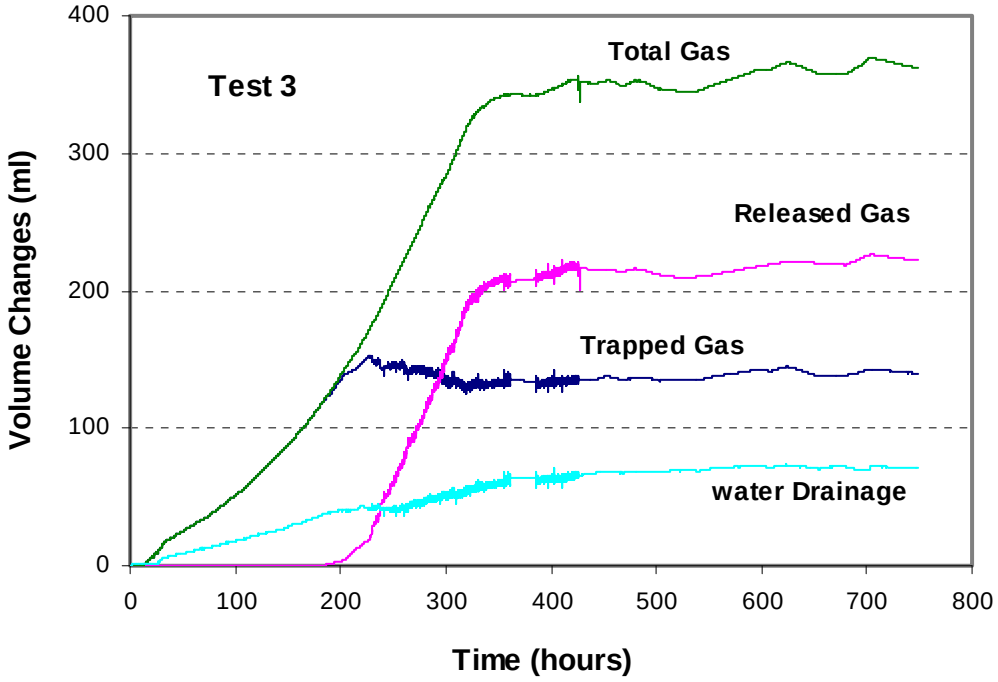

Figure 7-15 Volumetric Changes in Sample 3 during Microbial Activity

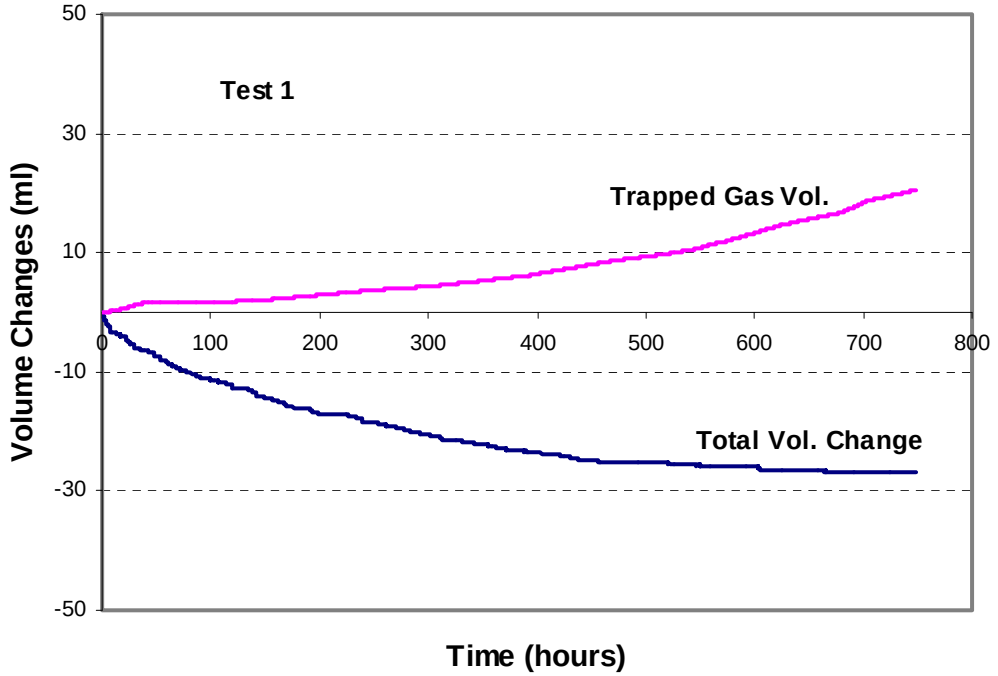

Figure 7-16 Changes of Trapped Gas Volume and Total MFT Volume in Sample 1

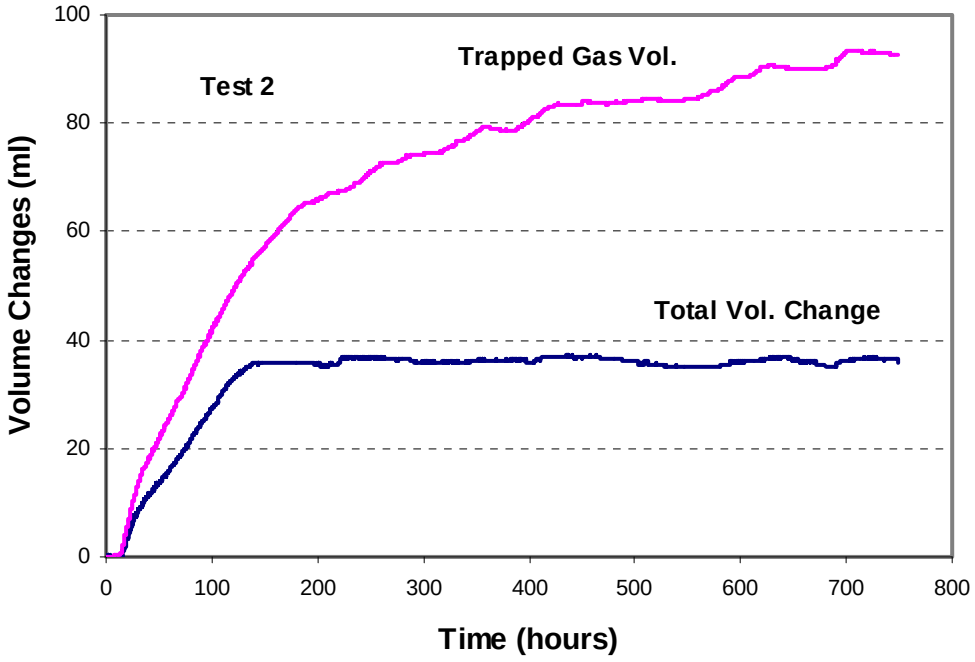

Figure 7-17 Changes of Trapped Gas Volume and Total MFT Volume in Sample 2

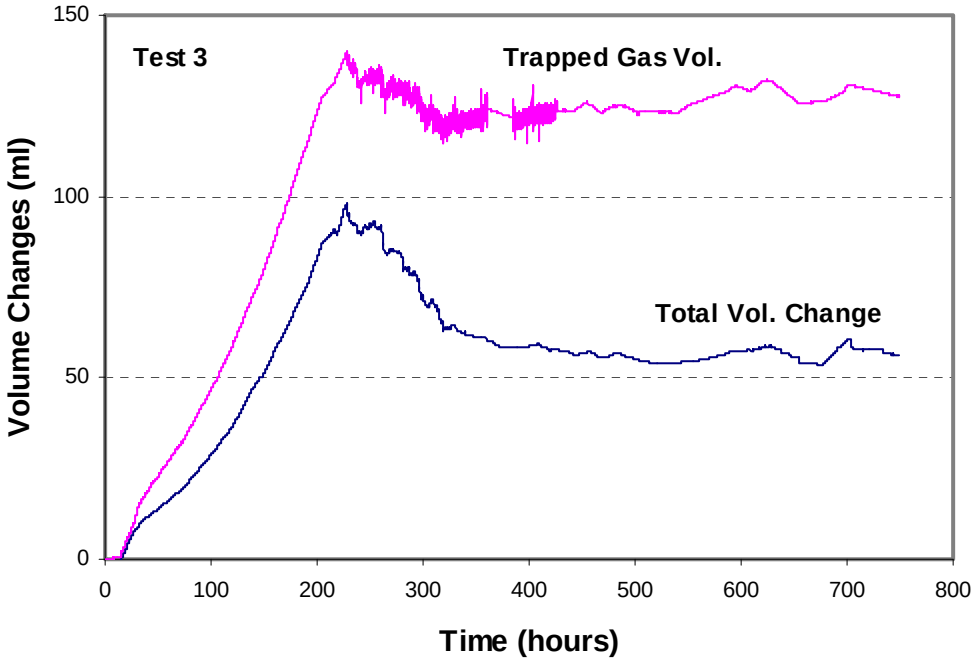

Figure 7-18 Changes of Trapped Gas Volume and Total MFT Volume in Sample 3

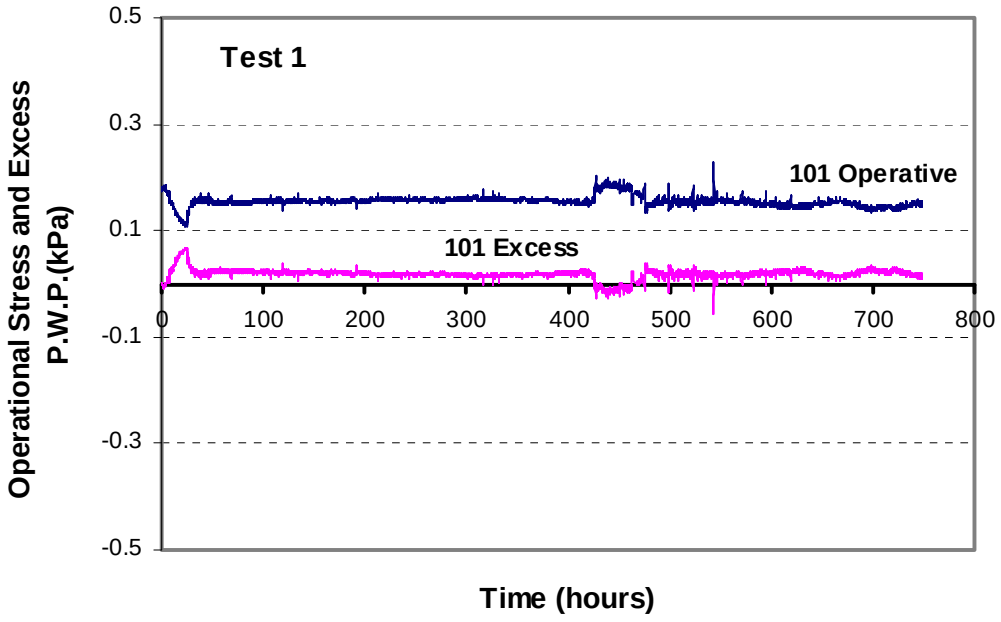

Figure 7-19 Changes of Excess Pore Water Pressure and Operative Stress at E1 of Test 1

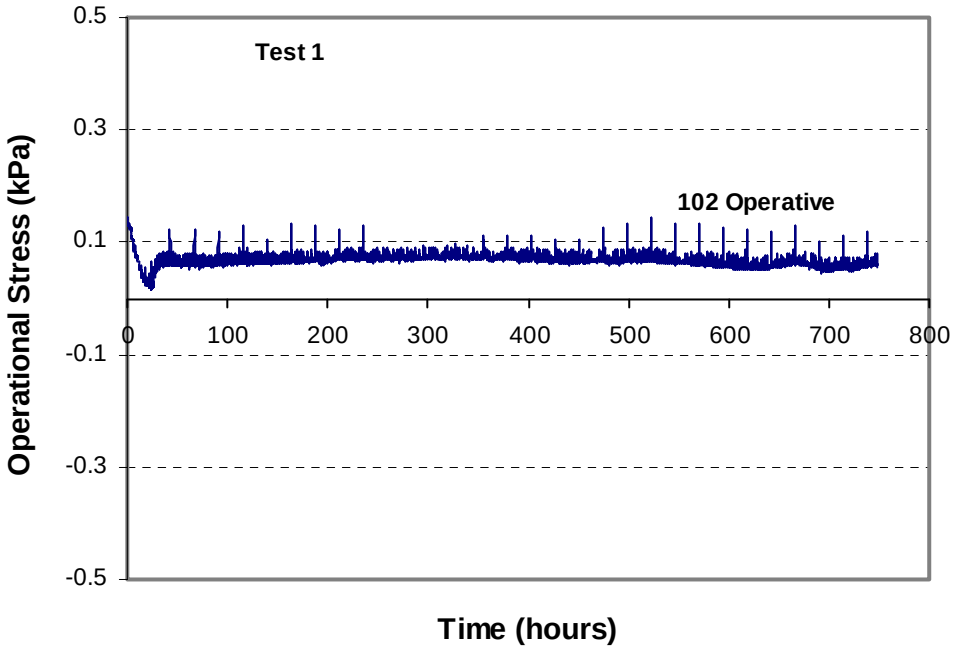

Figure 7-20 Changes of Operative Stress at E2 of Test 1

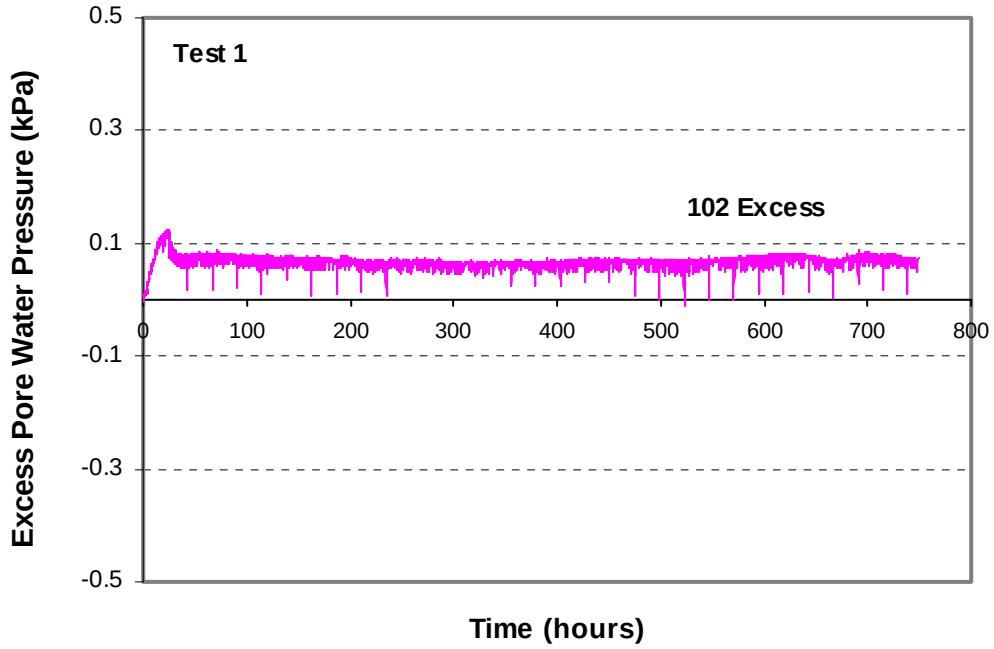

Figure 7-21 Changes of Excess Pore Water Pressure at E1 of Test 2

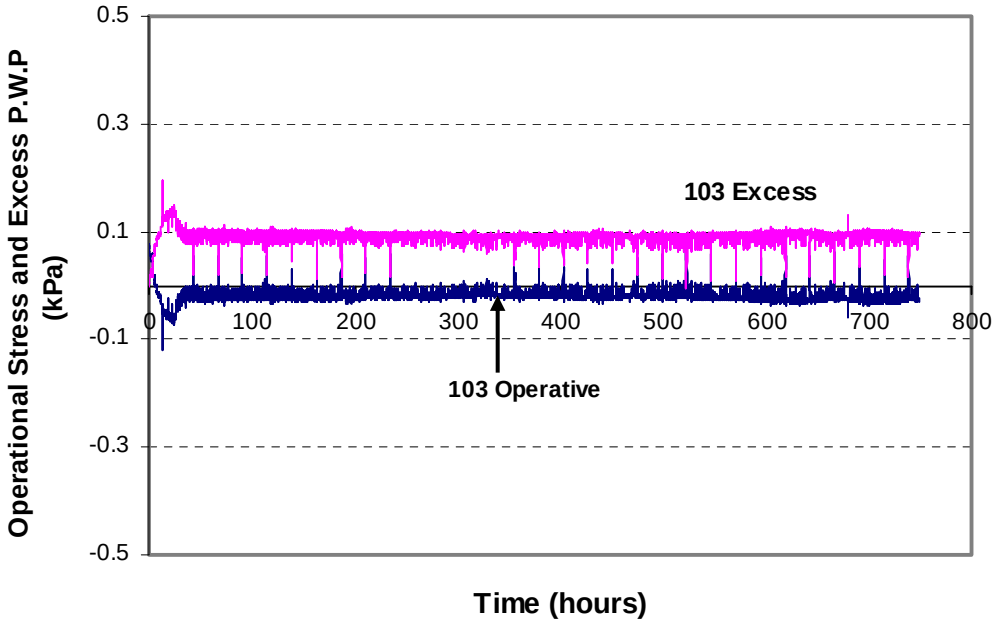

Figure 7-22 Changes of Excess Pore Water Pressure and Operative Stress at E3 of Test 1

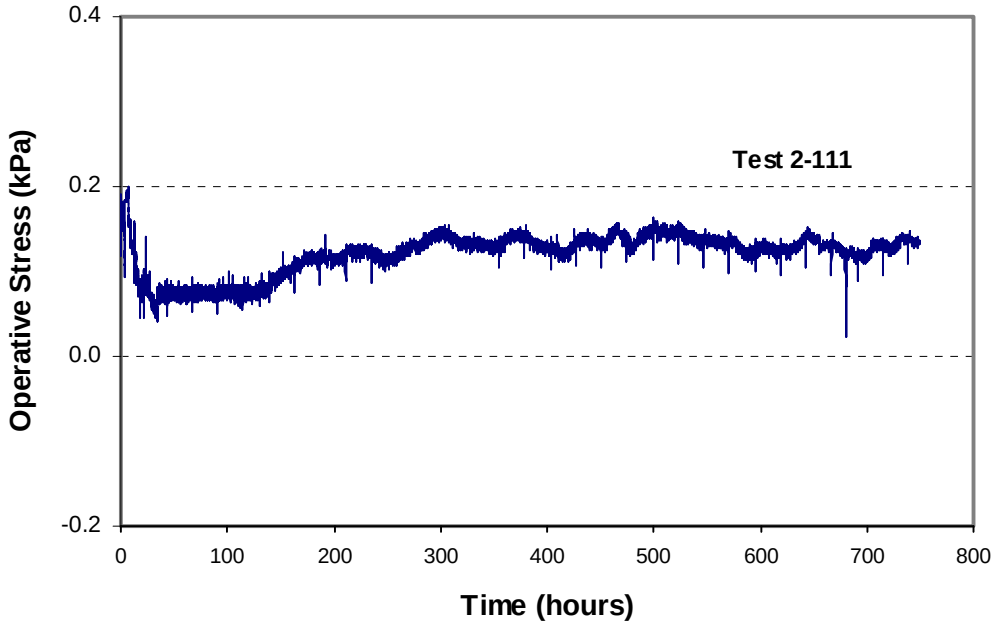

Figure 7-23 Changes of Operative Stress at E1 of Test 2

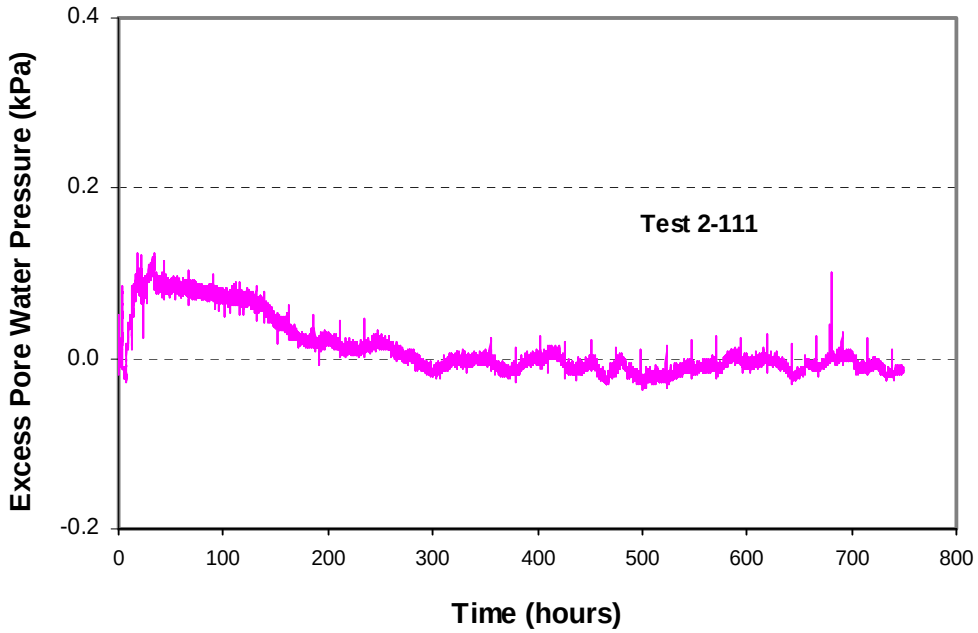

Figure 7-24 Changes of Excess Pore Water Pressure at E1 of Test 2

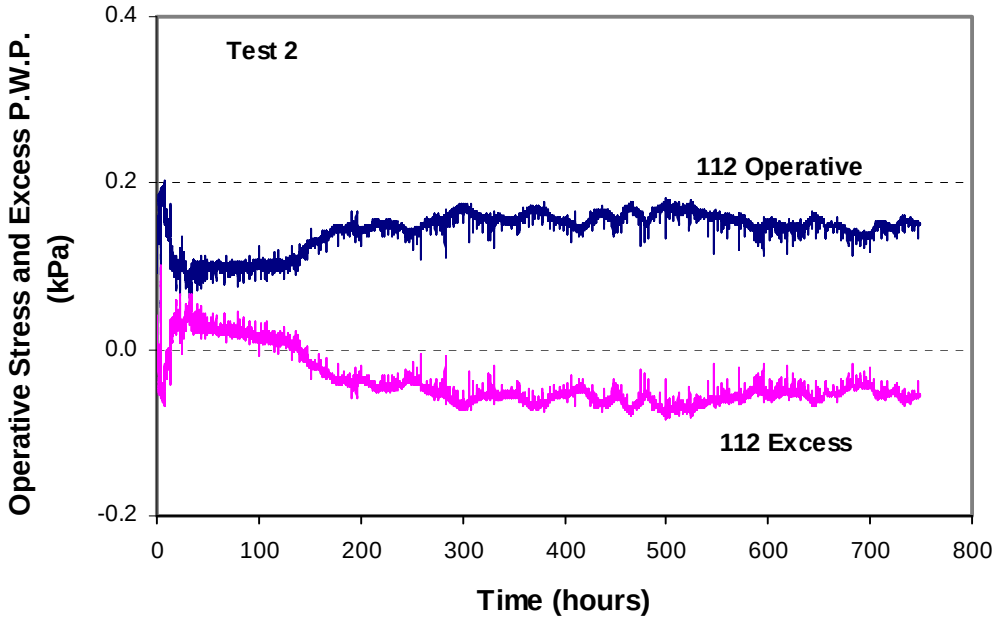

Figure 7-25 Changes of Excess Pore Water Pressure and Operative Stress at E2 of Test 2

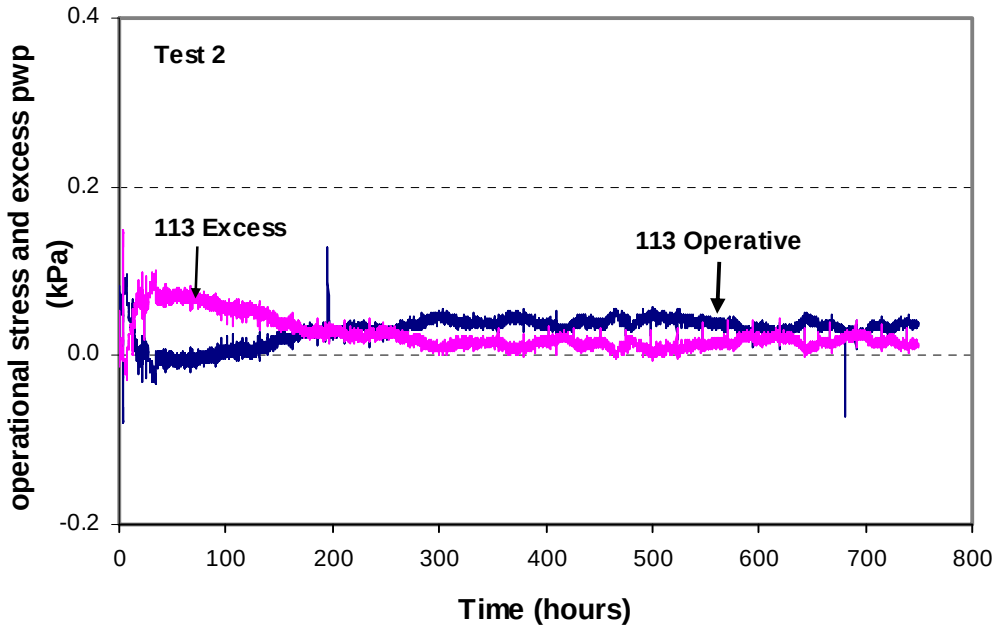

Figure 7-26 Changes of Excess Pore Water Pressure and Operative Stress at E3 of Test 2

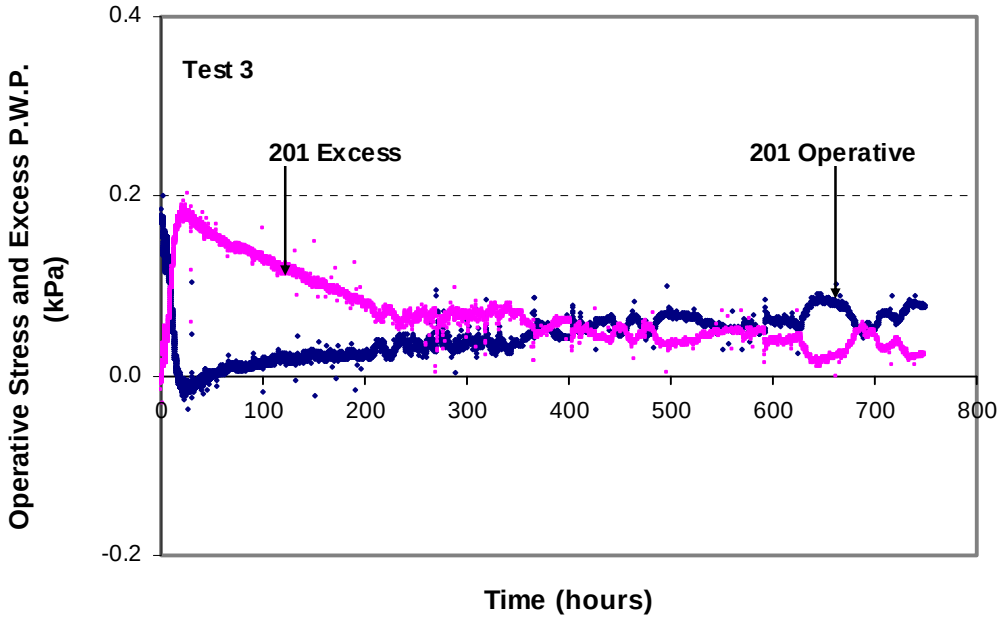

Figure 7-27 Changes of Excess Pore Water Pressure and Operative Stress at E1 of Test 3

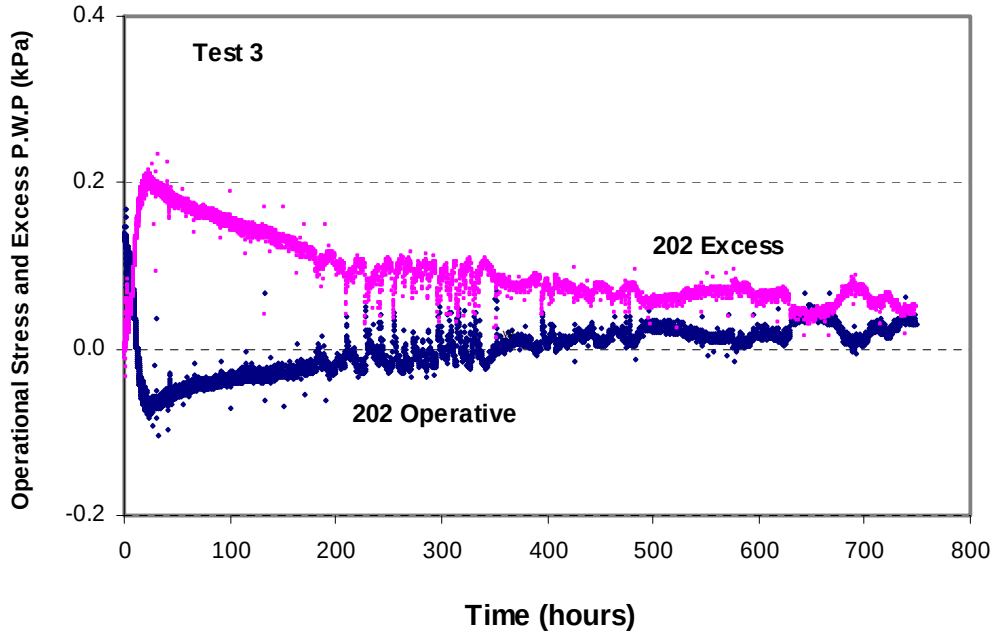

Figure 7-28 Changes of Excess Pore Water Pressure and Operative Stress at E2 of Test 3

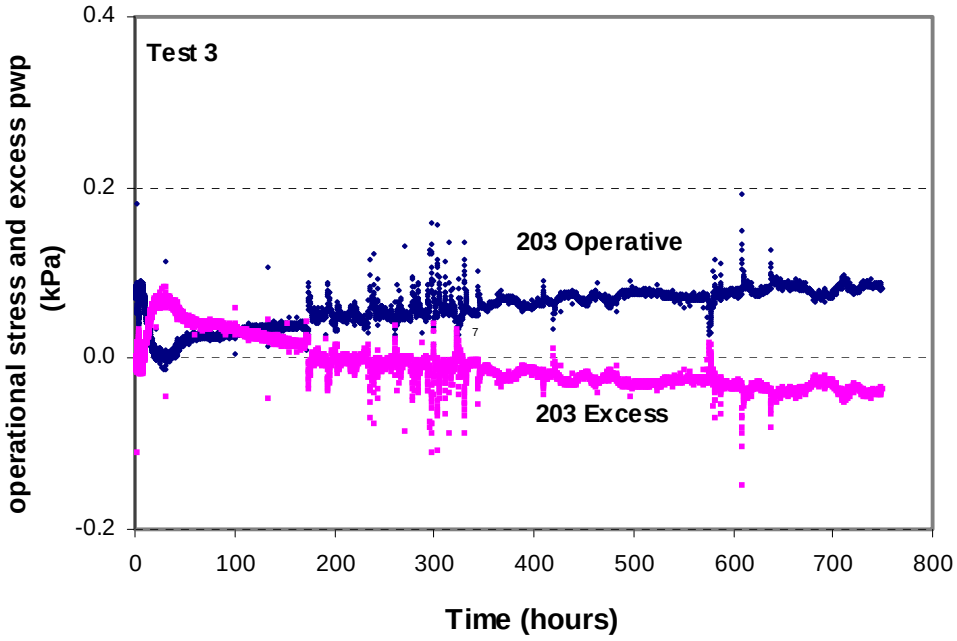

Figure 7-29 Changes of Excess Pore Water Pressure and Operative Stress at E3 of Test 3

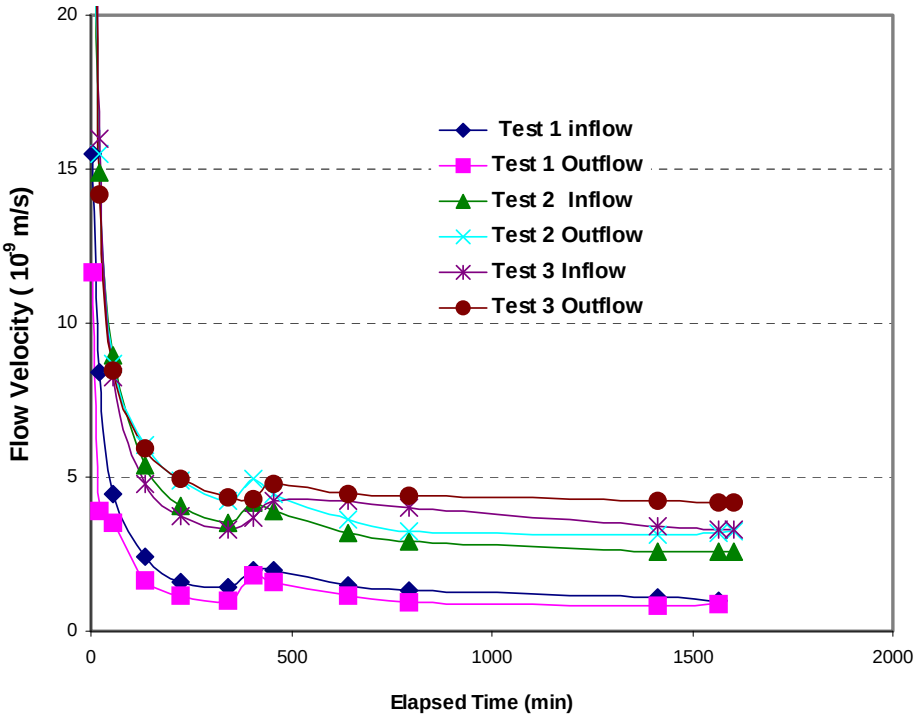

Figure 7-30 Flow Velocity vs. Time in Permeability Tests 1-3 after Microbial Activity

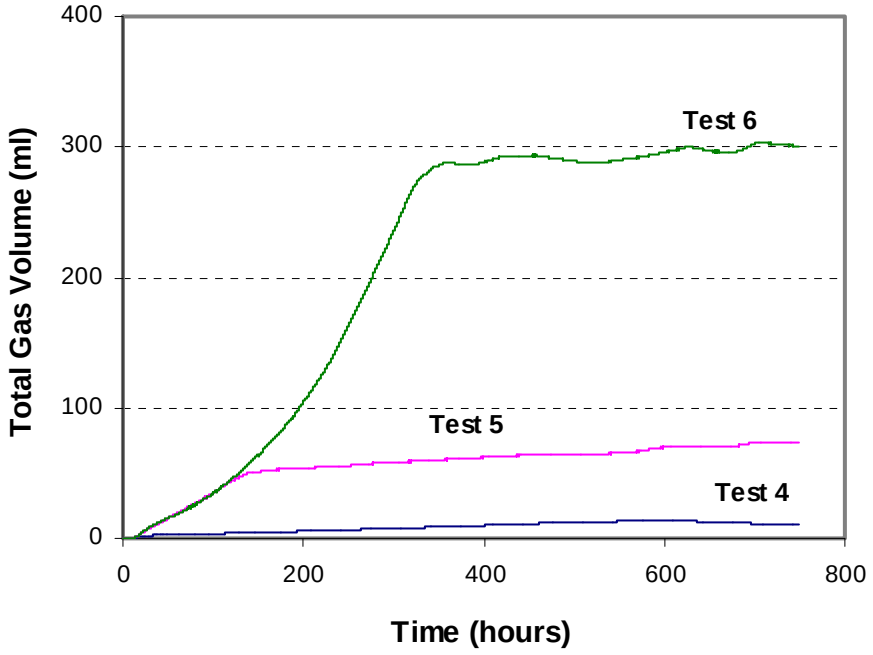

Figure 7-31 Total Gas Volume vs. Time in Samples 4-6

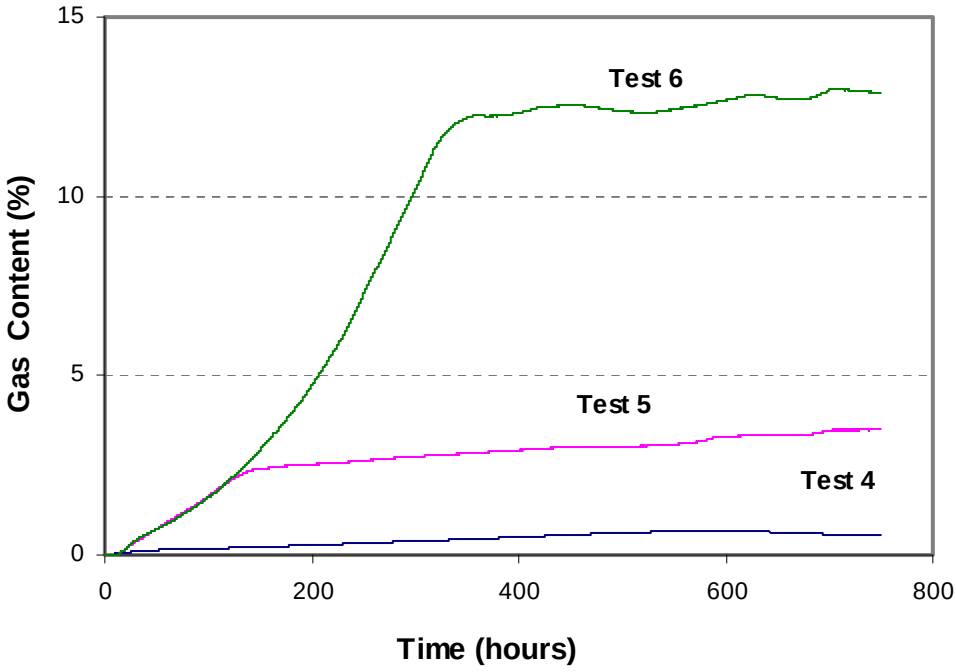

Figure 7-32 Gas Content vs. Time in Samples 4-6

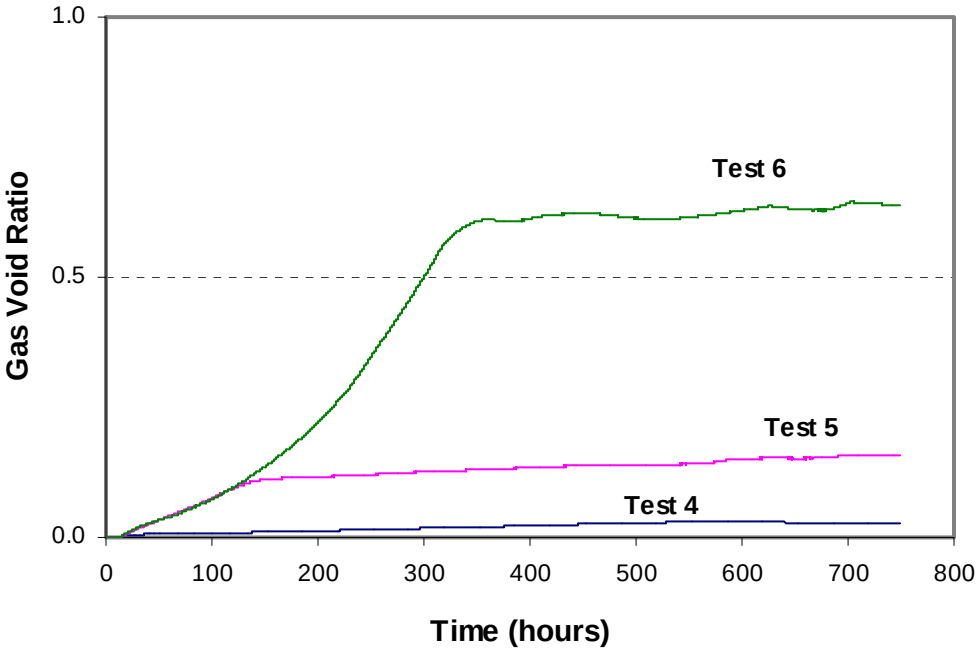

Figure 7-33 Gas Void Ratio vs. Time in Samples 4-6

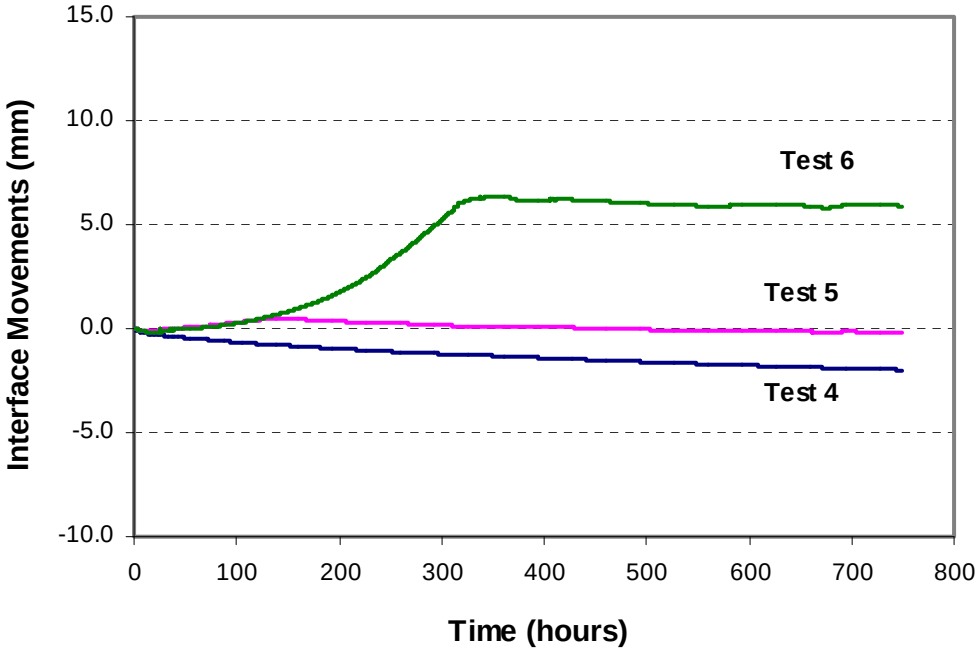

Figure 7-34 Interface Movements in Samples 4-6 during Microbial Activity

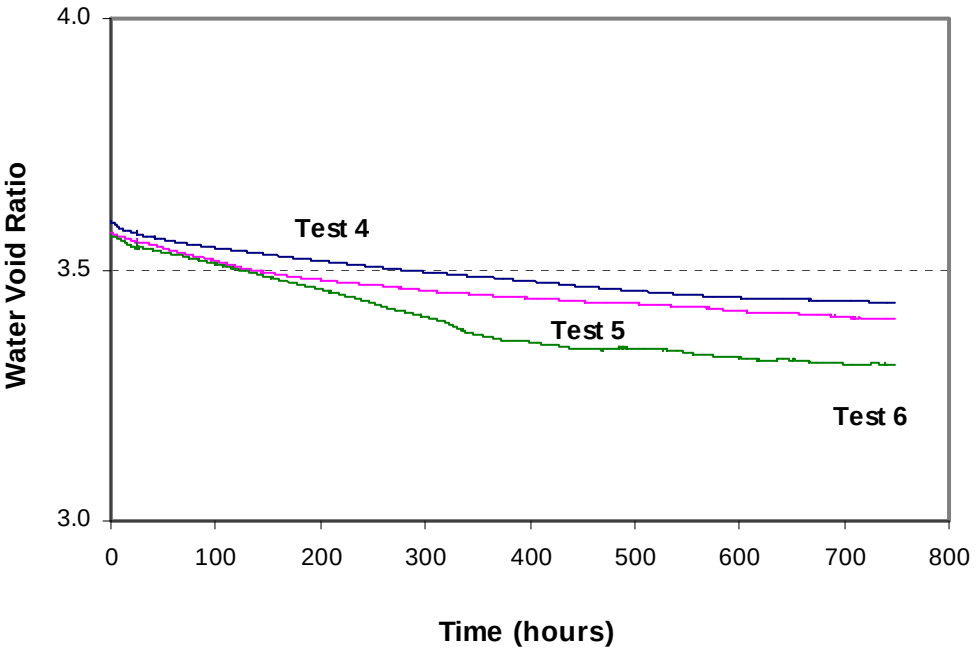

Figure 7-35 Water Void Ratio vs. Time in Samples 4-6

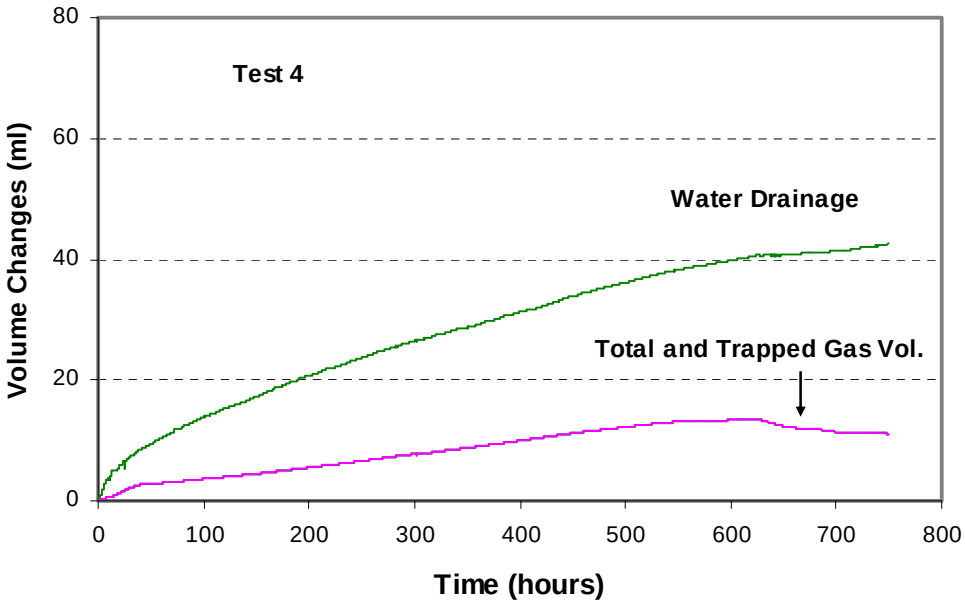

Figure 7-36 Volumetric Changes in Sample 4 during Microbial Activity

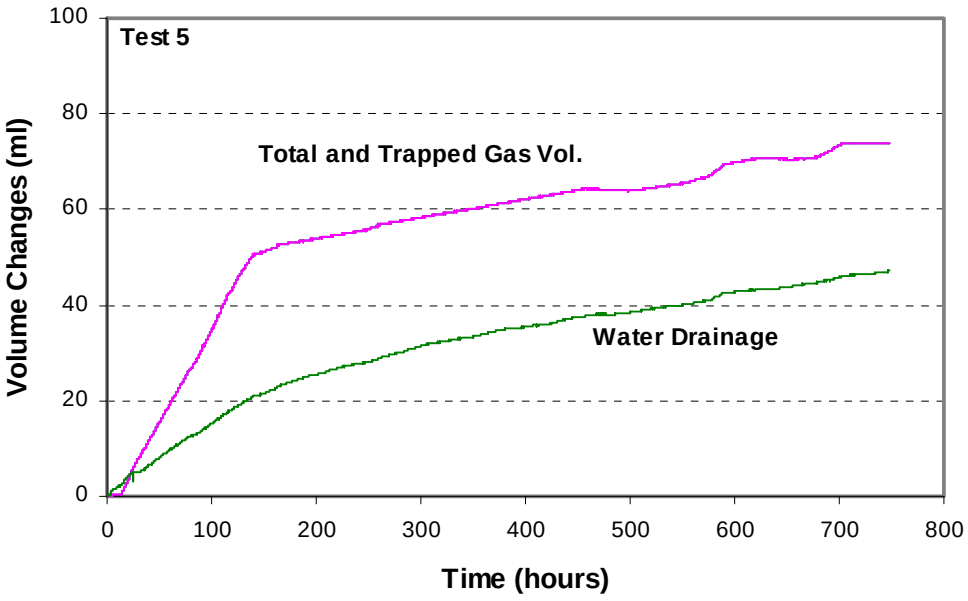

Figure 7-37 Volumetric Changes in Sample 5 during Microbial Activity

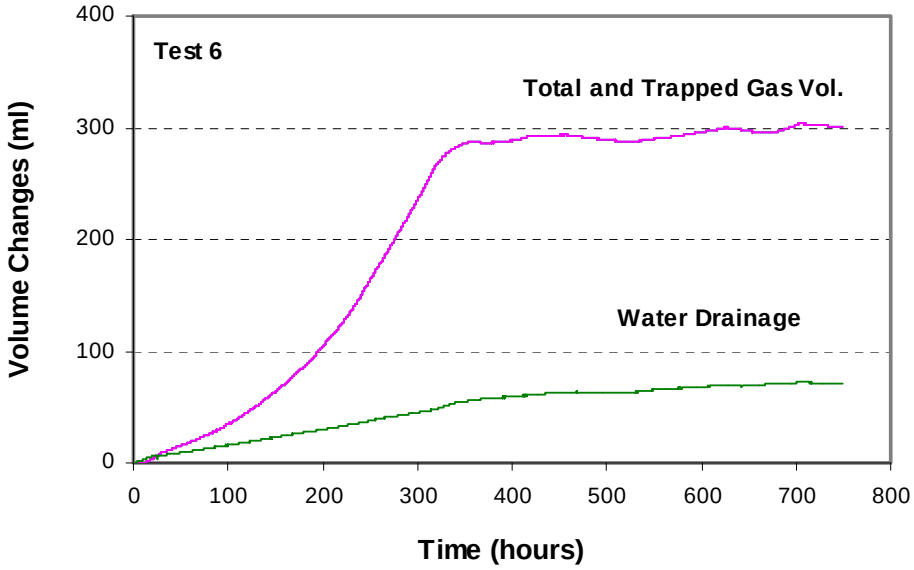

Figure 7-38 Volumetric Changes in Sample 6 during Microbial Activity

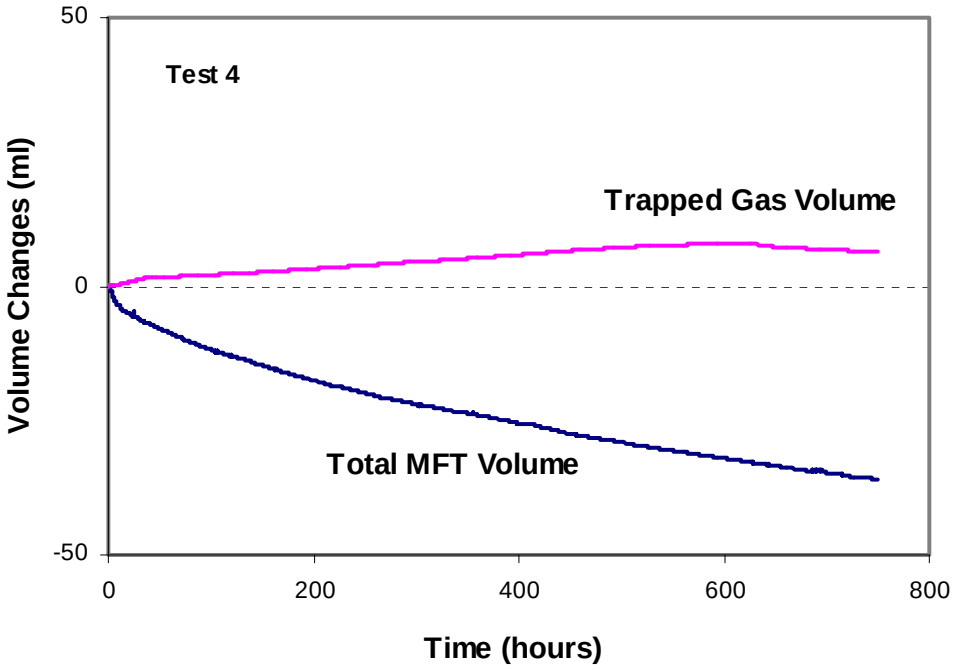

Figure 7-39 Changes in Trapped Gas Volume and Total MFT Volume in Sample 4

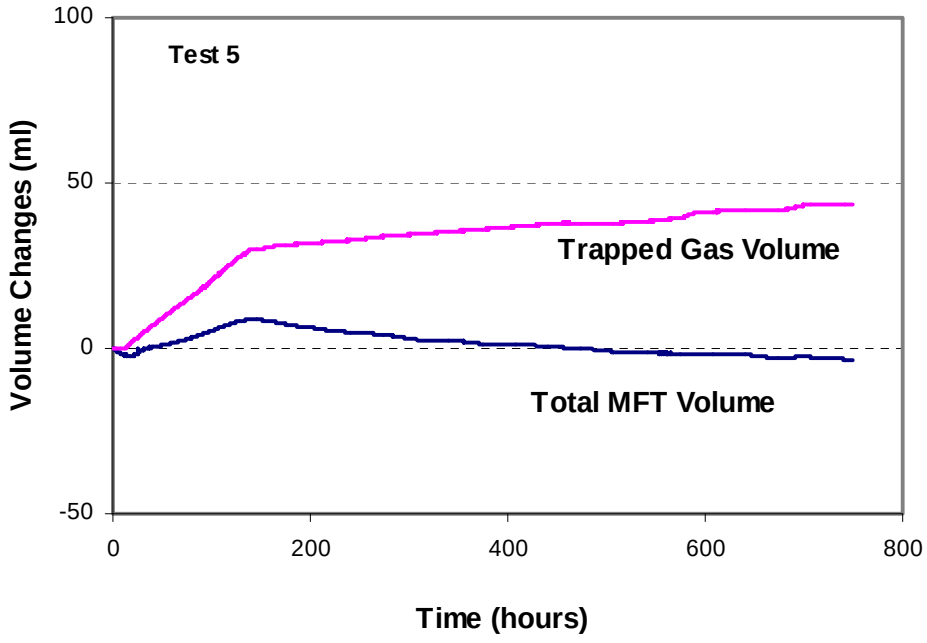

Figure 7-40 Changes in Trapped Gas Volume and Total MFT Volume in Sample 5

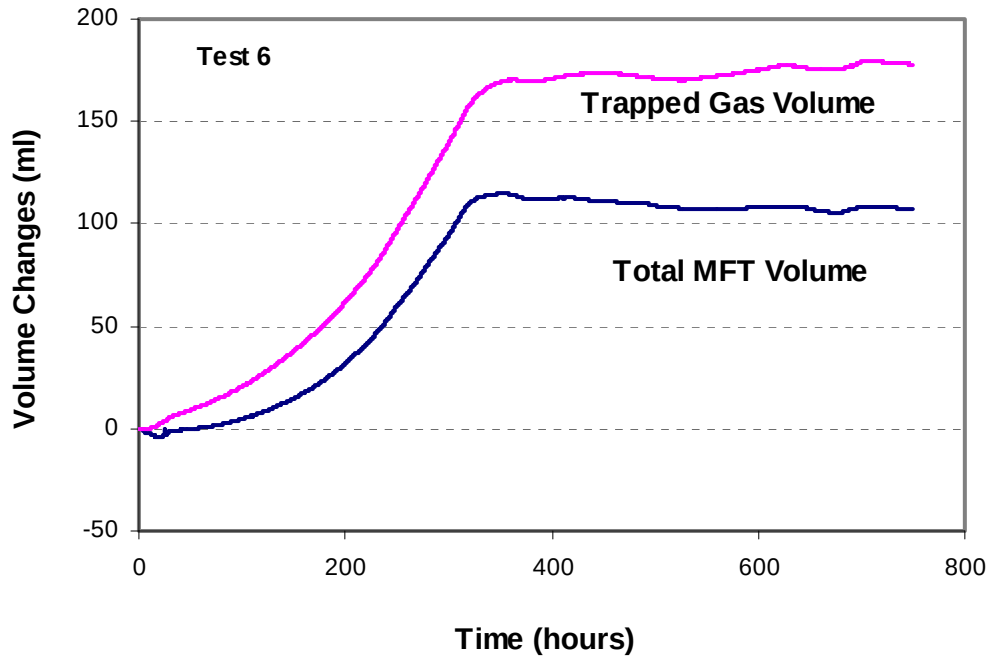

Figure 7-41 Changes in Trapped Gas Volume and Total MFT Volume in Sample 6

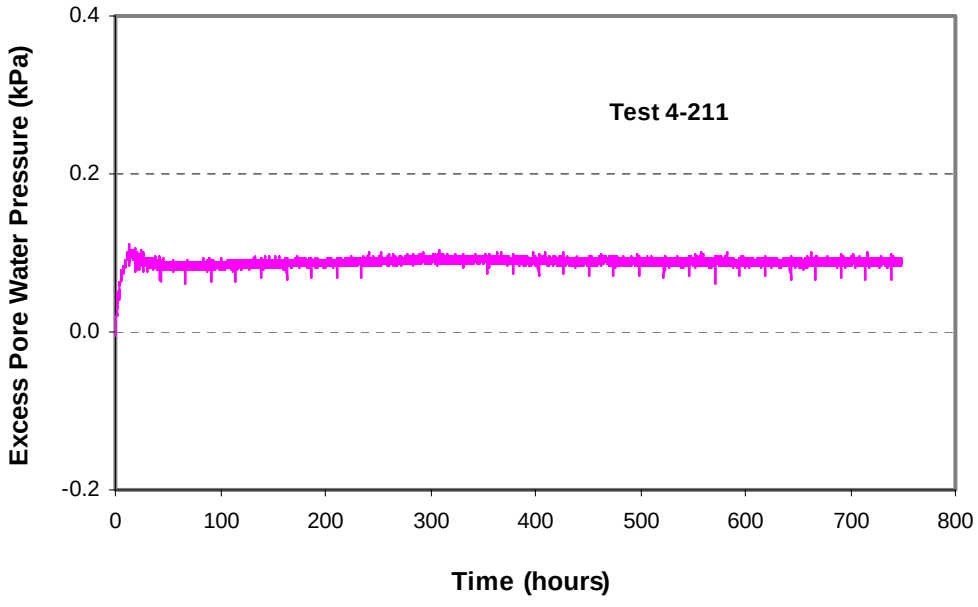

Figure 7-42 Excess Pore Pressure vs. Time at E1 in Sample 4

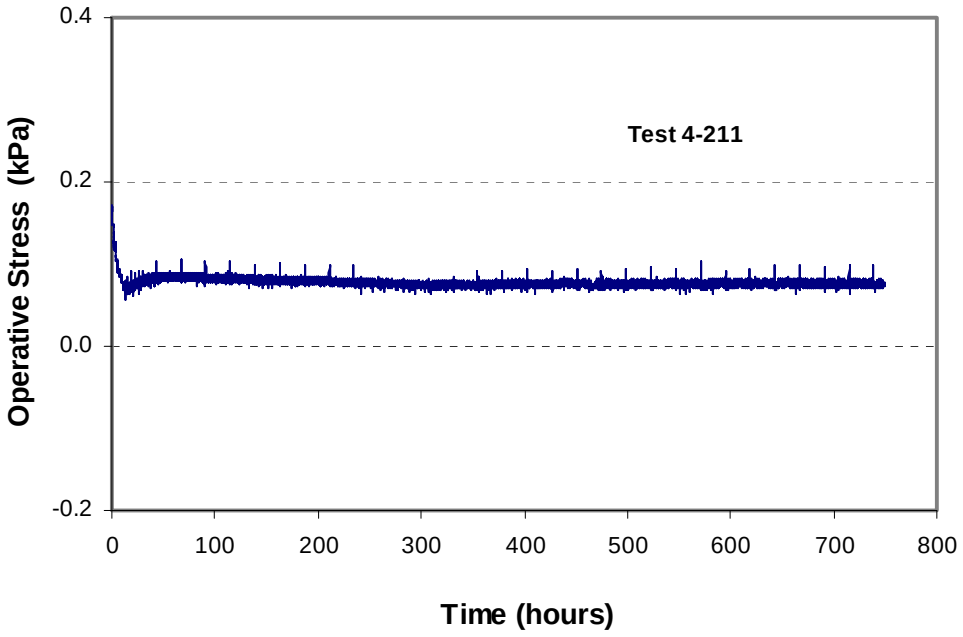

Figure 7-43 Operative Stress vs. Time in at E1 in Sample 4

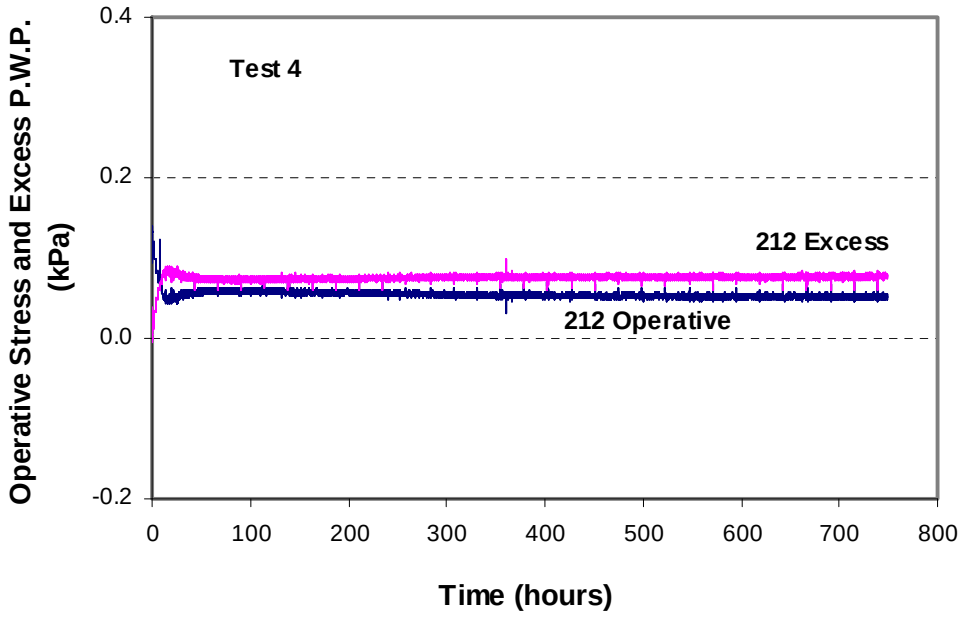

Figure 7-44 Changes in Excess Pore Pressure and Operative Stress at E2 in Sample 4

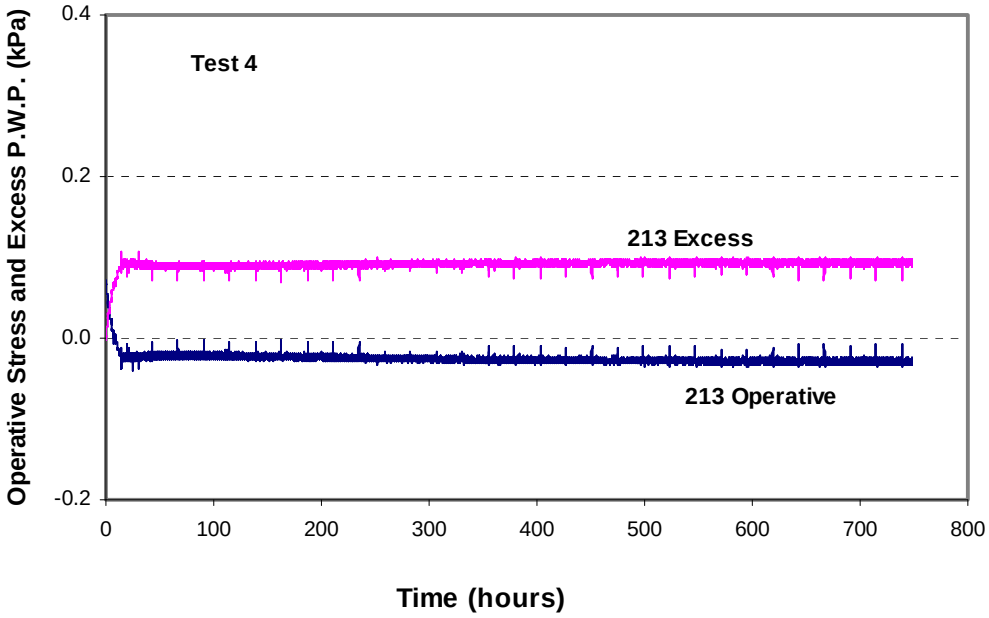

Figure 7-45 Changes in Excess Pore Pressure and Operative Stress at E3 of Test 4

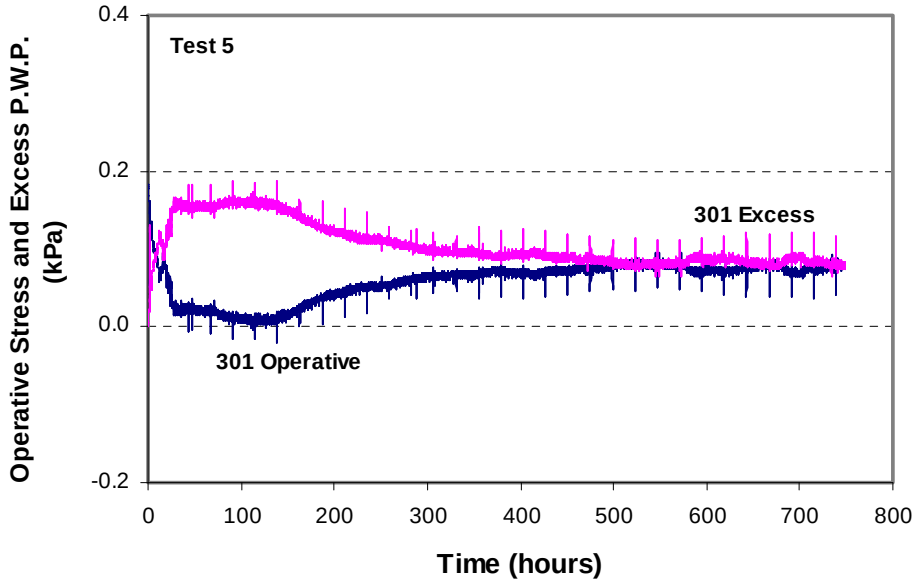

Figure 7-46 Changes in Excess Pore Pressure and Operative Stress at E1 of Test 5

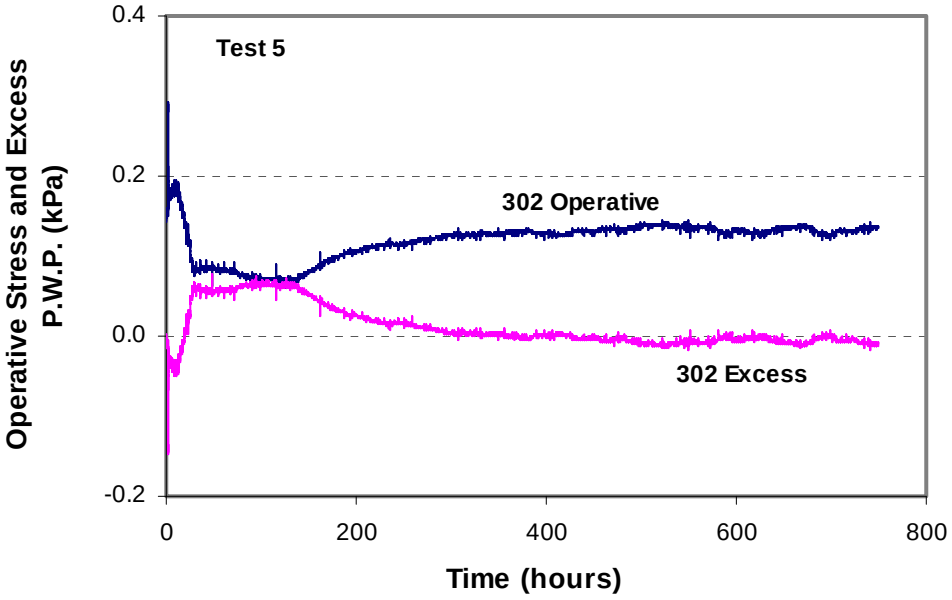

Figure 7-47 Changes in Excess Pore Pressure and Operative Stress at E2 of Test 5

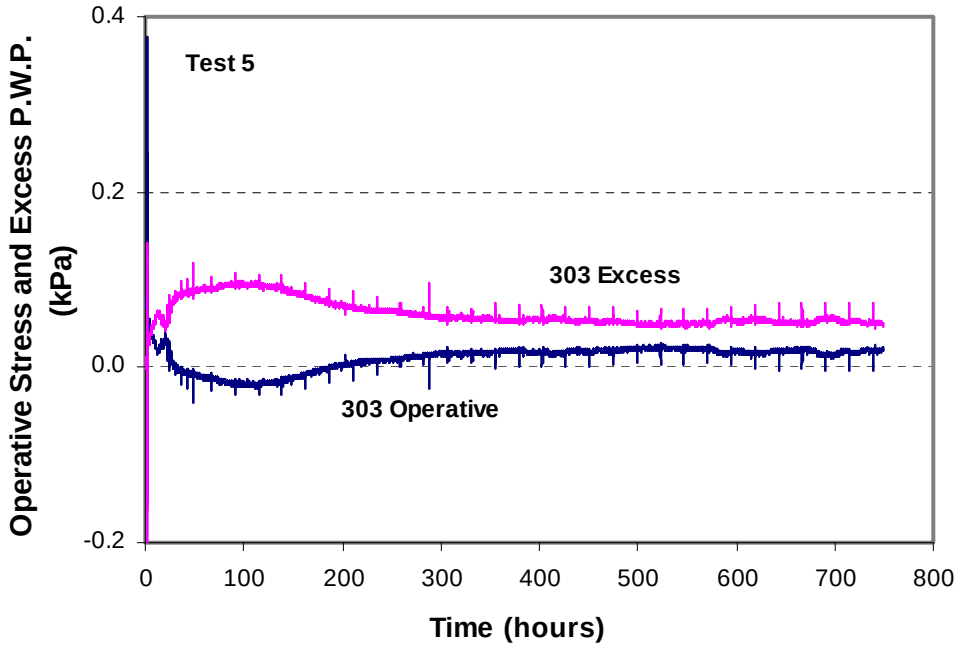

Figure 7-48 Changes in Excess Pore Pressure and Operative Stress at E3 of Test 5

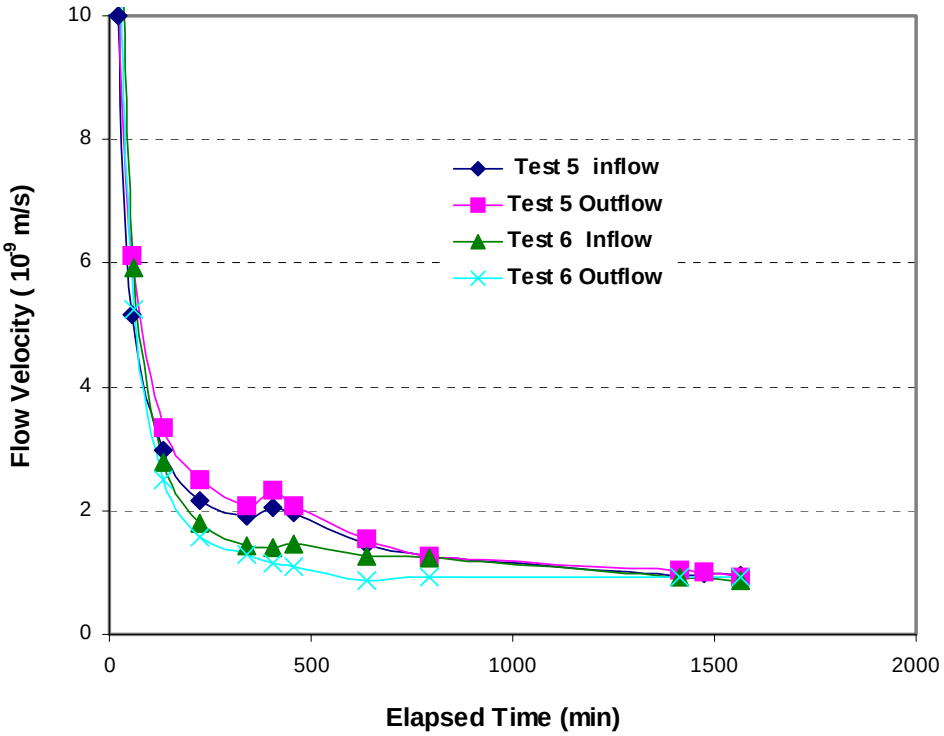

Figure 7-49 Flow Velocity vs. Time in Permeability Tests 5-6 after Microbial Activity

CHAPTER 8

8 INFLUENCE OF BIOLOGICAL GAS GENERATION FOR MFT UNDER VARYING STRESS HISTORIES

8.1 Introduction

Samples 1 to 6 had been consolidated under self-weight before microbial activity started. The stress condition of Samples 1 to 6 was similar to those of normally consolidated soils. However, an over-consolidated stress condition might exist in the field. For example, the MFT has been self-weight consolidated to a certain structural strength until part of the upper loading (effective stress) is reduced due to material transferring (or removal of the material at upper part). This may cause an over-consolidated stress condition in the MFT. This section presents the test results of the over-consolidated MFT during microbial activity.

Different amounts of sodium acetate, 0, 0.6 g, and 1.75 g per litre MFT, were added to Samples 10 to 12, respectively, to control microbial activity. At first, the samples were consolidated to 1.0 kPa at 4^{o}C temperature. Then, the loadings were released to create an over-consolidation stress condition in the MFT. Shortly after discharging the loadings, the room temperature was raised to 24^{o}C to activate microbial activity. The samples were under atmospheric pressure plus about 1 m water head during microbial activity.

Tests 1 to 6 and Tests 10 to 12 had been consolidated (under self-weight or under additional loading) before microbial activity was started, but, the MFT in the tailings pond was very soft when microbial activity began. Tests 13 to 15 were performed to study the densification properties of the very soft MFT (without pre-consolidation) during microbial activity. During microbial activity, Samples 13 to 15 were under atmospheric pressure plus about 1.0 m water head. Tests 13 to 15 were used to model the microbial activity of the very soft MFT at shallow depths of the tailings pond.

8.2 Test Materials and Sample Preparation

As with Tests 1 to 6, the initial MFT was taken from about 2.5 m below the water-MFT interface at Sta. 2 of the MLSB. The properties of the field material have been shown in Section 7.2. Sample preparation for Tests 10 to 12 and Tests 13 to 15 followed the same procedure as Tests 1 to 6. Pond water was added to the field material and they were completely mixed. Table 8.1 shows some parameters of the mixed samples of Samples 10 to 12, and Table 8.2 gives a summary of some information of Samples 10 to 12. Table 8.3 shows some parameters of the mixed samples of Samples 13 to 15, and Table 8.4 summarizes some initial information of Samples 13 to 15.

8.3 Consolidation before Microbial Activity

The consolidation and permeability tests of Samples 10 to 12 were conducted at 4^{o}C temperature. The test method was similar to that of Tests 1 to 6. A loading pressure of 1.0 kPa was applied by two steps: 0.5 kPa and 1.0 kPa. A plastic bowl filled with lead shots was placed on the surface of a porous plastic plate to apply the loading on each sample. Figure 8.1 shows a sketch of the consolidation test using lead shots as loadings.

Since the mixed MFT sample was very soft, direct application of 0.5 kPa loading might have squeezed the MFT out of the loading plate and damaged the sample. To avoid this situation, the sample was consolidated under its self-weight and the weight of the loading plate (the underwater weight of the loading plate was 45 g) at the beginning. After about 11 days of consolidation, certain structure strength was gained. After this time, 937 g lead shots were added into the plastic bowls to apply 0.5 kPa loading to the MFT. During consolidation, the interface movements of the MFT were measured using a Linear Potentiometer (LP). Excess pore pressure changes were monitored by pressure transducers at two elevations, 1.45 cm and 3.95 cm, above the bottom of Sample 11. The detailed

results of the consolidation tests are shown in Appendix G. After 0.5 kPa consolidation, the void ratio was about 2.8, and solids content was about 46.5%. Table 8.5 summarizes some parameters of Samples 10 to 12 after 0.5 kPa consolidation.

After 0.5 kPa consolidation was finished, Samples 10 to 12 were moved to a moisture room with 4^{o}C temperature to continue the consolidation tests under 1.0 kPa loadings (the room temperature of the cooler was raised to 24^{o}C to start microbial activity of Samples 1 to 6). Additional lead shots were added into the plastic bowls to apply another 0.5 kPa loading to each sample.

Table 8.6 summarizes some parameters of Samples 10 to 12 after 1.0 kPa consolidation. After 1.0 kPa consolidation, the average void ratio of Samples 11 to 12 was about 2.51, the average solids content was about 49%, and the excess pore water pressure was dissipated to close to zero. The detailed results are also shown in Appendix G.

After 1.0 kPa consolidation was finished, the valve at the bottom of each cell was closed and the plastic bowl filled with lead shots was taken out of the consolidation cell to release the loading. After unloading, the measured excess pore water pressures at three elevations, the bottom (E1), 1.45 cm (E2) and 3.95 cm (E3) above the bottom, of Sample 11 were –0.908 kPa, -0.926 kPa and –0.959 kPa, respectively. Negative excess pore water pressures were generated in the MFT after unloading.

8.4 Results of Tests 10, 11, and 12

8.4.1 Volume Change during Microbial Activity

After unloading, Cells 10 to 12 were moved back to the temperature-controlled cooler, and the gas MFT densification apparatus was installed as shown in Figure

6.1. The room temperature was then raised to 24°C to initiate microbial activity. The samples were under atmospheric pressure plus about 1.0 m water head.

Figure 8.2 shows the changes of room temperature with time during microbial activity. It took about 30 hours for the room temperature to increase from 4°C to 24°C. Due to defrosting operations of the temperature-controlling device, the room temperature fluctuated about 2°C (sometimes 4-5°C) for every 5 hours. The temperature variation could slightly affect the rate of biogas generation. Also, the water front (Figure 6.3) in the plastic tube fluctuated due to temperature effect on water volume. This could cause small fluctuations of the hydrostatic pressure and total pressure in the sample.

By using Henry's Law, the dissolved gas volumes in Samples 10 to 12 were calculated. Table 8.7 shows equivalent volumes (at STP) of the dissolved gas in Samples 10-12.

Figure 8.3 shows the changes of total gas volume (trapped gas plus released gas at STP) with time in Samples 10 to 12. In Test 10, gas bubbles started to form after about 100 hours, but in Tests 11 to 12, gas bubbles started to form shortly after temperature increased. In Test 12, the total gas volume increased rapidly during the first 200 hours, then increased slowly. In Test 11, gas was generated rapidly during the first 40 hours, then increased at a slower rate. In Sample 10, gas was generated at a slow rate after about 100 hours. At the end of testing (about 670 hours), total gas generation volumes (at STP) of Samples 10 to 12 were 10.3 mL, 23.4 mL and 120.7 mL, respectively.

Figure 8.4 shows the changes of the released gas volume (at STP) with time in Sample 12. Gas started to be released from Sample 12 after about 110 hours. At the end of testing, about 45 mL of gas was released from Sample 12, and there was no visible gas bubble release from Samples 10 to 11.

Figure 8.5 shows the changes of gas content with time in Samples 10 to 12. In Sample 12, the gas content rapidly increased during the first 200 hours, then remained almost constant. This suggests that after 200 hours, gas generation rates were almost equal to gas release rates. At the end of testing, the gas contents in Samples 10 to 12 were 1.1%, 2.5% and 6.9%, respectively. Figure 8.6 shows the changes of gas void ratios with time in Samples 10 to 12. At the end of testing, the gas void ratios in Samples 10 to 12 were 0.04, 0.1 and 0.28, respectively.

Figure 8.7 shows the interface movements at different times in Samples 10 to 12. Due to the existence of negative excess pore water pressure and biogas generation, Samples 10 to 12 continuously expanded during testing. The total volume of Sample 12 rapidly increased during the first 200 hours, and then, with gas generation slowing down, increased at slower rates. The total volume of Sample 11 rapidly expanded during the first 40 hours, and then increased slowly at an almost constant rate. The volume of Sample 10 slowly increased during microbial activity.

Figure 8.8 shows the changes of the water drainage volume with time. The negative values indicate that water went back into the MFT during microbial activity. In Test 12, water rapidly flowed back into the MFT during the first 200 hours, after which time the water volume in the MFT increased more slowly. The water volume in Sample 11 rapidly increased during the first 30 hours, then increased at a slower rate. The water volume in Sample 10 slowly increased throughout the test. At the end of testing (about 670 hours), the increased water volumes of Samples 10 to 12 were 26 mL, 33 mL and 61 mL, respectively. Figure 8.9 shows the changes of the water void ratio in Samples 10 to 12 at different times. At the end of testing, the water void ratios of Samples 10-12 were 2.61, 2.64 and 2.76, respectively.

Figure 8.10 shows the changes in bulk density of Samples 10 to 12 during microbial activity. In Sample 12, the bulk density rapidly decreased from 1.4

g/mL to 1.283 g/mL during the first 200 hours, and then decreased slowly. In Sample 11, the bulk density rapidly decreased during the first 30 hours, then decreased slowly. In Sample 10, the bulk density decreased at a slow rate all through the test. At the end of testing, the bulk densities of Samples 10 to 12 were 1.372 g/mL, 1.349 g/mL and 1.279 g/mL, respectively.

Figure 8.11 shows the volumetric changes (total gas, trapped gas and released gas volumes at STP, and water drainage volume) with time in Sample 12. During rapid biogas generation, the water volume in the MFT rapidly increased. When the gas generation rate decreased, the water volume in the MFT increased slowly. Figure 8.12 shows the volumetric changes of Sample 11 with time. During the first 40 hours, the total gas volume rapidly increased, as did the water volume of the MFT. After 40 hours, both the total gas volume and water volume in Sample 11 slowly increased. Figure 8.13 shows the volumetric changes in Sample 10. Both the gas generation volume and water volume slowly increased during microbial activity.

Figures 8.14 to 8.16 show the changes of the total MFT volume and trapped gas volume in Samples 10 to 12, respectively. In Sample 10, both the total MFT volume and trapped gas volume slowly increased with time. However, the MFT expansions were slightly faster than the trapped gas volume increases, so water slowly flowed back into the MFT. In Sample 12, both the trapped gas volume and total MFT volume increased during the first 200 hours, but the MFT volume increased more rapidly than the trapped gas volume. Water rapidly flowed back to fill the additional space. After 200 hours, the total MFT volume of Sample 12 slowly increased, but the trapped gas volume remained almost constant. Water traveled back into the MFT slowly. In Sample 11, both the trapped gas volume and total MFT volume rapidly increased during the first 40 hours, but the MFT volume expansions were more rapid than the trapped gas volume increases, and thus, water entered the MFT rapidly.

8.4.2 Excess Pore Pressure and Operative Stress

Figure 8.17 shows the changes of excess pore water pressure and operative stress at the bottom (E1) of Sample 10 during microbial activity. The total stress was relatively stable during the slow gas generation in Sample 10. During the first 100 hours, the excess pore water pressure increased from –0.91 kPa to –0.85 kPa, and the operative stress decreased from 1.1 kPa to 1.0 kPa. From 100 hours to 673 hours, excess pore water pressure slightly increased and operative stress slightly decreased.

Figure 8.18 shows the changes of excess pore water pressure and operative stress at 1.45 cm elevation (E2) above the bottom of Sample 10. During the first 40 hours, the excess pore water pressure obviously increased from –0.926 kPa to –0.522 kPa, and the operative stress obviously decreased from 1.06 kPa to 0.66 kPa. After 40 hours, excess pore water pressure slowly increased and operative stress slowly decreased.

Figure 8.19 shows the changes of excess pore pressure and operative stress at 3.95 cm elevation (E3) above the bottom of Sample 10. Similar changes to those seen at E1 and E2 are shown.

Figure 8.20 shows the changes of excess pore pressure and operative stress at the bottom (E1) of Sample 11. During the first 30 hours, excess pore water pressure slightly increased and the operative stress slightly decreased. After 30 hours, excess pore water pressure and operative stress were relatively stable.

Figure 8.21 shows the changes of excess pore pressure and operative stress at 1.45 cm elevation (E2) above the bottom of Sample 11 During the first 30 hours, the excess pore water pressure obviously increased from –0.926 kPa to –0.72 kPa, and operative stress decreased from 1.06 kPa to 0.85 kPa. After 30 hours, excess

pore water pressure slightly increased, and operative stress slightly decreased over time.

Figure 8.22 shows the changes of excess pore water pressure and operative stress at 3.95 cm elevation (E3) above the bottom of Sample 11. During microbial activity, excess pore water pressure slightly increased, and operative stress slightly decreased.

Figure 8.23 shows the changes of excess pore water pressure and operative stress at the bottom (E1) of Sample 12. The total stress slightly decreased during biogas generation. During the first 25 hours, excess pore water pressure slightly increased and operative stress slightly decreased. Then, both excess pore pressure and operative stress became relatively stable.

Figure 8.24 shows the changes of excess pore water pressure and operative stress at 1.45 cm elevation (E2) above the bottom of Sample 12. During the first 25 hours, excess pore water pressure increased from –0.926 kPa to -0.8 kPa, and operative stress decreased from 1.06 kPa to 0.93 kPa. Then, there were no obvious changes in either excess pore water pressure or operative stress.

Figure 8.25 shows the changes of excess pore pressure and operative stress at 3.95 cm elevation (E3) above the bottom of Sample 12. The changes at E3 were similar to those at E2.

Table 8.8 shows some parameters of Samples 10 to 12 after microbial activity. At the end of testing, Sample 12 had the highest water void ratio and gas void ratio among the three samples.

8.4.3 Permeability Tests after Microbial Activity

After microbial activity diminished, the room temperature was lowered to 4^{o}C to inhibit microbial activity. Constant head differences were applied to Samples 10 to 12 to cause upward flow. Figure 8.26 shows the flow velocity vs. time in permeability Tests 10 to 12. In each test, the inflow velocity was greater than the outflow velocity. This is likely because small part of the inflow water filled some voids (cracks and fractures) in the MFT. Table 8.9 summarizes the results of constant head permeability Tests 10 to 12 after microbial activity. The coefficients of permeability were calculated using the average flow velocities (the average value of inflow and outflow velocities). The coefficient of permeability of Sample 12 was about twice that of Sample 10. With the increases of microbial activity and biogas generation, the coefficients of permeability slightly increased.

8.5 Discussion of Tests 10, 11, and 12

8.5.1 Volume Change

After 1.0 kPa consolidation, the void ratio of the MFT decreased from 4.4 to 2.5, and the solids content increased from 35.1% to 49%. The densification states (void ratio, solids content, etc.) of Samples 10 to 12 were close at the end of the 1.0 kPa consolidation. After unloading the samples, negative excess pore water pressures were produced. Samples 10 to 12 were similar to over-consolidated soils.

With the increase of sodium acetate amendments in Samples 10 to 12, gas generation volumes increased. At the end of testing, the total gas generation volume in Sample 11 was slightly larger than that in Sample 10, but the gas generation volume in Sample 12 was much larger than those in Samples 10 and 11. Gas generation volumes in Samples 10 to 12 were obviously smaller than those in Samples 1 to 3, respectively. This might have been caused by two factors: (1) after 1.0 kPa consolidation, Samples 10 to 12 became much denser than Samples 1 to 3; more water was drained out of Samples 10 to 12 than Samples 1

to 3. Part of the sodium acetate dissolved in the pore solution migrated out of the sample along with water drainage; (2) during long-term consolidation, part of the sodium acetate was depleted or degraded. In Test 11, rapid gas generation lasted only a short period (about 40 hours), and then slowed down. Rapid gas generation in Sample 12 lasted much longer (about 200 hours) than in Sample 11. Gas was generated at slow rates in Sample 10 all through the test. Part of the generated gas in Sample 12 was released, while all of the generated gas in Samples 10 and 11 was trapped. Due to the over-consolidated behavior of the MFT, Samples 10 to 12 continually expanded during testing. During rapid gas generation, MFT volume expansion was obviously accelerated. During microbial activity and biogas generation, water flowed back into the MFT due to the existence of negative excess pore water pressure. With the increases of microbial activity, more water travelled back into the MFT. For each sample, the water volume quickly increased during rapid gas generation.

Analyzing the relative changes of the total MFT volume and trapped gas volume can help to clarify the process of water drainage from the MFT. In Sample 12, gas was generated rapidly during the first 200 hours. But the increase rates of the total MFT volume were more rapid than those of the trapped gas volume during this period, and as a result, water rapidly flowed back into the MFT to fill the space. After 200 hours, gas generation in Sample 12 slowed down. Both the trapped gas volume and total MFT volume increased slowly, and the water volume of the MFT increased slowly. It appears, based on the obtained observations, that rapid gas generation can accelerate MFT expansion and increase the relative difference between the total MFT volume and trapped gas volume. This is what allowed water to flow into the MFT more easily.

8.5.2 Excess Pore Pressure and Operative Stress

After unloading Samples 10 to 12, negative excess pore water pressures were produced. Since pore water pressures in Samples 10 to 12 were lower than hydrostatic pressure, water flowed into the MFT under downward gradients.

There were obvious excess pore water pressure increases in Sample 10 during the early period. These increases were likely caused by two factors: (1) a rapid temperature increase which produced extra excess pore water pressure; (2) water flowing back into the MFT and filling some voids. The rapid temperature increase was the main factor during the early period. After temperature became stable, excess pore water pressure continually increased and operative stress decreased. These changes were likely caused by the second factor.

The changes of excess pore water pressure and operative stress in Samples 11 and 12 were similar to those in Sample 10. Obvious changes occurred during the early periods. They were mainly caused by a rapid temperature increase. In Samples 11 and 12, the increases of excess pore water pressure were less obvious than those in Sample 10 after temperature became stable. In Sample 12, the excess pore water pressure was almost constant after temperature stabilized. This was attributed to two factors: (1) the rapid increase of the trapped gas volume in Samples 11 and 12, caused the total stress to decrease with time. This could retard the increase of excess pore water pressure; (2) the rapid structure dilation caused by rapid gas generation could also retard excess pore water pressure increases in the MFT.

8.5.3 Structure and Permeability

The details of the structural changes in Samples 10 to 12 are shown in Appendix I. In Sample 10, some large gas bubbles and cracks developed within a small range (about 1 cm below the interface). These cracks were likely caused by tensile stress after unloading the sample. Gas bubbles migrating into the tensile cracks further enlarged them. Below this narrow range, there were no visible gas

bubbles or cracks. In Sample 11, some ellipsoidal gas bubbles and cracks were observed, most of which were small and discontinuous. The structural changes in Sample 12 were more obvious than those in Samples 10 and 11. Some large gas bubbles and interconnected fractures were observed.

After microbial activity diminished, constant head permeability tests were conducted at 4^{o}C temperature. With the increases of microbial activity and biogas generation in Samples 10 to12, the coefficients of permeability slightly increased. The coefficient of permeability of Sample 12 was about twice that of Sample 10. The increase was due to two factors: (1) some large structures (fractures, cracks) might have become convenient drainage paths; (2) the water void ratio increased after microbial activity.

8.6 Results for Tests 13, 14 and 15

Before the MFT was poured, the test cell was flushed with nitrogen gas to create an anaerobic environment. The densification test device, as shown in Figure 6.1, was then installed. Without pre-consolidation and permeability tests, the room temperature was raised to 24^{o}C to start microbial activity. By Henry's Law, the dissolved gas mass was calculated. Table 8.10 shows the equivalent volumes (at STP) of dissolved gas in Samples 13-15.

8.6.1 Volume Change

Figure 8.27 shows the changes of total gas volume (trapped gas plus released gas at STP) during microbial activity. There was no obvious gas generation in Sample 13 during the first 100 hours. It is likely that any generated gas was dissolved in the pore solution during this period. After 100 hours, gas was generated at slow rates in Sample 13. In Sample 14, the total gas volume increased slowly during the first 80 hours, after which time gas generation rates started to accelerate. After about 340 hours, microbial activity in Sample 14

diminished and the total gas generation volume became stable. In Sample 15, gas was generated at slow rates during the first 100 hours. From 100 to 200 hours, gas generation rates gradually increased. From 200 to 550 hours, gas was generated very rapidly. After about 550 hours, microbial activity in Sample 15 diminished and the total gas volume became stable. At the end of testing, the total gas volumes (at STP) in Samples 13 to 15 were 9 mL, 179 mL and 510 mL, respectively.

Figure 8.28 shows the changes of the released gas volumes, with time, from Samples 13 to 15. In Sample 13, all the generated gas was trapped. In Samples 14 and 15, gas bubbles started to be released after about 300 hours. At the end of testing, the released gas volumes from Samples 14 and 15 were 58 mL and 358 mL, respectively. In Sample 15, the released gas volume accounted for about 70% of the total gas volume (at STP).

Figure 8.29 shows the changes of gas content with time in Samples 13 to 15. In Sample 15, the gas content rapidly increased with time during the first 320 hours. After reaching a threshold value of 8.2%, gas bubbles started to be released, and the gas content increased at slower rates. In Sample 14, the gas content rapidly increased during the first 300 hours. When it reached the threshold value of 8.5%, gas bubbles were released from the MFT. After this time, the gas content slightly decreased. After about 380 hours, the gas content in Sample 14 became stable. At the end of testing, the gas contents in Samples 13 to 15 were 0.6%, 7.4% and 9.4%, respectively. Figure 8.30 shows the changes of the gas void ratio, with time, in Samples 13 to 15. At the end of testing, the gas void ratios in Sample 13 to 15 were 0.03, 0.38 and 0.48, respectively.

Figure 8.31 shows the interface movements of Samples 13 to 15 during microbial activity. The interface level of Sample 15 was relatively stable during the first 30 hours. From 30 hours to 100 hours, the interface settled. From 100 hours to 160 hours, with biogas generation accelerating, the settlement was retarded, and slight

expansion was observed. From 160 hours to 320 hours, the MFT volume rapidly expanded due to rapid increase of the trapped gas volume. After 320 hours, due to gas release from the MFT, the interface settled down. At the end of testing, the MFT interface was 1.6 mm below the initial interface level (before microbial activity). In Sample 14, the interface slightly settled during the first 80 hours. From 80 hours to 160 hours, the interface level was almost constant due to accelerated gas generation. From 160 hours to 300 hours, the MFT volume expanded due to a rapid increase of the trapped gas volume. From 300 hours to 340 hours, the interface went down due to gas release from the MFT. After 340 hours, the interface became relatively stable. At the end of testing, the interface of Sample 14 was about 0.94 mm above the initial interface level. In Sample 13, the interface was relatively stable during the first 60 hours, then settled during the test.

Figure 8.32 shows the changes of the water void ratio during microbial activity. In Sample 13, the water void ratio decreased with time at slow rate. In Sample 14, the water void ratio slowly decreased during the first 80 hours, then, as biogas generation accelerated, the water void ratio rapidly decreased. After about 340 hours, with microbial activity diminishing, the water void ratio became relatively stable. In Sample 15, the water void ratio slowly decreased during the first 160 hours, then with intense microbial activity and biogas generation, rapidly decreased. After 550 hours, with microbial activity diminishing, the water void ratio became almost stable. At the end of testing, the water void ratios of Samples 13 to 15 were 4.04, 3.91 and 3.68, respectively.

Figure 8.33 shows the changes of the bulk density with time during microbial activity. The bulk density of Sample 13 slightly increased from 1.237 to 1.241g/mL due to slow gas generation. With the increases of trapped gas volume in Samples 14 and 15, the bulk densities decreased with time. When the trapped gas volume became stable, the bulk density showed less changes. At the end of

testing, the bulk densities of Samples 13 to 15 were 1.24 g/mL, 1.16 g/mL and 1.15 g/mL, respectively.

Figure 8.34 shows the changes of the degree of saturation, with time. The degree of saturation of each sample was closely related to the trapped gas volume in the MFT. At the end of testing, the degree of saturation of Sample 13 was about 99%. The values of the degree of saturation of Samples 14 and 15 slowly decreased during the first 100 hours, due to slow gas generation. Then, as gas generation accelerated, the values of the degree of saturation rapidly decreased with time. At the end of testing, the values of the degree of saturation of samples 14 and 15 were 91% and 88%, respectively.

Figures 8.35 to 8.37 show the volumetric changes (trapped gas volume, released gas volume and total gas volume at STP, and water drainage volume) of Samples 13 to 15, respectively. Gas was generated very slowly in Sample 13, and correspondingly, water was drained out of the MFT slowly. Water drainage volumes in Sample 14 were almost equal to the total gas volumes during the first 160 hours. After about 340 hours, with microbial activity diminishing, the water drainage volume from Sample 14 was almost stable. Water was drained out of Sample 15 at relatively slow rates during the first 160 hours, due to slow gas generation. As the gas generation accelerated, the water drainage rate increased. After about 550 hours, with biogas generation diminishing, the water drainage volume from Sample 15 became stable. Figure 8.38 shows water void ratio vs. total gas volume (at STP) in Samples 13 to 15 during microbial activity. Due to very slow gas generation, water drainage from Sample 13 was less affected by microbial activity (Sample 13 was similar to saturated soil). The plots of water void ratio vs. total gas volume of Samples 14 and 15 appear to be a single plot. This strongly supports the idea that during intense microbial activity, the water drainage from the MFT was controlled by biogas generation.

Figures 8.39 to 8.41 show the changes of the trapped gas volume and total MFT volume with time in Samples 13 to 15, respectively. The slow gas generation in Sample 13 had little effect on the MFT behavior. The sample was similar to saturated soil. During testing, the trapped gas volume increased very slowly and the total MFT volume slowly decreased. In Sample 14, the trapped gas volume slowly increased during the first 160 hours, and the total MFT volume was almost constant. Water was drained out of the MFT at a slow rate during this period. From 160 to 300 hours, both the total MFT volume and trapped gas volume rapidly increased with time, but the expansion of the global MFT volume lagged behind the increase of the trapped gas volume. As such, water was pushed out of the sample at rapid rates. In Sample 15, the trapped gas volume slowly increased with time during the first 160 hours, but the total MFT volume slightly decreased or stabilized. From 160 hours to 320 hours, the trapped gas volume rapidly increased with time, but the MFT volume expansion lagged far behind the increase of the trapped gas volume. As a result, part of the space required by trapped gas bubbles was obtained by pushing water out of the sample. After 320 hours, gas started to be released from Sample 15. The trapped gas volume slowly increased with time or stabilized, but the global MFT volume rapidly decreased, due to a structural collapse during gas bubble release. More water was rapidly drained out of Sample 15.

8.6.2 Excess Pore Pressure and Operative Stress

Figure 8.42 shows the changes of excess pore water pressure and operative stress at the bottom (E1) of Sample 13 during microbial activity. Due to very slow biogas generation, the total stress was relatively stable (the obvious fluctuations were likely due to the hydrostatic changes caused by water front movements in the plastic tube). During the first 24 hours, due to a rapid temperature increase, excess pore water pressure slightly increased, and operative stress slightly decreased. From 24 hours to the end of testing (660 hours), excess pore water

pressure slowly decreased from 0.201 kPa to 0.138 kPa, and operative stress slowly increased from 0 to 0.05 kPa.

Figures 8.43 and 8.44 show the changes of excess pore water pressure and operative stress at 1.45 cm elevation (E2) and 3.95 cm elevation (E3), respectively, above the bottom of Sample 13. Similar changes to those observed at E1 are shown.

Figure 8.45 shows the changes of excess pore water pressure and operative stress at the bottom (E1) of Sample 14. Due to a rapid increase of the trapped gas volume in the MFT, and water being partly pushed out from the test cell, total stress obviously decreased over the first 300 hours. When the trapped gas volume became stable (after 330 hours), the total stress was relatively stable. During the first 24 hours, due to a temperature increase, excess pore water pressure slightly increased and operative stress slightly decreased. From 24 hours to 80 hours, gas generation was relatively slow. Excess pore water pressure decreased from 0.198 kPa to 0.18 kPa, and operative stress increased from 0 to 0.013 kPa. It seems that the slow gas generation during this period had minor effects on the behaviour of the MFT, and that excess pore water pressure was dissipated very slowly, as in Sample 13. From 80 to 160 hours, biogas generation gradually accelerated, and the total stress decreased with time. Excess pore water pressure increased from 0.139 kPa to 0.168 kPa, and operative stress decreased from 0.013 kPa to –0.02 kPa. During this period, gas generation likely produced additional excess pore water pressure while excess pore water pressure was partly dissipated. From 160 hours to 300 hours, gas was generated very rapidly and all the gas bubbles were trapped in the MFT. The MFT volume was rapidly expanded, and water was drained out of the sample quickly. During this period, the total stress noticeably decreased. While excess pore water pressure decreased from 0.168 kPa to 0.046 kPa, operative stress was relatively stable. Both the total stress and pore water pressure decreased at almost the same rate during this period, so the operative stress was relatively stable. From 300 hours to 450 hours, gas was released from

the MFT, and total stress became relatively stable. Excess pore water pressure obviously decreased from 0.168 kPa to 0.046 kPa, and operative stress increased from –0.016 kPa to 0.044 kPa.

Figures 8.46 and 8.47 show the changes of excess pore water pressure and operative stress, respectively, at 1.45 cm elevation (E2) above the bottom of Sample 14. Figure 8.48 shows the changes of excess pore water pressure and operative stress at 3.95 cm elevation (E3) above the bottom of Sample 14. The changes at E2 and E3 were similar to those observed at E1.

Figures 8.49 and 8.50 show the changes of excess pore water pressure and operative stress, respectively, at the bottom (E1) of Sample 15. During the first 320 hours, the total stress obviously decreased due to the increase of the trapped gas volume in the MFT, and water being expelled out of the test cell. The changes of excess pore pressure and operative stress were not obvious during the rapid temperature increase. From 24 to 100 hours, gas was generated at slow rates, excess pore water pressure slowly decreased, and operative stress slowly increased. From 100 to 160 hours, biogas generation gradually accelerated and the trapped gas volume increased with time. Excess pore water pressure slightly increased, and operative stress decreased within this time frame. As was the case in Sample 14. From 160 to 320 hours, the trapped gas volume rapidly increased in the MFT, and the total stress noticeably decreased. There was rapid water drainage from the MFT during this period. Excess pore water pressure obviously decreased from 0.142 kPa to 0.089 kPa, but operative stress had only a slight increase. This was mainly due to a decrease in total stress. It was not appropriate to compare the operative stress changes, as the total stress was not constant. An obvious increase in operative stress would have been anticipated if the total stress were constant. This was proven by the subsequent period of microbial activity. From 320 hours to 550 hours, gas was intensely released from the MFT. The trapped gas volume and the total stress were relatively stable. During this period, excess pore water pressure obviously decreased from 0.089 kPa to 0.034 kPa, and

operative stress obviously increased from 0.016 kPa to 0.062 kPa. After 550 hours, with microbial activity diminishing, both excess pore water pressure and operative stress became stable, and water drainage from the MFT became very slow.

Figures 8.51 and 8.52 show the changes of excess pore water pressure and operative stress, respectively, at 1.45 cm elevation (E2) above the bottom of Sample 15. Figures 8.53 and 8.54 show the changes of excess pore water pressure and operative stress, respectively, at 3.95 cm elevation (E3) above the bottom of Sample 15. The changes in excess pore water pressure and operative stress at E2 and E3 were similar to those at E1.

Table 8.11 summarizes some parameters of Samples 13 to 15 at the end of the gas densification tests. Sample 15 had the lowest water void ratio and highest gas void ratio. After microbial activity, the total void ratio of Sample 15 was lower than the initial total void ratio.

8.6.3 Permeability Tests after Microbial Activity

After microbial activity diminished, the room temperature was lowered to 4^{o}C to inhibit microbial activity. Constant head permeability tests were conducted by applying upward gradients to Samples 13 to 15. Figure 8.55 shows the flow velocity vs. time in Tests 13 to 15. The inflow velocity was slightly larger than the outflow velocity for each sample. This is because part of the inflow water was used to fill voids (cracks) in the MFT. Table 8.12 summarizes the results of permeability Tests 13 to 15. The coefficient of permeability of Sample 15 was about three times that of Sample 13. With the increases of microbial activity and biogas generation, the coefficients of permeability increased.

8.6.4 Scanning Electric Microscopy (SEM) Analyses

MFT structural changes during microbial activity are an important factor affecting permeability and MFT densification. Observation of micro-structural changes can help to understand the mechanism of MFT densification during microbial activity. Scanning Electrical Micrograph (SEM) images were used to analyze the micro-structural changes of Samples 13 to 15 after microbial activity. The tests were conducted at the SEM Laboratory of the Department of Renewable Resources at the University of Alberta.

At the end of testing, a small copper tube was inserted into Samples 13 to 15 and nitrogen gas with a temperature of -70^{o}C was introduced into the tube to freeze the nearby MFT. After about five minutes, a cylindrical zone of about 1-2 cm was frozen around the tube. Because the freezing operation was conducted carefully, the MFT structure was well preserved. The frozen samples were used to analyze the structural properties of the MFT. The tests were conducted at the Scanning Electron Microscope Laboratory at the Department of Earth and Atmospheric Science, the University of Alberta. Cryo-electron Microscopy method (Al-Amoudi, A., et. al., 2004) was used during analysis.

Figure 8.56 shows a SEM image of Sample 13. Since no sodium acetate was added, microbial activity was weak. A typical dispersed structure was observed; the particles or particle domains (a group of particles with close face-face contacts) were parallel to each other with large spaces in between. This image reflects the loose MFT structure with high water content. The net repulsive force between the particles caused the meta-stable face-to-face arrangements (Craig, 1993).

Figure 8.57 shows a SEM photo of Sample 15 after microbial activity. With respect to Sample 13, more edge-to-face and edge-to-edge contacts were shown, and the structure became more flocculated and dense.

Figure 8.58 shows a large ellipsoidal gas bubble with a size of about 3 mm × 2 mm in Sample 14. A crack was observed on the wall of the large gas bubble.

Figure 8.59 shows the clay particle arrangements near the large crack in Sample 14. Some clay particle "domains" were cut off by the crack. On one side of the crack, the clay particles were re-oriented with faces parallel to the surrounding wall of the large gas bubble. The crack might have been caused by local stress concentration or tensile stress during gas bubble growth.

Figure 8.60 shows a thin membrane of clay on the sidewall of the large gas bubble. Within the membrane, the clay particles were re-oriented with faces parallel to the wall. It is likely that the clay particles surrounding the gas bubble were compressed and re-oriented during gas bubble formation.

Figures 8.61 and 8.62 show the clay particle (domain) distribution near the large gas bubble. In Figure 8.61, the particles or particle domains near the gas bubble were obviously disturbed and some of them were twisted. In Figure 8.62, some clay particles (domains) near the large gas bubble were cut off or re-oriented. Figure 8.63 shows the clay particle arrangements on the sidewall of the gas bubble. The clay particles were re-oriented with faces parallel to the sidewall.

From these images, some micro-structural properties of the MFT can be summarized as follows:

- After intense microbial activity and biogas generation, the structure of Sample 15 became denser and more aggregated than that of Sample 13.
- During microbial activity, some large gas bubbles were formed in Samples 14 and 15. Due to local stress concentration or tensile stress, cracks were formed near the large gas bubbles.

- Around each large gas bubble, a thin membrane of clay was formed. Within the membrane, the particles were re-oriented with faces parallel to the sidewall.
- Near the large gas bubbles, some soil particles (domains) were obviously disturbed. Some of them were re-oriented, cut off or twisted during gas bubble formation.
- Intense microbial activity and biogas generation significantly changed the MFT structure. During intense microbial activity, the meta-stable dispersed structure was disturbed and partly collapsed. After intense microbial activity and gas generation, the new structure became denser and more aggregated.

8.7 Discussion of Tests 13, 14, and 15

8.7.1 Volume Change

Due to the fact that different amounts of sodium acetate were added to each of Samples 13 to 15, gas generation rates were significantly different. Microbial activity in Sample 15 was much more intense than that in Sample 13. Gas generation volumes in Samples 14 and 15 were obviously larger than those in Samples 2 and 3, respectively. This might be related to two factors: firstly, during self-weight consolidation tests of Samples 2 and 3, part of the sodium acetate was depleted or degraded; secondly, part of the sodium acetate in Samples 2 and 3 migrated out of the MFT along with water which drained during the consolidation.

In Sample 13, gas was slowly generated at an almost constant rate. In Samples 14 and 15, gas generation rates were more variable during microbial activity. During the early period (about 100 hours) gas generation rates in Samples 14 and 15 were slow. Gas generation was then accelerated in the two samples. In Samples 14 and 15, microbial activity started to diminish after 340 hours and 550 hours, respectively. Small amounts of gas were released from Sample 14, but large

amounts (up to 70% the gas generation volume) were released from Sample 15. There was rapid gas generation and intense gas release in Sample 15. At the end of testing, Sample 15 had the highest gas content among the three samples. Although a large amount of gas was trapped in Sample 15, the total MFT volume was smaller than the MFT volume before microbial activity. This indicates that a large amount of water was drained out of the sample.

The process of rapid water drainage in Samples 14 and 15 can be divided into two periods: (1) the period before gas release, about 300 hours in Sample 14 and about 320 hours in Sample 15; (2) the period during intense gas release, from 300 to 340 hours in Sample 14 and from 320 to 550 hours in Sample 15. During the first period, the trapped gas volume rapidly increased; during the second period, the trapped gas volume was stable or had slightly decreased. For Sample 15, both periods played important roles in rapid water drainage, but for Sample 14, the first period dominated the water drainage process.

With the increases of microbial activity and biogas generation in Samples 13 to 15, came an increase in water drainage volumes. For each sample, water drainage rates were related to gas generation rates. In Sample 15, gas was generated slowly during the first 160 hours, and correspondingly, water was drained out of the MFT slowly. From 160 to 550 hours, with gas generation accelerating, water was rapidly drained out. After 550 hours, with microbial activity diminishing, water drainage from the MFT became very slow. In Sample 13, the degree of saturation was greater than 99% at the end of testing. The behavior of this sample was similar to that of a saturated soil; water was drained out slowly during the test.

Due to very slow gas generation, the water drainage volume in Sample 13 was almost equal to the total MFT volume decrease. In Samples 14 and 15, trapped gas volumes increased at relatively slow rates during the first 160 hours, and the MFT volumes were relatively stable. During this period water drainage volumes were close to trapped gas volumes. From 160 to 320 hours (160 to 300 hours in

Sample 14), both the trapped gas volume and total MFT volume in Sample 15 increased, but the increase of the trapped gas volume was more rapid than the expansion of the MFT volume. Water was rapidly pushed out of the sample. From 320 to 550 hours, gas was intensely released from Sample 15, the trapped gas volume was relatively stable, and the total MFT volume rapidly decreased with time. The initial meta-stable structure rapidly collapsed due to gas bubbles escaping and to intense disturbances. After 550 hours, both the trapped gas volume and total MFT volume were stable, and water drainage from the MFT became very slow.

Figure 8.64 compares the effects of biogas generation on MFT water drainage between Samples 1 to 3 and Samples 13 to 15. The impact of biogas generation on Samples 13 to 15 was more significant than that on Samples 1 to 3. Due to pre-consolidation of Samples 1 to 3 before microbial activity initiation, the MFT structure was at more stable and denser condition relative to Samples 13 to 15, in which structural collapse was less significant than Samples 1 to 3 during biogas activity.

8.7.2 Excess Pore Water Pressure and Operative Stress

Since microbial activity began without pre-consolidation, there existed positive excess pore water pressures in Samples 13 to 15. The initial effective stress was close to zero. Due to very slow gas generation and weak microbial activity, Sample 13 was similar to a saturated soil during testing. While the total MFT volume decreased with time, excess pore water pressure slowly dissipated, and operative stress slowly increased. Water was drained out slowly.

Due to variable gas generation rates, gas bubble release, and total stress changes during microbial activity, the changes of excess pore water pressure and operative stress in Samples 14 and 15 were much more complex than those in Sample 13.

In Sample 14, gas generation rates were slow from 24 to 80 hours, and the degree of saturation was greater than 99%. The sample behaved like a saturated soil. Excess pore water pressure slowly decreased and operative stress slowly increased with time. Correspondingly, water was drained out slowly. From 80 to 160 hours, gas generation was gradually accelerated. The trapped gas volume increased rapidly, but the total MFT volume was almost constant. Gas bubble growth had to overcome the structural resistance. While excess pore water pressure was partly dissipated, extra excess pore water pressure was likely produced. There was accelerated water drainage during the period from 80 to 160 hours. From 160 to 300 hours, as gas was rapidly generated, excess pore water pressure decreased rapidly, but the operative stress was almost constant (or very slowly increased). There was rapid water drainage during this period. Due to a rapid increase of the trapped gas volume, part of the water volume in the MFT was occupied by gas bubbles. This led to an obvious decrease in the total stress during rapid gas generation. An observable operative stress increase would be anticipated if the total stress were stable, that is, if all the water were kept in test cell, and the hydrostatic level increased with time. Sills et al. (2001) reported obvious operative stress increases during rapid gas generation in gas column tests in which the water level continuously rose and total stress at the bottom of the column was constant.

From 300 to 450 hours, a small amount of gas was released from Sample 14, and the trapped gas volume slightly decreased. Total stress was relatively stable. Excess pore water pressure rapidly decreased, and operative stress obviously increased.

In Sample 15, the changes of excess pore water pressure and operative stress before gas release (the first 320 hours) were similar to those in Sample 14. From 320 to 550 hours, gas was intensely released from Sample 15. There were rapid excess pore water pressure decreases, obvious operative stress increases, and rapid water drainage during this period.

8.7.3 Structure Change and Permeability

The structural changes of Samples 13 to 15 are shown in Appendix I. In Sample 13, some occluded gas bubbles in spherical or ellipsoidal shapes were observed at the upper part of the sample. No obvious cracks were observed. In Samples 14 and 15, during the early period (about five-seven days) gas generation was slow. Most of the gas bubbles were small and in a spherical shape. With gas generation accelerating, some cracks and ellipsoidal gas bubbles appeared at the upper parts of the samples.

Both Sample 15 and Sample 3 had intense microbial activity and rapid gas generation, however, the macro-structure changes in Sample 3 were more significant than those in Sample 15. Relative to Sample 15, more interconnected large fractures were formed in Sample 3. This might be attributed to different structural strengths between Sample 3 and Sample 15. After self-weight consolidation, Sample 3 became more similar to a "soil." Sample 15, in contrast, was more similar to a "slurry" which was not "stiff" enough to form large fractures. During rapid gas generation and release, the structure of Sample 15 evidently collapsed and became dense.

With the increases of microbial activity and biogas generation in Samples 13 to 15, the coefficients of permeability increased. Although the water void ratio of Sample 15 was smaller than that of Sample 13, the coefficient of permeability of Sample 15 was higher than that of Sample 13 at the end of testing. This indicates that after intense microbial activity, the coefficients of permeability in Samples 14 and 15 were controlled by structural changes (cracks, fractures and gas release holes), not only by the water void ratio.

By comparing the results of permeability tests of Samples 2 and 3 with those of Samples 14 and 15, it was concluded that after microbial activity, the increases of the coefficients of permeability of Samples 2 and 3 were more obvious than those

of Samples 14 and 15. This is because the structural changes in Samples 2 and 3 were more significant than those in Samples 14 and 15 during microbial activity.

8.8 Results for Tests 16©, 17©, and 18©

Tests 16© to 18© were the duplicating tests of Samples 13 to 15, respectively. They were used to sacrificially get samples for chemical and microbiological measurements during microbial activity. Different amounts of sodium acetate, 0 g, 0.6 g and 1.75 g per liter MFT, were added to Samples 16© to 18©, respectively. Applying the lessons learned from chemical sampling Tests 7© to 9©, a larger height of 11 cm was used for Samples 16© to 18©. During testing, the MFT was under atmospheric pressure plus about 1.0 m water head.

A plastic piston syringe connected with a hollow copper tube of small diameter was used as the sampler. When sampling, the small copper tube was inserted into the cell through a valve mounted at 1.45 cm elevation above the bottom of the sample. By pulling back the piston of the syringe, the MFT slurry was sucked into the sampler. The samples were then retrieved into glass jars and sealed.

Chemical measurements were performed at Syncrude Edmonton Research Centre using standard industry methods (Syncrude, 1995; Holowenko, 2000). The analyses included pH, EC, alkalinity, cations, anions, and selected trace elements. In this research, some parameters, including pH, EC, and the concentrations of some ions (Na^+, K^+, Ca^{2+}, Mg^{2+}, SO_4^{2-}, Cl^-, HCO_3^-), were analyzed. The detailed chemical changes are shown in Appendix J.

During microbial activity, acetate concentrations decreased with time and were completely depleted at the end of testing. The pH values slightly increased from 7.4~7.5 at the start of testing to 7.7~7.8 by the end of microbial activity. SO_4^{2-} concentrations decreased from 46 .3 mg/L to below 10 mg/L after microbial activity. Cl^- concentrations were relatively stable, HCO_3^- concentrations decreased

with time. During microbial activity, the concentrations of the cations (Na^+, K^+, Ca^{2+}, Mg^{2+}) decreased with time. The values of Electrical Conductivity also decreased with time in three samples. The chemical changes in Test 18© were more obvious than those in Tests 16© and 17©.

8.8.1 MPNs of Methanogens and Sulfate-Reducing Bacteria (SRB)

Methanogens and Sulfate-reducing Bacteria (SRB) are two important microorganisms active in the MLSB (Sobolewski, 1992; Fedorak et al., 2002). They compete with each other for energy sources. For a given substrate, SRB obtain more energy than do methanogens, so they out-compete the latter for the substrate if sulfate is abundant (Fedorak et al., 2002). It has been found that methanogenesis at the MLSB became significant only after the sulfate concentrations dropped (Holowenko et al., 2000).

During the tests, samples were obtained for chemical and microbiological measurements. The sampling methods and device have been described in Section 7.7. Small amounts (about 5 mL) of the samples in the plastic syringe were retrieved into glass tubes for enumerations of methanogens and SRB. These glass tubes were flushed with nitrogen gas to create an anaerobic environment prior to sampling. The microbiological tests were performed at Dr. Fedorak's Laboratory, Department of Biological Sciences at the University of Alberta. Microbiological enumeration tests were performed using the standard five-tube Most Probable Number (MPN) method, with serial 10-fold dilutions of the MFT samples **(**Fedorak et al., 2002). Holowenko et al. (2000**)** have described this method in detail.

During the test, three samples were obtained at different times from each sample. The first sampling was conducted at 4^oC before microbial activity was initiated. The second sampling was conducted on the eighth day of microbial activity at 24^oC temperature. The third sampling was conducted at the end of testing at 4^oC.

The detailed results of the MPN tests are shown in Appendix J. During the tests, the methanogen MPN values of Samples 16© to 18© ranged from 10^2 to 10^3 MPN/mL, and the SRB MPN values ranged from 10^4 to 10^5 MPN/mL. There were no significant changes in both MPN values during microbial activity. Some fluctuations were probably due to material heterogeneity, sampling, or testing errors.

8.8.2 Gas Chromatography (GC) Analyses

The gas released from the MFT might be a contaminant to the atmosphere, and could also be an indicator of microbial activity. According to Holowenko et al. (2000), about 60-80% of the released gas across the water surface of the tailings pond is methane. This indicates the intense methanogen activity in the MFT. During gas MFT densification tests, the released gas in the headspace was collected and analyzed by Gas Chromatography (GC). These tests were conducted in the Environmental Engineering Laboratory at the University of Alberta. Luo (2004) has given a detailed description about the test mechanism, equipment, operation and calibration used.

A Varian CP-2003 portable Micro-GC with two channels of A and B was used for GC analyses of the released gas. Channel A was suitable for measuring H_2, O_2, N_2, and CH_4, and Channel B was suitable for measuring CH_4, CO_2, C_2H_4, and H_2S (Luo, 2004). During GC tests, He gas was used as carrier gas. For each gas sample, three GC tests were conducted. A Cole-Parmer 01409-11 Tedlar bag was used to collect gas from the top of the released gas cylinder. Before sampling gas from the headspace, the Tedlar bag was flushed with nitrogen gas. During the GC test, the Tedlar bag was directly connected to the GC sampling port. An internal sampling pump in the Micro-GC instrument automatically retrieved the gas samples. The sample injection time was 40 ms (Luo, 2004).

Table 9.13 shows the percentages of some major gas components in the headspaces of Cells 17© and 18©. In Cell 18©, the methane accounted for more than 80% of the released gas in the headspace. This indicates that methanogenesis was the dominant microbial activity during the test. Trace amounts of O_2 (0.07%) found likely came from the atmosphere during sampling or GC testing. Small amounts of CO_2 (1.24%) were detected. In the Tedlar bag of Cell 17©, N_2 was the major gas, and the measured O_2 gas content was 11.5%. Since the released gas volume in headspace of Cell 17© and the volume of methane gas collected in Tedlar bag were small, the results of the GC analyses were greatly affected by environmental gases (gases in the air or nitrogen gas when flushing the Tedlar bag). Some gases such as H_2S were not detected by the equipment. It's likely that the concentrations of these gases were relatively small and the device was not sensitive enough to detect them.

8.9 Summary

Eighteen gas MFT densification tests and nine chemical sampling tests were carried out within 14 months. The MFT densification properties were studied under different conditions, such as different stress histories (normally consolidated Samples 1 to 6 and 19 to 24; under-consolidated Samples 13 to 15 and over-consolidated Samples 10 to 12), different pressures (0 and 60 kPa air pressures) and different microbial activities (0, 0.6 and 1.75 g sodium acetate added per liter MFT). During the densification tests, various parameters were measured and structural changes were observed. This section summarizes the results of Tests 10 to 15 and 16©-18©.

Tests 10-12

1. Gas generation volumes in Samples 11 and 12 were smaller than those in Samples 2 and 3, respectively. This was likely because part of the sodium

acetate had either depleted or migrated out of the MFT, along with water drained during long-term consolidation.

2. Due to the existence of negative excess pore water pressures after unloading Samples 10-12, water flowed back into the MFT. With the increases of microbial activity, more water flowed back. For each sample, water volume rapidly increased during rapid gas generation.
3. During rapid gas generation, MFT volume expansions were more rapid than trapped gas volume increases. As a result, water rapidly flowed back into the MFT to fill the spaces. Thus, rapid gas generation was seen to accelerate MFT expansion.
4. With water flowing back into the MFT, excess pore water pressures in Samples 10-12 increased and operative stresses decreased with time. But excess pore water pressure increases in Sample 10 were more obvious than those in Sample 12. This was attributed to a total stress decrease and rapid structural dilation in sample 12 during rapid gas generation.
5. With the increases of microbial activity in Samples 10-12, macro-structural changes became obvious, and the coefficients of permeability slightly increased. At the end of testing, the coefficient of permeability of Sample 12 was about twice that of Sample 10. This made water flow more easily back into the MFT.

Tests 13-15 and 16©-18©

1. With the increases of microbial activity and gas generation in Samples 13-15, water drainage volumes increased. For each sample, water drainage rates were related to gas generation rates.
2. In Samples 14 and 15, rapid water drainage occurred during two periods: before and during intense gas release. Before gas release, the trapped gas volume increased rapidly. MFT expansion lagged behind trapped gas volume increases, and as such, water was rapidly pushed out. During intense gas

release, the trapped gas volume was relatively stable, but the total MFT volume rapidly decreased due to rapid structural collapse.

3. Due to variable gas generation rates, total stress changes, and gas bubble release, the changes of excess pore water pressure and operative stress in Samples 14-15 were complex. During accelerated gas generation, excess pore water pressures slightly increased, and operative stresses slightly decreased in Samples 14 and 15. During this period, extra excess pore pressures were likely produced. Throughout the period of rapid gas generation in Samples 14 and 15, excess pore water pressures obviously decreased over time, while operative stresses increased very slowly due to MFT dilation and total stress decreases. In Sample 15, excess pore water pressure rapidly decreased and operative stress obviously increased during the phase of intense gas release.
4. With the increases of microbial activity in Samples 13-15, macro-structural changes became more visible. A SEM photo showed that Sample 13 had a typical dispersed structure which was less flocculated than that of Sample 15.
5. Around the large gas bubbles, the clay particle domains were visibly re-oriented or disturbed. Cracks were observed near the large gas bubbles. Gas bubble formation and migration was seen to significantly change MFT structure.
6. With the increases of microbial activity in Samples 13-15, coefficients of permeability increased. The coefficients of permeability in Samples 1-3 and Samples 13-15 were affected by structural changes, not just by the water void ratio.
7. GC analysis results show that the major component of the released gas was methane (up to 80% in Test 18). A small amount of CO_2 gas was also detected in the released gas.
8. During microbial activity, acetate concentration was depleted, sulfate concentration decreased with time, and the concentrations of the cations (Na^+, K^+, Ca^{2+}, Mg^{2+}) decreased with time. The chemical changes in Test 18© were more obvious than those in Tests 16© and 17©.

9. There were no obvious changes in the MPNs of either methanogens or SRB in Samples 16©-18© during microbial activity.

Table 8-1 Some Parameters of Samples 10-12 before Consolidation

Solids Content (%)	Fines/(fines + water) (%)	Void Ratio (e)	Density (g/ml)	Water Content (%)	Bitumen Content (%)
35.1	32.6	4.4	1.257	184.9	4.29

Table 8-2 Summary of Some Initial Information of Samples 10-12

Test No	Total Mass (g)	Solids Mass (g)	Water Mass (g)	Total Volume (ml)	Solids Volume (ml)	Height (cm)	Sodium Acetate (g/L MFT)
10	1726.1	605.9	1120.3	1373	252.7	7.63	0
11	1682.1	590.4	1091.7	1338	246.3	7.43	0.6
12	1702.3	597.5	1104.8	1353.2	248.4	7.59	1.75

Table 8-3 Some Initial Parameters of Samples 13-15

Solids Content (%)	Fines/(fines + water) (%)	Void Ratio (e)	Density (g/ml)	Water Content (%)	Bitumen Content (%)
34.5	32.1	4.3	1.237	189.9	4.29

Table 8-4 Summary of Some Initial Information of Samples 13-15

Test No	Total Mass (g)	Solids Mass (g)	Water Mass (g)	Total Volume (ml)	Solids Volume (ml)	Height (cm)	Sodium Acetate (g/L MFT)
13	1844.9	635.4	1209.5	1491.4	281.9	8.2	0
14	1884.9	652.4	1232.5	1523.8	291.2	8.2	0.6
15	1872.4	646.4	1226	1513.7	287.6	8.3	1.75

Table 8-5 Some Parameters of Samples 10-12 after 0.5 kPa Consolidation

Test No	Sample Height (cm)	Density (g/ml)	Void Ratio (e)	Solids Content (%)
10	5.3	1.37	2.76	46.5
11	5.2	1.37	2.77	46.4
12	5.3	1.37	2.80	46.3

Table 8-6 Some Parameters of Samples 10-12 after 1.0 kPa Consolidation

Test No	Sample Height (cm)	Density (g/ml)	Void Ratio (e)	Solids Content (%)
10	4.93	1.399	2.5	48.95
11	4.8	1.399	2.51	48.89
12	4.96	1.401	2.51	48.83

Table 8-7 Dissolved Gas Volumes in Samples 10-12

Test No	10	11	12
Dissolved Methane Gas (10^{-3} mol)	0.938	0.902	0.917
Equivalent Vol. at STP (ml)	22.9	22.1	22.4

Table 8-8 Some Parameters of Samples 10-12 after Microbial Activity

Test NO	Solids Content (%)	Density (g/ml)	Water Void Ratio	Gas Void Ratio	Total Void Ratio	Degree of Saturation (%)
10	47.9	1.372	2.605	0.04	2.65	98.5
11	47.6	1.349	2.64	0.095	2.74	96.5
12	46.5	1.279	2.76	0.28	3.03	90.8

Table 8-9 Results of Permeability Tests 10-12 after Microbial Activity

Test No.	10	11	12
Gradient	0.273	0.293	0.256
Average Flow Velocity (10^{-9} m/s)	0.665	1.0	1.312
Coefficient of permeability (10^{-9} m/s)	2.436	3.413	5.125

Table 8-10 Dissolved Gas Volumes in Samples 13-15

Test No	13	14	15
Dissolved Methane Gas (10^{-3} mol)	1.787	1.795	1.8
Equivalent Vol. at STP (ml)	43.7	43.9	44

Table 8-11 Some Parameters of Samples 13-15 after Microbial Activity

Test NO	Solids Content (%)	Density (g/ml)	Water Void Ratio	Gas Void Ratio	Total Void Ratio	Degree of Saturation (%)
13	35.8	1.241	4.04	0.031	4.07	99.2
14	36.4	1.161	3.91	0.38	4.29	91.1
15	37.9	1.147	3.68	0.48	4.16	88.5

Table 8-12 Results of Permeability Tests 13-15 after Microbial Activity

Test No.	13	14	15
Gradient	0.166	0.163	0.166
Average Flow Velocity (10^{-9} m/s)	1.21	2.25	3.26
Coefficient of permeability (10^{-9} m/s)	7.29	13.8	19.64

Table 8-13 GC Analysis Results of the Released Gas from Tests 17© and 18©

Test NO.	CH4 (%)	N_2 (%)	O_2 (%)	CO_2 (%)
17©	23.4	66.8	11.5	0.17
18©	80.6	2.22	0.07	1.24

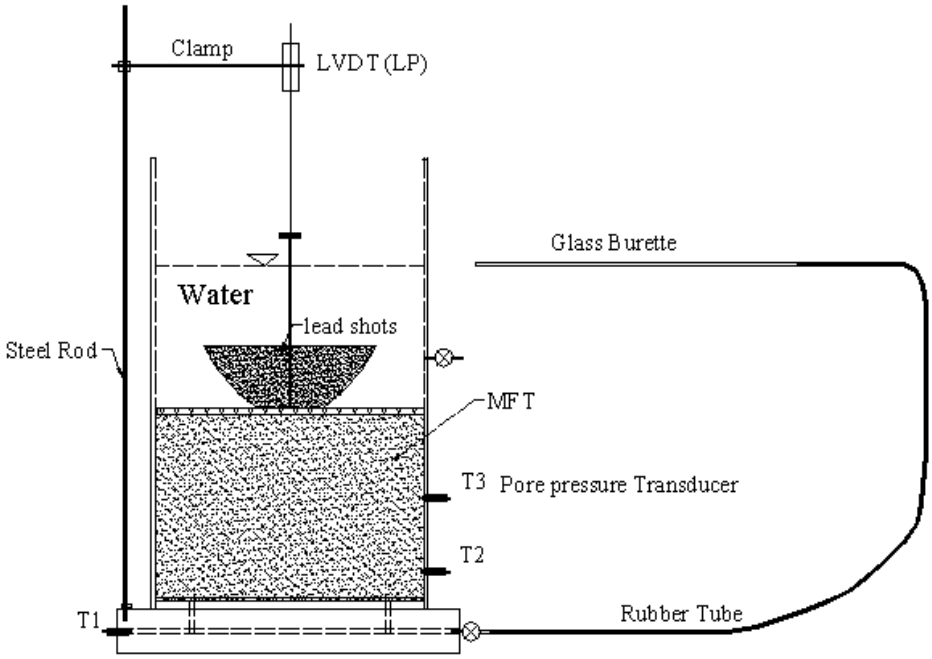

Figure 8-1 Schematic of Consolidation Tests 10-12

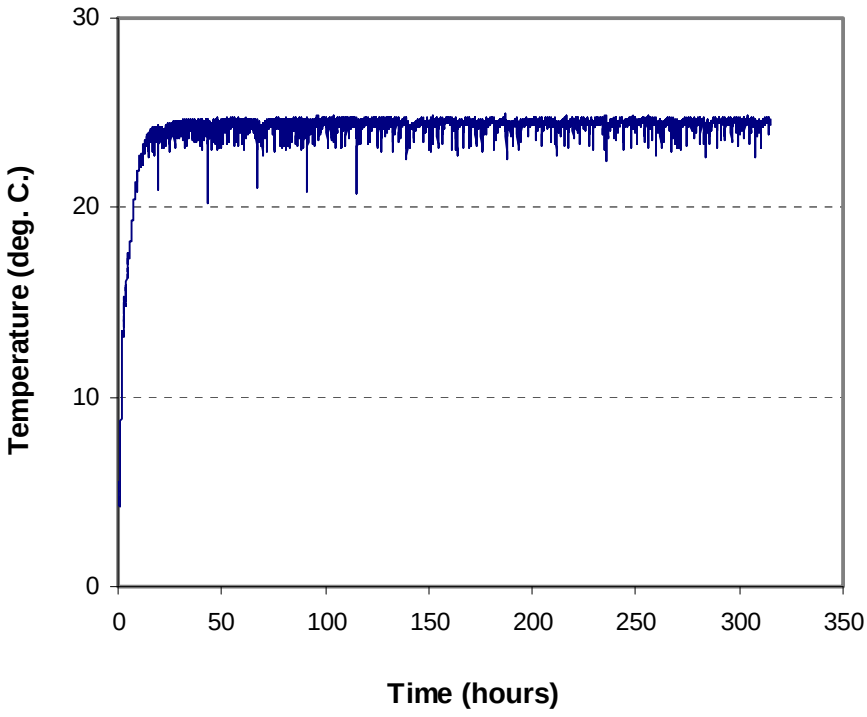

Figure 8-2 Room Temperature Changes during Gas Densification Tests 10-12

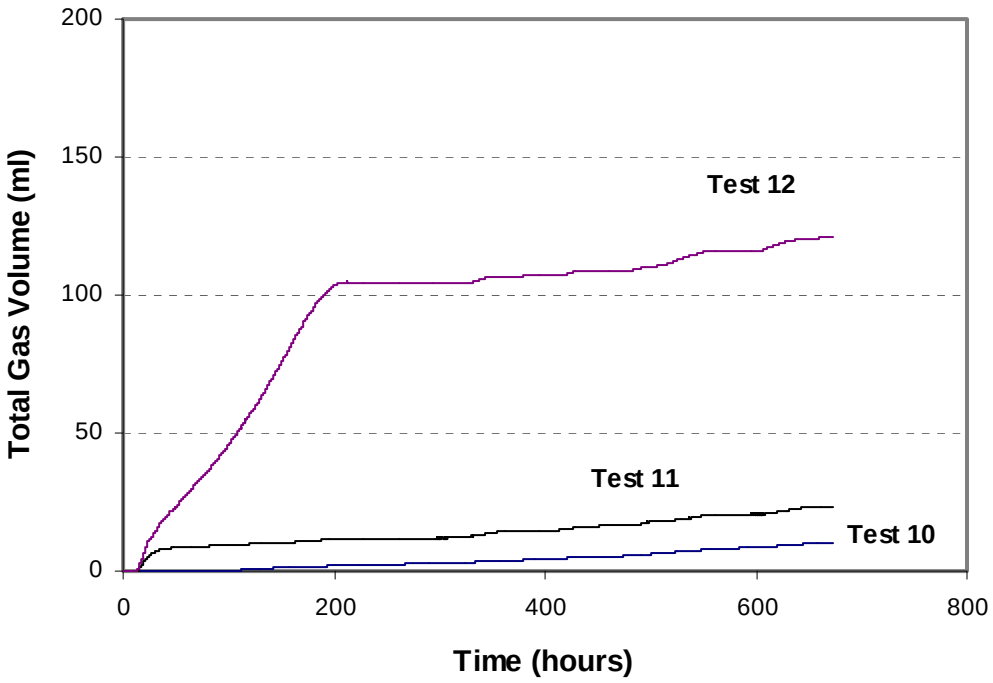

Figure 8-3 Total Gas Volume Changes (at STP) in Samples 10-12

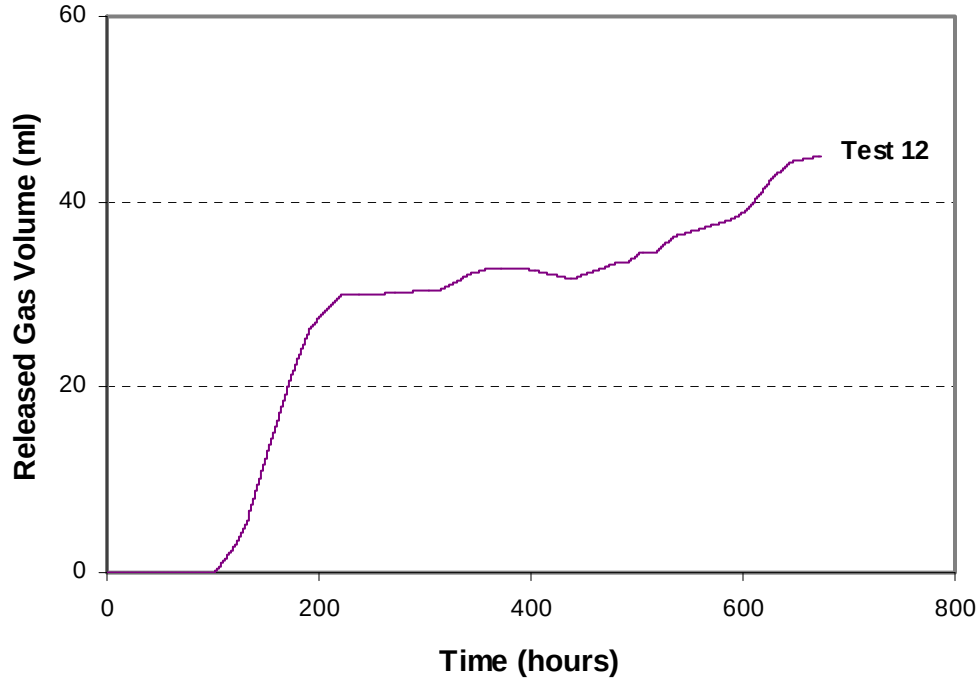

Figure 8-4 Released Gas Volumes (at STP) in Sample 12 during Microbial Activity

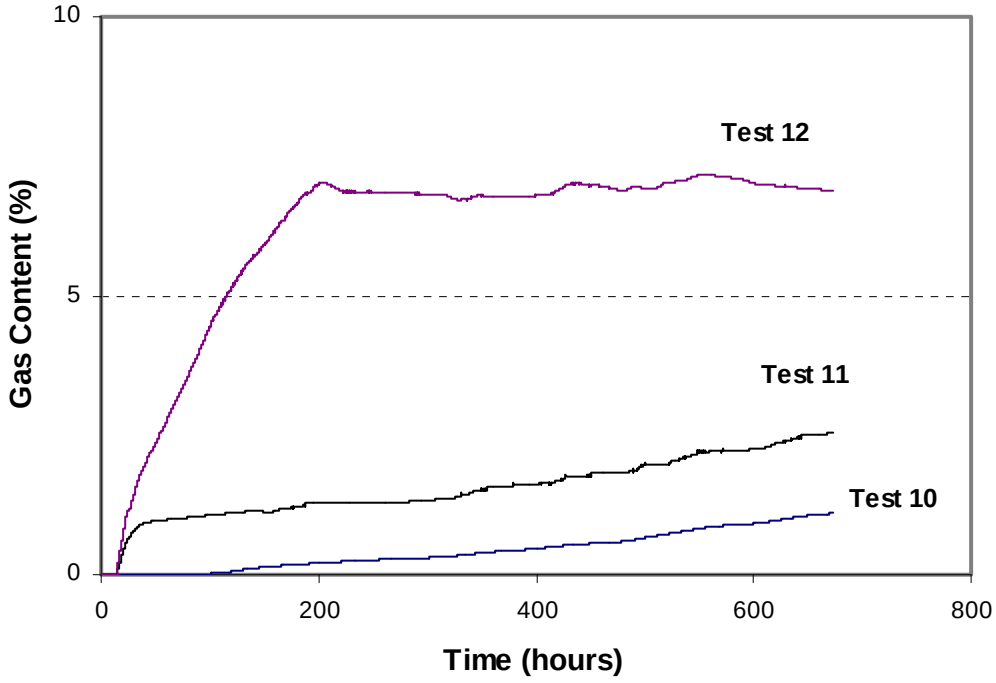

Figure 8-5 Gas Contents in Samples 10-12 during Microbial Activity

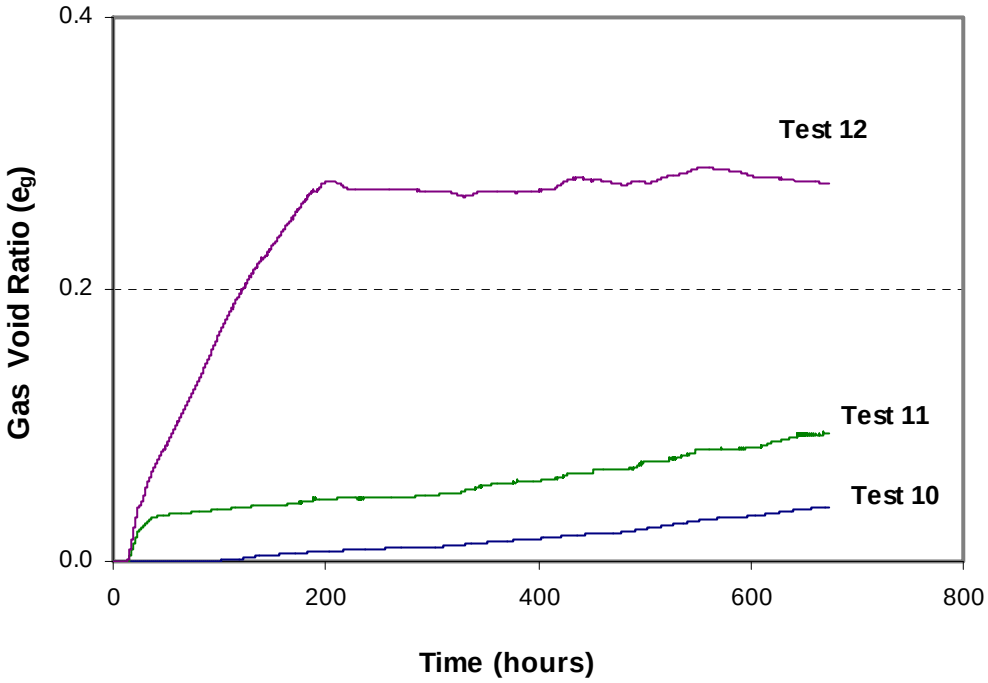

Figure 8-6 Gas Void Ratios in Samples 10-12 during Microbial Activity

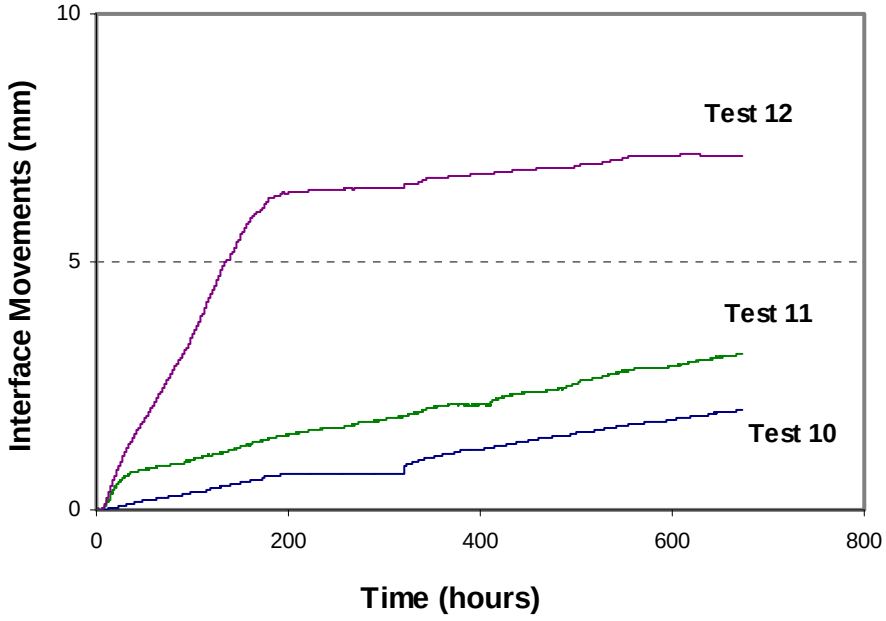

Figure 8-7 Interface Movements in Sample 10-12 during Microbial Activity

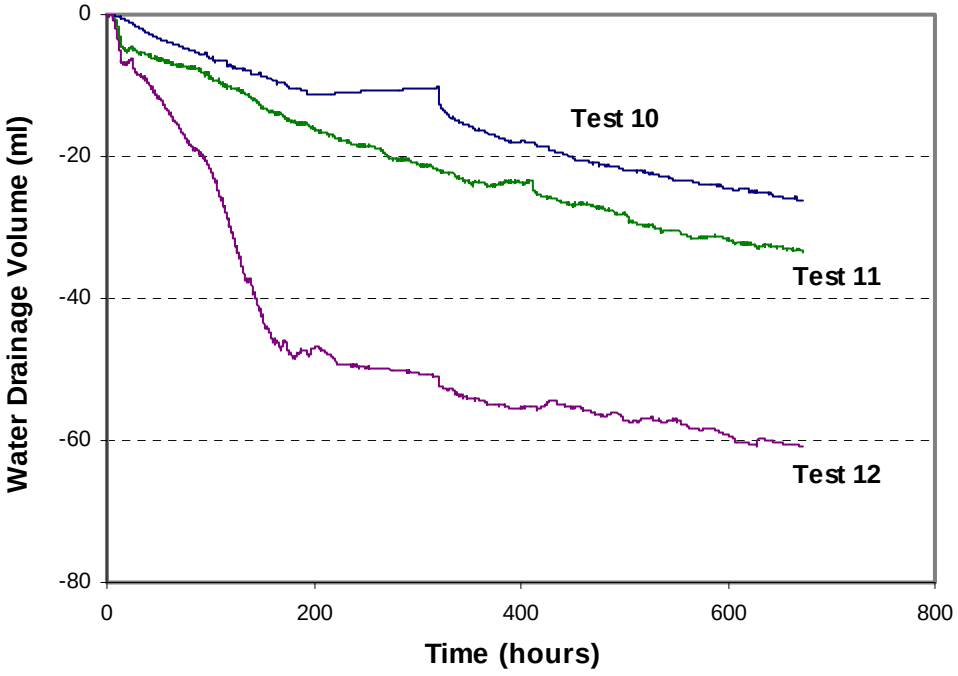

Figure 8-8 Water Drainage Volumes in Samples 10-12 during Microbial Activity

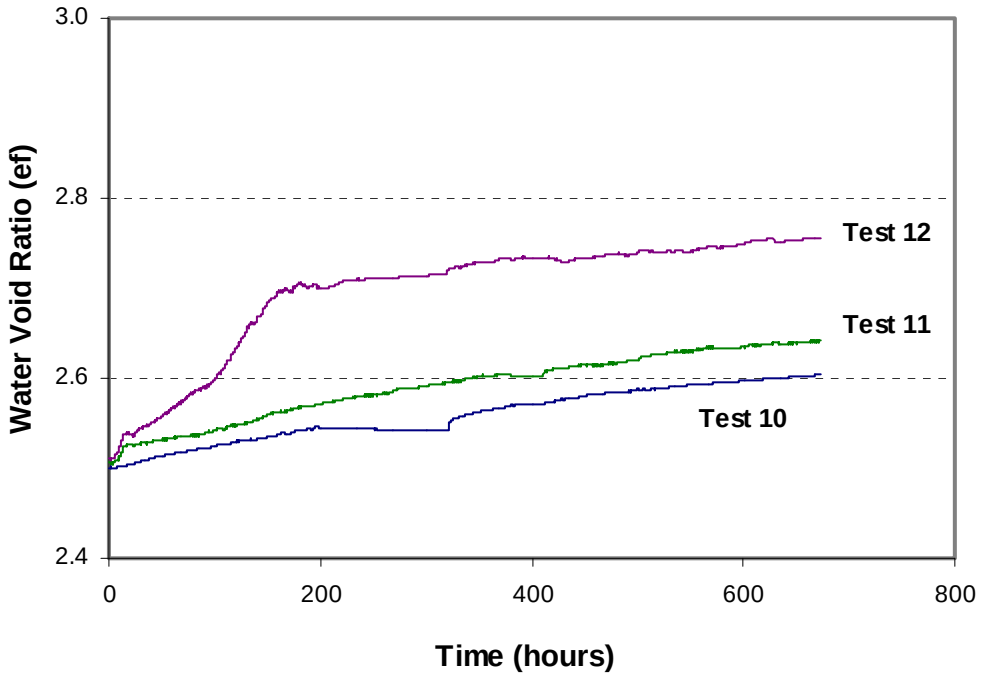

Figure 8-9 Water Void Ratio Changes in Samples 10-12 during Microbial Activity

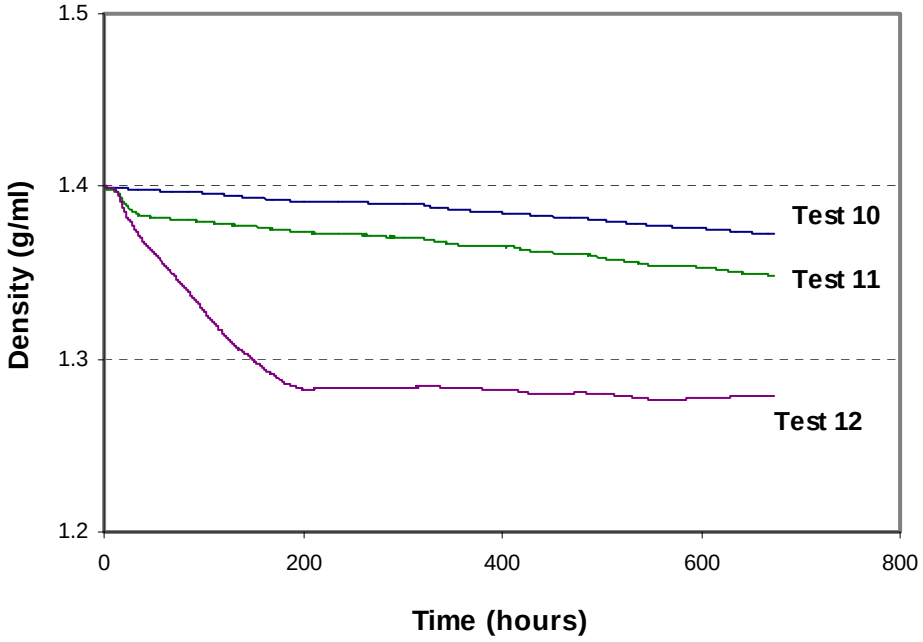

Figure 8-10 Bulk Density Changes of Samples 10-12 during Microbial Activity

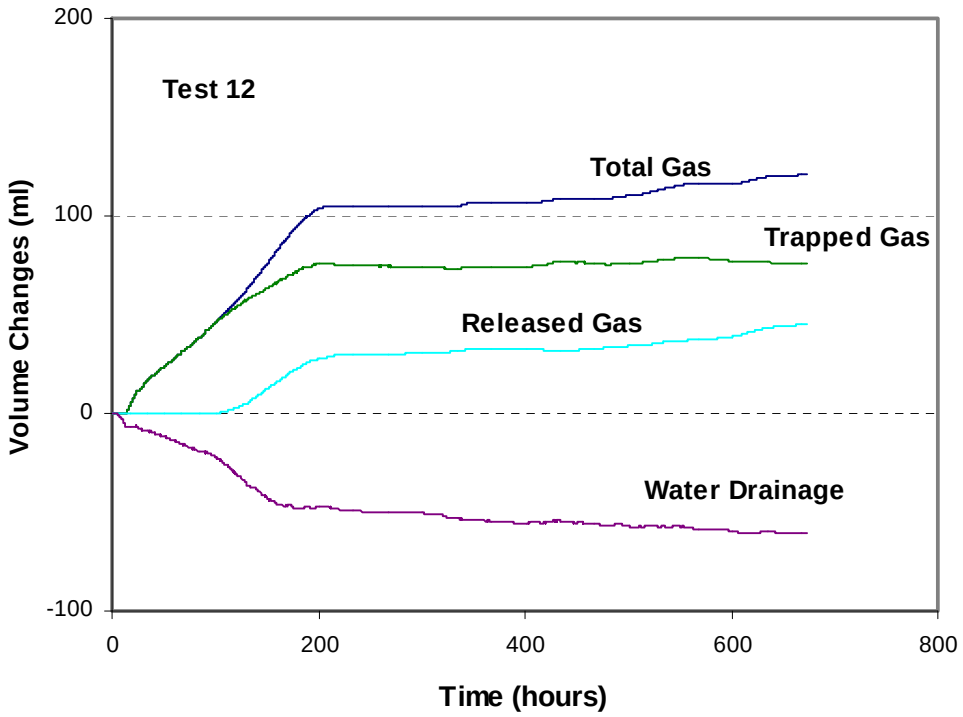

Figure 8-11 Volumetric Changes in Sample 12 during Microbial Activity

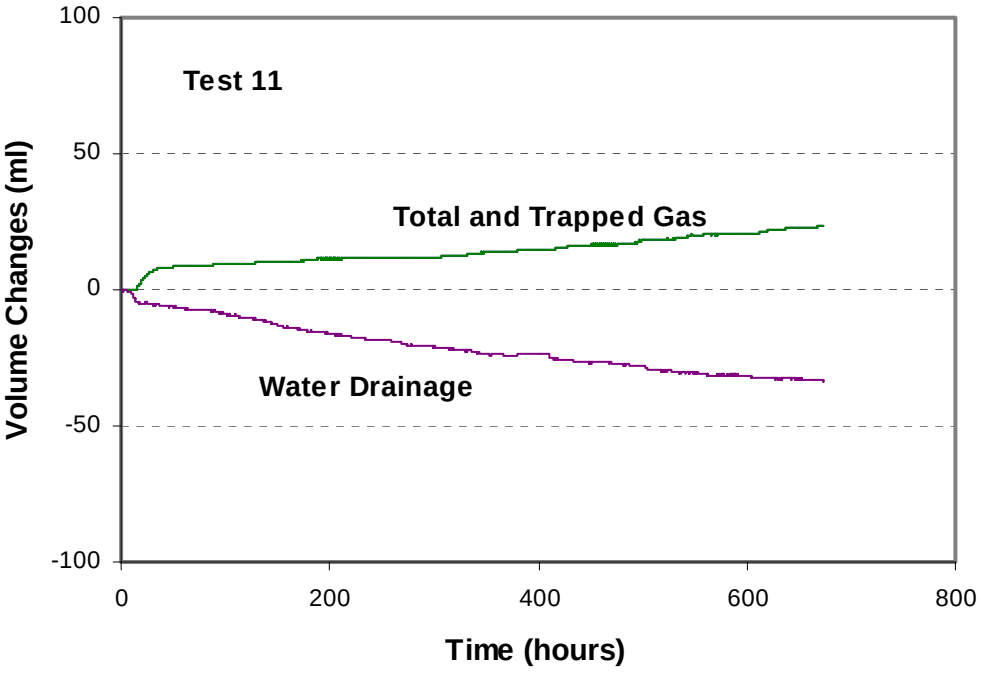

Figure 8-12 Volumetric Changes in Sample 11 during Microbial Activity

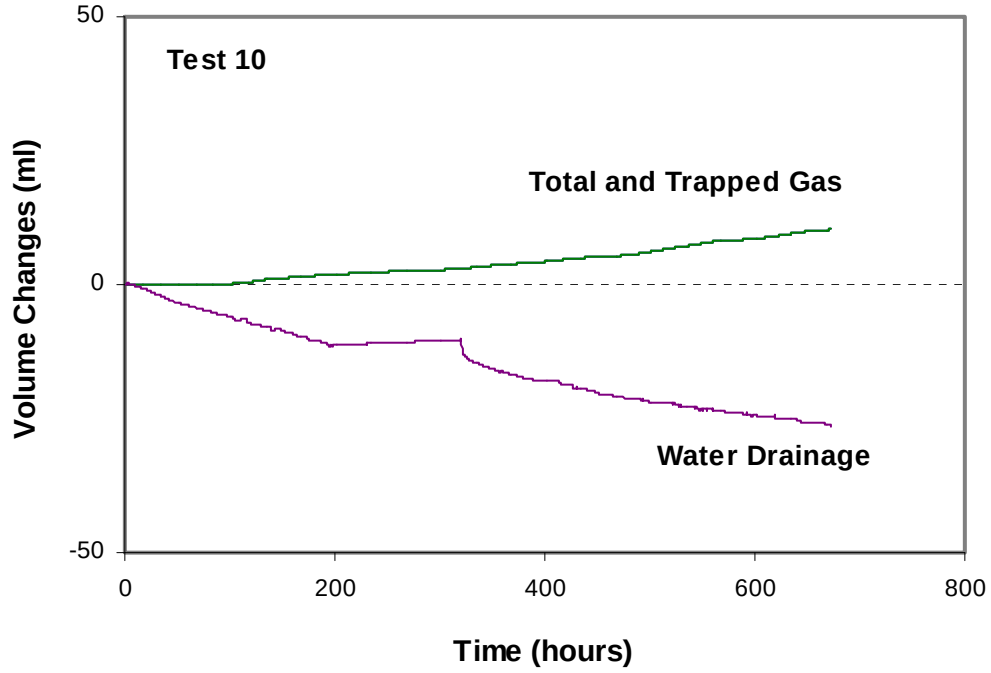

Figure 8-13 Volumetric Changes in Sample 10 during Microbial Activity

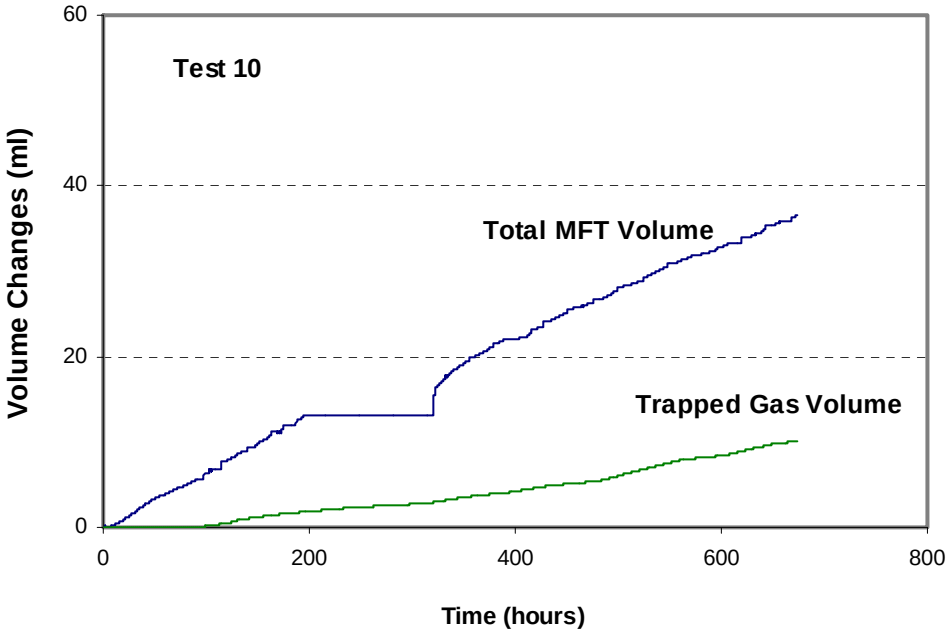

Figure 8-14 Changes in Trapped Gas Volume and Total MFT Volume in Sample 10

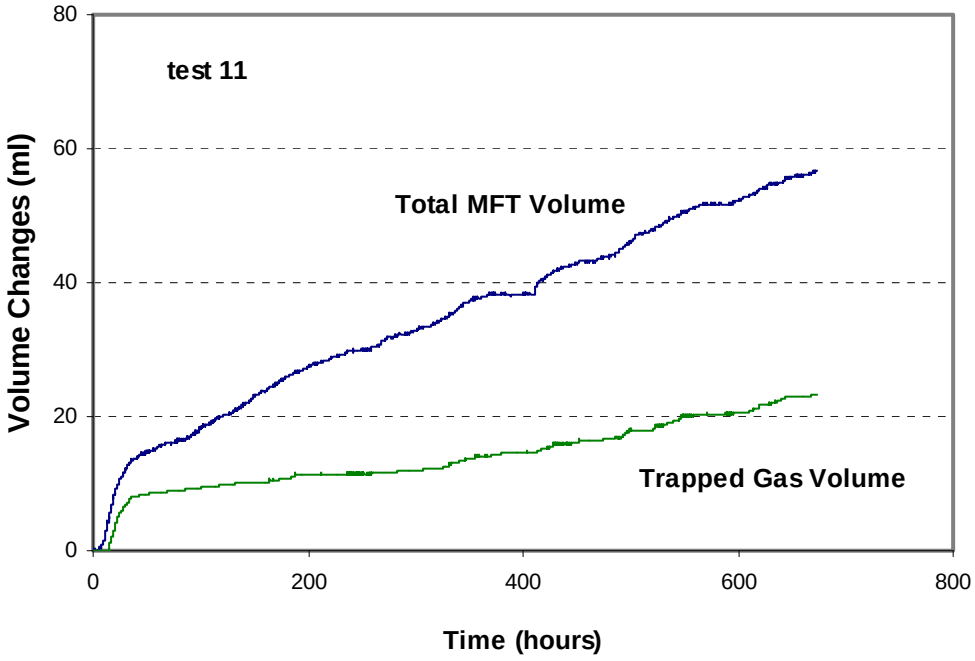

Figure 8-15 Changes in Trapped Gas Volume and Total MFT Volume in Sample 11

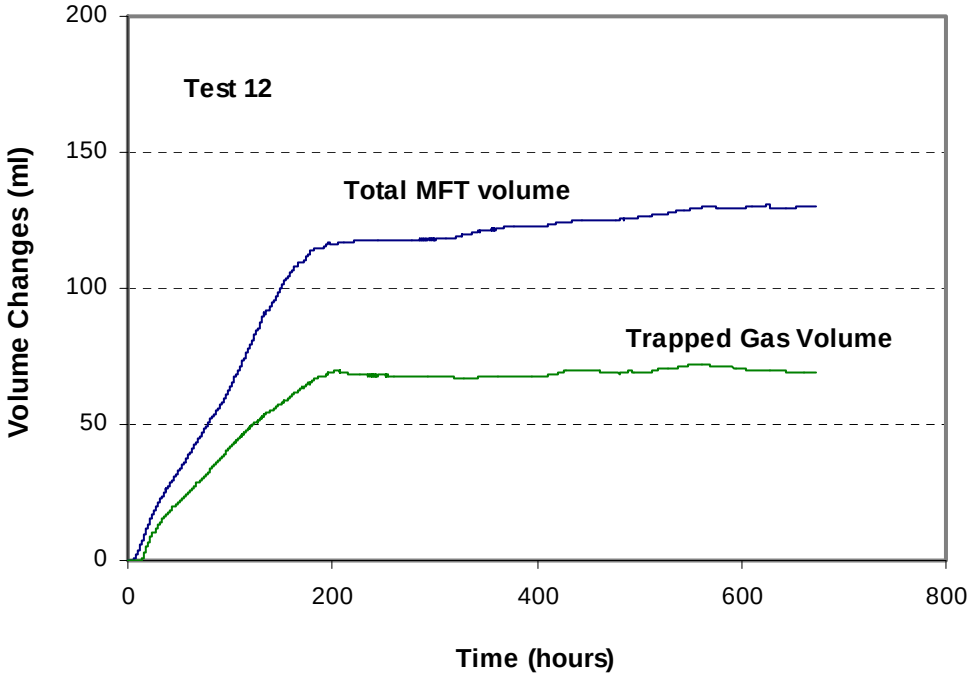

Figure 8-16 Changes in Trapped Gas Volume and Total MFT Volume in Sample 12

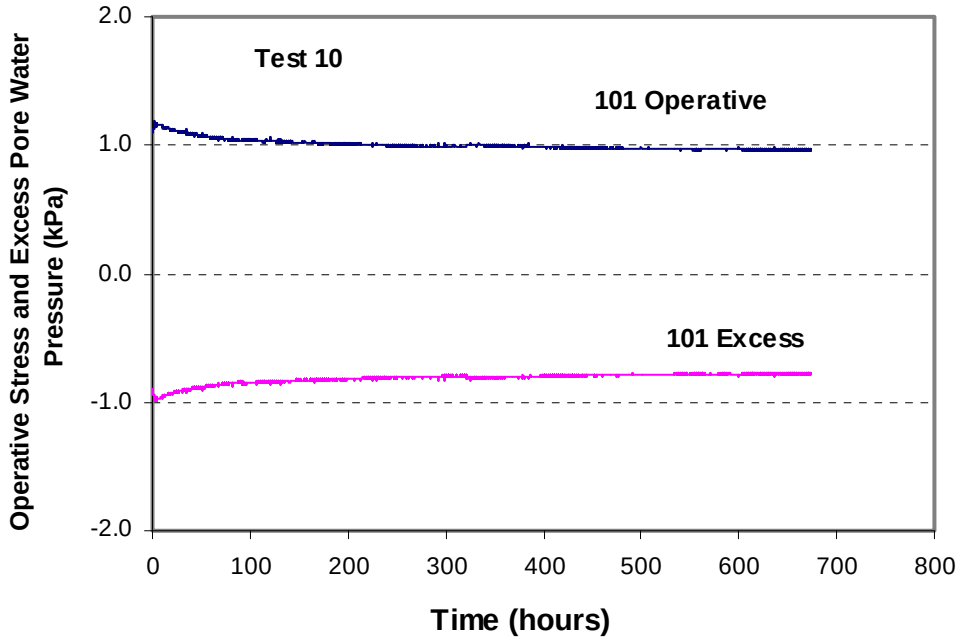

Figure 8-17 Changes of Excess Pore Pressure and Operative Stress at E1 of Test 10

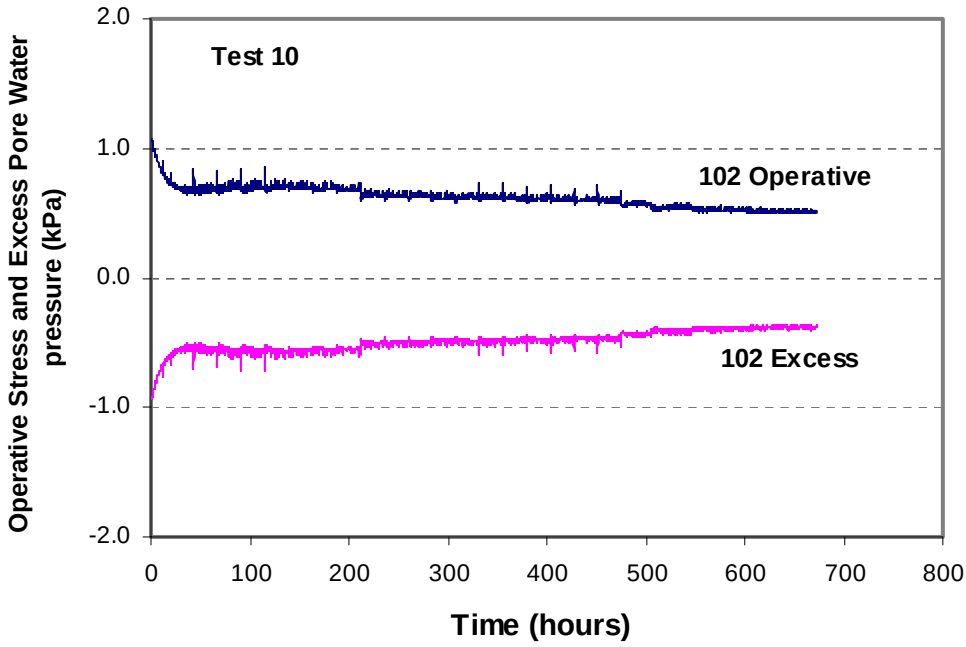

Figure 8-18 Changes of Excess Pore Pressure and Operative Stress at E2 of Test 10

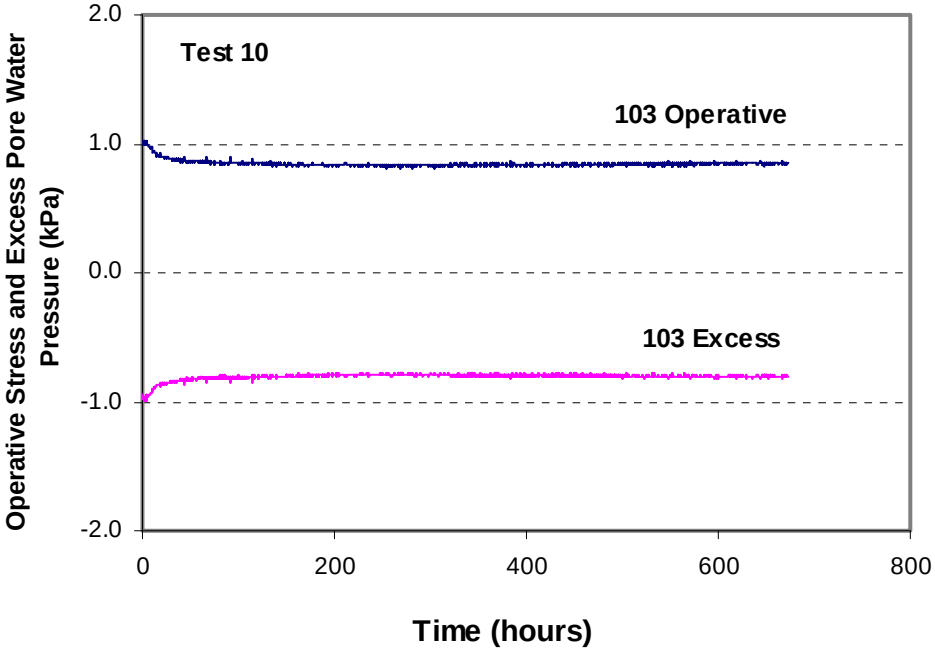

Figure 8-19 Changes of Excess Pore Pressure and Operative Stress at E3 of Test 10

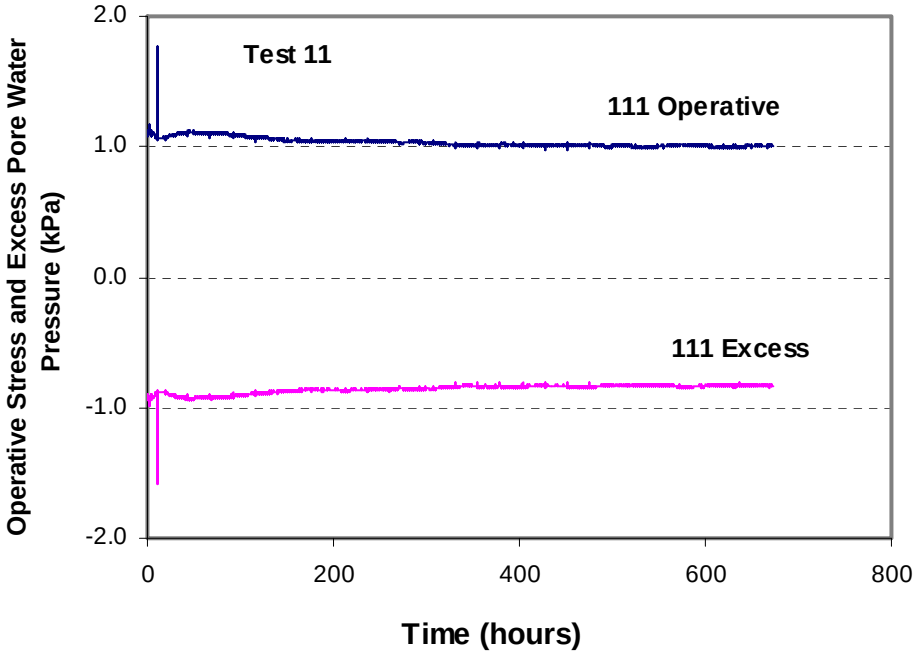

Figure 8-20 Changes of Excess Pore Pressure and Operative Stress at E1 of Test 11

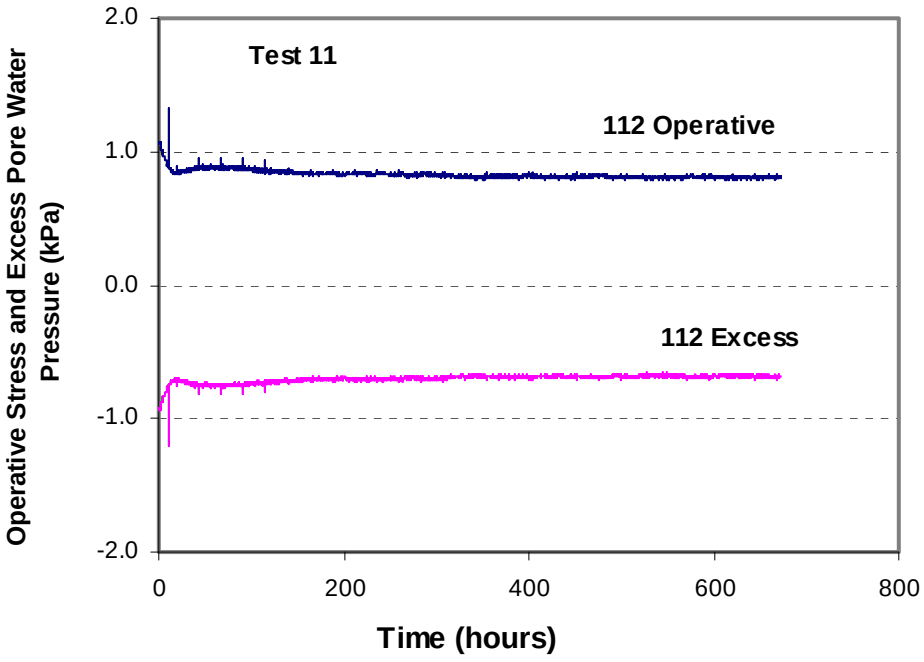

Figure 8-21 Changes of Excess Pore Pressure and Operative Stress at E2 of Test 11

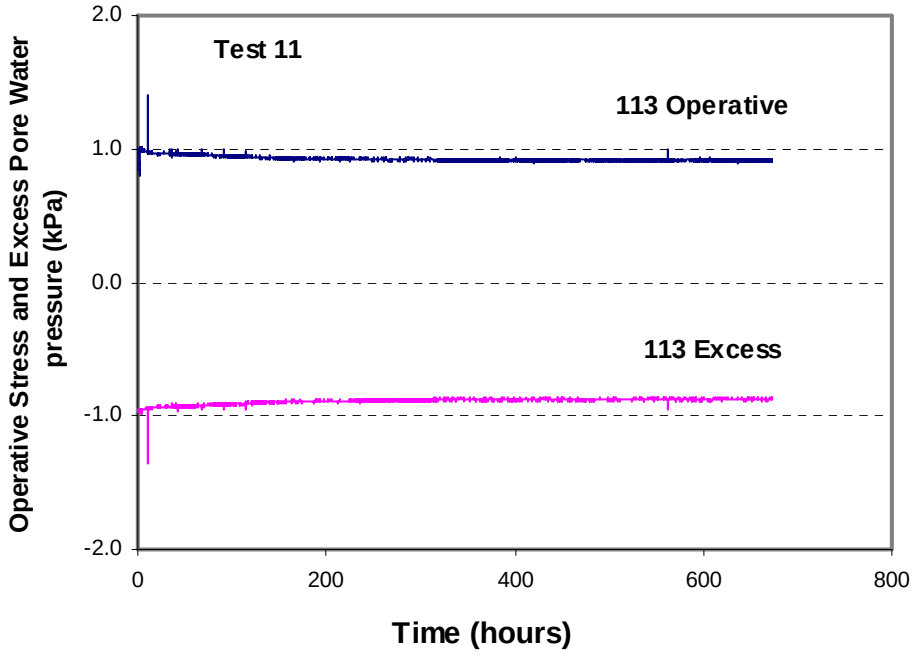

Figure 8-22 Changes of Excess Pore Pressure and Operative Stress at E3 of Test 11

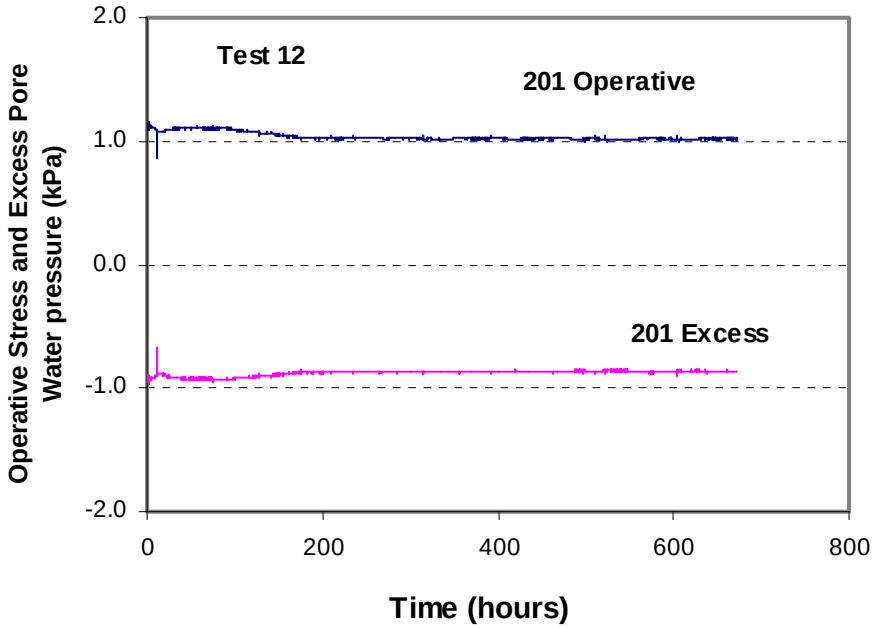

Figure 8-23 Changes of Excess Pore Pressure and Operative Stress at E1 of Test 12

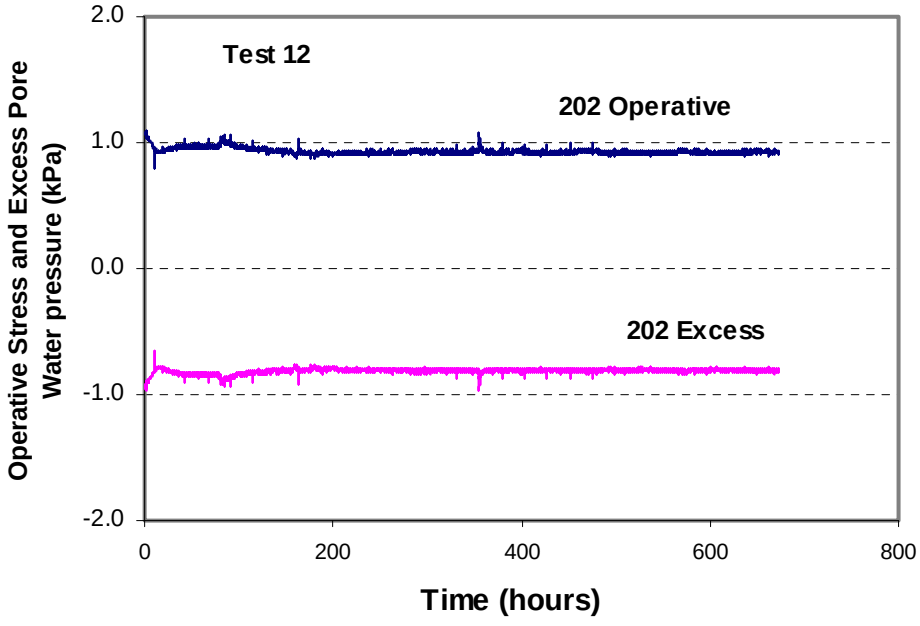

Figure 8-24 Changes of Excess Pore Pressure and Operative Stress at E2 of Test 12

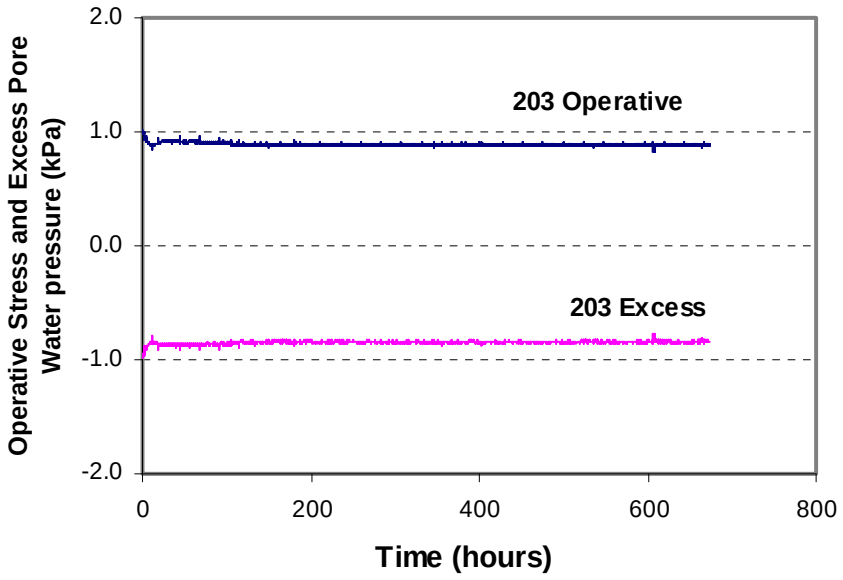

Figure 8-25 Changes of Excess Pore Pressure and Operative Stress at E3 of Test 12

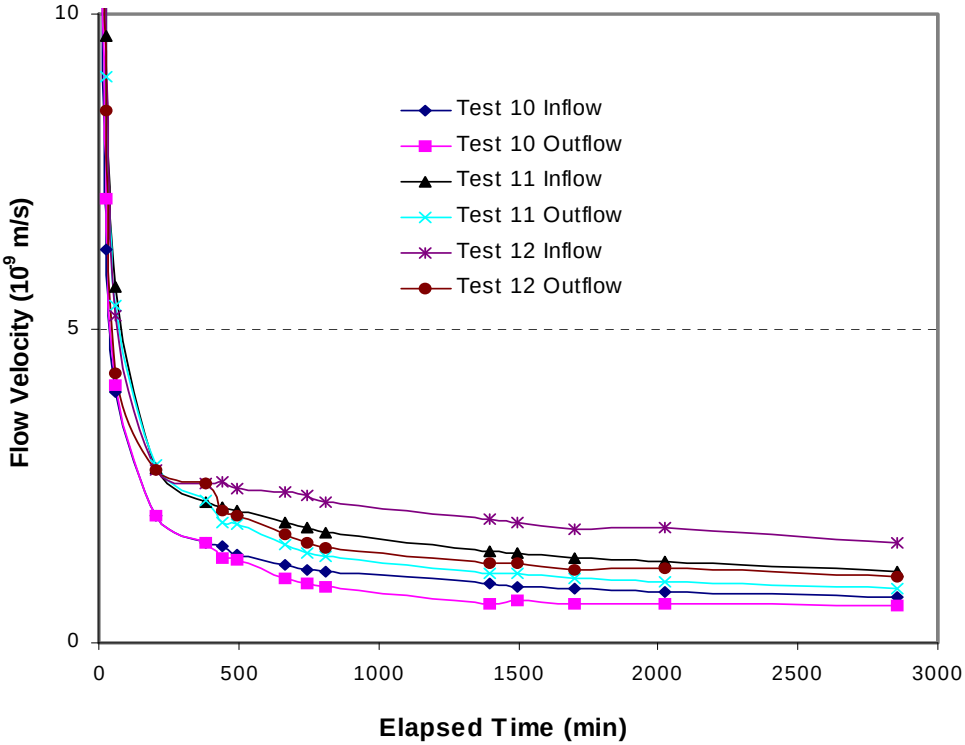

Figure 8-26 Flow Velocity vs. Time in Permeability Tests 10-12 after Microbial Activity

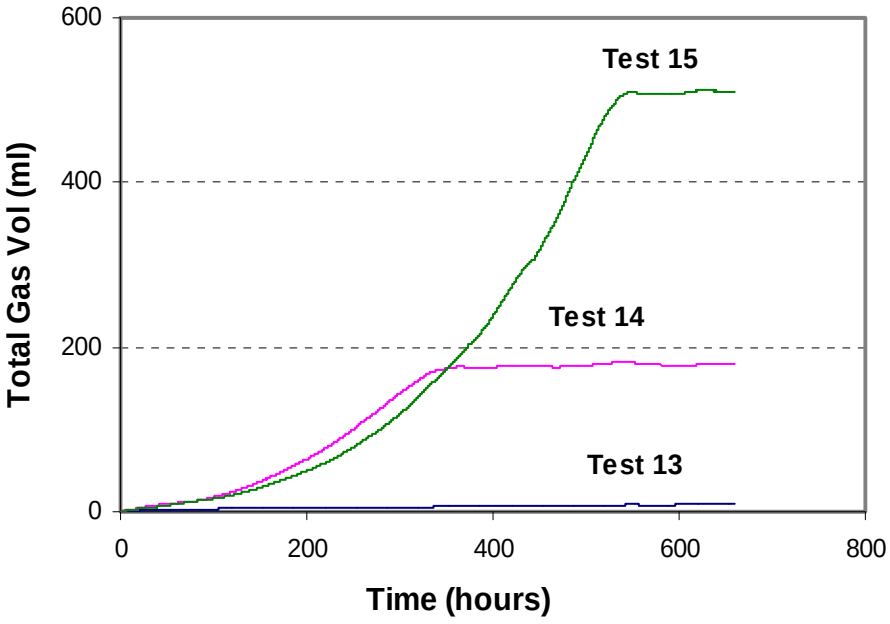

Figure 8-27 Total Gas Volume (at STP) vs. Time in samples 13-15

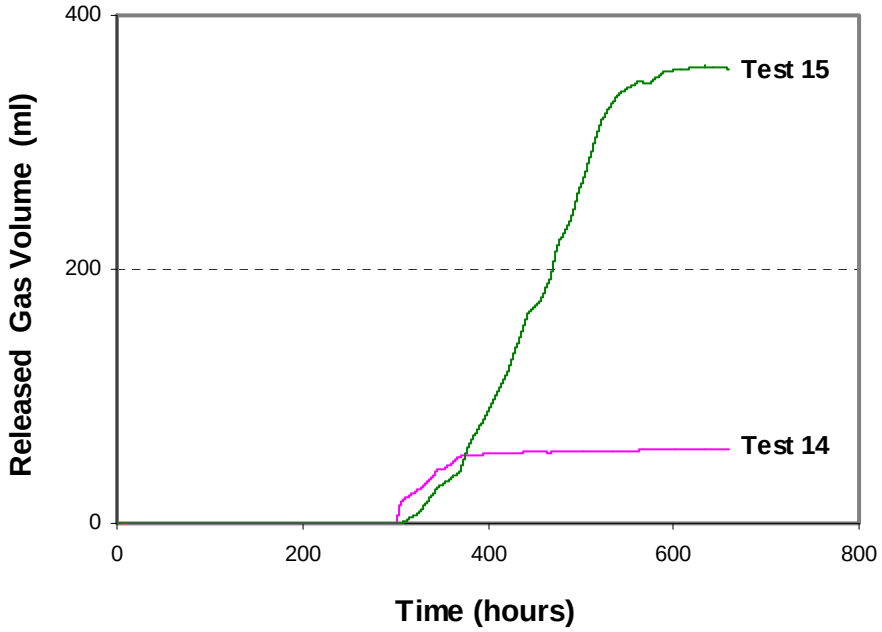

Figure 8-28 Released Gas Volume (at STP) vs. Time in Samples 13-15

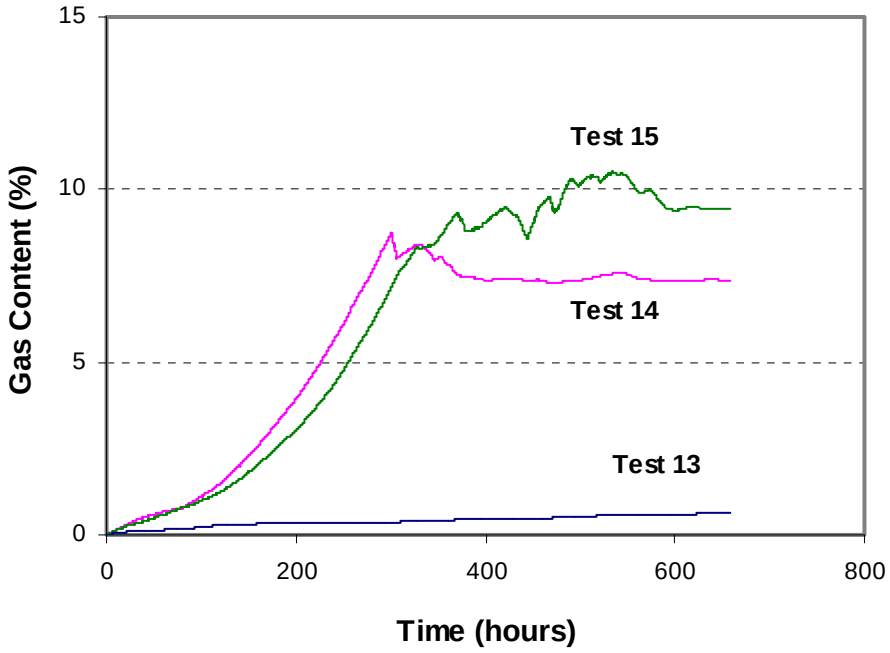

Figure 8-29 Gas Content vs. Time in Samples 13-15

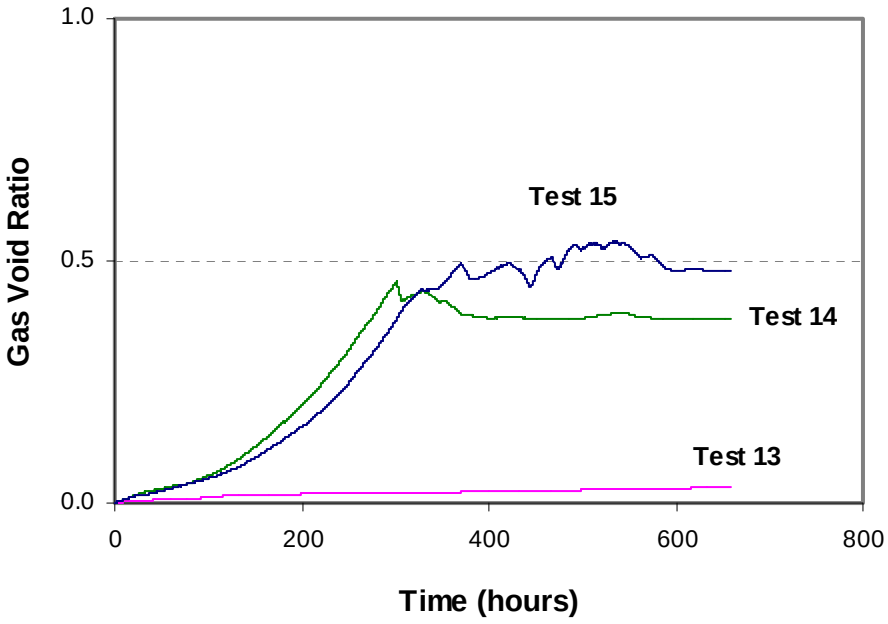

Figure 8-30 Gas Content vs. Time in Samples 13-15

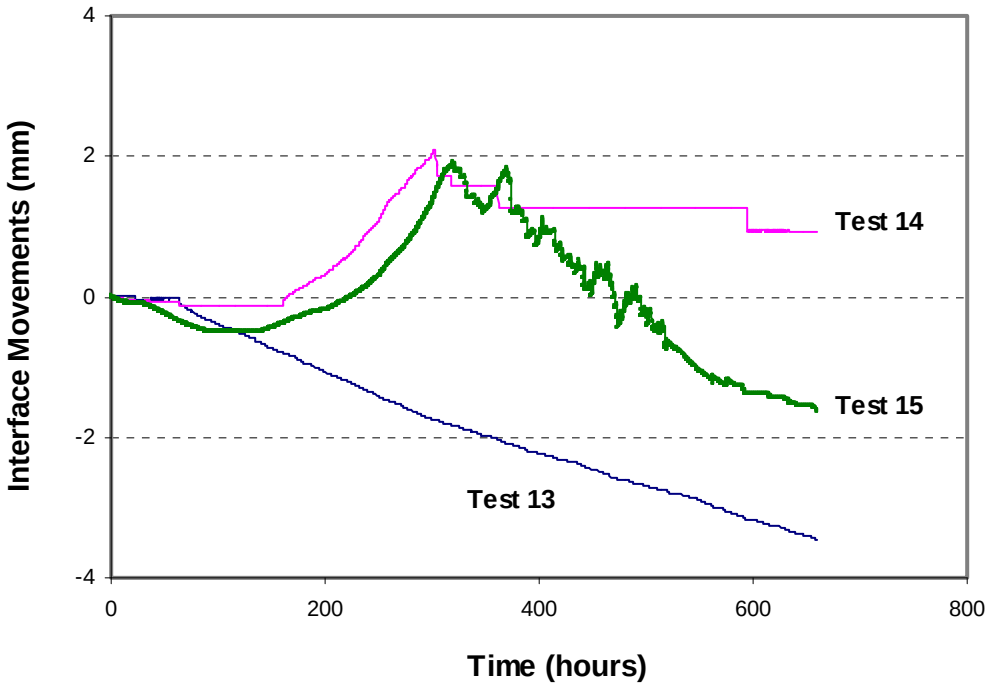

Figure 8-31 Interface Movements vs. Time in Samples 13-15

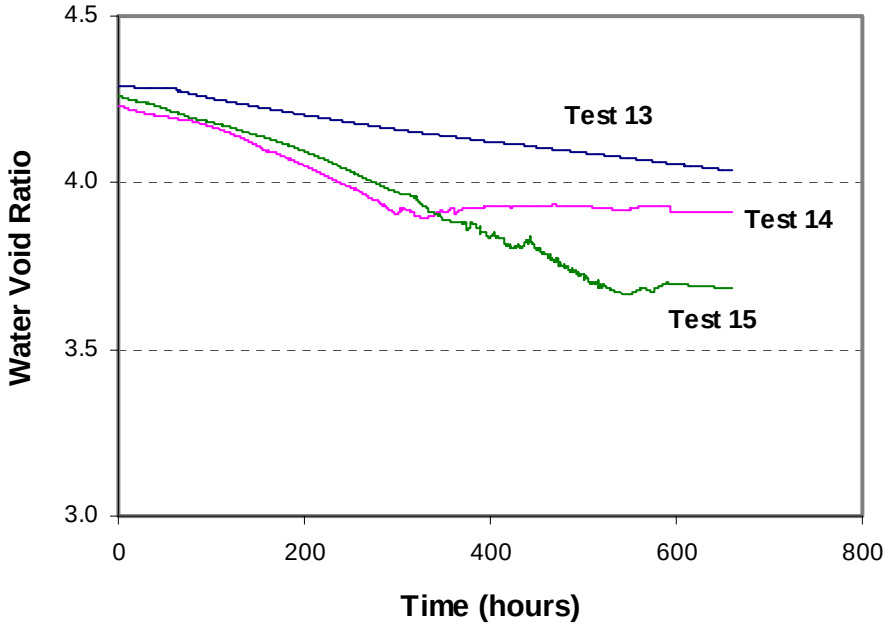

Figure 8-32 Water Void Ratio vs. Time in Samples 13-15

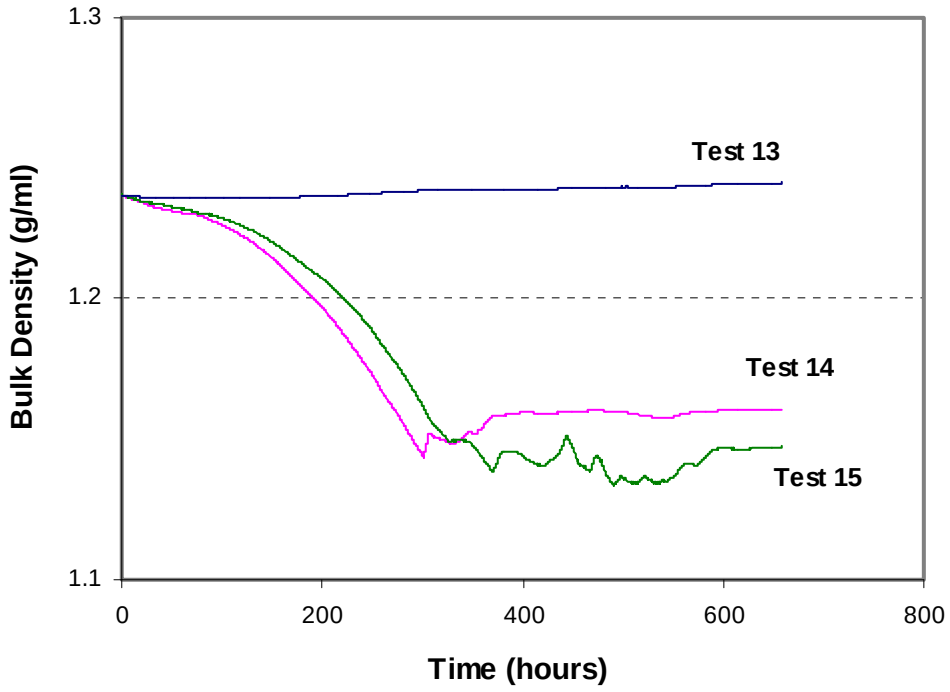

Figure 8-33 Bulk Density vs. Time in Samples 13-15

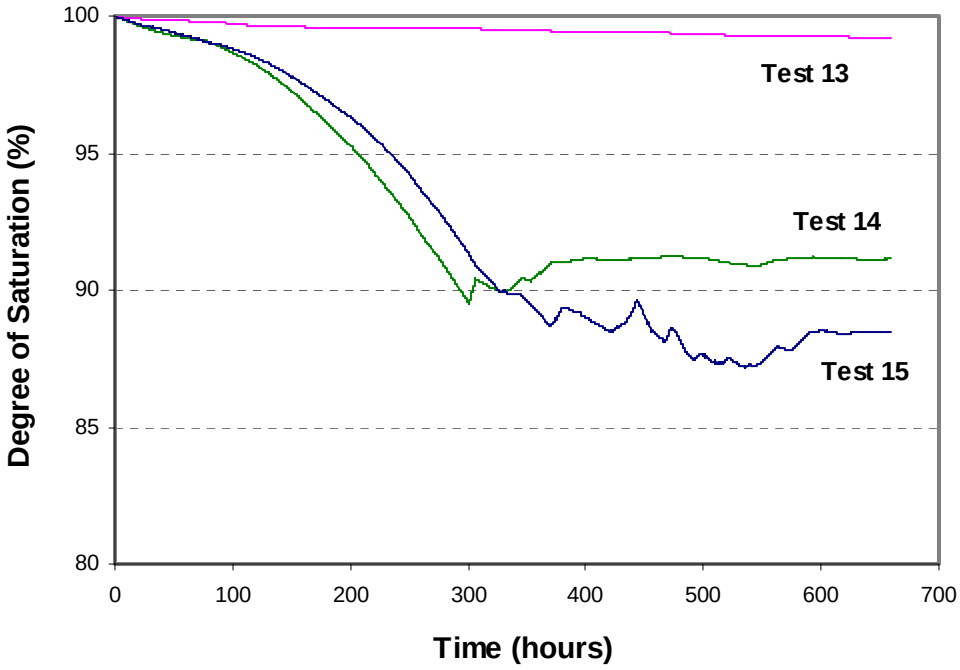

Figure 8-34 Degree of Saturation vs. Time in Samples 13-15

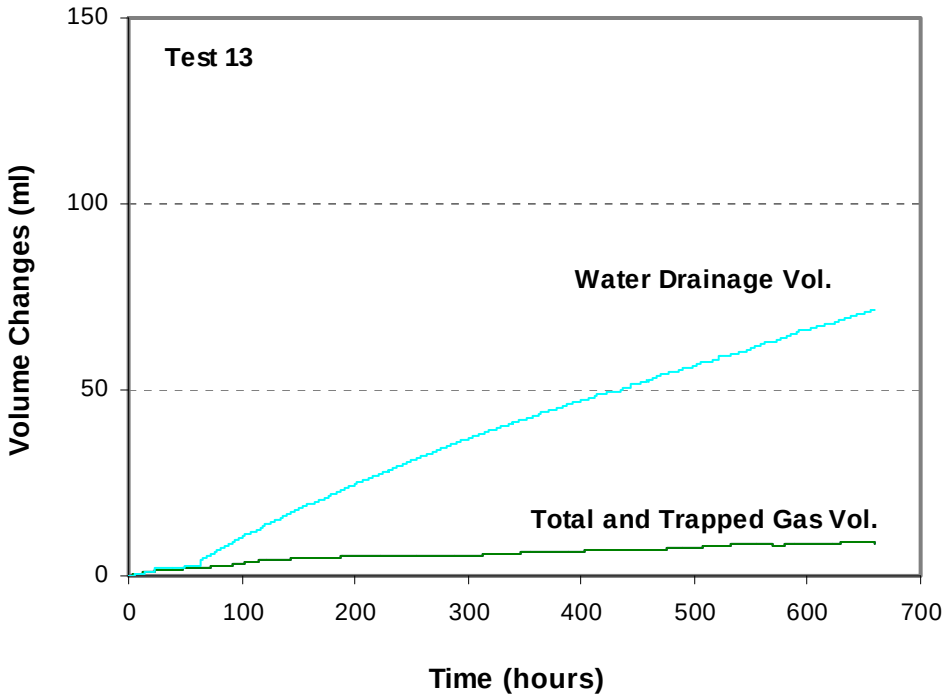

Figure 8-35 Volumetric Changes in Sample 13 during Microbial Activity

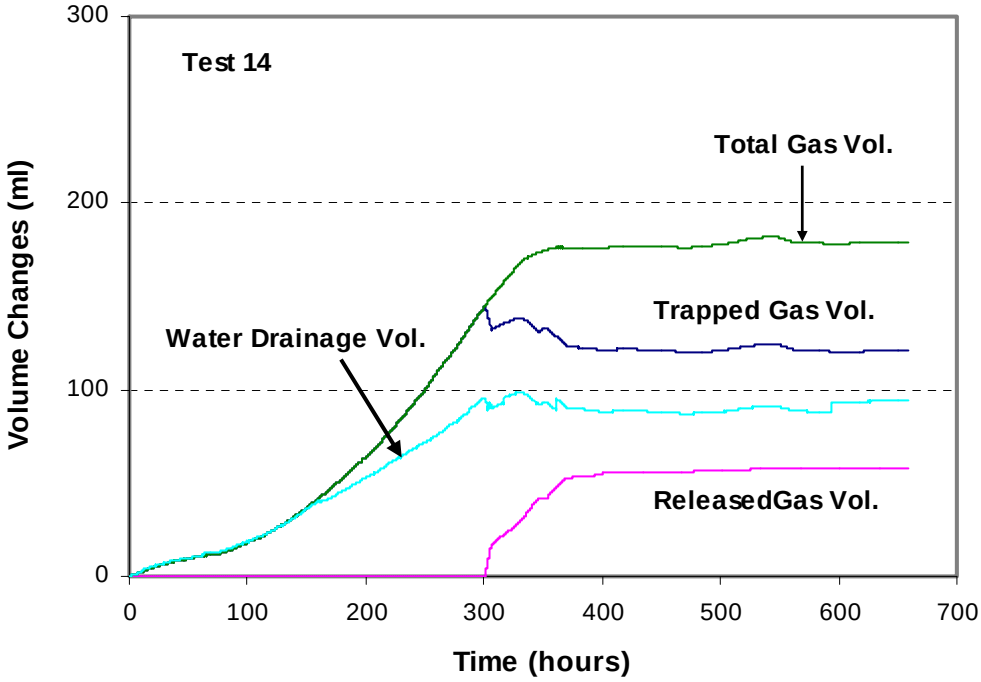

Figure 8-36 Volumetric Changes in Sample 14 during Microbial Activity

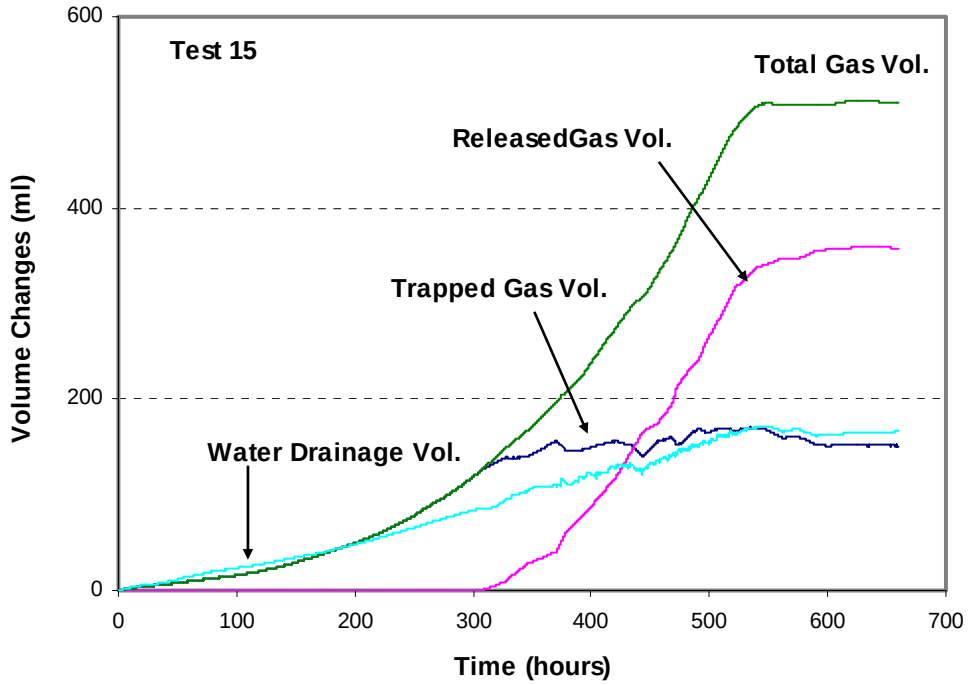

Figure 8-37 Volumetric Changes in Sample 15 during Microbial Activity

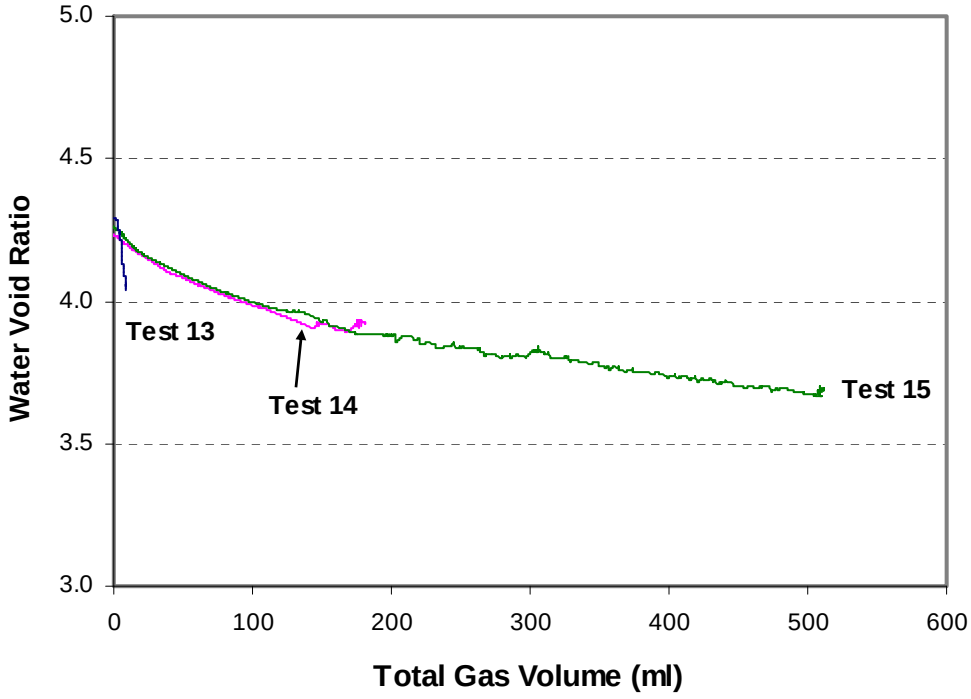

Figure 8-38 Water Void Ratio vs. Total Gas Volume (STP) in Samples 13-15

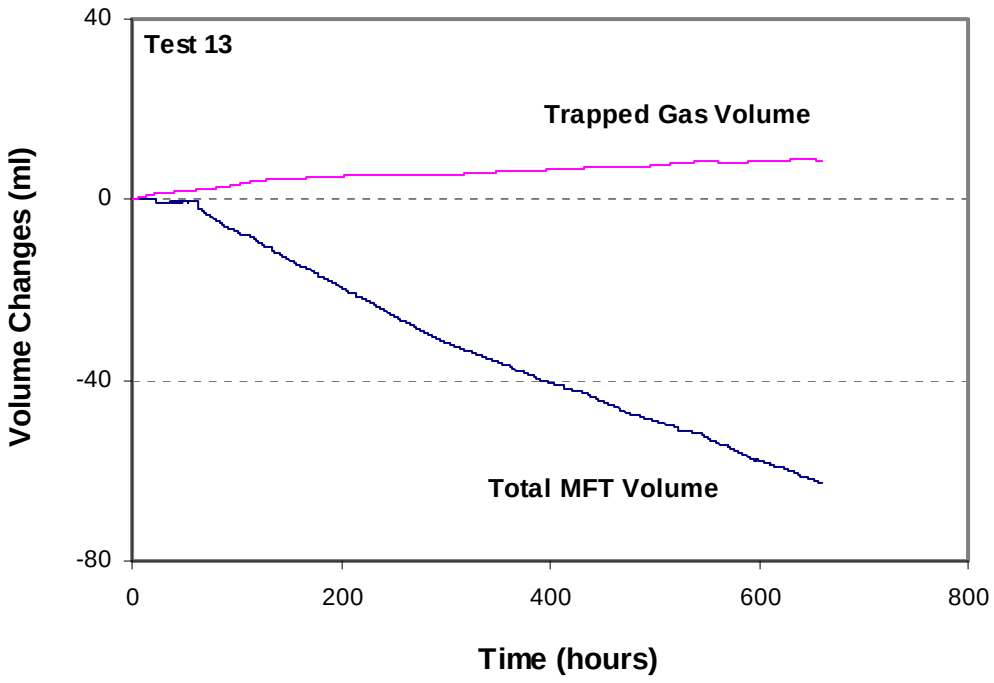

Figure 8-39 Changes in Trapped Gas Volume and Total MFT Volume (STP) in Sample 13

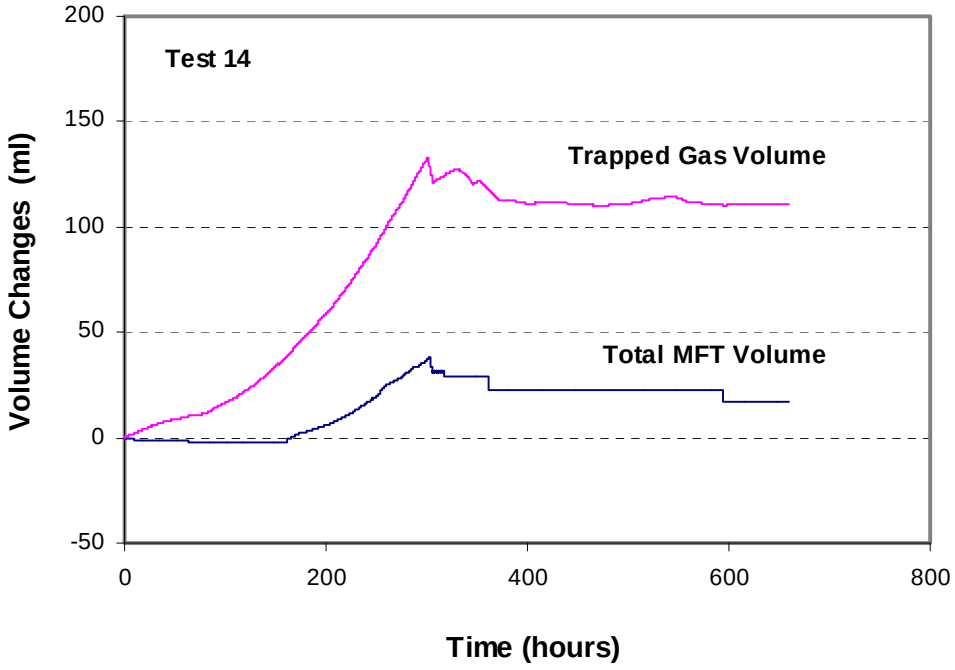

Figure 8-40 Changes in Trapped Gas Volume and Total MFT Volume (STP) in Sample 14

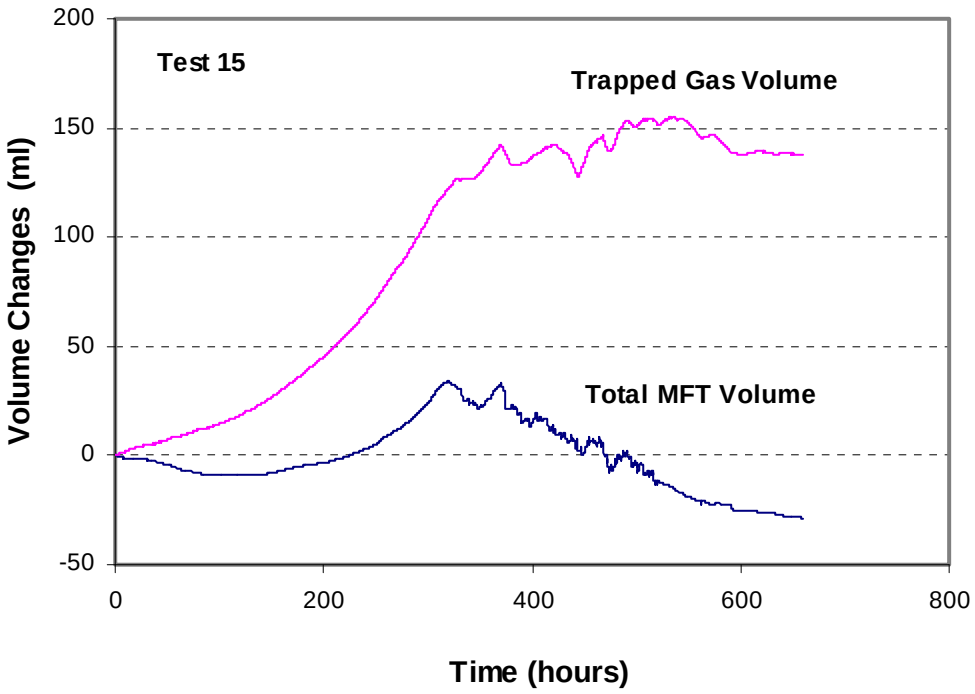

Figure 8-41 Changes in Trapped Gas Volume and Total MFT Volume (STP) in Sample 14

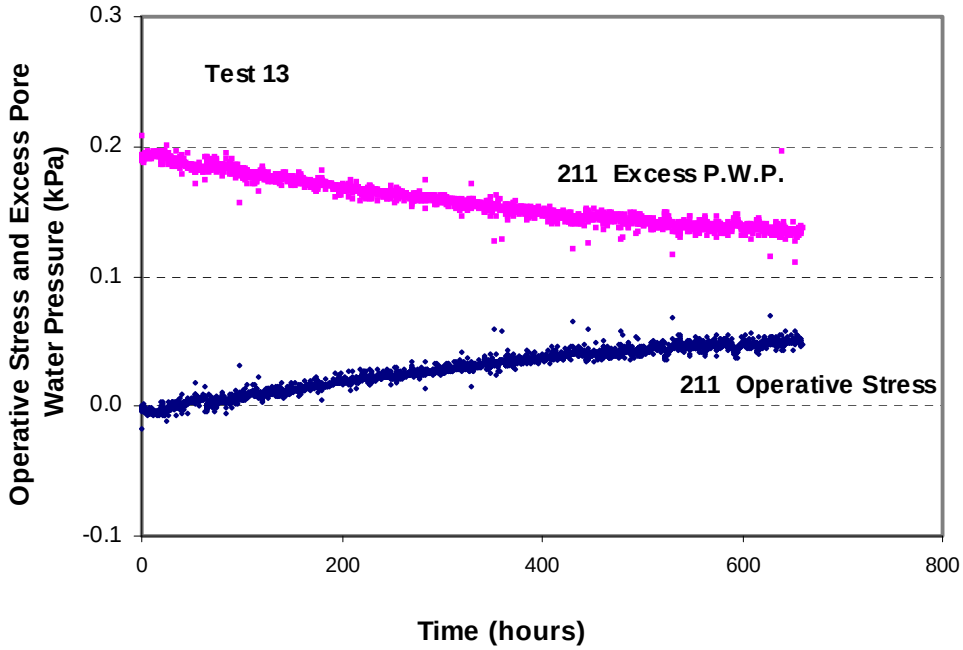

Figure 8-42 Changes in Excess Pore Pressure and Operative Stress at E1 of Test 13

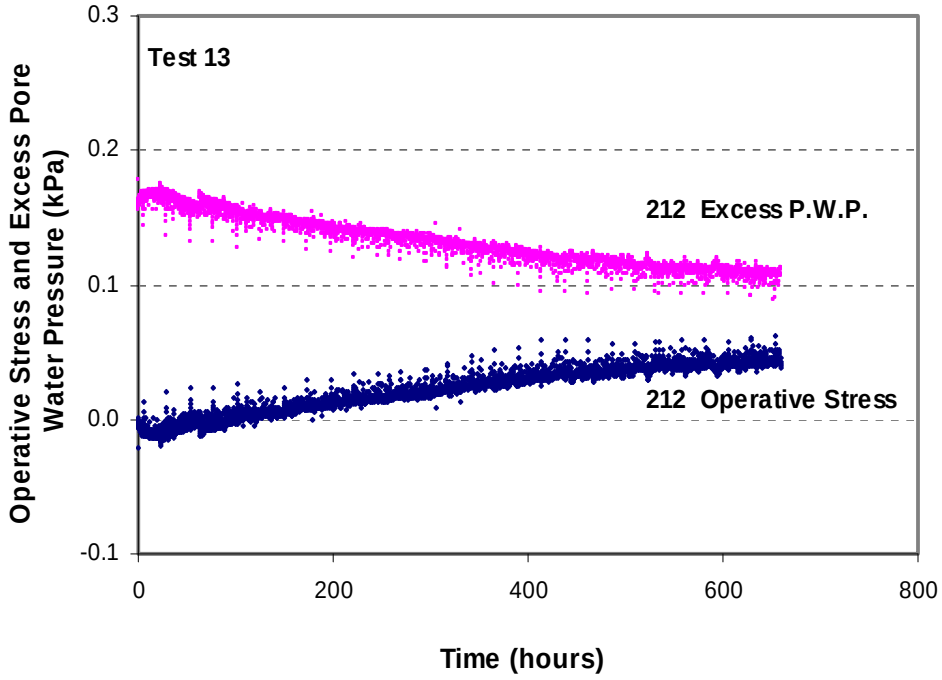

Figure 8-43 Changes in Excess Pore Pressure and Operative Stress at E2 of Test 13

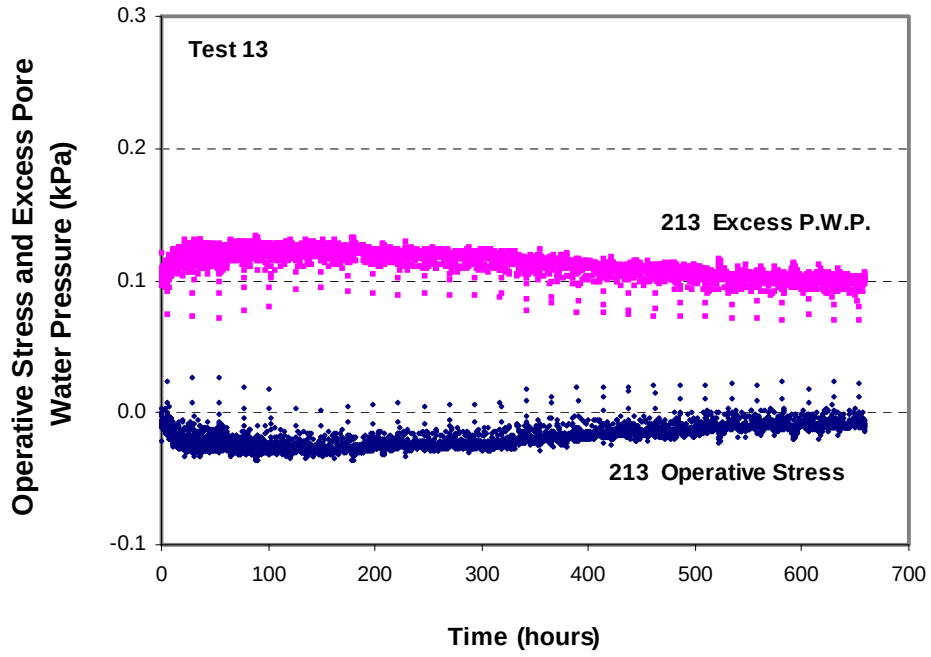

Figure 8-44 Changes in Excess Pore Pressure and Operative Stress at E3 of Test 13

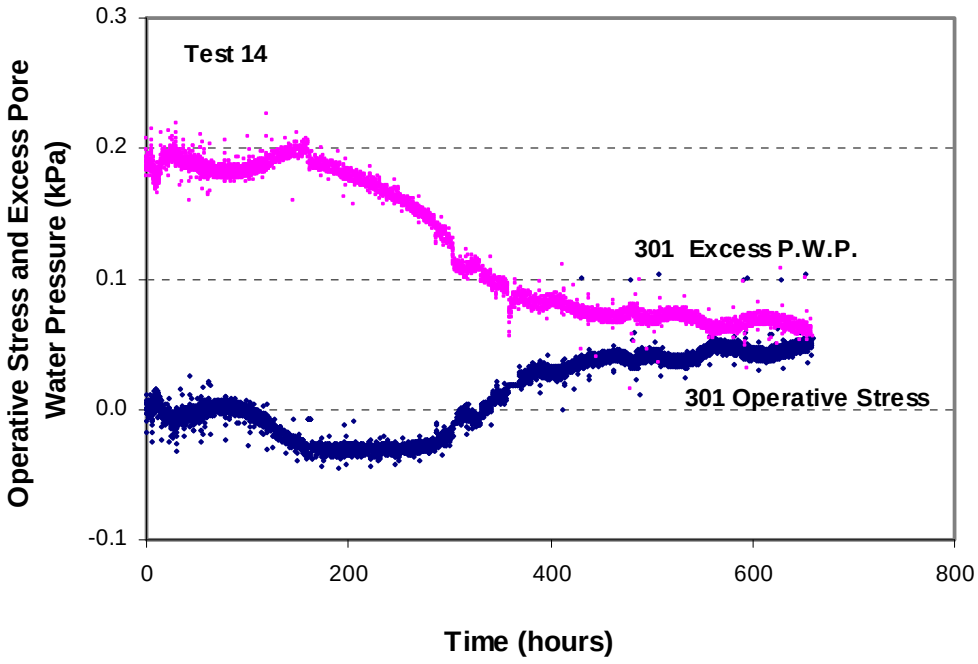

Figure 8-45 Changes in Excess Pore Pressure and Operative Stress at E1 of Test 14

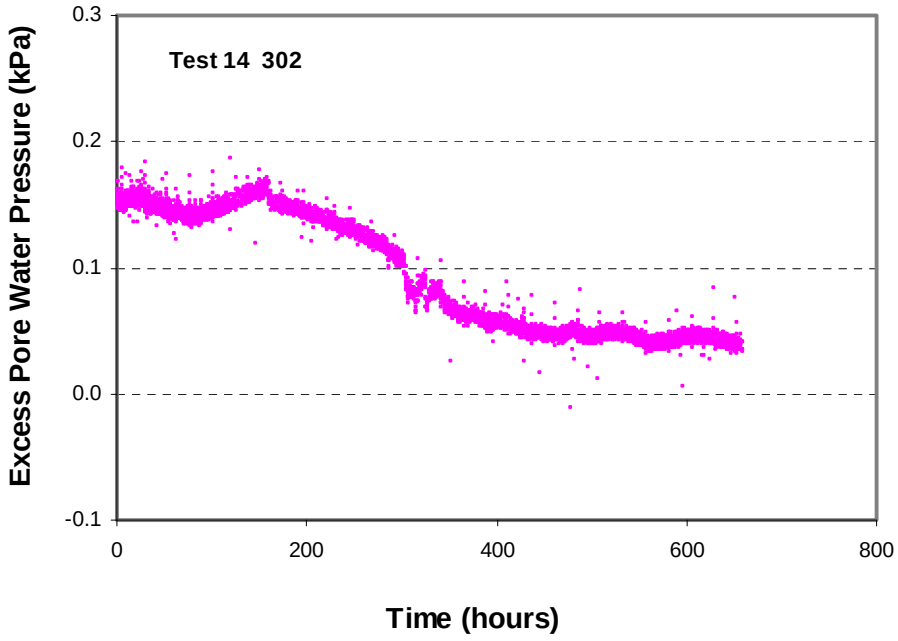

Figure 8-46 Changes in Excess Pore Pressure at E2 of Test 14

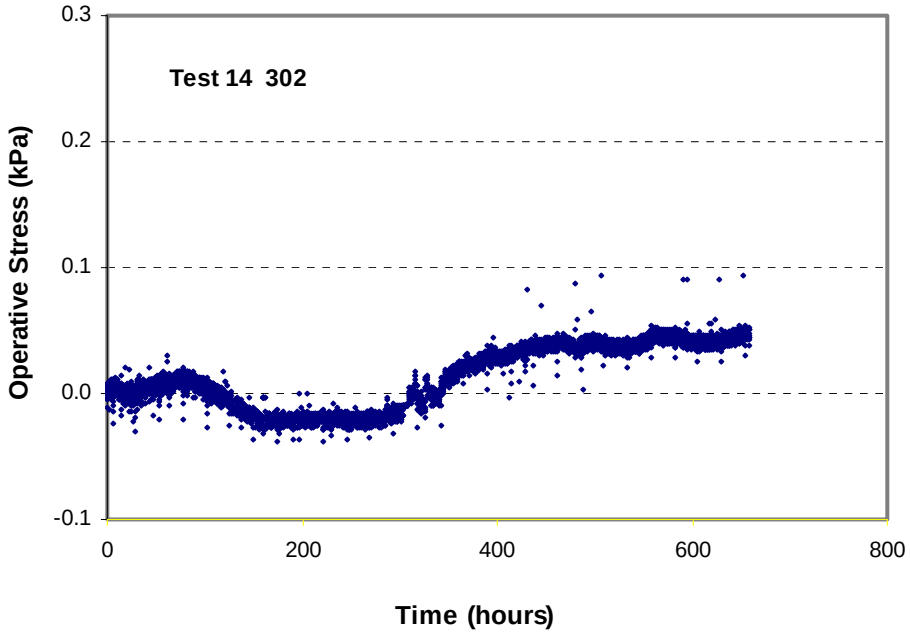

Figure 8-47 Changes in Operative Stress at E2 of Test 14

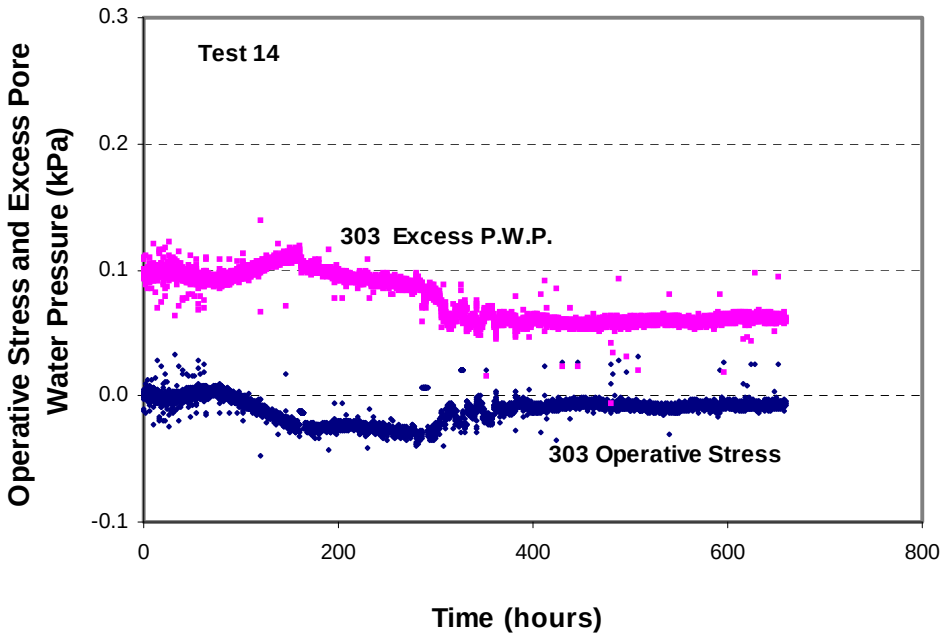

Figure 8-48 Changes in Excess Pore Pressure and Operative Stress at E3 of Test 14

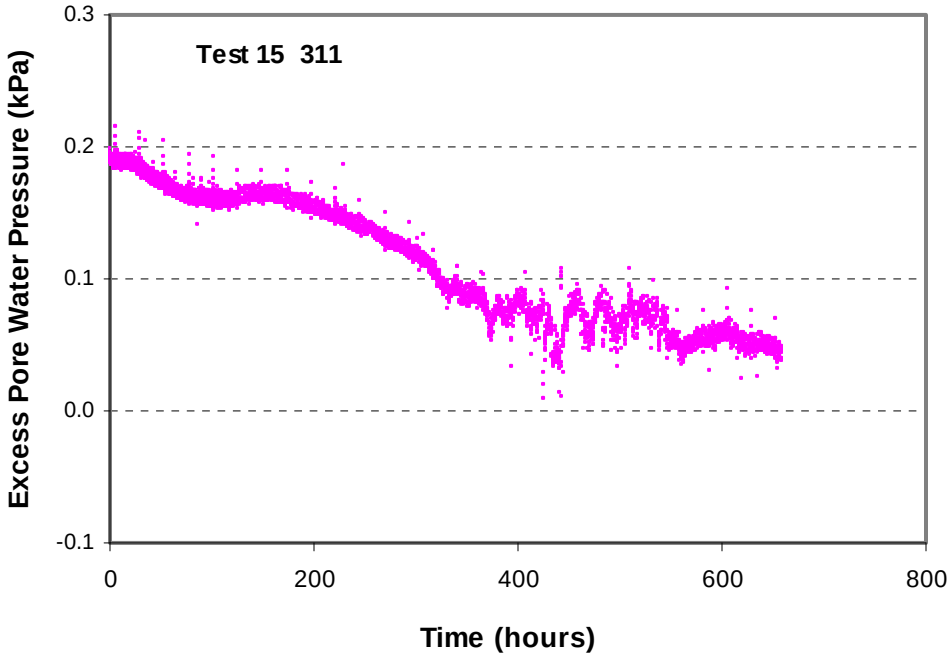

Figure 8-49 Changes in Excess Pore Pressure at E1 of Test 15

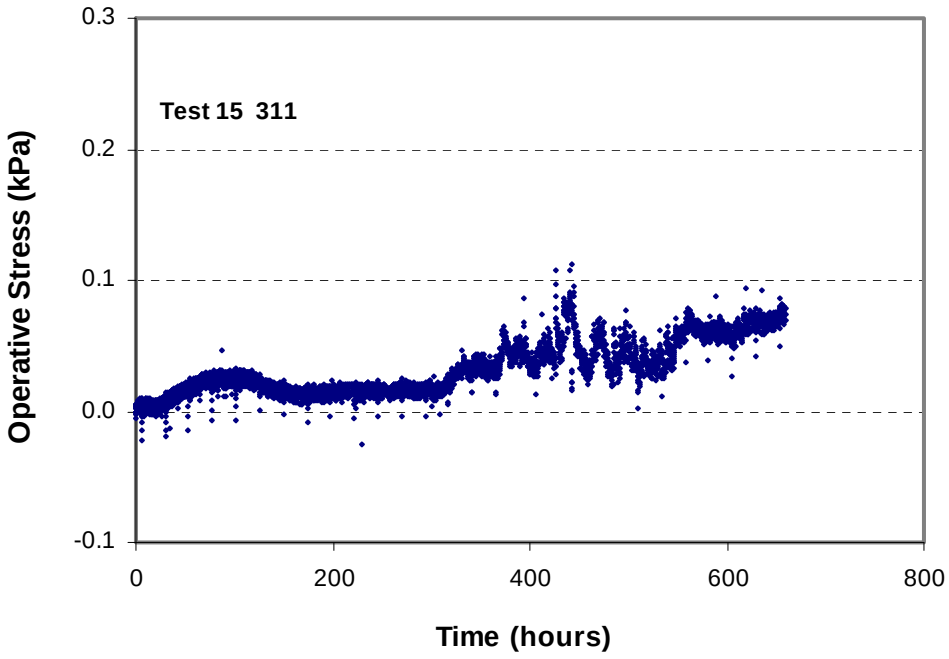

Figure 8-50 Changes in Operative Stress at E1 of Test 15

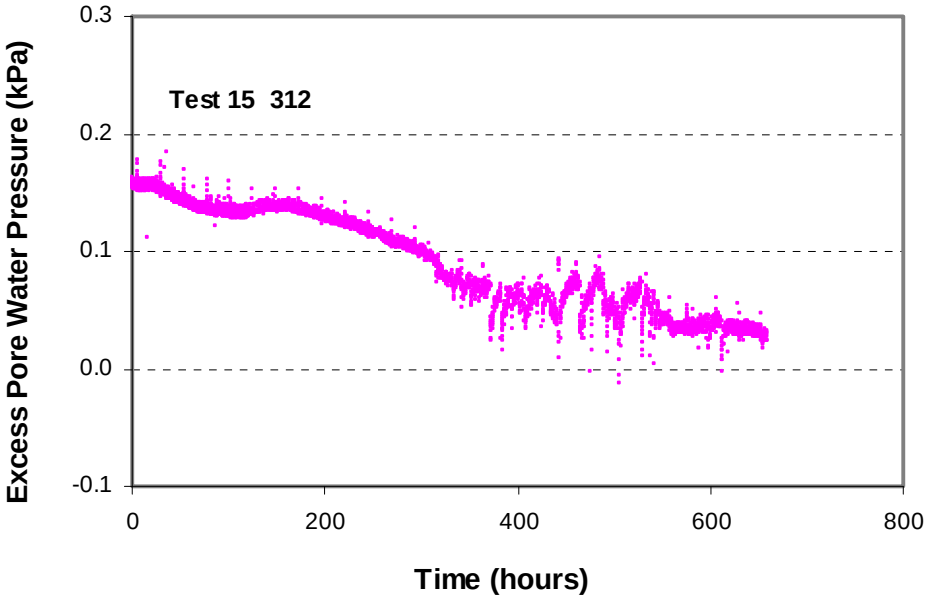

Figure 8-51 Changes in Excess Pore Pressure at E2 of Test 15

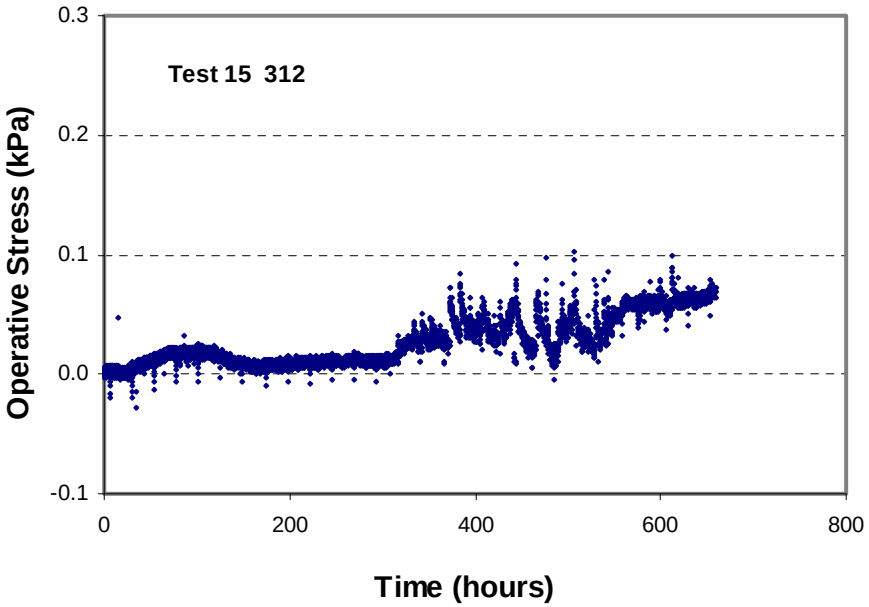

Figure 8-52 Changes in Operative Stress at E2 of Test 15

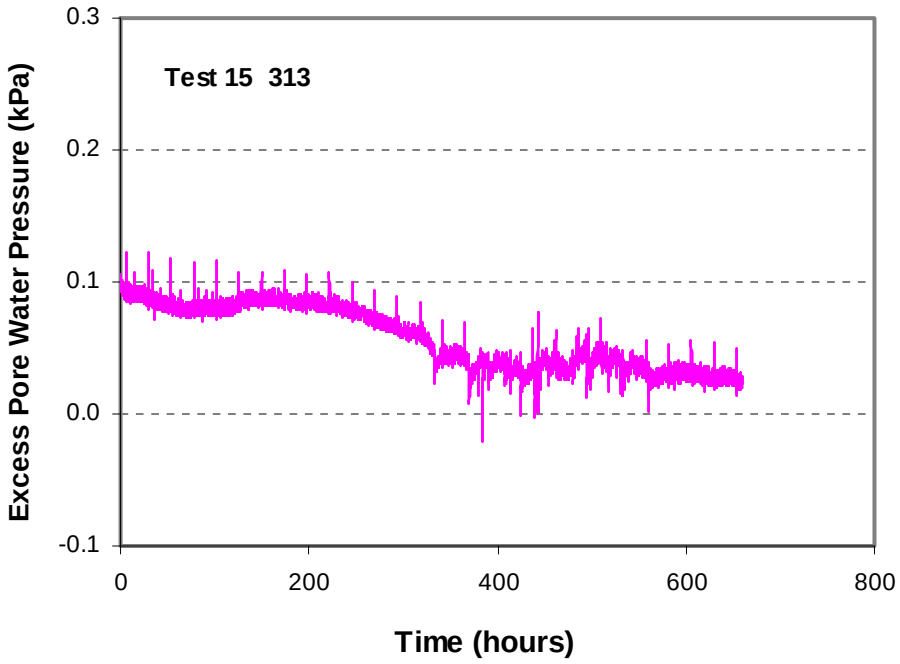

Figure 8-53 Changes in Excess Pore Pressure at E3 of Test 15

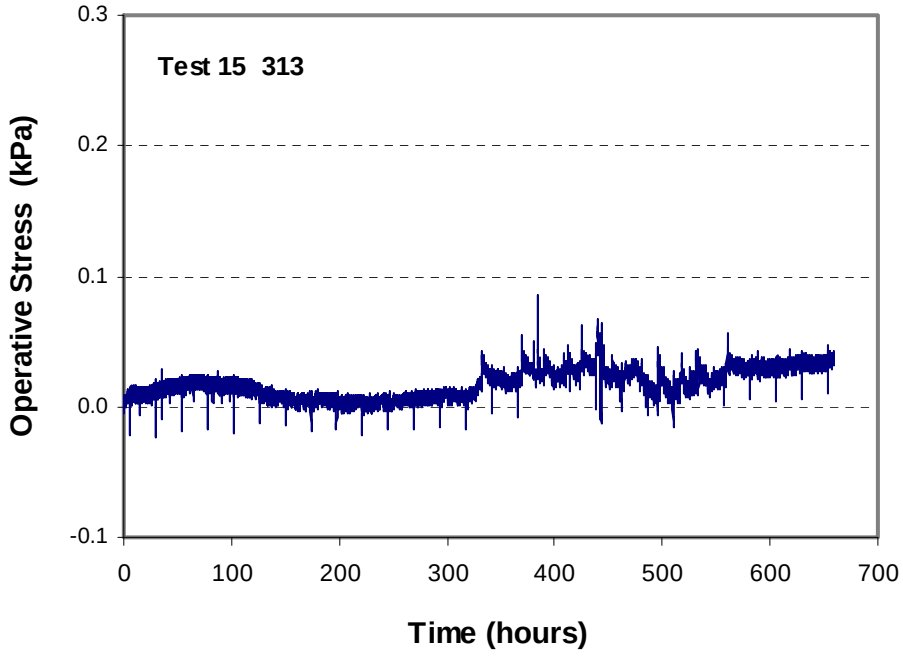

Figure 8-54 Changes in Operative Stress at E3 of Test 15

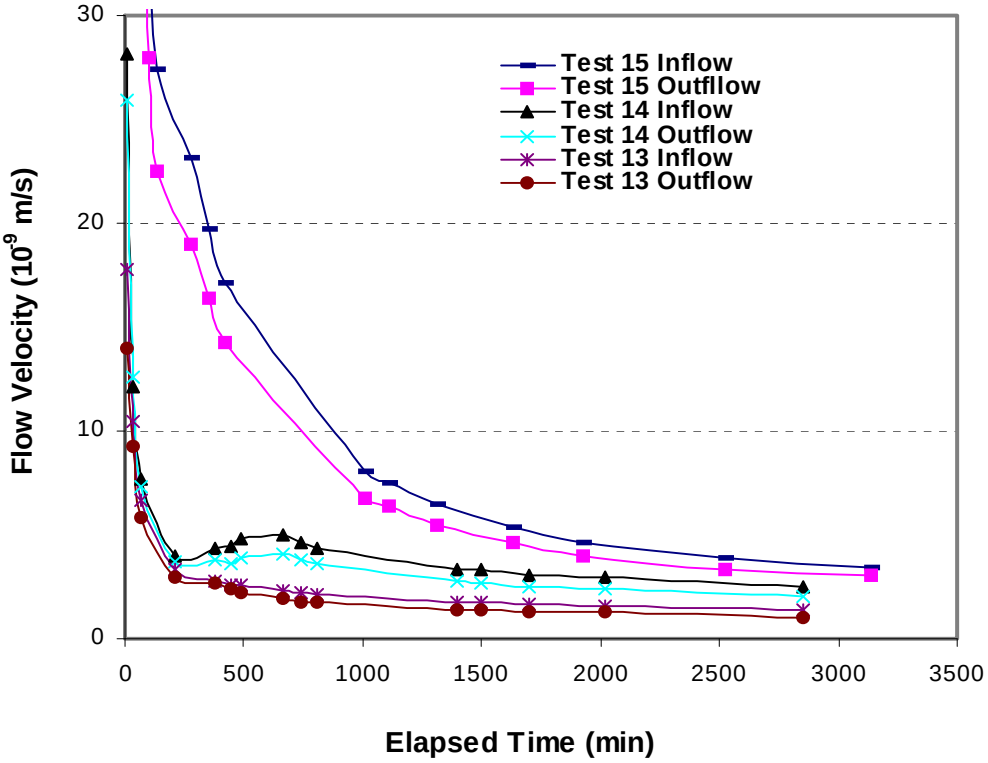

Figure 8-55 Flow Velocity vs. Time in Permeability Tests 13-15 after Microbial Activity

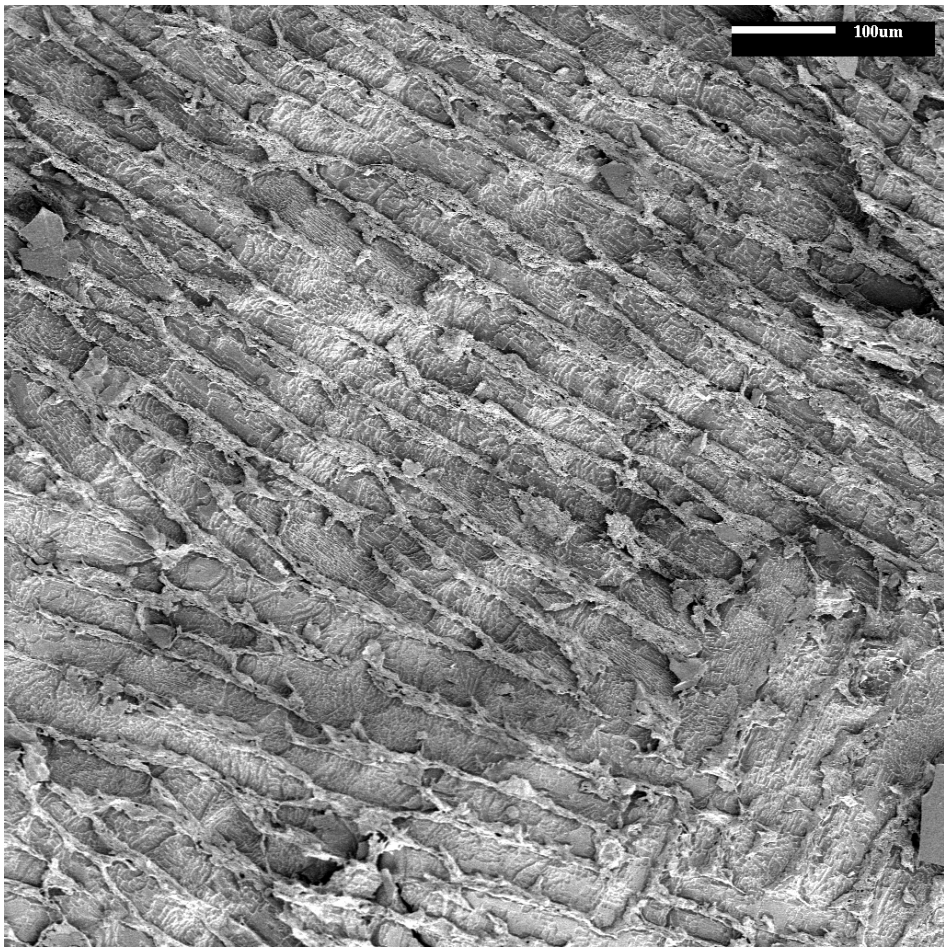

Figure 8-56 The Structure of Sample 13 after Microbial Activity

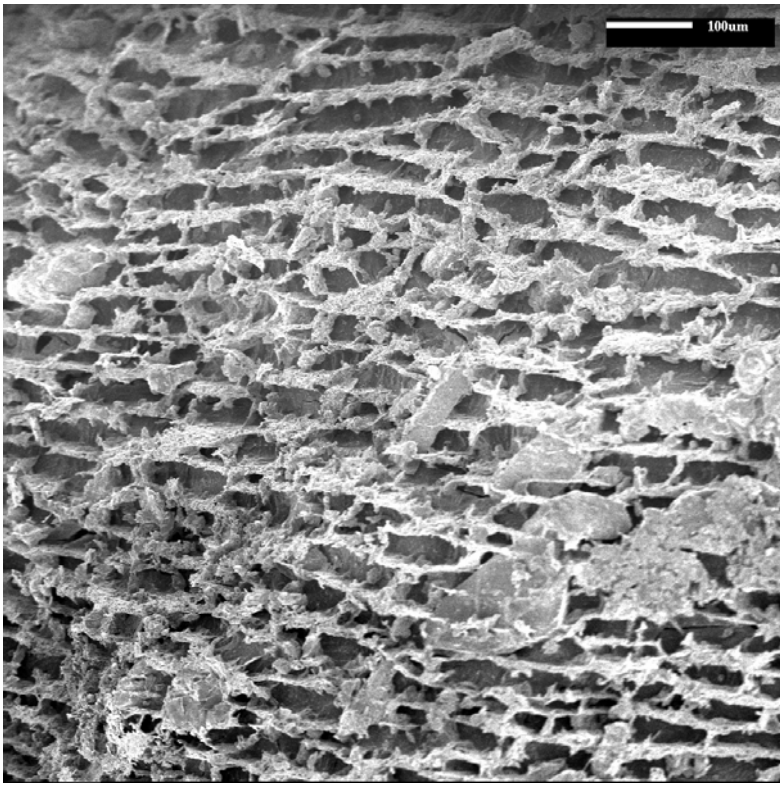

Figure 8-57 The Structure of Sample 15 after Microbial Activity

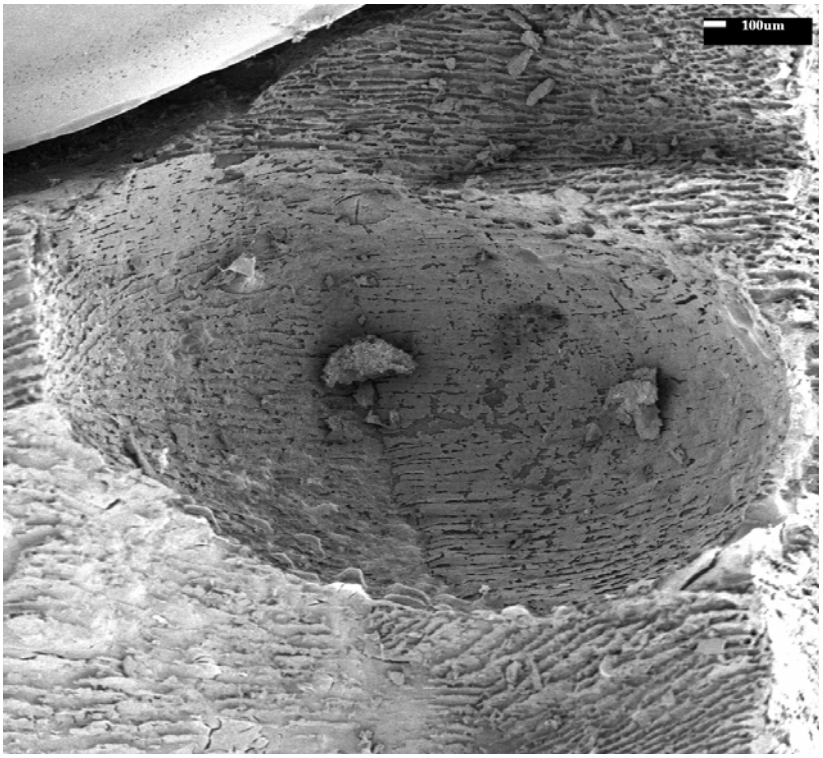

Figure 8-58 Large Gas Bubble in Sample 14 after Microbial Activity

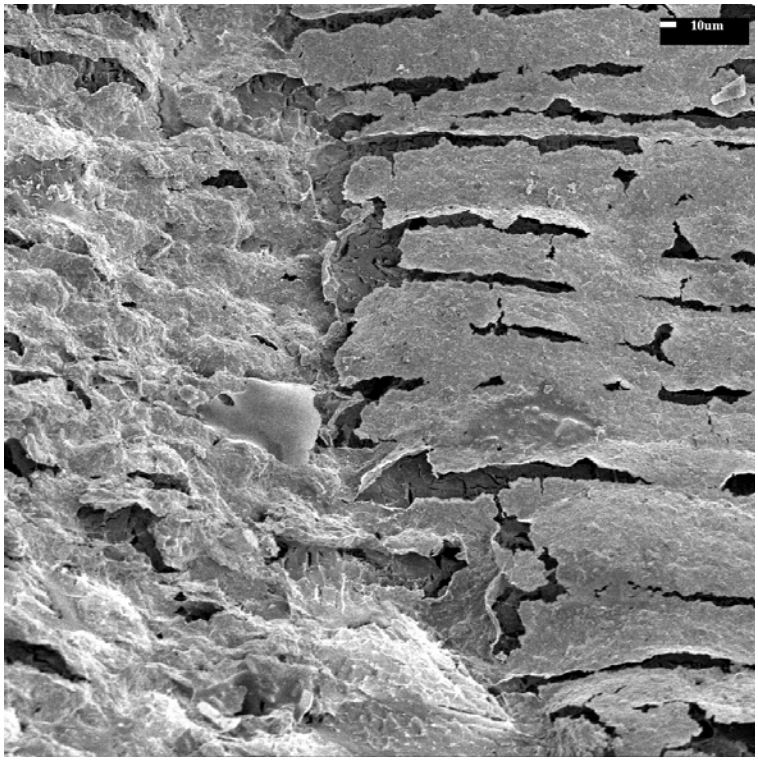

Figure 8-59 Clay Particle Arrangements near the Crack

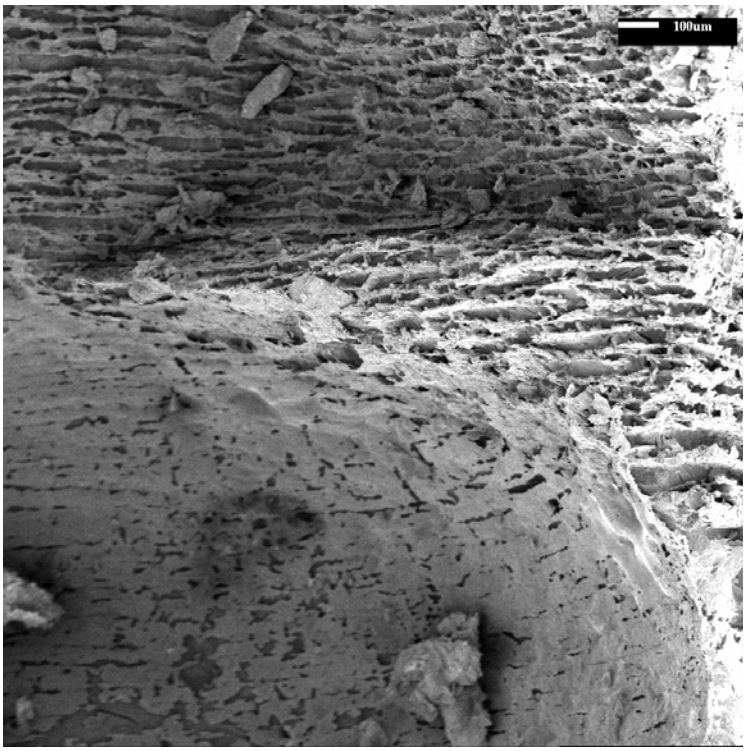

Figure 8-60 A Thin Membrane Surrounding the Large Gas Bubble

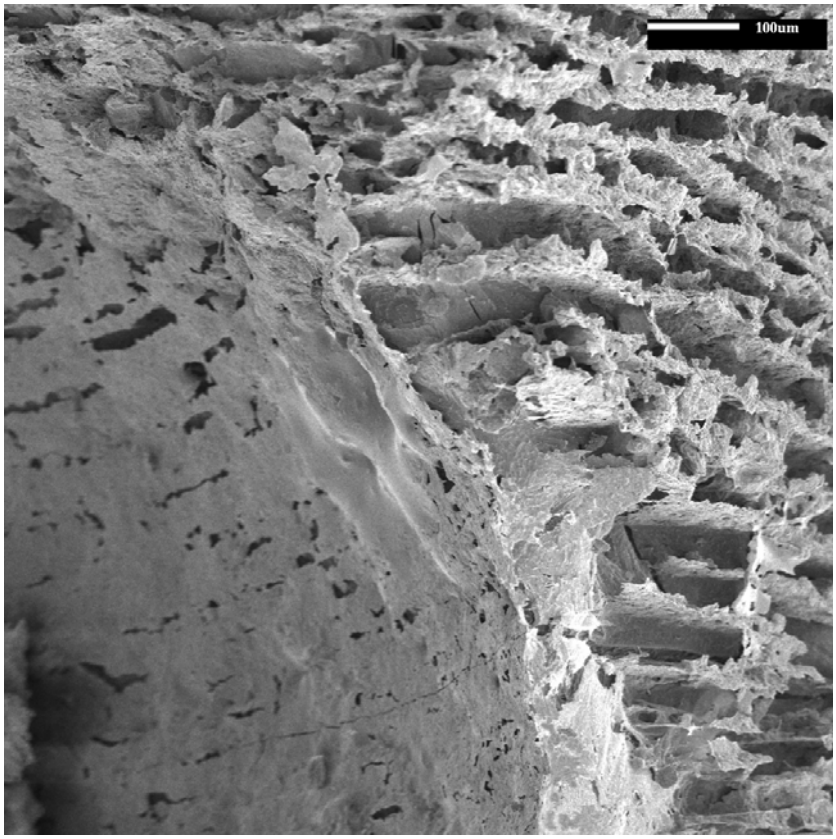

Figure 8-61 Structural Changes near the Large Gas Bubble

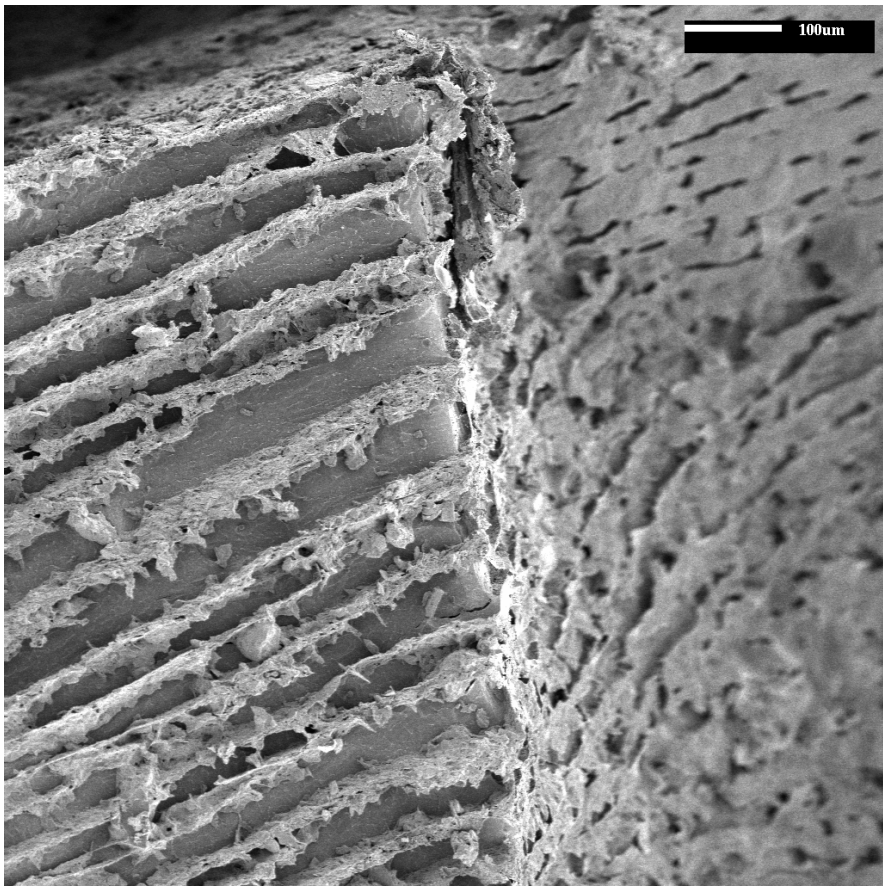

Figure 8-62 Structural Changes near the Large Gas Bubble

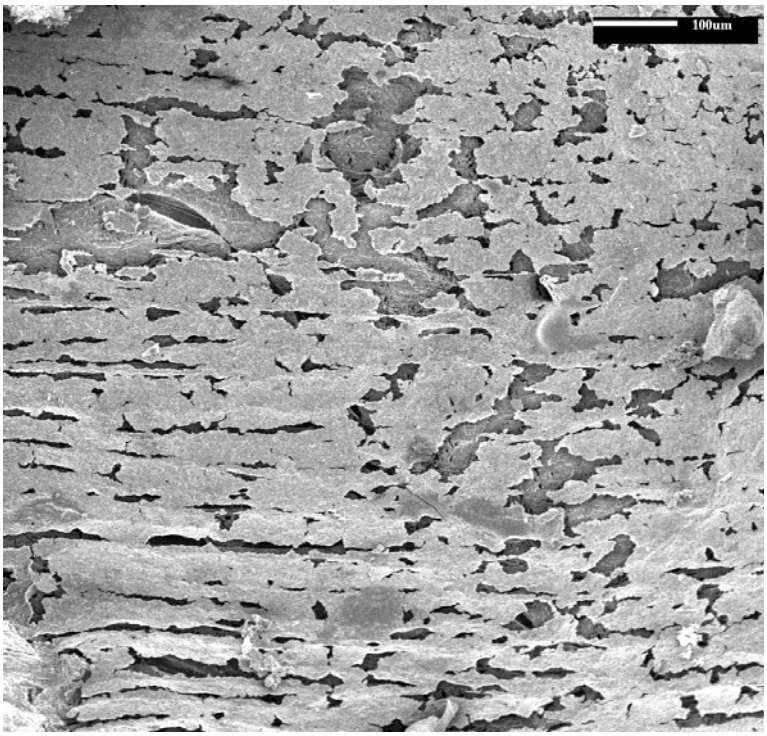

Figure 8-63 Reorientation of Clay Particles Surrounding the Large Gas Bubble

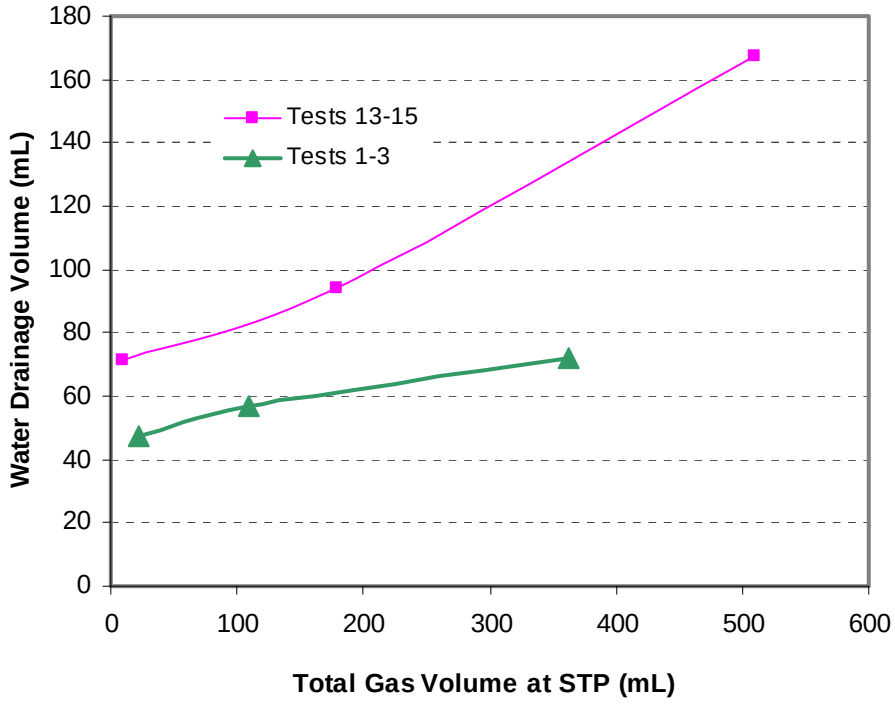

Figure 8-64 Comparison of Biogas Generation on Water Drainage between Tests 1 to 3 and Tests 13 to 15

CHAPTER 9

9 INFLUENCE OF BIOLOGICAL GAS GENERATION UNDER A PRECONSOLIDATION STRESS

9.1 Introduction

Tests 19 to 24 and 25© to 27© were conducted to study the effects of microbial activity on MFT which had been consolidated under external loadings. In Tests 10 to 12, the loadings were released before microbial activity had started. But in Tests 19 to 24, the loadings were maintained during microbial activity. Before microbial activity, the stress condition of Samples 19 to 24 was similar to that of normally consolidated soils under external loadings. Samples 19 to 24 had higher structural strengths than Samples 1-6 before microbial activity. This could be related to the field conditions such as, future biogas generation when tailings pond is capped (by sand, coke, etc.) for consolidation and reclamation.

Before microbial activity, Samples 19 to 24 and 25© to 27© were consolidated to 1.0 kPa, then the loading was maintained. During microbial activity, Samples 19 to 21 were under atmospheric pressure plus about 1.0 m water head. They were used to model the microbial activity of the MFT at shallow depths of the tailings pond. Samples 22 to 24 and 25© to 27© were under 60 kPa air pressure plus about 1.0 m water head. They were used to model the microbial activity of the MFT at 6-7 m depth below the water surface at the tailings pond. Tests 25© to 27© were conducted to sacrificially obtain chemical and microbiological samples during microbial activity. The test conditions of Samples 25© to 27© were identical to those of Samples 22 to 24.

9.2 Test Materials and Sample Preparation

The initial MFT material was obtained from about 2.5 m depth below the water–MFT interface at Sta. 2 of the MLSB. The properties of the field material are

described in Section 7.2. The initial MFT had a solids content of 40.6% and ratio of fines/(fines + water) of about 0.39. The field material was mixed with pond water to reconstitute the sample. Table 9.1 shows some parameters of the reconstituted sample, and Table 9.2 shows some initial information of Samples 19 to 21.

9.3 Consolidation before Microbial Activity

Since the reconstituted samples were very soft (the solids content was 34.7%), direct application of 1.0 kPa might have damaged them. Instead, the 1.0 kPa loading was applied by two steps: 0.4 kPa and 1.0 kPa. Each step was applied by placing a steel ring on a plastic loading plate (holes were drilled in the plate to allow gas bubbles to escape). A filter paper and a geotextile sheet were placed between the MFT interface and the plate to protect the solid particles from squeezing out of the loading plate. The gas bubbles could be released to the headspace from the gap between the plate and the cell wall. When gas releasing, the dynamic interaction between the sample and the plate also helped gas bubble escape. The consolidation tests were conducted at 4^{o}C temperature. A sketch of the consolidation test is shown in Figure 9.1. Water was drained from the top and bottom of the sample. The interface movements were measured using a Schaevitz LVDT for each test, and the pore water pressure changes in Sample 19 were monitored during consolidation testing. The detailed results of the consolidation tests are shown in Appendix G. Table 9.3 summarizes some parameters of Samples 19 to 24 at the end of 0.4 kPa consolidation. After 0.4 kPa consolidation, the average void ratio was about 3.1, the solids content was about 43%.

After the consolidation under 0.4 kPa loading was finished, additional 0.6 kPa loading was applied by placing another steel ring above the existing one. Table 9.4 summarizes some parameters of Samples 19 to 24 at the end of 1.0 kPa consolidation. After the test, the average void ratio was about 2.65, the solids

content was about 47.5%, and excess pore water pressure was dissipated to close to zero.

9.4 Permeability Tests before Microbial Activity

After 1.0 kPa consolidation was finished, the apparatus for gas-MFT densification and permeability tests were installed as shown in Figure 6.1. Constant head difference was applied to each sample to induce upward flow. During permeability tests, Samples 19 to 21 were under atmospheric pressure plus about 1.0 m water head, and Samples 22 to 24 were under 60 kPa back pressure plus about 1.0 m water head. The room temperature was kept at 4^{o}C.

Figure 9.2 and Figure 9.3 show the flow velocity vs. time for Tests 19 to 21 and Tests 22 to 24, respectively. Table 9.5 summarizes the results of the constant head permeability tests. The coefficients of permeability of Samples 19 to 24 were close before microbial activity.

9.5 Results for Tests 19 to 21

9.5.1 Volume Change during Microbial Activity

After consolidation and permeability tests were finished, the room temperature was raised to 24^{o}C to activate microbial activity.

Figure 9.4 shows the room temperature changes over time during microbial activity. It took about 40 hours for the temperature to increase from 4^{o}C to 24^{o}C. Due to defrosting operations of the temperature-controlling system, the room temperature fluctuated about 2-3^{o}C for every 10 hour interval. Due to some problems with the temperature-controlling device, significant fluctuations in

temperature occurred during two periods: from 610 hours to 660 hours, and from 1390 hours to 1570 hours.

Henry's law was used to calculate the dissolved gas masses in Samples 19 to 21. It is assumed that the generated gas was mainly methane. The calculated gas masses were converted to the equivalent gas volumes at standard temperature and pressure (STP). The results are shown in Table 9.6.

Figure 9.5 shows the changes of the total gas volume (trapped gas plus released gas at STP) with time in Samples 19 to 21. Gas generations in Sample 19 and Sample 20 were similar. During the first 350 hours, total gas volumes slowly increased with time in Samples 19 and 20. From 350 hours to 650 hours, gas generation was gradually accelerated in the two samples. This period can be regarded as the transitional period from slow gas generation to rapid gas generation. After 650 hours, gas was generated very rapidly in both Samples 19 and 20. After about 1400 hours, gas generation in Samples 19 and 20 obviously slowed down. In Sample 21, during the first 200 hours, gas was generated very rapidly, and then obviously slowed. At the end of testing, total gas generation volumes (at STP) in Samples 19 to 21 were 240 mL, 198 mL, and 350 mL, respectively. Although no sodium acetate was added to Sample 19, after more than 100 day incubation a large amount of gas was generated. This indicates that the natural MFT at the tailings pond has strong potential to become active with methanogens if a suitable environment is provided.

Figure 9.6 shows the changes of the released gas volume with time in Samples 19 to 21. Gas started to be released from Samples 19 and 20 after 450 hours. From 450 hours to 650 hours, gas was slowly released from the MFT. After 650 hours, with rapid biogas generation, gas bubbles were rapidly released from the two samples. From Sample 21, gas was released at slow rates from 270 hours to 550 hours. After 550 hours, gas release obviously accelerated. At the end of testing, the released gas volumes (at STP) from Samples 19 to 21 were 134 mL, 105 mL

and 187 mL, respectively. For each sample, the released gas volume accounted for more than 50% the total gas generation volume.

Figure 9.7 shows the changes of gas content with time in Samples 19 to 21. In Samples 19 and 20, the gas contents slowly increased during the first 350 hours. From 350 to 650 hours, the gas contents quickly increased in the two samples with rapid gas generation. During this period, most of the generated gas was trapped in the samples. After 650 hours, gas contents in the MFT increased approximately linearly with time. In Sample 21, the gas content rapidly increased during the first 200 hours, then increased at slower rates. At the end of testing, the gas contents in Samples 19 to 21 were 10.7%, 9.4% and 15.2%, respectively. Figure 9.8 shows the changes of the gas void ratio with time in Samples 19 to 21. At the end of testing, the gas void ratios in Samples 19 to 21 were 0.39, 0.34 and 0.58, respectively.

Figure 9.9 shows the interface movements of Samples 19 to 21 during microbial activity. During the first 350 hours, the interfaces of Samples 19 to 20 slowly settled. After 350 hours, the interfaces were stable or slowly expanded due to accelerated gas generation. During the first 200 hours, the interface of Sample 21 rapidly moved up due to rapid increases of the trapped gas volume. From 200 to 550 hours, it was stable. After 550 hours, due to rapid gas release, the interface continuously settled with time. At the end of testing, the interfaces of Samples 19 and 20 were close to the initial elevations, and the interface elevation of Sample 21 was 2.25 mm above its initial location.

Figure 9.10 shows the changes of the water drainage volume from Samples 19 to 21 during microbial activity. During the first 40 hours, water was rapidly drained out from Samples 19 and 20. This might be related to the rapid temperature increase. From 40 hours to 350 hours, water drainage from the two samples was slow. From 350 to 650 hours, with biogas generation accelerating, water drainage rates in the two samples increased. After 650 hours, water drainage volumes

increased approximately linearly with time. In Sample 21, during the first 200 hours, water was rapidly drained out from the sample and gas was rapidly generated. After 200 hours, water drainage rates obviously decreased. At the end of testing, the drained water volumes from samples 19 to 21 were 97 mL, 89 mL and 106 mL, respectively. Figure 9.11 shows the changes of the water void ratios in Samples 19 to 21 during microbial activity. At the end of testing, the water void ratios of Samples 19 to 21 were 2.25, 2.32 and 2.23, respectively.

Figure 9.12 shows the changes of bulk density of Samples 19 to 21 during microbial activity. With the increase of the trapped gas volume in the MFT, the bulk density of the MFT decreased with time. In Samples 19 and 20, during the first 350 hours, the bulk densities were relatively stable due to slow gas accumulation in the MFT. After 350 hours, the bulk densities in the two samples had obviously decreased. In Sample 21 the bulk density rapidly decreased during the first 200 hours due to rapid gas generation. After 600 hours, the bulk density in Sample 21 was relatively stable since the gas content was not significantly changed.

Figures 9.13 to 9.15 show the volumetric changes (total gas volume, trapped gas volume, released gas volume (at STP), and water drainage volume) in Samples 19 to 21, respectively. In Samples 19 and 20, gas was generated slowly from 40 to 350 hours, and correspondingly, water was drained out of the MFT slowly at this time. From 350 to 650 hours, with gas generation accelerating, water drainage rates increased. In Sample 21, both rapid gas generation and rapid water drainage occurred during the first 200 hours, then with gas generation slowing down, water drainage rates visibly decreased.

Figures 9.16 to 9.18 show the changes of the trapped gas volume and total MFT volume in Samples 19 to 21, respectively. From 50 hours to 350 hours, trapped gas volumes in Samples 19 and 20 increased slowly, and the total MFT volumes slightly decreased with time. Water was drained out at slow rates during this

period. After 350 hours, both the trapped gas volumes and total MFT volumes increased, but the trapped gas volumes increased more rapidly than the total MFT volumes. Water was pushed out by a rapid increase in trapped gas bubbles. In Sample 21, both the trapped gas volume and total MFT volume increased with time during the first 200 hours, but MFT expansion rates lagged behind the increase rates of the trapped gas volume. As a result, water was rapidly pushed out from the MFT. From 200 hours to 600 hours, the trapped gas volume slowly increased with time, the global MFT volume was relatively stable, and more water was drained out from the MFT. After 600 hours, the total MFT volume slightly decreased with time, and the trapped gas volume increased very slowly. Water was drained out at slow rates during this period. During intense microbial activity and the rapid accumulation of trapped gas volume, MFT expansion lagged behind the increase of the trapped gas volume due to the structural resistance. Water was pushed out of the MFT rapidly.

9.5.2 Excess Pore Pressure and Operative Stress

Figure 9.19 shows the changes of excess pore water pressure and operative stress at the bottom (E1) of Sample 19 during microbial activity. During the first 350 hours, due to slow gas generation, total stress was relatively stable. After 350 hours, with accelerated gas generation, there was a slight decrease in total stress. During the first 45 hours, due to a rapid temperature increase, excess pore water pressure increased from 0 to 0.28 kPa, and operative stress decreased from 1.19 kPa to 0.96 kPa. From 45 hours to 350 hours, gas generation occurred at slow rates. During this period, excess pore water pressure decreased from 0.28 kPa to 0 kPa, and operative stress increased from 0.96 kPa to 1.2 kPa. From 350 hours to 650 hours, with gas generation accelerating, both the trapped gas volume and total MFT volume increased with time, but the trapped gas volume increased more rapidly than did the total MFT volume. Excess pore water pressure increased from 0 to 0.1 kPa, and operative stress decreased from 1.2 kPa to 1.1 kPa. During this period, the accelerated gas generation was restricted by slow

structure expansion, and as a result, some small gas bubbles pushed the surrounding pore water. This caused additional excess pore water pressure. While the excess pore water pressure was partially dissipated, accelerated gas bubble growth generated additional excess pore water pressure. Water drainage from the MFT was accelerated during this period. After 650 hours, both excess pore water pressure and operative stress were relatively stable, and water drainage rates were slow.

Figure 9.20 shows the changes of excess pore water pressure and operative stress at 1.45 cm elevation (E2) above the bottom of Sample 19, Similar changes to those seen at E1 are shown. The pore pressure transducer at 3.95 cm elevation (E3) above the bottom of Sample 19 was out of order shortly after warming up, due to some unknown electrical or mechanical problems of the transducer itself. Unfortunately, no useful data was available at this location.

Figures 9.21 to 9.23 show the changes of excess pore water pressure and operative stress E1, E2, and E3, respectively, in Sample 20. Similar changes to those observed in Sample 19 are shown.

Figure 9.24 shows the changes of excess pore water pressure and operative stress at the bottom (E1) of Sample 21 during microbial activity. The total stress noticeably decreased during the first 200 hours, due to rapid gas generation and a significant decrease in bulk density. After 200 hours, the total stress became relatively stable (the obvious fluctuations came from those of the water head in the plastic tube). During the first 40 hours, excess pore water pressure rapidly increased from 0 to 0.71 kPa, and operative stress rapidly decreased from 1.19 kPa to 0.48 kPa, mainly due to a rapid temperature increase. From 40 hours to 200 hours, gas was generated very rapidly and there was swift water drainage from the MFT. Excess pore water pressure and operative stress were relatively stable, however, from 40 hours to 100 hours, there were slight excess pore water pressure increases. From 200 hours to 600 hours, excess pore water pressure

rapidly decreased from 0.67 kPa to 0 kPa, and operative stress increased from 0.48 kPa to 1.1 kPa. From 600 hours to 2424 hours, biogas generation continually proceeded, but most of the generated gas was released from the MFT. There were no obvious changes in excess pore water pressure or operative stress at this time. Water drainage from the MFT was attributed to structural adjustments of the MFT.

Figure 9.25 shows the changes of excess pore water pressure and operative stress at 1.45 cm elevation (E2) above the bottom of Sample 21 during microbial activity. Similar changes to those at E1 can be observed.

Figure 9.26 shows the changes of excess pore water pressure and operative stress at 3.95 cm elevation (E3) above the bottom of Sample 21. The total stress at E3 was less affected by gas generation than at the lower elevations E1 and E2. During the first 40 hours, excess pore water pressure increased from 0 to 0.58 kPa due to a rapid temperature increase, and operative stress decreased from 1.04 kPa to 0.46 kPa. From 40 hours to 200 hours, excess pore water pressure obviously increased from 0.58 kPa to 0.7 kPa, and operative stress decreased from 0.46 kPa to 0.35 kPa. This strongly confirms that additional excess pore water pressure can be produced during rapid gas generation. From 200 hours to 600 hours, gas generation slowed down, and gas started to be released from the MFT. Excess pore water pressure rapidly decreased from 0.7 kPa to 0.29 kPa, and operative stress increased from 0.35 kPa to 0.75 kPa. From 600 to 2424 hours, there were no obvious changes in excess pore water pressure or operative stress.

Table 9.7 gives a summary of some parameters of Samples 19 to 21 at the end of the gas densification tests. Although the water void ratios of the three samples were close at the end of testing, the drainage rates for each sample were related to gas generation rates.

9.5.3 Permeability Tests after Microbial Activity

After microbial activity had diminished, the room temperature was lowered to 4°C to inhibit it. Constant head differences were applied to the samples to cause upward flow. Figure 9.27 shows the flow velocity vs. time in Tests 19 to 21. After about 2000 minutes, outflow velocities of Samples 20 and 21 slightly increased with time. This was likely caused by the existence of weak microbial activity and very slow biogas generation at 4° C temperature.

Table 9.8 gives a summary of constant head permeability Tests 19 to 21. After microbial activity, the coefficients of permeability of Samples 19 to 21 were very close, and were slightly lower than those before microbial activity.

9.5.4 Discussion

9.5.4.1 Volume Change

During the long-term consolidation tests (more than four months) at 4°C, part of the added sodium acetate in Samples 20 and 21 was likely depleted by very weak microbial activity; a few occluded gas bubbles were observed in Samples 20 and 21 before the temperature was raised. In addition, part of the dissolved sodium acetate migrated out of the MFT along with water drained during consolidation. It is likely that only a small amount of sodium acetate remained in Sample 20 after 1.0 kPa consolidation. This may explain why the microbial activities in Samples 19 and 20 were similar.

Water drainage rates of Samples 19 to 21 were affected by gas generation rates. From 40 to 350 hours, gas was slowly generated in Samples 19 and 20, and correspondingly, water drained out from these samples slowly. From 350 to 650 hours, with gas generation accelerating, water drainage rates increased. In Sample 21, gas was generated very rapidly during the first 200 hours, and in the mean time, water drained out rapidly. After 200 hours, with gas generation slowed down, water drainage rates decreased. Compared with Samples 13 to 15, water

drainage in Samples 19 to 21 was less affected by gas generation. This is because after 1.0 kPa consolidation, the structures of Samples 19 to 21 were denser and more stable than those of Samples 13 to 15, and the compressibility coefficients of Samples 19 to 21 were much smaller. Structural collapse in Samples 19 to 21 was not as obvious as in Samples 13 to 15 during periods of intense gas release.

In Sample 21, the trapped gas volume increased rapidly during the first 200 hours while the MFT expansions lagged far behind them, due to structural resistance. This led to rapid water drainage from the MFT. After 200 hours, the trapped gas volume slowly increased, and the total MFT volume slowly decreased. Water was drained out at slow rates during this period.

9.5.4.2 Excess Pore Water Pressure and Operative Stress

Since microbial activity in Sample 19 was very similar to that in Sample 20, the changes of excess pore water pressure and operative stress in the two samples were similar. After the temperature was raised to 24^{o}C, the increases of excess pore water pressures in Samples 19 to 21 were more significant than those in Samples 1 to 3 and Samples 13 to 15. This is because of the higher initial operative stresses in Samples 19 to 21 before temperature was raised.

In Samples 19 and 20, excess pore water pressures decreased, and operative stress increased from 35 to 350 hours. With excess pore water pressure dissipating, water drained out from the MFT. From 350 to 650 hours, with excess pore water pressures increasing, water drainage accelerated in samples 19 and 20. During this period, trapped gas volumes rapidly increased, while MFT volume expansion was restricted by structural resistance. Small gas bubble growth pushed the nearby pore water. This led to excess pore water pressure increases. While excess pore water pressure was partly dissipated, extra excess pore water pressure was produced. After 650 hours, excess pore water pressures and operative stresses were almost stable in the two samples, and water drained out very slowly.

In Sample 21, gas was generated rapidly during the first 200 hours. With the increase of the trapped gas volume in the MFT, total stress decreased over time. However, the decreases in the total stress were not uniform in the sample. The decreases in total stress at lower elevations (for example, at E1 and E2) were more obvious than at the higher elevation (E3). From 40 to 200 hours, excess pore water pressures at E1 and E2 were stable or slightly increased with time, operative stresses were stable or slightly decreased. In contrast, excess pore water pressure obviously increased, and operative stress obviously decreased at E3 during rapid gas generation. When the total stress maintained stability, the increases of excess pore water pressure became more obvious. While excess pore water pressure was partly dissipated, extra excess pore water pressure was generated. In the mean time, rapid water drainage occurred. From 200 to 600 hours, with gas generation slowing down and gas being released from the MFT, less (or no) extra excess pore water pressure was produced. As such, the dissipation of excess pore water pressure became more obvious than in the prior period. After 600 hours, both excess pore water pressure and operative stress became stable. The slow water drainage can be attributed to MFT structural adjustments.

In Samples 19 to 21, when trapped gas volumes rapidly increased, extra excess pore water pressures were generated. In the mean time, there was rapid water drainage. This process can be considered an internal loading process. This internal loading process was not an immediate one, for it took a long time. During this period, excess pore water pressure dissipation and excess pore water pressure generation proceeded concurrently**.**

9.5.4.3 Structure Change and Permeability

The detailed structural changes of Samples 19 to 21 during microbial activity are shown in Appendix I. Before the room temperature was raised to 24^{o}C, a few gas bubbles appeared at the upper parts of Samples 20 and 21. This indicates that very weak microbial activity occurred during the long-term consolidation at 4^{o}C. Parts of the added sodium acetate were likely depleted.

Macro-structural changes in Samples 19 and 20 were very similar. There were no obvious changes during the early period (about 10-15 days). With accelerated gas generation and gas bubble release, some occluded gas bubbles and small cracks were observed. No large cracks and fractures were seen.

In Sample 21, gas was generated very rapidly after temperature was raised. Large cracks were formed after a few days. Some ellipsoidal gas bubbles were trapped in the large cracks. With gas bubbles being released, the large cracks became small and tight.

After microbial activity, the coefficients of permeability of Samples 19 to 21 were close. There were no obvious changes in the coefficients of permeability in Samples 19 to 21 after microbial activity. The structural strength and operative stress restricted the development of some open structures (cracks and fractures). Most of the cracks were tightly filled with large gas bubbles. They could not act as convenient drainage paths, so the coefficient of permeability was controlled by the water void ratio.

9.6 Results for Tests 22, 23, and 24

During microbial activity, Samples 22 to 24 were under 60 kPa air pressure plus about 1.0 m water head. The tests were used to model the microbial activity of MFT at about 6-7 m depth below the water surface at the tailings pond. The 1.0 kPa loading was maintained during microbial activity. By Henry's law, the

dissolved gas mass was calculated. Table 9.9 shows the equivalent volumes (at STP) of the dissolved gas in Samples 22 to 24.

9.6.1 Volume Change

Figure 9.28 shows the changes of the total gas volume (trapped gas plus released gas at STP) in Samples 22 to 24 during microbial activity. In Sample 22, the total gas volume slowly increased during the first 850 hours. After 850 hours, gas generation gradually accelerated. After about 1400 hours, gas was generated rapidly in this sample. In Sample 23, the total gas volume rapidly increased during the first 50 hours. From 50 to 400 hours, gas was generated at slow rates. After 400 hours, gas generation gradually accelerated. After about 650 hours, the total gas volume rapidly increased with time. In Sample 24, the total gas volume rapidly increased during the first 200 hours. After 200 hours, gas generation slowed down. At the end of testing, total gas volumes (at STP) in Samples 22 to 24 were 101 mL, 148 mL and 241 mL, respectively.

Figure 9.29 shows the changes of the released gas volume (at STP) in Samples 22 to 24. Gas bubbles started to be released from Samples 22 to 24 after 1700 hours, 1050 hours and 520 hours, respectively. At the end of testing, the released gas volumes from Samples 22 to 24 were 22 mL, 30 mL and 44 mL, respectively. Most of the generated gas was trapped in the MFT and only small parts of the generated gas were released.

Figure 9.30 shows the changes of the gas content in Samples 22 to 24 during microbial activity. Since most of the generated gas was trapped in the MFT, the gas content changes in each sample were similar to the total gas volume changes. At the end of testing, the gas contents in Samples 22 to 24 were 5.2%, 7.6% and 12.5%, respectively. Figure 9.31 shows the changes of the gas void ratio with time in Samples 22 to 24. At the end of testing, gas void ratios in Samples 22 to 24 were 0.19, 0.27 and 0.46, respectively.

Figure 9.32 shows the interface movements of Samples 22 to 24 during microbial activity. During the first 850 hours, with slow biogas generation, the interface of Sample 22 slightly settled, then became relatively stable. During the first 400 hours, gas generation in Sample 23 was slow, and the interface slightly settled with time. From 400 hours to 2420 hours, as gas generation accelerated, the interface of Sample 23 moved up slightly. During the first 100 hours, the interface of Sample 24 was stable. From 100 hours to 200 hours, the interface of Sample 24 moved up slightly, then became relatively stable.

Figure 9.33 shows the water drainage volumes from Samples 22 to 24 during microbial activity. In Sample 24, with rapid biogas generation, water was rapidly drained out of the MFT during the first 200 hours. After 200 hours, with biogas generation slowing down, water drainage rates obviously decreased. At the end of testing, water drainage volumes from Samples 22 to 24 were 65 mL, 76 mL and 106 mL. Figure 9.34 shows the changes of the water void ratio in Samples 22 to 24 during microbial activity. At the end of testing, the water void ratios of Samples 22 to 24 were 2.38, 2.33 and 2.23, respectively.

Figure 9.35 shows the changes in bulk densities of Samples 22 to 24 during microbial activity. In Sample 22, the bulk density was relatively stable during the first 850 hours due to slow gas generation. After 850 hours, the bulk density slightly decreased. In Sample 23, the bulk density was relatively stable during the first 400 hours, and then slowly decreased. In Sample 24, the bulk density obviously decreased during the first 200 hours due to a rapid increase of trapped gas bubbles in the MFT. After 200 hours, the bulk density decreased slowly. At the end of testing, the bulk densities of Samples 22 to 24 were 1.34 g/mL, 1.31 g/mL and 1.25 g/mL, respectively.

Figures 9.36 to 9.38 show the volumetric changes (total gas volume, trapped gas volume, released gas volume at STP and drained water volume) of Samples 22 to

24, respectively. In Sample 22, water drainage rates were almost constant during most of the time intervals. From 850 to 1400 hours, with gas generation accelerating, the water drainage rates of Sample 22 slightly increased. In Sample 23, from 400 hours to 650 hours, water drainage rates increased in accordance with accelerating gas generation. There was a clear connection observed between gas generation rates and water drainage rates in Sample 24. During the first 200 hours, as rapid gas generation occurred, water was rapidly drained out. After 200 hours, with biogas generation slowing down, water drainage from Sample 24 became slow. Figure 9.39 shows the water void ratio vs. total gas volume in Samples 22 to 24. With the increases of the gas generation volume, water void ratios in Samples 22 to 24 decreased.

Figures 9.40 to 9.42 show the changes of the trapped gas volume and total MFT volume with time in Samples 22 to 24. Similar changes occurred as in Samples 19 to 21. In Test 24, the trapped gas volume increased very rapidly during the first 200 hours, but the total MFT volume stayed relatively stable or increased slowly. As such, water was pushed out rapidly. After 200 hours, biogas generation lost its strong momentum. While the trapped gas volume increased at slow rates, the total MFT volume remained almost stable. Water was drained out at slower rates.

9.6.2 Excess Pore Pressure and Operative Stress

Figure 9.43 shows the changes of excess pore water pressure and operative stress at the bottom (E1) of Sample 22 during microbial activity. Since biogas generation in Sample 22 was slow and the test took place under 60 kPa air pressure, the trapped gas volume in the MFT was relatively small (the maximum gas content was 5.2%). During the test, the total stress was not obviously affected by biogas generation. During the first 50 hours, excess pore water pressure increased from 0 to 0.25 kPa, and operative stress decreased from 1.18 kPa to 0.94 kPa due to a rapid temperature increase. From 50 hours to 350 hours, excess pore water pressure decreased from 0.2 kPa to 0.15 kPa, and operative stress

increased from 0.94 kPa to 1.03 kPa. From 350 hours to 850 hours, both excess pore water pressure and operative stress were stable. After 850 hours, with accelerated biogas generation, excess pore water pressure slightly increased with time. It is likely that extra excess pore water pressure was produced during this period. After 1400 hours, both excess pore water pressure and operative stress again became stable. Throughout the test, the changes of excess pore water pressure and operative stress were not significant.

Figure 9.44 and Figure 9.45 show the changes of excess pore water pressure and operative stress at 1.45 cm (E2) and 3.95 cm (E3), respectively, above the bottom of Sample 22. Similar changes as those observed at E1 are shown.

Figure 9.46 shows the changes of excess pore water pressure and operative stress at the bottom (E1) of Sample 23. In the span of the first 45 hours, due to a rapid temperature increase, excess pore water pressure increased from 0 to 0.23 kPa, and operative stress decreased from 1.2 kPa to 0.9 kPa. From 45 to 400 hours, excess pore water pressure decreased from 0.23 kPa to 0.03 kPa, and operative stress increased from 0.94 kPa to 1.22 kPa. From 400 hours to 650 hours, excess pore water pressure increased from 0.4 kPa to 0.5 kPa, and operative stress decreased from 0.73 kPa to 0.66 kPa. With biogas generation accelerating from 400 to 650 hours, additional excess pore water pressure was likely produced. There was slight acceleration in the water drainage rate during this period. After 650 hours, there were no obvious changes in excess pore water pressure or operative stress.

Figure 9.47 shows the changes of excess pore water pressure and operative stress at 1.45 cm elevation (E2) above the bottom of Sample 23. During the first 45 hours, excess pore water pressure increased from 0 to 0.58 kPa, and operative stress decreased from 1.14 kPa to 0.59 kPa due to a rapid temperature increase and gas generation. From 45 to 400 hours, excess pore water pressure decreased and operative stress increased. From 400 to 650 hours, excess pore water

pressure slightly increased, and operative stress slightly decreased. After 650 hours, both excess pore water pressure and operative stress were stable.

Figure 9.48 shows the changes of excess pore water pressure and operative stress at 3.95 cm elevation (E3) above the bottom of Sample 23. Similar changes as those seen at E1 and E2 are shown.

Figure 9.49 shows the changes of excess pore water pressure and operative stress at the bottom (E1) of Sample 24. Due to a rapid increase in the trapped gas volume, as well as water being pushed out of the test cell, total stress decreased during the first 200 hours. During the first 50 hours, excess pore water pressure increased from 0 to 0.37 kPa due to a rapid temperature increase. Within the same period operative stress decreased from 1.19 kPa to 0.85 kPa. From 50 hours to 200 hours, excess pore water pressure increased from 0.37 kPa to 0.62 kPa, and operative stress decreased from 0.85 kPa to 0.6 kPa. While excess pore water pressure was partly dissipated, extra excess pore water pressure was generated during rapid gas generation. From 200 to 330 hours, with gas generation slowing down, the MFT interface slightly settled. Excess pore water pressure rapidly decreased from 0.62 kPa to near zero kPa, as operative stress increased from 0.6 kPa to 1.25 kPa. From 330 to 2420 hours, excess pore water pressure slightly decreased and operative stress slightly increased.

Figure 9.50 shows the changes of excess pore water pressure and operative stress at 1.45 cm elevation (E2) above the bottom of Sample 24. During the first 50 hours, excess pore water pressure increased due to a rapid temperature increase and gas generation. From 50 hours to 200 hours, with very rapid biogas generation taking place, excess pore water pressure increased from 0.35 kPa to 0.64 kPa, and operative stress decreased from 0.79 kPa to 0.5 kPa. In this time frame it was clear to see that additional excess pore water pressure had been generated during rapid gas generation, and that water was drained out rapidly.

Figure 9.51 shows the changes of excess pore water pressure and operative stress at 3.95 cm elevation (E3) above the bottom of Sample 24. Similar changes as those seen at E1 and E2 are outlined.

Table 9.10 summarizes some parameters of Samples 22 to 24 at the end of gas densification testing. Sample 24 had the highest gas void ratio and the lowest water void ratio among the three samples.

9.6.3 Permeability Tests after Microbial Activity

After microbial activity diminished, the room temperature was lowered to 4^{o}C, at which time constant head permeability tests were conducted. During permeability testing, 60 kPa air pressure was equally applied to the inflow and outflow tubes. Figure 9.52 shows the flow velocity vs. time in permeability Tests 22 to 24. For each test, the inflow velocity was slightly higher than the outflow velocity. It is likely that part of the inflow water replaced some gas bubbles which were pushed out by the upward gradient. Table 9.11 summarizes the results of the permeability tests. After microbial activity, the coefficients of permeability of Samples 22 to 24 were similar. For each sample, the coefficient of permeability after microbial activity was close to that before microbial activity.

9.6.4 Discussion of Tests 22 to 24

9.6.4.1 Consolidation and Permeability before Microbial Activity

After summarizing a series of consolidation tests on oil sands fine tailings, Suthaker (1995) concluded that, a single void ratio vs. effective stress relationship was not enough to describe the consolidation behaviour. The compressibility was affected by the initial void ratio (or solids content). The higher the initial solids content of the sample, the smaller the final void ratio it reached under an applied effective stress. From Suthaker's testing results, after 1.0 kPa consolidation the

void ratios for the MFT samples with initial solids contents 20%, 25%, and 30% were 6.7, 5.4, and 3.7, respectively. With the increase of initial solids content, the void ratio after consolidation obviously decreased. The initial solids contents of Samples 10 to 12 and Samples 19 to 24 were about 35%. No consolidation data was found for the MFT with 35% initial solids content. A value obviously below 3.7 is anticipated. After 1.0 kPa consolidation, the void ratios of Samples 10 to 12 and Samples 19-24 ranged from 2.5 to 2.65, which appear to be reasonable compared with Suthaker's tests.

By fitting the results of laboratory permeability tests on oil sands mature fine tailings, Pollock (1988) recommended the following relationship between coefficient of permeability and void ratio:

$$k = 7.425 \times 10^{-11} \times e^{3.847} \quad [9\text{-}1]$$

k: coefficient of permeability in m/s, e: void ratio, at 20°C.

After self-weight consolidation, the void ratios of Samples 1 to 6 were about 3.6. From Pollock's equation, the coefficient of permeability is 1.03×10^{-8} m/s. The measured coefficients of permeability (at 4°C) of Samples 1 to 6 after self-weight consolidation were $2.6 \sim 4.0 \times 10^{-9}$ m/s. The viscosity of water at 4°C is about 1.56 times that at 20°C (Head, 1989). From the following equation (Head, 1989):

$$k_{20} = (\square_T/\square_{20})\, k_T \quad [9\text{-}2]$$

The coefficients of permeability of Samples 1 to 6 at 20°C were $4.06 \sim 6.24 \times 10^{-9}$ m/s. The calculated coefficient of permeability from Pollock's equation is 1.7~ 2.5 times of the measured.

After 1.0 kPa consolidation, the void ratios of Samples 19 to 24 were about 2.65. The calculated coefficient of permeability from Pollock's equation is 3.15×10^{-9}

m/s. The measured coefficients of permeability (at 4°C) of the three samples were 7.3~ 11.4 × 10^{-10} m/s which were 1.1~ 1.8 × 10^{-9} at 20°C by Equation 9-2. The calculated coefficient of permeability from Pollock's equation is 1.8 ~ 2.8 times of the measured.

The calculated coefficients of permeability from Pollock's equation were slightly larger than the measured. Pollock's equation was obtained in 1988. The difference is likely due to MFT property changes after more than 10 years sedimentation.

9.6.4.2 Volume Change

During microbial activity, 60 kPa air pressure was applied to the test systems of Samples 22 to 24. This accounted for the major differences between Tests 19 to 21 and Tests 22 to 24.

Only small parts of the generated gas (less than 30%) were released from Samples 22 to 24. Gas release from Samples 22 to 24 occurred with more difficulty than that of Samples 19 to 21. Similar phenomena occurred in Tests 4 to 6. Under high pressure, the MFT structures (fractures and cracks) were at tightly closed conditions, and the sizes of gas bubbles were small.

With the increases of microbial activity and biogas generation in Samples 19 to 24, water drainage volumes increased. Figure 9.53 shows the total gas generation volume (at STP) vs. water drainage volume in Samples 19 to 24. There existed a strong relationship between the total gas volume (trapped + released gas volume at STP) and the water drainage volume.

For each sample, water drainage rates were related to gas generation rates. With gas generation accelerating from 850 to 1400 hours, the water drainage rate in Sample 22 increased. Similarly, the water drainage rate in Sample 23 increased after 400 hours as gas generation accelerated. There was rapid water drainage in

Sample 24 during the first 200 hours, due to rapid gas generation. After 200 hours, with gas generation slowing down, the water drainage rate decreased.

In Sample 22, gas generation was slow during the first 850 hours (the degree of saturation was greater than 98%). The behavior of the sample was similar to that of a saturated soil. The trapped gas volume increased slowly, and the total MFT volume decreased with time. The water drainage volume increases were approximately equal to the MFT volume decreases. With gas generation accelerating after 850 hours, MFT settlements were hindered. While the trapped gas volume increased rapidly, the total MFT volume was almost constant. During this period, water drainage volume increases were approximately equal to trapped gas volume increases. The volumetric changes in Sample 23 were similar to those in Sample 22. In Sample 24, the trapped gas volume increased rapidly during the first 200 hours, but the total MFT volume was relatively stable (or slightly increased) due to structural resistance. Water was rapidly pushed out at this time. After 200 hours, the trapped gas volume increased at slower rates, but the total MFT volume was almost constant. Water was drained out at slower rates.

9.6.4.3 Excess Pore Pressure and Operative Stress

In Sample 22, excess pore water pressure and operative stress were relatively stable during most times of testing. Changes occurred when temperature or gas generation rate was altered. During the first 50 hours, excess pore water pressure increased and operative stress decreased due to a rapid temperature increase. From 50 to 350 hours, excess pore water pressure decreased and operative stress increased. During this period, the MFT behavior was similar to that of a saturated soil. From 850 to 1400 hours, with gas generation accelerating, excess pore water pressure slightly increased with time, as did the water drainage rates. During the other periods, there were no obvious changes in excess pore water pressure or operative stress in Sample 22. The slow water drainage during these periods was likely due to structural adjustments. The changes in Sample 23 were similar to those in Sample 22.

The changes of excess pore water pressure and operative stress in Sample 24 were more significant than those in Samples 22 and 23. During the first 200 hours, excess pore water pressure significantly increased due to a rapid temperature increase and gas generation. Excess pore water pressure continually increased once temperature became stable. This strongly supports the idea that extra excess pore water pressure can be produced during rapid gas generation. Water was drained out of the MFT very rapidly during this period. This process is similar to an internal loading process. Since the internal loading process was not an immediate one (it took about 200 hours), excess pore water pressure dissipation and extra excess pore water pressure production could proceed concurrently. From 200 to 330 hours, with gas generation noticeably slowing, excess pore water pressure rapidly decreased and operative stress rapidly increased.

9.6.4.4 Macro-Structure and Permeability

Due to the application of 60 kPa back pressure and the existence of structural strengths, macro- structural changes in Samples 22 to 24 were less evident than those in Samples 19 to 21. Most of the occluded gas bubbles were small and not very visible, and cracks were tightly closed and short. There was no large crack observed. The details of the structural changes are shown in Appendix I.

There were no obvious changes in coefficients of permeability of Samples 19 to 24 after microbial activity. This is because the structural strength and high total stress restricted the development of some open structures (cracks and fractures), so the coefficient of permeability was mainly controlled by the water void ratio.

9.7 Results for Chemical Tests 25©, 26©, and 27©

The test conditions and procedures of Samples 25© to 27© were similar to those of Samples 22 to 24, respectively. Different amounts of sodium acetate, 0 g, 0.6 g,

and 1.75 g per liter MFT, were added to Samples 25© to 27©, respectively. The initial sample heights (before consolidation) were about 11 cm. 60 kPa air pressure was applied to the test system to model the microbial activity of the MFT at 6-7 m depth below the water surface at the tailings pond.

During consolidation (at 4°C) and microbial activity (at 24°C), four chemical sub-samples were obtained at different times from each cell. The time when sodium acetate was mixed with the MFT was defined as zero time. The four samples were obtained on Day 3, Day 12, Day 154 and Day 267, respectively. The first two samples were obtained during consolidation testing at 4°C, the third sample was obtained during microbial activity (15 days after warming up) at 24°C, and the fourth sample was obtained at the end of testing at 4°C. The detailed chemical changes of Samples 25© to 27© are shown in Appendix J.

The chemical changes in Tests 25© to 27© were similar to those in Tests 16© to 18©. After microbial activity, the pH values slightly increased, the Electrical Conductivity values decreased with time. Sulfate concentrations decreased to near 0 from the first to the second sampling, then, slightly increased. HCO_3^- concentrations decreased with time in Tests 27©, but were relatively stable in Tests 25© to 26©. During microbial activity, the concentrations of the cations (Na^+, K^+, Ca^{2+}, Mg^{2+}) decreased with time. Relative to Tests 27©, the chemical parameters in Tests 25© and 26© were less changed.

9.7.1 MPNs of Methanogens and Sulphate Reducing Bacteria (SRB)

During testing, four microbiological sub-samples were obtained from each cell of Tests 25© to 27© at different times. The zero sampling was defined as the time when sodium acetate was mixed with the MFT. The first and second samples were obtained at 4°C after three and 120 days, respectively. The room temperature was raised to 24°C after 139 days. The third sample was obtained after 154 days (15 days after microbial activity had started) at 24°C. The fourth

sampling was conducted after 267 days (at the end of testing) at 4^{o}C. The details of the MPN test results of Samples 25© to 27© are shown in Appendix J.

During testing, the methanogen MPN values of Samples 25© to 27© ranged from 10^2 to 10^4, and the MPN values of Sulphate Reducing Bacteria (SRB) ranged from 10^3 to 10^5. The overall changes of the MPNs were not significant. During microbial activity (15 days after microbial activity had started), Sample 27© slightly had the highest MPN value of methanogens and the lowest MPN value of SRB among the three samples. This should have been favorable for methanogen activity and methane gas generation in Sample 27©.

9.8 Summary

Eighteen gas MFT densification tests and nine chemical sampling tests were carried out within 14 months. The MFT densification properties were studied under different conditions, such as different stress histories (normally consolidated Samples 1 to 6 and 19 to 24; under-consolidated Samples 13 to 15 and over-consolidated Samples 10 to 12), different pressures (0 and 60 kPa air pressures) and different microbial activities (0, 0.6 and 1.75 g sodium acetate added per liter MFT). During the densification tests, various parameters were measured and structural changes were observed. This section summarizes the results of Tests 19 to 24 and 25©-26©.

1. Most of the generated gas in Samples 19-21 was released to the headspace, but only small parts of the generated gas in Samples 22-24 was released. Under higher pressure, the generated gas had more difficulty escaping. This can be attributed to the different structural changes which occur under different pressures.
2. With the increase of microbial activity in Samples 19-24, water drainage increased. Water drainage rates in Samples 19-24 were affected by gas generation rates.

3. When gas was generated rapidly in Samples 19-24, MFT volume expansions lagged behind trapped gas volume increases due to structural resistance. As a result, water was rapidly pushed out of the MFT.
4. For Samples 19–20 and 22-23, MFT behavior in early periods was similar to that of a saturated soil; gas generation was slow. Temperature-induced excess pore water pressures were gradually dissipated, and water was drained out at slow rates.
5. During rapid gas generation in Samples 19-24, excess pore water dissipation and extra excess pore water pressure generation proceeded concurrently, and water was drained from the MFT rapidly.
6. During the late periods of microbial activity in Samples 19-24, gas was intensely released from the MFT and trapped gas volumes increased slowly. There were no obvious changes in excess pore water pressure or operative stress. The slow water drainage during this period could have been attributed to MFT structural adjustments.
7. Due to the structural strength and operative stress in Samples 19-24, and to the high pressure in Samples 22-24, cracks and fractures were mostly in a closed condition and tightly filled with gas bubbles. There were no obvious changes in coefficients of permeability after microbial activity.
8. The chemical changes in Samples 25©-26© were similar to those in Samples 16©-18©. After microbial activity, pH values slightly increased, the Electrical Conductivity values decreased with time. The concentrations of the cations (Na^+, K^+, Ca^{2+}, Mg^{2+}) decreased with time.
9. During rapid gas generation, Sample 27© had the highest methanogen MPN and lowest SRB MPN among the three samples. This was expected to be favorable for methanogenesis activity and methane gas production.

Table 9-1 Some Parameters of Samples 19-24 before Consolidation Tests

Solids Content (%)	Fines/(fines + water) (%)	Void Ratio (e)	Density (g/ml)	Water Content (%)	Bitumen Content (%)
34.65	32.2	4.5	1.252	188.6	4.29

Table 9-2 Summary of Some Initial Information of Samples 19-24

Test No	Total Mass (g)	Solids Mass (g)	Water Mass (g)	Total Volume (ml)	Solids Volume (ml)	Height (cm)	Sodium Acetate (g/L MFT)
19	1706.3	591.2	1115.1	1362.9	247.8	7.53	0
20	1708.4	592	1116.4	1364.5	248.1	7.55	0.6
21	1752.3	607.2	1145.1	1399.6	254.5	7.69	1.75
22	1711.5	593	1118.5	1367	248.5	7.52	0
23	1763.3	611	1152.3	1408.3	256	7.78	0.6
24	1727.8	598.7	1129.1	1380	250.9	7.67	1.75

Table 9-3 Some Parameters of Samples 19-24 after 0.4 kPa Consolidation

Test No	Sample Height (cm)	Density (g/ml)	Void Ratio (e)	Solids Content (%)
19	5.6	1.339	3.09	43.5
20	5.71	1.333	3.16	43.0
21	5.85	1.332	3.18	42.9
22	5.63	1.337	3.12	43.4
23	5.87	1.333	3.15	43.1
24	5.77	1.335	3.14	43.2

Table 9-4 Some Parameters of Samples 19-24 after 1.0 kPa Consolidation

Test No	Sample Height (cm)	Density (g/ml)	Void Ratio (e)	Solids Content (%)
19	4.98	1.38	2.64	47.5
20	5.04	1.38	2.67	47.2
21	5.10	1.38	2.64	47.4
22	4.98	1.38	2.64	47.5
23	5.14	1.38	2.63	47.5
24	5.09	1.38	2.65	47.4

Table 9-5 Results of Permeability Tests 19-24 before Microbial Activity

Test No	19	20	21	22	23	24
Gradient	0.843	0.774	0.804	0.783	0.817	0.746
Average Flow Velocity (10^{-10} m/s)	7.13	7.64	5.93	7.2	9.29	6.46
Coefficient of permeability (10^{-10} m/s)	8.46	9.87	7.38	9.2	11.37	8.66

Table 9-6 Dissolved Gas Volumes in Samples 19-21

Test No	19	20	21
Dissolved Methane Gas (10^{-3} mol)	0.982	0.981	1.0
Equivalent Vol. at STP (Ml)	24	24	24.5

Table 9-7 Some Parameters of Samples 19-21 after Microbial Activity

Test NO	Solids Content (%)	Density (g/ml)	Water Void Ratio	Gas Void Ratio	Total Void Ratio	Degree of Saturation (%)
19	51.5	1.274	2.25	0.39	2.64	85.2
20	50.8	1.287	2.32	0.34	2.66	87.1
21	51.7	1.213	2.23	0.58	2.81	79.4

Table 9-8 Results of Permeability Tests 19-21 after Microbial Activity

Test No.	19	20	21
Gradient	0.904	0.857	0.752
Average Flow Velocity (10^{-10} m/s)	6.66	6.71	5.17
Coefficient of Permeability (10^{-10} m/s)	7.37	7.83	6.88

Table 9-9 Dissolved Gas Volumes in Samples 22-24

Test No	22	23	24
Dissolved gas (10^{-3} mol)	1.502	1.53	1.52
Equivalent Vol. at STP (ml)	36.7	37.3	37.1

Table 9-10 Some Parameters of Samples 22-24 after Microbial Activity

Test NO	Solids Content (%)	Density (g/ml)	Water Void Ratio	Gas Void Ratio	Total Void Ratio	Degree of Saturation (%)
22	50.1	1.336	2.38	0.19	2.57	92.7
23	50.6	1.308	2.33	0.27	2.61	89.5
24	51.7	1.249	2.23	0.46	2.69	82.8

Table 9-11 Results of Permeability Tests 22-24 after Microbial Activity

Test No.	22	23	24
Gradient	0.882	0.843	0.816
Average Flow Velocity (10^{-9} m/s)	0.693	0.65	0.847
Coefficient of Permeability (10^{-10} m/s)	7.86	7.71	10.4

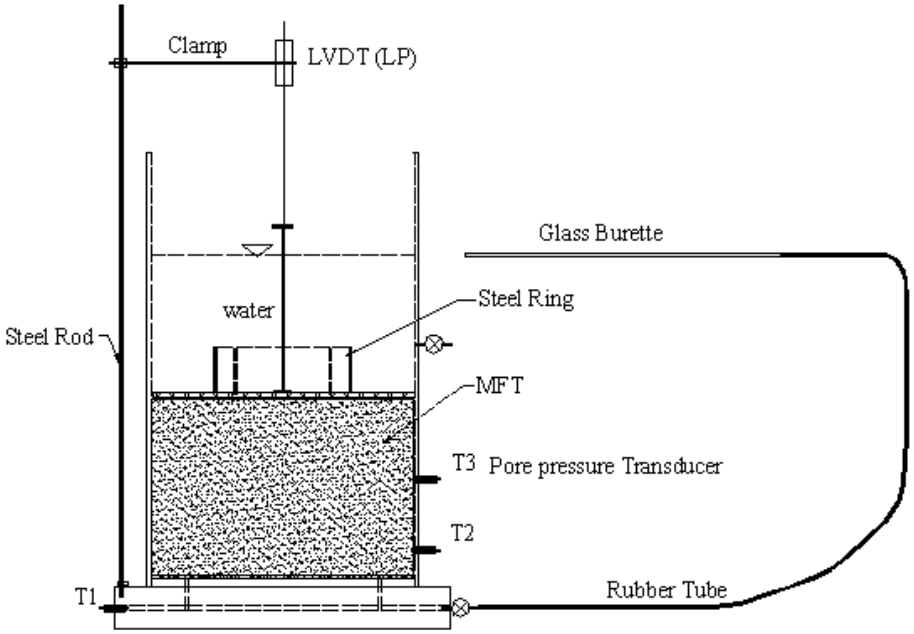

Figure 9-1 Schematic of Consolidation Tests 19-24

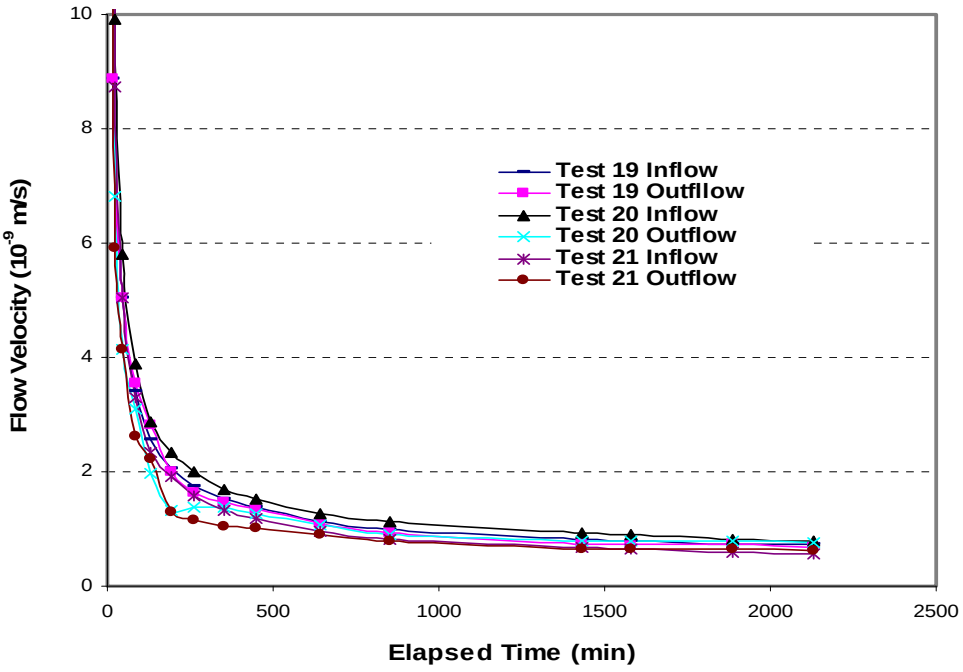

Figure 9-2 Flow Velocity vs. Time in Permeability Tests 19-21 before Microbial Activity

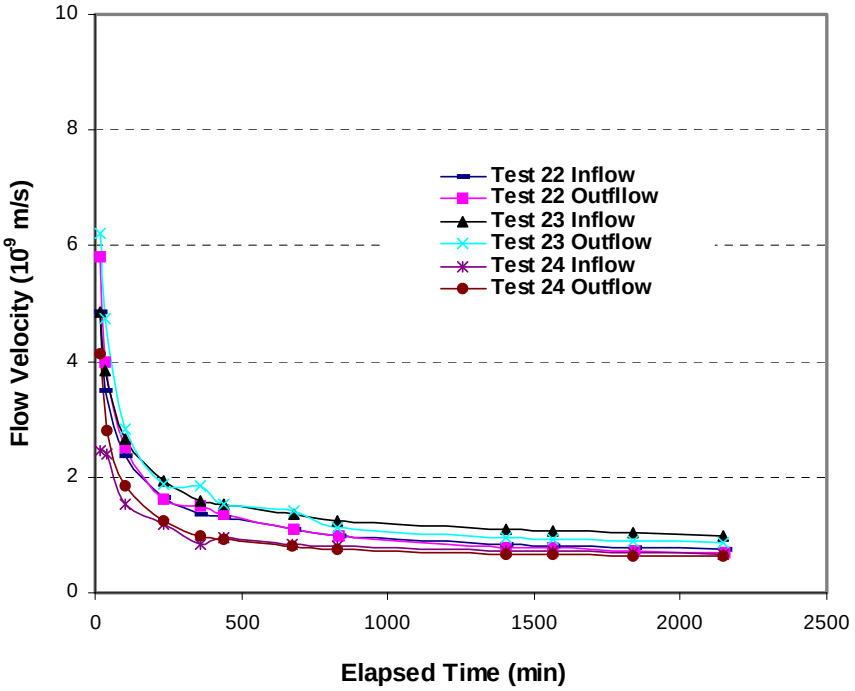

Figure 9-3 Flow Velocity vs. Time in Permeability Tests 22-24 before Microbial Activity

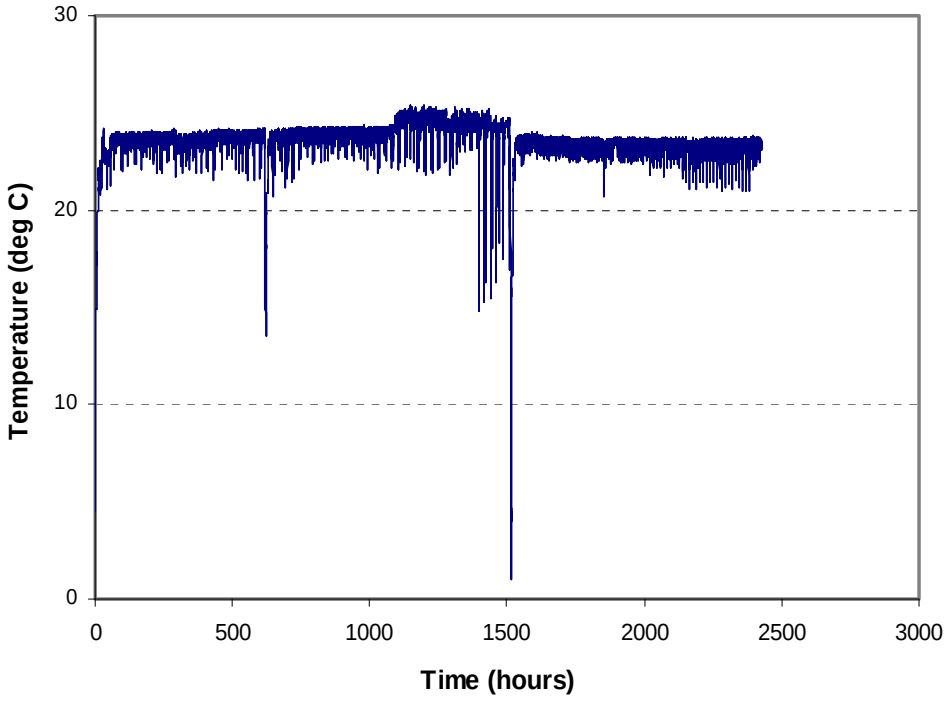

Figure 9-4 Temperature Changes during Gas MFT Densification Tests of Samples 19-24

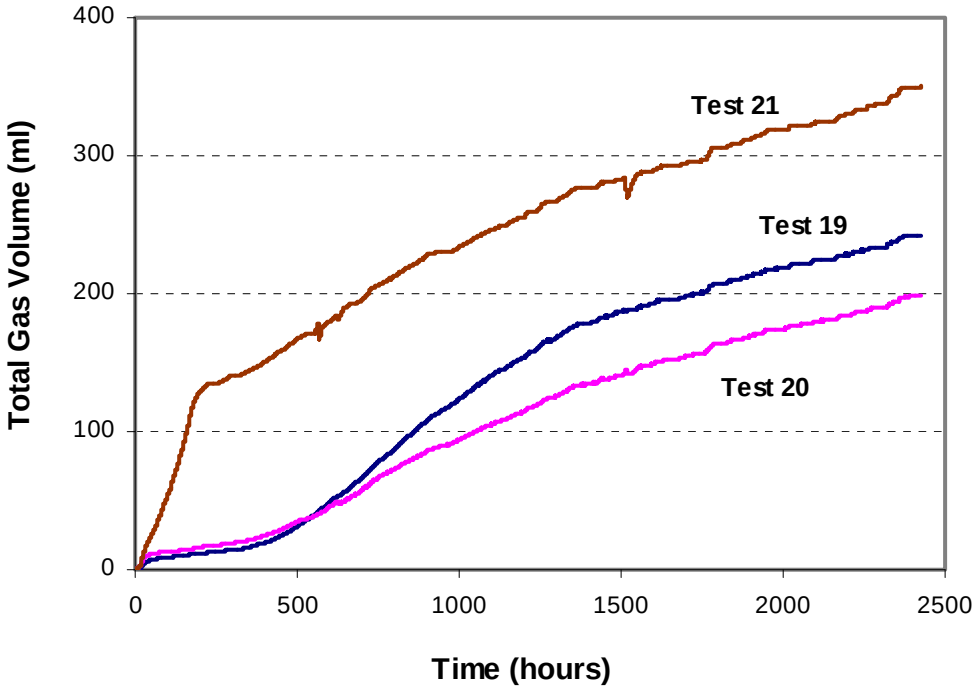

Figure 9-5 Total Gas Volume (STP) vs. Time in Tests 19-21

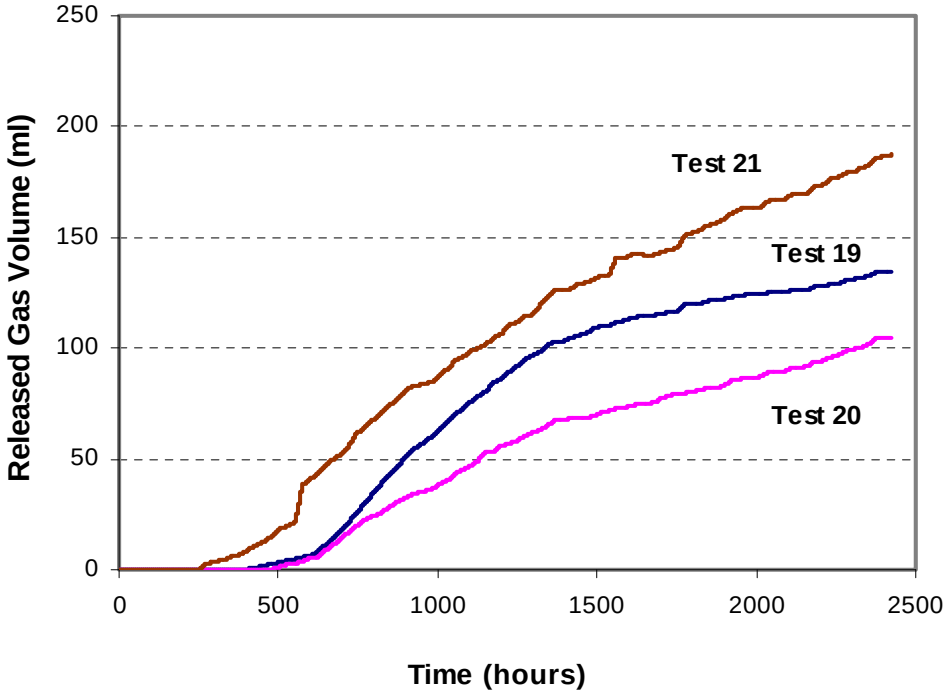

Figure 9-6 Released Gas Volume (STP) vs. Time in Tests 19-21

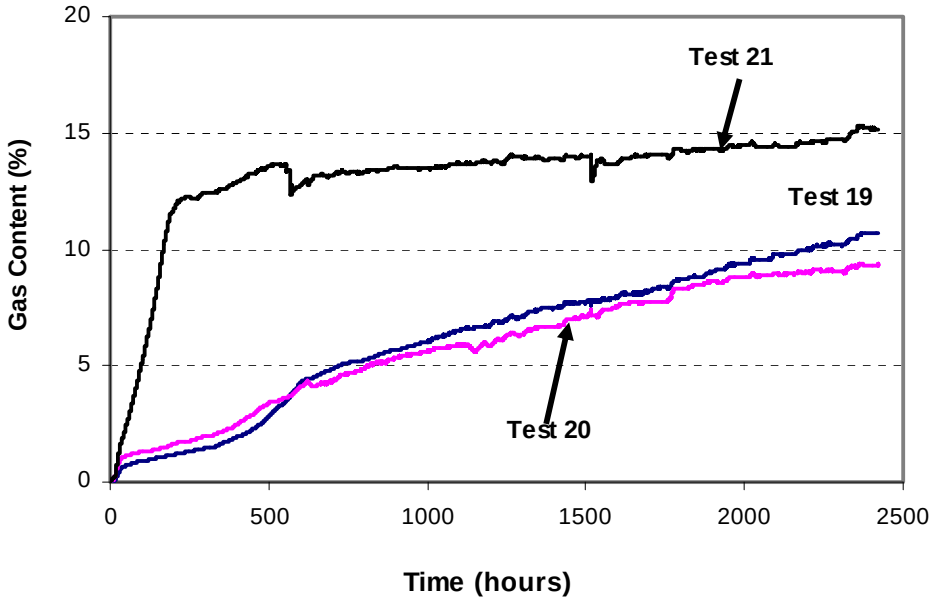

Figure 9-7 Gas Content vs. Time in Tests 19-21

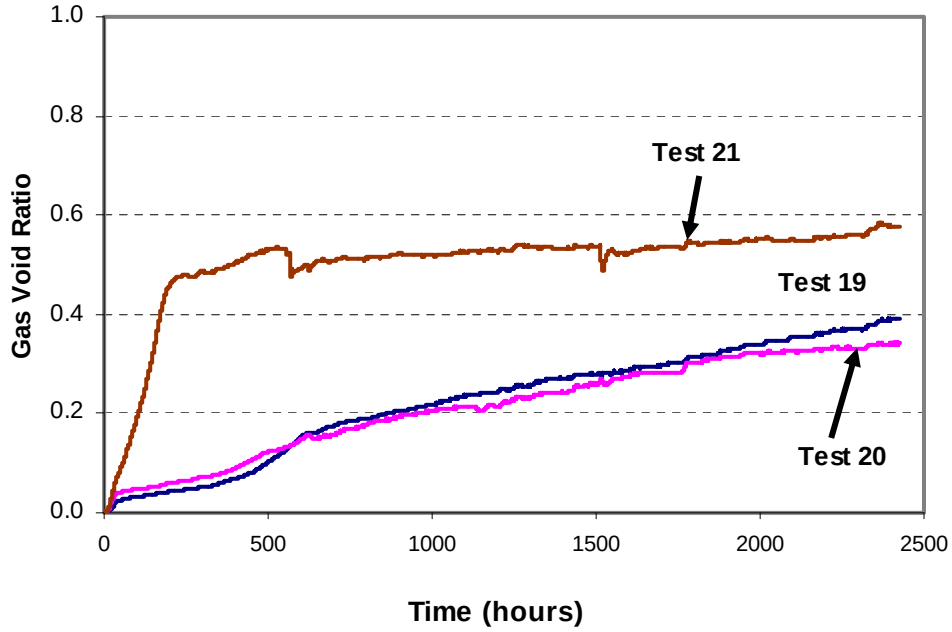

Figure 9-8 Gas Void Ratio vs. Time in Samples 19-21

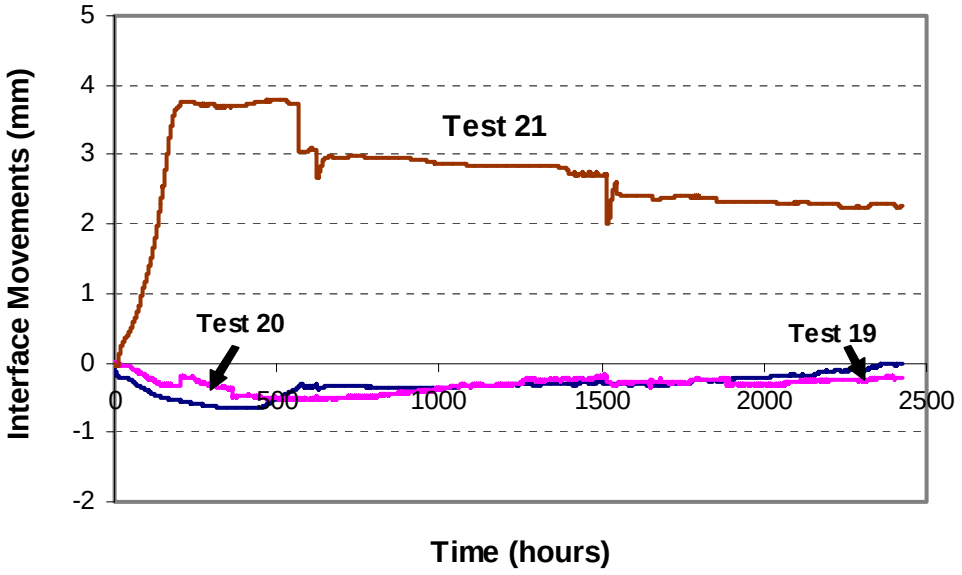

Figure 9-9 Interface Movements of Samples 19-21 during Microbial Activity

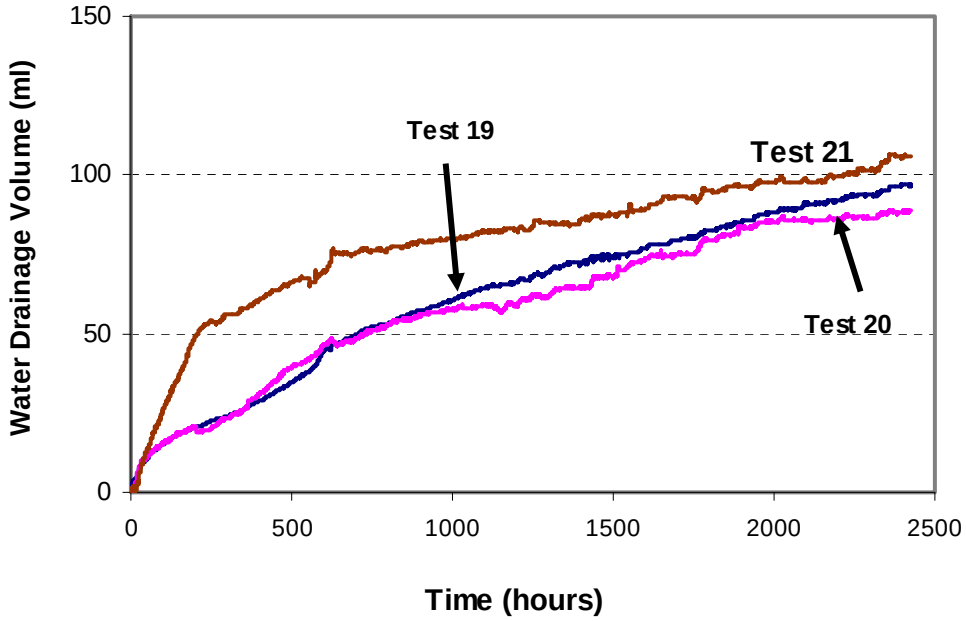

Figure 9-10 Water Drainage Volume vs. Time in Tests 19-21

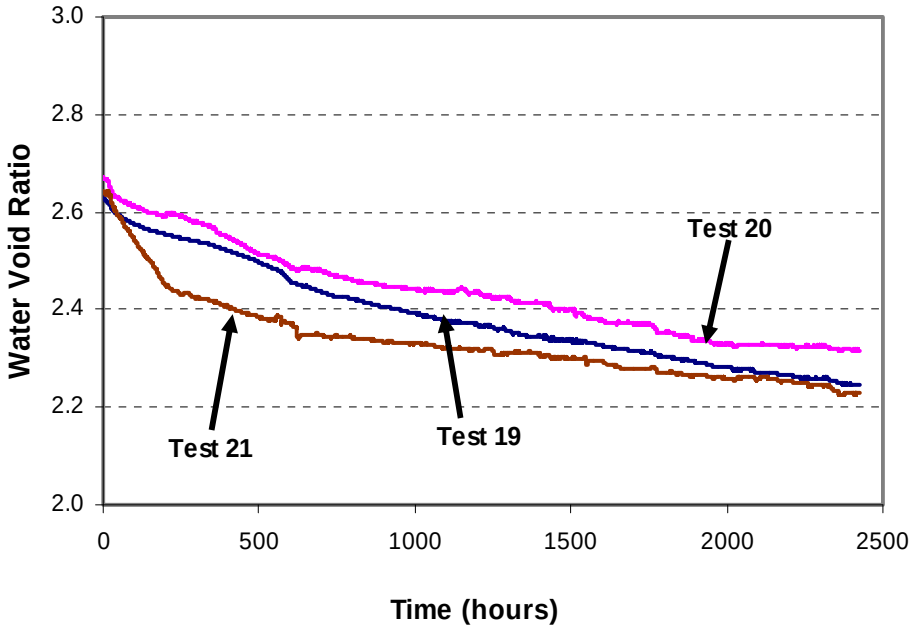

Figure 9-11 Water Void Ratio vs. Time in Samples 19-21

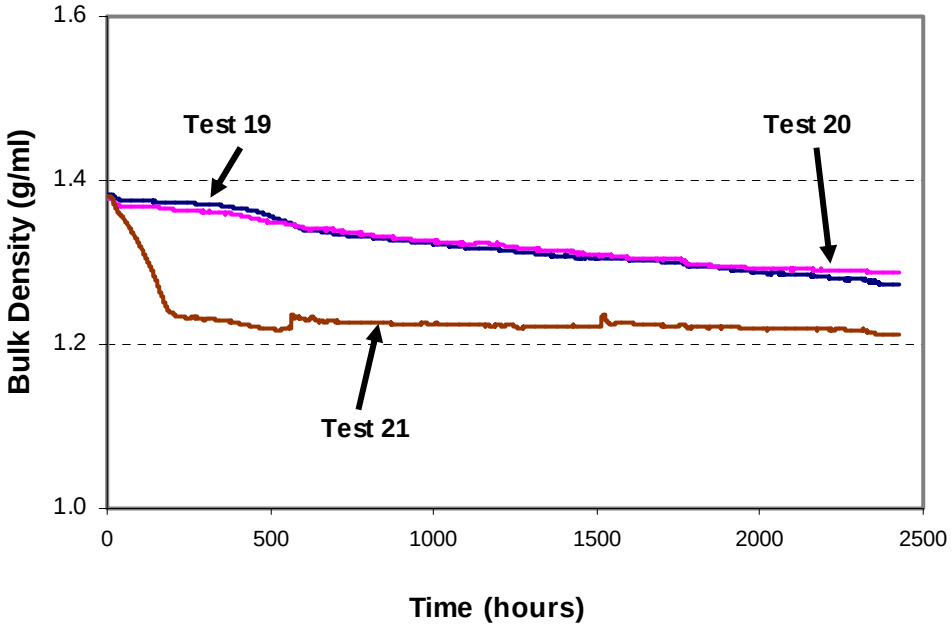

Figure 9-12 Bulk Density vs. Time in Samples 19-21

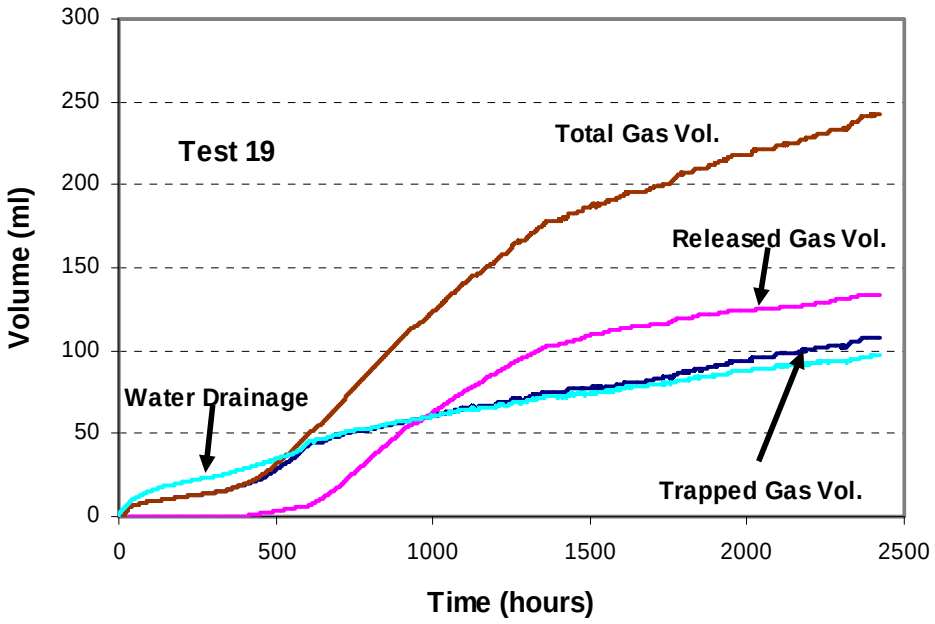

Figure 9-13 Volumetric Changes in Sample 19 during Microbial Activity

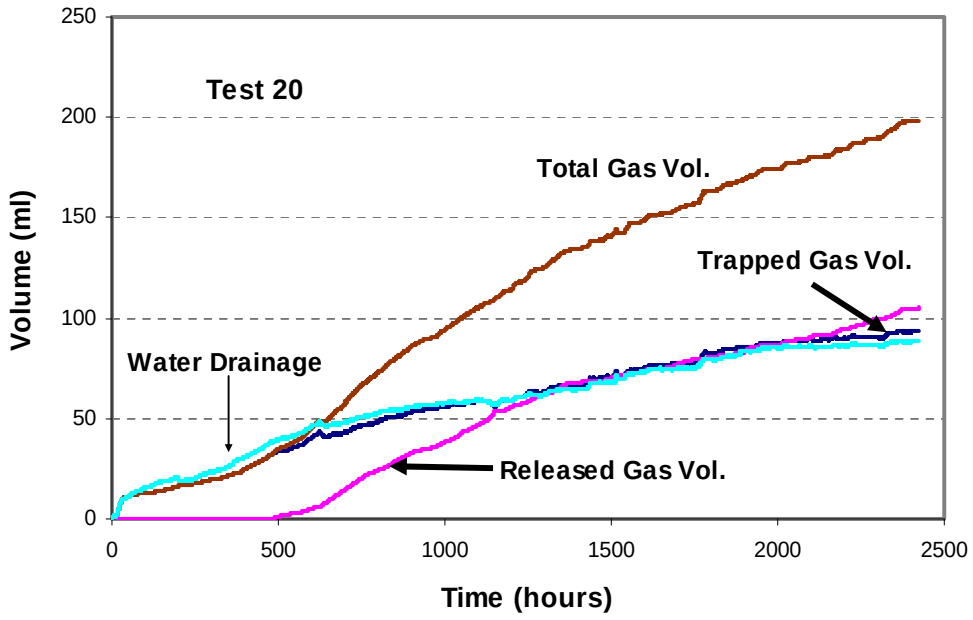

Figure 9-14 Volumetric Changes in Sample 20 during Microbial Activity

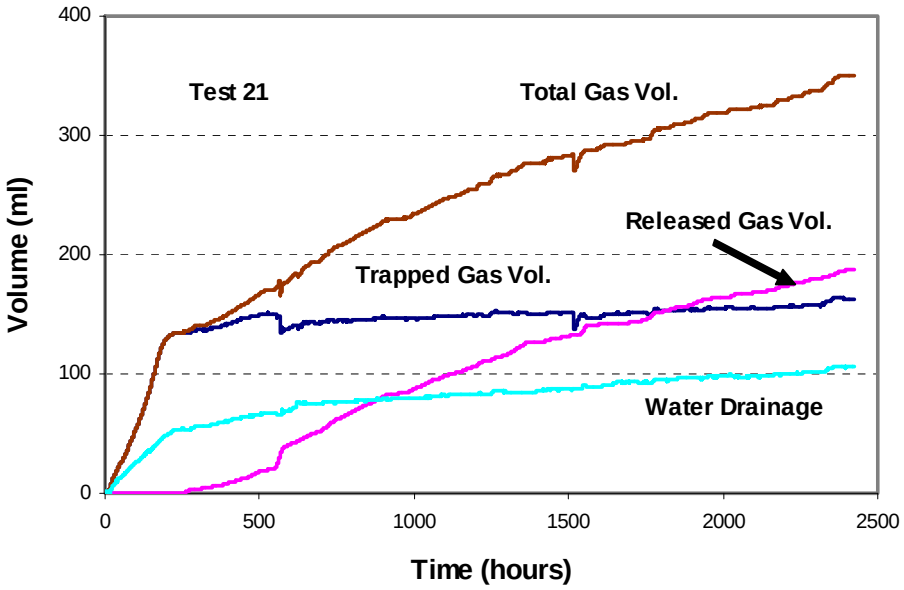

Figure 9-15 Volumetric Changes in Sample 21 during Microbial Activity

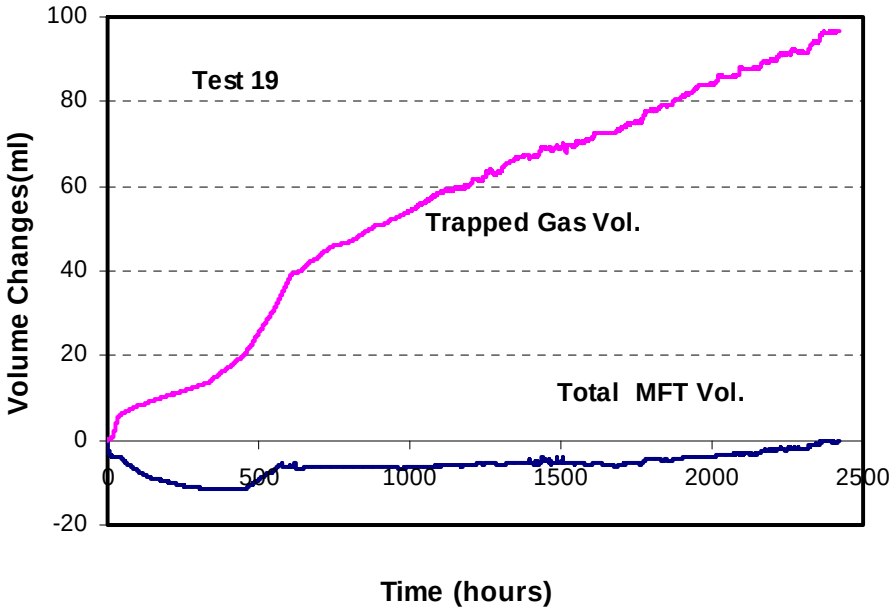

Figure 9-16 Changes in Trapped Gas Volume and Total MFT Volume in Sample 19

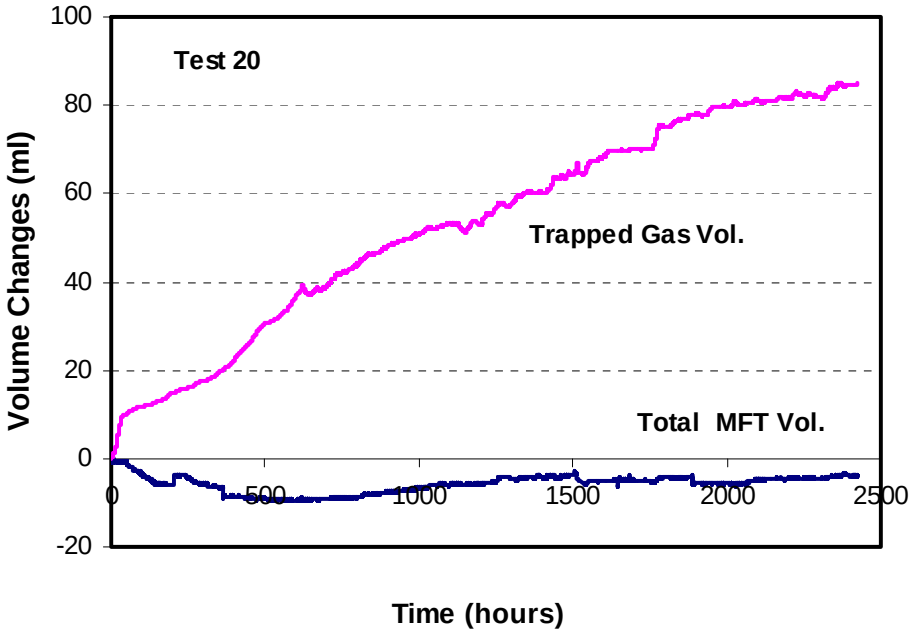

Figure 9-17 Changes in Trapped Gas Volume and Total MFT Volume in Sample 20

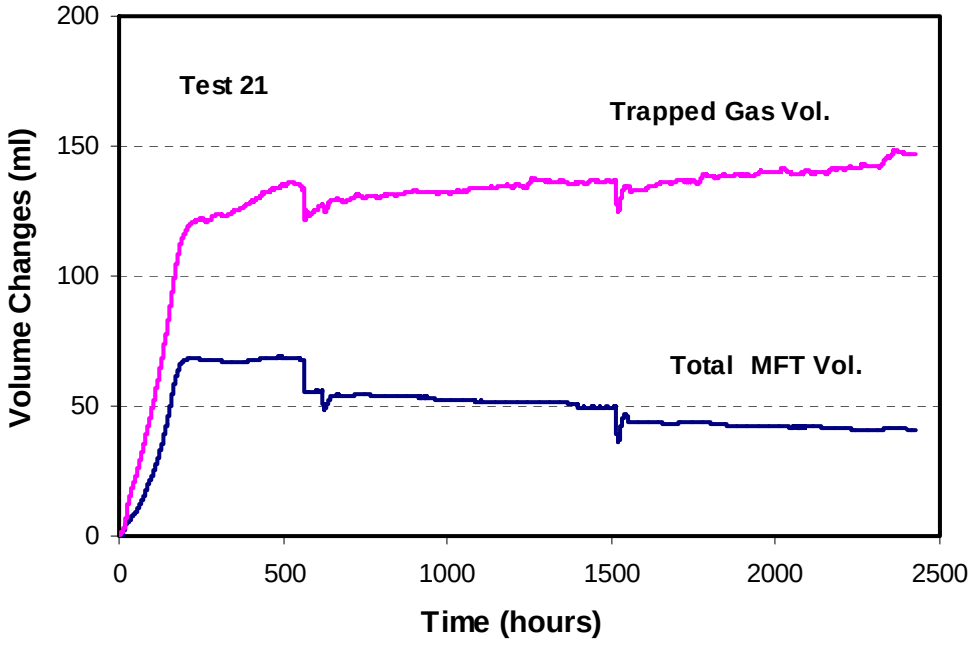

Figure 9-18 Changes in Trapped Gas Volume and Total MFT Volume in Sample 21

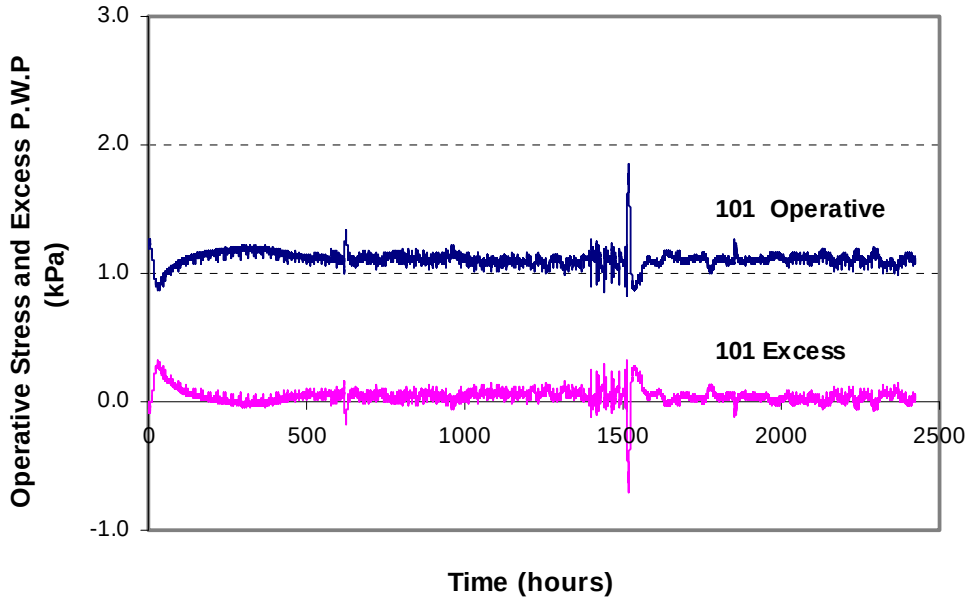

Figure 9-19 Changes in Excess Pore Pressure and Operative Stress at E1 of Test 19

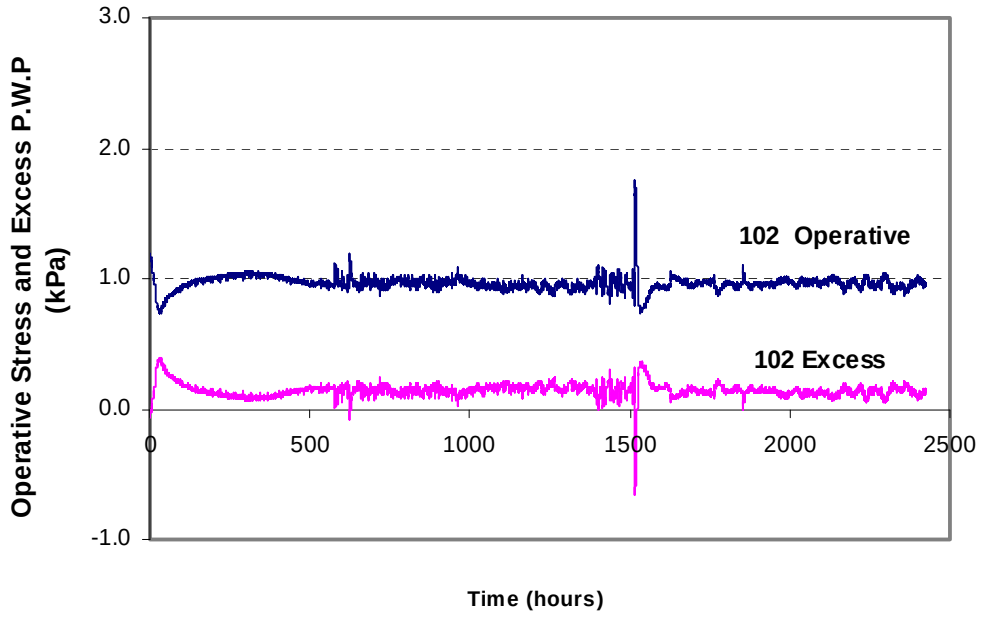

Figure 9-20 Changes in Excess Pore Pressure and Operative Stress at E2 of Test 19

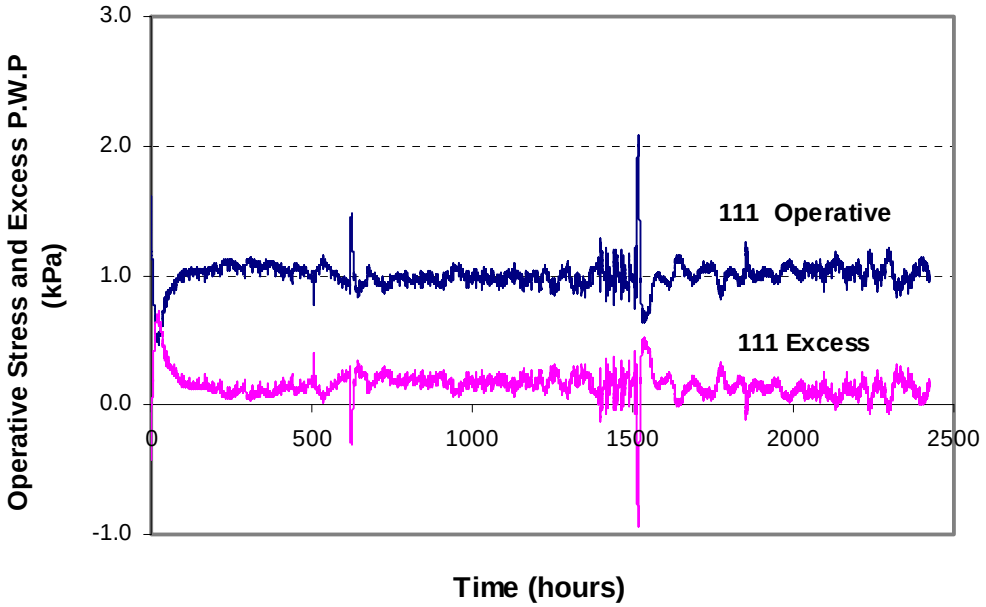

Figure 9-21 Changes in Excess Pore Pressure and Operative Stress at E1 of Test 20

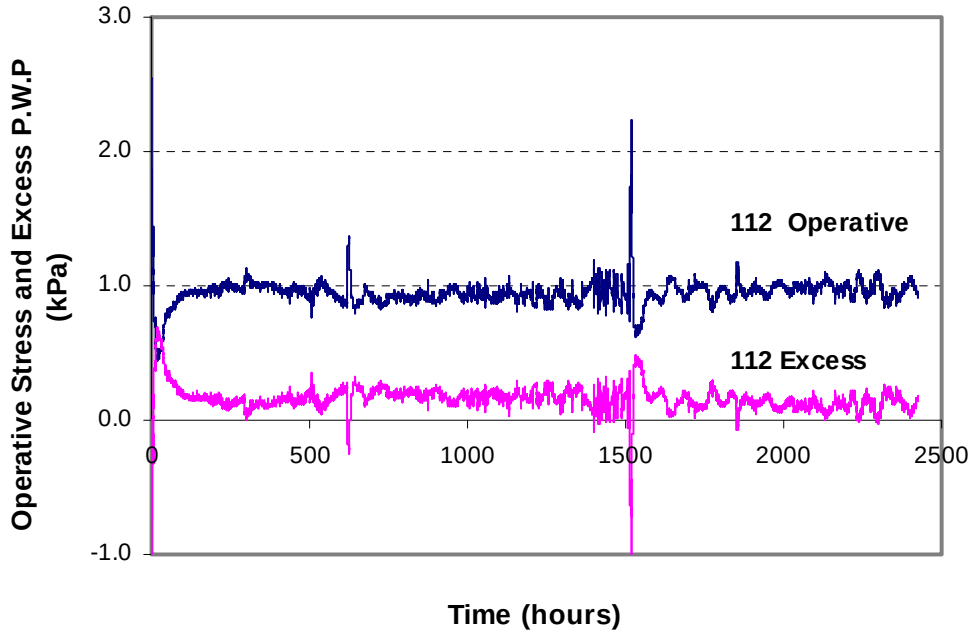

Figure 9-22 Changes in Excess Pore Pressure and Operative Stress at E2 of Test 20

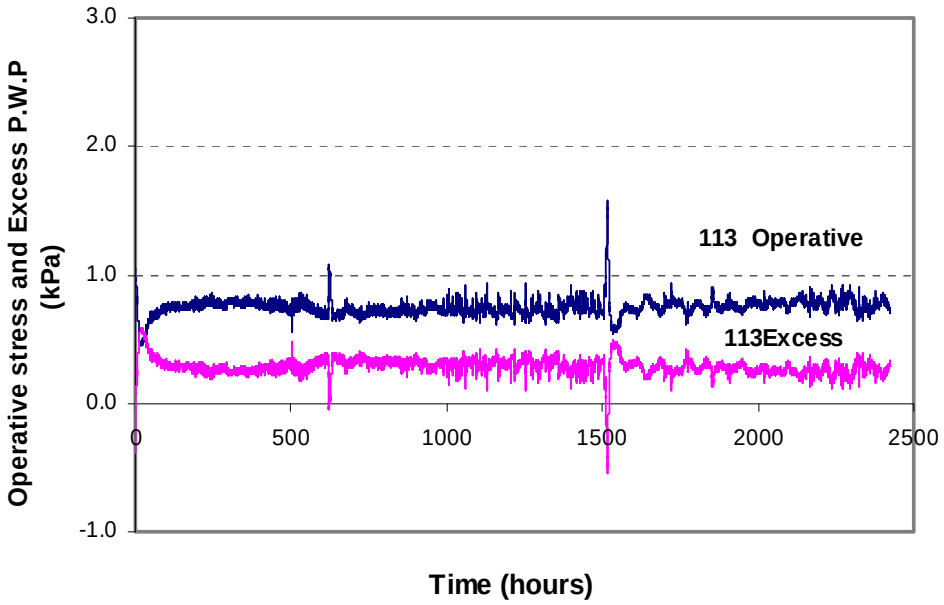

Figure 9-23 Changes in Excess Pore Pressure and Operative Stress at E3 of Test 20

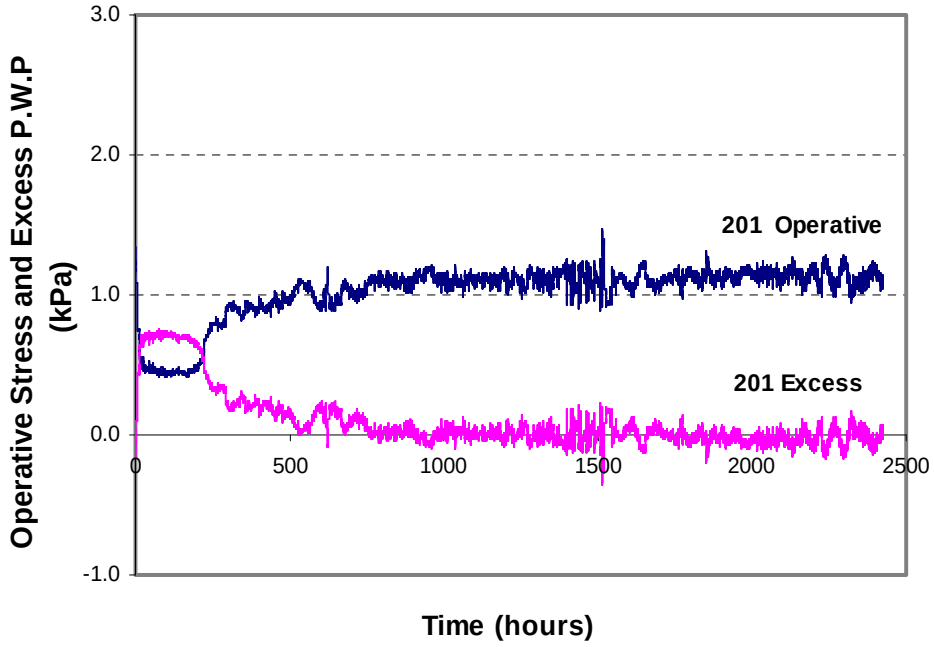

Figure 9-24 Changes in Excess Pore Pressure and Operative Stress at E1 of Test 21

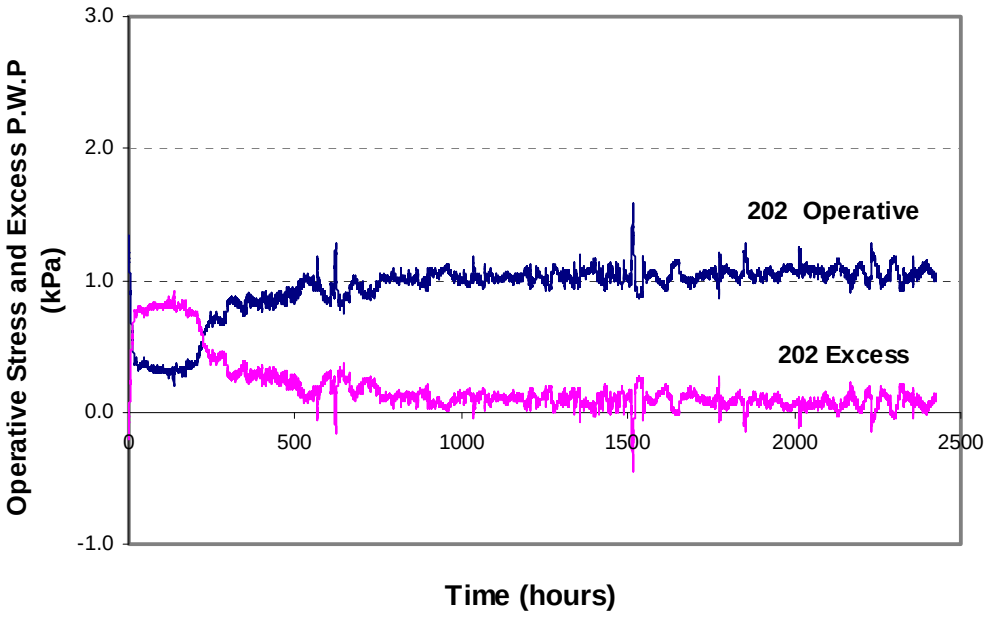

Figure 9-25 Changes in Excess Pore Pressure and Operative Stress at E2 of Test 21

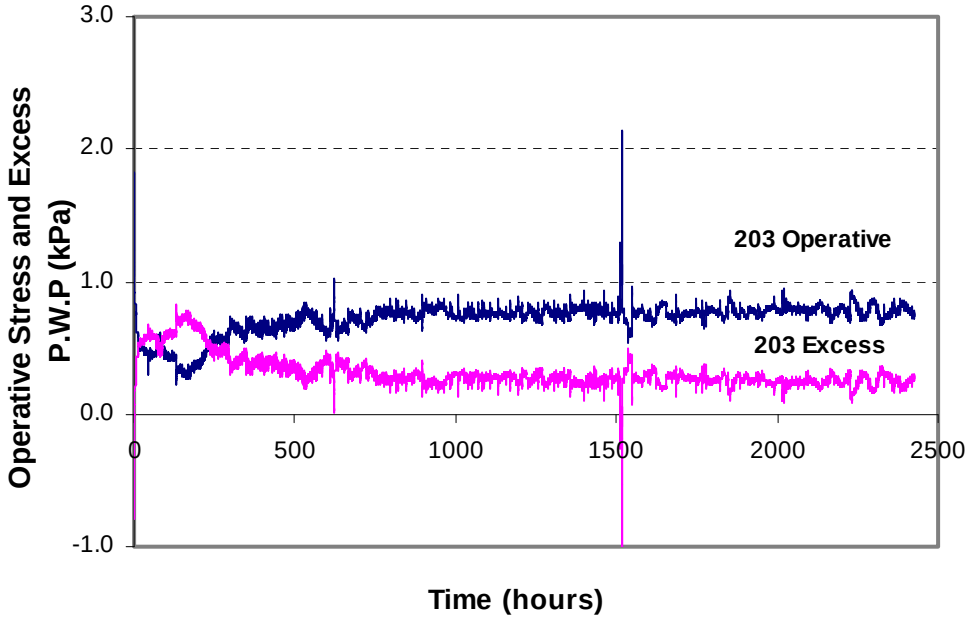

Figure 9-26 Changes in Excess Pore Pressure and Operative Stress at E3 of Test 21

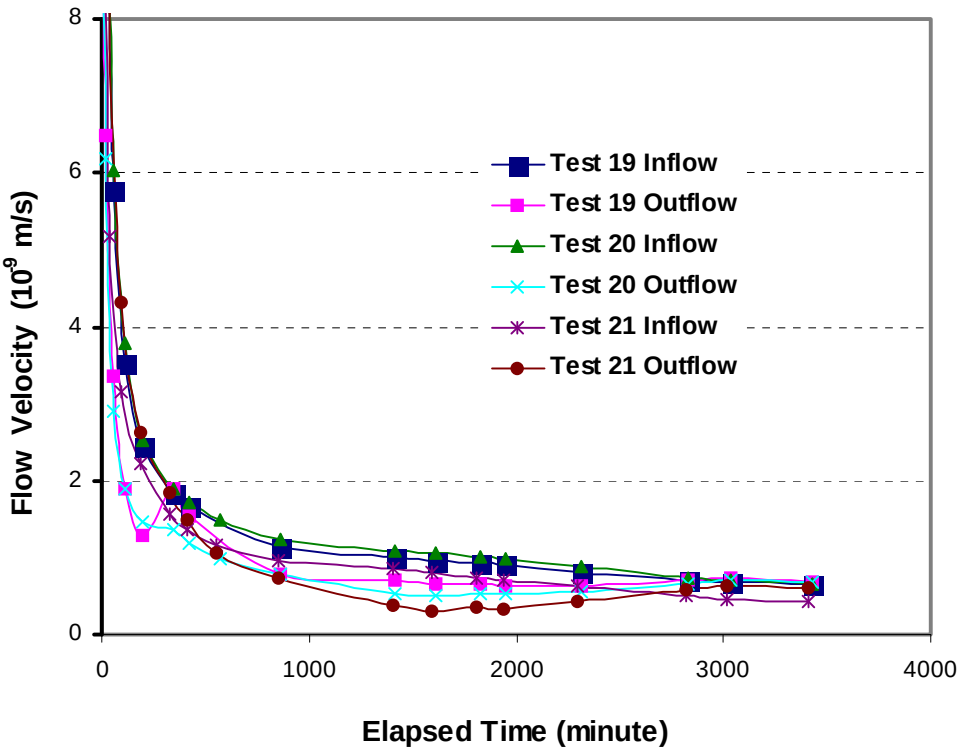

Figure 9-27 Flow Velocity vs. Time in Permeability Tests 19-21 after Microbial Activity

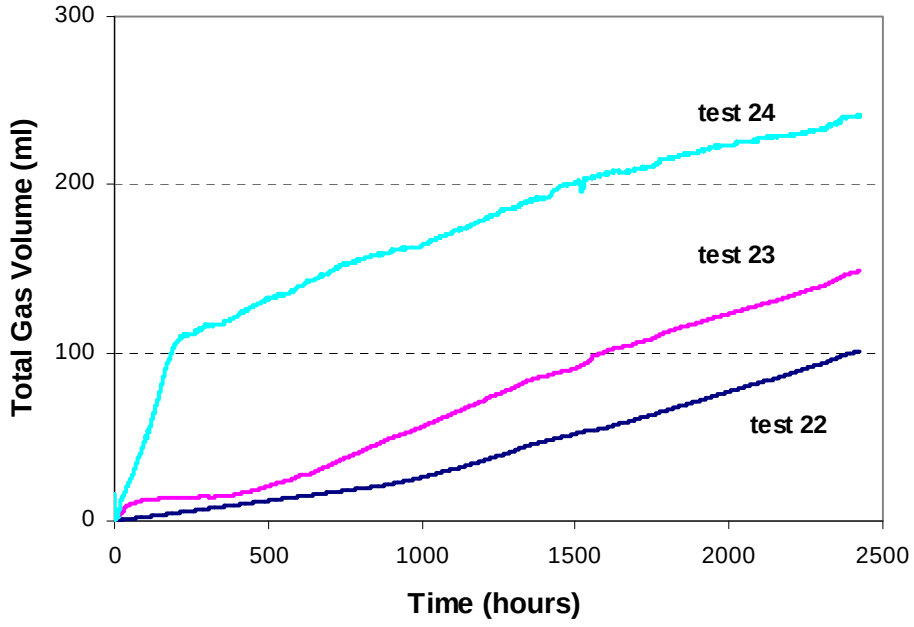

Figure 9-28 Total Gas Volume (STP) vs. Time in Samples 22-24

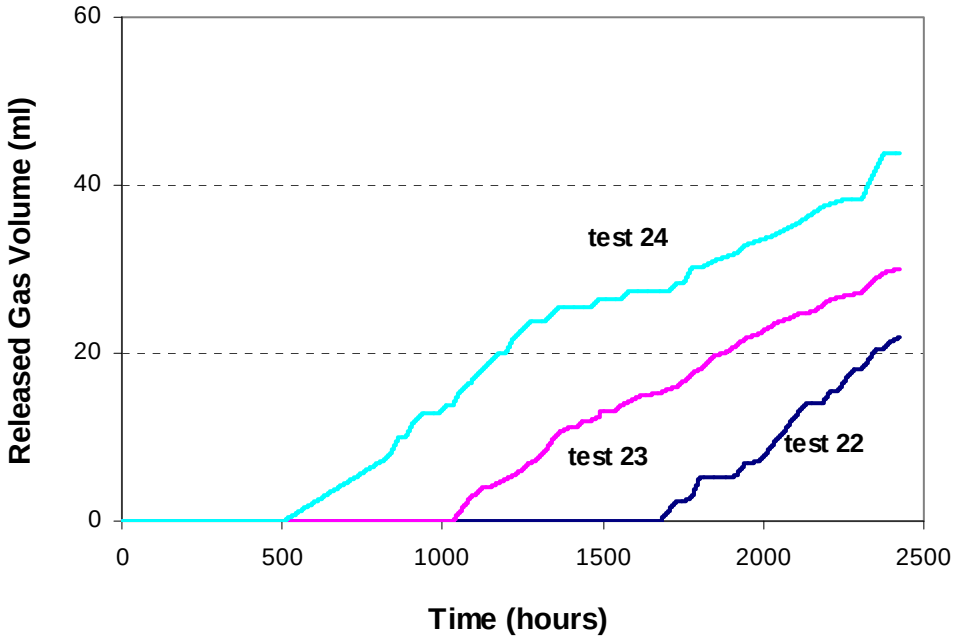

Figure 9-29 Released Gas Volume vs. Time in Samples 22-24

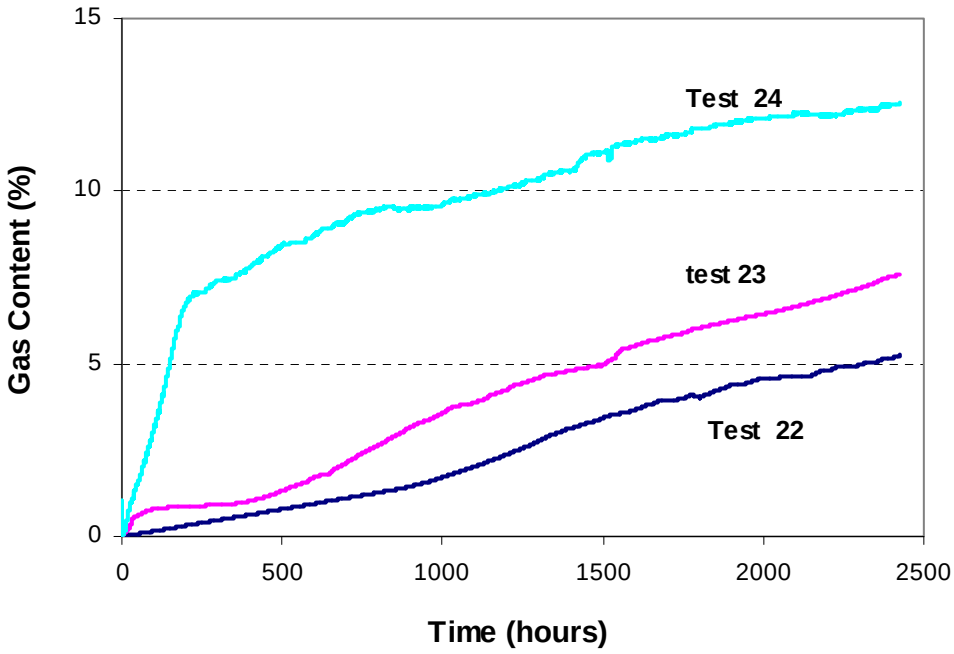

Figure 9-30 Gas Content vs. Time in Samples 22-24

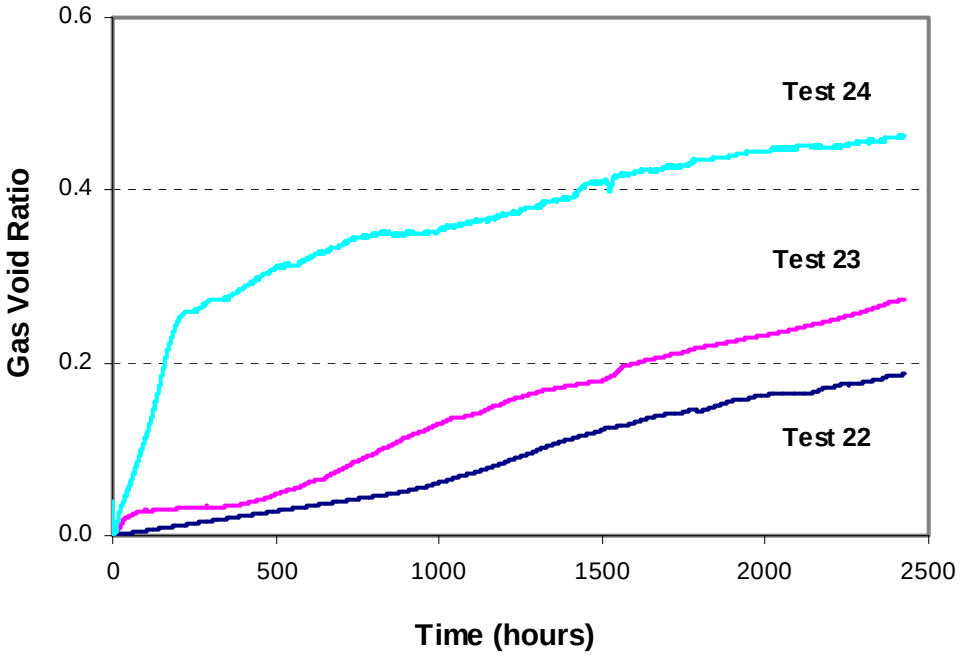

Figure 9-31 Gas Void Ratio vs. Time in Samples 22-24

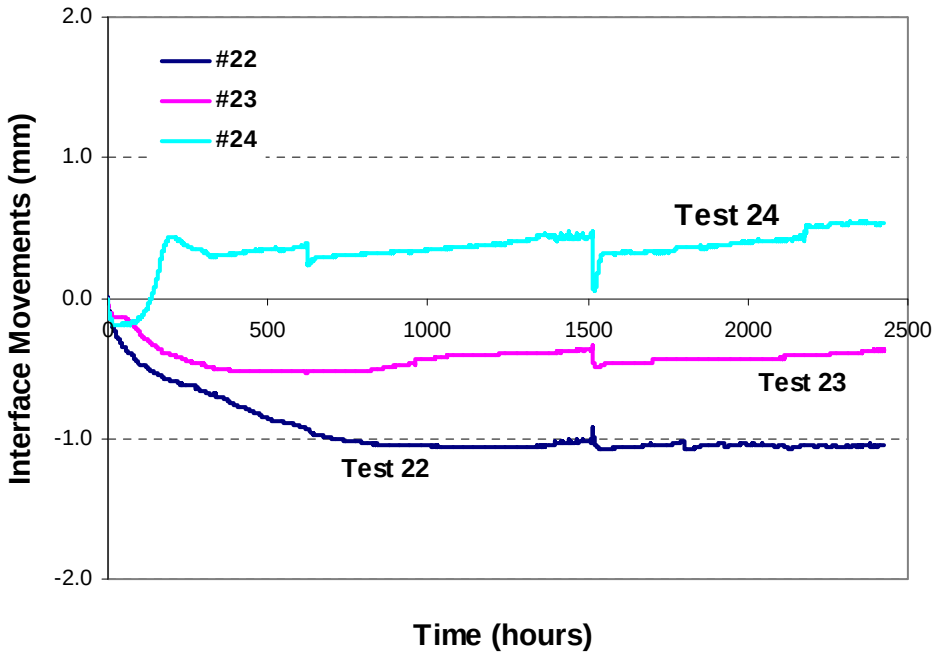

Figure 9-32 Interface Movements with Time in Samples 22-24

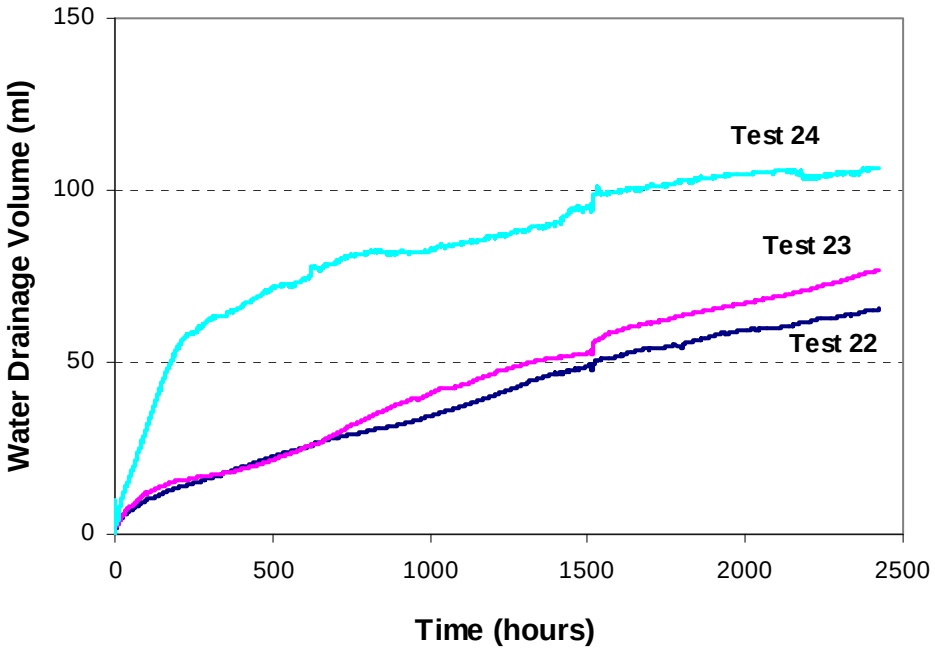

Figure 9-33 Water Drainage Volume vs. Time in Samples 22-24

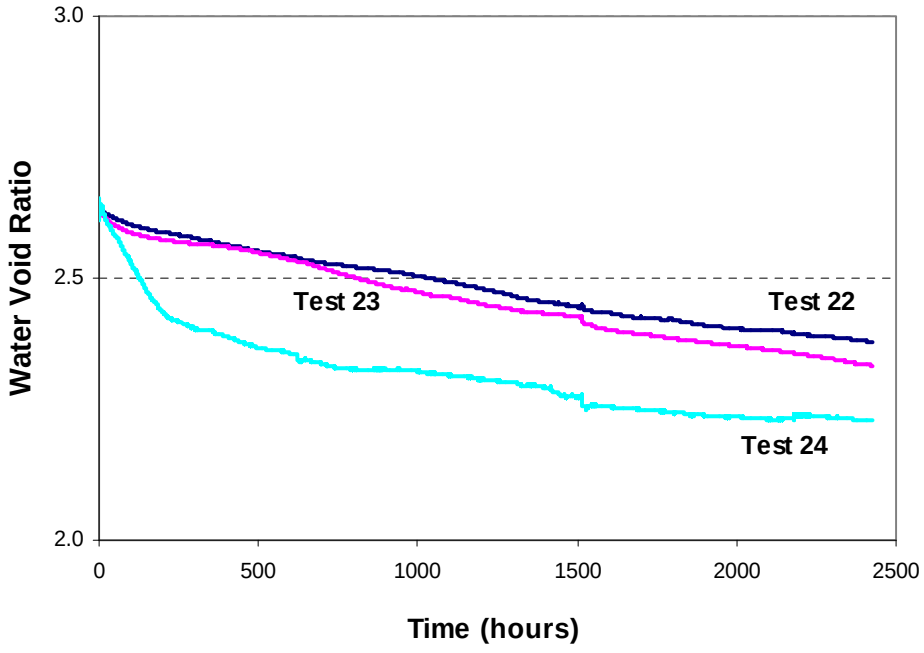

Figure 9-34 Water Void Ratio vs. Time in Samples 22-24

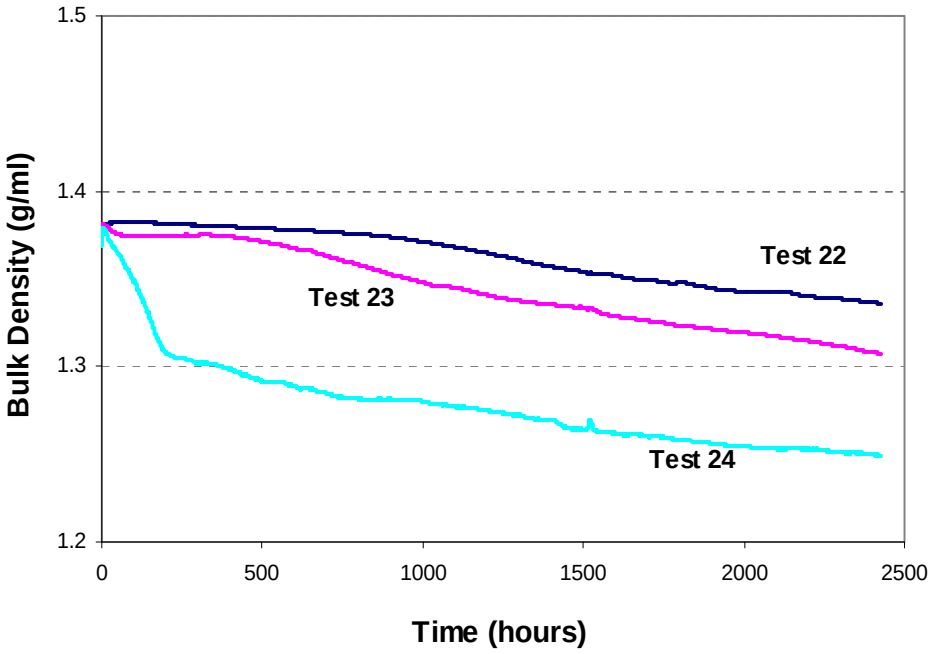

Figure 9-35 Bulk Density vs. Time in Samples 22-24

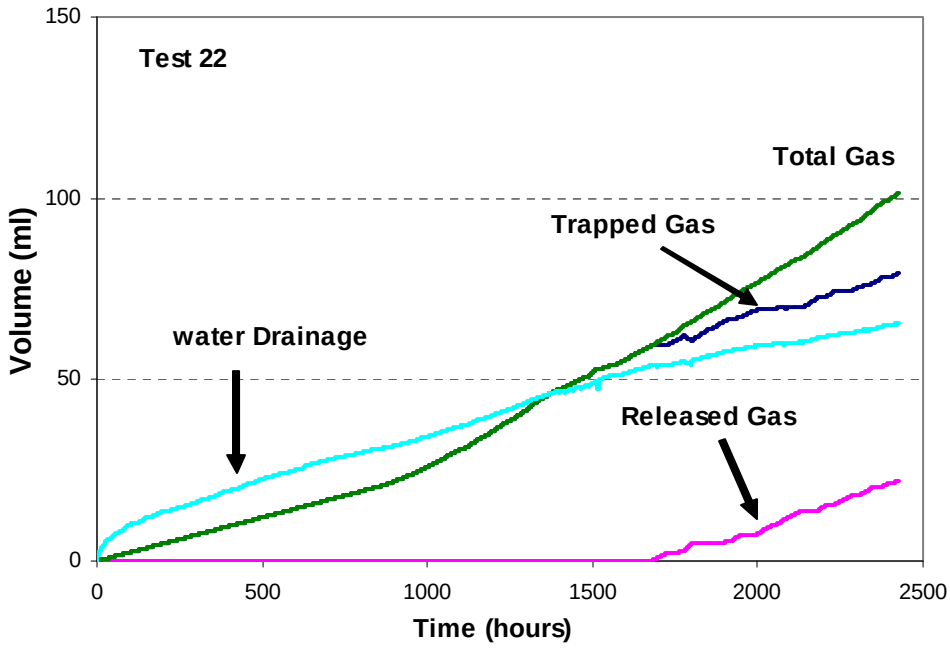

Figure 9-36 Volumetric Changes in Sample 22 during Microbial Activity

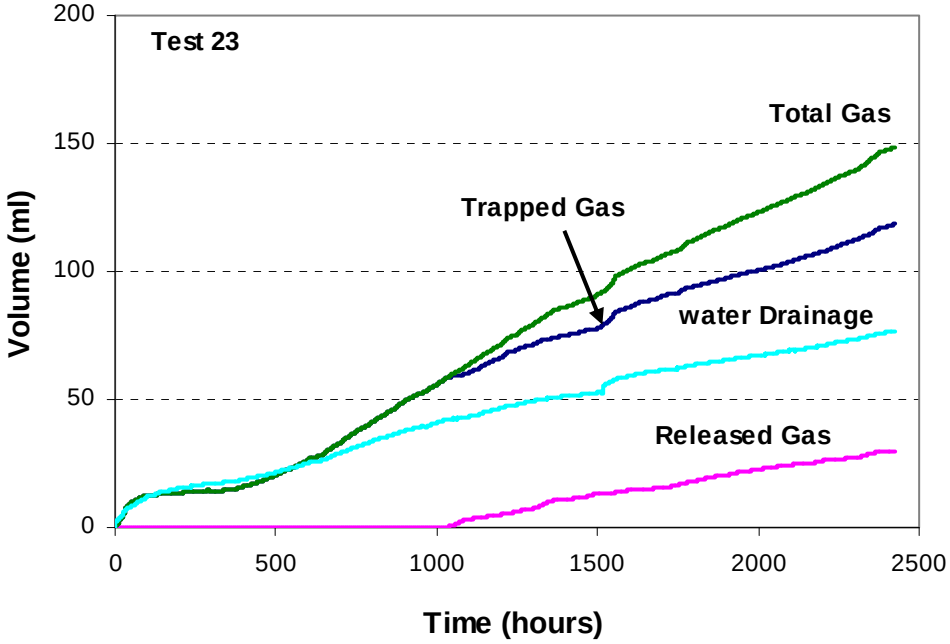

Figure 9-37 Volumetric Changes in Sample 23 during Microbial Activity

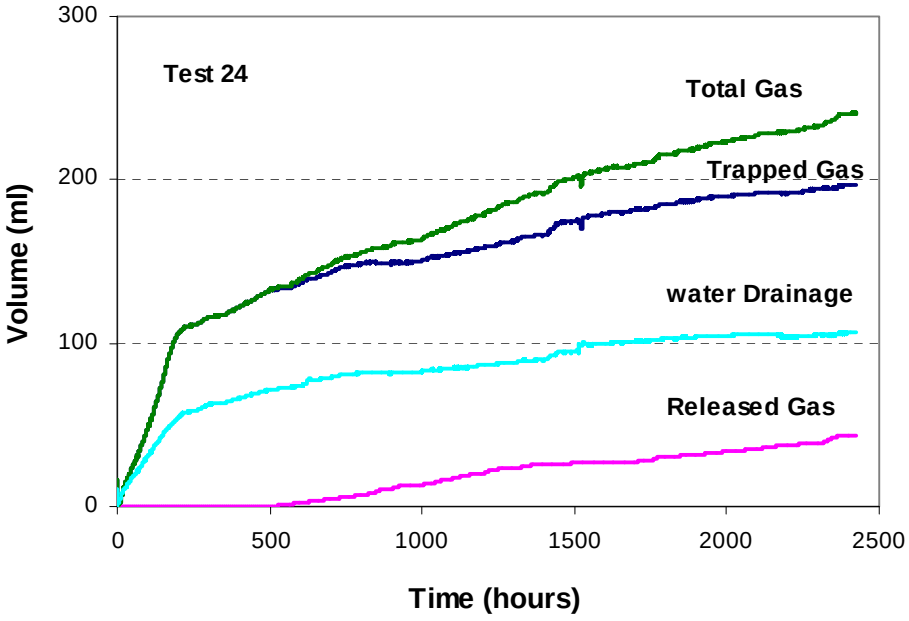

Figure 9-38 Volumetric Changes in Sample 24 during Microbial Activity

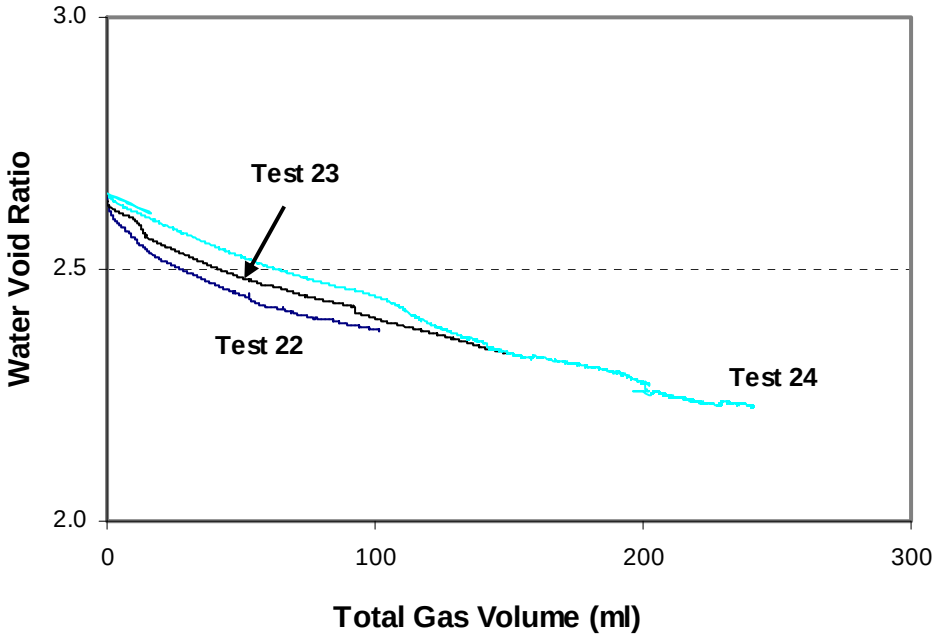

Figure 9-39 Water Void Ratio vs. Total Gas Volume (STP) in Tests 22-24

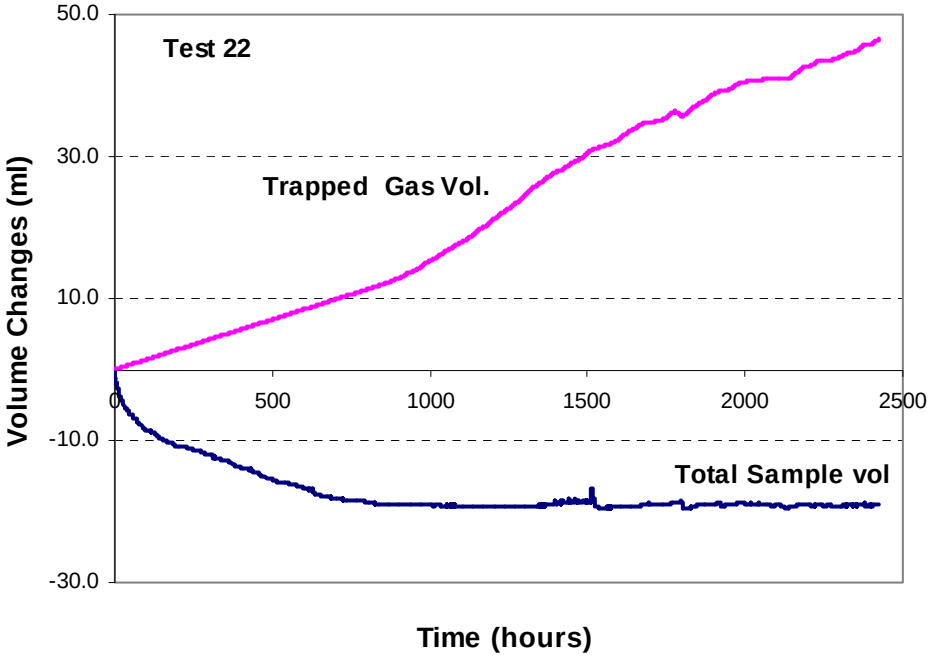

Figure 9-40 Changes in Trapped Gas Volume and Total MFT Volume in Sample 22

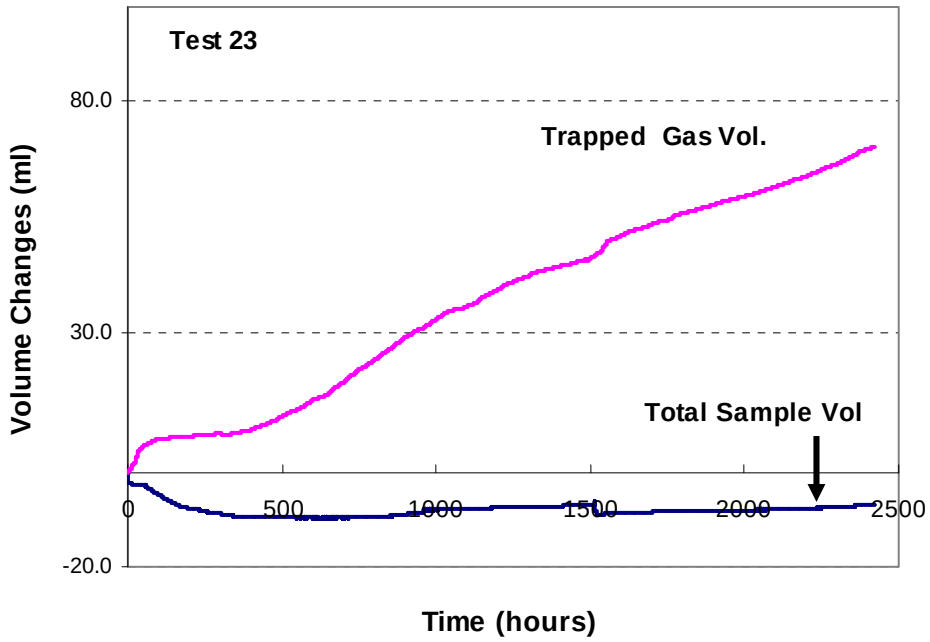

Figure 9-41 Changes in Trapped Gas Volume and Total MFT Volume in Sample 23

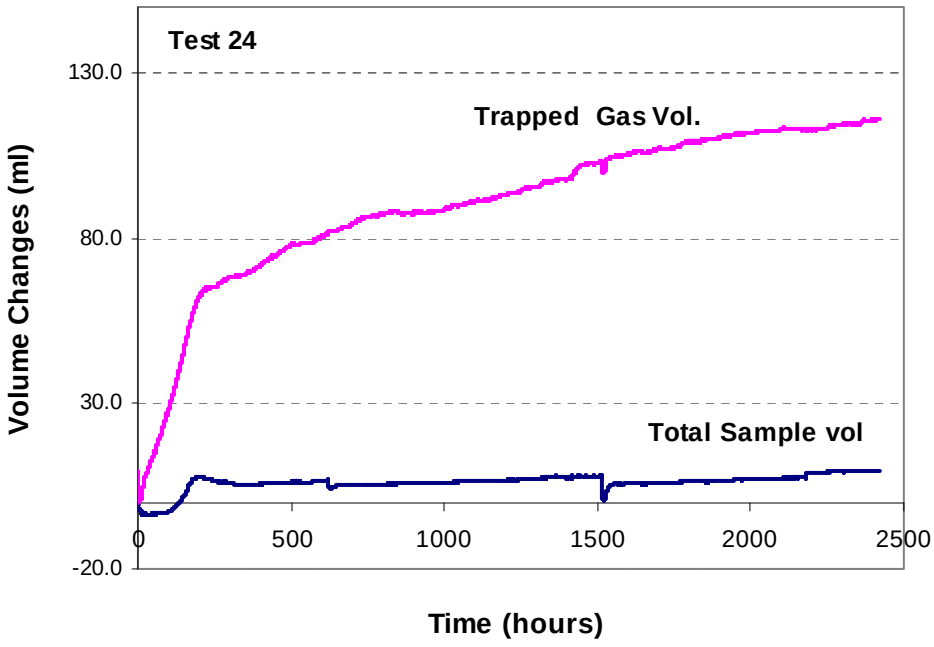

Figure 9-42 Changes in Trapped Gas Volume and Total MFT Volume in Sample 24

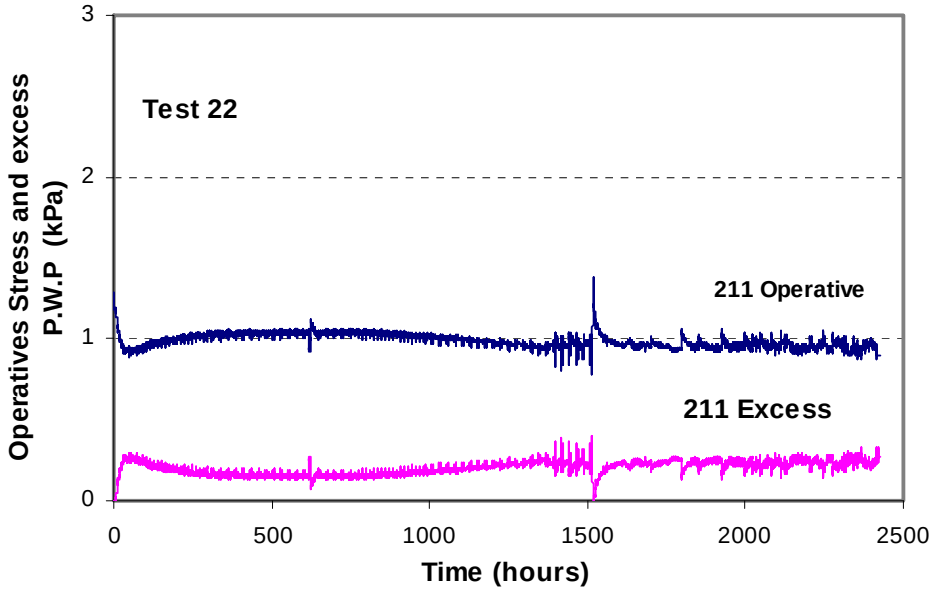

Figure 9-43 Changes in Excess pore Pressure and Operative Stress at E1 of Test 22

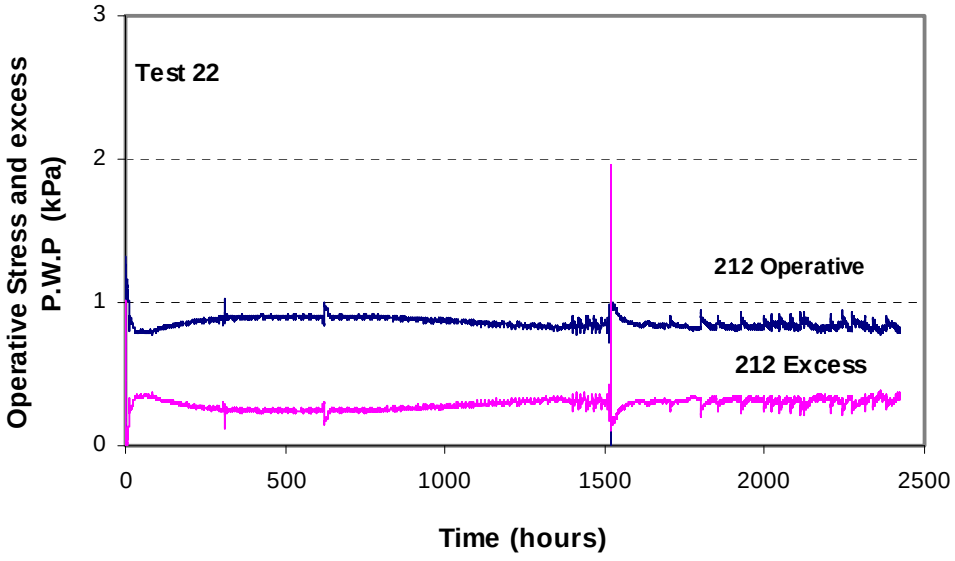

Figure 9-44 Changes in Excess pore Pressure and Operative Stress at E2 of Test 22

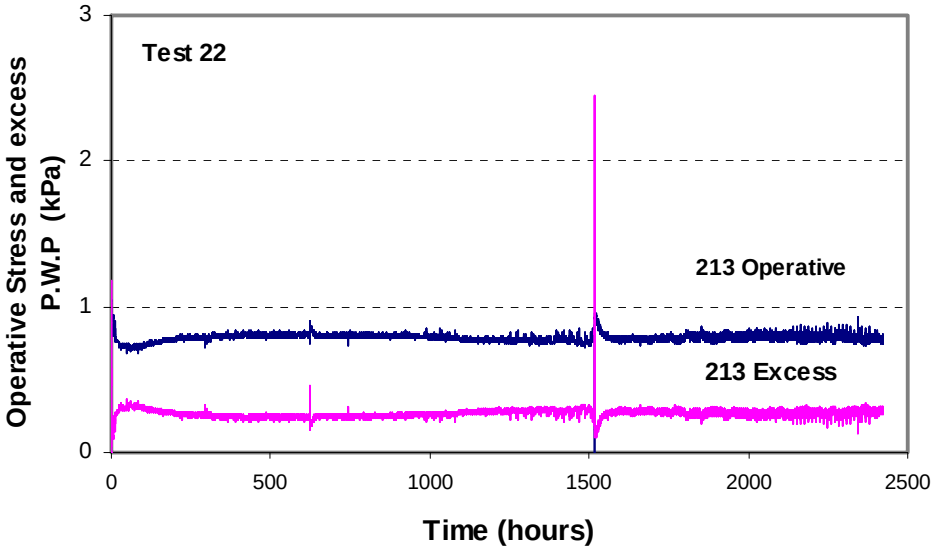

Figure 9-45 Changes in Excess pore Pressure and Operative Stress at E3 of Test 22

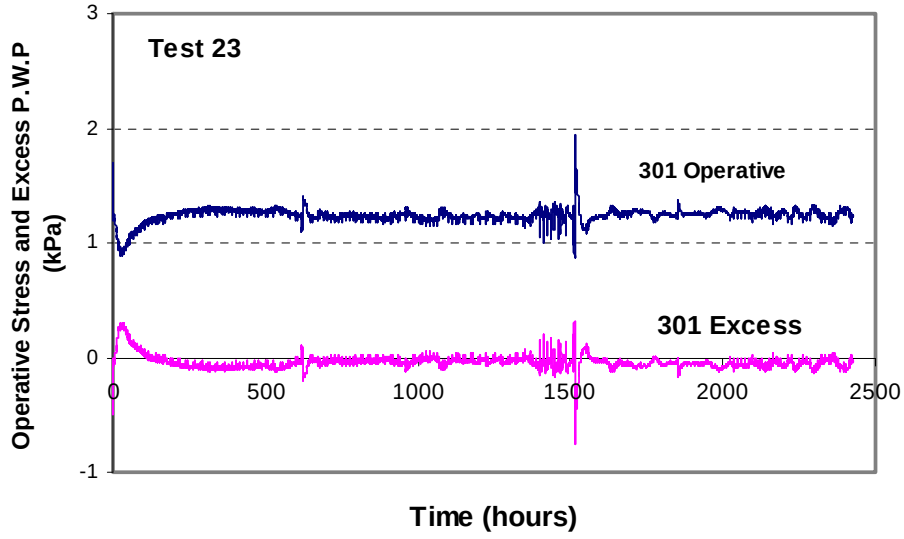

Figure 9-46 Changes in Excess pore Pressure and Operative Stress at E1 of Test 23

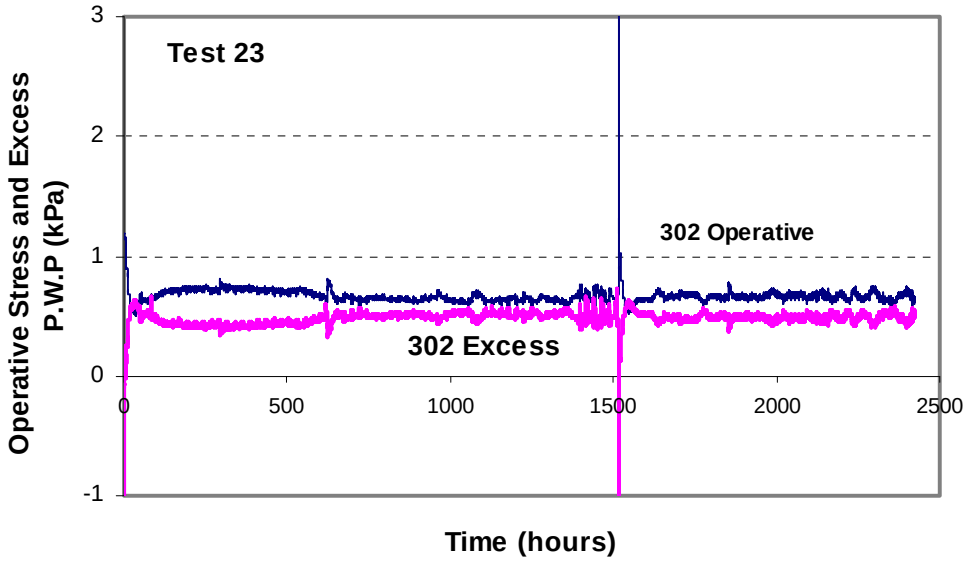

Figure 9-47 Changes in Excess pore Pressure and Operative Stress at E2 of Test 23

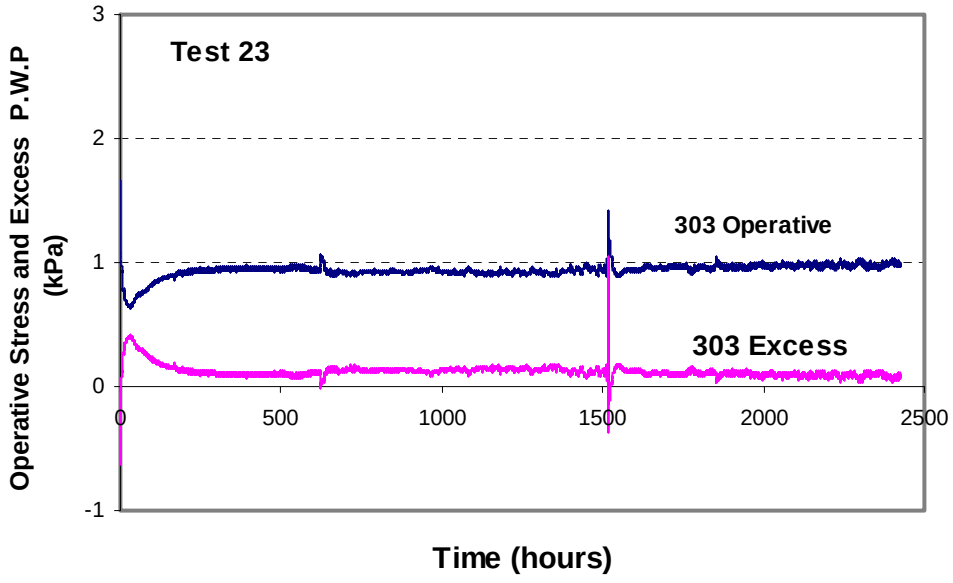

Figure 9-48 Changes in Excess pore Pressure and Operative Stress at E3 of Test 23

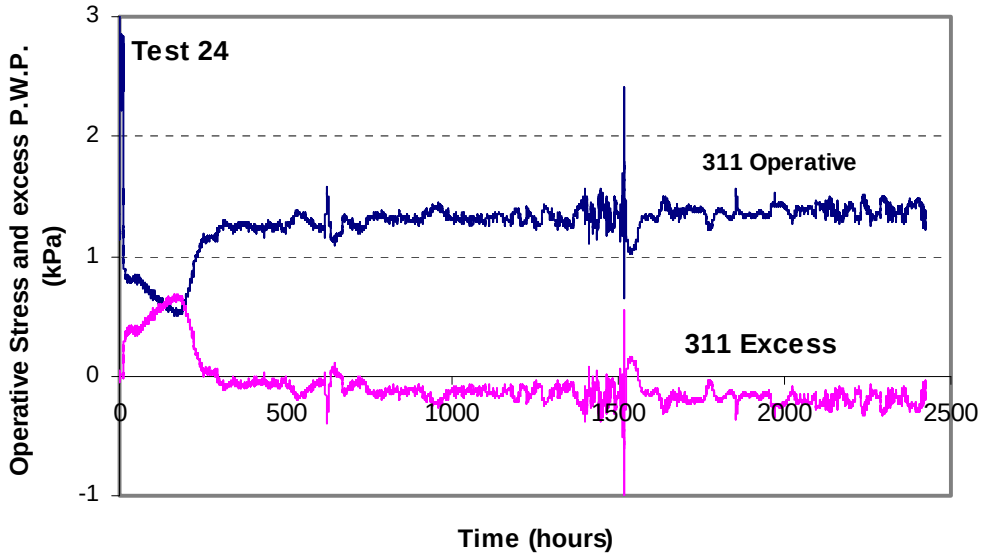

Figure 9-49 Changes in Excess pore Pressure and Operative Stress at E1 of Test 24

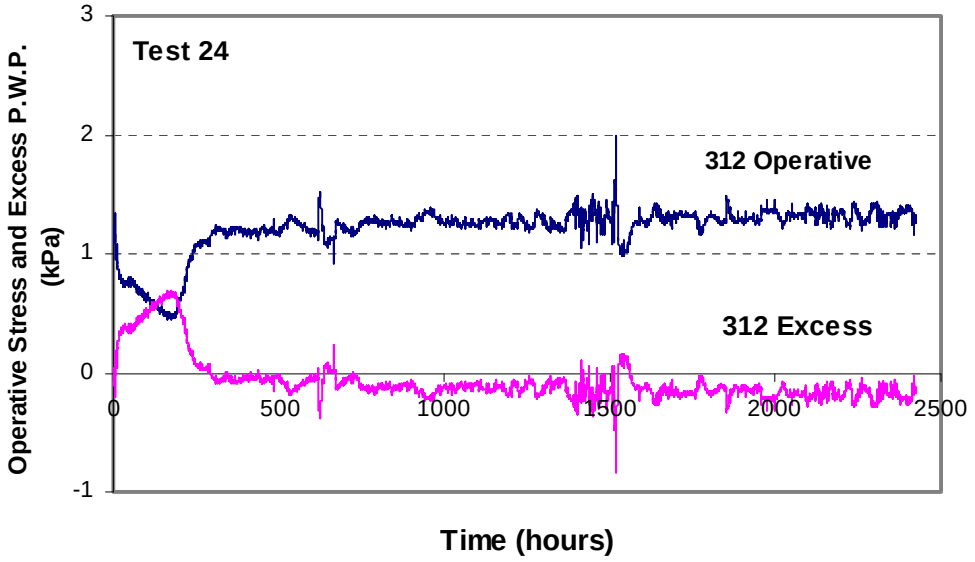

Figure 9-50 Changes in Excess pore Pressure and Operative Stress at E2 of Test 24

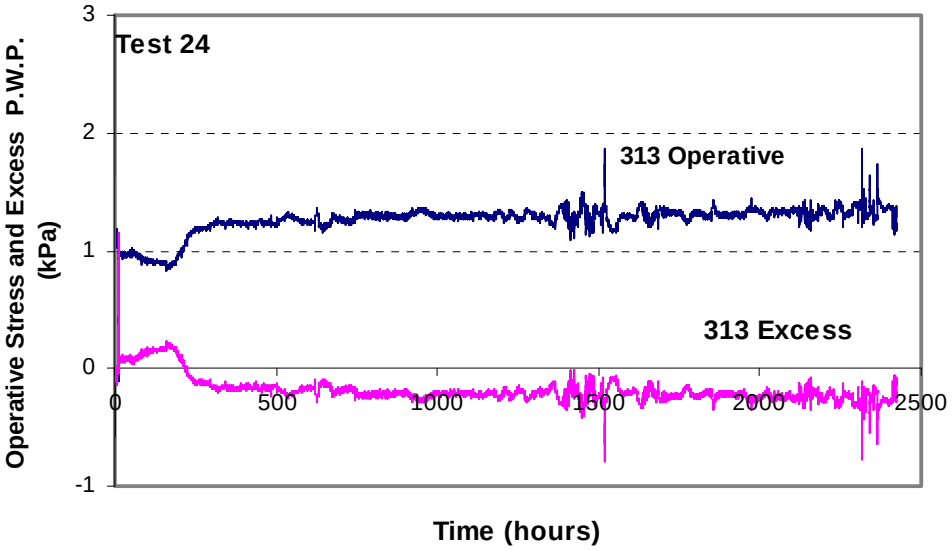

Figure 9-51 Changes in Excess pore Pressure and Operative Stress at E3 of Test 24

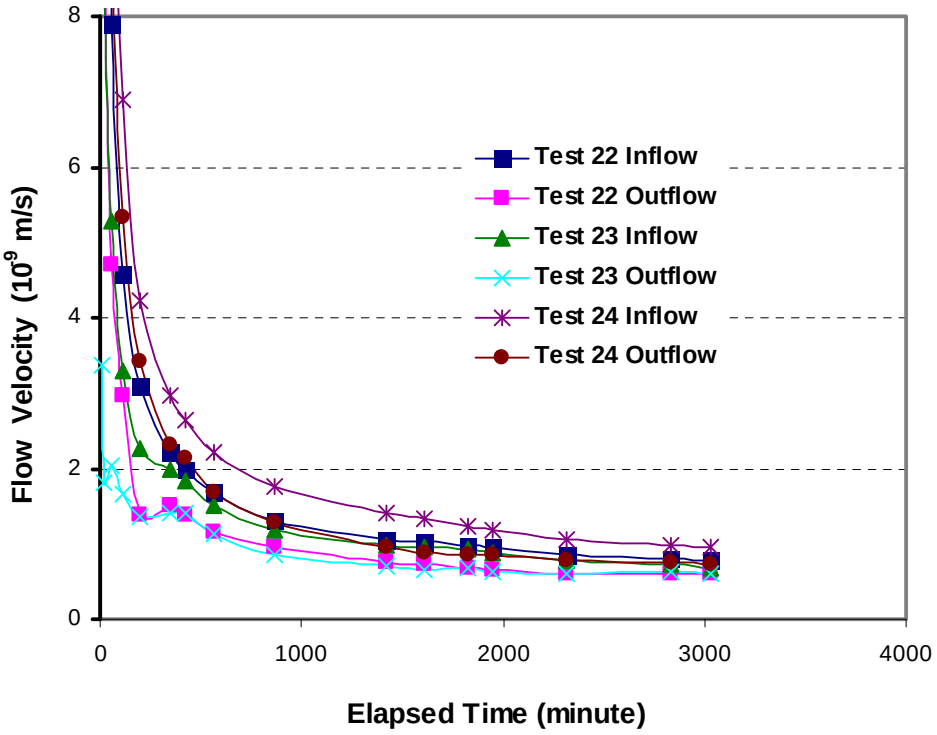

Figure 9-52 Flow Velocity vs. Time in Permeability Tests 22-24

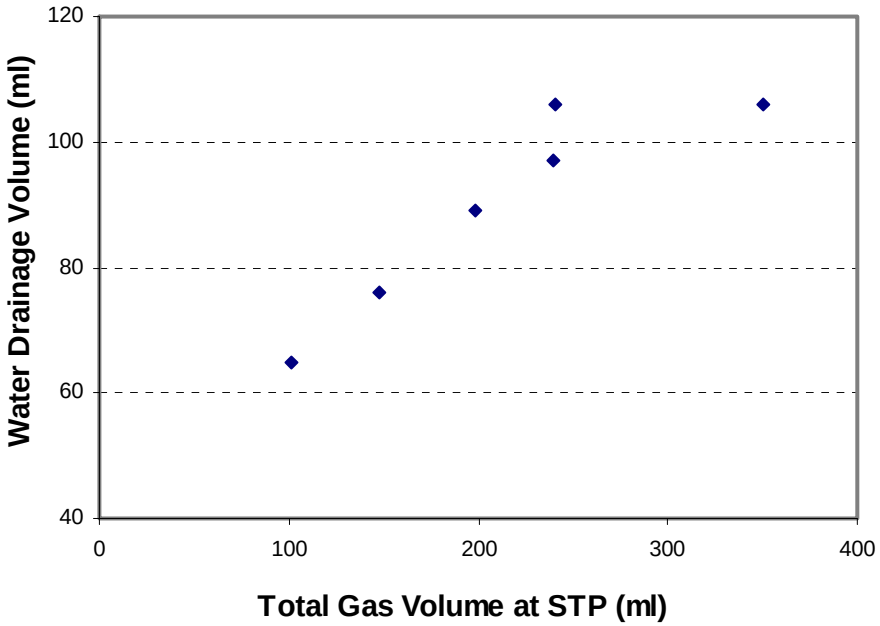

Figure 9-53 Water Drainage Volume vs. Total Gas Volume (STP) in Samples 19-24

CHAPTER 10

10 CONCLUSIONS AND RECOMMENDATIONS

10.1 Historical Monitoring Data

The historical monitoring data is used to study the depositional environmental changes and densification properties of MFT at the MLSB. The changes of some physical and chemical parameters, including solids content, fines/(fines + water), temperature, pH, electrical conductivity, and the concentrations of some major ions, are analyzed. The historical data has provided important information in helping understand the development of microbial activity and densification of MFT at the tailings pond.

Significant changes have occurred at the southern part of the MLSB since the mid 1990s. The rapid temperature increases have mainly been caused by the warm tailings discharge from the extraction plant. Since the mid 1990s, the tailings discharge has been focused at the southern part of the MLSB. The released heat from the discharged tailings has warmed up the MFT at that location. MFT temperatures have been caused to gradually decrease from the south to the north end of the pond. Although released energy from microbial activity can change the MFT temperature, its effect is minor relative to the significant temperature changes at the southern part of the MLSB.

Sulphate concentrations at both the southern and northern parts of the MLSB have decreased with time, and in 1995 reached about 20 mg/L, a value through which methanogen activity can develop at a large scale (Fedorak et al., 2002). However, the microbial activity at the southern part of the tailings pond was more intense than that at the northern end. The different intensities of microbial activity were likely due to different temperatures and some biochemical properties**.** The lower temperatures at the northern part of the MLSB were less favourable for microbial activity. The high percentage (about 60-80%) of methane in the released gas on

the water surface of the MLSB indicates that methanogenesis was the major microbial activity in the MFT at the pond.

Although the collected gas from the field syringe samples cannot provide accurate data of the gas contents of MFT in the field, it does reflect the relative changes of the trapped gas volumes in the MFT. After 1996, the gas contents of the MFT at both Sta. 1 and Sta. 3 increased, but the increases at Sta. 1 were more significant than those at Sta. 3. This indicates that microbial activity at Sta. 1 was more intense than at Sta.3. The rapid decreases in gas content after 1999 were likely caused by intense gas release. At about 5-6 m below the water-MFT interface, the gas content reached its peak value at its depth profile at Sta.1. This demonstrates that microbial activity is not uniform throughout different depths of the pond. Holowenko et al., (2000) have shown that the differences of methanogen MPNs were not obvious at different depths, and that the in situ abundance of methanogenic substrates has affected microbial activity.

The depth profiles of fines/(fines + water) show that the densification of the MFT at both Sta. 1 and Sta. 3 was accelerated after 1996, but the densification phenomenon at Sta. 1 was more significant than that at Sta. 3. The rapid MFT densification started at a time when obvious microbial activity was observed. The most rapidly densified MFT zone was about 5-6 m below the water-MFT interface, which was also the zone which had the most intense microbial activity. All of this evidence supports that microbial activity plays a very important role in rapid densification of MFT at the MLSB.

Historical chemical data shows that the concentrations of some major ions, including Na^+, Ca^{2+}, Mg^{2+}, HCO_3^-, and Cl^-, at the southern part of the MLSB have obviously increased, and that the pH value has obviously decreased since the mid 1990s. The possible reasons for the changes include the chemical variations in oil sands ore, the bitumen extraction process, and tailings/water managements. During the past years, the water chemical property of oil sands ore has become more brackish (MacKinnon, 2003, personal communications). Because pond

water is recycled for bitumen extraction, the pore water of the oil sands tailings will become more brackish with time.

With the increases of cation concentrations, especially some multivalent cations, the thickness of the diffuse double layer decreases. The chemical changes can reduce the repulsive force between clay particles and make the MFT structure more flocculated. The pH decrease can also decrease the repulsive force between clay particles. The chemical changes at the southern part of the MLSB should have potentially favorable effects on MFT densification.

10.2 Field Investigations

The field investigations have suggested that there existed rapid densification at the southern part of the MLSB, and that the densification phenomenon at the northern part of the MLSB was not observed. After a series of field investigations, the properties of the dense MFT at the MLSB have become clearer. There were good agreements between the un-drained shear strengths measured by the field vane shear test, steel plate penetration test, and cone penetration test. The steel plate penetration test is a simple and effective method to determine the range of the rapidly dense MFT. The un-drained shear strengths of the dense MFT can be approximated using this method. The rapidly dense MFT ranged from 8 m to 15 m below the water surface of the pond. The un-drained shear strength of the dense MFT was more than 2 kPa, and its physical condition was close to a plastic state. Gas bubble distribution mapping has demonstrated that the microbial activity at the southern part of the MLSB was more significant than that at the northern part. There existed a strong relationship between the intense microbial activity zone and rapid densification zone. Historical monitoring data and field investigations have all confirmed that the densification of the MFT was closely related to microbial activity.

Observations of the macro- and micro- structures of the frozen samples have suggested that the structure of the dense MFT has become more aggregated than before microbial activity. Some large fractures were observed to become favorable paths for water drainage and gas bubble migration.

Pumping operations can significantly change the stress state of MFT in the surrounding area. The disturbances brought about by the operations could have accelerated gas bubble release and thus increased the density of the MFT. On the other hand, MFT pumping obviously lowered the water-MFT interface level in the surrounding area. This would have reduced the total stress, and could have changed the effective stress of the MFT. In addition, the strong disturbances from pumping operations could have, in part, destroyed the effective stress in the MFT.

Piezometric and earth pressure measurements have shown that the vertical and lateral earth pressures and pore water pressure were close at a certain depth of the pond. This indicates that, if there existed effective stress in the MFT, it should have been very small. Since it is very difficult for an earth pressure cell to further penetrate into a dense MFT zone, the effective stresses at the lower part of dense MFT are not clear.

The effective stress at the southern part of the MLSB is affected by various factors, including MFT densification, pumping operations, and microbial activity. The densification of the MFT could have increased the effective stress, but the pumping operation might have reduced or destroyed the effective stress for the reasons discussed previously.

10.3 Small-Scale Column Tests

Small-scale column tests can be used to preliminarily model the microbial activity of MFT. The results of the tests show that nutrients (such as sodium acetate) and temperature are very important factors in the development of microbial activity.

At 24°C temperature, with the increase of added sodium acetate, microbial activity and gas generation volume increased, and water drainage from the MFT was accelerated. The results from the two columns incubated at 4°C temperature have shown that sodium acetate itself has very little influence on MFT densification, apart from its role in stimulating microbial activity. Significant temperature changes can in turn change pore water viscosity of MFT, and thus directly affect the water drainage rate. This makes it difficult to analyze the effect of microbial activity on water drainage rates of MFT (Sills et al., 2001). The results of the small-scale column tests suggest that changing sodium acetate amendments is a more effective way to study the effects of microbial activity on MFT densification than changing temperature.

10.4 Gas MFT Densification Tests

Sodium acetate was used to control the microbial activity during gas MFT densification tests. With the increase amount of added sodium acetate, the total gas generation in the MFT increased. During long-term consolidation tests at 4°C, it is likely that very weak microbial activity occurred in the MFT as acetate was added. This has been confirmed by the small gas bubbles shown on the side walls of the test cells. In the samples with no acetate added, no visible gas bubbles were observed during long-term consolidation tests. During consolidation, part of the added sodium acetate was likely depleted or was made to migrate out of the MFT along with the water drained.

During intense microbial activity, gas generation occurred during two periods: rapid gas generation with all gas bubbles trapped, and gas generation with intense gas release. The gas bubbles generated under low pressure were much more easily released than those under high pressure. This was mainly due to the presence of some large open structures (cracks and fractures) in the MFT under low pressure. The interconnected fractures allowed the gas bubbles to migrate easily and escape from the MFT. This suggests that, in a relatively stable

environment, the released gas bubbles mainly came from the shallow zone of the pond. At the southern part of the MLSB, pumping operations were said to greatly accelerate gas release from the MFT. Wheeler (1990) has indicated that gas bubbles of a realistic size can move upward only in extremely weak sediments. The results from our tests demonstrate that total pressure and structure are also very important factors in gas migration and release. Under high pressure, gas bubbles are small and tend to be tightly confined within the matrix. They are also difficult to move. Under low pressure, gas bubbles tend to move upward due to buoyancy, and small gas bubbles generally move toward large gas bubbles due to the differences in gas pressure and gas concentration. Large gas bubble formations can cause tensile stress and local stress concentrations, which in turn cause the formation of cracks and fractures within MFT.

Although Samples 1 to 6 were incubated at different pressures, the total gas generation volumes (at STP) were close for samples with the same amount of sodium acetate added. This demonstrates that microbial activity and gas generation were not obviously affected by the total pressure. However, total pressure did affect the MFT structure and gas release.

For normally consolidated Samples 1 to 6 , Samples 19 to 24, and the samples without pre-consolidation (Samples 13 to 15), with the increases of microbial activity and biogas generation, water drainage volumes from the MFT increased. During rapid gas generation, water was quickly drained out of the samples under different pressures. For each sample, water drainage rates were related to gas generation rates. Water drainage from the MFT was shown to be accelerated even if the generated gas bubbles were trapped.

During intense microbial activity under low pressures, for example, Samples 3, 15, and 21, rapid water drainage occurred at two periods: rapid gas generation with all gas trapped, and gas generation with intense gas release. During the first period, total MFT expansion lagged behind the trapped gas volume increase, so water was rapidly pushed out of the MFT. During the second period, the structures

were significantly cracked and fractured. The meta-stable dispersed structure was obviously destroyed and had collapsed. Through the duration of this period, the trapped gas volumes were almost constant, but the total MFT volumes rapidly decreased with time. There was rapid water drainage during both periods.

For the MFT with very weak microbial activity, as in Samples 1, 4 and 13, the samples were similar to saturated soils. The trapped gas volumes increased very slowly, and the total MFT volumes decreased over time. Water drainage from the samples was very slow, and the drainage volumes were approximately equal to the total MFT volume decreases.

For over-consolidated Samples 10 to 12, water flowed back into the MFT due to the presence of negative excess pore water pressure. With the increases of microbial activity, more water flowed back. For each sample, the water flow rates were related to gas generation rates. During rapid gas generation, the total MFT volume increased more rapidly than did the trapped gas volume. It appears from this observation that biogas generation can accelerate MFT expansion, and increase the difference between the total MFT volume and trapped gas volume. This causes more water to flow back into the increased number of voids.

The influences of microbial activity on MFT structures are clearly different for samples under different pressures, or with different structural strengths. Samples 1 to 3 and Samples 13 to 15 were incubated under low pressures. With the increases of microbial activity, the structural changes became significant. Some open structures (interconnected cracks and fractures) may have become favorable drainage paths. The structural changes in Sample 3 were more obvious than those in Sample 15, although more gas was generated in the latter. This is due to the different structural strengths of each sample. Before microbial activity, Sample 3 was more similar to a “soil”, while Sample 15 was more like a “slurry,” which was less “stiff” and therefore better able to form large fractures. With the increases of microbial activity and biogas generation, the coefficients of

permeability of Samples 1 to 3 and Samples 13 to 15 increased after testing. The increase of Sample 3 was more obvious than that of Sample 15. This can be attributed to their different structural changes. Due to the high pressures applied to Samples 4 to 6 and Samples 22 to 24, and the structural strengths of Samples 19 to 21, their structural changes were less obvious than those of Samples 1 to 3 and Samples 13 to 15. The cracks and fractures in these samples were mostly at closed conditions and tightly filled with gas bubbles. They could not act as convenient drainage paths for this reason. There were no obvious changes in the coefficients of permeability after microbial activity.

Rapid temperature increases may have raised excess pore water pressures in the MFT. With the increases of initial effective stress, excess pore water pressure increased more obviously. In addition, small gas bubble formation during the rapid temperature increase could have further increased the excess pore water pressure.

Due to the very slow gas generation present in Samples 1, 4 and 13, they were similar to saturated soils. The water drainage from these samples was very slow due to their low coefficients of permeability. There were no obvious changes in excess pore water pressure or operative stress during microbial activity. During rapid gas generation in Samples 2, 3, 5, 6, 14 and 15, water was rapidly drained out of the MFT. The overall changes of excess pore water pressure and operative stress were more obvious than those in Samples 1, 4, and 13.

During rapid gas generation, excess pore water pressures in Samples 2 and 3 rapidly decreased, but the operative stresses increased slowly. This was mainly due to total stress decreases during rapid gas generation. When total stresses became stable, operative stresses obviously increased. When microbial activity diminished, both excess pore water pressures and operative stresses became stable, and water drainage rates became very slow.

The changes of excess pore water pressure and operative stress in Samples 14 and 15 were more complex than those in Samples 2 and 3. During microbial activity, the changes of the coefficients of permeability of Samples 14 and 15 were less significant than those of Samples 2 and 3 for the reasons discussed previously. During the early period of accelerated gas generation in Samples 14 and 15, excess pore water pressures slightly increased with time. It is likely that extra excess pore water pressures were generated at this stage. During very rapid gas generation, the changes of excess pore water pressure and operative stress in Samples 14 and 15 were similar to those in Samples 2 and 3.

During the period of rapid gas generation there was swift water drainage from Samples 5, 6, 20, 21, 23 and 24. The changes of excess pore water pressure and operative stress in these samples were different from those of Samples 2, 3, 14 and 15. During rapid gas generation, the coefficients of permeability were less changed in Samples 5, 6, 20, 21, 23 and 24 than in 2, 3, 14 and 15. Excess pore water pressure dissipations in Samples 5, 6, 20, 21, 22, and 24 were relatively slow. The small gas bubbles that developed in these samples had to overcome greater restrictions than those in Samples 2, 3, 14, and 15. While excess pore water pressures were partly dissipated, extra excess pore water pressures were likely produced during rapid gas generation. This process can be explained as one of internal loading. Water was rapidly pushed out of the MFT when extra excess pore water pressure was produced. The changes of excess pore water pressure and operative stress were complex during microbial activity as both were affected by fluctuations of gas generation, total stress, structural strength, and permeability.

During microbial activity in the laboratory, the cation concentrations (like Na^{+}, K^{+}, Ca^{2+}, Mg^{2+}) decreased with time, anions like sulfate and bicarbonate decreased with time, pH slightly increased. The acetate concentrations were completely depleted by the end of testing. The changes in the laboratory testing were different from those in the field. The changes in the field were mainly affected by ore chemical changes, process water management, and bitumen extraction, not only

by microbial activity. The chemical changes in the field were more favorable to MFT densification compared with those occurred during microbial activity in the laboratory testing.

The MPN values of both methanogens and SRB in Samples 16© to 18© had no obvious changes during microbial activity, and the differences of the MPN values among the three samples were small. However, there were significant differences in microbial activity among the three samples. This suggests that microbial activities in Samples 16© to 18© were mainly controlled by the different amounts of nutrients (sodium acetate) added to each one. The major component (up to 80%) of the released gas from Sample 18© was methane. This demonstrates that methanogenesis was the major microbial activity during testing. The sulfate concentrations in Samples 16© to 18© were less than 10 g/mL of MFT. Although the MPN value of SRB in each sample was larger than that of methanogens, no sufficient substrate was available during testing for SRB activity.

There were some inconsistencies between the MPNs of methanogens and SRB in Samples 25© to 27©. During microbial activity (about 15 days after the temperature increased), the methanogen MPN value in Sample 27© was higher than that in Sample 25©, while the MPN value of SRB in Sample 27© was lower than that in Sample 25©. This could have helped to accelerate methane production in Sample 27©.

The test results show that methane production of the MFT can be accelerated by increasing nutrients or the methanogen MPN. It should be noted, however, that methane production can be significantly accelerated even if the MPN is stable. Holowenko et al. (2000) have demonstrated that there are no significant differences in methanogen MPN values for samples attained from 5-20 m below the water-MFT interface at the southern part of the MLSB. The obvious differences in methane gas production at different depths were likely due to the diversity among methanogenic substrates (Holowenko, 2000; Penner et al., 2004).

The microbial activity at the southern part of the MLSB has been observed to be more significant than at the northern part of the pond. The difference in MFT temperature is likely another factor.

10.5 Conclusions

10.5.1 Field Investigations

A series of field investigations were carried out from 2000 to 2002 using different methods, including piston and freeze sampling, the field vane shear test, steel plate penetration test (SPP), cone penetration test (CPT), piezometer and earth pressure measurements, and gas bubble distribution mapping. The field investigations have greatly improved our understanding of the microbial activity and densification properties of MFT at the MLSB, as outlined below:

- The rapid densification mainly occurred at the southern part of the MLSB. The densification phenomena at the northern part of the MLSB were not obvious at testing times.
- There existed obvious un-drained shear strengths in the MFT from 8 m to 15 m depths at Sta. 1 and Sta. 2. The maximum vane shear strength at Sta. 1 was more than 2 kPa. The vane shear strengths of the MFT at Sta.3 were negligible at testing times. Similar results were obtained from the cone penetration tests and steel plate penetration tests.
- Field observations of the piston samples show that the physical condition of the dense MFT was close to a plastic state.
- The steel plate penetration test (SPP) is a simple and effective method to investigate the dense MFT. The test results show that the rapidly dense MFT was mainly at the southern part of the MLSB with an area of about 3 km^2, and at depths ranging from 8 m to 15 m below the water surface. The undrained shear strength of the dense MFT can be approximated by this method.

- Piezometer and earth pressure measurements show that in situ lateral and vertical earth pressures, and pore water pressure at a certain depth of the MLSB were close. Effective stress in the dense MFT was not obvious at testing times.
- Pumping operations can significantly change the stress condition of the MFT near the pumping barge. If the operations act to accelerate gas bubble release, it could contribute to the increase of MFT density, and decrease the total MFT volume.
- Gas bubble distribution mapping shows the clear connection between the intense microbial activity zone and rapid densification zone at the MLSB.
- MFT temperatures obviously increased from the north to the south of the MLSB. The obvious temperature differences between the two locations might be a factor in bringing about the non-uniform distributions of microbial activity at the pond.
- SEM images of the frozen samples show the existence of some large gas bubbles in the MFT, and the evidence which relates to gas bubbles causing cracks and being released. Some large fractures were visually observed in the frozen samples. These could act as convenient paths for gas bubble migration and water drainage.

10.5.2 Small-Scale Column Tests

Small-scale column test is a simple and effective method to preliminarily model the microbial activity of MFT under controlled laboratory conditions. It can be used to observe microbial activity and MFT structural changes, and to initially study the influences of microbial activity on MFT densification. The successful implementation of small-scale column tests laid a solid foundation for the more comprehensive gas MFT densification test. Some conclusions derived from the small-scale column tests are summarized as follows:

- Sodium acetate can be used to effectively stimulate microbial activity at room temperature (about 25^{o}C). With the increases of added sodium acetate, the gas generation volumes and rates increased.
- Sodium acetate itself has very little influence on MFT densification, except for its role in stimulating microbial activity. Changing sodium acetate amendments is a more effective way to study the effects of microbial activity on MFT densification than changing the temperature.
- At 25^{o}C temperature, with increases of microbial activity and gas generation, water drainage volumes were seen increasing. During microbial activity and gas generation, water drainage from the MFT can be improved even if there is no gas release.
- The limitations of the small-scale column test include its inability to model the microbial activity at deep depths of the pond, and its weakness in explaining the in-depth mechanisms of the rapid densification of MFT during microbial activity.

10.5.3 Gas MFT Densification Tests

Eighteen gas MFT densification tests and nine chemical tests were carried out to study the behaviors of MFT during microbial activity. The effects of different microbial activities, stress histories, and total pressures on MFT densification were tested. The test results have been used to analyze the mechanism of rapid densification of MFT and to interpret some of the phenomena occurring at the MLSB.

- In the samples with sodium acetate amendments, very weak microbial activity was able to proceed during long-term consolidation tests at 4^{o}C temperature. Parts of the added sodium acetate were depleted or forced to migrate out of the samples along with water drained.
- Microbial activity and the total gas generation volume (at STP) were not obviously altered by total pressure, but the changes in total pressure greatly

affected the MFT structure and gas bubble release. Under high pressure, the generated gas had difficulty releasing from the MFT. This suggests that, in a stable depositional environment, the released gas bubbles are mainly from shallow depths.

- For normally consolidated samples, and those without pre-consolidation, with the increases of microbial activity and gas generation, water drainage volumes from the MFT increased. For each sample, water drainage rates were related to gas generation rates.
- In the over-consolidated MFT samples, with increases of microbial activity and gas generation, more water flowed back into the MFT. During rapid gas generation, water flowed rapidly back into the MFT.
- During rapid gas generation, water drainage from the MFT can be accelerated regardless of whether the generated gas is mostly trapped or intensely released.
- In MFT with intense microbial activity under low pressure, rapid water drainage occurred during two periods: rapid gas generation with all gas trapped, and gas generation with intense release. In MFT with intense microbial activity under high pressure, swift water drainage occurred during rapid gas generation and while most of the generated gas trapped.
- The samples under low pressures with low structural strengths (Samples 1-3 and 13-15), had intense microbial activity which significantly changed the structures of each one. The coefficients of permeability of the samples increased after microbial activity. The coefficients of permeability were affected by some open structures (cracks and fractures).
- In the samples under high pressures (Samples 4-6 and 22-24) or with high structural strengths (Samples 19-21), the fractures were mostly at closed conditions and tightly filled with gas bubbles. The coefficients of permeability of the samples were not obviously changed after intense microbial activity.
- In the MFT samples with very weak microbial activity, the MFT behavior was similar to that of saturated soil. There were no obvious changes in excess pore water pressure or operative stress after the temperature stabilized.

- For the samples with intense microbial activity under low pressure, excess pore water pressure quickly decreased during rapid gas generation, while operative stress increased slowly. This was mainly due to total stress decreases. When total stress became stable, operative stress obviously increased. With microbial activity diminishing, both excess pore water pressure and operative stress became stable, and water drainage from the MFT was very slow.
- The samples under high pressures or with high structural strengths had an increase in excess pore water pressure and decrease in operative stress during rapid gas generation. It is likely that extra excess pore water pressure was produced during rapid gas generation. Excess pore water pressure dissipation and extra excess pore water pressure generation proceeded concurrently. This process was similar to one of internal loading. There was rapid water drainage during rapid gas generation.
- The chemical changes during microbial activity in the laboratory tests were different from those occurred in the field. The field chemical changes were affected by ore chemical changes, process water management, rapid densification, and bitumen extraction. The chemical changes of the MFT in the pond should have favorable effect on its densification.
- There were no significant differences in MPN values of methanogens in the samples with different microbial activities. This demonstrates that the different intensities of microbial activity during densification tests were mainly controlled by the presence of different nutrients.

10.6 Recommendations for Future Research

Considerable progress has been made in understanding the behavior of MFT with microbial activity and gas generation. The results of this research program will be beneficial in the management of oil sands tailings, landfills, and other mine wastes with microbial activity. In order to better understand MFT properties and

to utilize microbial activity in accelerating MFT reclamation, further investigation and research is recommended as follows:

- With the increase of microbial activity at the northern part of the MLSB, it is likely that the densification of the MFT will be accelerated. The depositional environmental (physical, chemical, and biological) changes and densification properties at the northern part of the MLSB should be closely monitored.
- MFT behavior in the small samples has been studied by small-scale column tests and gas MFT densification tests. It is strongly recommended that, in the future, large-scale column tests be conducted in order to model MFT densification during microbial activity. In addition, it's suggested that numerical modeling is conducted to predict the densification of the MFT at certain conditions.
- The significant chemical changes, including decreases in pH values, increases in electrical conductivity and the concentrations of some cations, have been assumed to directly benefit MFT densification. Chemical changes at the southern part of the MLSB might be a contributing factor in the rapid densification of MFT. The influences of the chemical changes on MFT densification should be further studied.
- Recent molecular analyses of methanogens in oil sands tailings (Penner, 2006) indicate that acetate might not be the best amendment to stimulate methanogenesis. With the progress of microbiological research, a more effective amendment may be available to stimulate microbial activity.
- Microbial activity might be an option for improving MFT treatment. To rapidly increase the density of MFT to a large scale by this method, it is important to find a more effective amendment in the acceleration of microbial activity. In addition, the microbial activity method could be combined with other methods, such as non-segregated tailings (NST), to accelerate MFT densification.
- It's suggested that oil sands industry make greater efforts to develop alternative tailings technologies to accelerate tailings treatment and land

reclamation. So, we can minimize greenhouse gas release from tailings ponds and avoid long-term tailings storage and transferring costs.

REFERENCES

ACR (Alberta Chamber of Resources), 1995. Canada's oil sands industry: yesterday, today and tomorrow. Prepared by National Task Forces on Oil Sands Strategies of the Alberta Chamber of Resources. Alberta.

AGRA, 1997. Progress on MFT modeling, Report to Syncrude Canada Ltd. by AGRA Earth & Environmental limited, Edmonton, Alberta. 29 pages

Alberta Energy and Utilities Board (AEUB), 2004. Alberta's Reserves 2003 and Supply/Demand Outlook 2004-2013. Calgary, Alberta.

Al-Amoudi, A., Norlen, L.P., Doborchet, J., 2004. Cryo-electron microscopy of vitreous sections of native biological cells and tissues. Journal of Structural Biology, 148 (1):131-5.

AOSD (Alberta Oil Sands Developers), 1998. From Potential to Prosperity: Progress in Canada's Oil Sands. Alberta, Canada.

Bjerrum, L. 1967. Engineering geology of Norwegian normally-consolidated marine clays as related to settlements of buildings. Geotechnique, 17, pp. 81-118.

Bo, M.W., Choa, V., Wong, K.S.2000. Compression tests on a slurry using a small-scale consolidometer. Canadian Geotechnical Journal 39:388-398.

Campanella, R.G., 1984. Piezometer-friction cone investigation at the tailings dam. Canadian Geotechnical Journal, 21 (3), 551-562.

Chandler, R.J., 1987. The in-situ measurements of the un-drained shear strength of clays using the field vane. Vane Shear Strength Testing in Soils: Field and Laboratory Studies. Edited by Richards, A.F. STP 1014, ASTM, 1916 Race Street, Philadelphia, PA 19103.

Cooper, P. and Harrington, D. 1988. Biological effluent treatment. In Biotechnology for engineers (ed. A. H. Scragg), pp. 350-365. New York: John Wiley & Sons.

Craig, R.F. 1992. Soil Mechanics, the fifth edition. Chapman & Hall, London, UK.

Dawson, R.F., Sego, D.C., Pollock, G. W., 1999. Freeze-thaw dewatering of oil sands fine tailings. Canadian Geotechnical Journal Vol. 36, pp. 587-598.

Eckert, W.F., Masliyah, J.H., Gray, M.R., and Fedorak, P.M. 1996. Prediction of sedimentation and consolidation of fine tails. AIChE J. 42: 960-972.

Esrig, M.I., Kirby, R.C., 1977. Implications of gas content for predicting the stability of submarine slopes. Marine Geotechnology, Vol. 2, pp.

Fedorak P.M., Coy D.L, Dudas, M.J., Renneberg, A.J., Salloum, M.J., 2000. Role of microbiological processes on sulfate-enriched tailings deposits. Research Report, Department of Biological Sciences and Department of Renewable Resources, University of Alberta, Edmonton, Alberta.

Fedorak P.M., Coy D.L., Salloum M.J., and Dudas M.J., 2002. Methanogenic potential of tailings samples from oil sands extraction plants. Can. J. Microbiol. **48**: 21-33.

Fedorak P.M., 2003. Personal Communications.

Fourie, A. B., Hofman, B.A., Mikula, R.J., Lord, E.R.F., Robertson, P.K., 2001.

Partially Saturated Tailings Sand below the Phreatic Surface, Geotechnique 51, NO.7, 577-585.

Fredlund, D.G. 1985. Soil mechanics principles that embrace unsaturated soils. Proc. 11th Int. Conf. Soil Mech. Fnd Engng, San Francisco 2, 465-472.

Fredlund, D.G., Rahardjo, H., 1993. Soil Mechanics for Unsaturated Soils, John Wiley & Sons ltd.

FTFC (Fine Tailings Fundamentals Consortium), 1995. Advances in Oil Sands Tailings Research. Alberta Department of Energy. Oil Sands and Research Division. Edmonton. Alberta.

Gardner, T.N., Goringe, M.J., 1988. The measurement of gas bubble size distributions: three phase laboratory gassy soil. Geotechnical Testing Journal, GTJODJ, Vol. 11, No. 1, pp. 49-55.

Guo, C., Chalaturnyk, R.J., Scott, J.D., MacKinnon, M., and Cyre, G., 2002. Geotechnical field investigation of the densification phenomenon in the oil sands mature fine tailings. 55th Canadian Geotechnical Conference, Niagara Falls, Ontario, 8 pages on a CD.

Guo, C., Chalaturnyk, R.J., Scott, J.D., MacKinnon, M., 2004. Densification of oil sands tailings by biological gas generation. 57th Canadian Geotechnical Conference, Quebec City, 8 pages on a CD.

Head, K.H., 1989. Soil Technicians' Handbook. John Wiley & Sons, New York. Toronto.

Holowenko, F.M., MacKinnon, M.D., and Fedorak, P.M. 2000. Methanogens and surfate-reducing bacteria in oil sands fine tailings wastes. Can. J. Microbial 46:927-937.

Jeeravipoolvarn, 2004. Compression Behavior of Thixotropic Oil Sands Tailings. Master's Thesis, the Department of Civil and Environmental Engineering, University of Alberta.

Langmuir, D. 1997. Aqueous Environmental Geochemistry. Prentice Hall, Upper Saddle River, new Jersey 07458.

Lunne, T., Robertson, P.K., Powell, J.J.M., 1997. Cone Penetration Testing in Geotechnical Practice. Blackie Academic and Professional, an imprint of Chapman & Hall, London, UK. 312 pages.

Luo, G.X., 2004. Investigation of CT Beneath MFT Deposition for Oil Sands Tailings Disposal. M.Sc thesis, Department of Civil and Environmental Engineering, University of Alberta, Edmonton, AB, Canada.

MacKinnon M. D. and Sethi A., 1993. A Comparison of the Physical and Chemical Properties of the Tailings Ponds at the Syncrude and Suncor Oil Sands Plants. Proceedings of Fine Tailings Symposium: "Oil Sands---Our Petroleum Future". Edmonton. Alberta.

MacKinnon M.D., Matthews J.G., Shaw W.H., and Cuddy R.G., 2000. Water Quality Issue Associated with Implementation of Composite Tailings (CT) Technology for Managing Oil Sands Tailings. Proceedings of SWEMP 2000. Calgary. Alberta.

MacKinnon,M.D., 2003. Personal Communications.

Marison, I.W., 1988. Growth kinetics. In Biotechnology for engineers (ed. A. H. Scragg), pp. 184-217. New York: John Wiley & Sons.

Matyas, E.L., Radhakrishna, H.S., 1968. Volume change characteristics of partially saturated soils. Geotechnique 18, No. 4, 432-448.

Mikula, R. J., Kasperski, K. L., Burns, R., MacKinnon, M.D. 1996. The nature and fate of oil sands fine tailings. Suspensions: Fundamentals and Applications in the Petroleum Industry. L. L. Schramm. Washington, D.C., ACS. **251:** 677-723.

Mitchell J.K., 1993. Fundamentals of Soil Behaviors. John Wiley & Sons, Inc. New York, USA.

Olson, R.E., 1986. State of the art: consolidation testing. Consolidation of Soils: Testing and Evaluation, ASTM STP 892, R.N.Yong and F.C. Townsend, Eds., American Society for Testing and Materials, Philadephia.

Penner, T., 2006. Analysis of methanogenic microbial communities from oil sands processing tailings. M. Sc. Thesis, University of Alberta, Edmonton, Canada.

Petroleum Communication Foundation, 2000. Canada's Oil Sands and Heavy Oil. Alberta, Canada.

Pollock, G.W. 1988. Large Strain Consolidation of Oil Sand Tailings Sludge. M. Sc. Thesis, University of Alberta, Edmonton, Alberta.

Sheeran, D.E., 1993. An improved understanding of fine tailings structure and behaviour. Proceedings of Fine Tailings Symposium: "Oil Sands---Our Petroleum Future". Edmonton. Alberta.

Sheeran, D.E., 2003. Personal Communications

Sidique, T., Fedorak, P.M., MacKinnon, M. D., Foght, J. M., 2006. Biodegradation of Short-Chain n-Alkanes in Oil Sands Tailings under Methanogenic Conditions. Environmental Science & Technology, Vol. 40, 5459-5464.

Sidique, T., Fedorak, P.M., MacKinnon, M. D., Foght, J. M., 2007. Metabolism of BTEX and Naphtha Compounds to Methane in Oil Sands Tailings. Environmental Science & Technology, Vol. 41, NO. 7, 2350-2356.

Sills, G.C., Wheeler, S.J., Thomas, S.D., and Gardner, T.N., 1991. Behaviour of offshore soils containing gas bubbles. Geotechnique 41, No. 2, 227-241.

Sills, G.C., Gonzalez, R. 2001. Consolidation of naturally gassy soft soil. Geotechnique 51, No. 7, 629-639.

Sobolewski, A. 1992. The microbial characteristics of oil sands tailings sludge. Consultant's report submitted to Alberta Oil Sands Technology Research Authority. Calgary, Alberta.

Sparks, A.D.W., 1963. Theoretical considerations of stress equations for partly saturated soils. Proc. 3rd African Conf. Soil Mech. Fdn Engng, Salisbury, Rhodesia 1, 215-218.

Suthaker, N.N., 1995. Geotechnics of Oil Sands Fine Tailings. PhD Thesis. Department of Civil and Environmental Engineering, University of Alberta, Edmonton, AB, Canada.

Syncrude Canada Ltd. 1995. Syncrude Analytical Methods (SAM) Manual. 4th ed. Syncrude Canada Ltd. Research Department. Edmonton, Alberta.

Terzaghi, K., 1936. The shear resistance of saturated soils and the angles between

the planes of shear. Proc. 1st Int. Conf. Soil Mech., Harvard, Vol. 1, pp. 54-56.

Thomas, S.D. 1987. The Consolidation Behaviour of Gassy Soil. D.Phil.thesis, Oxford University.

Tiner, R. W., 1999. Wetland Indicators: A Guide to Wetland Identification, Delineation, Classification, and Mapping. CRC Press, Taylor & Francis Group.

Touhidi, A., 1998. Absolute permeability of McMurray formation oil sands at low confining stresses. Department of Civil and Environmental Engineering, University of Alberta, Edmonton, AB, Canada.

Vidic, S.D., 1995. Profiling mine tailings with CPT. Proceedings of the International Symposium on Cone Penetration Testing, CPT'95, Linkoping, Swede, 2, 607-612, Swedish Geotechnical Society.

Wells, P.S., Riley, D. A., 2006. MFT drying – case study in the use of rheological modification and dewatering of fine tailings through thin life deposition in the oil sands of Alberta. Proceedings of the Tenth International Seminar on Paste and Thickened Tailings, 13-15 March 2007, Perth, Australia.

Whelan, T., J.M., Coleman, J.N. Suhayda, and H.H. Roberts. 1977. Acoustical penetration and shear strength in gas-charged sediment. Marine Geotechnology 2:147-159.

Wheeler, S.J., 1988. A concept model of soils containing large gas bubbles. Geotechnique 38, 389-397.

Wheeler, S.J., Sham, W.K., Thomas, S.D., 1990. Gas pressure in unsaturated

offshore soils. Canadian Geotechnical Journal, Vol. 27, 79-89.

Wheeler, S.J. 1990. Movement of large gas bubbles in unsaturated fine-grained sediments. Marine Geotechnology, Volume 9, pp.113-129.

Wichman, B.G.H.M. (1999). Consolidation behavior of gassy mud: theory and experimental validation. Ph. D thesis, Delft university, the Netherlands.

Wichman, B.G.H.M., 2000. A finite strain theory for gassy sludge. Geotechnique 50, No. 1, 35-41.

Wichman, B.G.H.M., Sills, G.C., and Gonzalez, R. 2000.Experimental validation of a fine strain theory for gassy mud. Canadian Geotechnical Journal, Vol. 37, pp.1227-1240.

Zinder, S.H., 1993. Physiological ecology of methanogens. In: J.G. Ferry (ed). Methanogenesis. Champpman and Hall, Inc. New York, NY. Pp. 128-206.

APPENDIX A Field Descriptions of the Piston Sampling

During the field investigations at the MLSB and WIP in 2001, the piston samples were recorded and described on the boat before they were stored into the glass jars. This section demonstrates the results of the field descriptions.

Table A. 1 Field Descriptions of the Piston Sampling at Sta.1 of the MLSB

Depth	Descriptions
0 ~ 4 m	Water
4 ~ 5 m	Light MFT (thin fine tailings slurry)
5 ~ 6 m	Medium MFT (flowing state tailings slurry)
7 ~ 9m	Dense to very dense MFT
10 ~ 11m	Very dense MFT
12.5 ~13.5m	Dense MFT
Sampling date: May 22, 2001; Coordinates: 461927 (Easting), 6324940 (Northing)	

Table A. 2 Field Descriptions of the Piston Sampling at Sta.2 of the MLSB

Depth	Descriptions
0 — 3m	Water
4 — 5m	Light tailings slurry
6 — 13m	Medium - dense MFT, flowing state tailings.
14 — 19m	Dense to very dense MFT. (At 15 m, very dense, plastic state. When the glass jar was turned upside down, the sample stayed inside the jar for long time without falling out.)
20 — 33m	Dense MFT and sandy tailings
36 — 45m	Beach sand
Sampling date: May 24, 2001; Coordinates: 461397 (Easting), 6325690 (Northing)	

Table A. 3 Field Descriptions of the Piston Sampling at Sta.3 of the MLSB

Depth	Descriptions
0 — 2m	Water
2 — 5m	Light MFT
5 — 28m	Medium to dense MFT and sandy tailings
29m	Beach sand
Sampling date: May 25, 2001; Coordinates: 460089 (Easting), 6327113 (Northing)	

Table A. 4 Field Descriptions of the Piston Sampling at Sta. A (near the pumping barge) of the WIP

Depth	Descriptions
0 — 3m	Water
4 — 8m	Light MFT
9 — 27m	Medium, or medium to dense MFT.
31 — 34m	Dense to very dense material, pit bottom
Sampling date: May 26, 2001; Coordinates: 462377 (Easting), 6319143 (Northing)	

Table A. 5 Field Descriptions of the Piston Sampling at Sta. B of the WIP

Depth	Descriptions
0 — 3m	Water
4 — 6m	Light MFT
7 — 12m	Medium MFT, a lot of gas bubbles are observed when sampling.
13 — 31m	Medium - dense MFT.
33 — 36m	Pit bottom, very dense material, plastic state
Sampling date: May 27, 2001; Coordinates: 4632145 (Easting), 6319022 (Northing)	

APPENDIX B Approximate Calculation of the Undrained Shear Strength by the Steel Plate Penetration Test

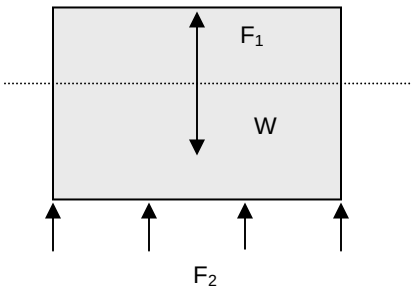

Figure B. 1 Schematic of the Forces on the Plate

Where:

W: weight of the steel plate
F_1: buoyant force of the fine tailings
F_2: net base resistance
Side friction neglected.

$$W = F_1 + F_2 \quad [1]$$

$$F_1 = V\gamma \quad [2]$$

$$\sigma_b = F_2 / A \quad [3]$$

Where:

V: the volume of the steel plate
γ: the average unit weight of the fine tailings
σ_b : net base stress of the steel plate
A: the base area of the steel plate

For Plate No.4:

$W = 0.381$ kN
$F_1 = V\gamma = 0.0565$ kN

(Assume the average unit weight of the fine tailings: 12 kN/m^3)

$F_2 = 0.325$ kN
$\sigma_b = F_2/A = 10.33$ kPa

The un-drained shear strength of the fine tailings can be approximately calculated as follows:

Assume the steel plate is a shallow foundation embedded in the fine tailings.

$q_f = N_c s_u + \gamma D$ [4]

Where:

q_f: ultimate limit bearing capacity

N_c: function of footing width and shape

s_u: undrained shear strength

D: the depth of the foundation base

$q_f - \gamma D = \sigma_b$ [5]

$s_u = \sigma_b / N_c$ [6]

For steel block No. 4:

Assume $N_c = 5.14$

$s_u = \sigma_b / 5.14 = 2.01$

APPENDIX C Piezometer and Earth Pressure Measurements

This appendix shows the results of the total lateral earth pressure and pore water pressure measurements at the MLSB in 2002.

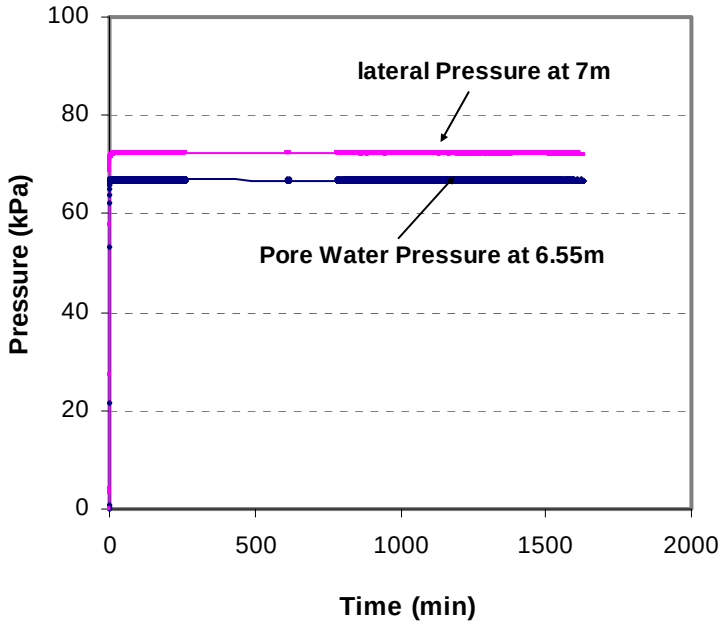

Figure C. 1 Total Lateral Pressure at 7 m and Pore Water Pressure at 6.55 m below Water Surface at Sta. 1

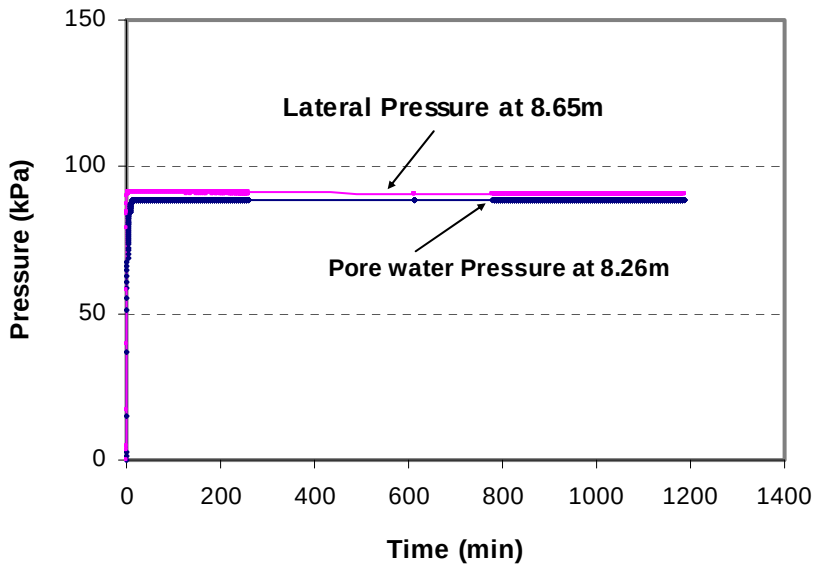

Figure C. 2 Total Lateral Pressure at 8.65 m and Pore Water Pressure at 8.26 m below Water Surface at Sta. 1

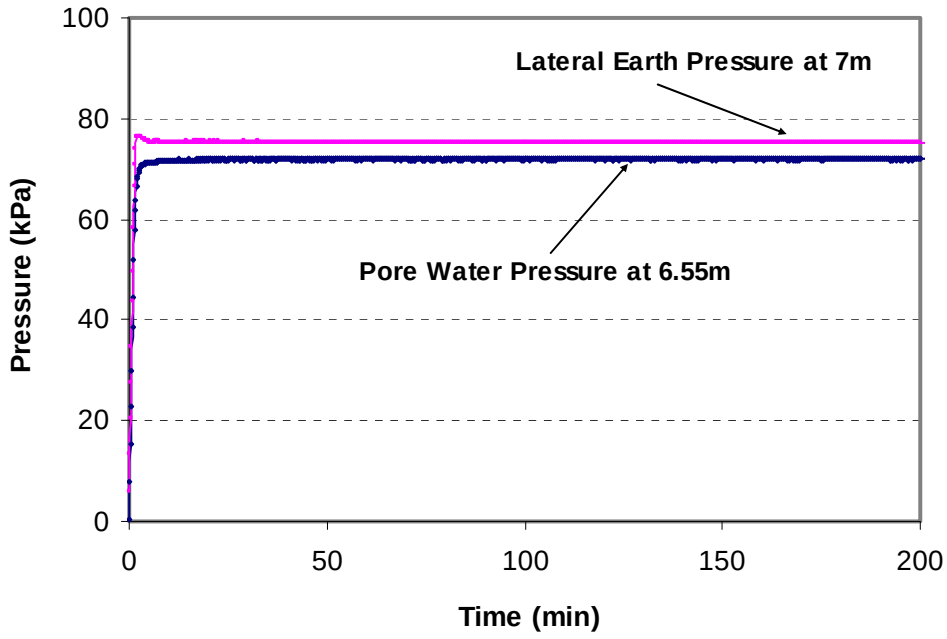

Figure C. 3 Total Lateral Pressure at 7 m and Pore Water Pressure at 6.55 m below Water Surface at Sta. 2

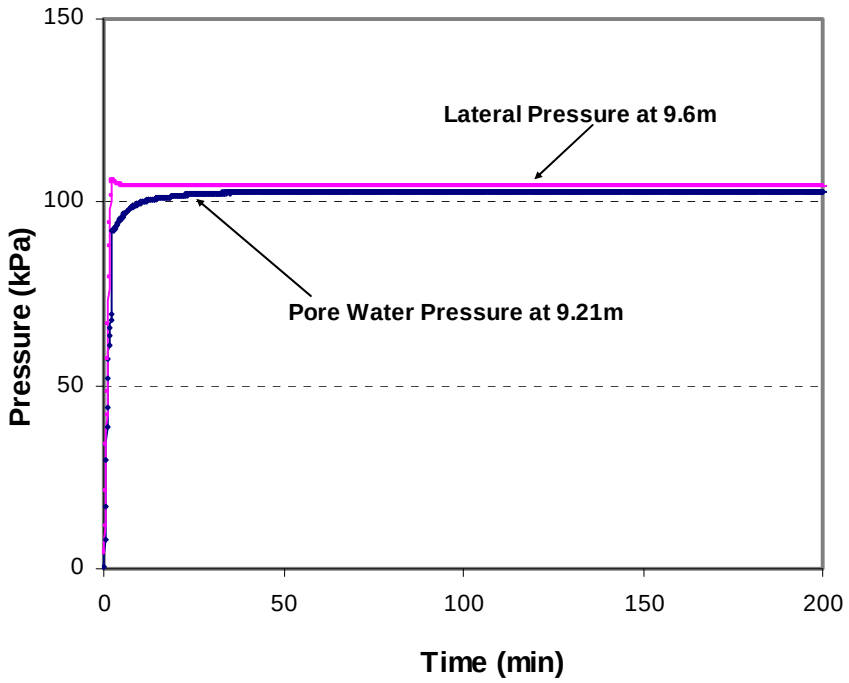

Figure C. 4 Total Lateral Pressure at 9.6 m and Pore Water Pressure at 9.21 m below Water Surface at Sta. 2

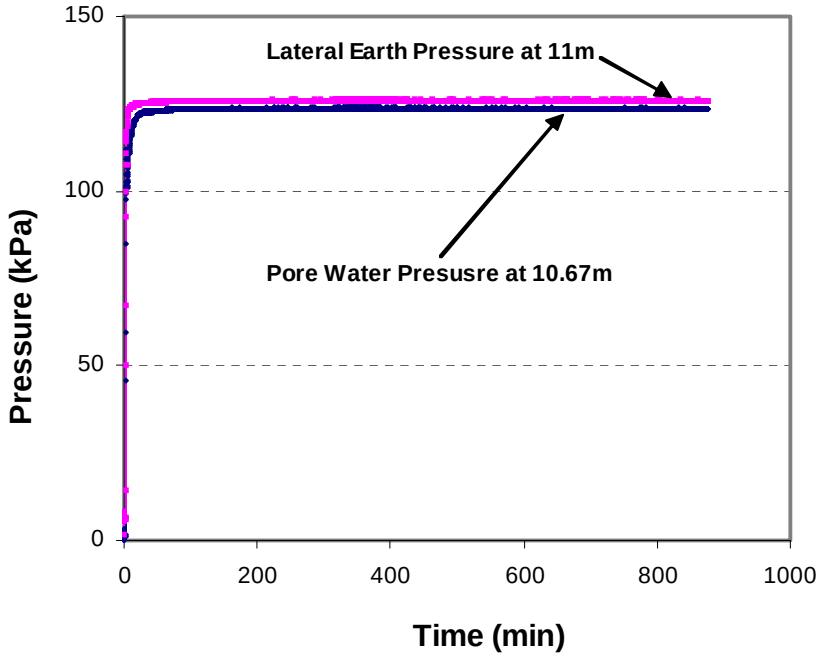

Figure C. 5 Total Lateral Pressure at 11 m and Pore Water Pressure at 10.67 m below Water Surface at Sta. 2

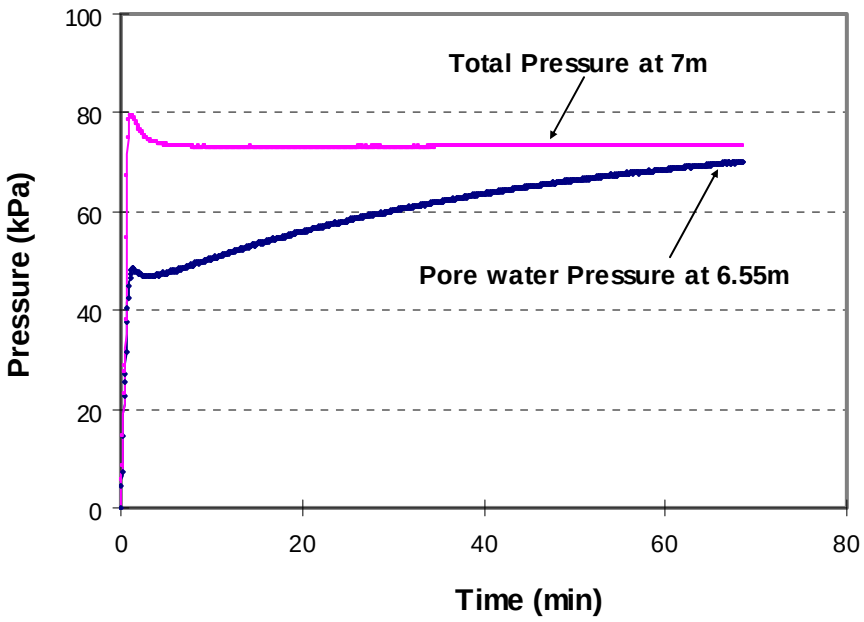

Figure C. 6 Total Lateral Pressure at 7 m and Pore Water Pressure at 6.55 m below Water Surface at Sta. 3

APPENDIX D Field Equipment Calibration Results

This appendix shows the calibration results of field vane shear tests, piezometers, earth pressure cells, and cone penetration tests.

Table D. 1 Calibration Coefficients of Piezometers and Total Pressure Cells in 2002

Serial No.	A	B	C	Calibration Temperature (Deg.C)	Temperature Coefficient (kPa/Deg.C)
74515	-0.000087975	-0.011452	876.58	23	0.1034
74516	-0.000090126	-0.039791	1011.7	23	-0.0146
74517	-0.00009502	-0.039572	1033.7	23	-0.0703
74518	-0.000074206	-0.081936	987.4	21.9	-0.1103
74519	-0.000092898	-0.057766	1102.8	21.9	-0.1358
74520	-0.0001011	-0.02654	1035.5	21.9	-0.1496
74521	-0.000093352	-0.063757	1106.8	21.9	-0.0189

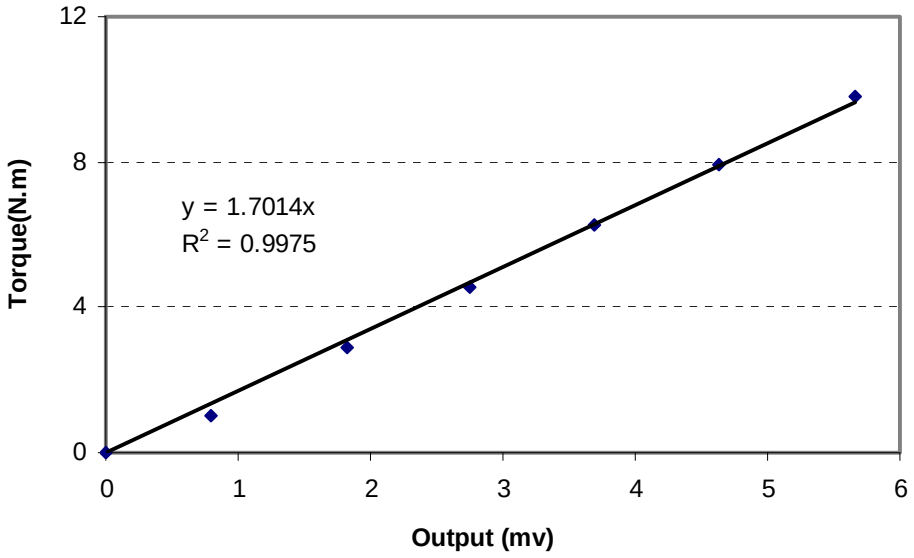

Figure D. 1 Calibration of the Field Vane Shear Test in 2001

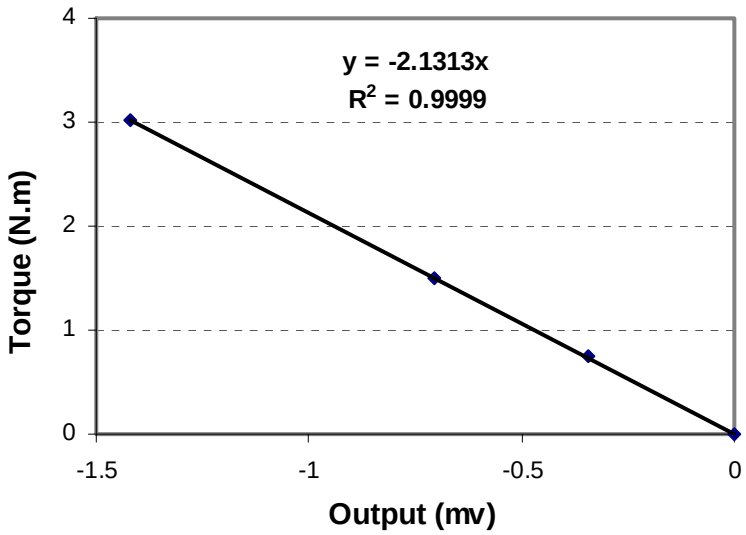

Figure D. 2 Calibration of the Field Vane Shear Test in 2002

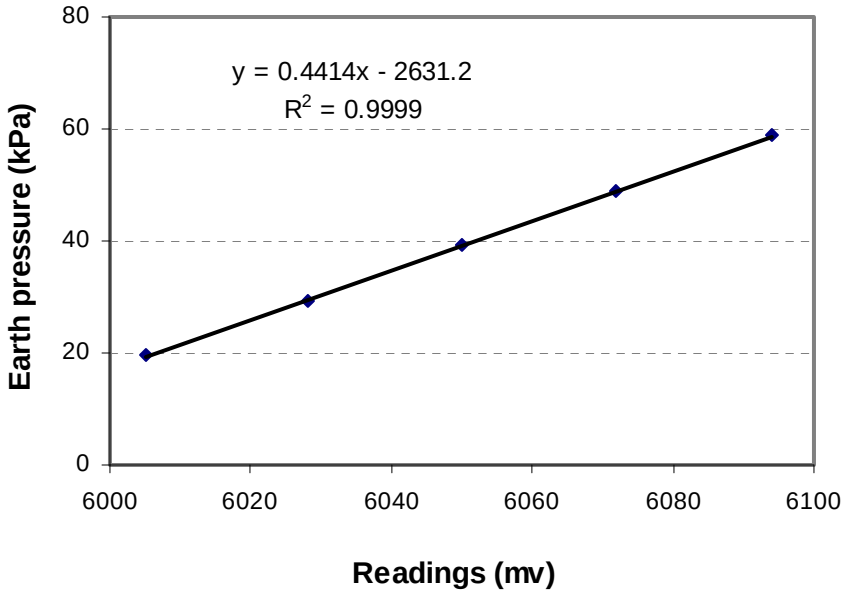

Figure D. 3 Calibration of the IRAD GAGE Earth Pressure Cell in 2001

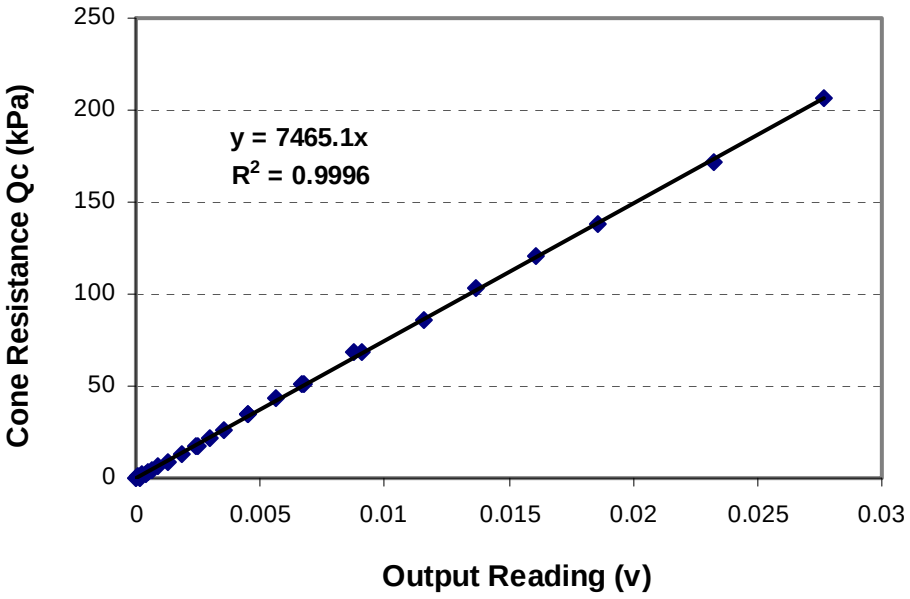

Figure D. 4 Calibration Results of 1.5" Cone Used in 2000

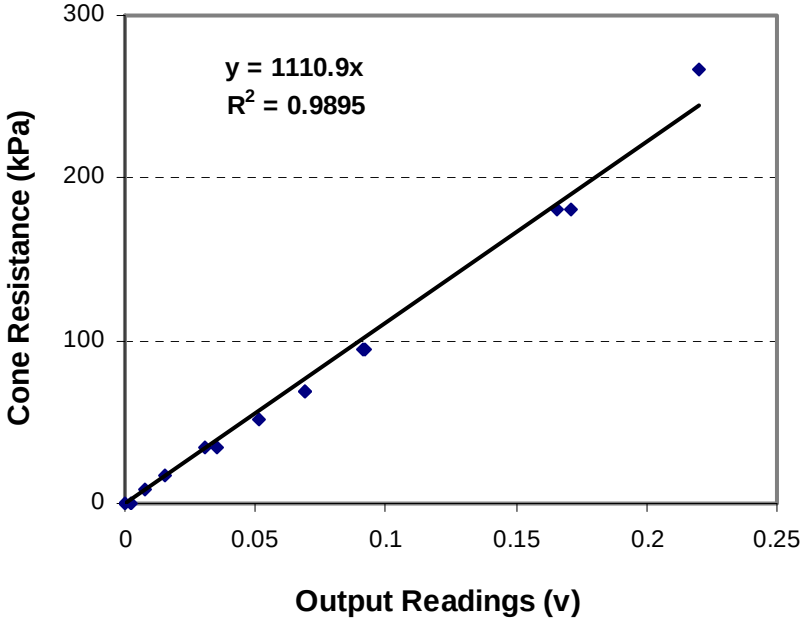

Figure D. 5 Calibration Result of 1.5" Cone Used in 2001

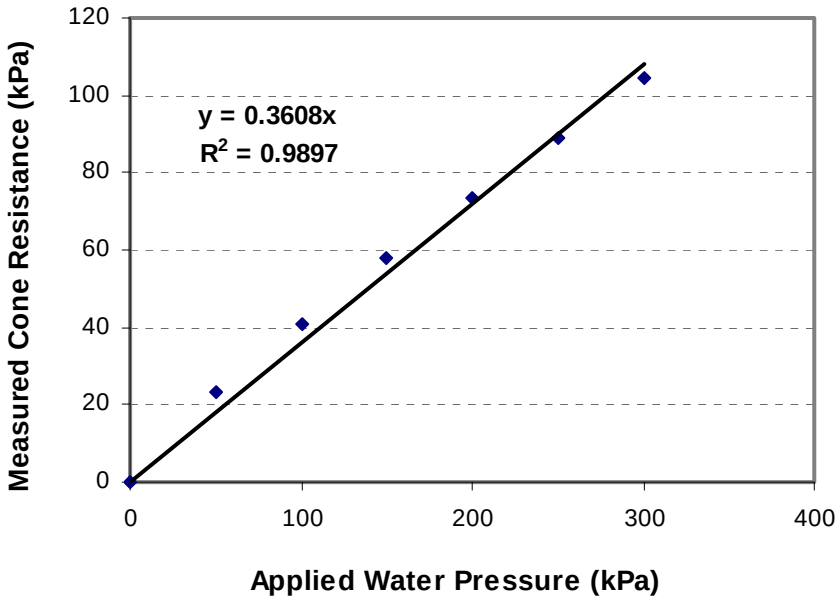

Figure D. 6 Determination of Area Ratio (a) for 1.5" Cone in 2001

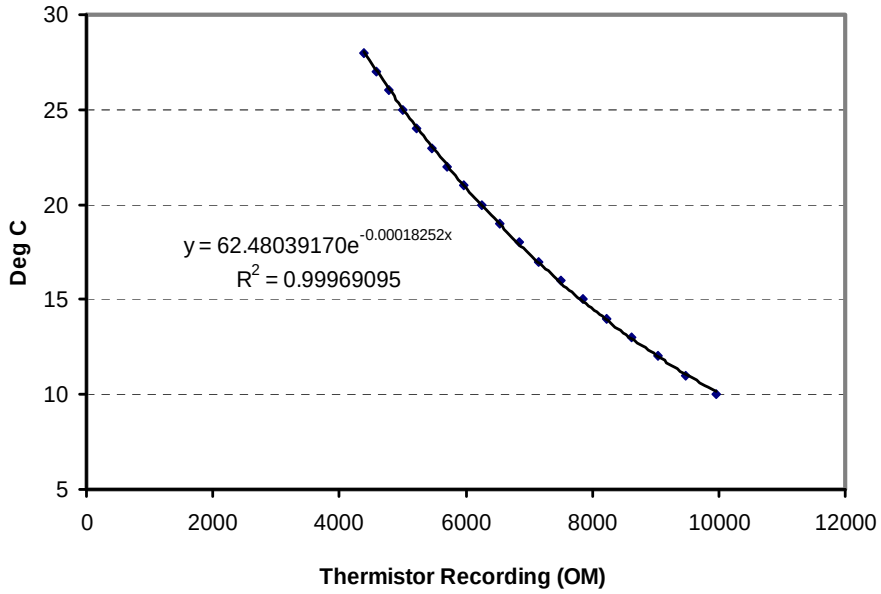

Figure D. 7 Thermister Calibration in 2002 Field Testing

APPENDIX E Observations of Microbial Activity in Small-Scale Columns 1 to 5

During microbial activity, the MFT structures were observed and photographed. This appendix demonstrates some the observations.

Column 5

All the columns were set up on March 7 (Day one). On Day two, some small gas fissures were observed at the upper part of the MFT sediment in column 5. On Day five the MFT interface level had obviously expanded, and some horizontal and vertical cracks appeared near the interface of the MFT. On Day seven **(**Figure E.1**)** these large cracks divided the top of the MFT into brick-shaped blocks. At a level of about 6 cm below the interface, a large crack 2.3 cm long and 0.3 cm wide was observed. Most of the large gas voids and cracks were above the elevation of about 10 cm from the bottom of the column. Below this elevation, only small gas voids were observed. There was no visible gas release until Day eight.

On Day nine **(**Figure E.2 and Figure E.3), gas accumulation within the MFT reached a critical state. The gas bubbles burst out of the interface. The brick-shaped blocks were broken due to sudden flooding of the gas bubbles. The interface of the MFT then settled downwards, and large gas cracks at 6 cm elevation below the interface disappeared. After gas release, some large voids (cracks) disappeared or became smaller, and some long and continuous cracks became shorter and occluded.

Gas bubbles continued to form, migrate and release until Day 18 (March 24). Some large cracks were formed, but then disappeared due to gas release. Later, new large cracks were formed, and disappeared again. These phenomena are shown in Figures E.1 (Day seven) through E.6 (Day 18). With increasing gas release, the MFT structure obviously collapsed, leaving some of the original large cracks as occluded voids. On Day 18, the interface level was very close to its initial elevation. The MFT matrix surrounding the large gas bubbles became very dense.

Column 3

Figure E.7 (Day seven) and Figure E.8 (Day 18) show the structural changes of the MFT in column 3. The changes are similar to those observed in column 5 in that most of the large voids were in the upper portion of the column. Although some inclined cracks were observed, most of the cracks extended in the horizontal direction. This is because the MFT could only expand in the vertical direction. There was no obvious difference in gas bubble distribution and morphology between Figure E.7 and Figure E.8. This indicates that microbial activity became less significant after Day eight. There was no visible gas release during testing.

Column 1

Gas generation in column 1 was much slower than that in columns 3 and 5. On Day nine, some tiny gas fissures extending horizontally appeared at the upper part of the column, as shown in Figure E.9. On Day 13, a fissure with 0.5 mm width, extending almost around the entire perimeter of the column, was observed at the upper part of the column. On Day 18 (Figure E.10**)** the crack was about 1 mm wide. The interface of the MFT heaved up 0.32 mm. There was no visible gas release.

Columns 2 and 4

Different amounts of sodium acetate were added to the MFT in columns 2 and 4, both of which were incubated in a 4^{o}C temperature room. No visible gas bubbles were observed in these two columns during testing. Figure E.11 shows a photo of column 4 on Day 18. The interfaces in both columns settled down slightly during the testing period.

Figure E.12 shows a photo of the five columns at the end of testing (Day 18). Obvious differences in gas generation and structural changes can be observed from the photo.

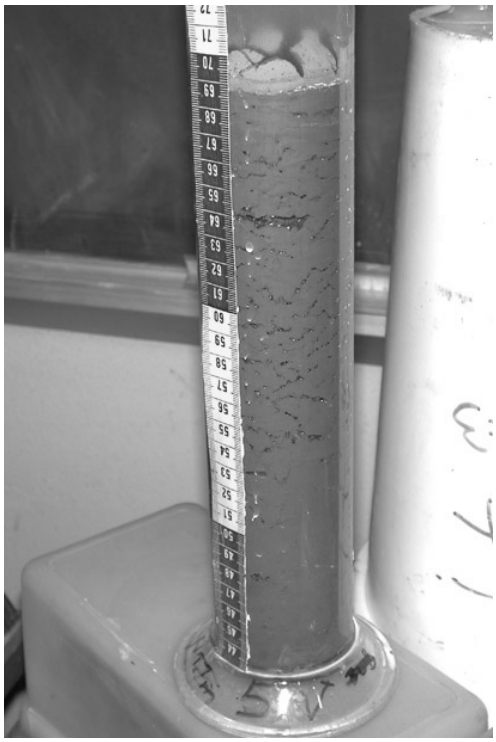

Figure E. 1 Column 5 on Day 7 (March 13)

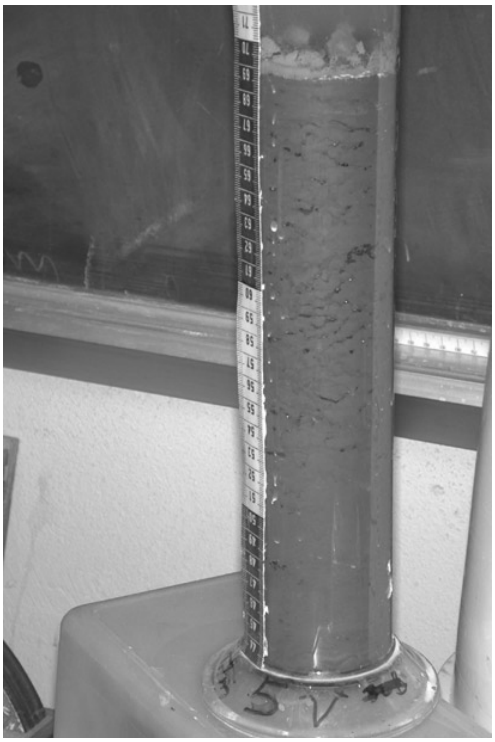

Figure E. 2 Column 5 on Day 9 (March 15)

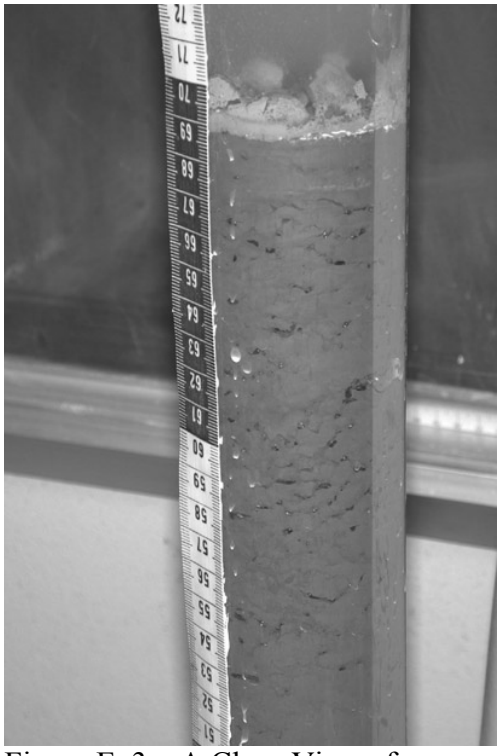

Figure E. 3 A Close View of Column 5 on Day 9

Figure E. 4 Column 5 on Day 11

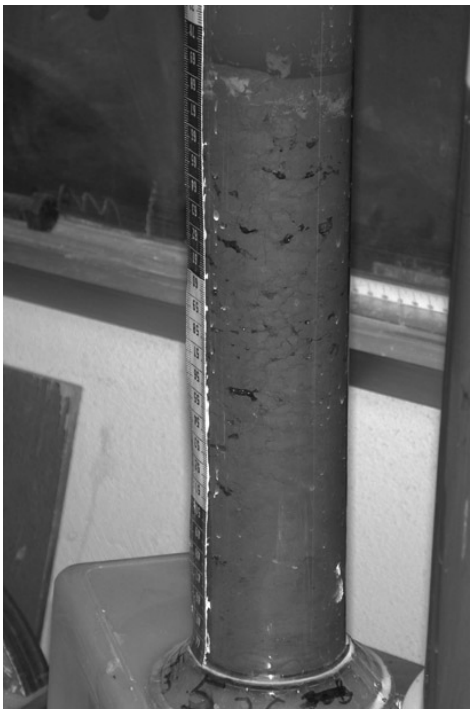

Figure E. 5 Column 5 on Day 13

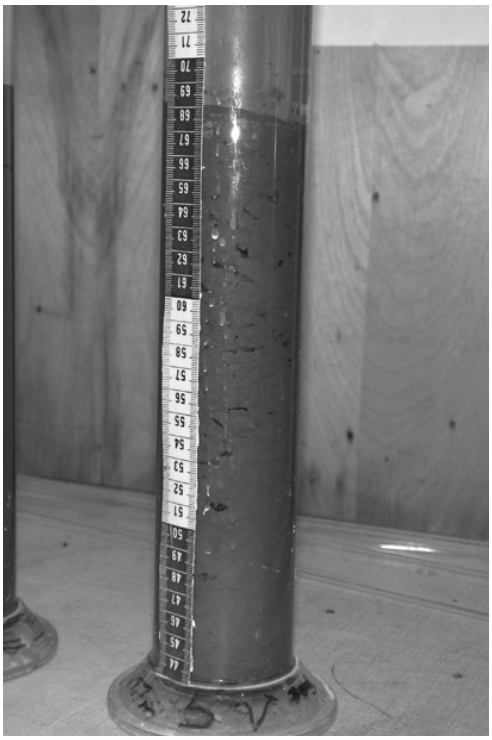

Figure E. 6 Column 5 on Day 18 (March 24)

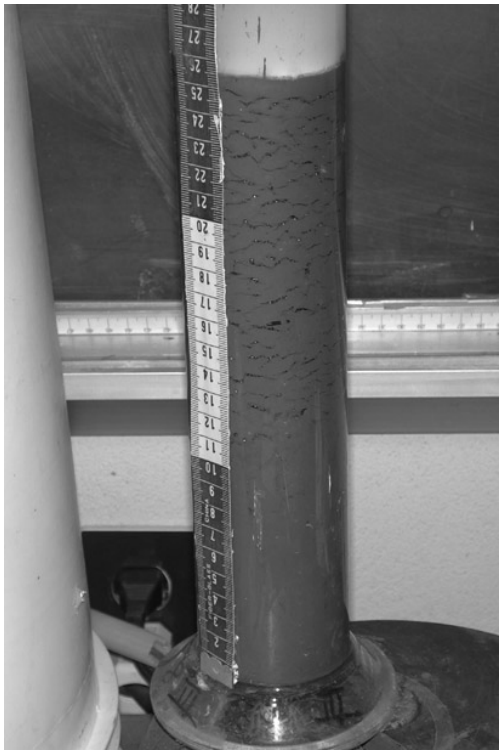

Figure E. 7 Column 3 on Day 7 (March 13)

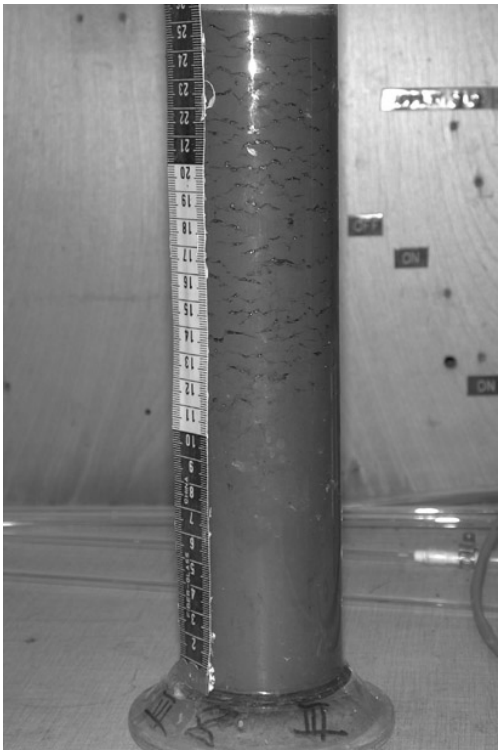

Figure E. 8 Column 3 on Day 18 (March 24)

Figure E. 9 Column 1 on Day 9 (March 15)

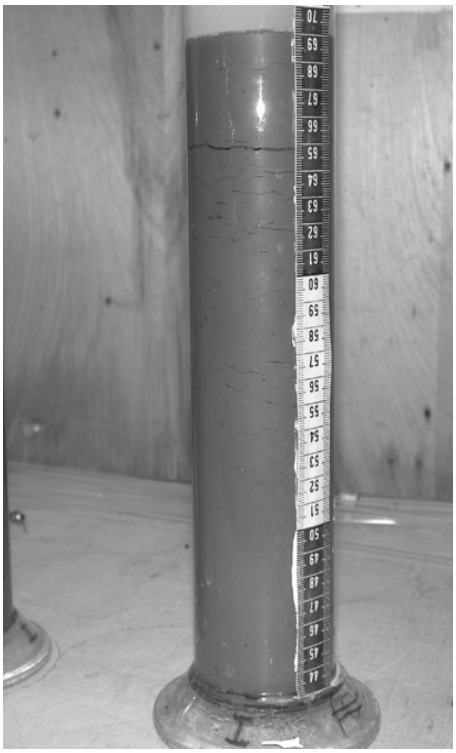

Figure E. 10 Column 1 on Day 18 (March 24)

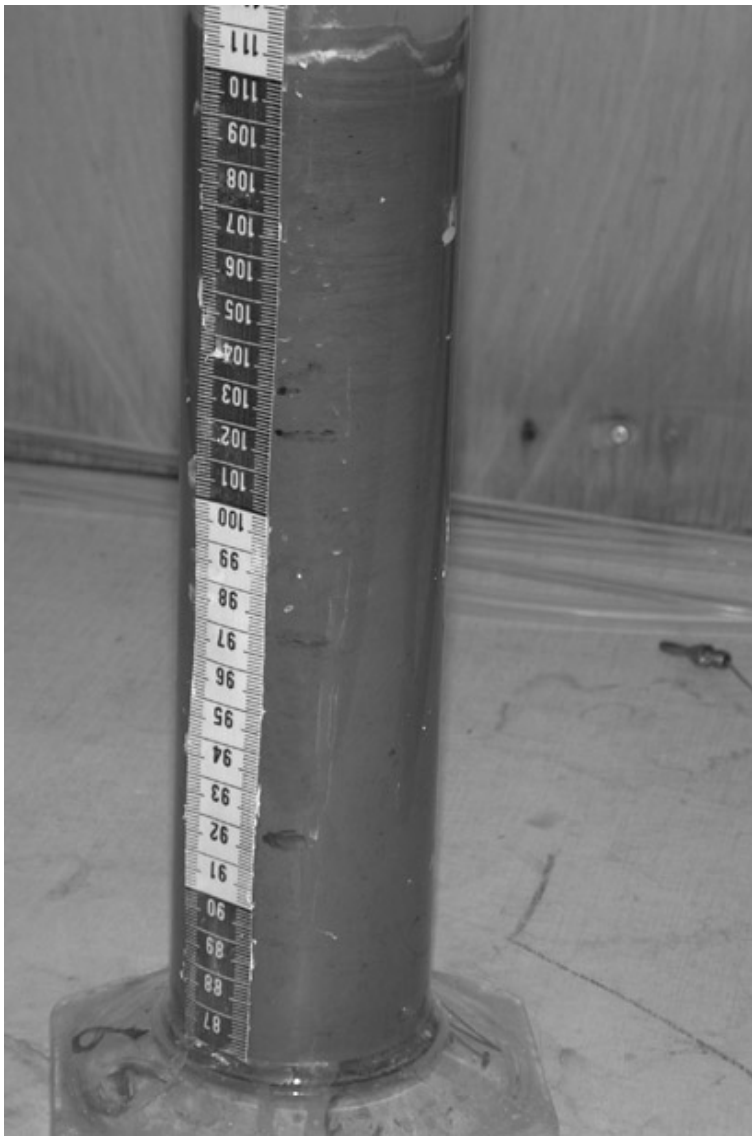

Figure E. 11 Column 4 on Day 18 (March 24)

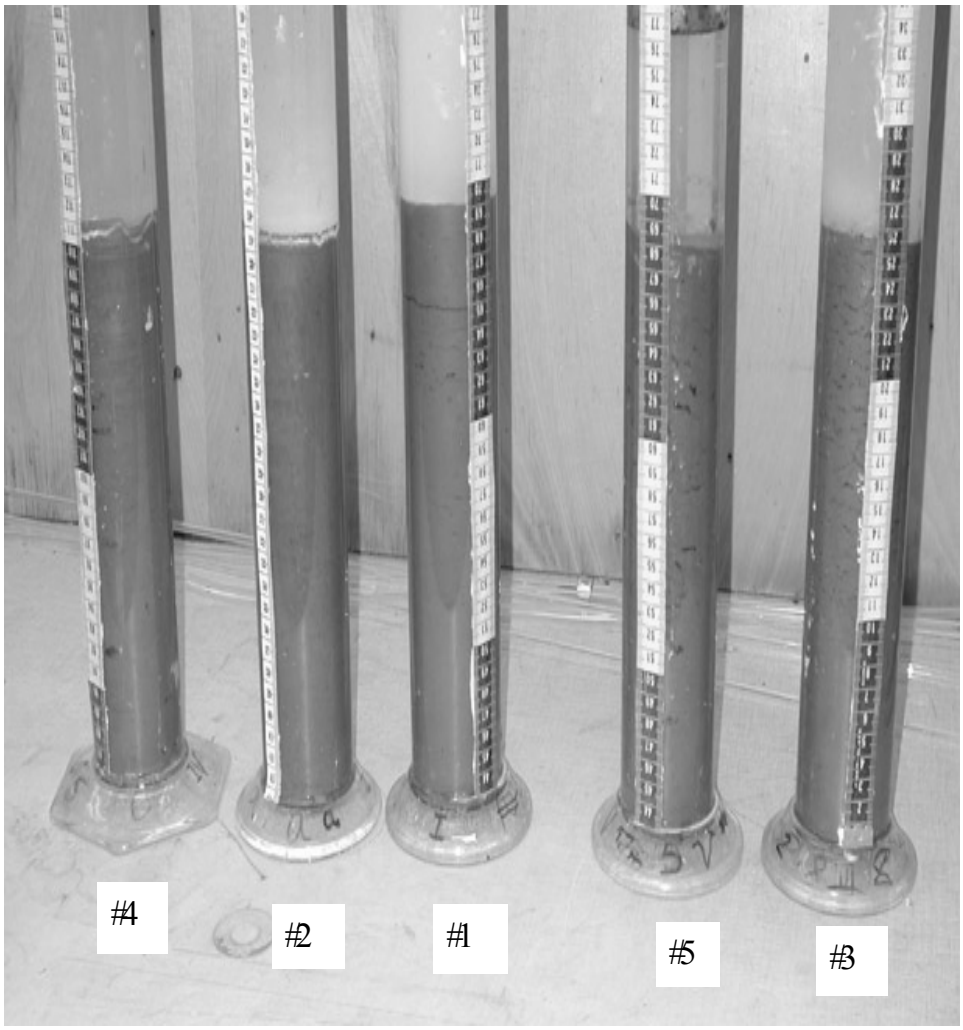

Figure E. 12 Columns 1~5 on Day 18 (March 24)

APPENDIX F Laboratory Equipment Calibration Results

This section presents the calibration results of pore pressure transducers and LVDT (LP) used for consolidation and gas MFT densification tests. The schematic diagrams of the measurement and recording systems for gas MFT densification test are also shown.

Table F. 1 Calibration Results of Pore Pressure Transducers

Test No	Location	Model	Calibration Equation	Correlation Coefficient (R^2)
Test 1	T1	PX26-001 GV	Y=0.708 X	1.000
	T2	PX26-005 GV	Y= 1.153X	1.000
	T3	PX26-005 GV	Y=1.153 X	1.000
	T4	PX26-001 GV	Y=0.713X	1.000
	T5	PX26-001 GV	Y=0.714 X	1.000
Test 2	T1	PX26-005 GV	Y=1.166 X	1.000
	T2	PX26-005 GV	Y=1.171X	1.000
	T3	PX26-005 GV	Y=1.15 X	1.000
	T4	PX26-001 GV	Y=0.713 X	1.000
	T5	PX26-001 GV	Y=0.706X	1.000
Test 3	T1	PX26-005 GV	Y=1.176X	1.000
	T2	PX26-005 GV	Y=1.156 X	1.000
	T3	PX26-005 GV	Y=1.171X	1.0000
	T4	PX26-001 GV	Y=0.720 X	1.000
	T5	PX26-001 GV	Y=0.713 X	1.000
Test 4	T1	PX26-005 GV	Y=1.146X	1.000
	T2	PX26-005 GV	Y=1.156X	1.000
	T3	PX26-005 GV	Y=1.153X	1.000
	T4	PX26-001 GV	Y=0.720 X	1.000
	T5	PX26-001 GV	Y=0.712 X	1.000
Test 5	T1	PX26-005 GV	Y=1.165 X	1.000
	T2	PX26-005 GV	Y=1.157 X	1.000
	T3	PX26-005 GV	Y=1.149 X	1.000
	T4	PX26-001 GV	Y=0.705 X	1.000
	T5	PX26-001 GV	Y=0.712 X	1.000
Test 6	T1	PX26-005 GV	Y=1.167 X	1.000
	T2	PX26-005 GV	Y=1.164 X	1.000
	T3	PX26-005 GV	Y=1.153 X	1.000
	T4	PX26-001 GV	Y=0.714 X	1.000
	T5	PX26-001 GV	Y=0.732 X	1.000
Notes: Y-Changes in pore pressure (kPa), X-Changes in output reading (10^{-3} voltage)				

Table F.1 Calibration Results of Pore Pressure Transducers (Continuing)

Test No	Elevation	Range (kPa)	Calibration equation	Correlation coefficient (R^2)
Test 10	T1	PX26-005 GV	Y=1.167X	1.000
	T2	PX26-005 GV	Y= 1.228X	0.999
	T3	PX26-005 GV	Y=1.161X	1.000
	T4	PX26-001 GV	Y=0.704X	1.000
	T5	PX26-001 GV	Y= 0.714X	1.000
Test 11	T1	PX26-005 GV	Y=1.234X	1.000
	T2	PX26-005 GV	Y=1.168X	1.000
	T3	PX26-005 GV	Y=1.15X	1.000
	T4	PX26-001 GV	Y=0.699 X	1.000
	T5	PX26-001 GV	Y=0.702X	1.000
Test 12	T1	PX26-005 GV	Y=1.17X	1.000
	T2	PX26-005 GV	Y=1.171 X	1.000
	T3	PX26-005 GV	Y=1.153X	0.999
	T4	PX26-001 GV	Y=0.707 X	1.000
	T5	PX26-001 GV	Y= 0.706X	1.000
Test 13	T1	PX26-001 GV	Y=0.707X	1.000
	T2	PX26-005 GV	Y=1.149X	1.000
	T3	PX26-005 GV	Y=1.145X	1.000
	T4	PX26-001 GV	Y=0.702 X	1.000
	T5	PX26-001 GV	Y= 0.712X	1.000
Test 14	T1	PX26-005 GV	Y=1.136 X	1.000
	T2	PX26-005 GV	Y=1.135 X	1.000
	T3	PX26-005 GV	Y=1.140 X	1.000
	T4	PX26-001 GV	Y=0.718 X	1.000
	T5	PX26-001 GV	Y= 0.715X	1.000
Test 15	T1	PX26-005 GV	Y=1.152 X	0.999
	T2	PX26-005 GV	Y=1.143 X	1.000
	T3	PX26-005 GV	Y=1.142X	1.000
	T4	PX26-001 GV	Y=0.701 X	1.000
	T5	PX26-001 GV	Y=0.701X	1.000
Notes: Y-Change in pore pressure (kPa), X-Change in output reading (10^{-3} voltage)				

Table F.1 Calibration Results of Pore Pressure Transducers (Continuing)

Test No	Elevation	Range (kPa)	Calibration equation	Correlation coefficient (R^2)
Test 19	T1	PX26-005 GV	Y=1.167X	1.000
	T2	PX26-005 GV	Y= 1.228X	1.000
	T3	PX26-005 GV	Y=1.161X	1.000
	T4	PX26-001 GV	Y=0.704X	1.000
	T5	PX26-001 GV	Y= 0.691X	1.000
Test 20	T1	PX26-005 GV	Y=1.234X	1.000
	T2	PX26-005 GV	Y=1.168X	0.996
	T3	PX26-005 GV	Y=1.15X	1.000
	T4	PX26-001 GV	Y=0.699 X	1.000
	T5	PX26-001 GV	Y=0.708X	1.000
Test 21	T1	PX26-005 GV	Y=1.17X	1.000
	T2	PX26-005 GV	Y=1.171 X	1.000
	T3	PX26-005 GV	Y=1.153X	1.000
	T4	PX26-001 GV	Y=0.707 X	1.000
	T5	PX26-001 GV	Y= 0.711X	1.000
Test 22	T1	PX26-001 GV	Y=0.707X	1.000
	T2	PX26-005 GV	Y=1.149X	1.000
	T3	PX26-005 GV	Y=1.145X	1.000
	T4	PX26-001 GV	Y=0.702 X	1.000
	T5	PX26-001 GV	Y= 0.712X	1.000
Test 23	T1	PX26-005 GV	Y=1.136 X	1.000
	T2	PX26-005 GV	Y=1.135 X	1.000
	T3	PX26-005 GV	Y=1.140 X	1.000
	T4	PX26-001 GV	Y=0.718 X	1.000
	T5	PX26-001 GV	Y= 0.715X	1.000
Test 24	T1	PX26-005 GV	Y=1.152 X	1.000
	T2	PX26-005 GV	Y=1.143 X	1.000
	T3	PX26-005 GV	Y=1.142X	0.999
	T4	PX26-001 GV	Y=0.701 X	1.000
	T5	PX26-001 GV	Y=0.709X	1.000
Notes: Y-Change in pore pressure (kPa), X-Change in output reading (10^{-3} voltage)				

Table F. 2 Calibration Results of LVDT (or LP)

Test No.	Periods	Sensor Type	Range (mm)	Calibration Equation	Correlation Coefficient (R2)
1	Consol. and Microbial	LVDT	±12.7 mm	Y=2.2384X	1.000
2	Consol. and Microbial	LVDT	±12.7 mm	Y=2.0035X	1.000
3	Consol. and Microbial	LVDT	±12.7 mm	Y=2.0392X	1.000
4	Consol. and Microbial	LVDT	±12.7 mm	Y=2.2158X	1.000
5	Consol. and Microbial	LVDT	±12.7 mm	Y=2.0732X	0.999
6	Consol. and Microbial	LVDT	±12.7 mm	Y=2.2528X	1.000
10	0.5 kPa Consol.	LP	0-25 mm	Y=8.5883X	1.000
11	0.5 kPa Consol.	LP	0-25 mm	Y=8.732X	1.000
12	0.5 kPa Consol.	LP	0-25 mm	Y=8.712X	1.000
10	1.0 kPa consoli.	LP	0-25 mm	Y=20.945X	1.000
11	1.0 kPa consoli.	LP	0-25 mm	Y=20.793X	1.000
12	1.0 kPa consoli.	LP	0-25 mm	Y=21.018X	1.000
10	Microbial	LVDT	±12.7 mm	Y=2.2384X	1.000
11	Microbial	LVDT	±12.7 mm	Y=2.0035X	1.000
12	Microbial	LVDT	±12.7 mm	Y=2.0392X	1.000
13	Microbial	LVDT	±12.7 mm	Y=2.2158X	1.000
14	Microbial	LVDT	±12.7 mm	Y=2.0732X	0.999
15	Microbial	LVDT	±12.7 mm	Y=2.2528X	1.000
19	Consol. and Microbial	LVDT	±12.7 mm	Y=2.2384X	1.000
20	Consol. and Microbial	LVDT	±12.7 mm	Y=2.0035X	1.000
21	Consol. and Microbial	LVDT	±12.7 mm	Y=2.0392X	1.000
22	Consol. and Microbial	LVDT	±12.7 mm	Y=2.2158X	1.000
23	Consol. and Microbial	LVDT	±12.7 mm	Y=2.0732X	0.999
24	Consol. and Microbial	LVDT	±12.7 mm	Y=2.2528X	1.000
Note: Y-Displacement (mm), X-Output reading (voltage)					

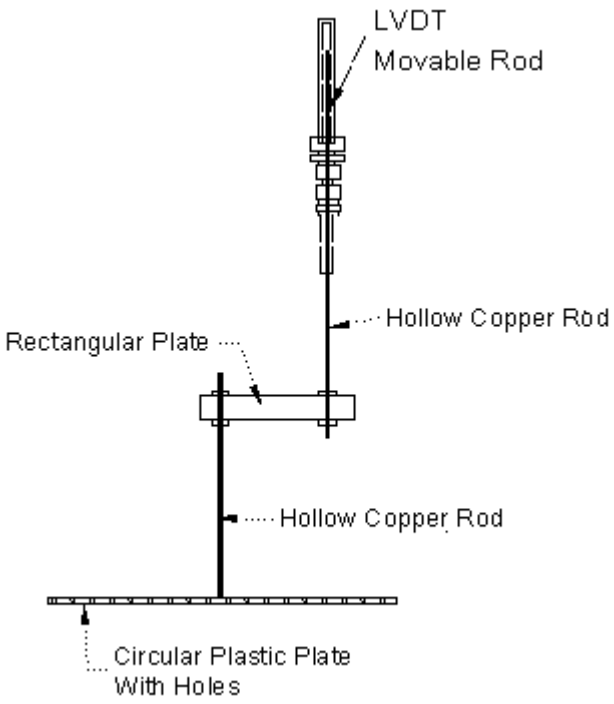

Figure F. 1 Displacement Measurement System in Gas MFT Densification Test

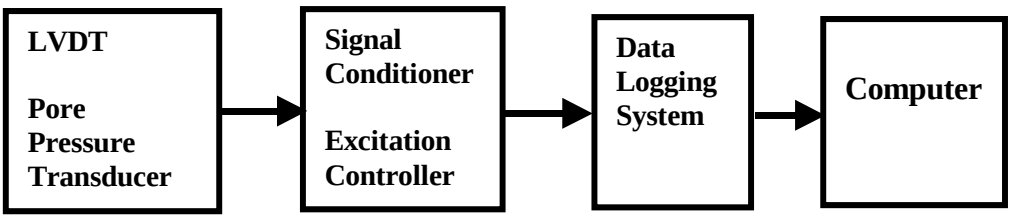

Figure F. 2 Schematic Diagram of the Data Collecting and Recording System

APPENDIX G Consolidation Test Results before Microbial Activity

This appendix presents the results of the consolidation tests (the plots of settlements vs. Log (t) and excess pore pressure dissipation with time) at $4^{o}C$ temperature before microbial activity.

Figures G.1 to G.6 show the water-MFT interface movements vs. log t in self-weight consolidation tests 1-6. Figure G.7 shows excess pore water pressure changes at 3.95 cm elevation (E3, close to the middle of the initial sample) above the bottom of sample 4. The initial excess pore pressure at this elevation was about 0.1 kPa. While water was drained out from the bottom and top of the sample, excess pore pressure decreased. After about 50000 minutes (35 days) the excess pore water pressure was close to zero. In Figure G.7, data from 4036 min to 10268 min was lost due to operation errors when downloading the data from the data logger.

Figures G.8 to G.10 show the interface movements vs. log t during 0.5kPa consolidation of Samples 10 to 12, respectively. The settlements of samples 10-12 before lead shots were added to the plastic bowls were 4.5 mm, 3.94 mm and 4.1 mm, respectively. In test 12, the measurements show some irregularities during the early period of consolidation. This might have been caused by the improper installation of the LP. Because the movable rod of the LP was not set vertically, it might have been temporarily hampered by the frictional resistance, and thus did not follow the interface movements. After being adjusted, the LP functioned well and the prior irregularities did not affect the total settlement measurement of sample 12.

Figures G.11 and G.12 show the changes of excess pore water pressure with time at 1.45 cm and 3.95 cm elevations above the bottom of sample 11, during 0.5 kPa consolidation. The sensor at 3.95 cm elevation (E3) was approximately in the middle of the sample at the beginning of consolidation. Excess pore water pressure dissipation was relatively slow during the first 12000 minutes (about 8 days) of 0.5 kPa consolidation, but after that was obviously accelerated. Because

the consolidation was large strain deformation, it caused the thickness of the sample to rapidly decrease. This greatly reduced the drainage path between the interface and E3. After about 35,000 minutes (about 24 days), excess pore water pressure at E3 decreased to close to zero. From the plots of interface movements vs. log t, as shown in Figures G.8 to G.10, the primary consolidation lasted about 45,000 minutes (31 days).

Figures G.13 and G.15 show the interface movements vs. log t for consolidation tests 10-12, respectively, under 1.0 kPa loading. Figures G.16 and G.17 show the changes of excess pore water pressure at 1.45 cm (E2) and 3.95 cm (E3) elevations above the bottom of sample 11. Compared with the results in Figures G.11 to G.12, the measurements from the moisture room were more fluctuated. This was mainly caused by the environmental noises and artificial disturbances in the moisture room. After about 30000 minutes (about 21 days), the excess pore water pressures in sample 11 decreased to close to zero.

Figures G.18–G.23 show the interface movements vs. log t during 0.4 kPa consolidation for samples 19-24, respectively. Figures G.24 and G.25 show the changes of excess pore water pressure at 1.45 cm and 3.95 cm elevations, respectively, above the bottom of sample 19. After about 60,000 minutes (about 45 days), excess pore water pressures in the MFT decreased to close to zero. The consolidation test under 0.4 kPa lasted about 66 days. Secondary consolidation was observed at the late period of testing.

After the consolidation under 0.4 kPa loading was finished, additional 0.6 kPa loading was applied by placing another steel ring above the existing one. Figures G.26–G.31 show the interface movements vs. log t in consolidation tests 19-24, respectively, and Figures G.32 and G.33 show the changes of excess pore water pressure at 1.45 cm and 3.95 cm elevations, respectively, above the bottom of sample 19. It took about 50,000 minutes (35 days) for excess pore water pressures to be completely dissipated in the sample.

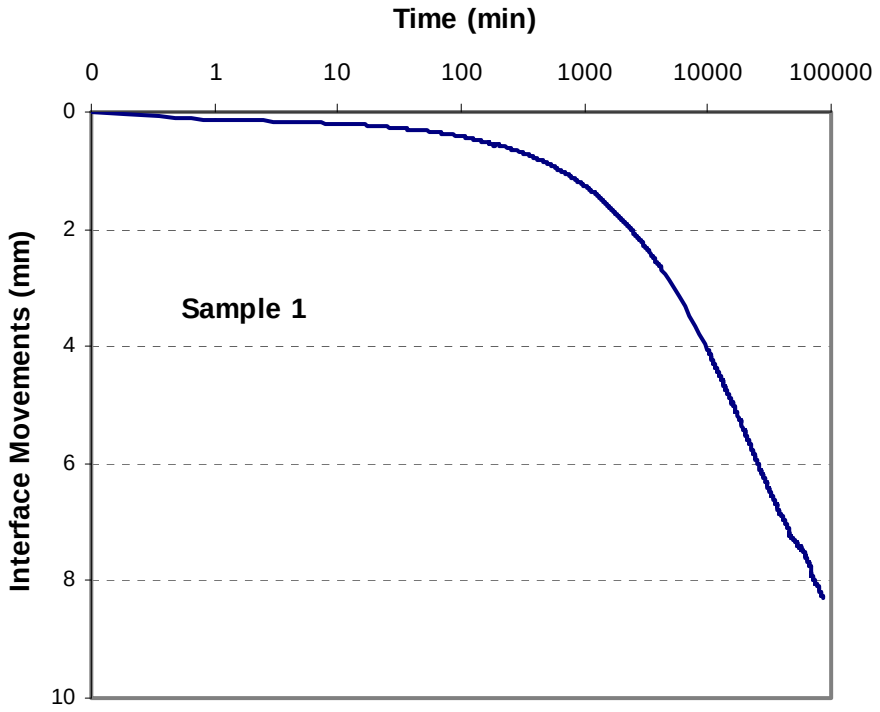

Figure G. 1 Interface Movements vs. Log (t) in Self-Weight Consolidation of Sample 1

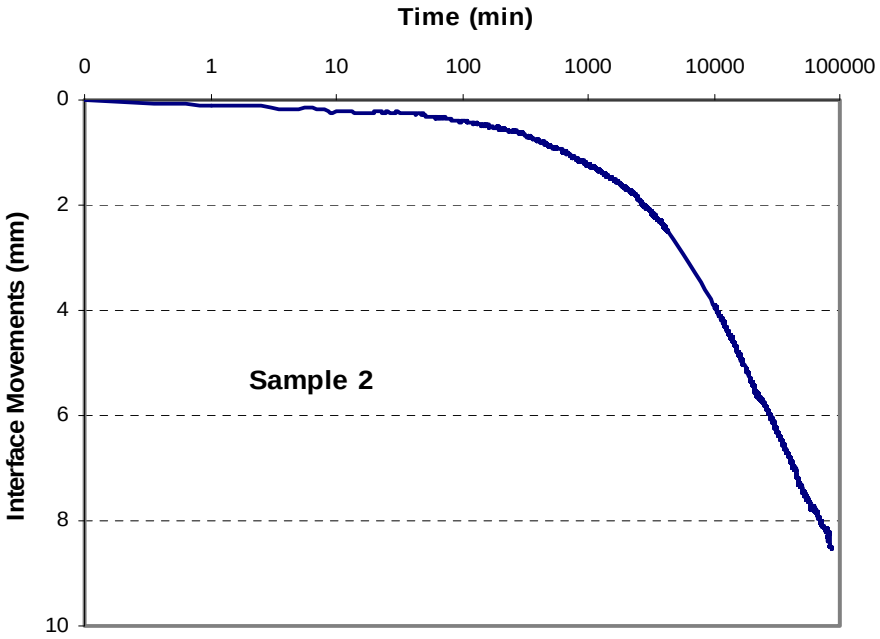

Figure G. 2 Interface Movements vs. Log (t) in Self-Weight Consolidation of Sample 2

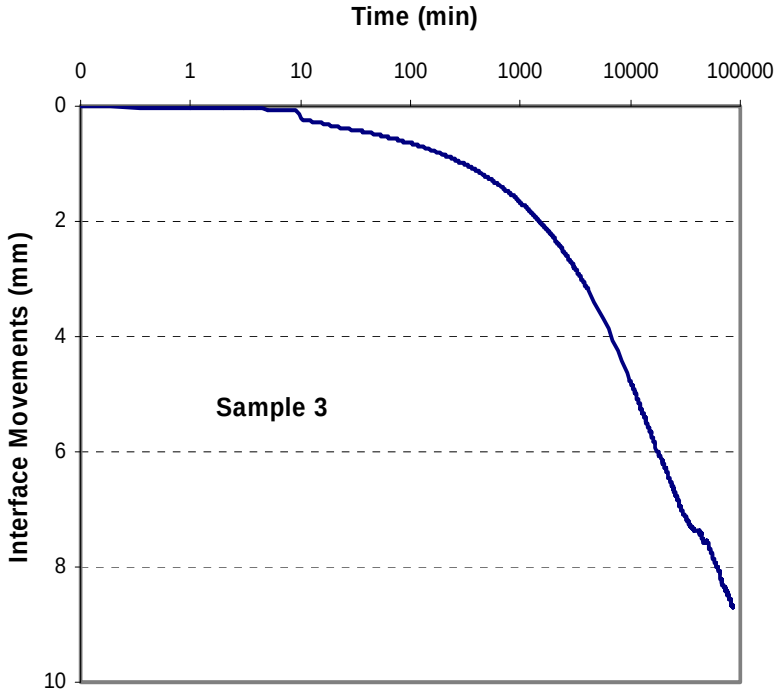

Figure G. 3 Interface Movements vs. Log (t) in Self-Weight Consolidation of Sample 3

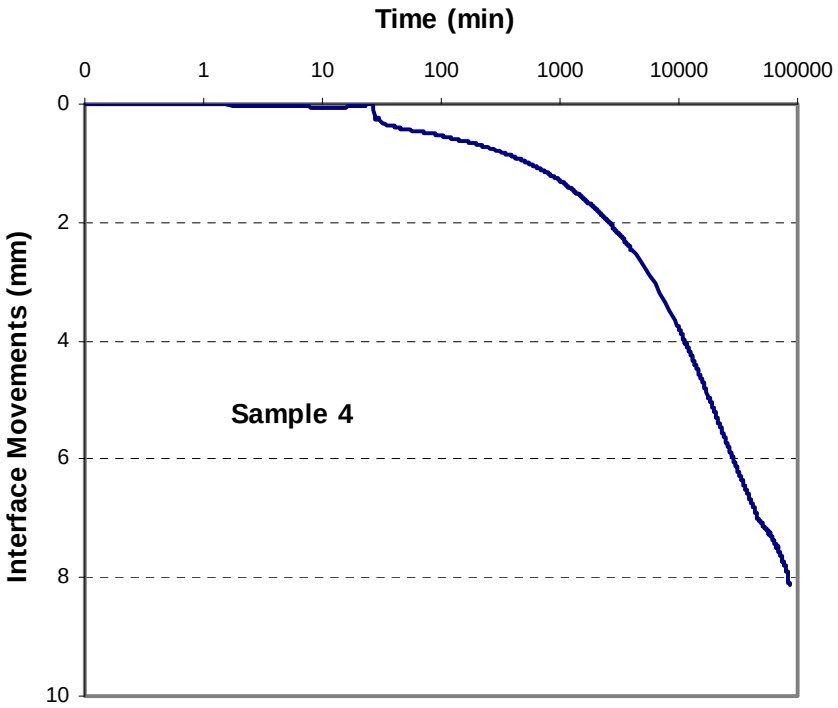

Figure G. 4 Interface Movements vs. Log (t) in Self-Weight Consolidation of Sample 4

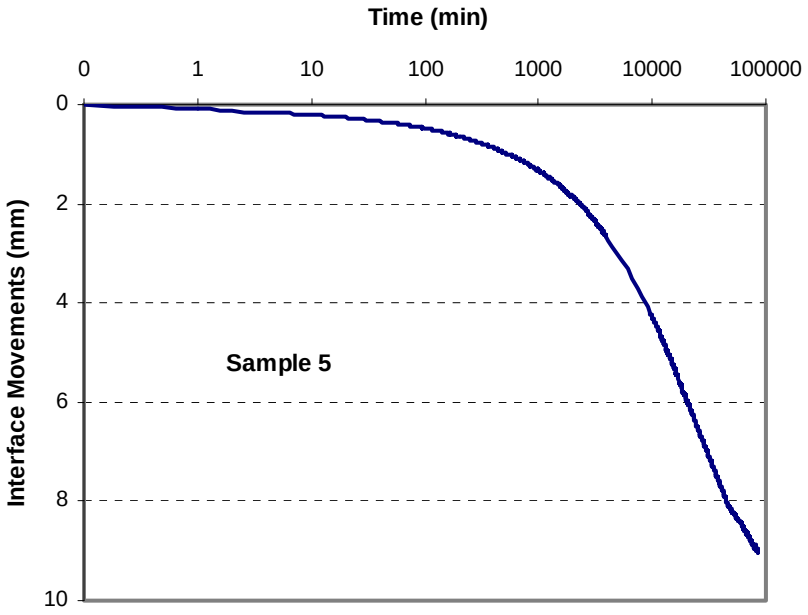

Figure G. 5 Interface Movements vs. Log (t) in Self-Weight Consolidation of Sample 5

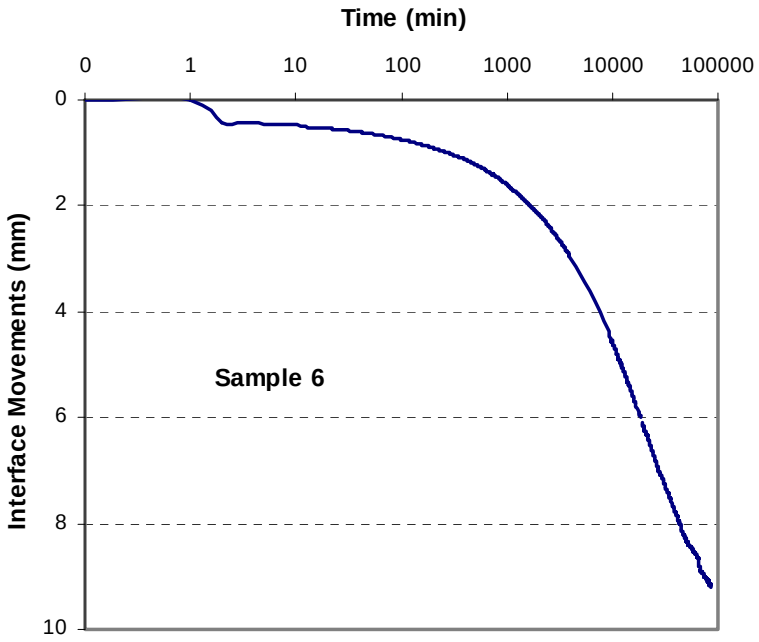

Figure G. 6 Interface Movements vs. Log (t) in Self-Weight Consolidation of Sample 6

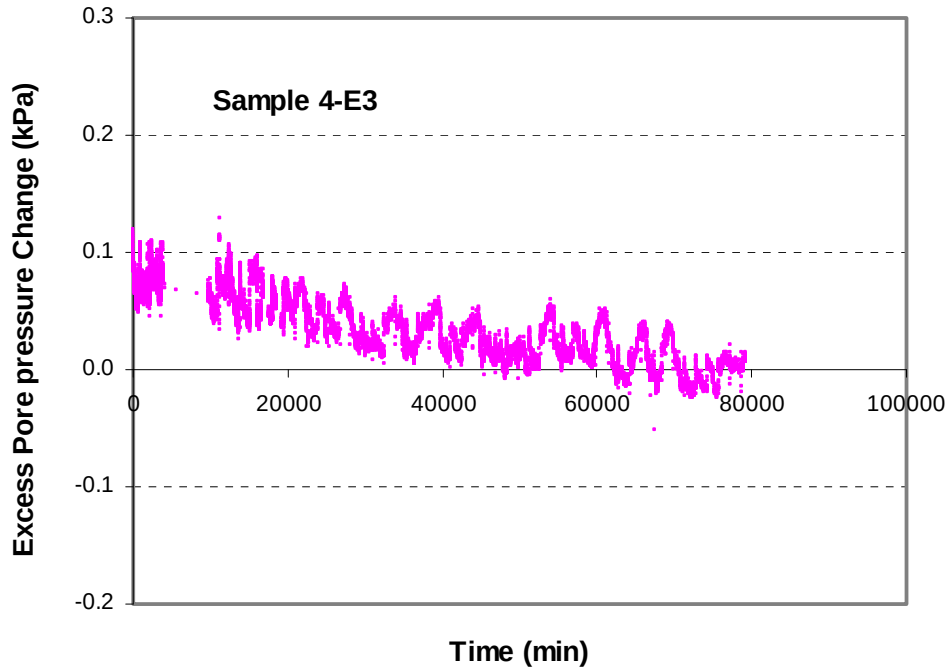

Figure G. 7 Excess Pore Pressure Changes during Self-Weight Consolidation at E3 in Sample 4

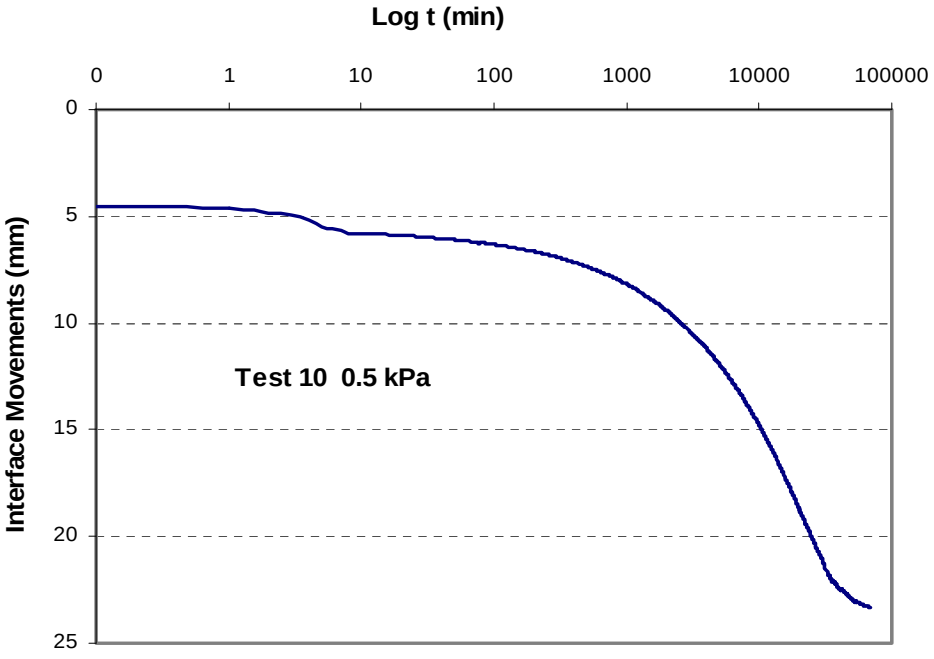

Figure G. 8 Interface Movements vs. Log (t) during 0.5 kPa Consolidation of Sample 10

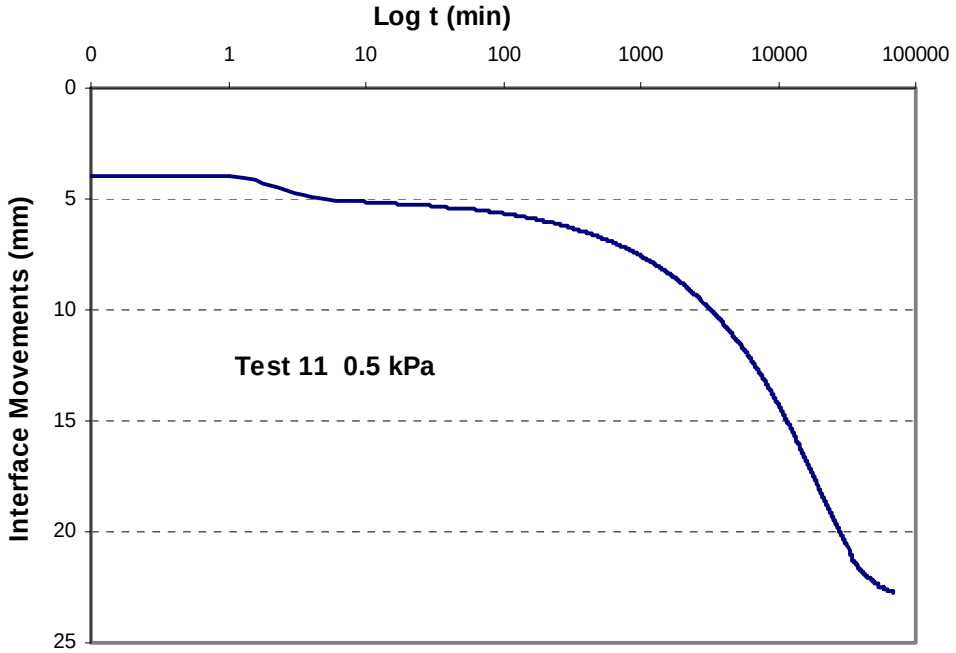

Figure G. 9 Interface Movements vs. Log (t) during 0.5 kPa Consolidation of Sample 11

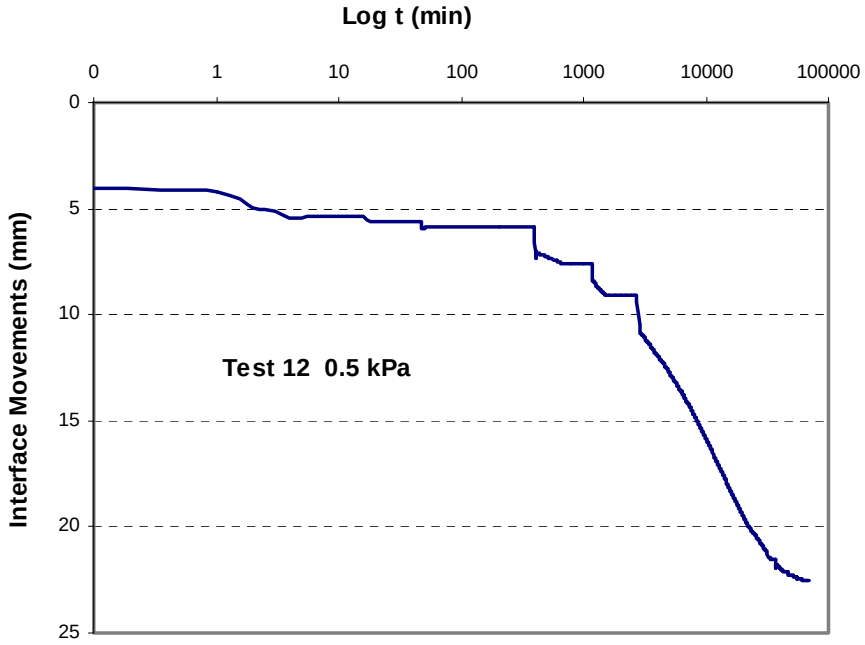

Figure G. 10 Interface Movements vs. Log (t) during 0.5 kPa Consolidation of Sample 12

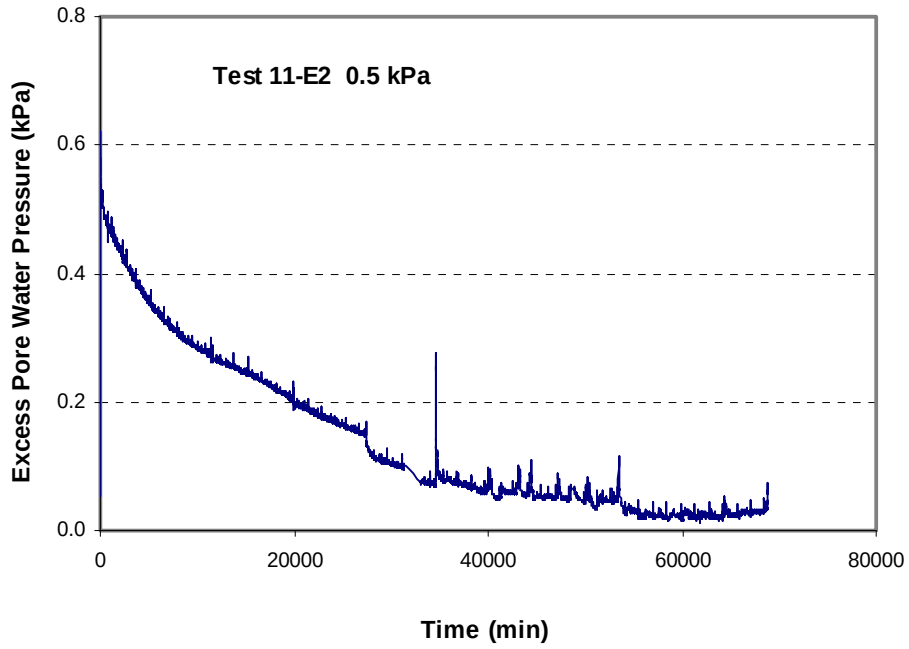

Figure G. 11 Excess Pore Pressure Changes during 0.5 kPa Consolidation at E2 of Sample 11

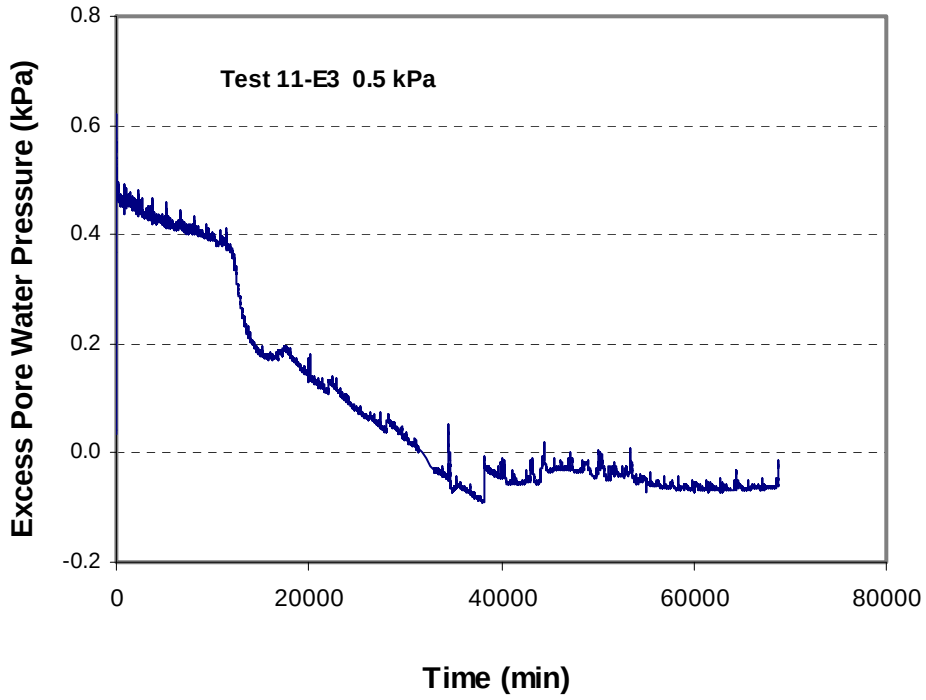

Figure G. 12 Excess Pore Pressure Changes during 0.5 kPa Consolidation at E3 of Sample 12

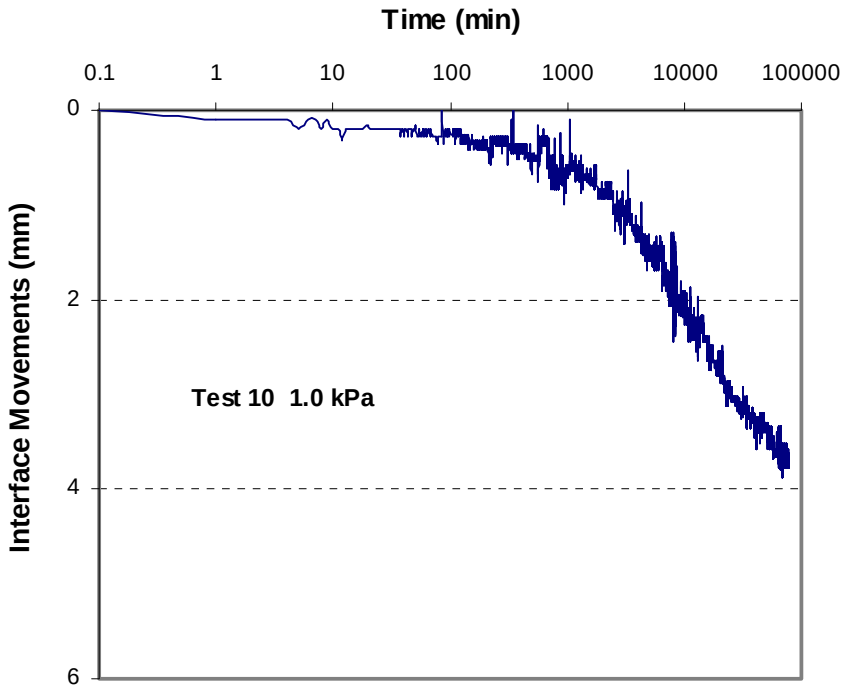

Figure G. 13 Interface Movements vs. Log t during the Consolidation of Sample 10 from 0.5 kPa to 1.0 kPa

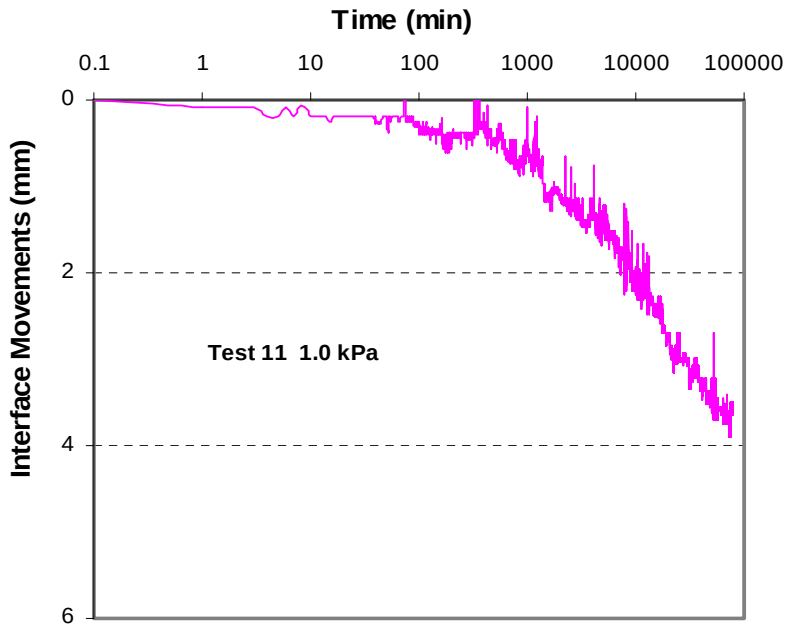

Figure G. 14 Interface Movements vs. Log t during the Consolidation of Sample 11 from 0.5 kPa to 1.0 kPa

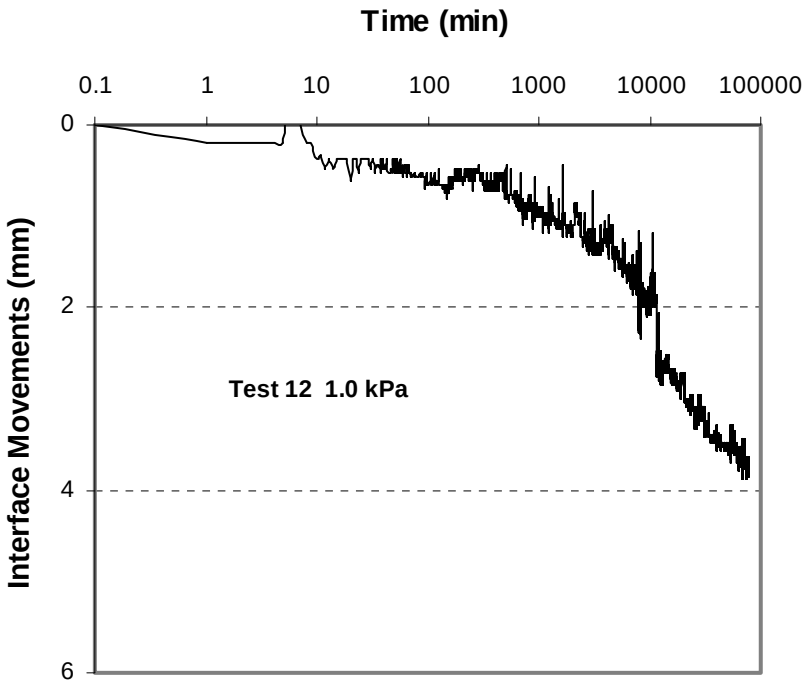

Figure G. 15 Interface Movements vs. Log t during the Consolidation of Sample 12 from 0.5 kPa to 1.0 kPa

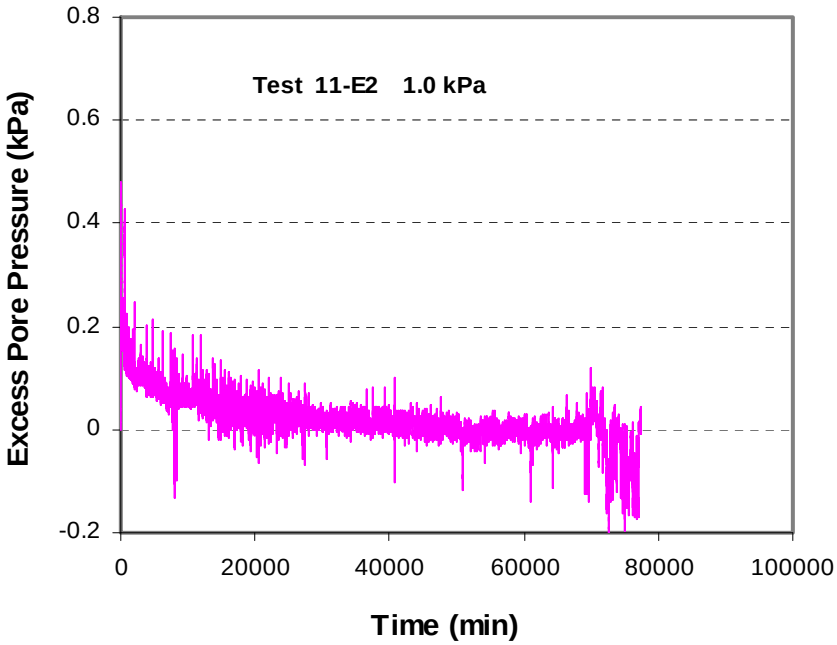

Figure G. 16 Excess Pore Pressure Changes at E2 of Sample 11 during the Consolidation from 0.5 to 1.0 kPa

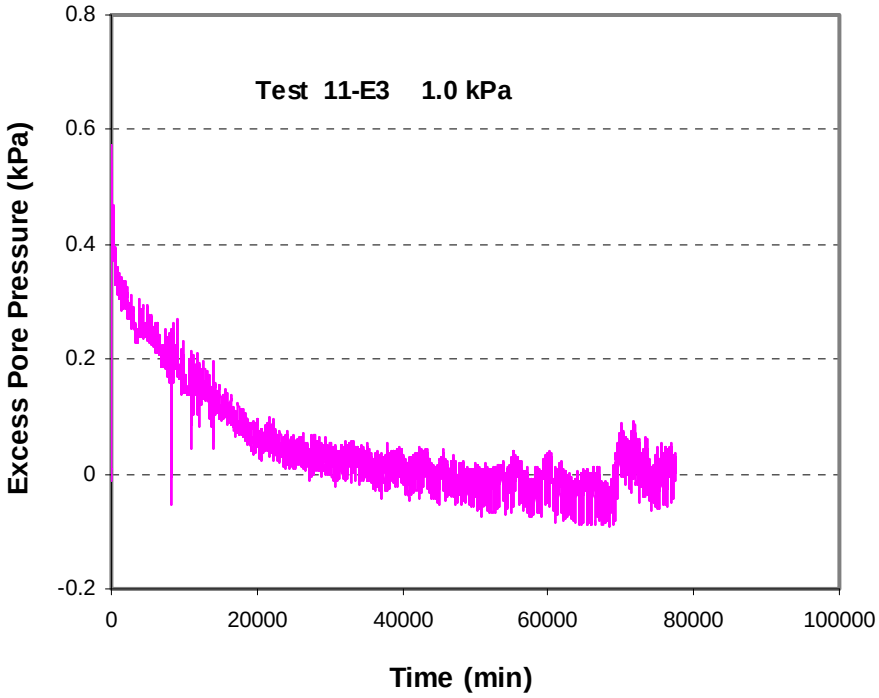

Figure G. 17 Excess Pore Pressure Changes at E3 of Sample 11 during the Consolidation from 0.5 to 1.0 kPa

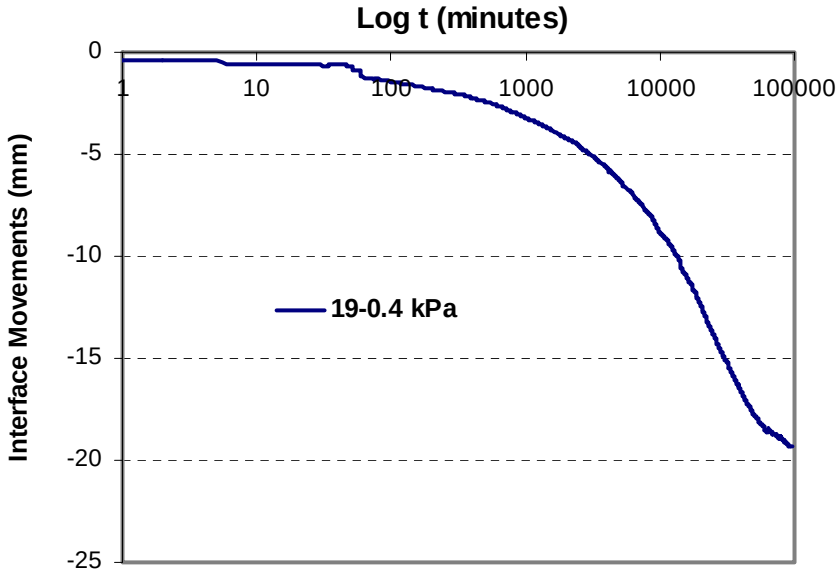

Figure G. 18 Interface Movements vs. Log t during 0.4 kPa Consolidation of Sample 19

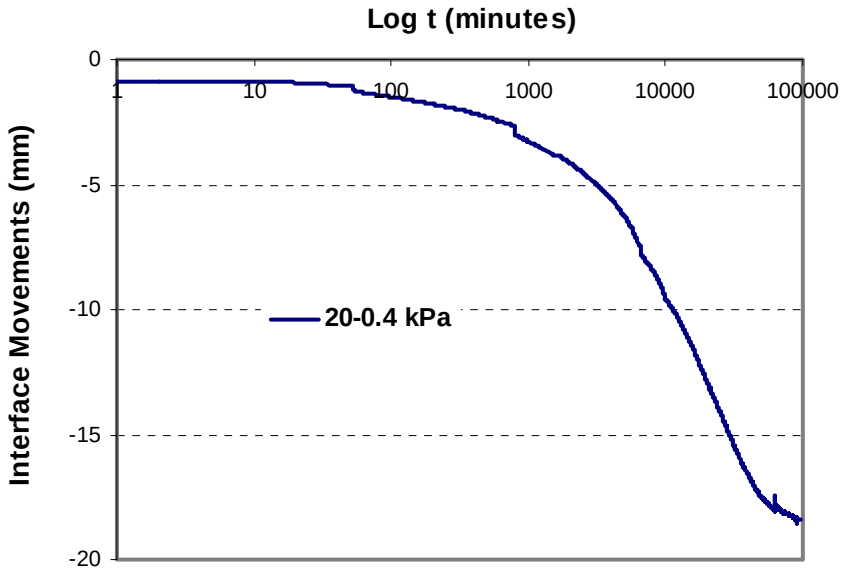

Figure G. 19 Interface Movements vs. Log t during 0.4 kPa Consolidation of Sample 20

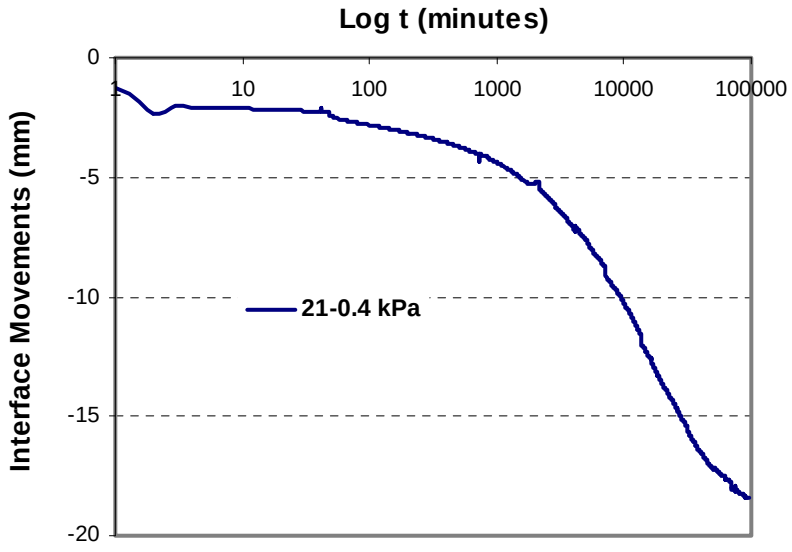

Figure G. 20 Interface Movements vs. Log t during 0.4 kPa Consolidation of Sample 21

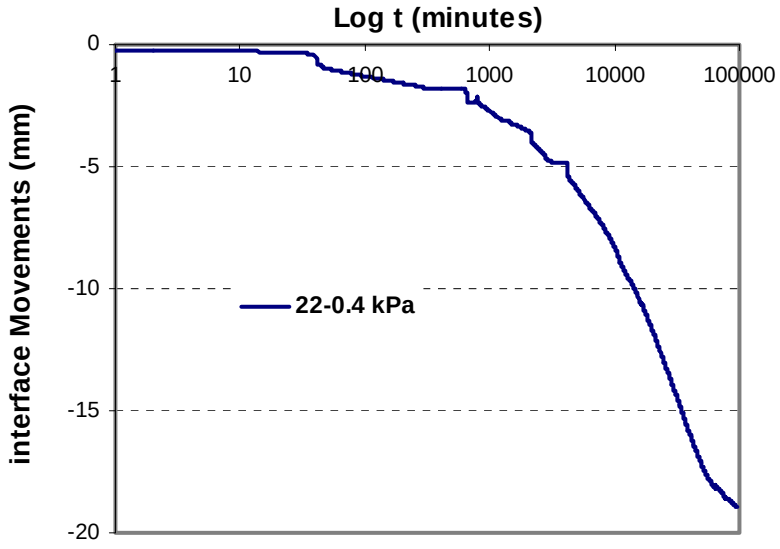

Figure G. 21 Interface Movements vs. Log t during 0.4 kPa Consolidation of Sample 22

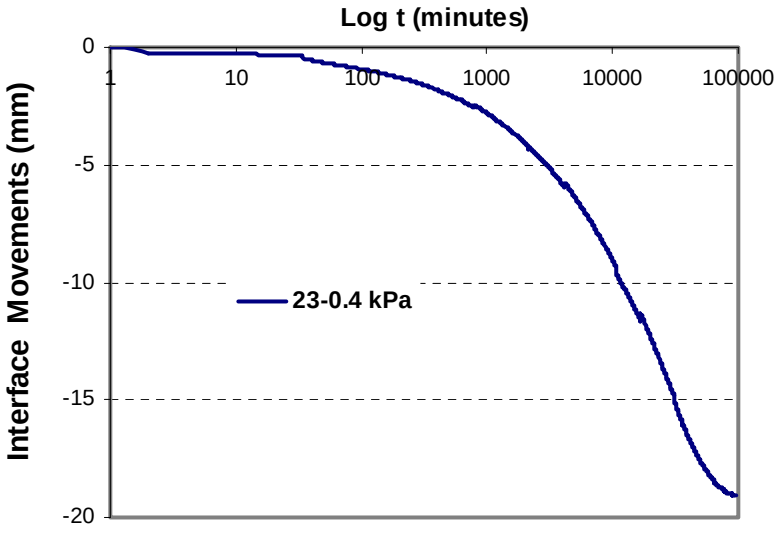

Figure G. 22 Interface Movements vs. Log t during 0.4 kPa Consolidation of Sample 23

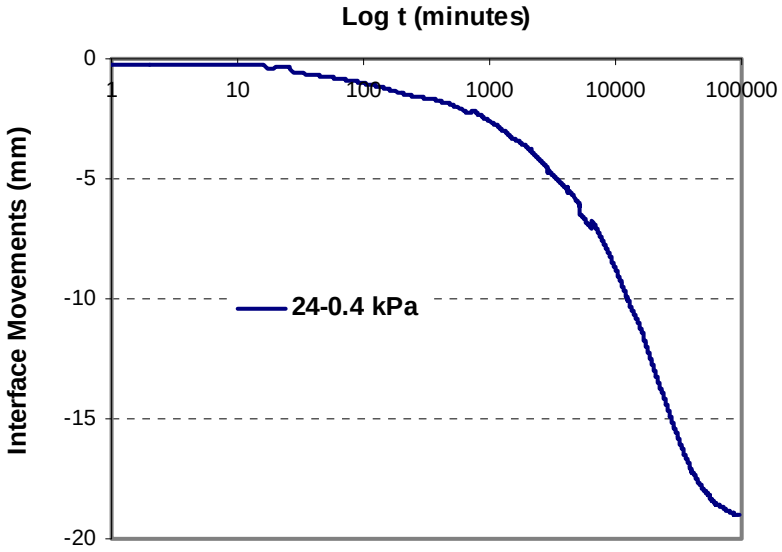

Figure G. 23 Interface Movements vs. Log t during 0.4 kPa Consolidation of Sample 24

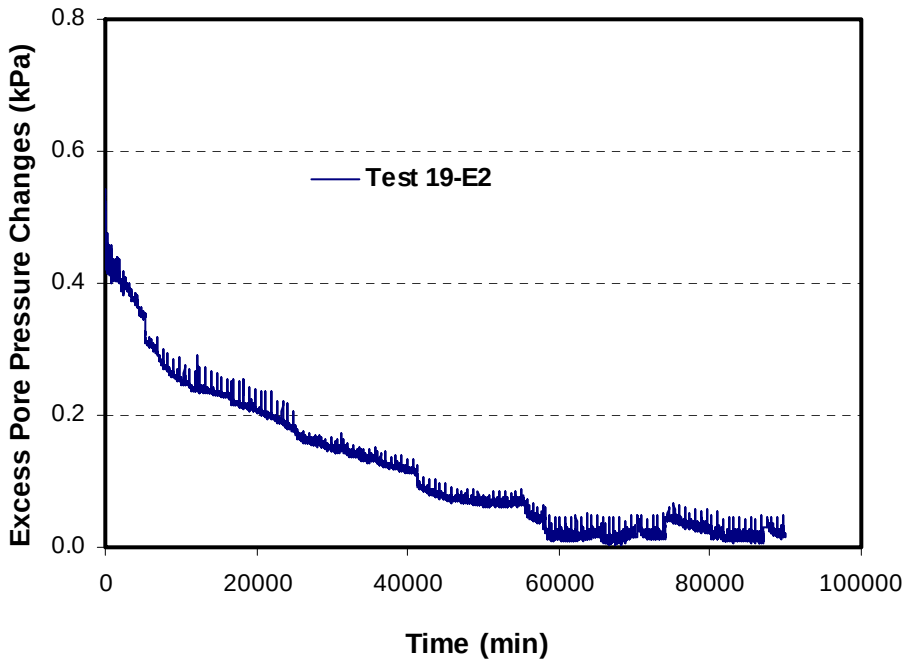

Figure G. 24 Excess Pore Pressure Changes during 0.4 kPa Consolidation at E2 of Sample 19

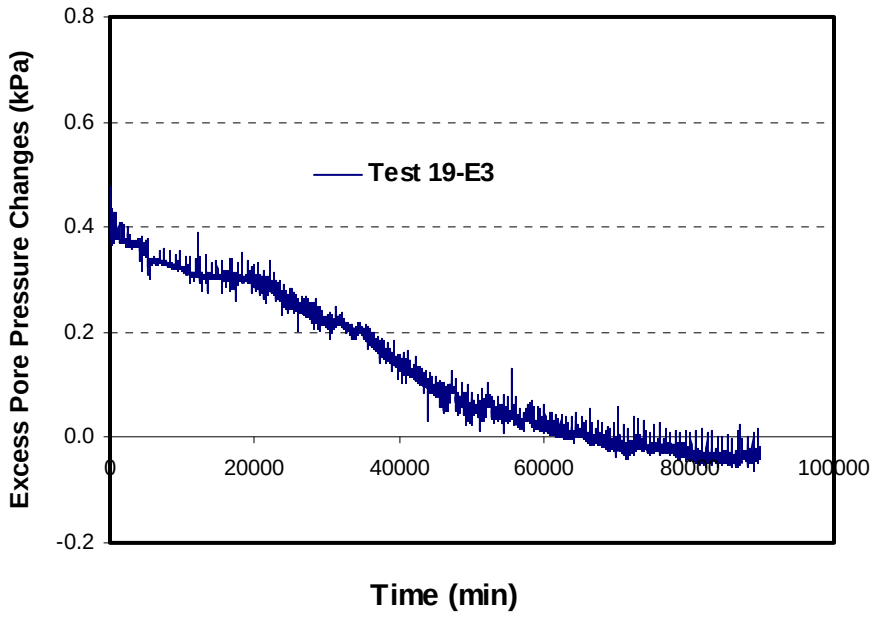

Figure G. 25 Excess Pore Pressure Changes during 0.4 kPa Consolidation at E3 of Sample 19

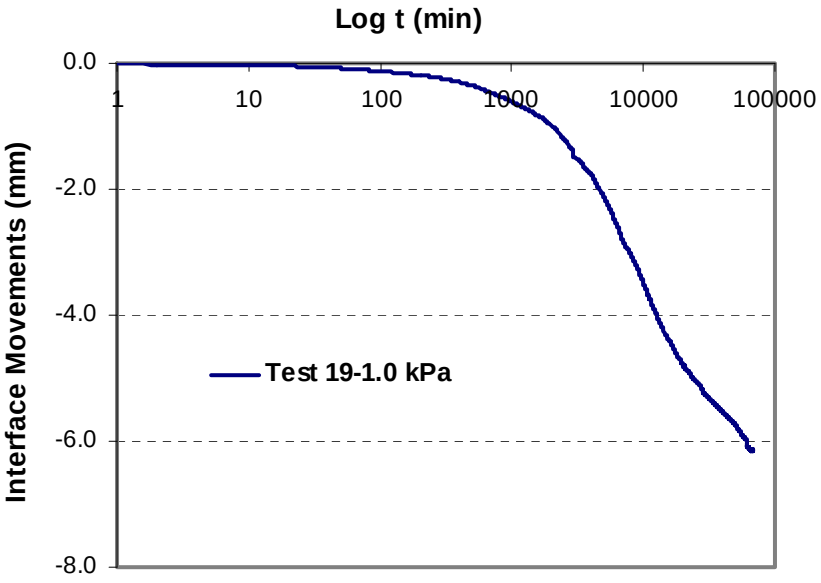

Figure G. 26 Interface Movements vs. Log t in Consolidation Test 19 from 0.4 to 1.0 kPa

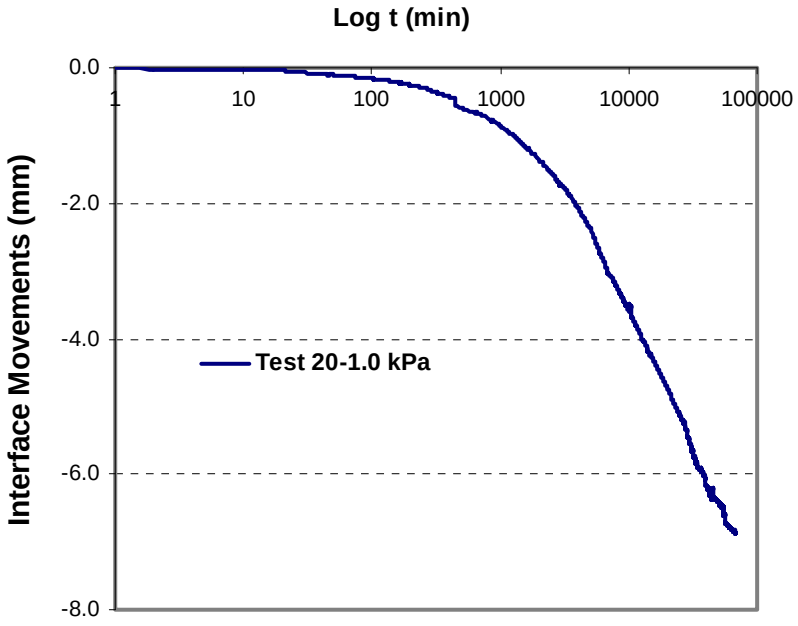

Figure G. 27 Interface Movements vs. Log t in Consolidation Test 20 from 0.4 to 1.0 kPa

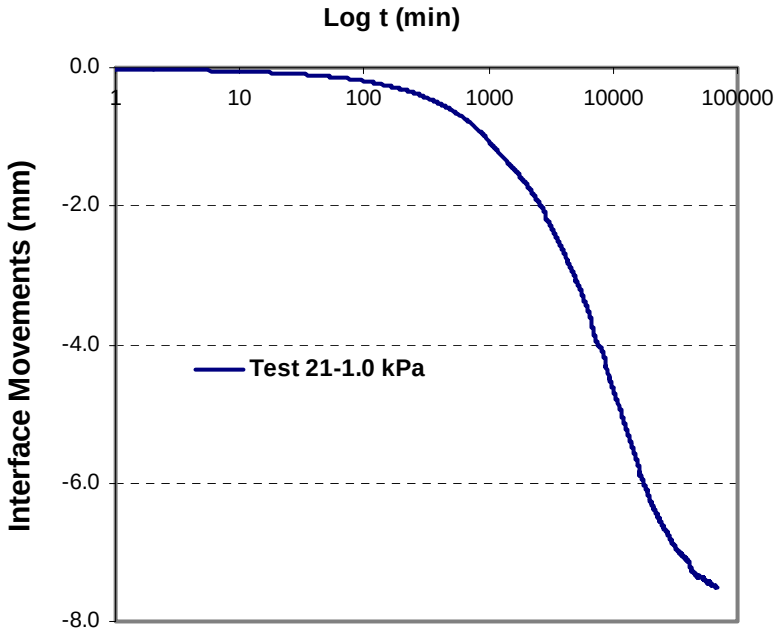

Figure G. 28 Interface Movements vs. Log t in Consolidation Test 21 from 0.4 to 1.0 kPa

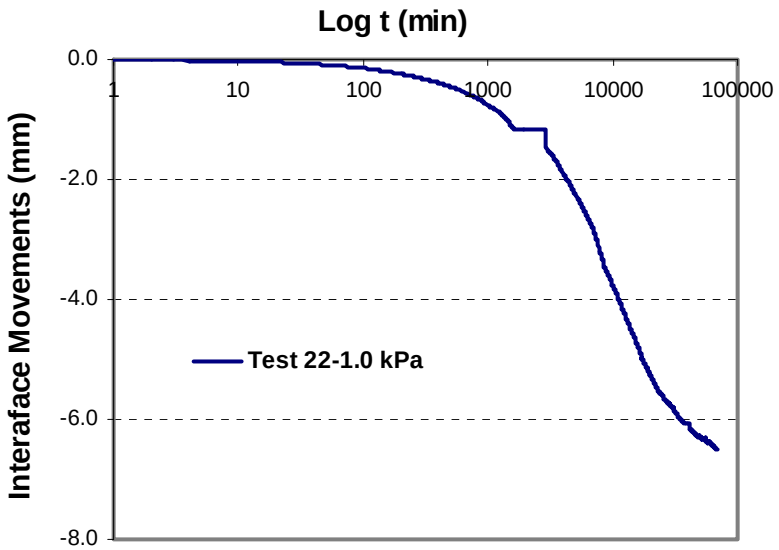

Figure G. 29 Interface Movements vs. Log t in Consolidation Test 22 from 0.4 to 1.0 kPa

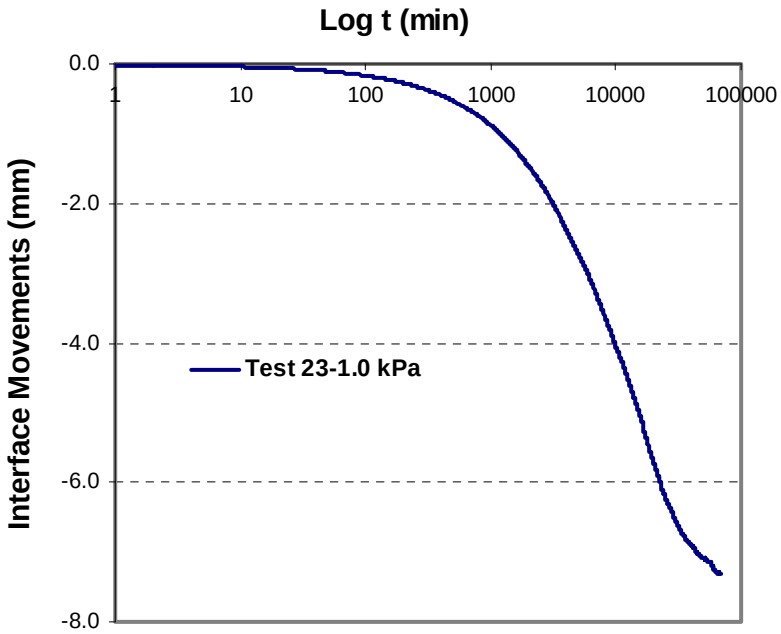

Figure G. 30 Interface Movements vs. Log t in Consolidation Test 23 from 0.4 to 1.0 kPa

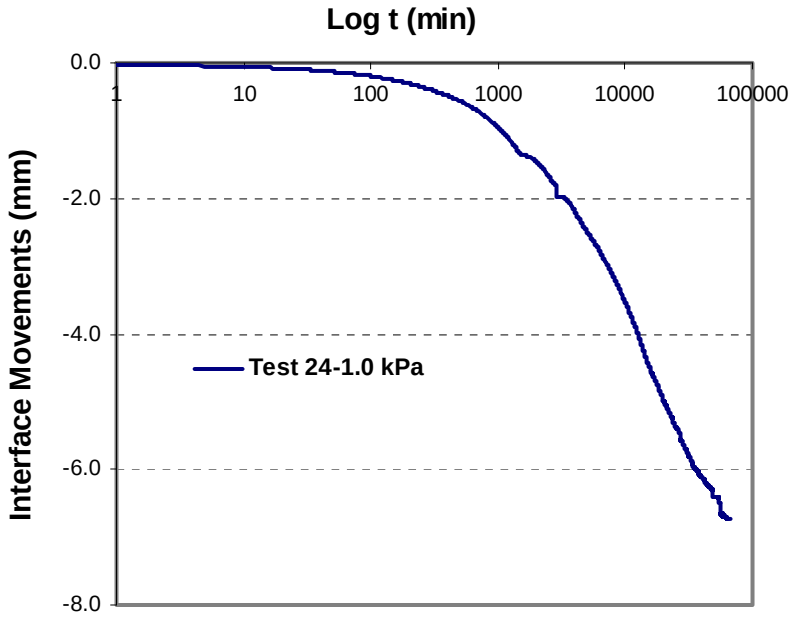

Figure G. 31 Interface Movements vs. Log t in Consolidation Test 24 from 0.4 to 1.0 kPa

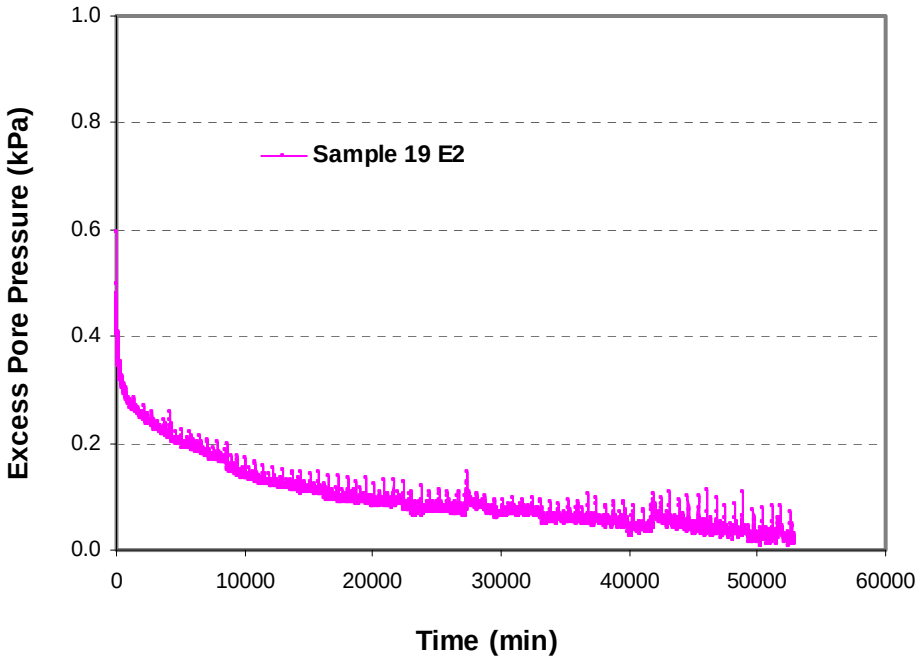

Figure G. 32 Excess Pore Pressure Changes at E2 of Consolidation Test 19 from 0.4 kPa to 1.0 kPa

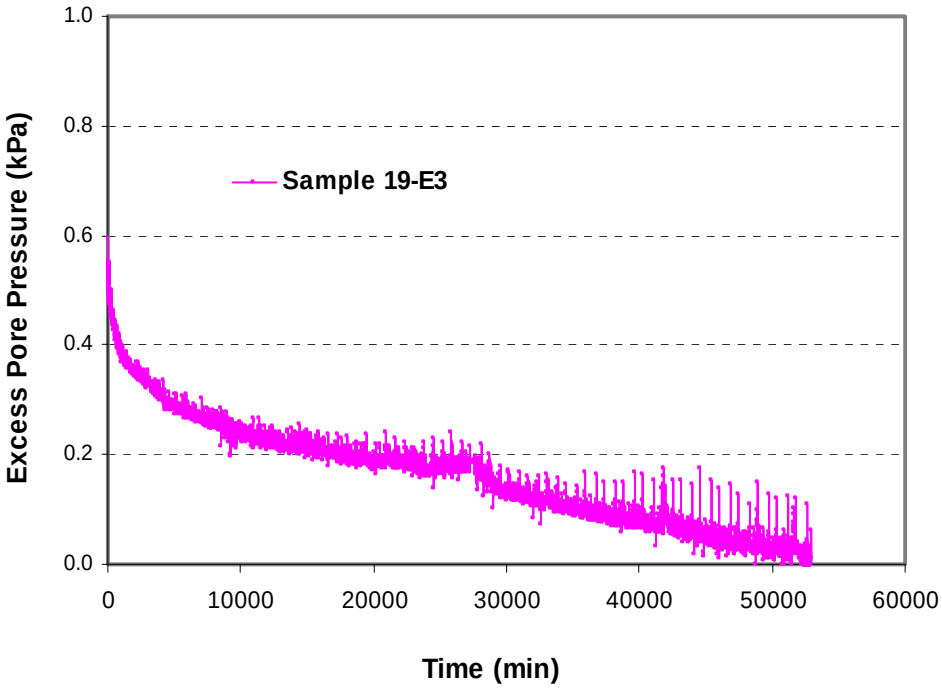

Figure G. 33 Excess Pore Pressure Changes at E3 of Consolidation Test 19 from 0.4 kPa to 1.0 kPa

APPENDIX H Changes of Total Stress and Pore Water Pressure during Microbial Activity

This appendix shows the plots of total stress and pore water pressure vs. time during microbial activity. The results of total stress and pore water pressure were used to calculate excess pore water pressure and operative stress (as shown in the Chapter 6) during microbial activity.

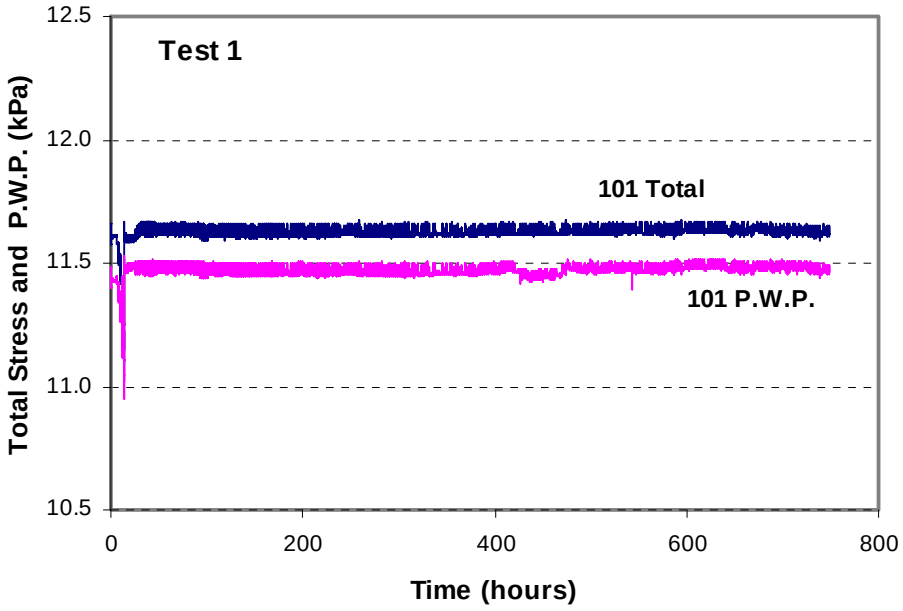

Figure H. 1 Changes in Total Stress and Pore Water Pressure at E1 of Test 1 during Microbial Activity

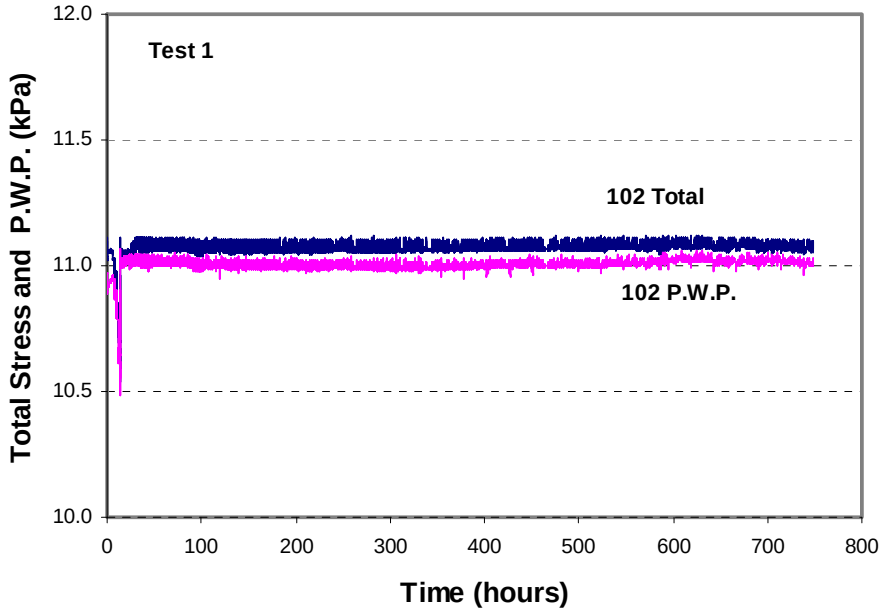

Figure H. 2 Changes in Total Stress and Pore Water Pressure at E2 of Test 1 during Microbial Activity

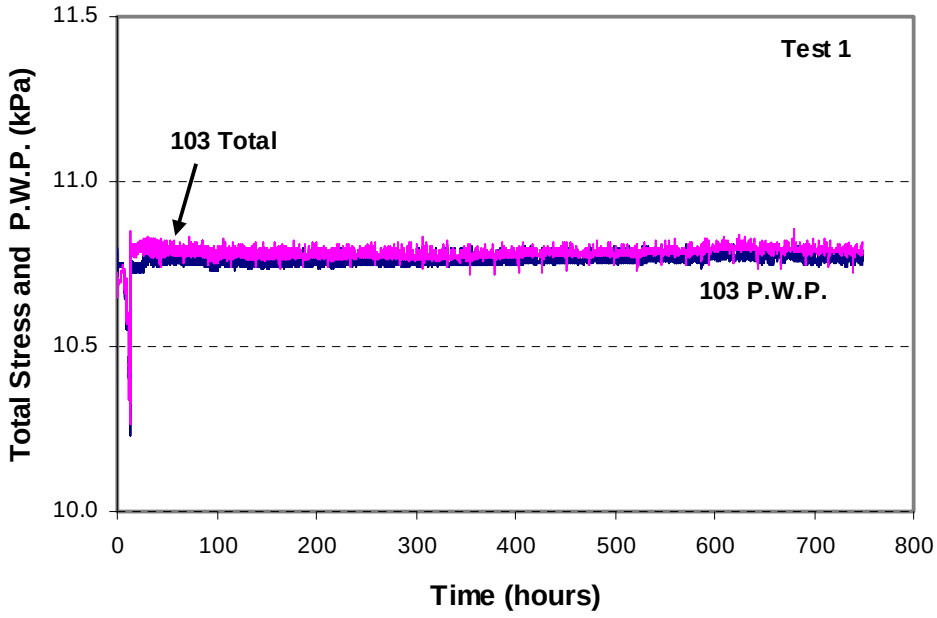

Figure H. 3 Changes in Total Stress and Pore Water Pressure at E3 of Test 1 during Microbial Activity

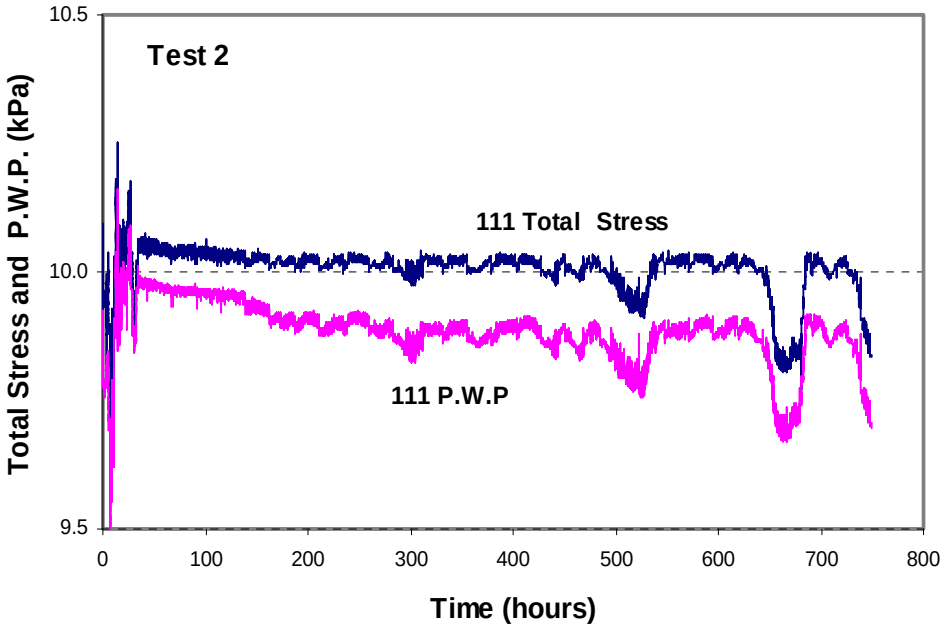

Figure H. 4 Changes in Total Stress and Pore Water Pressure at E1 of Test 2 during Microbial Activity

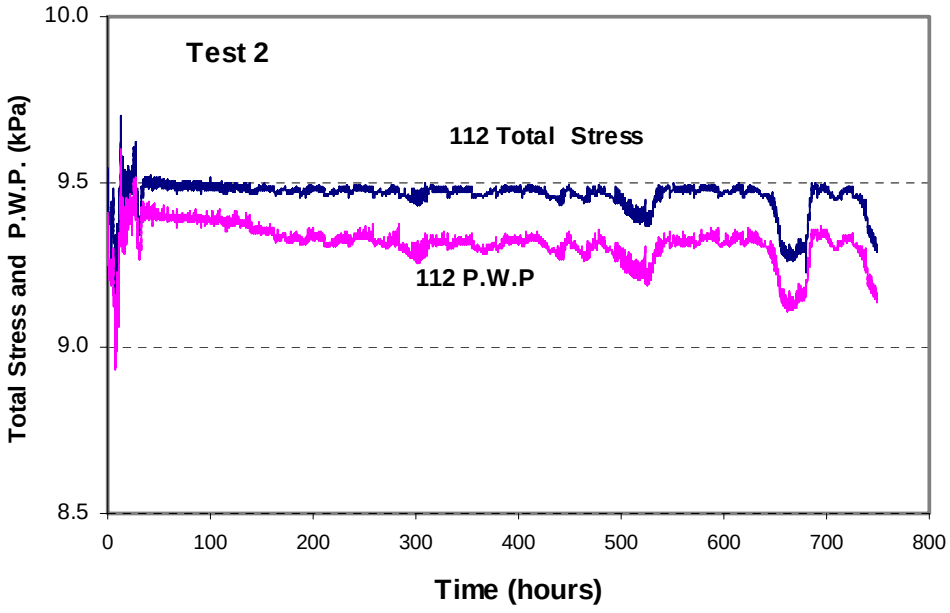

Figure H. 5 Changes in Total Stress and Pore Water Pressure at E2 of Test 2 during Microbial Activity

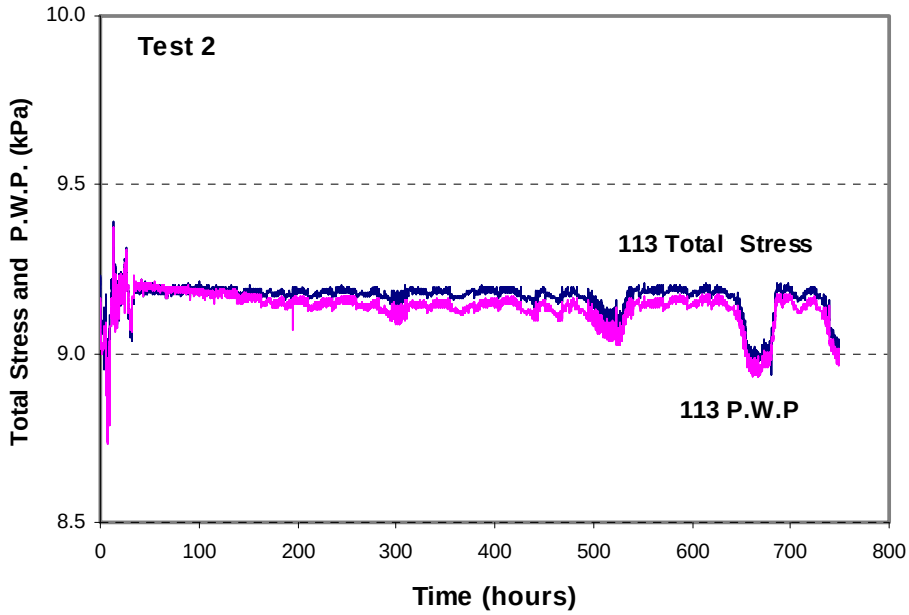

Figure H. 6 Changes in Total Stress and Pore Water Pressure at E3 of Test 2 during Microbial Activity

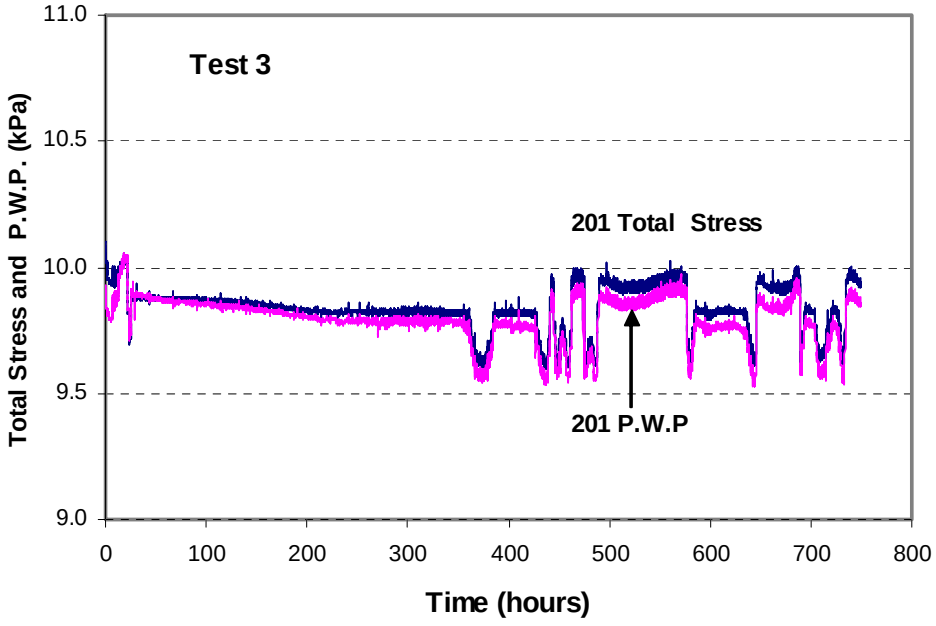

Figure H. 7 Changes in Total Stress and Pore Water Pressure at E1 of Test 3 during Microbial Activity

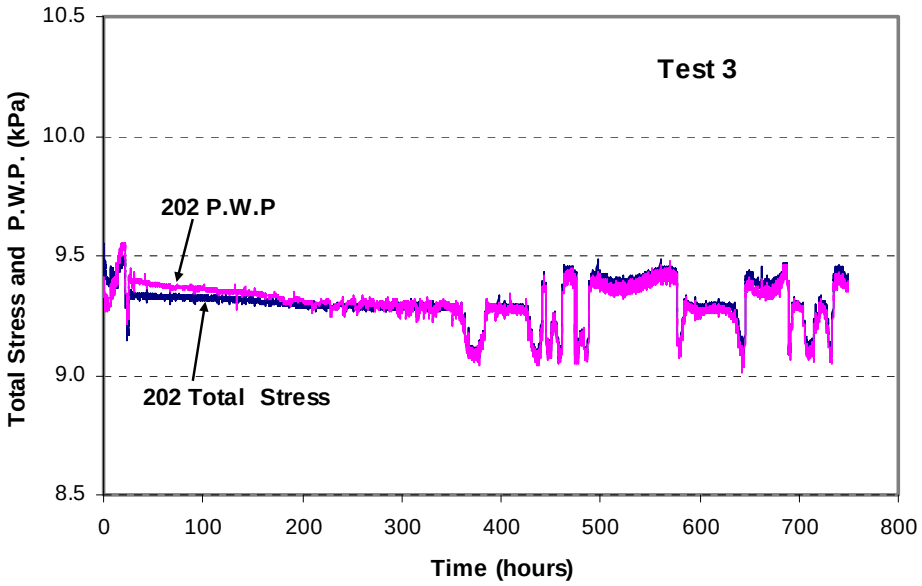

Figure H. 8 Changes in Total Stress and Pore Water Pressure at E2 of Test 3 during Microbial Activity

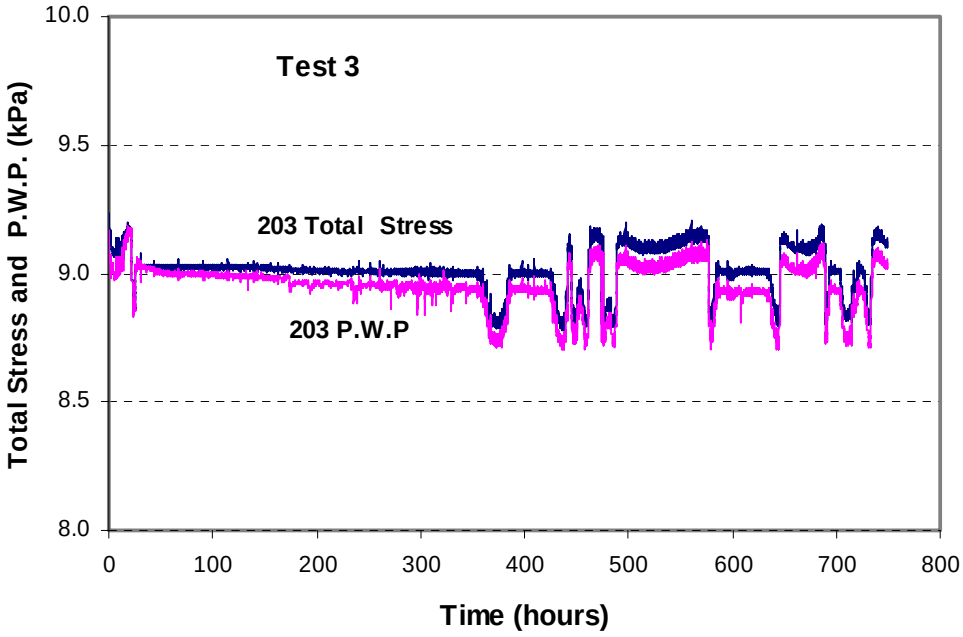

Figure H. 9 Changes in Total Stress and Pore Water Pressure at E3 of Test 3 during Microbial Activity

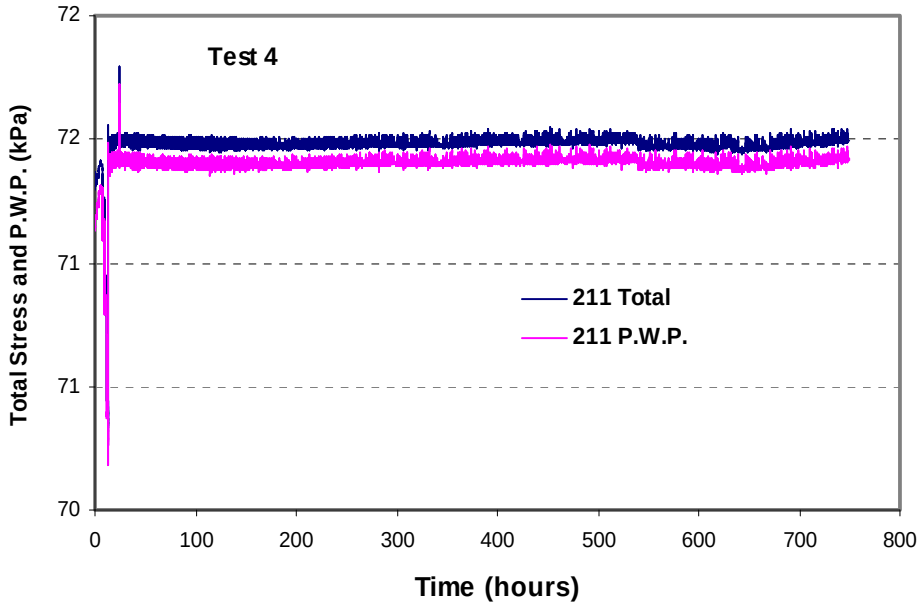

Figure H. 10 Changes in Total Stress and Pore Water Pressure at E1 of Test 4 during Microbial Activity

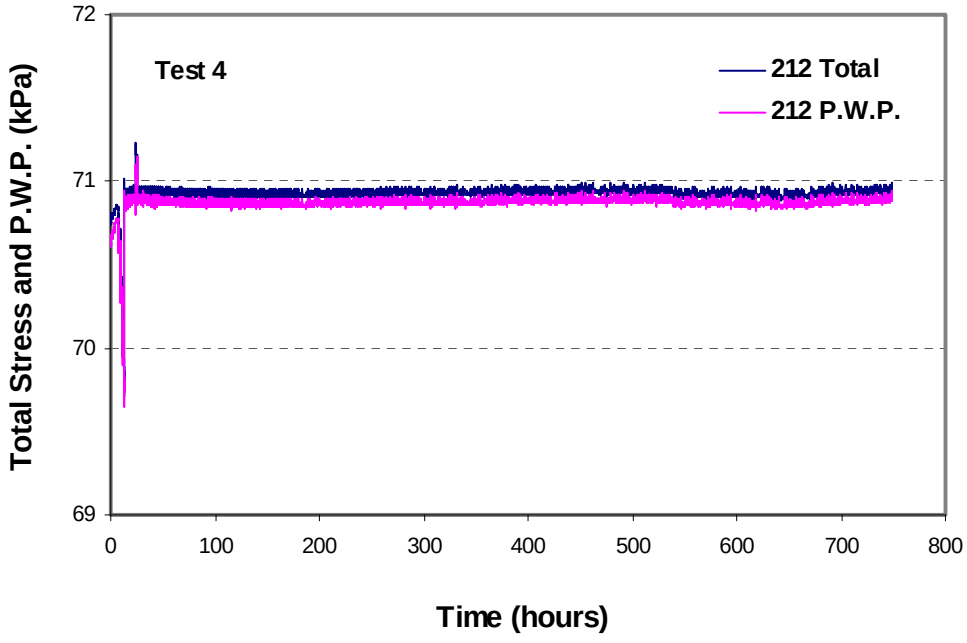

Figure H. 11 Changes in Total Stress and Pore Water Pressure at E2 of Test 4 during Microbial Activity

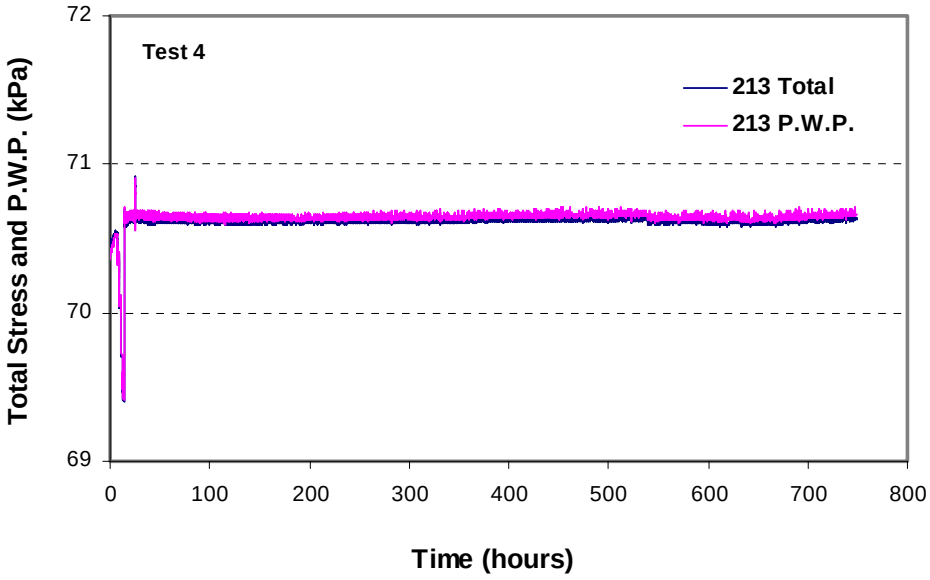

Figure H. 12 Changes in Total Stress and Pore Water Pressure at E3 of Test 4 during Microbial Activity

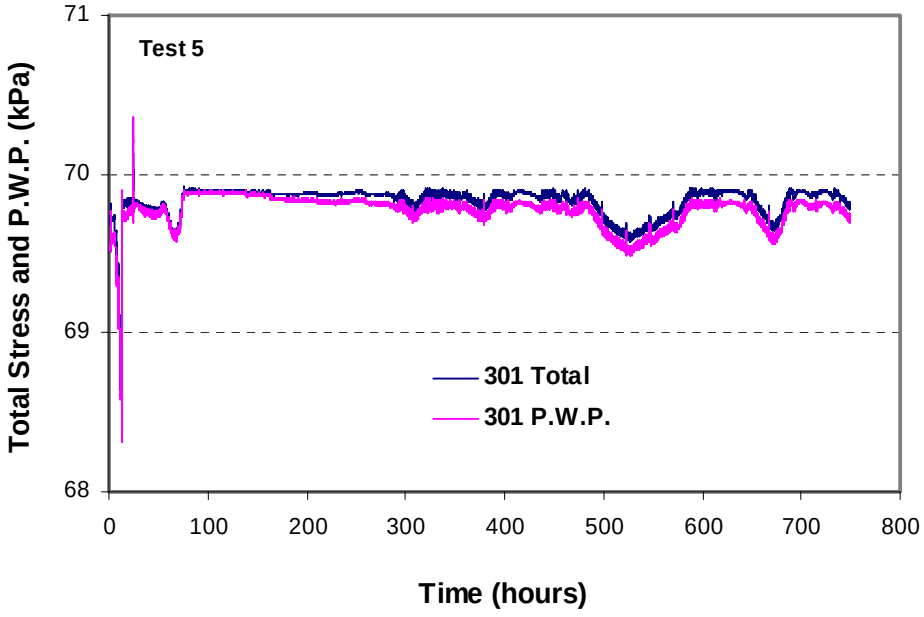

Figure H. 13 Changes in Total Stress and Pore Water Pressure at E1 of Test 5 during Microbial Activity

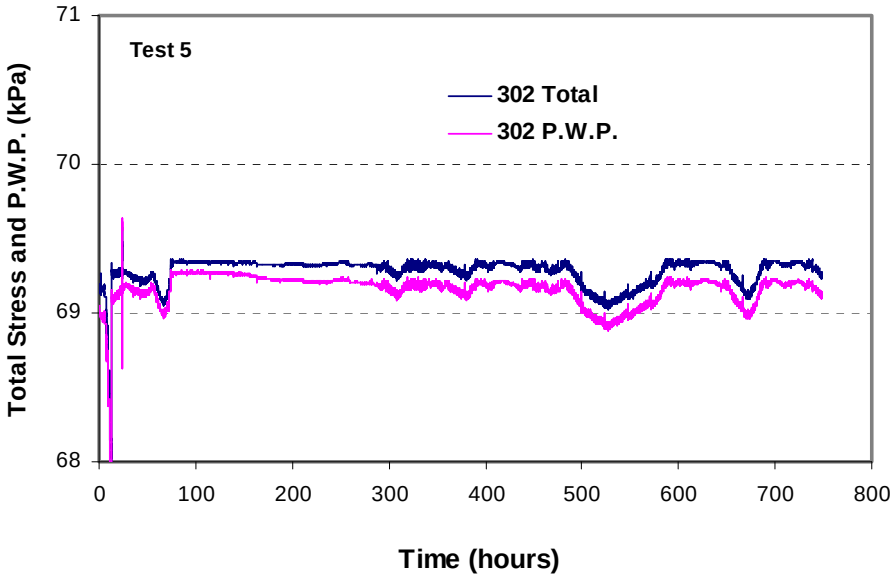

Figure H. 14 Changes in Total Stress and Pore Water Pressure at E2of Test 5 during Microbial Activity

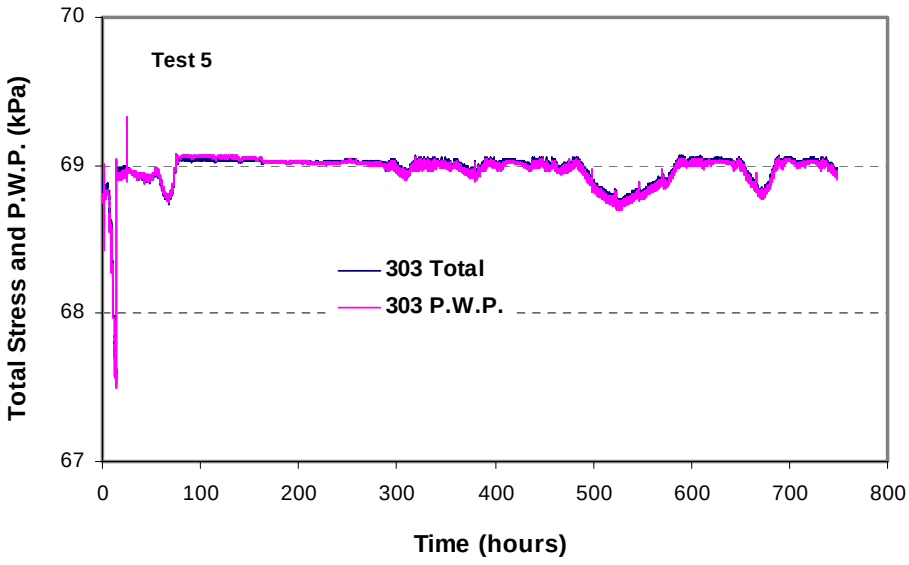

Figure H. 15 Changes in Total Stress and Pore Water Pressure at E3 of Test 5 during Microbial Activity

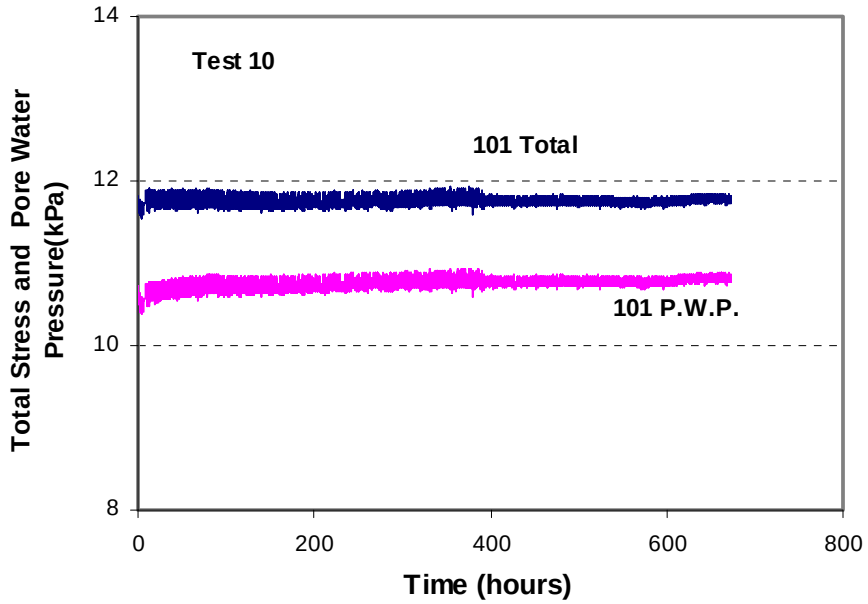

Figure H. 16 Changes in Total Stress and Pore Water Pressure at E1 of Test 10 during Microbial Activity

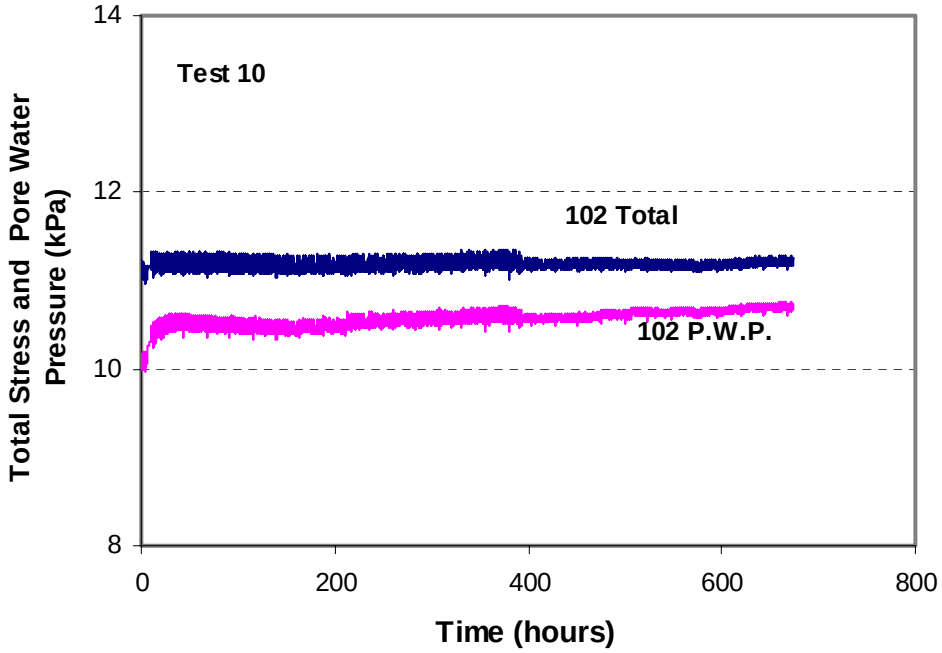

Figure H. 17 Changes in Total Stress and Pore Water Pressure at E2 of Test 10 during Microbial Activity

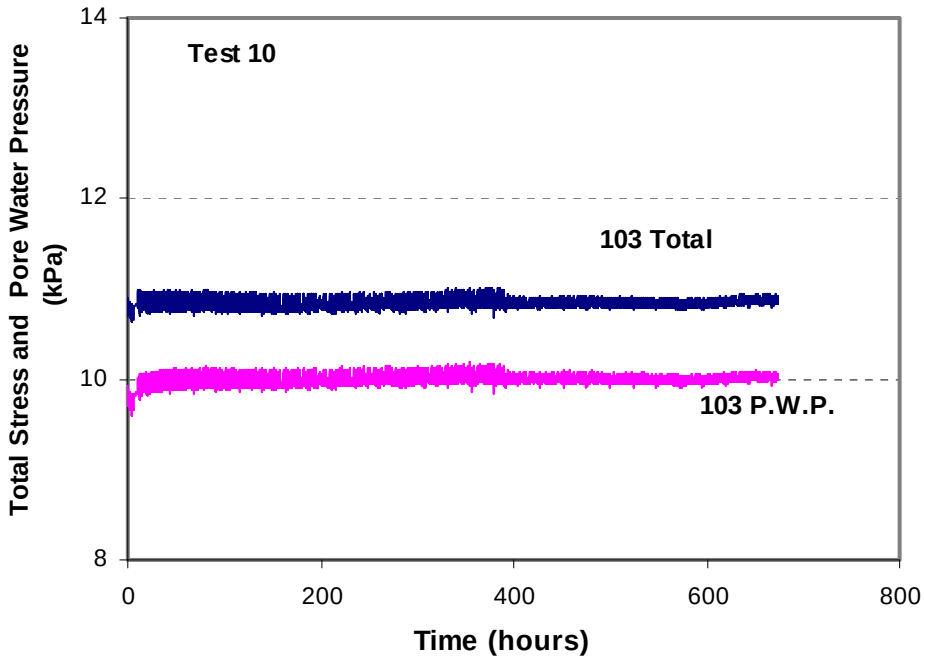

Figure H. 18 Changes in Total Stress and Pore Water Pressure at E3 of Test 10 during Microbial Activity

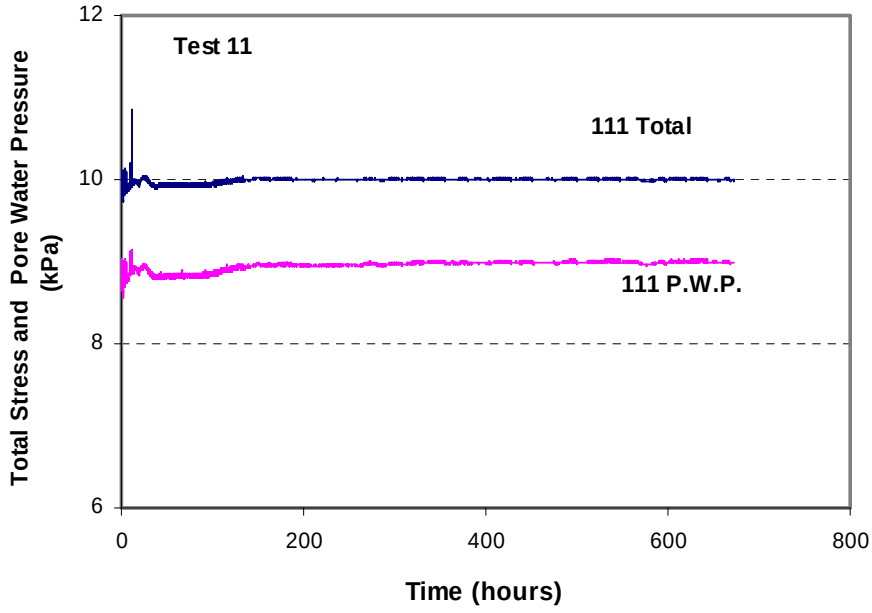

Figure H. 19 Changes in Total Stress and Pore Water Pressure at E1 of Test 11 during Microbial Activity

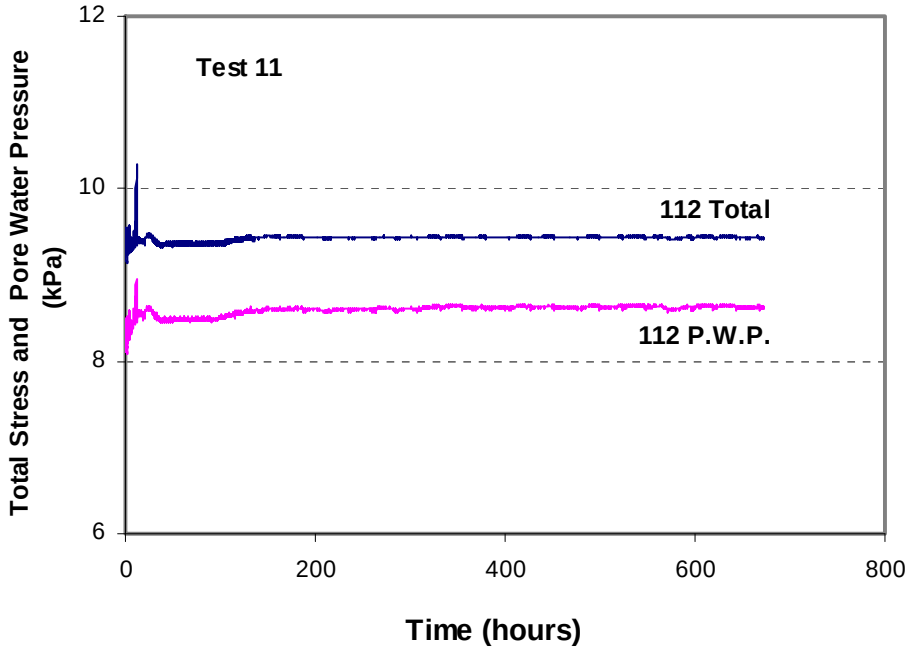

Figure H. 20 Changes in Total Stress and Pore Water Pressure at E2 of Test 11 during Microbial Activity

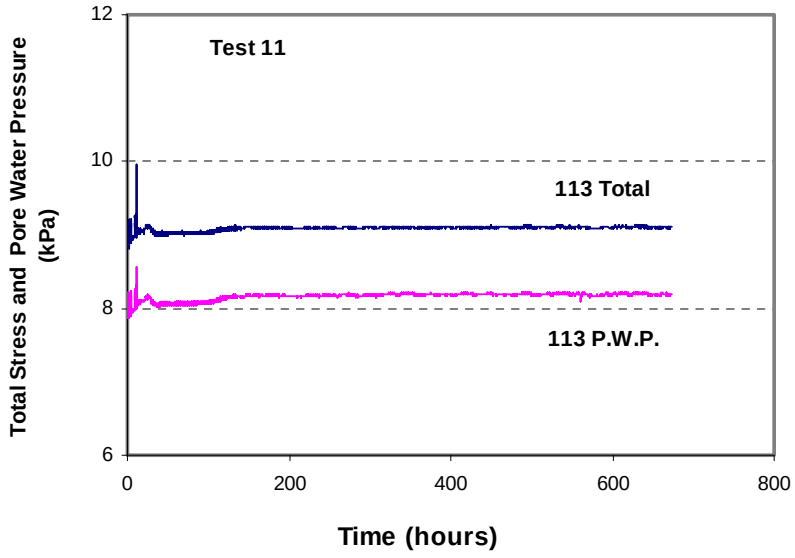

Figure H. 21 Changes in Total Stress and Pore Water Pressure at E3 of Test 11 during Microbial Activity

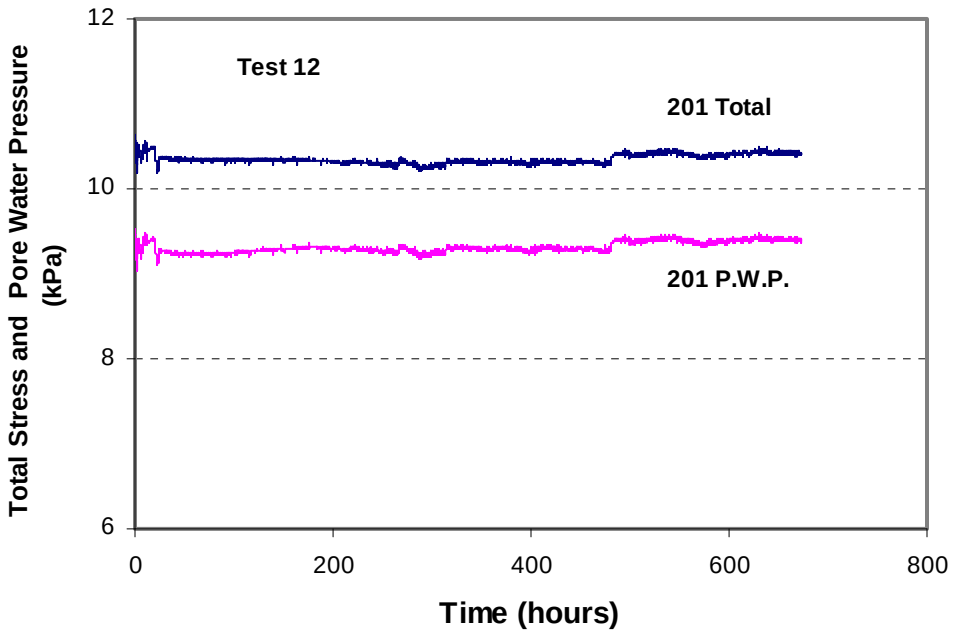

Figure H. 22 Changes in Total Stress and Pore Water Pressure at E1 of Test 12 during Microbial Activity

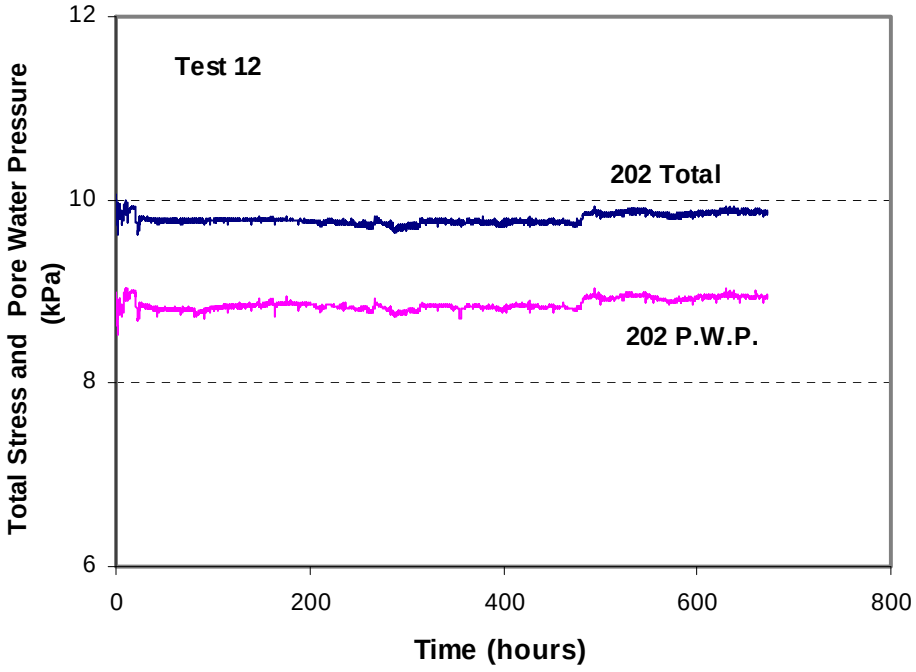

Figure H. 23 Changes in Total Stress and Pore Water Pressure at E2 of Test 12 during Microbial Activity

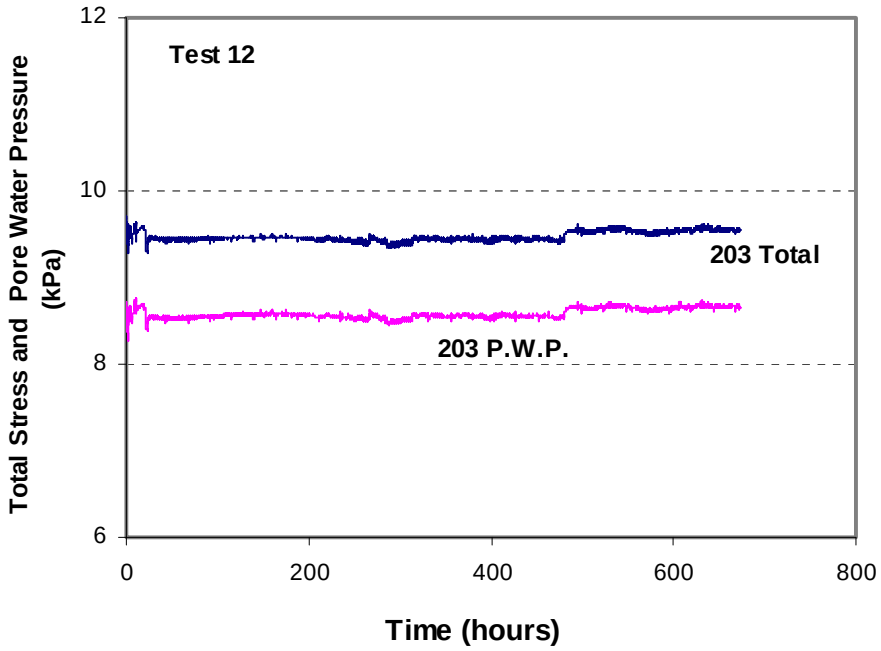

Figure H. 24 Changes in Total Stress and Pore Water Pressure at E3 of Test 12 during Microbial Activity

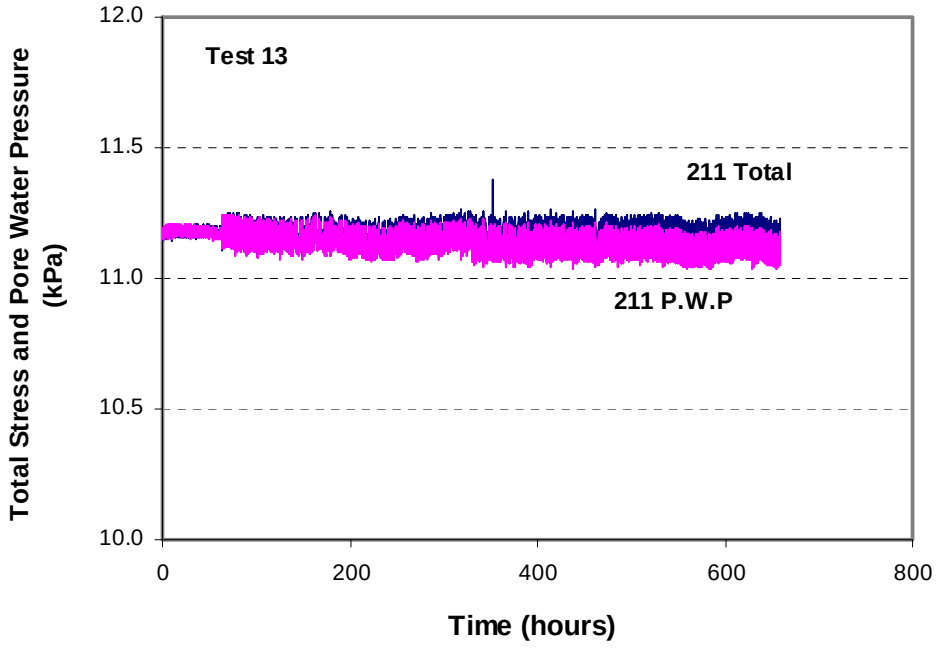

Figure H. 25 Changes in Total Stress and Pore Water Pressure at E1 of Test 13 during Microbial Activity

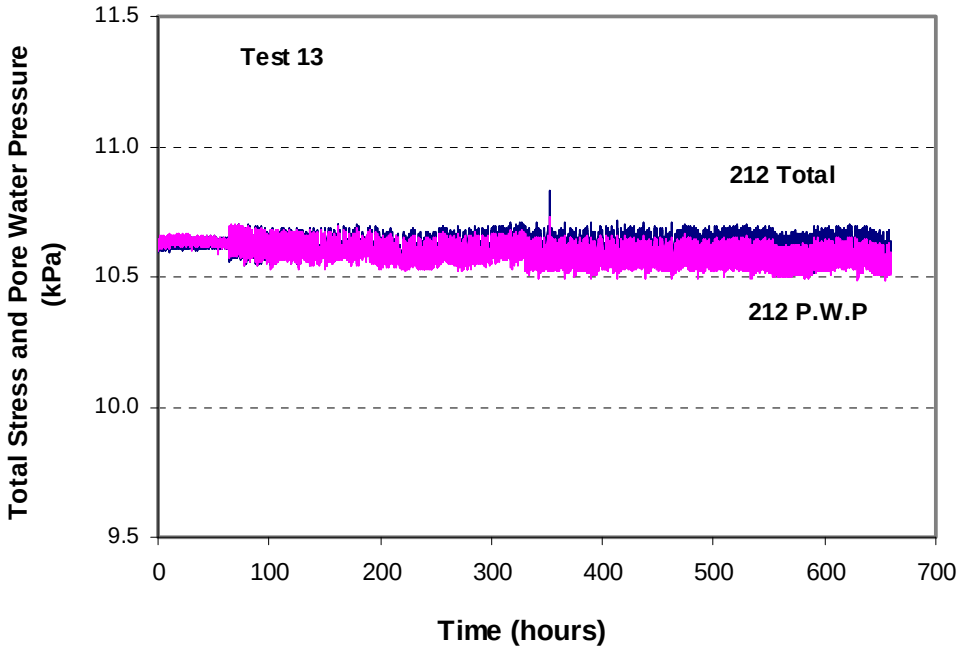

Figure H. 26 Changes in Total Stress and Pore Water Pressure at E2 of Test 13 during Microbial Activity

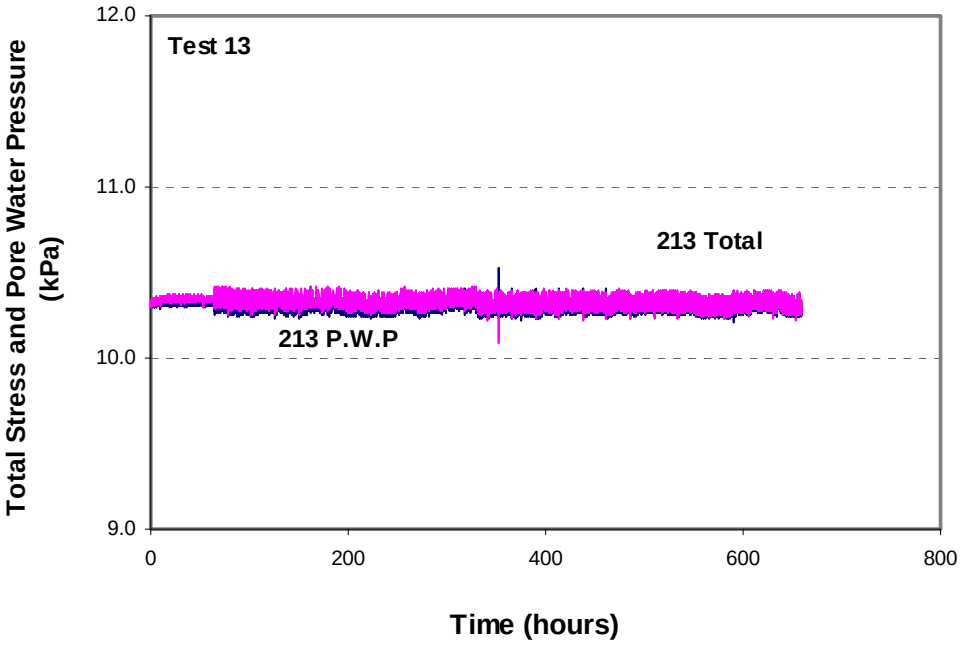

Figure H. 27 Changes in Total Stress and Pore Water Pressure at E3 of Test 13 during Microbial Activity

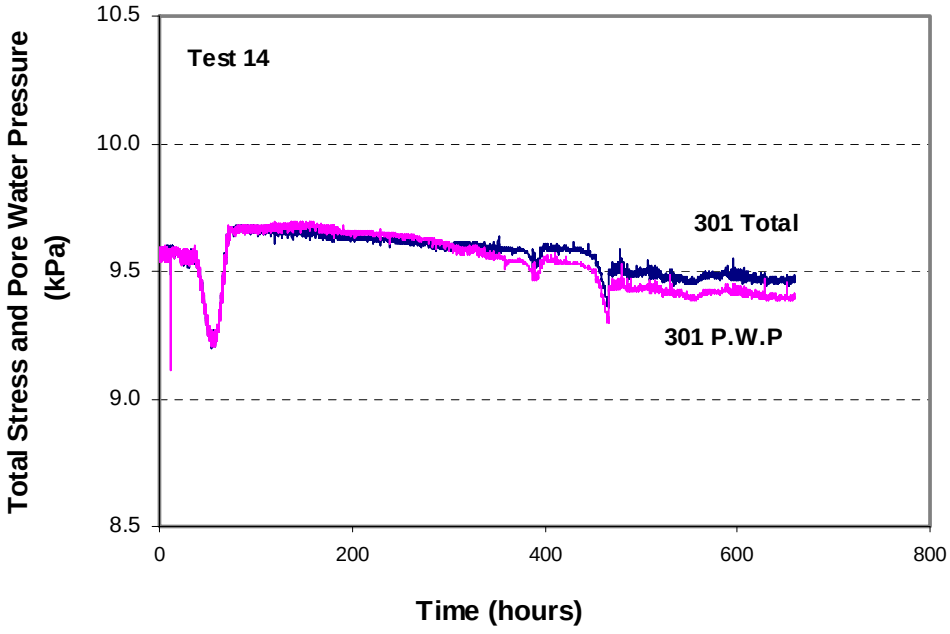

Figure H. 28 Changes in Total Stress and Pore Water Pressure at E1 of Test 14 during Microbial Activity

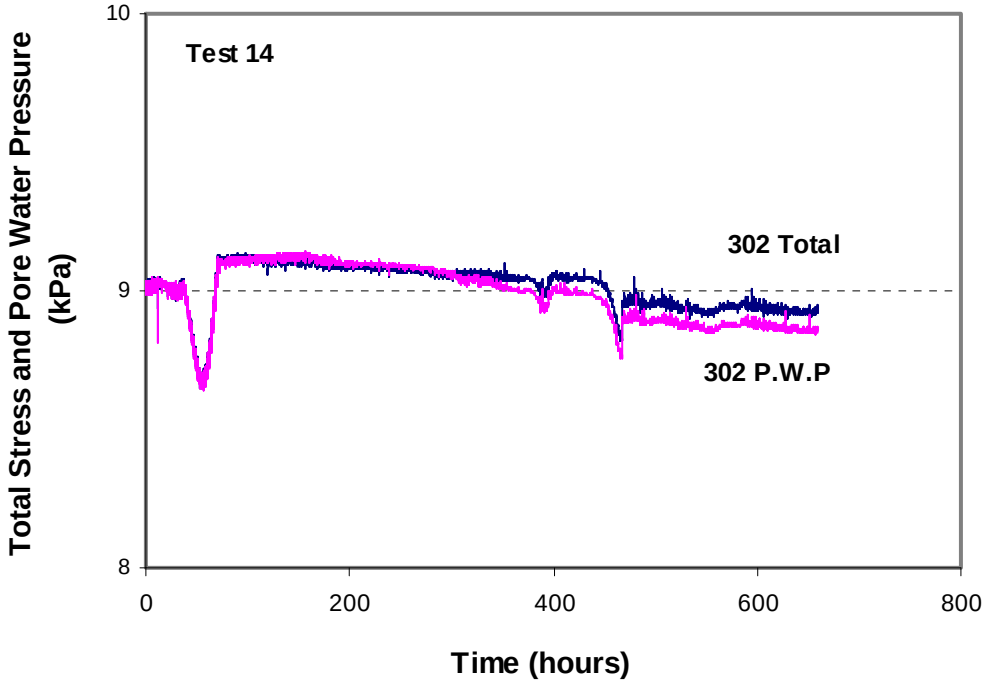

Figure H. 29 Changes in Total Stress and Pore Water Pressure at E2 of Test 14 during Microbial Activity

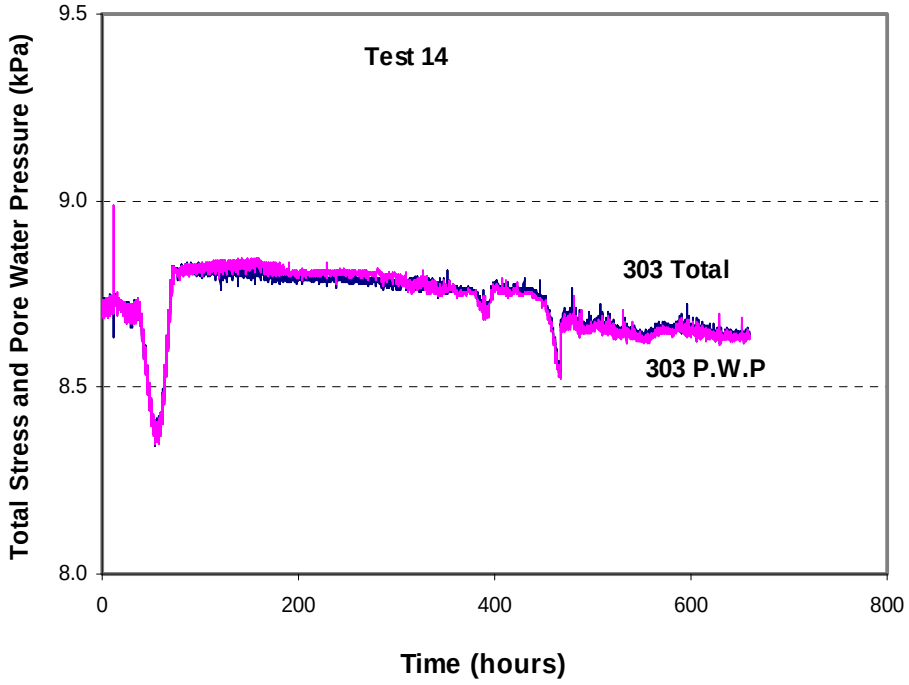

Figure H. 30 Changes in Total Stress and Pore Water Pressure at E3 of Test 14 during Microbial Activity

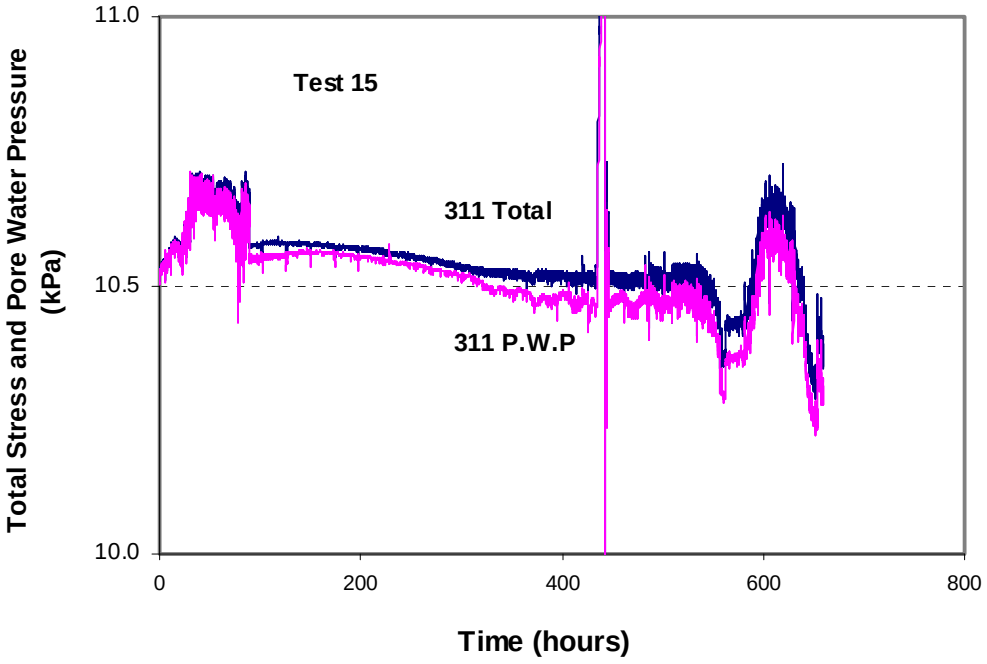

Figure H. 31 Changes in Total Stress and Pore Water Pressure at E1 of Test 15 during Microbial Activity

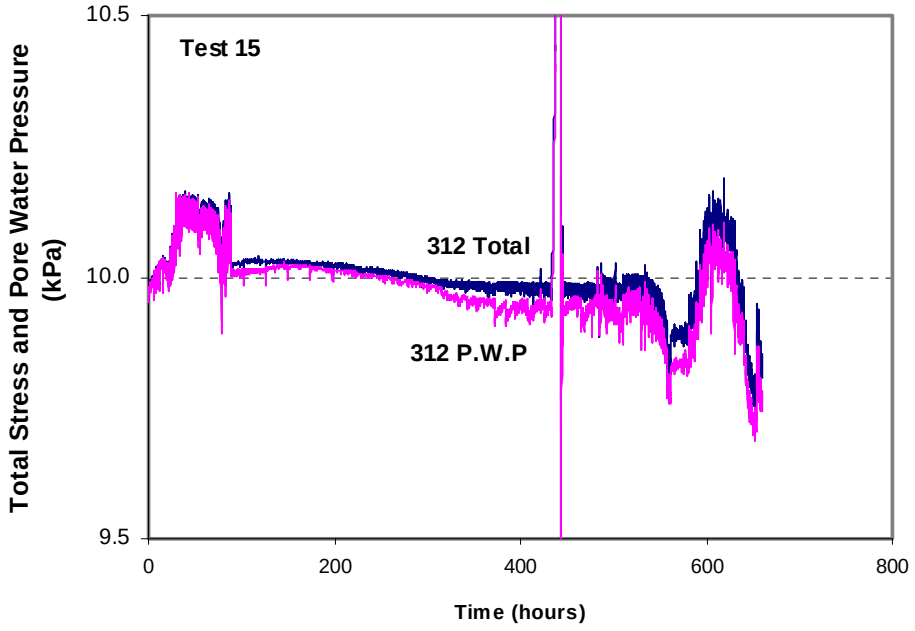

Figure H. 32 Changes in Total Stress and Pore Water Pressure at E2 of Test 15 during Microbial Activity

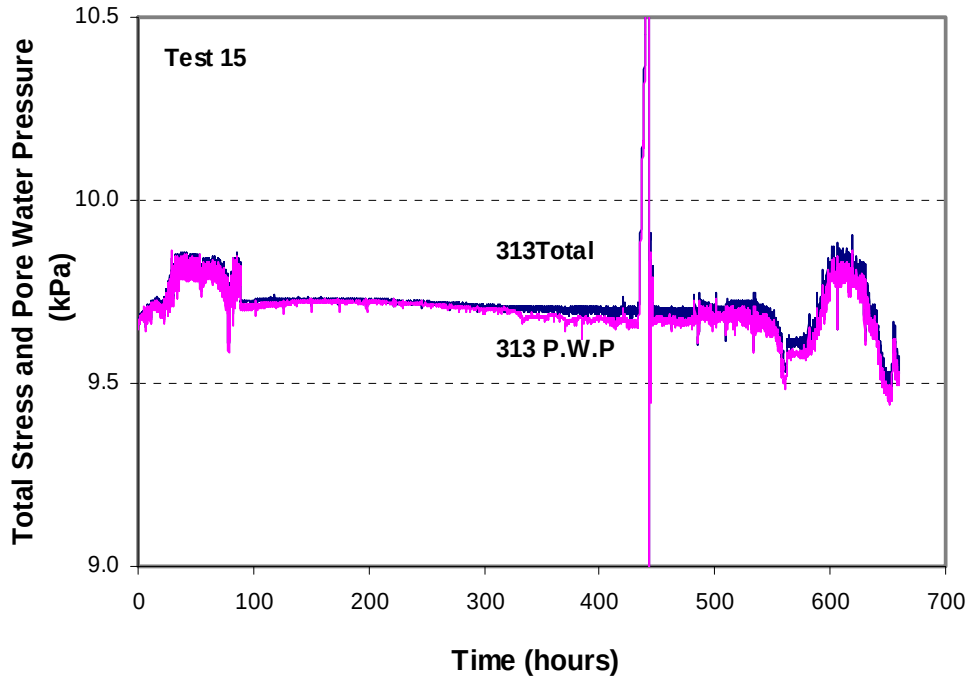

Figure H. 33 Changes in Total Stress and Pore Water Pressure at E3 of Test 15 during Microbial Activity

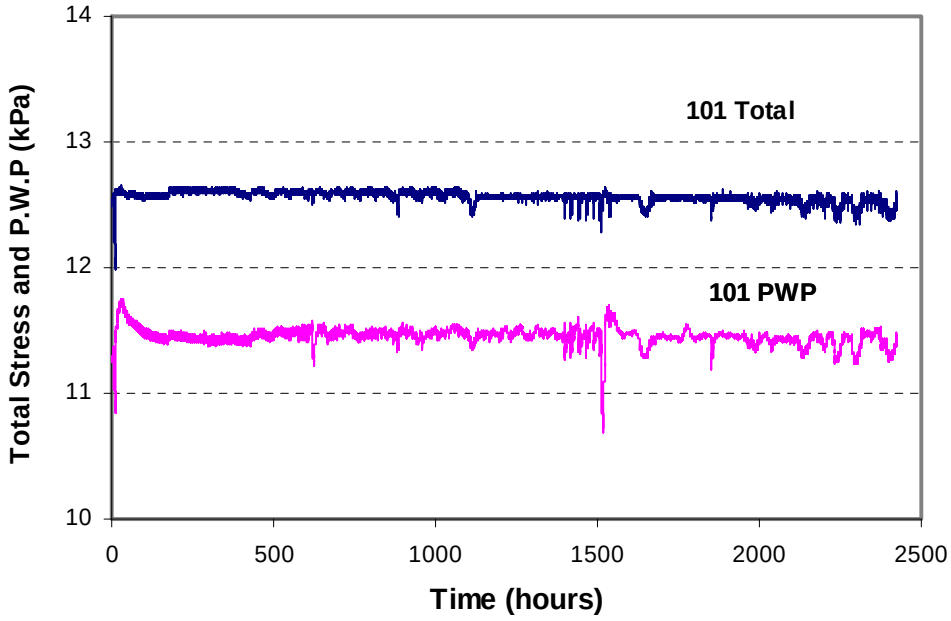

Figure H. 34 Changes in Total Stress and Pore Water Pressure at E1 of Test 19 during Microbial Activity

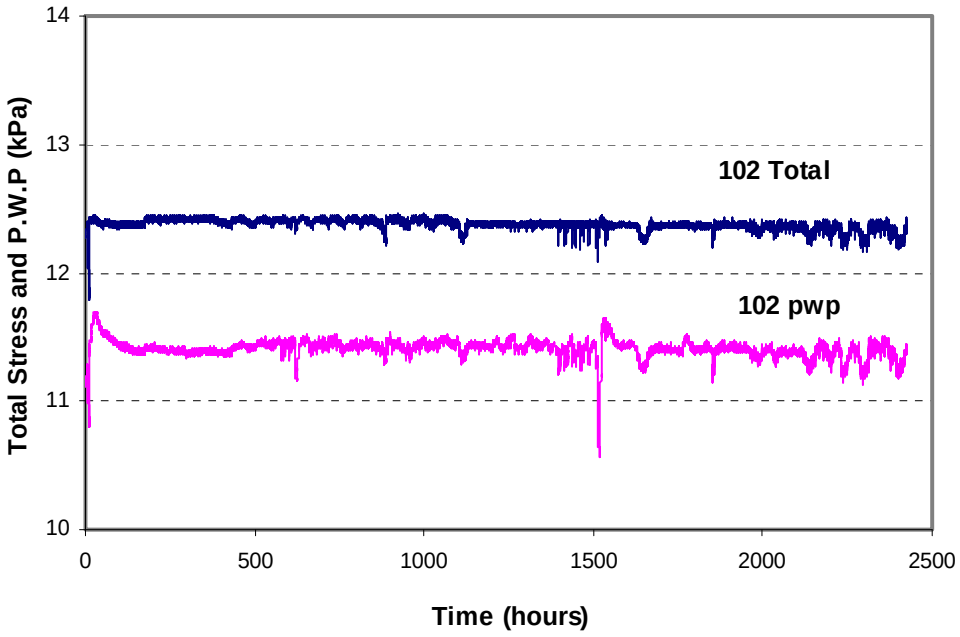

Figure H. 35 Changes in Total Stress and Pore Water Pressure at E2 of Test 19 during Microbial Activity

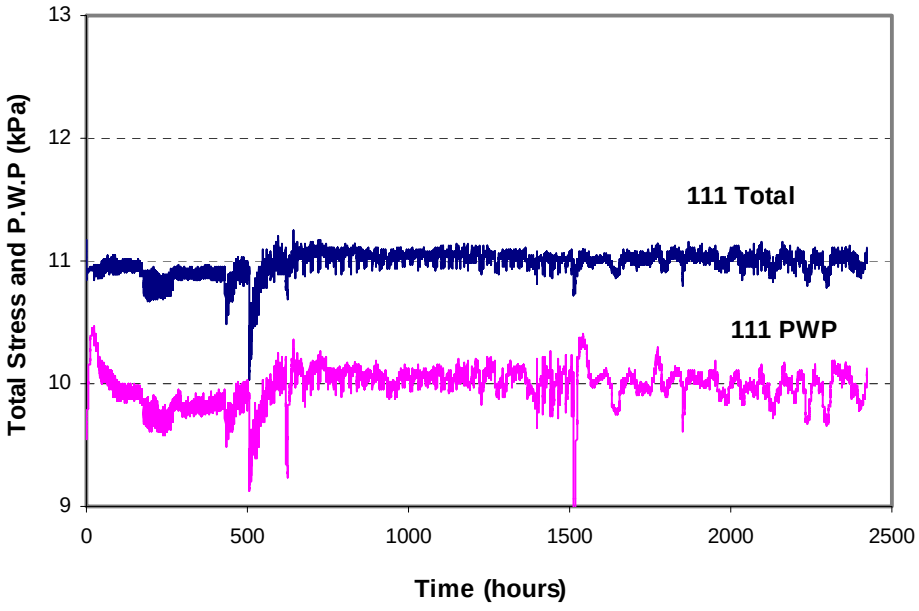

Figure H. 36 Changes in Total Stress and Pore Water Pressure at E1 of Test 20 during Microbial Activity

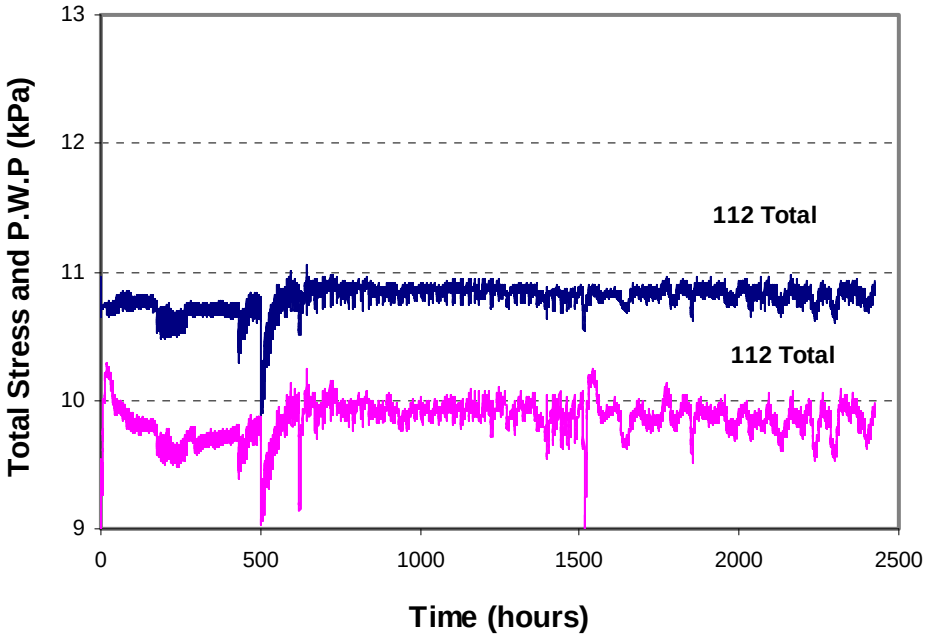

Figure H. 37 Changes in Total Stress and Pore Water Pressure at E2 of Test 20 during Microbial Activity

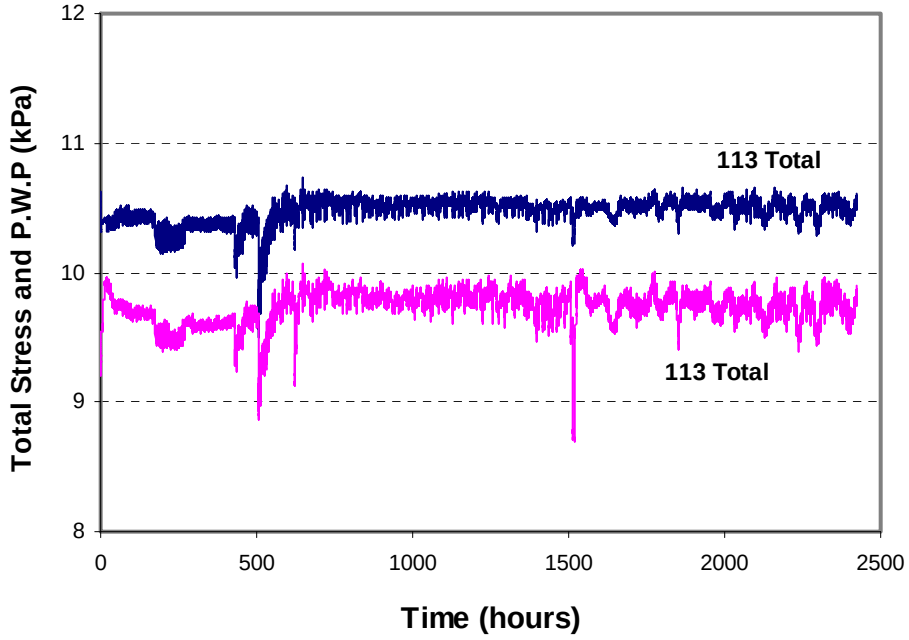

Figure H. 38 Changes in Total Stress and Pore Water Pressure at E3 of Test 20 during Microbial Activity

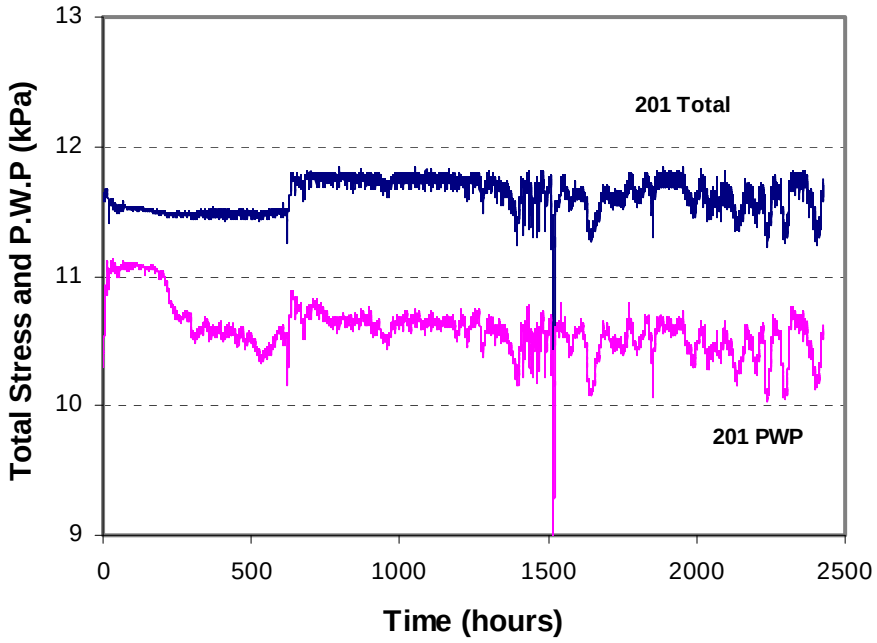

Figure H. 39 Changes in Total Stress and Pore Water Pressure at E1 of Test 21 during Microbial Activity

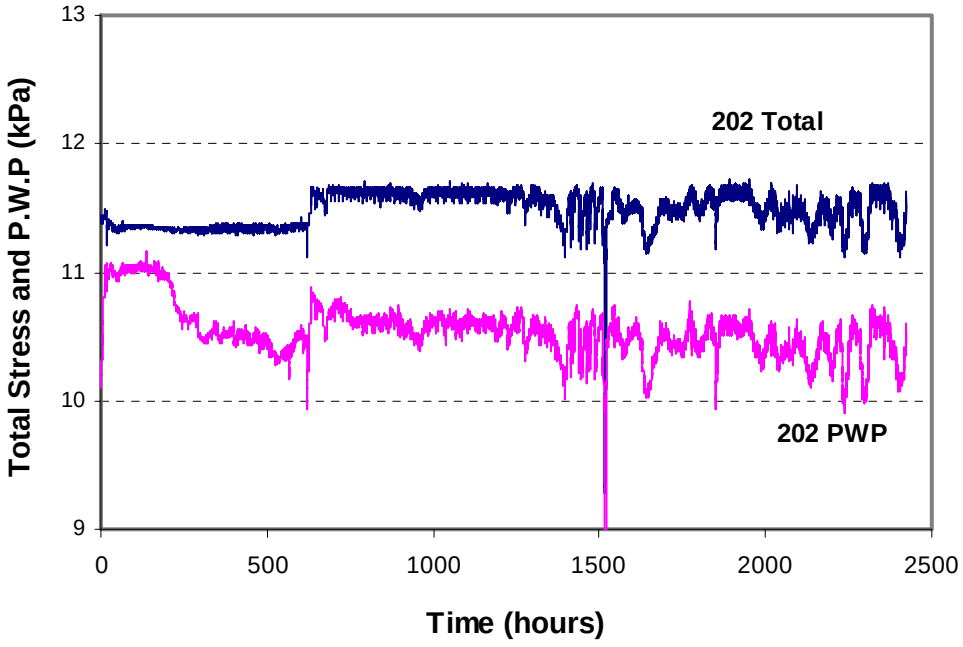

Figure H. 40 Changes in Total Stress and Pore Water Pressure at E2 of Test 21 during Microbial Activity

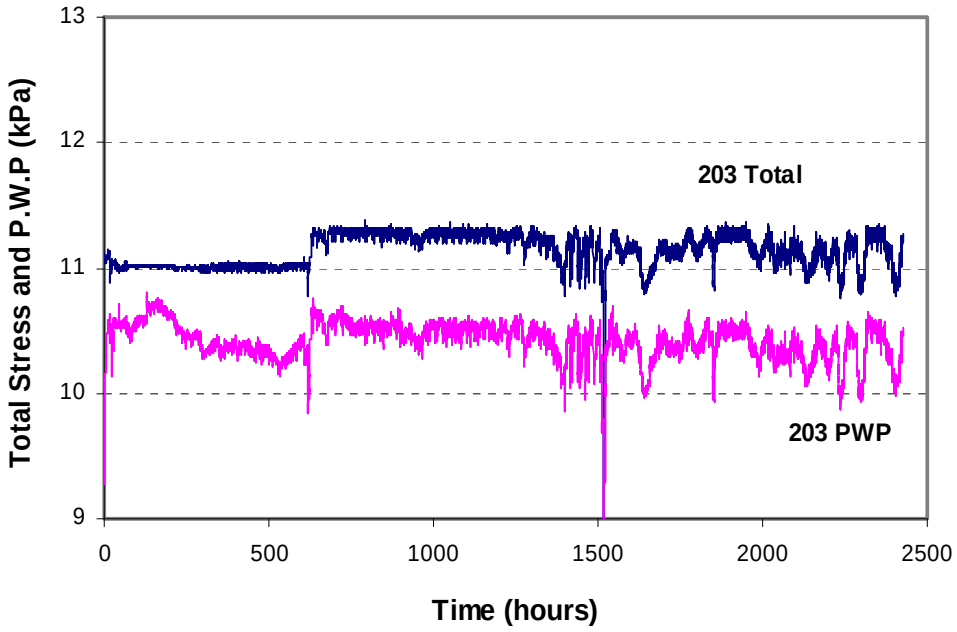

Figure H. 41 Changes in Total Stress and Pore Water Pressure at E3 of Test 21 during Microbial Activity

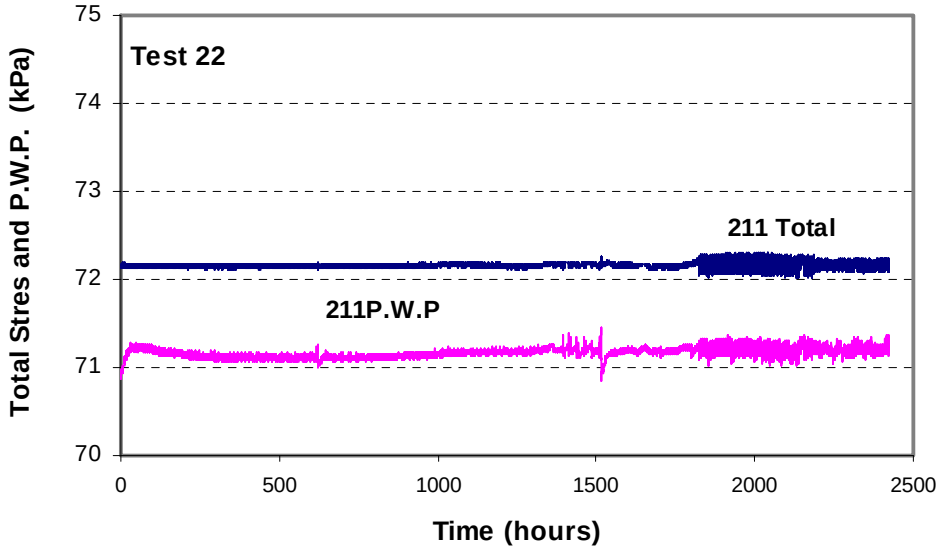

Figure H. 42 Changes in Total Stress and Pore Water Pressure at E1 of Test 22 during Microbial Activity

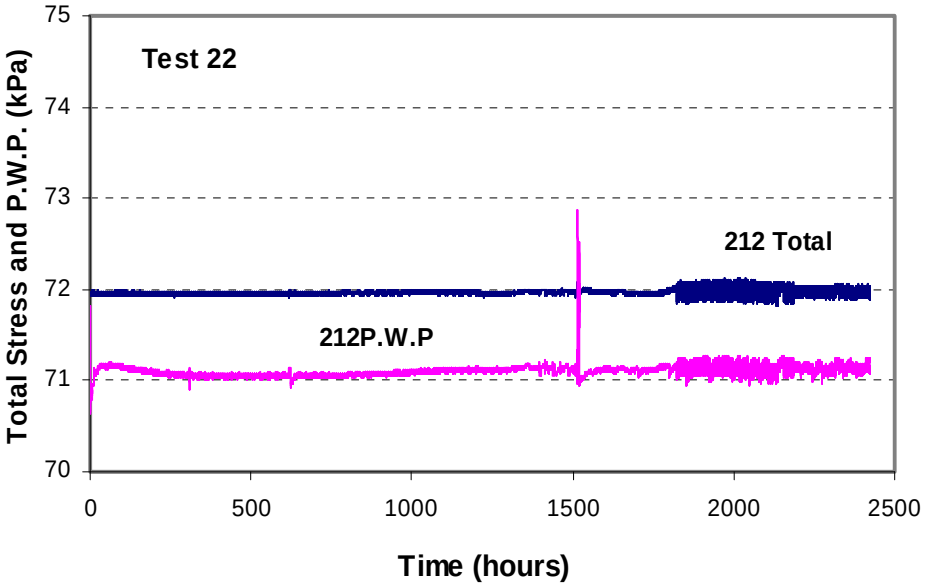

Figure H. 43 Changes in Total Stress and Pore Water Pressure at E2 of Test 22 during Microbial Activity

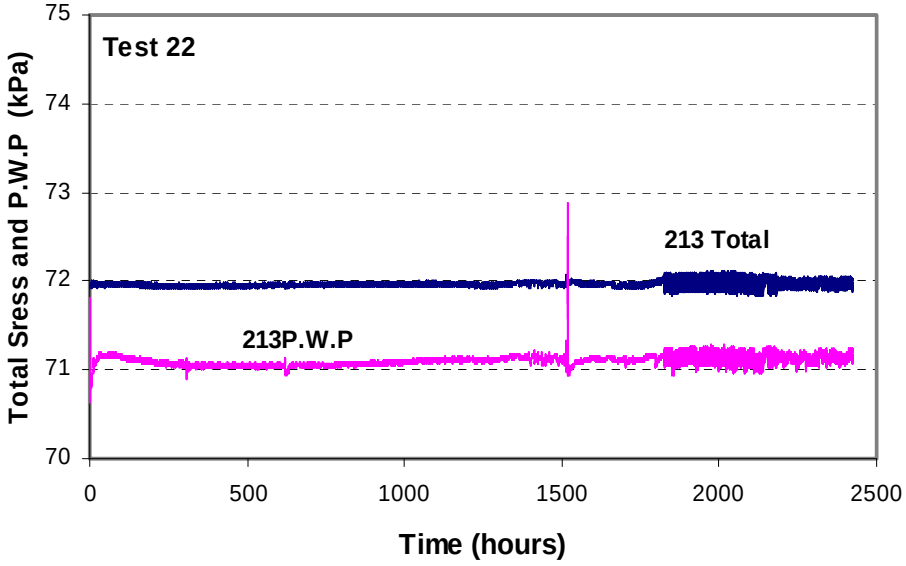

Figure H. 44 Changes in Total Stress and Pore Water Pressure at E3 of Test 22 during Microbial Activity

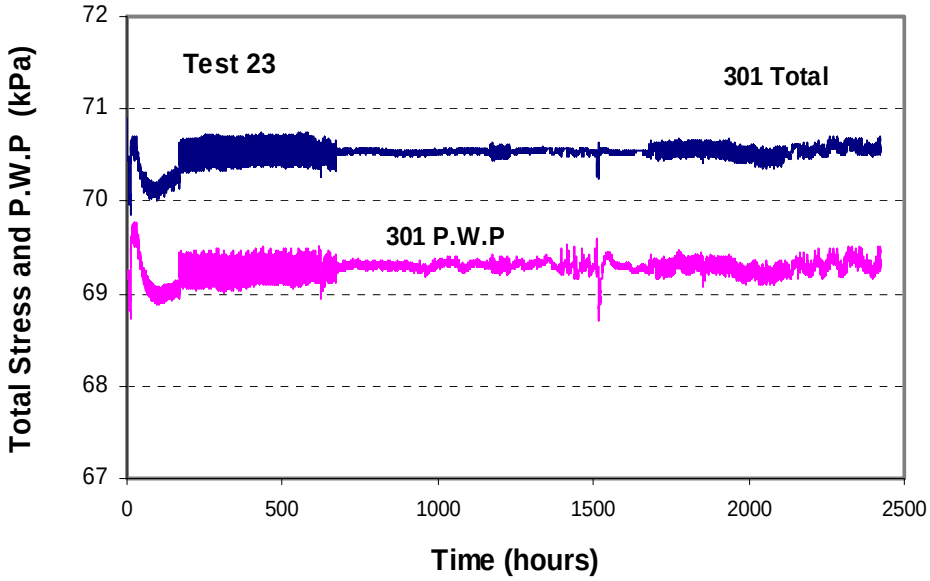

Figure H. 45 Changes in Total Stress and Pore Water Pressure at E1 of Test 23 during Microbial Activity

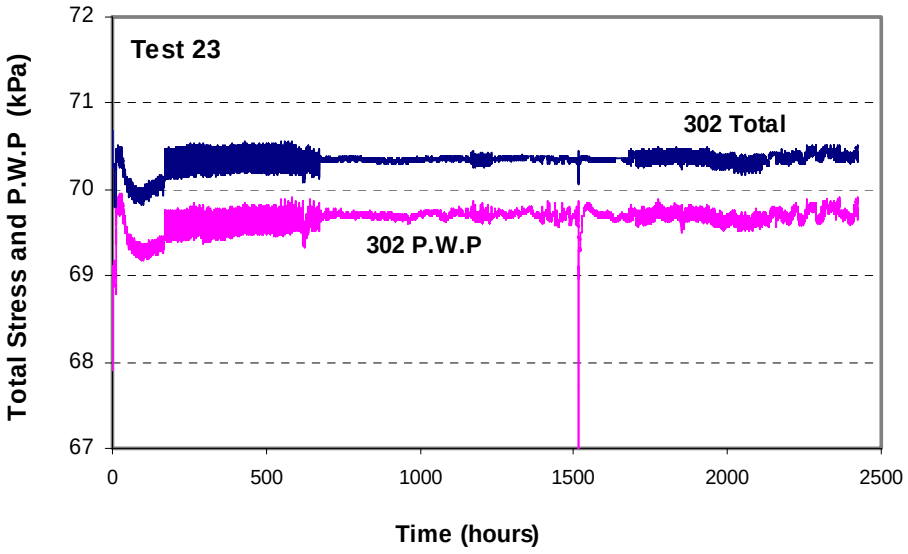

Figure H. 46 Changes in Total Stress and Pore Water Pressure at E2 of Test 23 during Microbial Activity

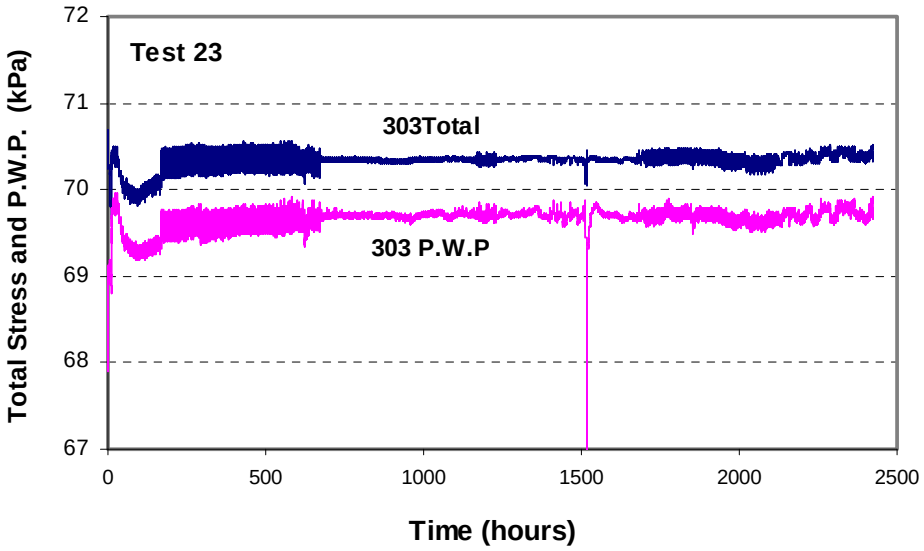

Figure H. 47 Changes in Total Stress and Pore Water Pressure at E3 of Test 23 during Microbial Activity

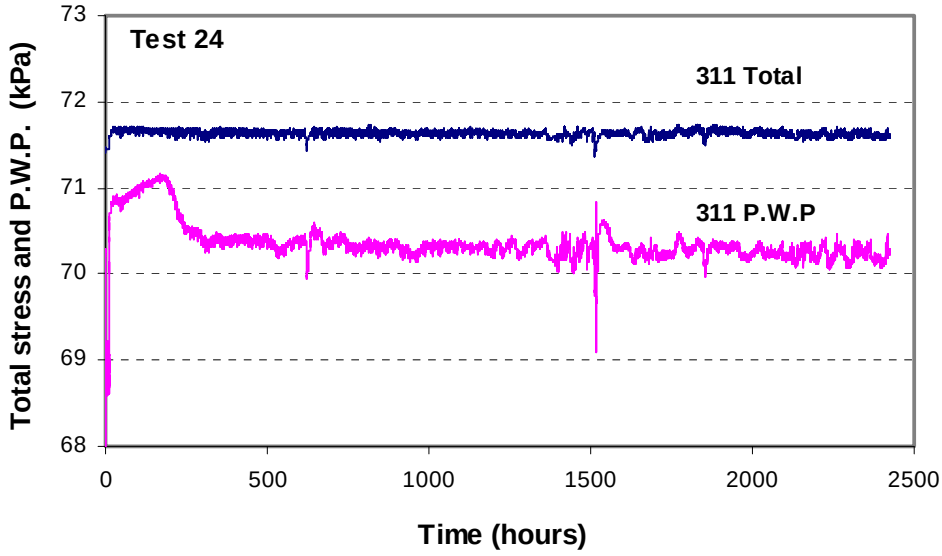

Figure H. 48 Changes in Total Stress and Pore Water Pressure at E1 of Test 24 during Microbial Activity

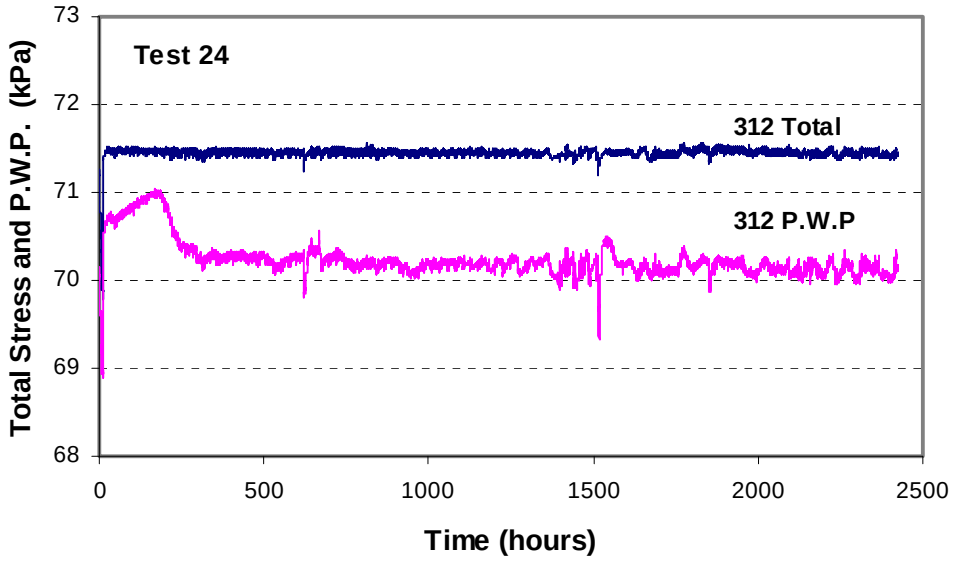

Figure H. 49 Changes in Total Stress and Pore Water Pressure at E2 of Test 24 during Microbial Activity

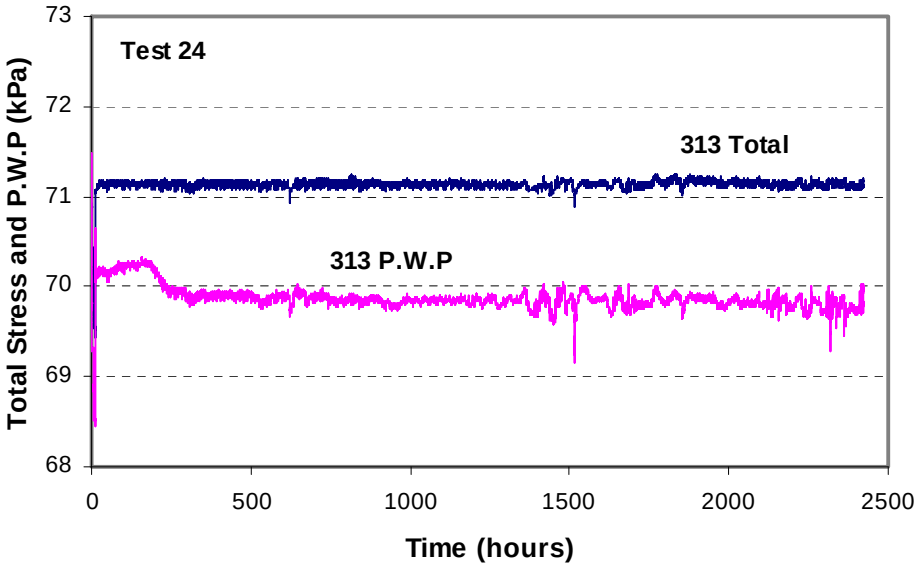

Figure H. 50 Changes in Total Stress and Pore Water Pressure at E3 of Test 24 during Microbial Activity

APPENDIX I Structure Observations during Gas MFT Densification Tests

This appendix shows observations and photos of the samples during gas MFT densification tests. The photos shown were used to analyze the macro-structure changes during microbial activity.

Sample 1

Since no sodium acetate was added, microbial activity in sample 1 was relatively weak. During the test, only small spherical gas voids with less than 0.1 mm diameters were observed. No obvious cracks and fractures appeared on the sidewall of the cell. All the generated gas was trapped within the MFT. Figure I.1 shows a photo of sample 1 at the end of testing (Day 32).

Sample 2

Some spherical gas voids with less than 0.1 mm diameters started to appear on November 2 (Day 3). On November 4 (Day 5), some cracks, 0.2-0.4 mm wide and 1-2 cm long, were shown close to the interface (Figure I.2). Figure I.3 shows a photo taken on November 14 (day 15). Most of the gas bubbles were in a spherical shape with a maximum size of about 0.2-03 mm. Some short and discontinuous cracks were observed close to the interface. During the test, no obvious large fractures were observed. A small amount of gas started to be released from the sample on November 16 (Day 17).

Sample 3

Figure I.4 shows a photo of sample 3 on October 30, 2003 (Day 1), when microbial activity was initiated. No visible gas bubbles and cracks were seen. After the room temperature was raised to 24^{o}C, biogas was rapidly generated. On November 2 (Day 3), small fissures started to appear on the upper part of the sample. On November 4 (Day 5), obvious cracks, 0.2 mm wide and 1-2 cm long, appeared at the upper part of the sample (Figure I.5**)**. Most of the cracks extended in horizontal or slightly inclined directions. On November 6 (Day 7, Figure I.6) some cracks were more than 1 mm wide and 2 cm long with ellipsoidal gas

bubbles trapped inside. Some of the cracks were interconnected and extended to the interface. On November 7 (Day 8), part of the trapped gas started to escape from the sample. With gas bubbles being released, the interface settled down and some of the cracks and trapped gas bubbles disappeared or became smaller. Figure I.7 shows a photo at the end of the test period (Day 32). Most of the large cracks and fractures appeared at the upper part of the sample (about 3 cm below the MFT interface). At the lower part of the sample, large cracks and gas voids rarely happened.

Sample 4

Since gas generation was slow and most of the generated gas was dissolved in the solution under the applied back pressure, no obvious structural change was observed during microbial activity. The MFT interface settled during testing.

Sample 5

On November 2 (Day 3), small spherical gas voids started to appear. Figure I.8 shows a photo of the gas bubbles on November 6 (Day 7). A few spherical gas bubbles with 0.2-0.4 mm diameters were observed. The white color strips shown on the sidewall might have been caused by the non-uniform distributions of dissolved gas or chemical concentrations. There was no visible crack observed during the test. Most of the generated gas existed as occluded small gas voids (less than 0.1 mm in diameter), which were less visible. All the generated gas was trapped in the sample. Structural changes during microbial activity were not significant.

Sample 6

After the room temperature was raised, gas was rapidly generated. On November 4 (Day 5), a small horizontal fissure, 0.1 mm wide and 1-2 cm long, appeared about 1.5 cm below the MFT interface. With rapid gas generation continuing, a large crack (Figure I.9), 0.3-0.4 mm wide, appeared about 1-2 cm below the interface on November 8 (Day 9). This large crack extended horizontally around

the periphery of the sidewall of the cell. Some large gas bubbles in an ellipsoidal shape were trapped within the large crack. As the accumulated gas volume increased, the size of the large crack gradually did the same. On November 17 (Figure I.10), the large crack developed to a width of about 3-4 mm. At this point, some ellipsoidal gas bubbles were trapped inside. Throughout the test, there was no visible gas bubble release from the MFT. Most of the cracks were filled with ellipsoidal gas bubbles, which were mostly in compressed and tightly closed conditions. It appears that the gas bubbles produced under lower pressure were better able to escape from the MFT than those under higher pressure. This might be related to the rapid expansion of the MFT volume and rapid development of some open structures (large cracks and fractures) when gas generation was under lower pressure.

Sample 10

After unloading the sample, negative excess pore water pressure was generated. Thus, the MFT had the potential to swell. Figure I.11 shows a photo of sample 10 on December 29 (Day 7, after warming up). A small horizontal tension crack was observed close to the interface due to MFT expansion. There was no other visible change during the early period besides this tension crack. With continuing expansion and gas generation, the tension crack near the interface further developed. Figure I.12 shows a photo from January 8 (Day 16). The crack was about 1-2 mm wide and 4-5 cm long, and some ellipsoidal gas bubbles were trapped within the it. Below the crack no visible change was observed. It is likely that some of the generated gas bubbles migrated to the upper part of the sample and became trapped in the tension crack. Figure I.13 shows a photo of the sample on January 20 (Day 28). The crack near the interface developed into interconnected fractures extending in different directions. Some large gas bubbles were trapped within the fractures. Below the fractured zone (about 1 cm below the interface), there was no obvious change observed. During microbial activity, all the generated gas was trapped in the MFT; there was no visible gas bubble release.

Sample 11

After temperature increased, biogas was rapidly produced in sample 11. Figure I.14 shows a photo of sample 11 on December 27 (Day 5). Some occluded gas voids in spherical or ellipsoidal shapes were observed on the sidewall. With continual gas generation in the MFT, more large gas bubbles were observed, and some cracks, filled with ellipsoidal gas bubbles, appeared at the upper part of the sample, as shown in

Figure I.15 (January 5, Day 13). Figure I.16 shows a photo taken on January 20 (Day 28). The maximum width of the cracks at the upper part of the sample was 2-3 mm. Most of the generated gas existed in occluded gas bubbles and discontinuous gas cracks. There was no obvious gas release during the test.

Sample 12

Figure I.17 shows a photo of sample 12 taken on December 23 (Day 1, when microbial activity began). The sample was uniform and no visible gas bubbles were observed. After the room temperature was increased, gas was rapidly produced in the sample. Figure I.18 shows a photo on December 27 (Day 5). Some large cracks, 1-3 mm wide and 3-4 cm long, appeared at the upper part of the sample. The large cracks were partly filled with gas bubbles, some of which started to escape from the MFT. Rapid gas generation significantly changed the MFT structure. Figure I.19 shows a photo taken on December 31 (Day 9) in which some interconnected fractures appeared at the upper part of the sample, and some extended to the interface. Some gas bubbles were trapped within the fractures. Figure I.20 shows a photo from Jan 20 (Day 29), in which some large gas bubbles, shown in Figure I.19 (Day 9), disappeared. It is likely that the large gas bubbles moved out of the sample through the interconnected fractures. The large fractures could have become convenient paths for water drainage or gas migration.

Sample 13

The room temperature started to warm up on December 23, 2003. Due to the slow biogas generation, there was no visible structural change in sample 13 until December 28 (Day 5). On December 31 (Day 9), some small discontinuous fissures appeared on the upper part of the sample, as shown in Figure I.21**.** A few spherical gas bubbles with 0.1-0.2 mm diameters were also observed. Figure I.22 shows a photo taken on January 20, 2004 (Day 29). Some ellipsoidal gas bubbles appeared on the upper part of the sample in the range of about 2-3 below the interface. There were no obvious cracks or fractures observed, and all the generated gas was trapped in the MFT.

Sample 14

There was no obvious structural change during the first several days. Figure I.23 shows a photo of sample 14 on December 29 (Day 7). Most of the gas bubbles were in spherical shape with a diameter less than 0.1 mm. This indicates that biogas generation was relatively slow during the early days of microbial activity.

Gas bubbles started to escape from the MFT on December 2 (Day 11). With accelerated gas generation, some cracks were formed at the upper part of the sample. Figure I.24 (January 17, Day 26) shows a vertical crack, 0.2 mm wide and 1 cm long, close to the interface. Figure I.25 (January 20, 2004, Day 29) shows some cracks at the upper part of the sample, some of which extended to the interface. Also, some large ellipsoidal gas bubbles were observed.

Sample 15

Figure I.26 shows a photo of sample 15 on December 27 (Day 5). Most of the gas bubbles observed at this time were in a spherical shape and were smaller than 0.1 mm in diameter. This indicates the slow gas generation during the early days of microbial activity. Small fissures started to appear at the upper part of the sample

on December 31 (Day 9). Gas bubbles started to be released from the MFT after 15 days.

Figure I.27 shows a photo taken on January 11, 2004 (Day 20). After large amounts of gas had been released from the MFT, some fissures, 0.1-0.2 mm wide and about 1 cm long, appeared on the upper part of the sample, and some occluded gas bubbles in spherical or ellipsoidal shapes were observed.

Figure I.28 shows a photo taken on January 17, 2004 (Day 26). After intense gas generation and gas release, the cracks at the upper part of the sample became obvious. Large occluded gas bubbles were mainly at the upper part of the sample. At the lower part, only small gas voids with diameters less than 0.1 mm were observed.

Figures I.29-I.30 show the MFT interfaces of samples 13 and 15, respectively, at the end of testing (Day 29). Some large particle assemblages were observed on the interface of sample 15. It appears that the structure of sample 15 became more aggregated than that of sample 13 after microbial activity.

Sample 19

The room temperature started to increase on June 29, 2004. Due to slow biogas generation, there was no obvious structural change in sample 19 during first 10 days. Figure I.31 shows a photo taken on July 14 (Day 15). A few ellipsoidal gas bubbles and some small fissures, 0.5 mm wide and 3-4 mm long, were seen on the upper part of the sample. Gas bubbles started to be released from the sample on July 20 (Day 21). Figure I.32 shows a photo taken on October 7. Most of the gas bubbles were in spherical or ellipsoidal shapes, and the cracks were discontinuous and short (less than 1 cm long). The short cracks might have been caused by local stress concentration or tensile stress near some large gas bubbles.

Sample 20

Figure I.33 shows a photo taken on June 28 (before the temperature increase). Some small spherical bubbles appeared on the sidewall. It seems that there existed very weak microbial activity even at 4^{o} C temperature. Sodium acetate might have assisted in bringing about this weak microbial activity. Figure I.34 shows a photo taken on July 14 (Day 15) in which some occluded gas bubbles and tiny fissures, less than 1 cm long, were observed. Since microbial activity was slow during the early period, MFT structure changes were not obvious.

With accelerated biogas generation, some short cracks started to appear and gas started to be released from the MFT on July 20 (Day 21). Figure I.35 shows a photo of the sample taken on October 7. Some occluded gas bubbles in spherical or ellipsoidal shapes, and some small cracks, 0.2 –0.3 mm wide and less than 5 mm long, were observed. No large crack or fracture was observed during the test.

Sample 21

Figure I.36 shows a photo taken on June 28 (before room temperature was increased) in which a few ellipsoidal gas bubbles are shown to have developed near the interface. This indicates the existence of very weak microbial activity in the MFT at 4^{o}C temperature. After the temperature increased, biogas was generated very rapidly. Figure I.37 shows a photo of sample 21 taken on July 5 (Day 6). Cracks 1-2 mm wide and 4-5 cm long were shown near the interface. Figure I.38 shows a photo taken on July 7 (Day 8). Some interconnected cracks with a maximum width of about 3-4 mm appeared at the upper part of the sample. Some ellipsoidal gas bubbles were contained within the large cracks. On July 10 (Day 11), gas started to be discharged from the MFT. Figure I.39 shows a photo taken on September 6. Most of the trapped gas bubbles shown in Figure 7.d.38 escaped from the sample, and the cracks became shorter and smaller with a few occluded gas bubbles trapped inside.

Sample 22

Due to very slow biogas generation, there was no obvious change in sample 22 during the first ten days. Figure I.40 shows a photo of sample 22 taken on July 14 (Day 15). Some occluded gas voids, 0.1-0.2 mm in size, and small vertical fissures, 3-4 mm long and 0.1-0.2 mm wide, were observed. Figure I.41 shows a photo of the sample taken on September 6 (Day 69). Small amounts of gas were released from the MFT. Some tiny vertical cracks and spherical gas bubbles less than 0.2 mm in diameter were observed. Most of the tiny cracks appeared near the gas bubbles and might have been caused by local stress concentration or tensile stress near the gas bubbles.

Sample 23

There was no obvious change to sample 23 during the early period, due to very slow microbial activity. Figure I.42 shows a photo of sample 23 taken on July 17 (Day 18). A few occluded gas bubbles in spherical or ellipsoidal shapes were observed, and no obvious cracks were seen. Figure I.43 shows a photo from October 10 (Day 103). Most gas voids seen at this time were small, and the structural changes were not obvious.

Sample 24

After the room temperature increased, gas was generated very rapidly in sample 24. Some occluded gas bubbles were observed, as shown in Figure I.44 (July 7, Day 8). Although the trapped gas volume rapidly increased with time, no obvious fractures or cracks were observed. This was due to the applications of backpressure and external loading. Figure I.45 shows a photo taken on September 6 (Day 72). Some small fissures, about 0.1-0.2 mm wide, appeared at the upper part of the sample. Most of the trapped gas existed as occluded gas bubbles.

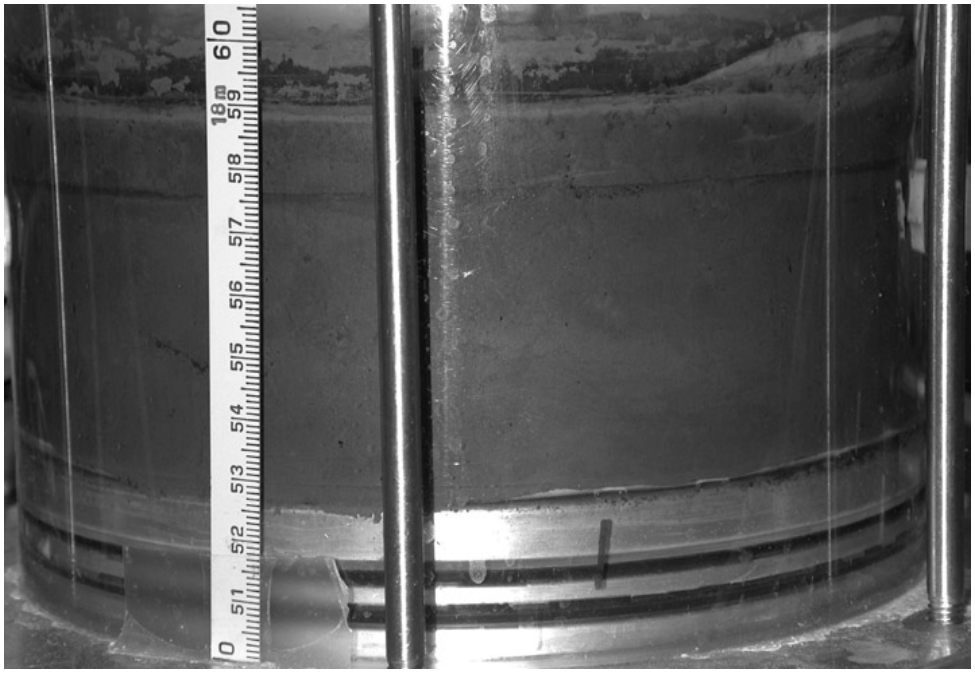

Figure I. 1 Sample 1 on December 2 (Day 32)

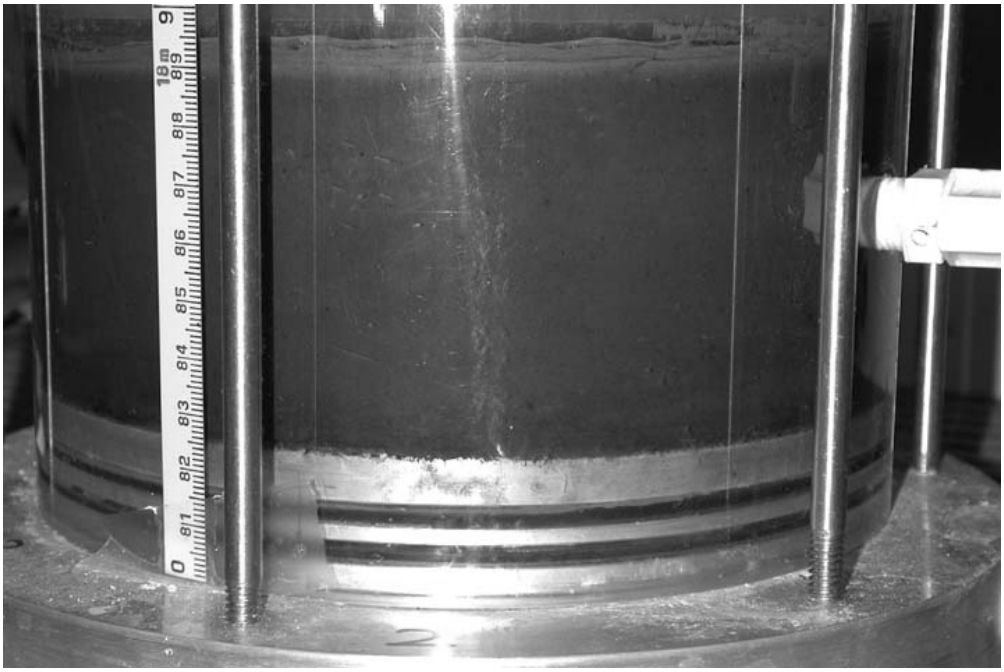

Figure I. 2 Sample 2 on November 4

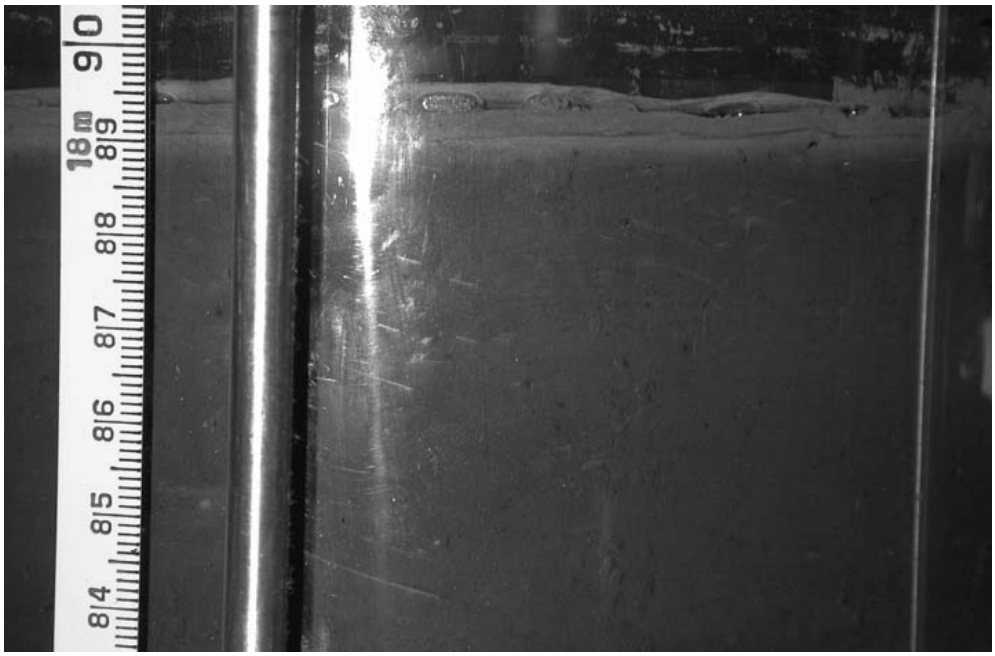

Figure I. 3 Sample 2 on November 14

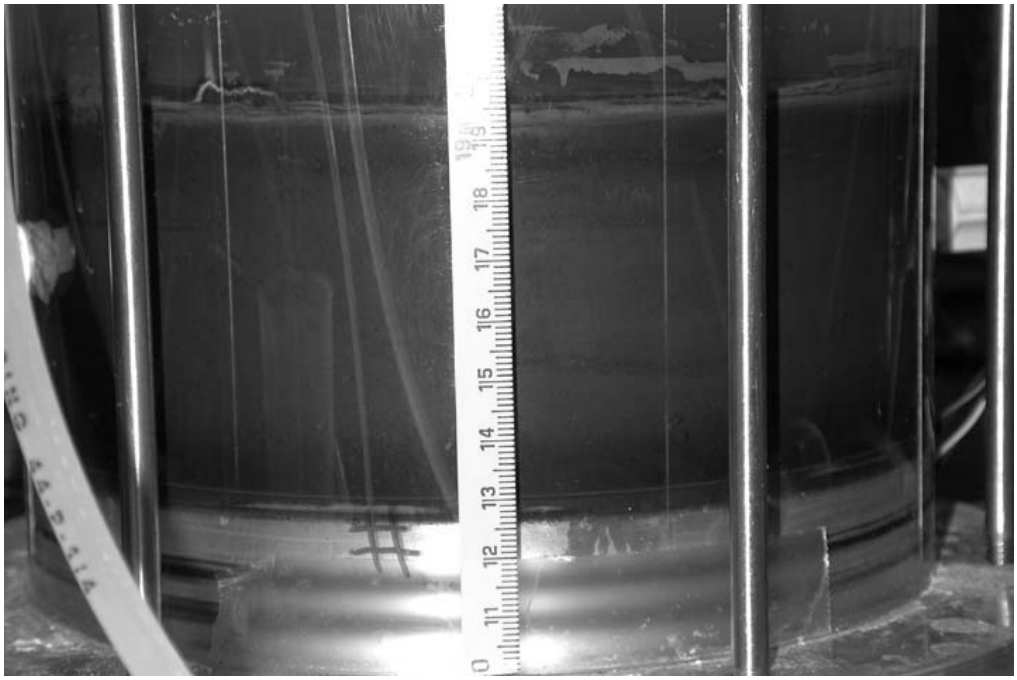

Figure I. 4 Sample 3 on October 30

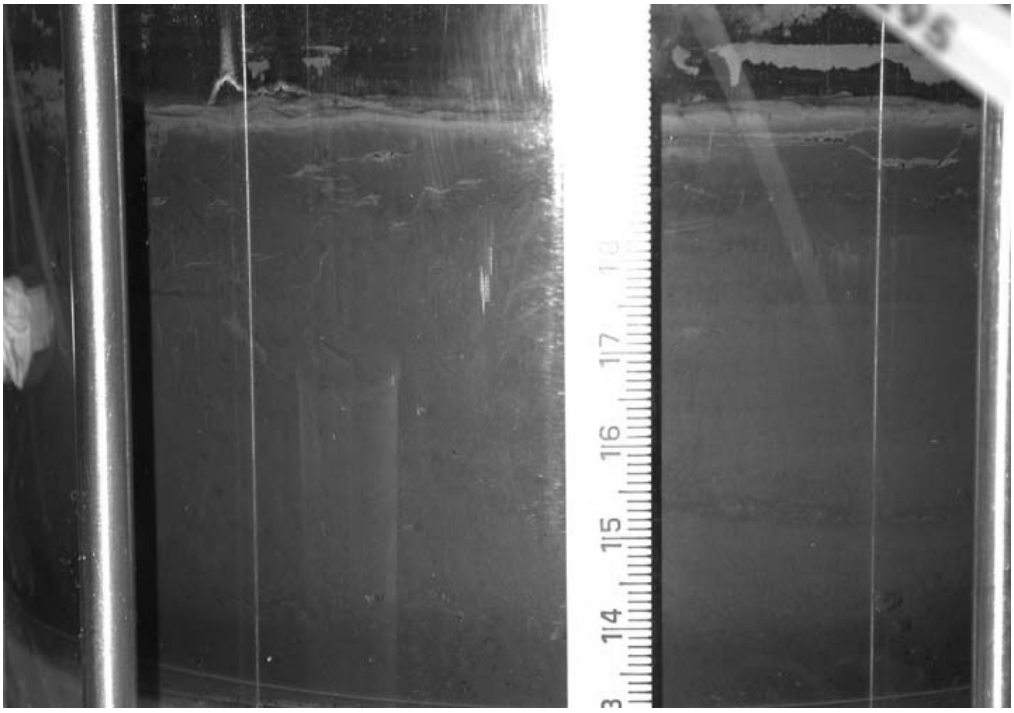

Figure I. 5 Sample 3 on November 4

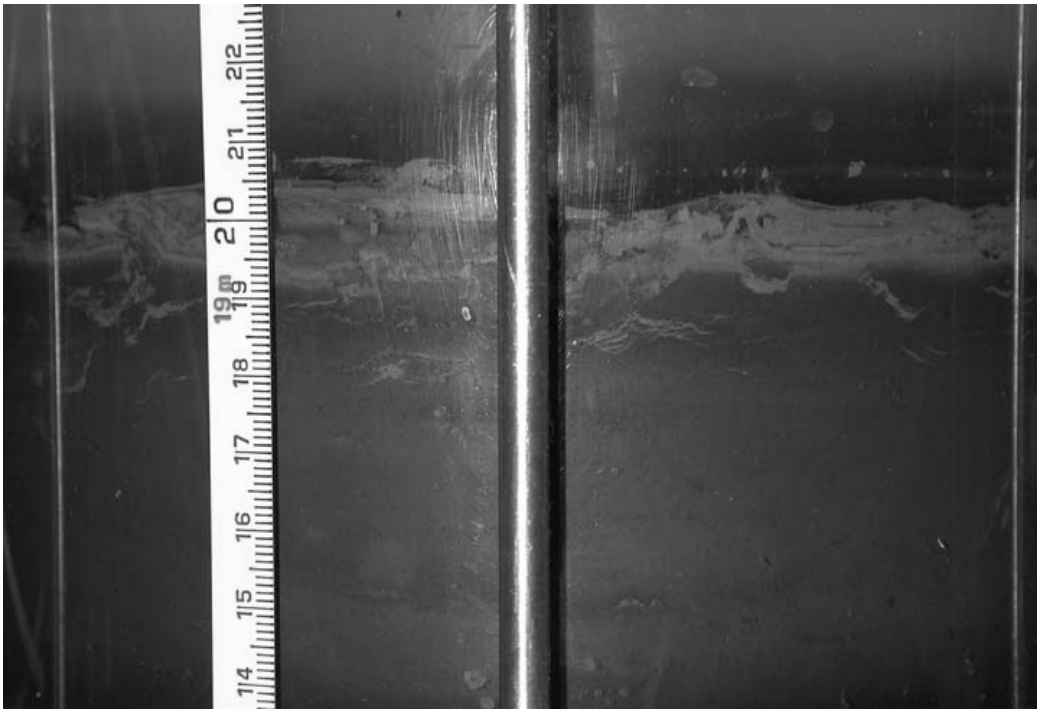

Figure I. 6 Sample 3 on November 6

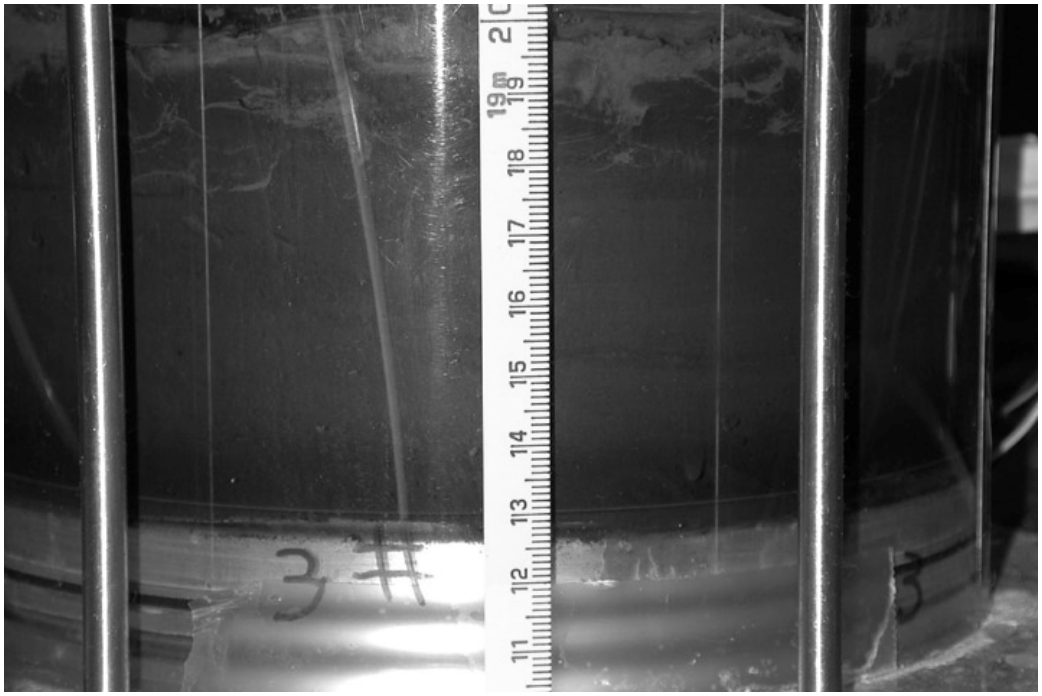

Figure I. 7 Sample 3 on December 2

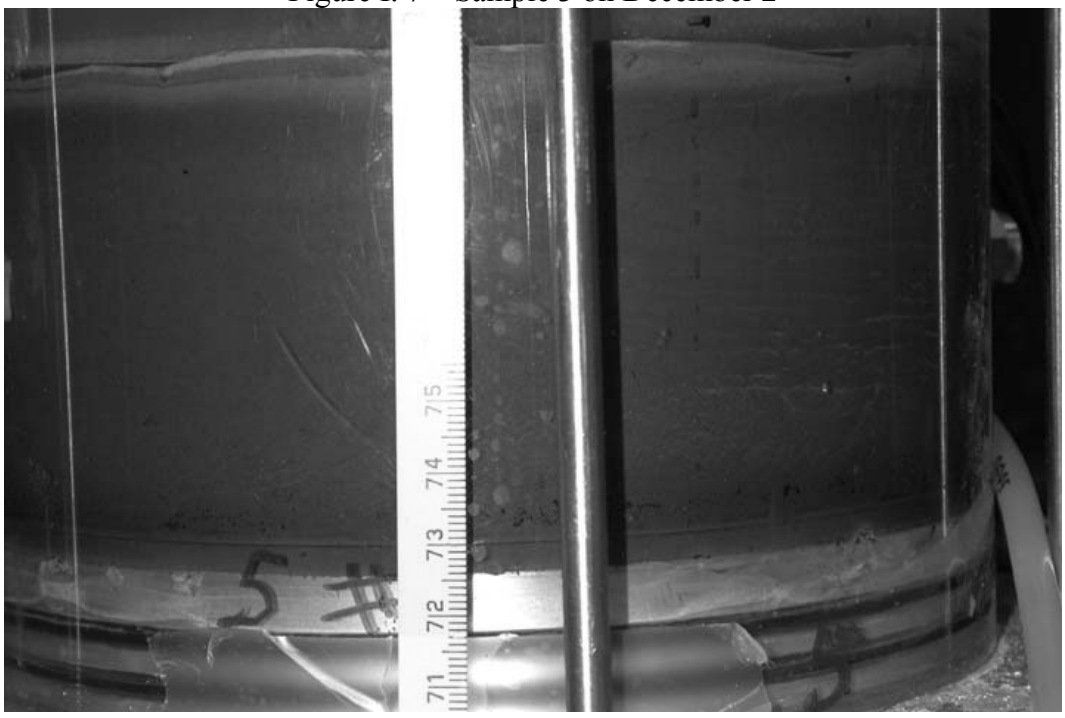

Figure I. 8 Sample 5 on November 6

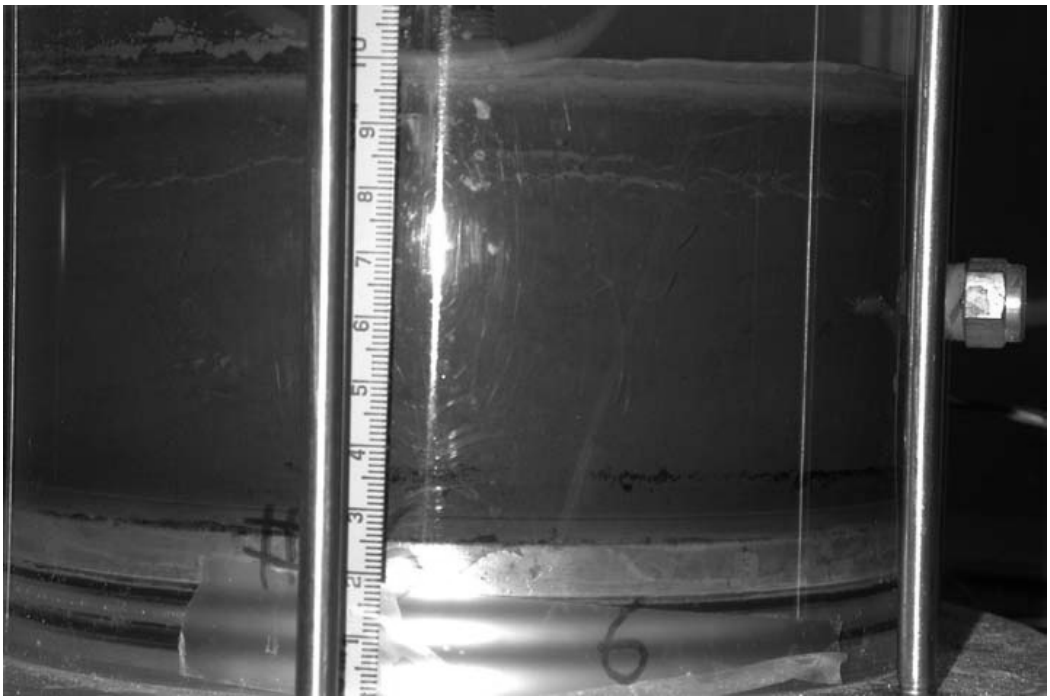

Figure I. 9 Sample 6 on November 8

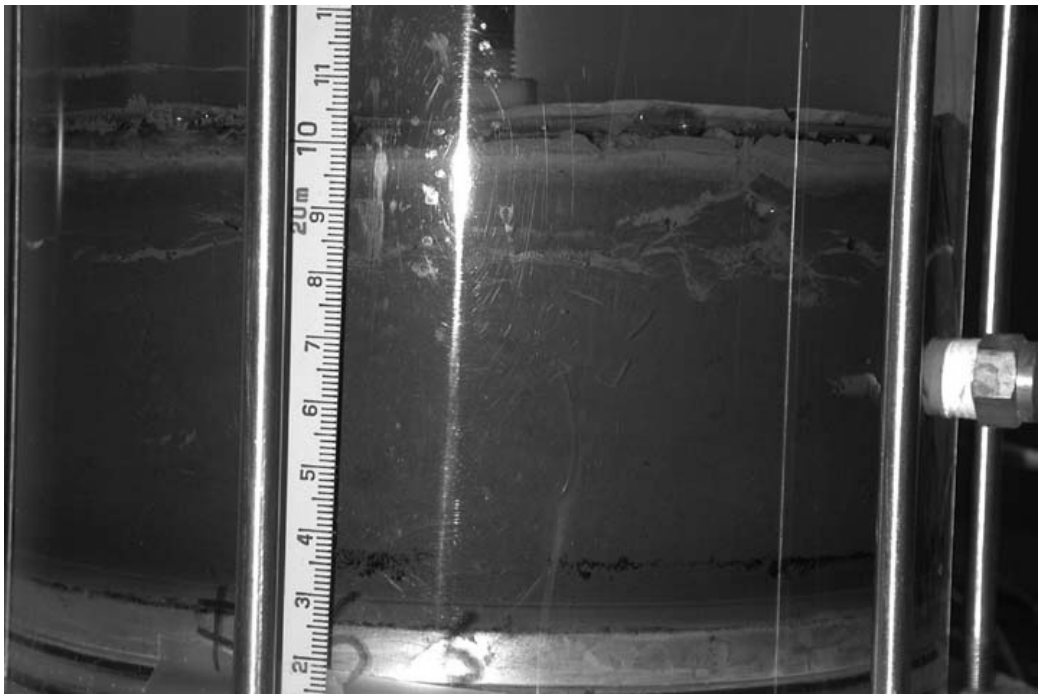

Figure I. 10 Sample 6 on November 17

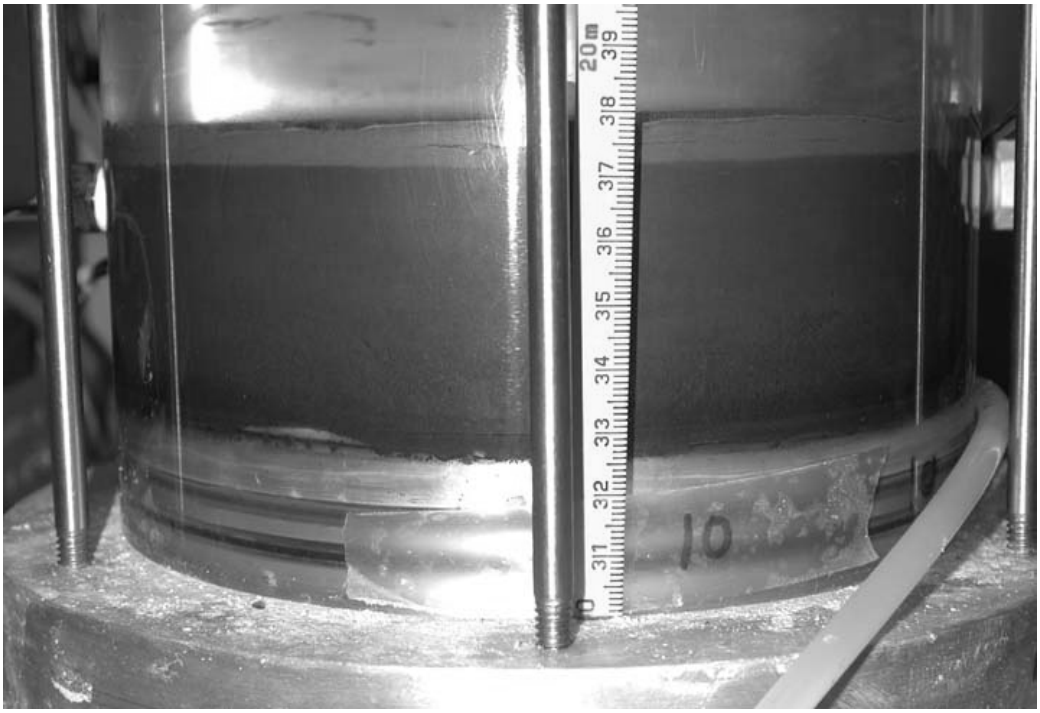

Figure I. 11 Sample 10 on December 29

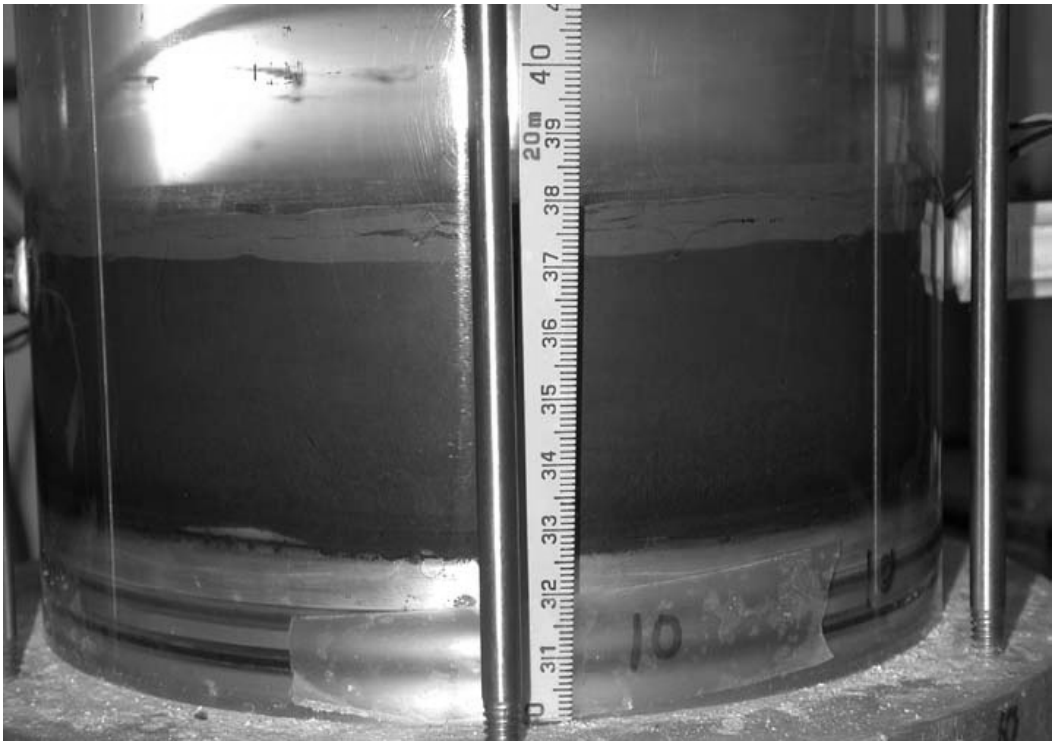

Figure I. 12 Sample 10 on January 8

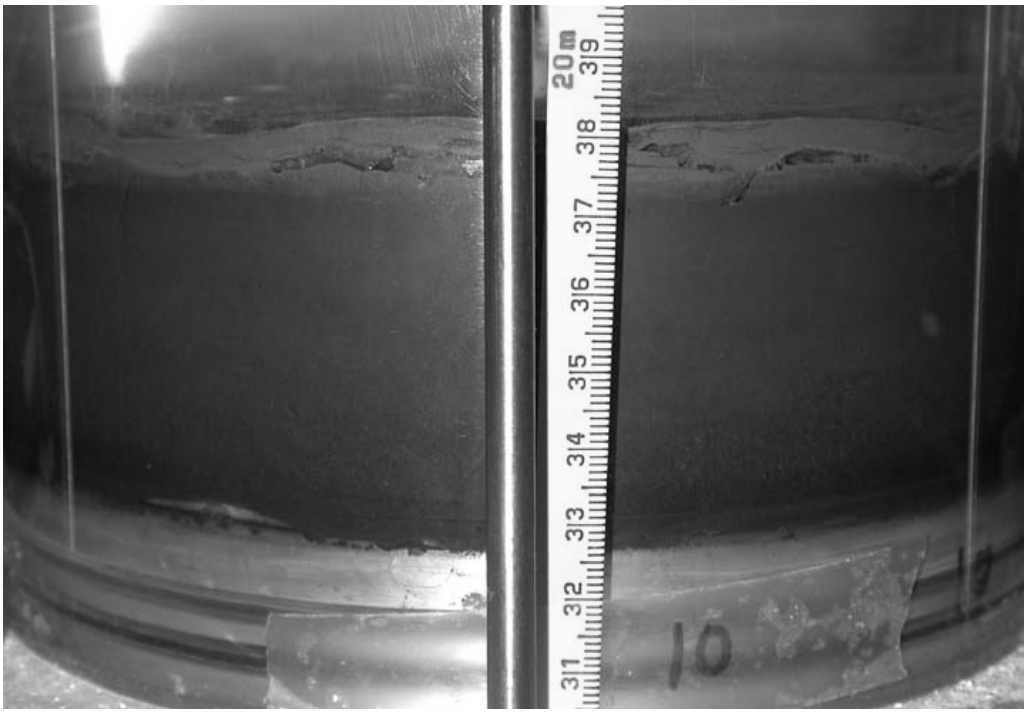

Figure I. 13 Sample 10 on January 20

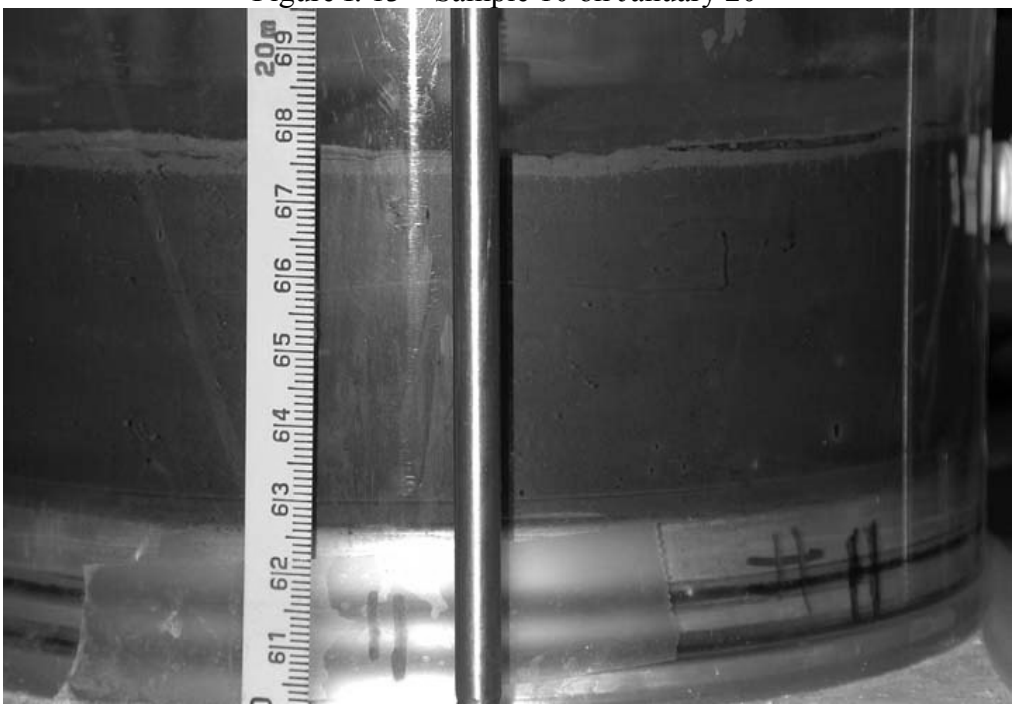

Figure I. 14 Sample 11 on December 27

Figure I. 15 Sample 11 on January 5

Figure I. 16 Sample 11 on January 20

Figure I. 17 Sample 12 on December 23

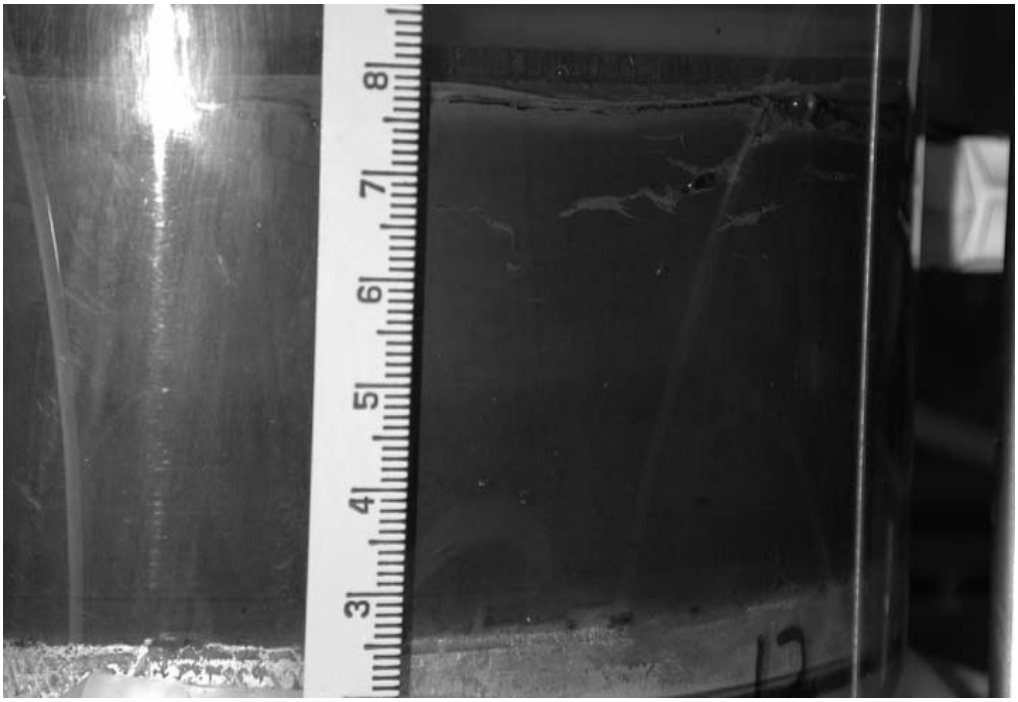

Figure I. 18 Sample 12 on December 27

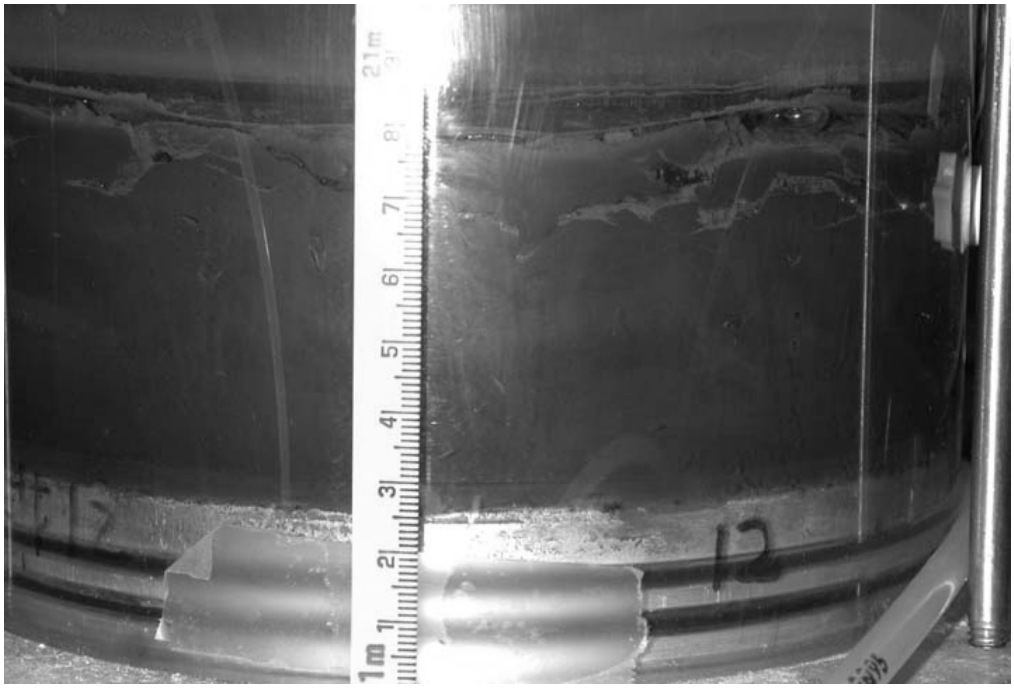

Figure I. 19 Sample 12 on December 31, 2003

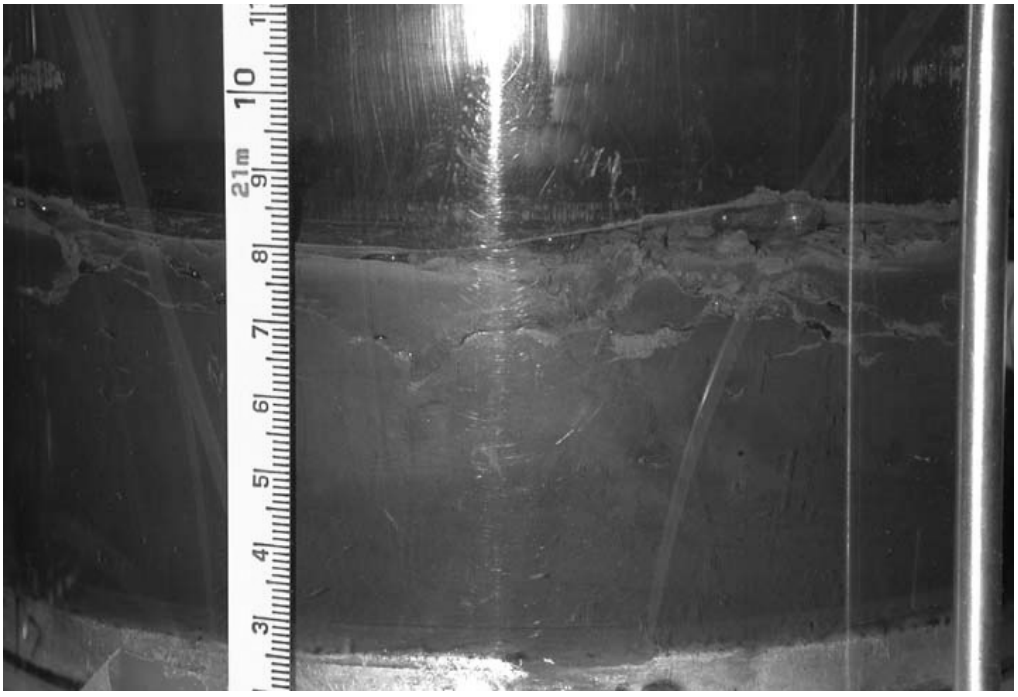

Figure I. 20 Sample 12 on January 20, 2004

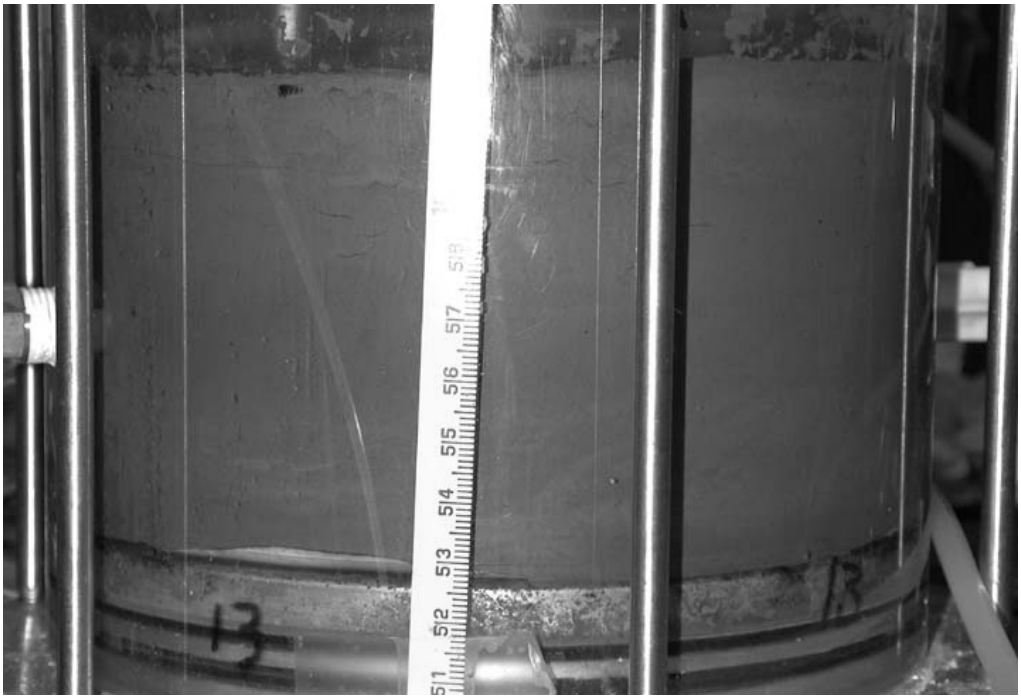

Figure I. 21 Sample 13 on December 31, 2003

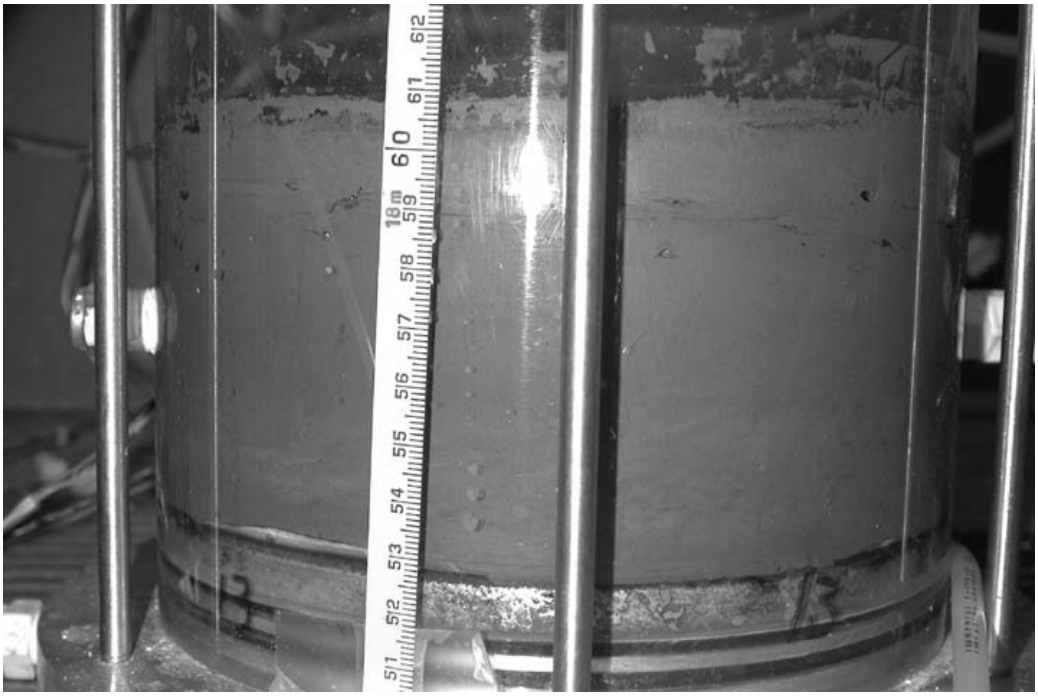

Figure I. 22 Sample 13 on January 20 2004

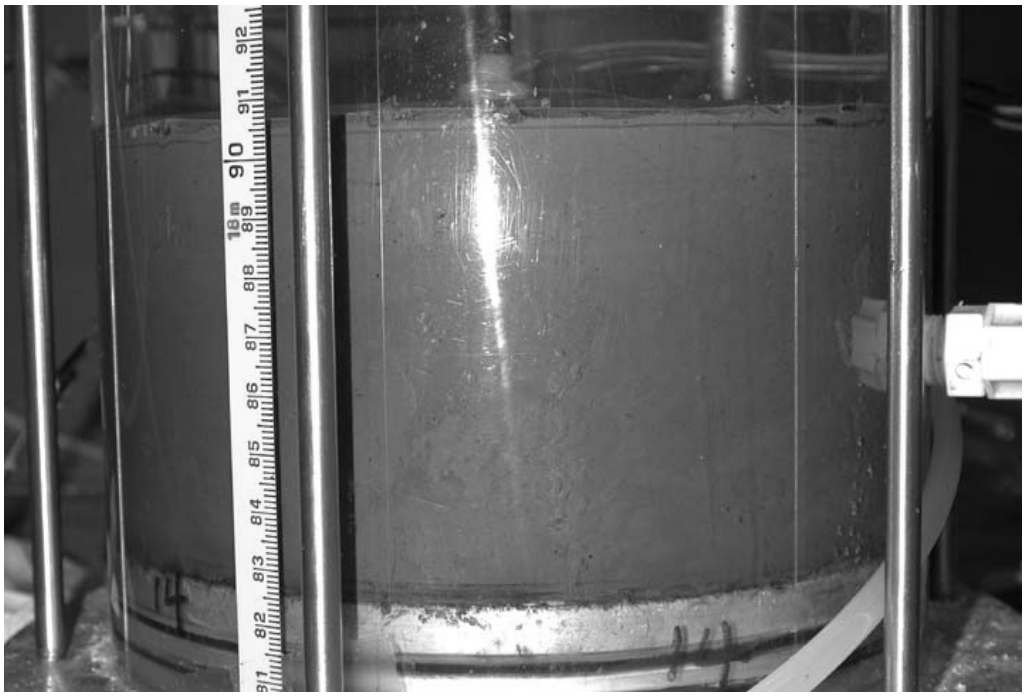

Figure I. 23 Sample 14 on December 29, 2003

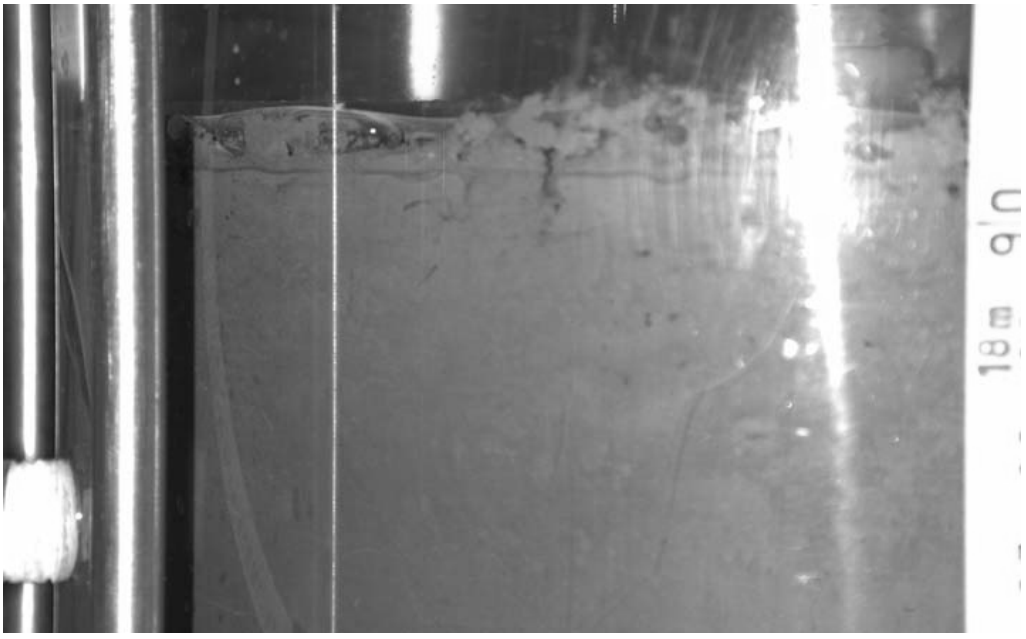

Figure I. 24 Sample 14 on January 17, 2004

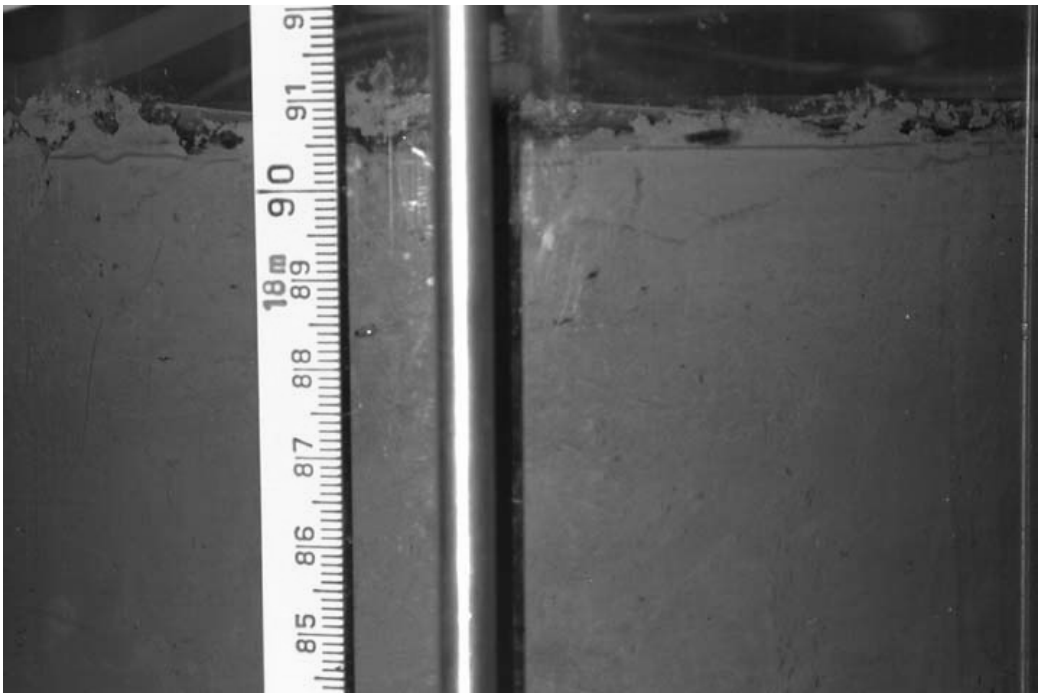

Figure I. 25 Sample 14 on January 20 2004

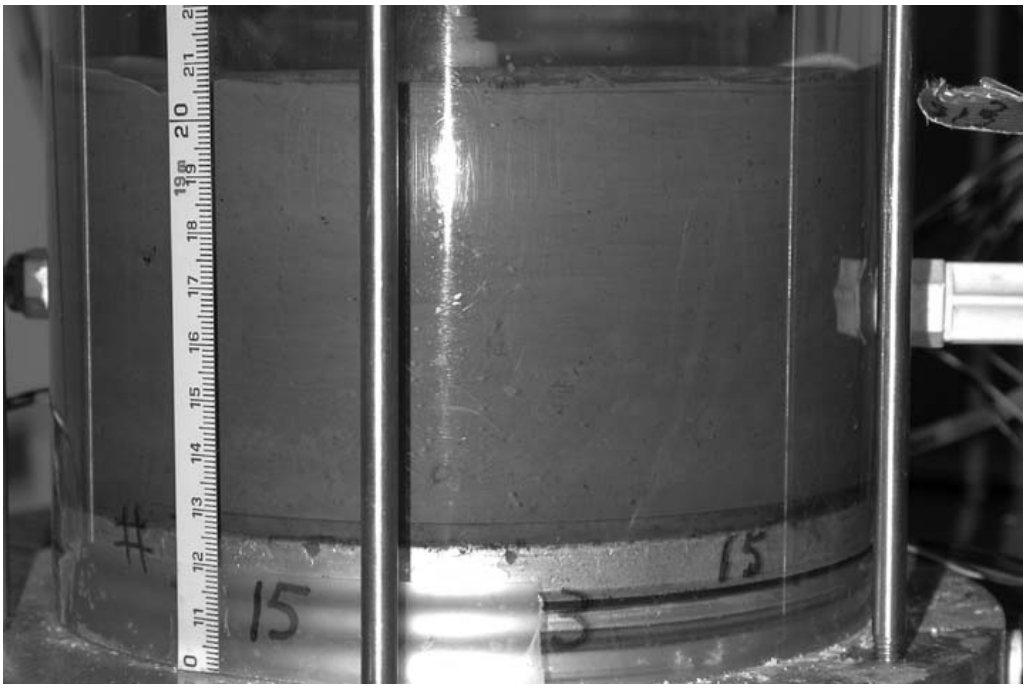

Figure I. 26 Sample 15 on December 27 2003

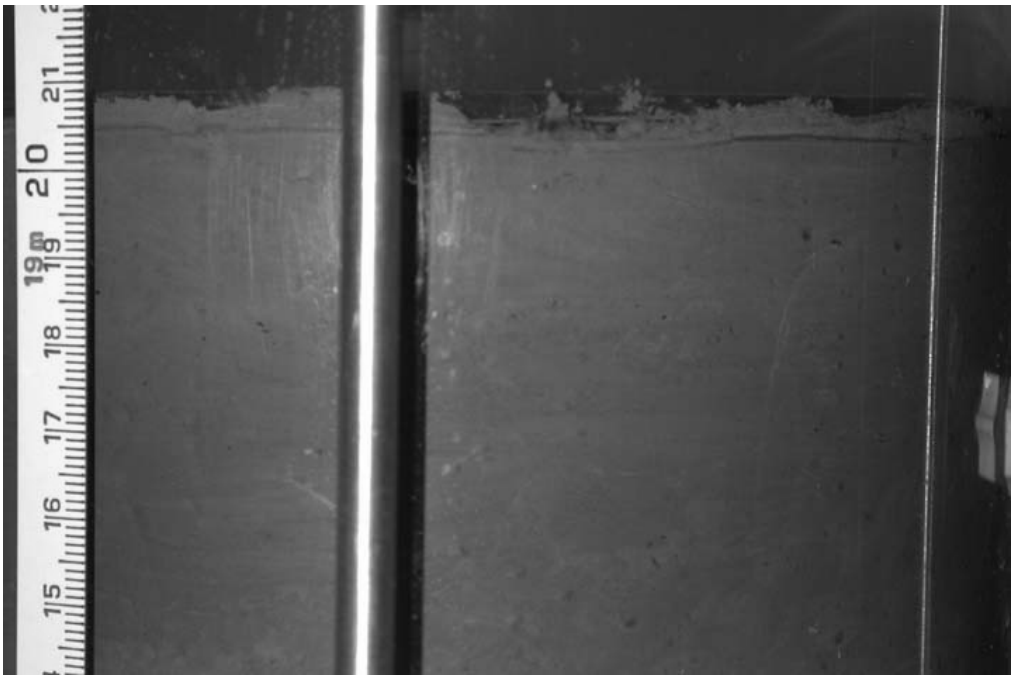

Figure I. 27 Sample 15 on January 11 2004

Figure I. 28 Sample 15 on January 17 2004

Figure I. 29 The Interface of Sample 13 at the End of Testing

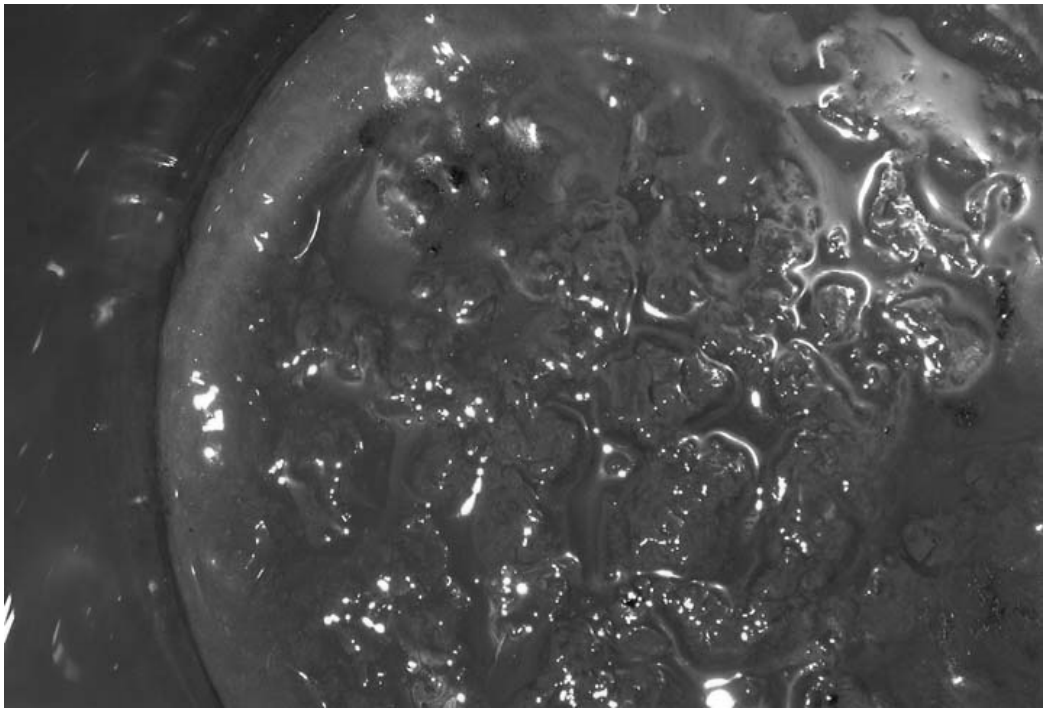

Figure I. 30 The interface of Sample 15 at the End of Testing

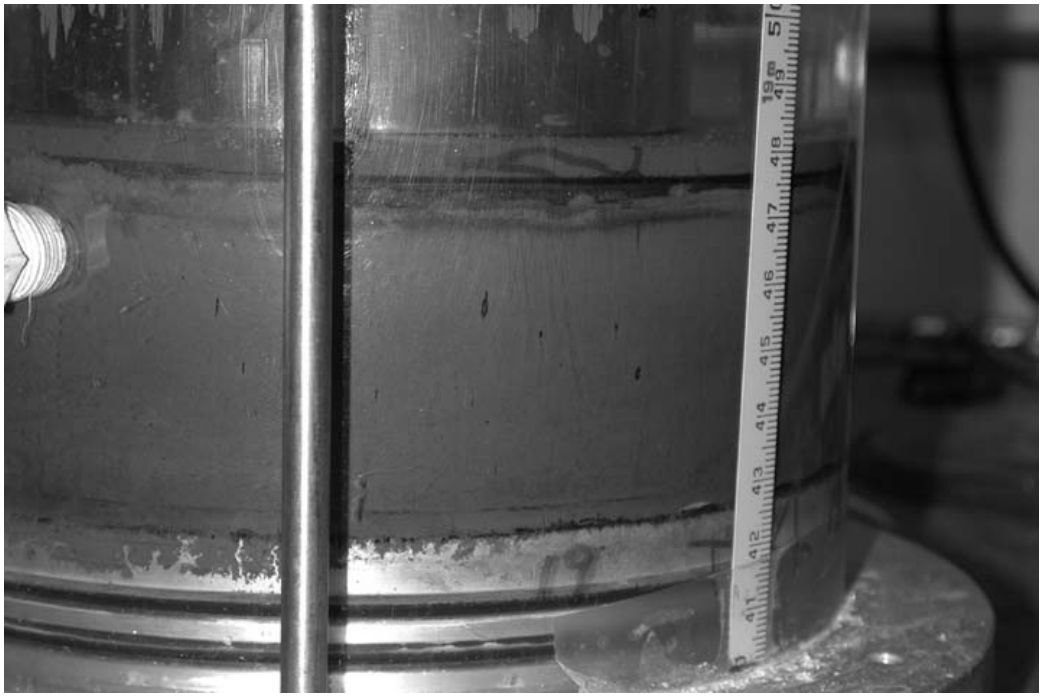

Figure I. 31 Sample 19 on July 14 2004

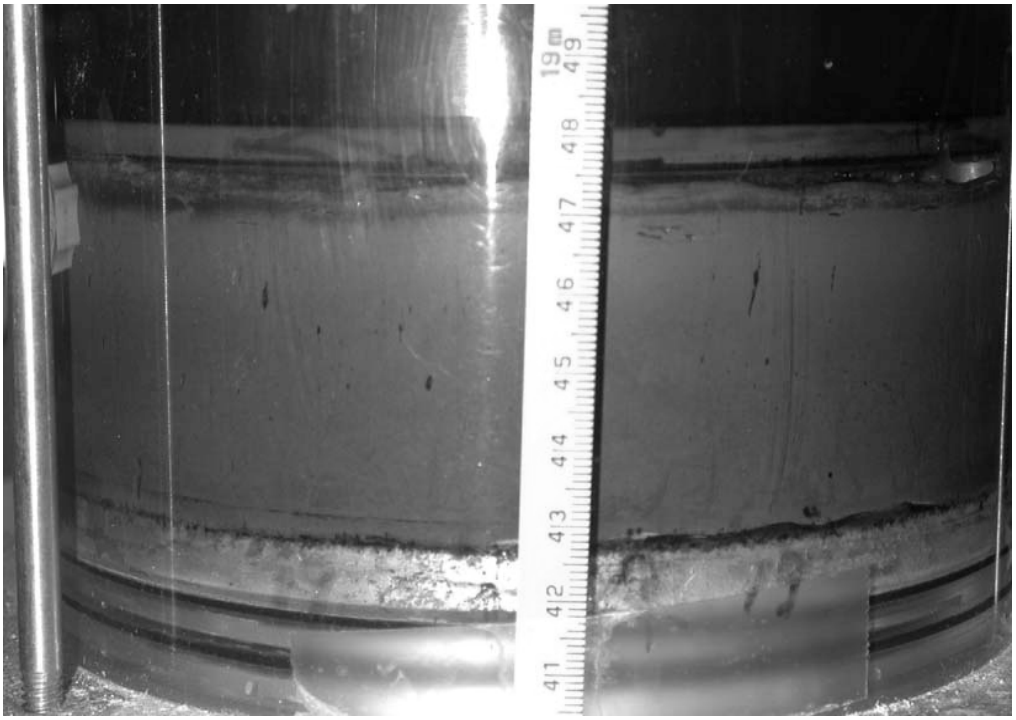

Figure I. 32 Sample 19 on October 7 2004

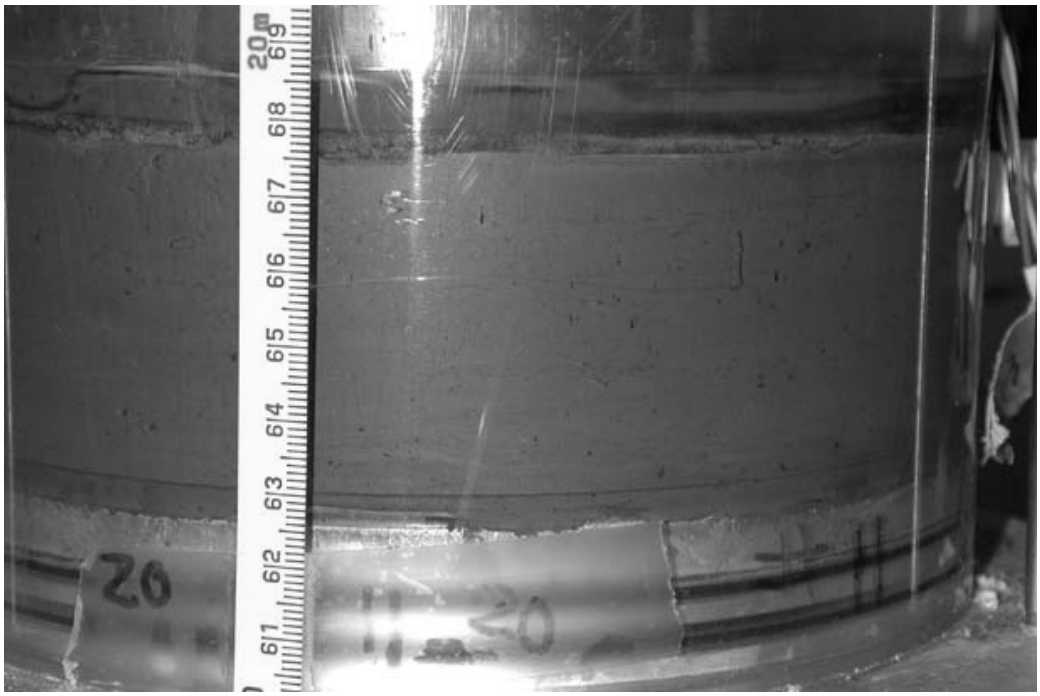

Figure I. 33 Sample 20 on June 28 2004

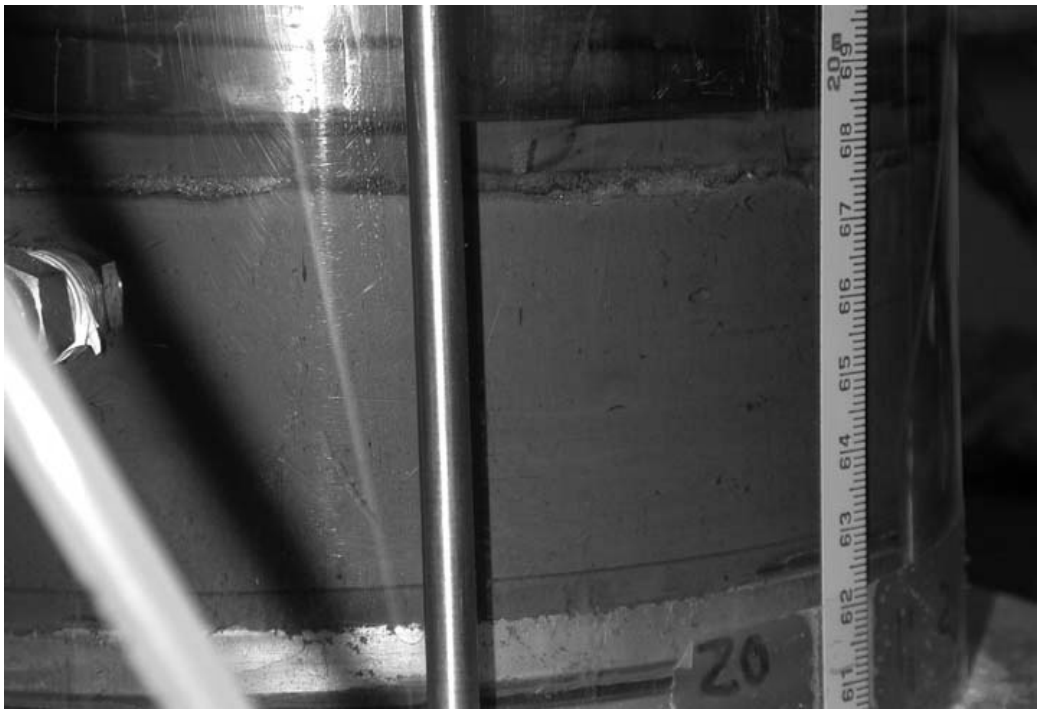

Figure I. 34 Sample 20 on July 14 2004

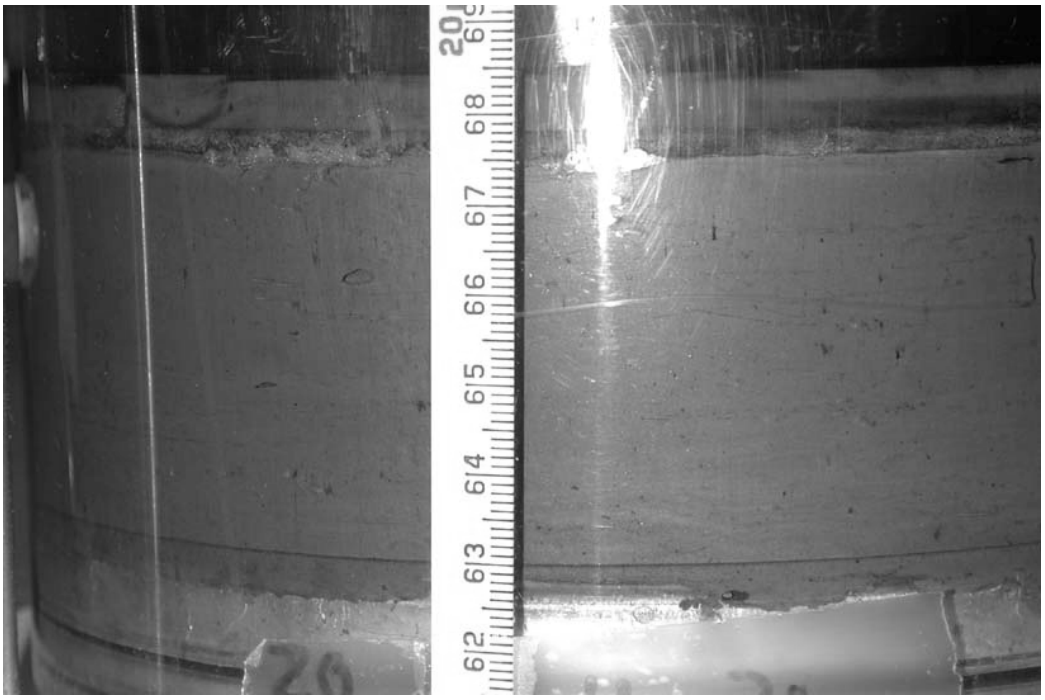

Figure I. 35 Sample 20 on October 7 2004

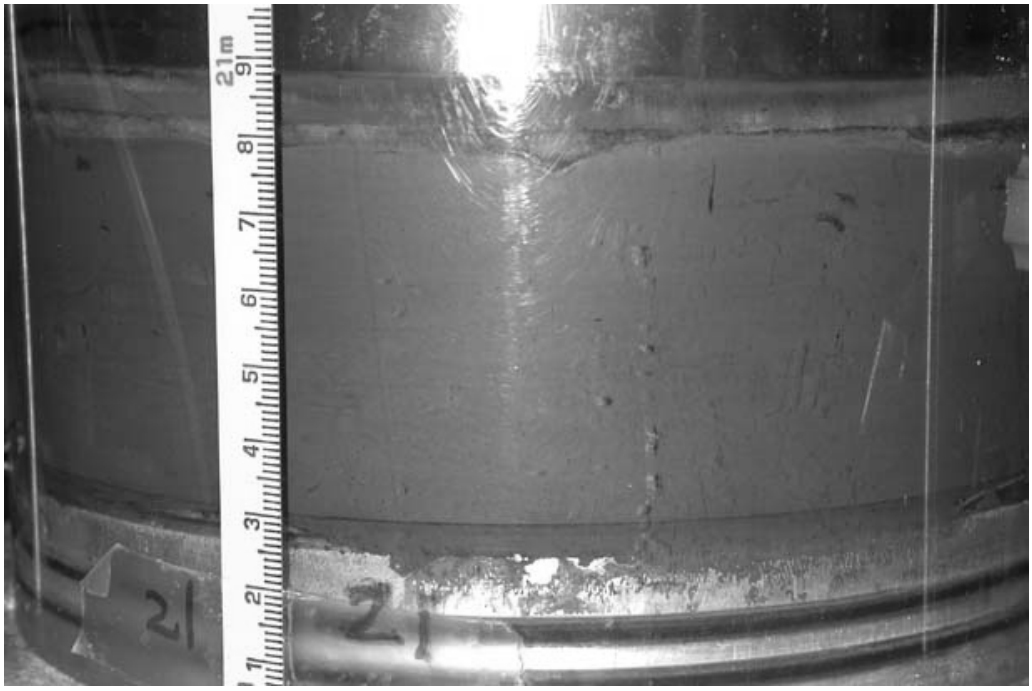

Figure I. 36 Sample 21 on June 28 2004

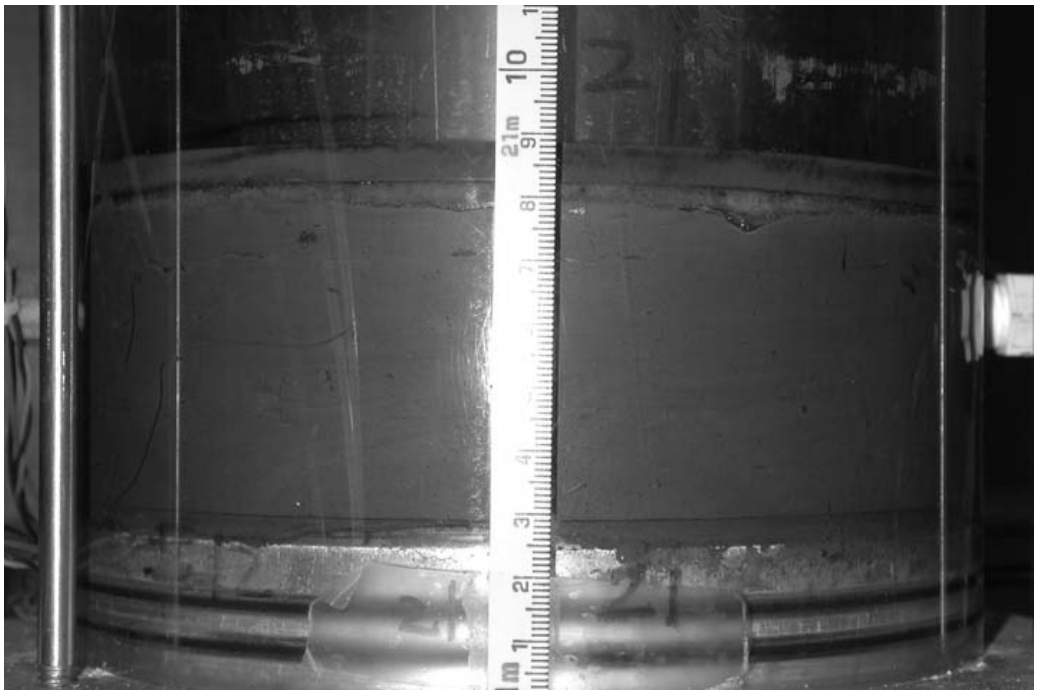

Figure I. 37 Sample 21 on July 5, 2004

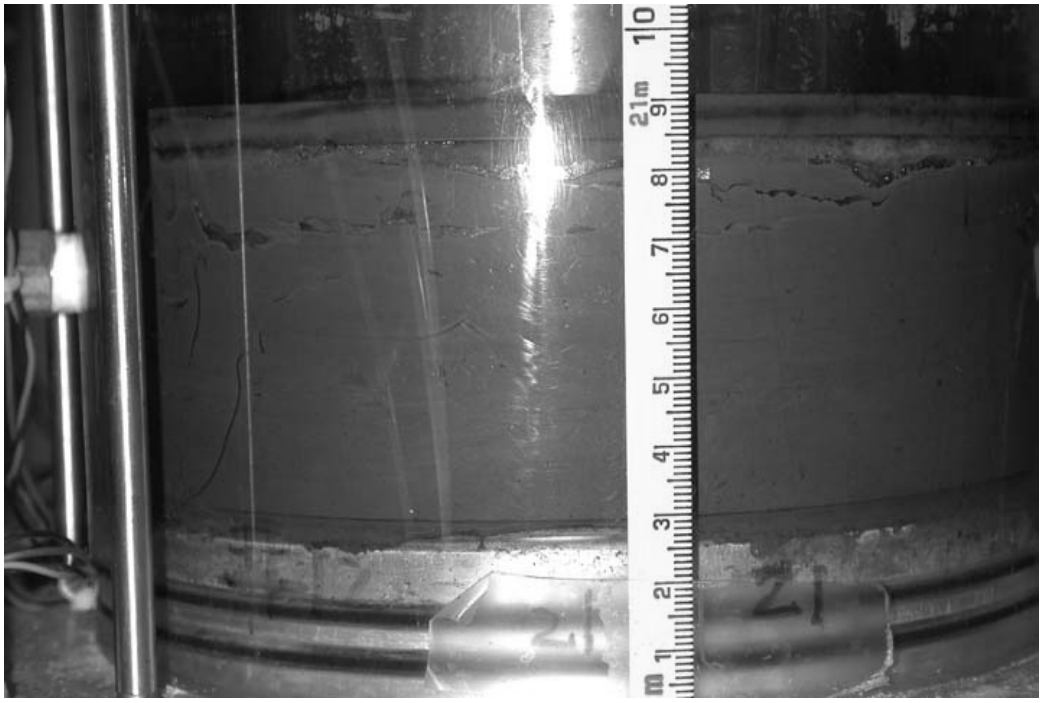

Figure I. 38 Sample 21 on July 7 2004

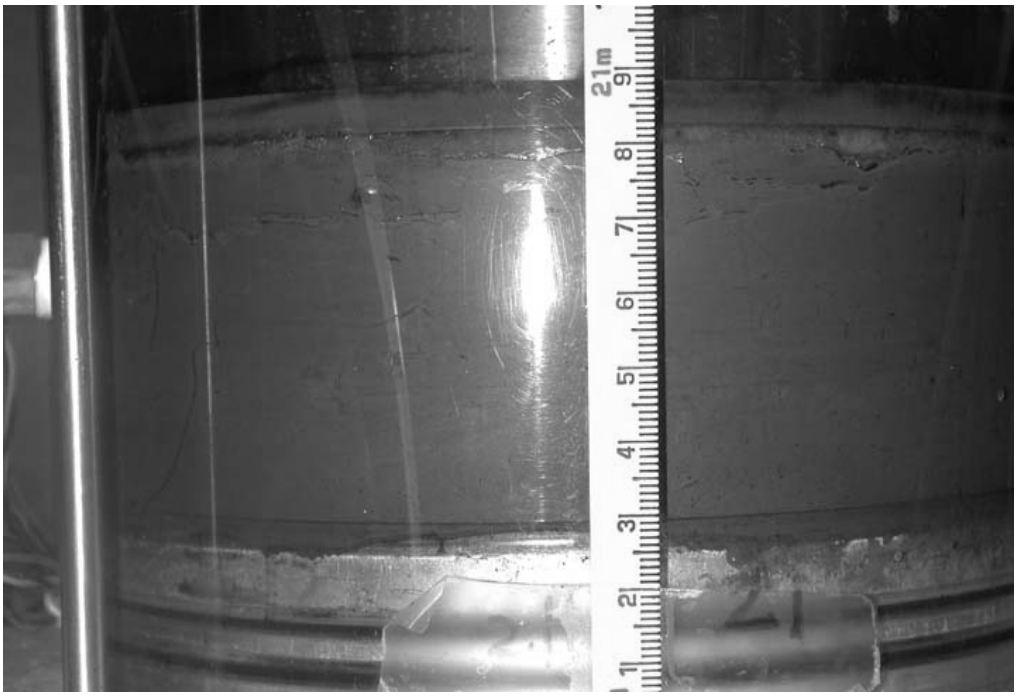

Figure I. 39 Sample 21 on September 6 2004

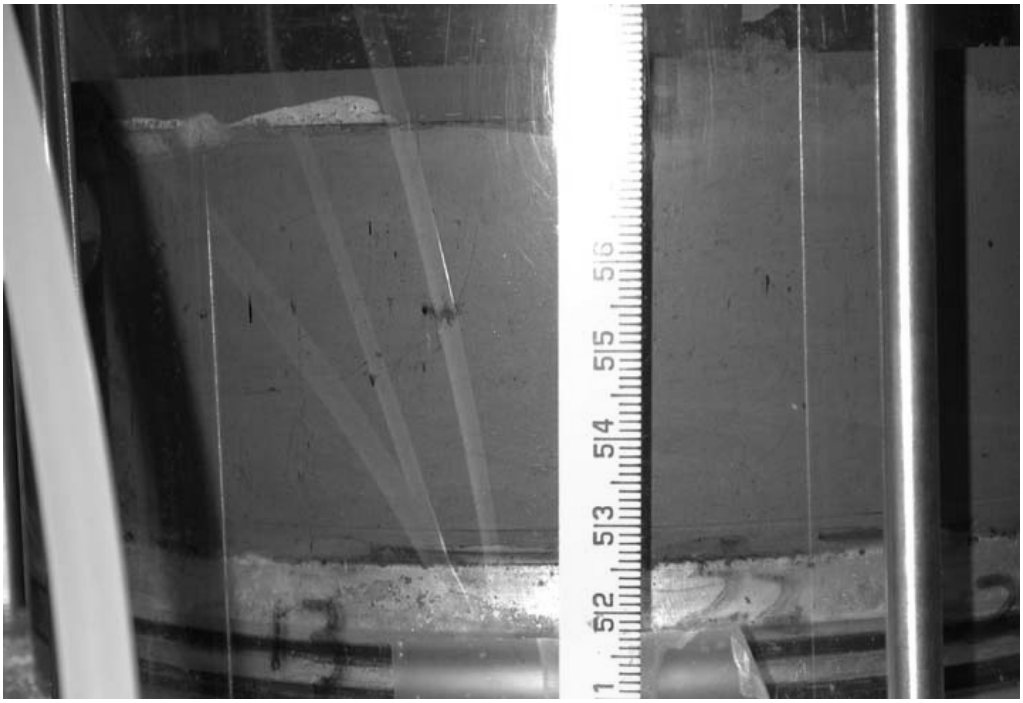

Figure I. 40 Sample 22 on July 14 2004

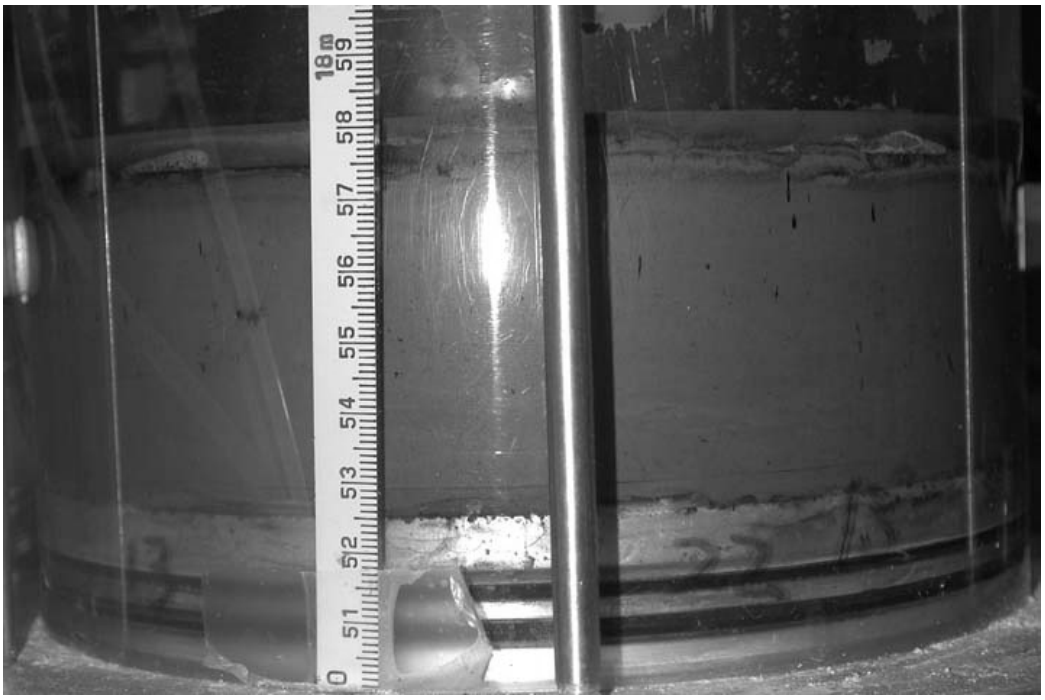

Figure I. 41 Sample 22 on September 6 2004

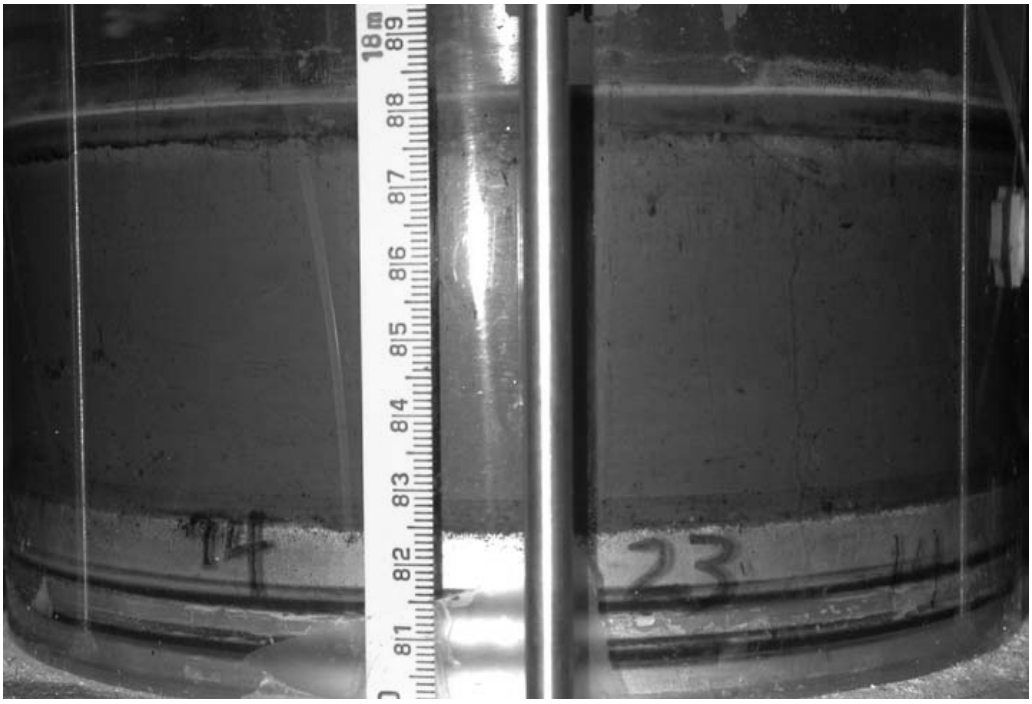

Figure I. 42 Sample 23 on July 17 2004

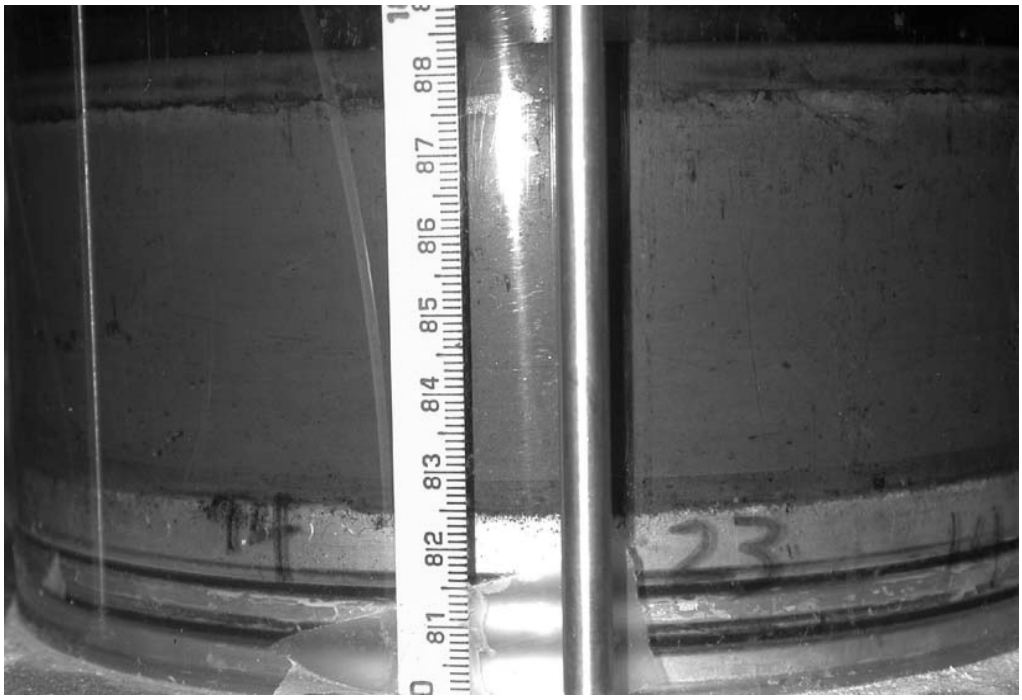

Figure I. 43 Sample 23 on October 10 2004

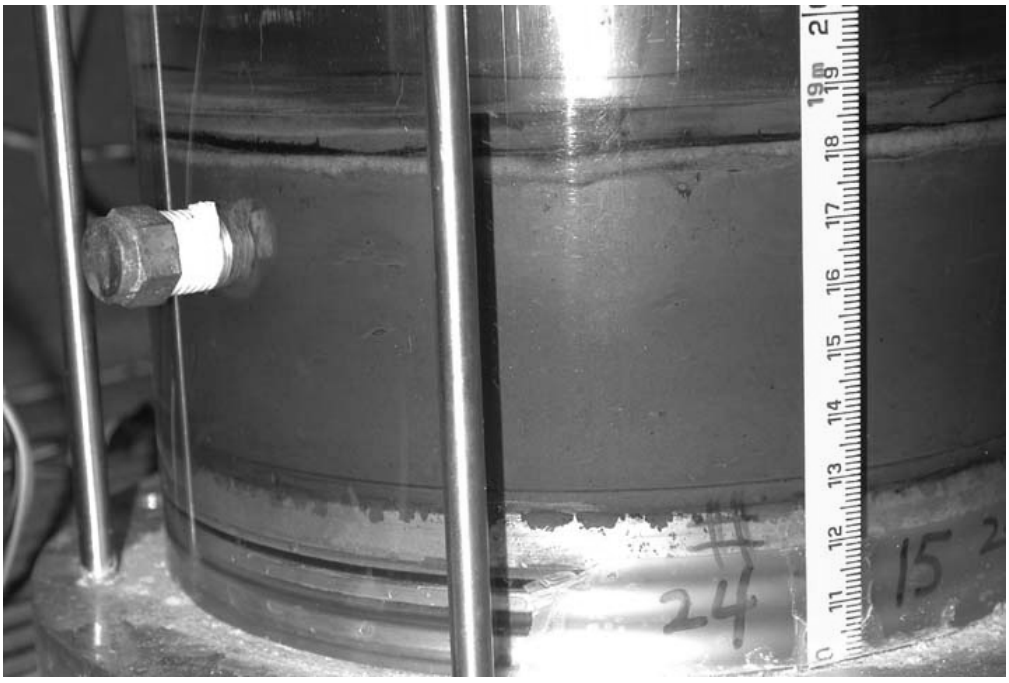

Figure I. 44 Sample 24 on July 7 2004

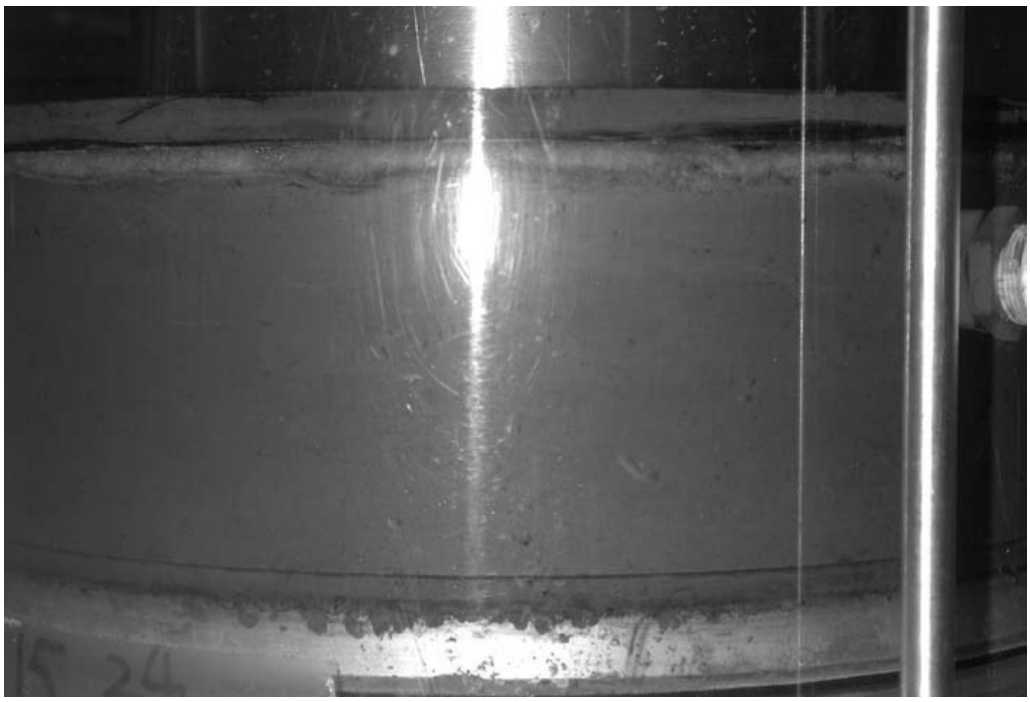

Figure I. 45 Sample 24 on September 6 2004

APPENDIX J Chemical and Microbiological Test Results

This Appendix presents the results of chemical and microbiological tests during microbial activity, including pH, conductivity, concentrations of some ions, and bacteria Maximum Probable Numbers (MPNs).

Samples 16© to 18©

Figure J.1 shows the changes of acetate concentrations in samples 16© to 18© during microbial activity. The samples at zero time were obtained before microbial activity was initiated at $4^{o}C$ temperature. The measured acetate concentrations of samples 16© to 18© at zero time were 119 mg/L, 376 mg/L, and 1625 mg/L, respectively. These measurements were lower than the acetate amendments. It is likely that parts of the added acetate were depleted before chemical measurements were conducted. During microbial activity, acetate concentration decreased with time. The concentration in sample 18© decreased more rapidly than did those in samples 16© and 17©. At the end of testing, the acetate concentrations in the three samples were close to zero.

Figures J.2 shows the pH changes of samples 16© to 18© during microbial activity, and Figure J.3 shows the changes of electrical conductivity (EC) in the samples. During microbial activity, the pH slightly increased, while electrical conductivity (EC) slightly decreased with time.

Figure J.4 shows the changes of Na^{+} concentrations during microbial activity. In samples 16© and 17©, there were no obvious changes. In sample 18©, the Na^{+} concentration decreased from 1500 mg/L to 1200 mg/L during the first eight days, and then remained stable. Figure J.5 shows the changes of K^{+} concentrations with time. During the first eight days, the concentrations in the three samples slightly decreased, then stayed almost stable. Figures J.6 and J.7 show the changes of Ca^{2+} and Mg^{2+} concentrations, respectively, during microbial activity. Both Ca^{2+} and Mg^{2+} concentrations decreased during testing.

Figure J.8 shows the changes of SO_4^{2-} concentrations with time. SO_4^{2-} concentrations in samples 17© and 18© decreased with time during the first eight days, then were almost stable. The concentrations in sample 16© were more variable than those in samples 17© and 18©. Figure J.9 shows the changes of Cl^- concentrations during microbial activity. In sample 18©, there was no obvious change in Cl^- concentrations during microbial activity. In samples 16© and 17©, the concentrations increased during the early period (eight days), and then stabilized. The increases might have been caused by sample heterogeneity, temperature change or some other factors. Figure J.10 shows HCO_3^- concentrations in samples 16© to 18©, which slightly decreased during microbial activity.

Figure J.11 shows the changes of Maximum Probable Numbers (MPNs) of methanogen bacteria, and Figure J.12 shows the MPNs of Sulfate- Reducing Bacteria (SRB) of samples 16© to 18©.

Samples 25© to 27©

During consolidation (at 4^oC) and microbial activity (at 24^oC), four chemical sub-samples were obtained at different times from each cell. The time when sodium acetate was mixed with the MFT was defined as zero time. The four samples were obtained on Day 3, Day 12, Day 154 and Day 267, respectively. The first two samples were obtained during consolidation testing at 4^oC, the third sample was obtained during microbial activity (15 days after warming up) at 24^oC, and the fourth sample was obtained at the end of testing at 4^oC.

Figure J.13 shows the pH changes at different times. The pH values increased from the second to third sampling (after room temperature had increased). During the other periods, the pH values were relatively stable. Figure J.14 shows the changes of electrical conductivity during testing. It was relatively stable in samples 25© and 26©. In sample 27©, electrical conductivity decreased from first to third sampling, and kept relatively stable from the third to fourth sampling.

Figure J.15 shows the changes of the Na^+ concentration at different times in samples 25© to 27©. The changes in samples 25© and 26© were not obvious. In sample 27©, the Na^+ concentration slightly decreased with time. Figure J.16 shows the changes of the K^+ concentration with time. K^+ decreased from the second to the third sampling in samples 25© to 27©, but the changes were relatively small during the other periods. Figure J.17 shows Ca^{2+} concentration changes in samples 25© to 27©. In samples 25© and 26©, Ca^{2+} concentration changes were minor. In sample 27©, Ca^{2+} decreased from the first to third sampling. From the third to fourth sampling, there was no obvious change. The changes of Mg^{2+} concentrations (Figure J.18) were similar to those of Ca^{2+} concentrations.

Figure J.19 shows the changes of SO_4^{2-} concentrations at different times. In samples 26© and 27©, SO_4^{2-} obviously decreased from the first to second sampling, then remained largely unchanged. The fluctuations in sample 25© might have come from sample heterogeneity or errors during sampling or chemical measuring. Figure J.20 shows Cl^- concentration changes. During microbial activity, Cl^- concentrations slightly increased in the three samples. Figure J.21 shows HCO_3^- concentration changes in the three tests. The changes in samples 25© and 26© were relatively small, but in sample 27©, a decrease from the second to fourth sampling (during microbial activity) was obvious.

During testing, four microbiological sub-samples were obtained from each cell of tests 25© to 27© at different times. The zero sampling was defined as the time when sodium acetate was mixed with the MFT. The first and second samples were obtained at 4^oC after three and 120 days, respectively. The room temperature was raised to 24^oC after 139 days. The third sample was obtained after 154 days (15 days after microbial activity had started) at 24^oC. The fourth sampling was conducted after 267 days (at the end of testing) at 4^oC.

Figure J.22 shows the methanogen MPN values of samples 25© to 27© at various times. They ranged from 10^2 to 10^4. The MPN values of samples 25© and 27© increased after microbial activity began. The increases in sample 27© were more obvious than those in sample 25©. From the third to fourth sampling, the MPN values in samples 25© and 27© decreased. The changes of metahanogen MPN in sample 26© were not obvious. During microbial activity (15 days after the room temperature had risen), the MPN values in samples 25© to 27© were 4.3×10^3, 9.3×10^2, and 2.3×10^4, respectively. The MPN value in sample 27© was higher than those in samples 25© and 26©.

Figure J.23 shows the MPN values of Sulphate Reducing Bacteria (SRB) in samples 25© to 27© during the tests. The values ranged from 10^3 to 10^5. After microbial activity was initiated, the MPN values in the three samples increased. The increase in sample 25© was more obvious than that in sample 27©. For the third sampling (15 days after microbial activity had started), the MPN values of SRB in samples 25© to 27© were 9.3×10^5, 4.3×10^5, and 9.3×10^4, respectively. Sample 27© had the lowest MPN value of SRB. From the third to fourth sampling, the MPN values in the three cells decreased. At the end of testing, the MPN values of SRB in the three samples were close.

During microbial activity (15 days after microbial activity had started), sample 27© had the highest MPN value of methanogens and the lowest MPN value of SRB among the three samples. This should have been favorable for methanogen activity and methane gas generation in sample 27©.

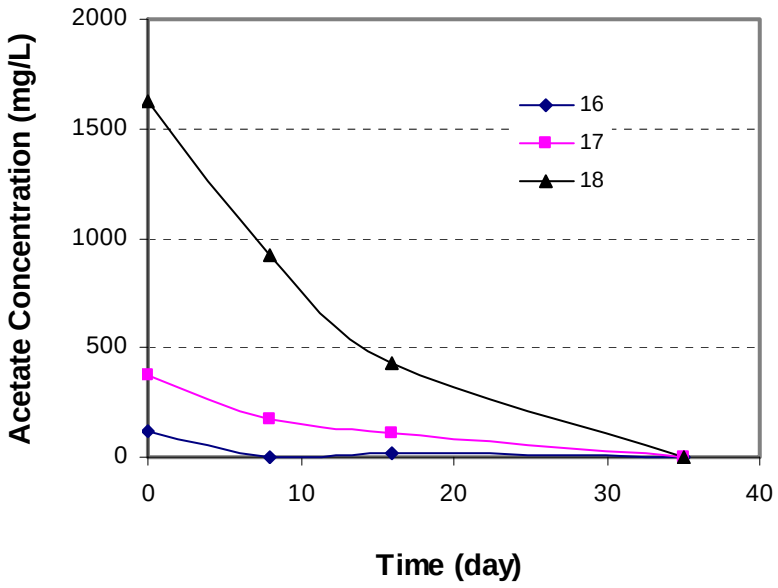

Figure J. 1 Changes in Acetate Concentration in Samples 16© to18©

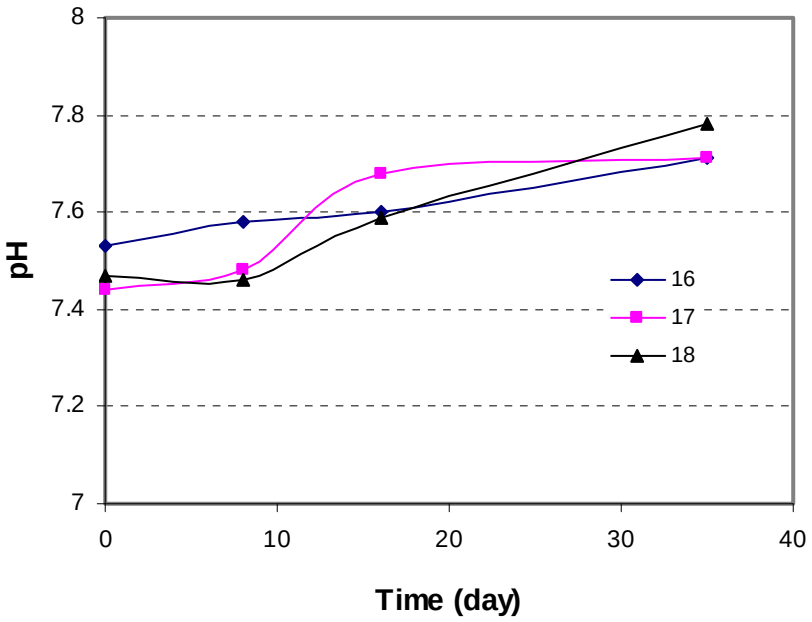

Figure J. 2 pH Changes in Samples 16© to 18©

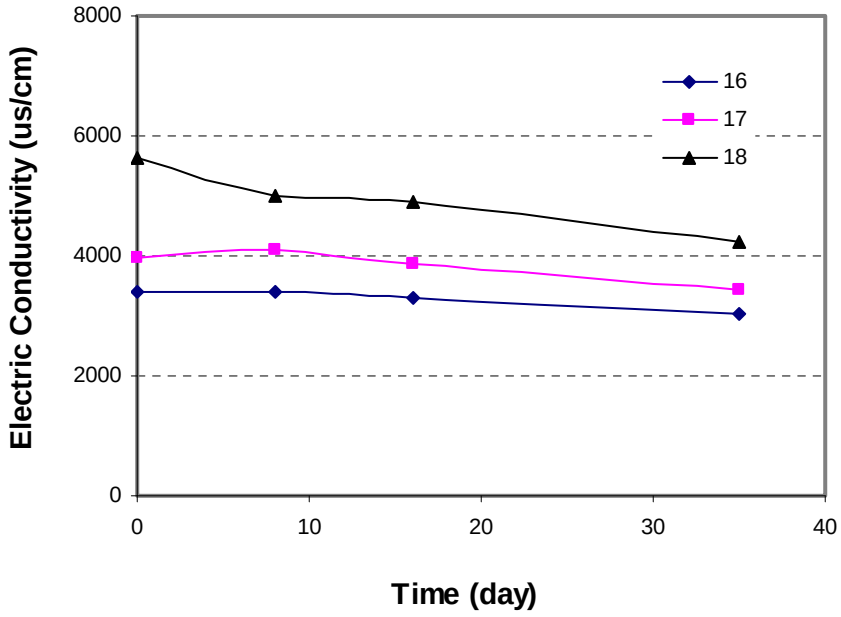

Figure J. 3 Changes in Electrical Conductivity in Samples 16© to 18©

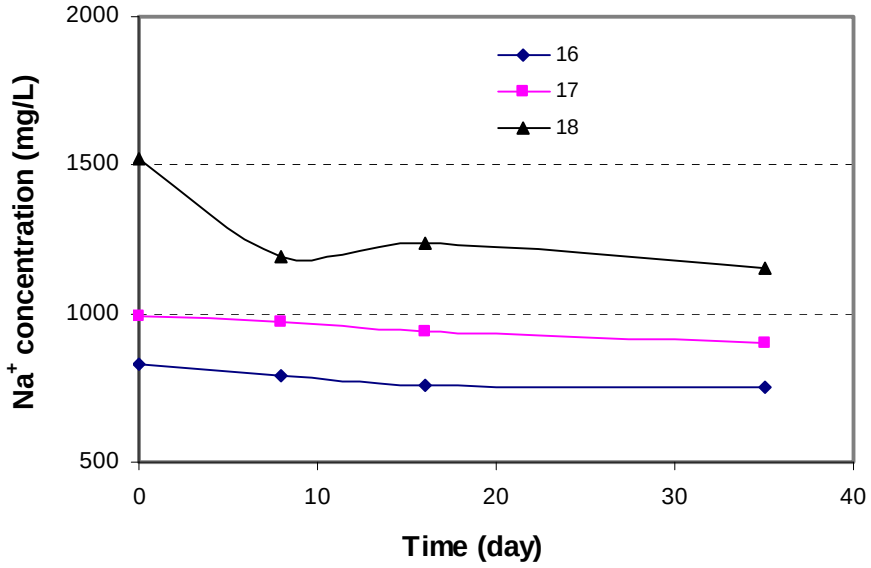

Figure J. 4 Changes in Na^+ Concentration in Samples 16© to 18©

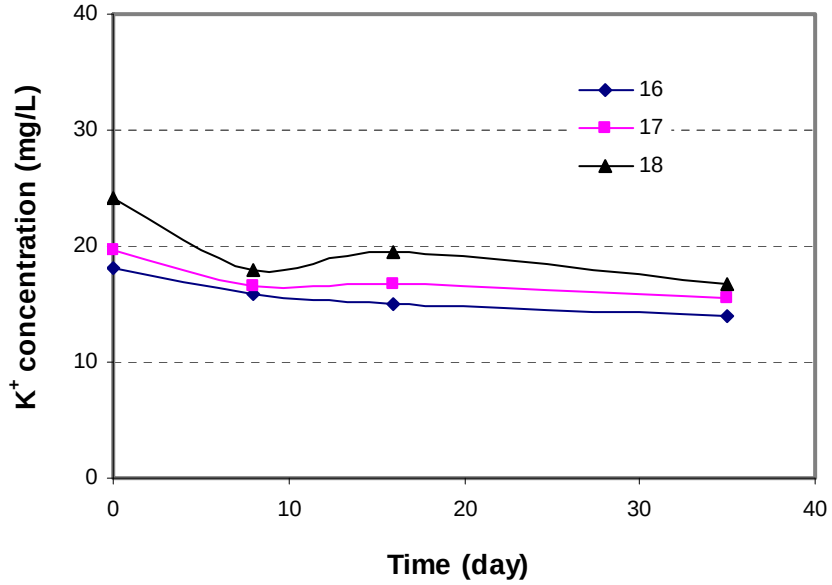

Figure J. 5 Changes in K^+ Concentration in Samples 16© to 18©

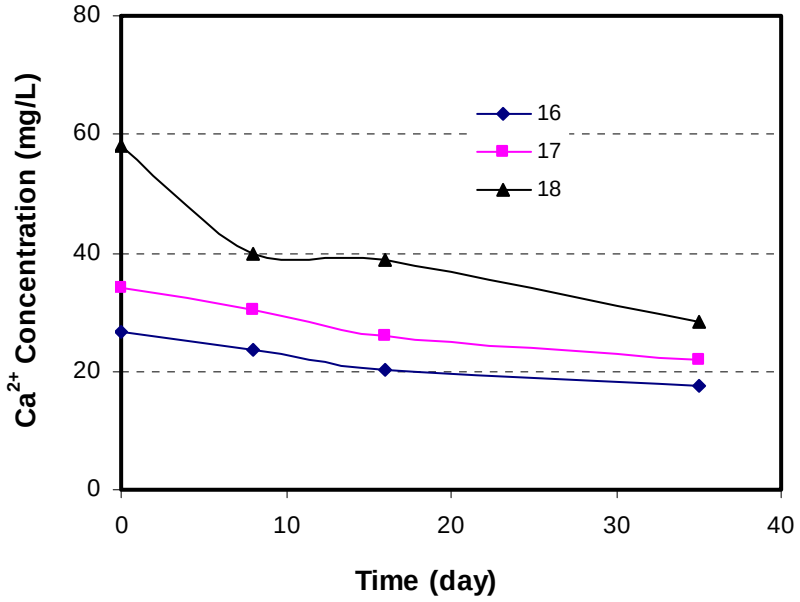

Figure J. 6 Changes in Ca^{2+} Concentration in Samples 16© to 18©

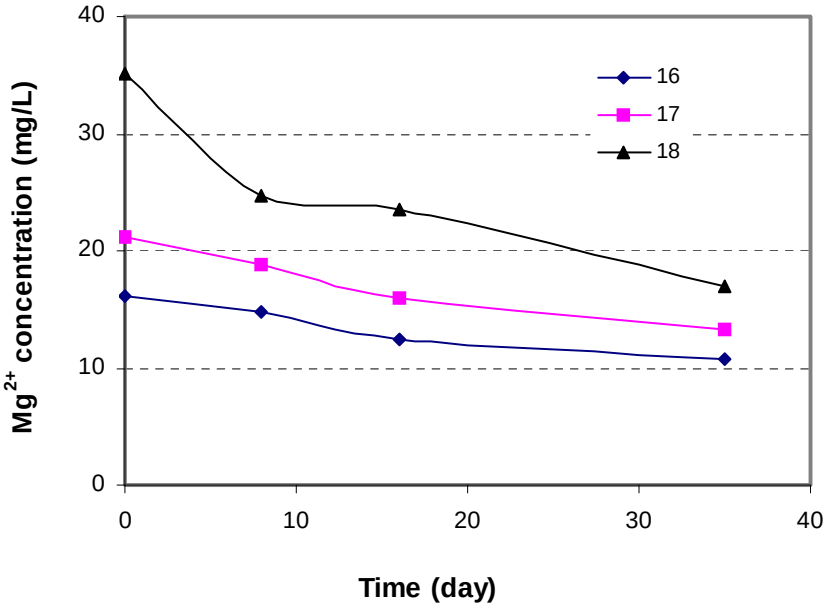

Figure J. 7 Changes in Mg^{2+} Concentration in Samples 16© to 18©

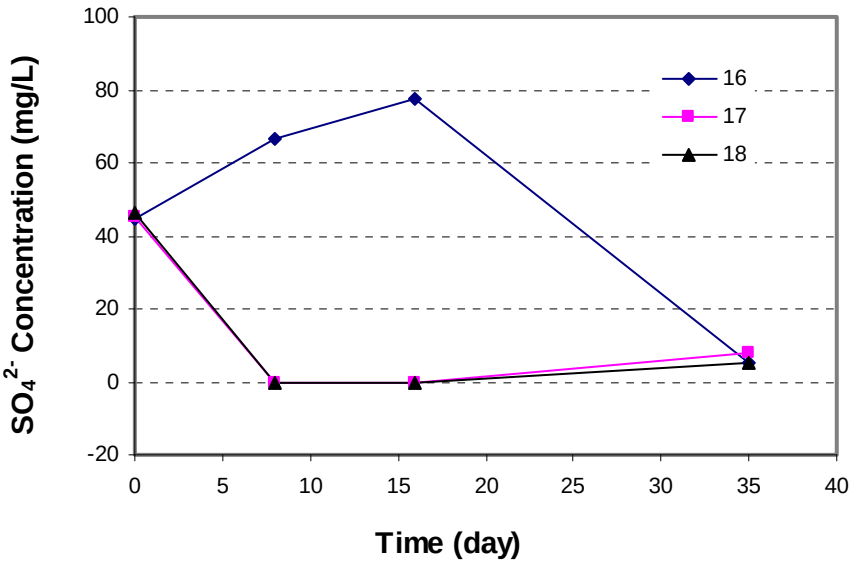

Figure J. 8 Changes in SO_4^{2-} Concentration in Samples 16© to 18©

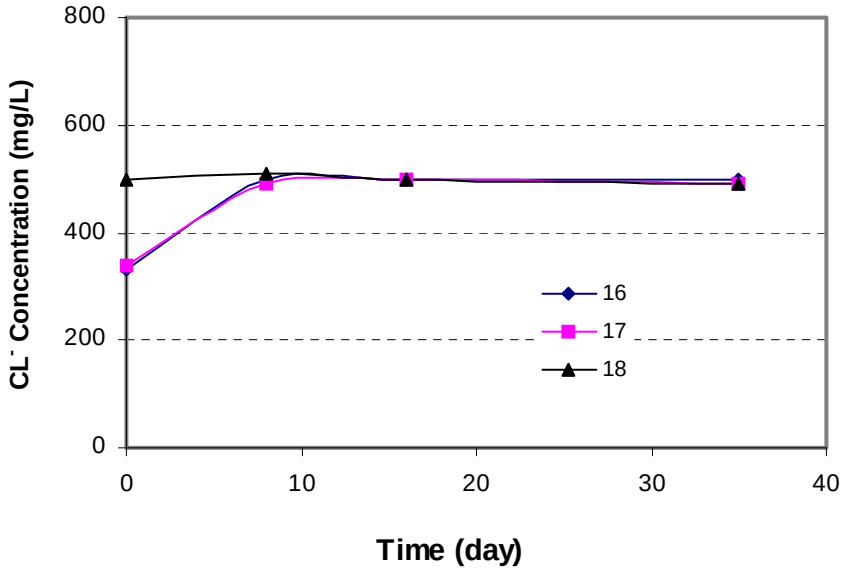

Figure J. 9 Changes in Cl^- Concentration in Samples 16© to 18©

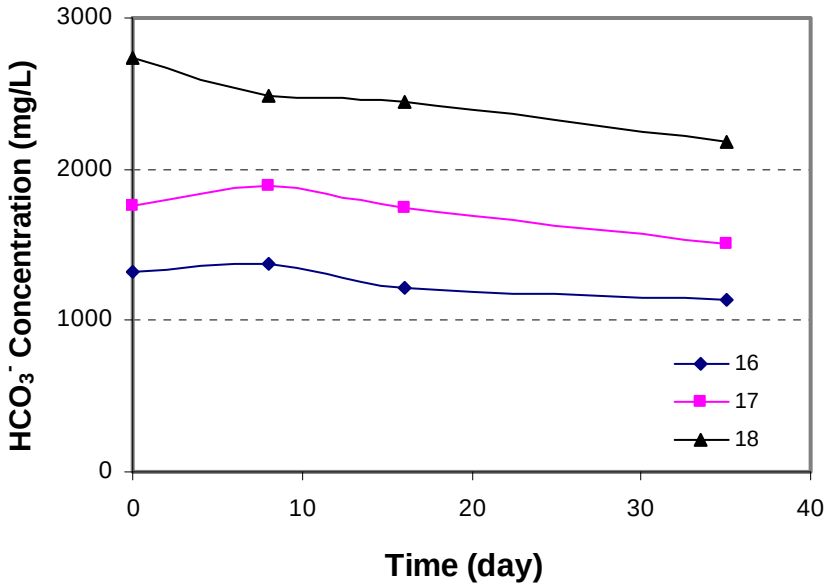

Figure J. 10 Changes in HCO_3^- Concentration in Samples 16© to 18©

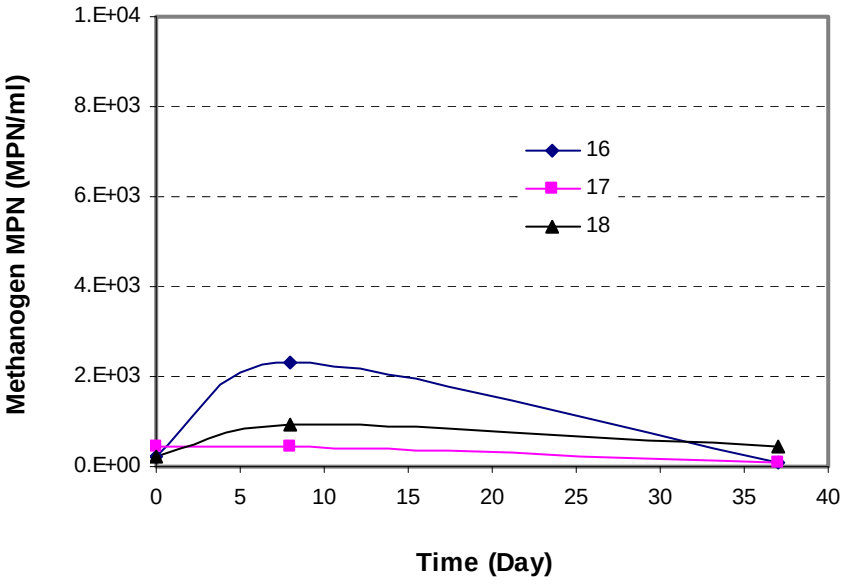

Figure J. 11 Changes of Methanogen MPN in Samples 16© to18©

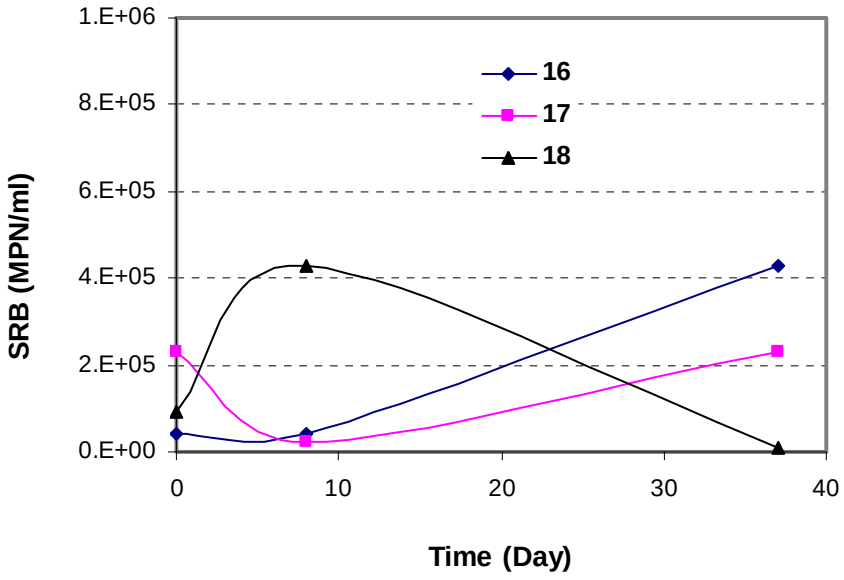

Figure J. 12 Changes of SRB MPN in Samples 16© to 18©

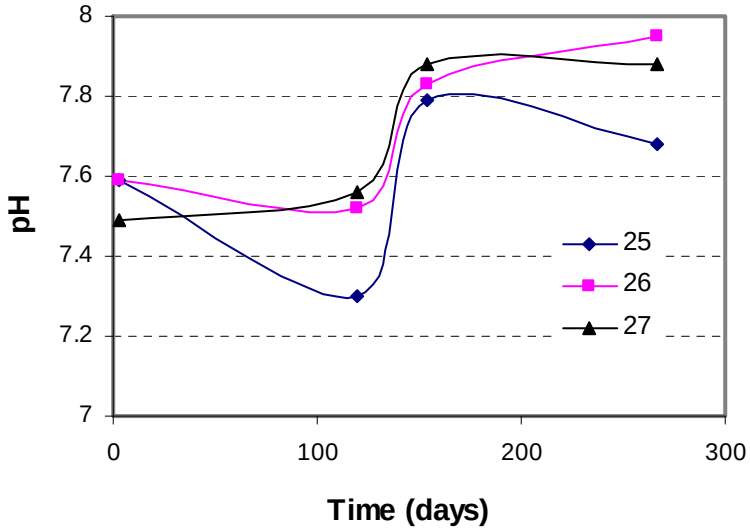

Figure J. 13 pH Changes in Samples 25© to 27©

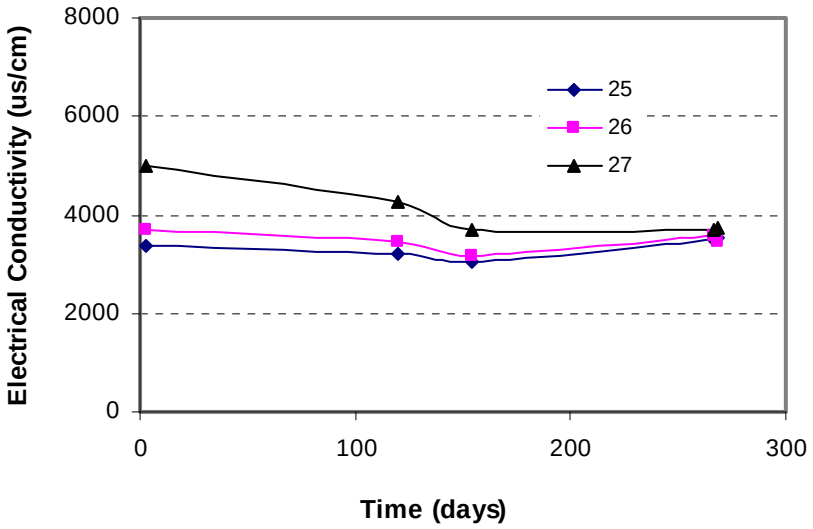

Figure J. 14 Changes in Electrical Conductivity in Samples 25© to 27©

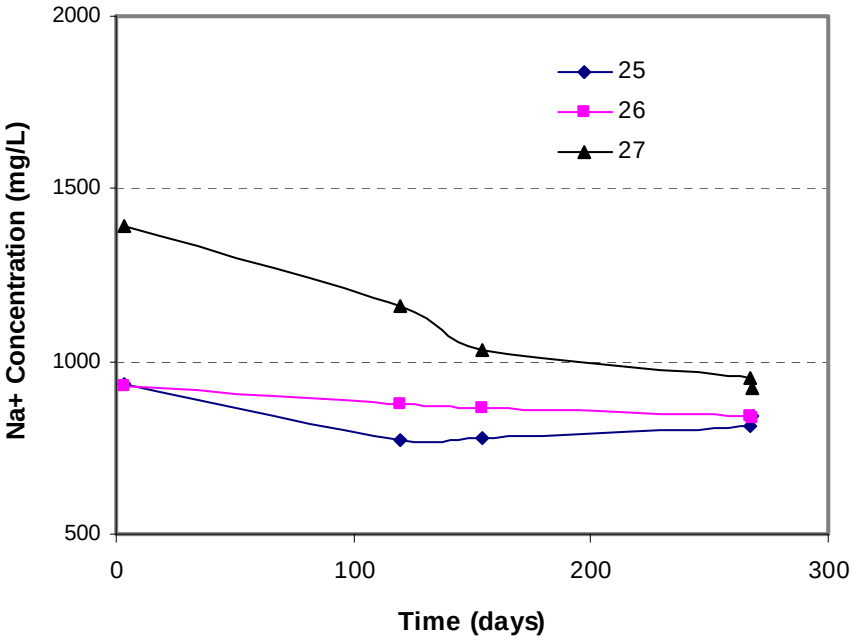

Figure J. 15 Changes in Na^+ Concentration in Samples 25© to 27©

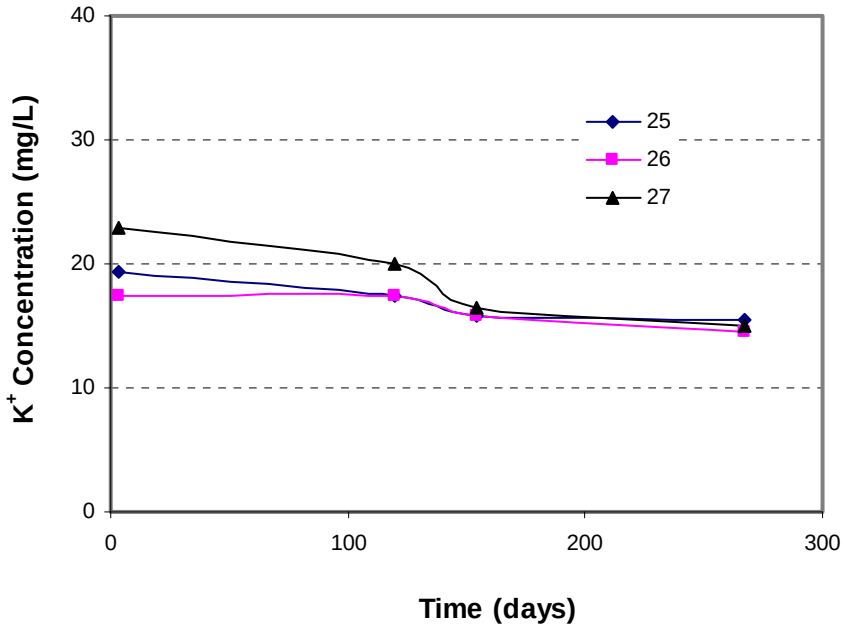

Figure J. 16 Changes in K^+ Concentration in Samples 25© to 27©

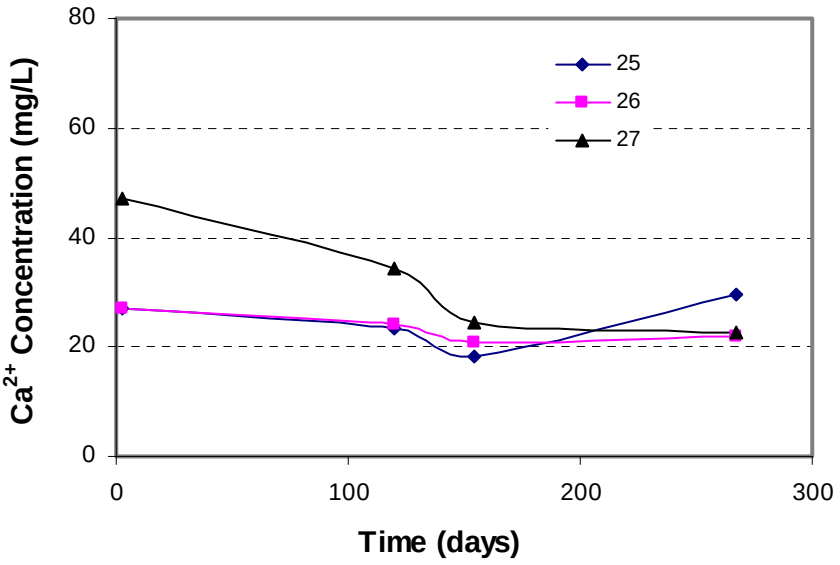

Figure J. 17 Changes in Ca^{2+} Concentration in Samples 25© to 27©

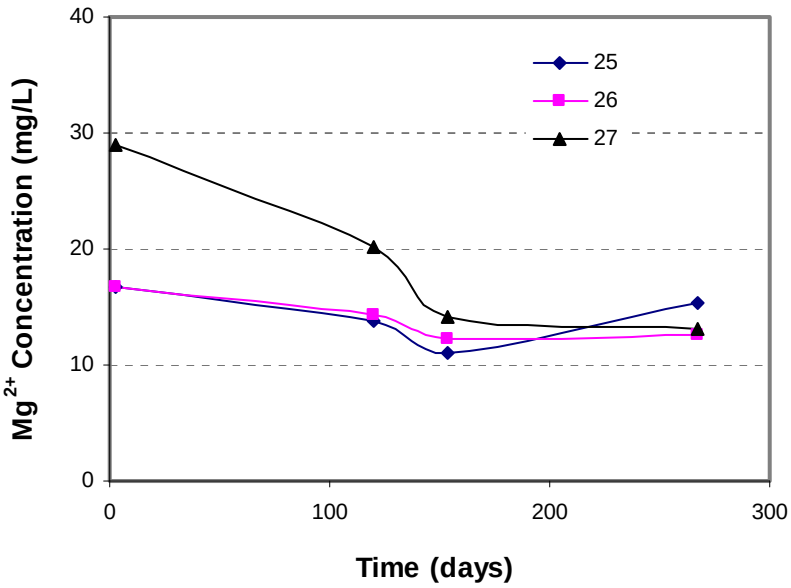

Figure J. 18 Changes in Mg^{2+} Concentration in Samples 25© to 27©

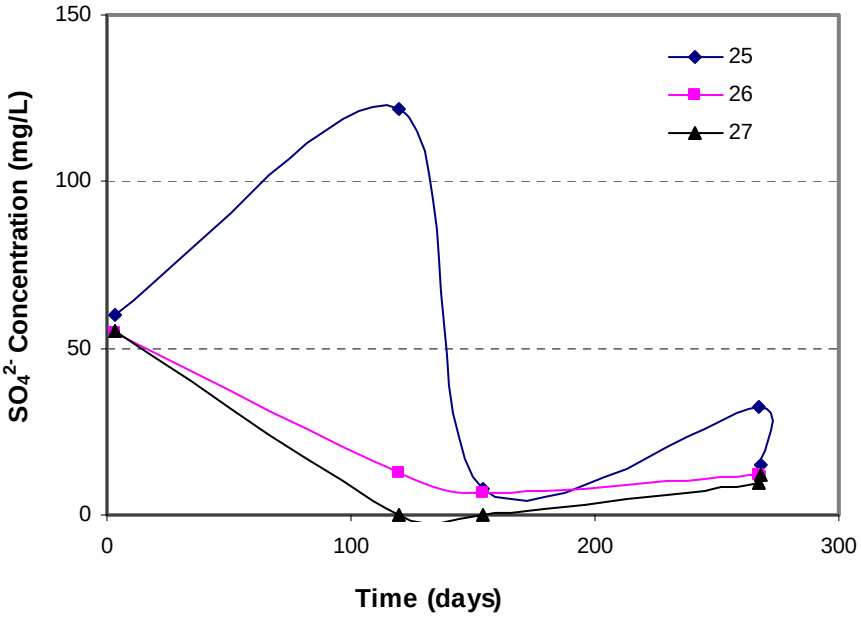

Figure J. 19 Changes in SO_4^{2-} Concentration in Samples 25© to 27©

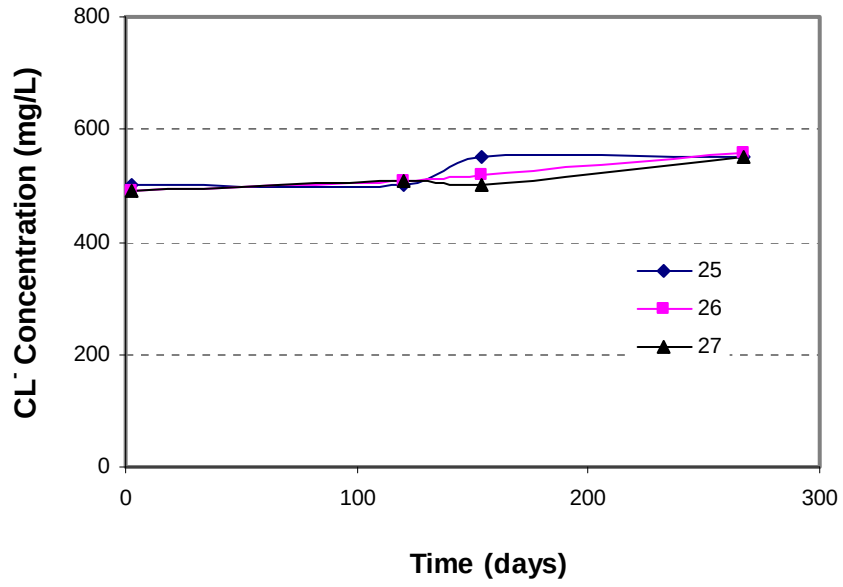

Figure J. 20 Changes in Cl^- Concentration in Samples 25© to 27©

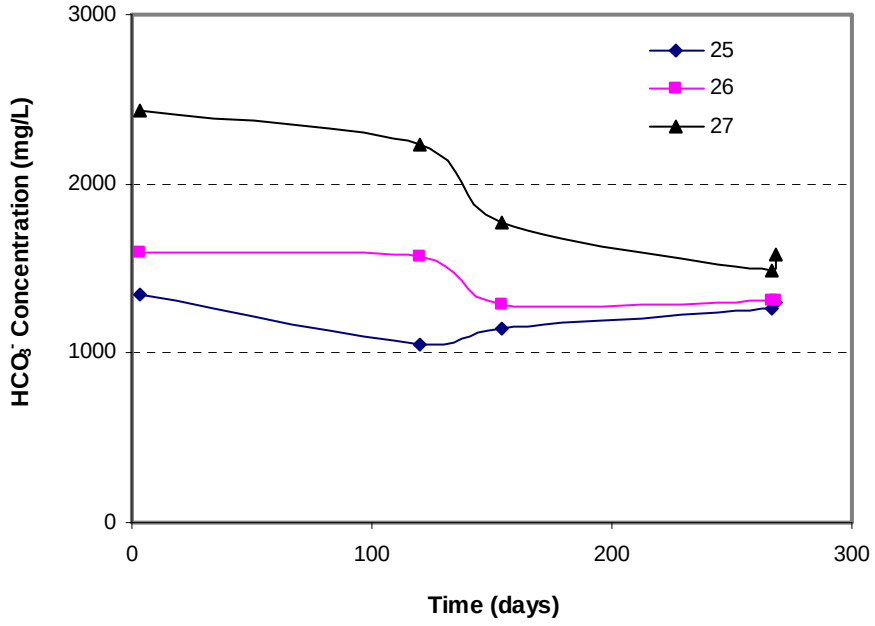

Figure J. 21 Changes in HCO_3^- Concentration in Samples 25© to 27©

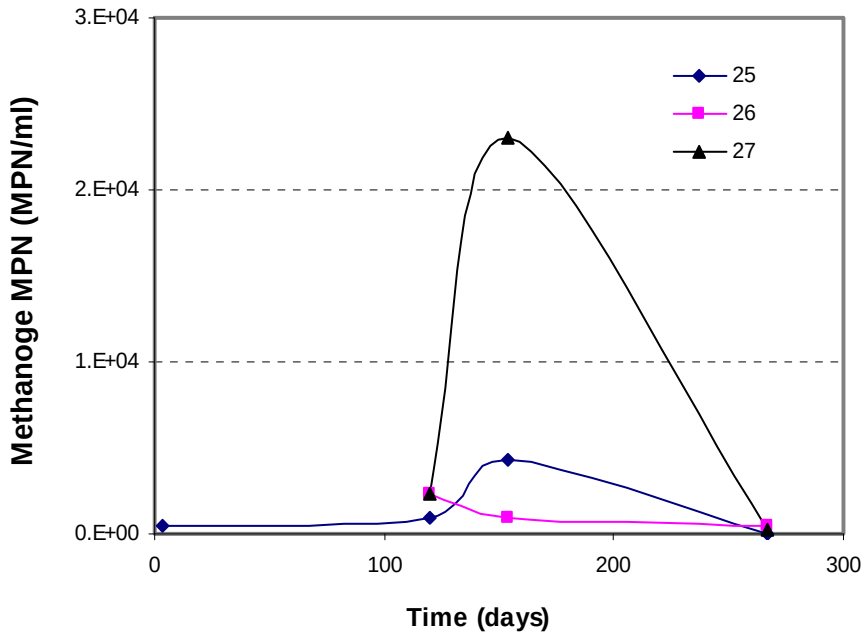

Figure J. 22 Changes in Methanogen MPN in Samples 25© to 27©

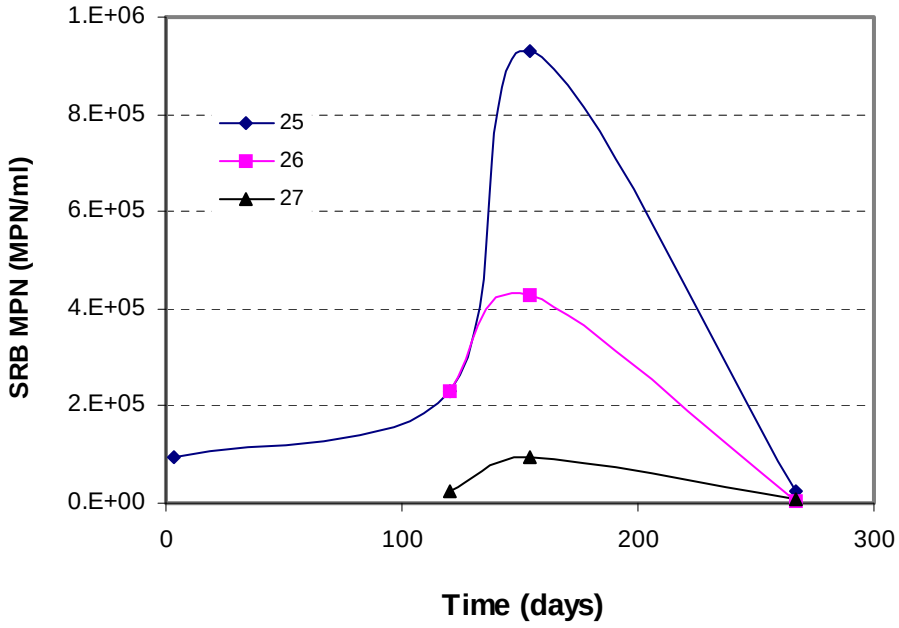

Figure J. 23 Changes in SRB MPN in Samples 25© to 27©

APPENDIX K Preliminary Permeability Test

The preliminary permeability tests were conducted to study the effects of microbial activity on the permeability of MFT, and to compare the results of coefficients of permeability measured by different methods, including constant head and constant flow rate permeability tests, and self-weight consolidation tests. This appendix presents some results of the preliminary permeability tests.

The original sample was obtained from about 2.5 m below the water-MFT interface at Sta. 2 of the MLSB. Before testing, the sample was completely remoulded. Some parameters of the remoulded sample are shown in Table K.1. The initial height of the MFT sample was 11.2 cm. 1.2 g of sodium acetate per liter MFT was added to stimulate microbial activity. Recycled water from the MLSB was used as a permeant. Figure K.1 shows a sketch of the constant flow rate permeability test. Constant inflow was injected at the bottom of the sample using a plastic syringe filled with recycle water from the MLSB. The injection rate of the inflow was controlled using a compression machine. The pore water pressure changes at the bottom and above the interface of the sample were measured by transducer T1 and T2, respectively. The water volume changes in the standpipe were measured by transducer T3. A LVDT (non-submergible) was used to measure interface movements during microbial activity. Unfortunately, the LVDT came to be out of order shortly after it was submerged in water. To remedy this issue, a submergible LVDT was used for the subsequent gas MFT densification tests.

Before microbial activity, the MFT sample was consolidated under self-weight at 4^{o}C room temperature. After the self-weight consolidation, the solids content was 39.1% and the total void ratio was 3.78. Figure K.2 and Figure K.3 show settlement vs. logarithm of time, and settlement vs. square root of time, respectively, for the self-weight consolidation test. The coefficient of permeability before microbial activity can be approximated by the root time method. After self-weight consolidation, constant head and constant flow rate permeability tests were conducted at 4^{o}C. Figure K.4 shows the flow rate vs. time

for the constant head permeability test, and Figure K.5 shows the changes of excess pore water pressure caused by upward injection at the bottom of the sample during the constant rate permeability test. Figures K.6 to K.8 show the structural changes of the MFT during microbial activity. Figure K.9 shows the changes of the total gas generation volume and released gas volume with time during microbial activity (at 25^{o}C and approximate atmospheric pressure). The total gas generation volume was equal to the water volume collected in the standpipe. The released gas volume was obtained by visual observations of the gas-water interface movements. During the early period of microbial activity, continuous inflow was injected into the MFT at the bottom of the sample to measure the continuous changes of the coefficients of permeability. During the continuous injection, it was found that the excess pore water pressure changes were not obvious. As such the injection was stopped after a few hours, and water was injected at the end of microbial activity. Due to the continuous water injection, gas started to be released from the MFT at the early stage of microbial activity. After microbial activity had diminished, the room temperature was lowered to 4^{o}C to further inhibit it. Constant head and constant rate permeability tests were conducted at this point. Figure K.10 shows the flow rate vs. time for the constant head permeability test, and Figure K.11 shows the changes of excess pore water pressure caused by upward injection at the bottom of the sample. From the test results, the coefficients of permeability before and after microbial activity were calculated and are summarized in Table K.2.

Some conclusions can be obtained from the preliminary permeability tests:

- Under low pressure (atmospheric pressure plus about 1 m water head), intense microbial activity notably changed the MFT structure and significantly increased the coefficients of permeability of each sample.
- There were strong agreements between the coefficients of permeability measured by constant head and constant flow rate permeability tests.

Table K. 1 Some Parameters of the Initial MFT Sample

Solids content (%)	Density (g/cm3)	Bitumen content (%)	Void ratio (e)	Fines content (<45u) (%)	Fines content (<22u) (%)	Water content (%)
37.75	1.285	4.27	4.12	92	83	164.9

Table K. 2 Summary of the Permeability Tests

Test Time	Test Method		
	Self-weight Consolidation (m/s)	Constant Head (m/s)	Constant Rate (m/s)
Before Microbial Activity	2.5×10^{-9}	3.44×10^{-9}	$<7.2 \times 10^{-9}$
After Microbial Activity		3.904×10^{-8}	4.06×10^{-8}

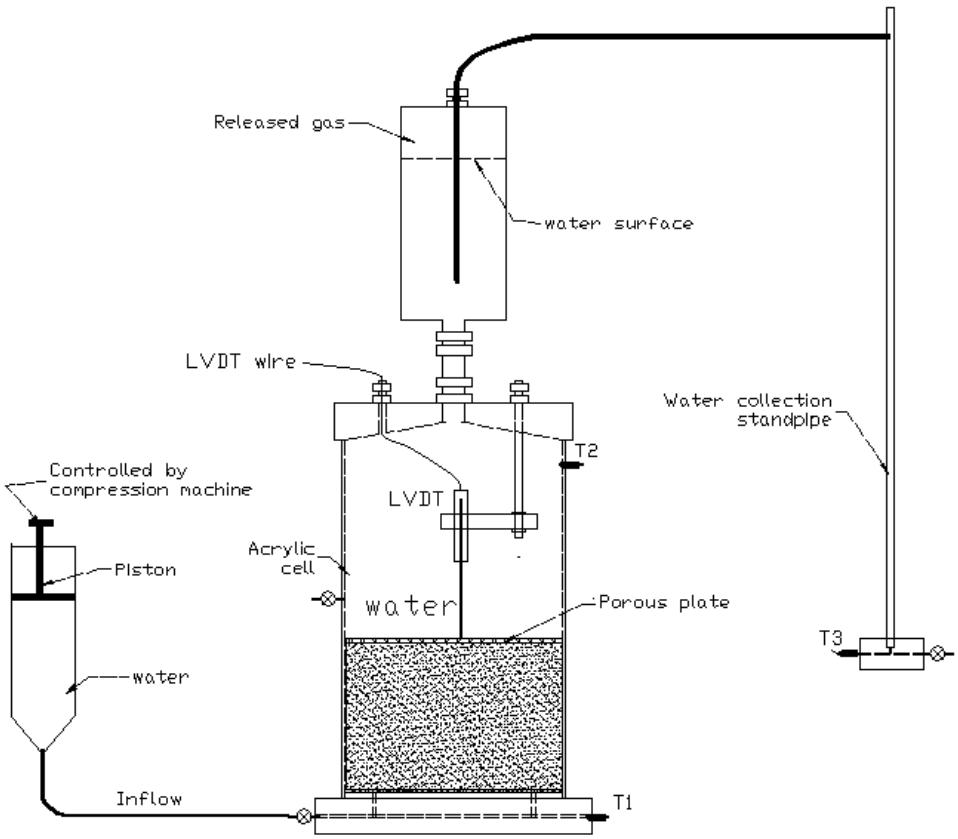

Figure K. 1 A Sketch of the Preliminary Permeability Test (Constant Flow Rate)

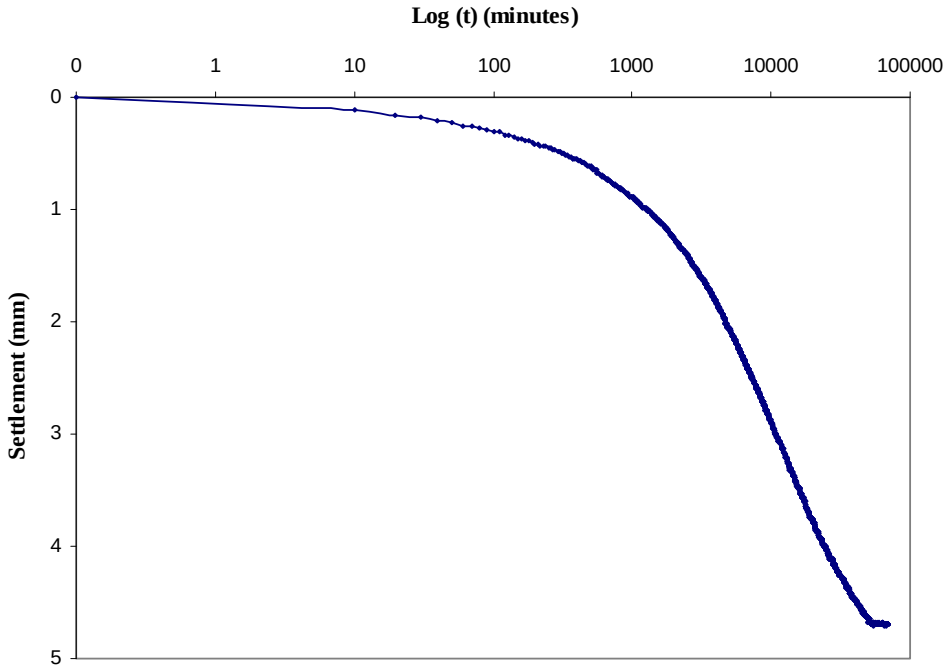

Figure K. 2 Settlement vs. Log (t) for Self-Weight Consolidation Test before Microbial Activity

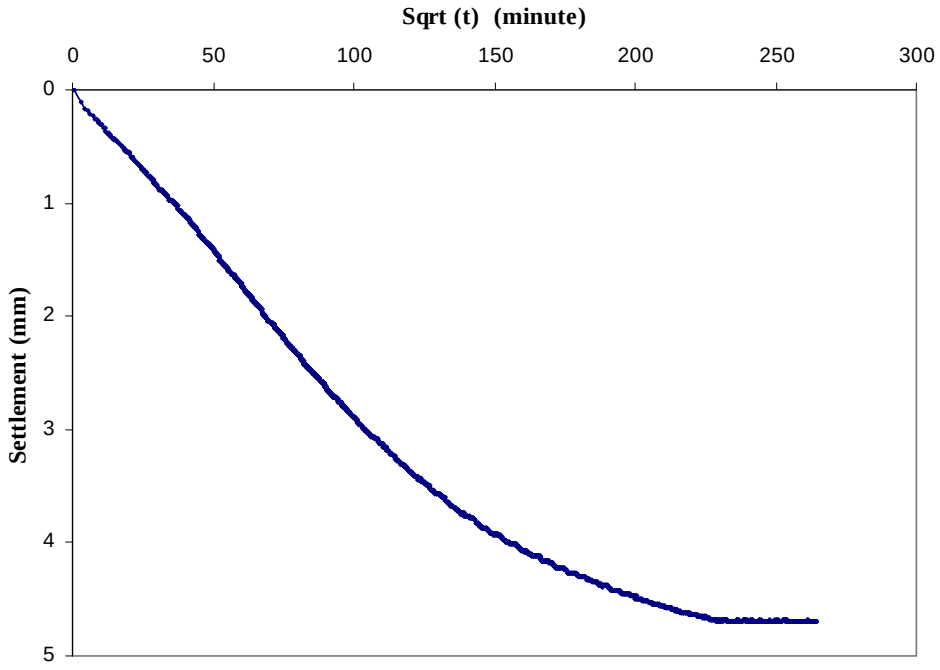

Figure K. 3 Settlement vs. Square Root of Time for Self-Weight Consolidation before Microbial Activity

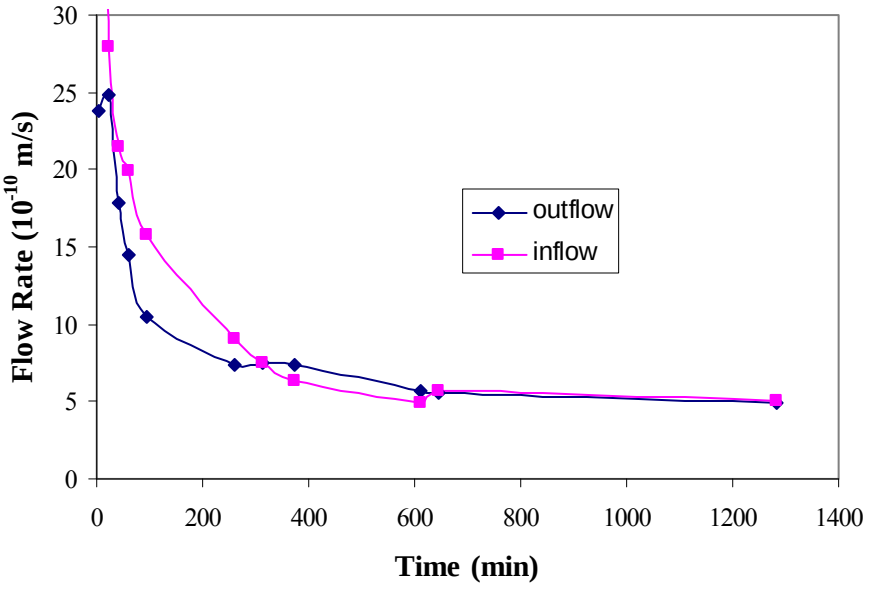

Figure K. 4 Constant Head Permeability Test before Microbial Activity

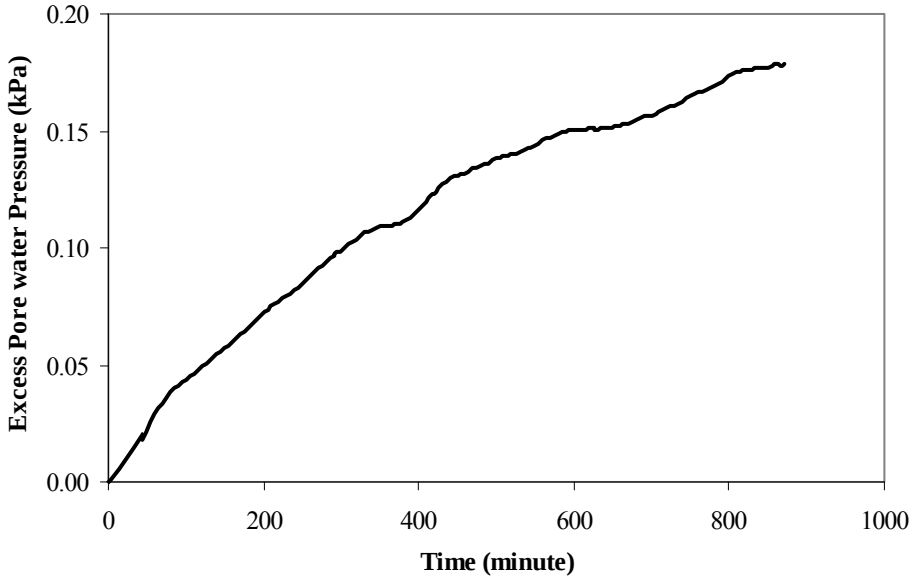

Figure K. 5 Constant Flow Rate Permeability Test before Microbial Activity

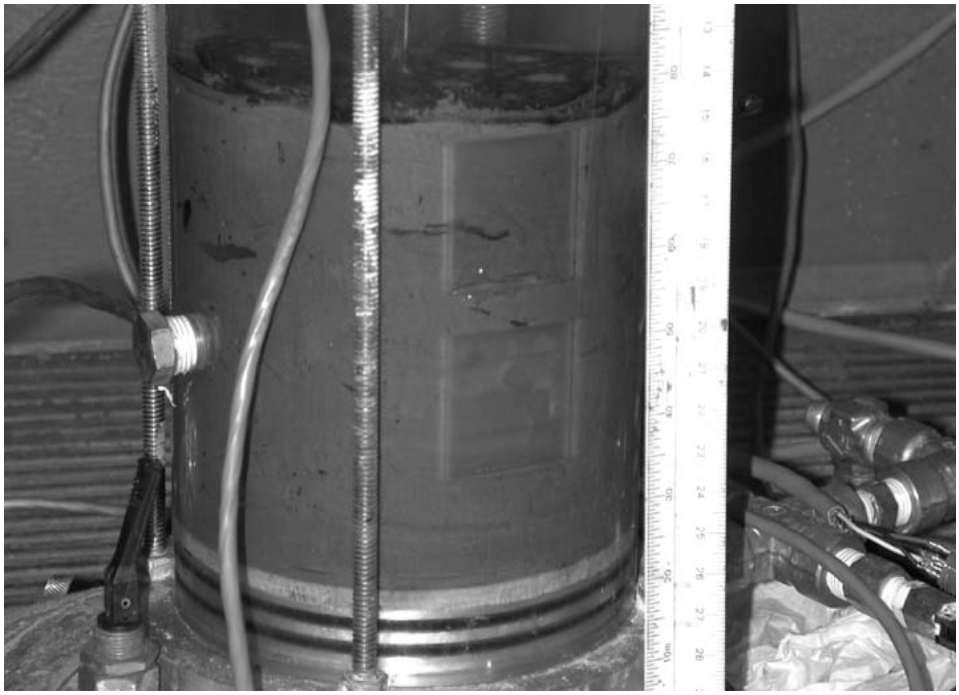

Figure K. 6 A Photo of the Sample on Sept 22 (Day 3)

Figure K. 7 A Photo of the Sample on September 25 (Day 6)

Figure K. 8 A Photo of the Sample on October 22 (Day 33)

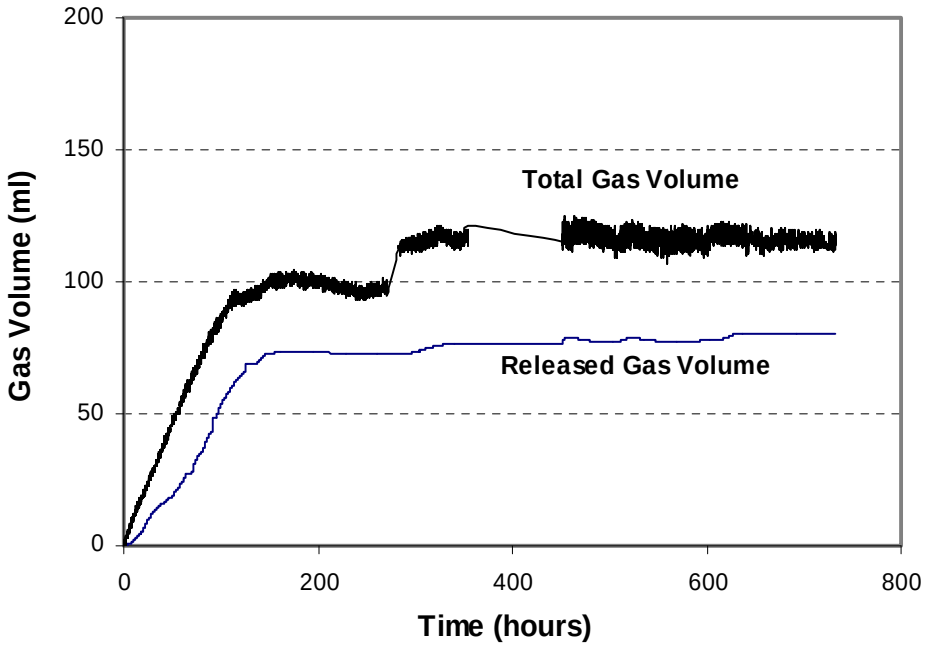

Figure K. 9 Changes of Total and Released Gas Volumes with Time during Microbial Activity

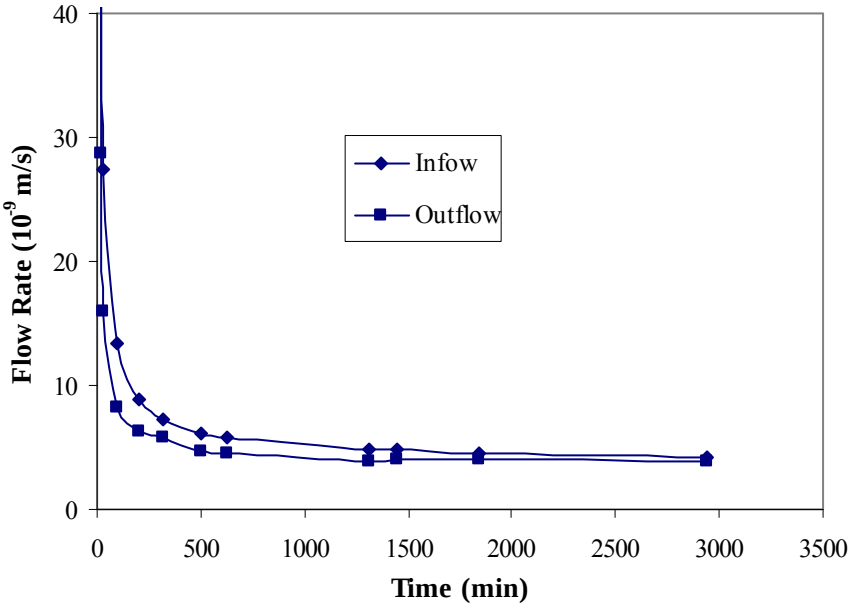

Figure K. 10 Constant Head Permeability Test after Microbial Activity

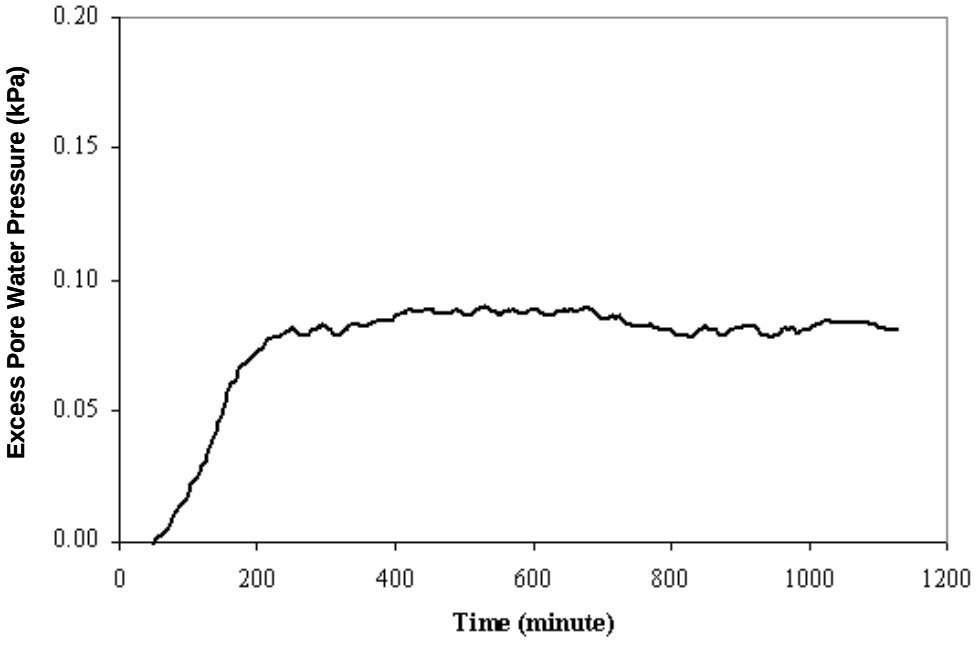

Figure K. 11 Constant Flow Rate Permeability Test after Microbial Activity